

2025



Aviation Higher Vocational School
Publication Number: 2



AVIATION TECHNOLOGIES AND APPLICATIONS

Editors

Asst. Prof. Dr. Gürcan LOKMAN
Prof. Dr. Rüstem Barış YEŞİLAY

İZMİR 2025



AVIATION TECHNOLOGIES AND APPLICATIONS



This book has been prepared in cooperation with the National Defence University Air NCO Higher Vocational School and Aviation Higher Vocational School of Ege University.

AVIATION TECHNOLOGIES AND APPLICATIONS

E-ISBN: 978-605-338-471-7

Published by the decision of Ege University Publishing Commission dated 16.01.2025 and numbered 01/14.

© 2025 by Ege University. All rights for this book reserved. No part of this book may be reproduced, stored in a retrieved system, or transmitted, in any form or by any means, electronic, mechanical, photocopying, recording or otherwise, without the prior permission of the copyright owner. However, it can be cited as a source.

Science, language and all kinds of liabilities of the work belong to its author/editor.

Ministry of Culture and Tourism Certificate No: 52149

Contact

Ege Üniversitesi Yayınları

Ege Üniversitesi Basım ve Yayınevi
Bornova-İzmir Tel: 0 232 342 12 52

E-mail: basimveyayinevisbm@mail.ege.edu.tr

Web: <https://basimveyayinevi.ege.edu.tr/>

Date of Publication: January, 2025



Bu eser, Creative Commons Atıf 4.0 Uluslararası lisansı (CC BY-NC-ND) ile lisanslanmıştır. Bu lisansla eser alıntı yapmak koşuluyla paylaşılabilir. Ancak kopyalanamaz, dağıtılamaz, değiştirilemez

ve ticari amaçla kullanılamaz.

This work is licensed under a Creative Commons Attribution 4.0 International license (CC BY-NC-ND). Under this license, the text can be shared with the condition of citation. However, it cannot be copied, distributed, modified or used for commercial purposes.

Contents

About The Editors.....	v
About the Contributors	vi
Editor’s Introduction	xviii
Chapter 1: STUDY OF QUALITY METRICS FOR SATELLITE BASED IMAGING: EFFECTS OF OPTICAL APERTURE OBSCURATIONS	1
Chapter 2: A COMPARATIVE NUMERICAL STUDY ON BUCKLING BEHAVIOUR OF SKIN- STRINGER AND SANDWICH PANELS	20
Chapter 3: NUMERICAL AEROELASTICITY ANALYSIS OF WINGS	41
Chapter 4: SMART ANTENNA SYSTEMS AND APPLICATIONS: A REVIEW	59
Chapter 5: INVESTIGATION OF DAMAGES OCCURRED DURING GRINDING OF B737- 800 MAIN LANDING GEAR INNER CYLINDER CHROME COATING	75
Chapter 6: FORMATION OF AVIATION EPOXY MATRIX ARALDITE LY5052 SOLUTION WITH GRAPHENE NANO ADDITIVE.....	92
Chapter 7: AUTONOMOUS LANDING OF A GENERAL AVIATION AIRPLANE ON AN AIRCRAFT CARRIER	107
Chapter 8: UNITY3D ORTAMINDA DERİN PEKİŞTİRMELİ ÖĞRENME İLE EĞİTİLEN UÇAKLARIN PERFORMANSI	128
Chapter 9: INVESTIGATION OF THE HUMAN FACTOR IN SEARCH AND RESCUE OPERATIONS: SHELL MODEL ANALYSIS.....	150
Chapter 10: DISCONTINUITY DETECTION IN GLASS FIBER REINFORCED THERMOSET LAMINATED COMPOSITES BY REVERSE THERMOGRAPHIC INSPECTION	167

Chapter 11:	
UNMANNED AERIAL VEHICLES IN DISASTER MANAGEMENT: AN INNOVATIVE APPROACH TO CIVIL ENGINEERING	177
Chapter 12:	
FLORESANS MANYETİK PARÇACIK TEST GÖRÜNTÜLERİNDE AKIM DEĞİŞİMLERİNİN ANALİZİ	191
Chapter 13:	
NUMERICAL AND EXPERIMENTAL INVESTIGATIONS ON THE RESPONSE AND COMPRESSIVE STRENGTH OF FOAM-CORED SANDWICH STRUCTURES SUBJECTED TO MEDIUM-VELOCITY IMPACT	205
Chapter 14:	
INVESTIGATING ON BEHAVIOUR OF TURBOPROP ENGINE BY CONSIDERING COMPONENT EFFICIENCY	225
Chapter 15:	
AUTONOMOUS ENERGY MANAGEMENT FOR ENHANCED UAV OPERATIONS.....	238
Chapter 16:	
İNSANSIZ HAVA ARACI KOMPOZİT KANATLARININ ISIL MODELLEMESİ VE ELEKTROTERMAL ISITMA UYGULAMASI.....	265
Chapter 17:	
ANALYTICAL PARAMETER STUDY FOR A WIND TURBINE BLADE	279
Chapter 18:	
ACTIVE CONTROL OF STORE SEPARATION INDUCED FLAPWISE BENDING VIBRATIONS ON SIMPLIFIED WING STRUCTURES	300
Chapter 19:	
BENEFITS OF END-TO-END TRACEABILITY ON PROJECT PROCESSES WITHIN THE SCOPE OF PLM- DEFENSE AND AVIATION CASE STUDY....	316
Chapter 20:	
INVESTIGATION OF MECHANICAL PROPERTIES OF NACA 2024 DROP WING ACCORDING TO STATIC AND MODAL BEHAVIOUR OF DIFFERENT ROOT AND TIP VETER POSITIONS.....	341

About The Editors

Gürcan LOKMAN, Ph.D., Asst. Prof. Dr., National Defence University Air NCO Higher Vocational School.



Asst. Prof. Dr. Lokman is the Program Coordinator for the Computer Programming Program at the Technology Sciences Department, National Defence University Air NCO Higher Vocational School, where he has been serving as an Assistant Professor doctor since 2020. From 2009 to 2012, he held positions as a Research Assistant and Lecturer at Haliç University, and from 2012 to 2022, he served as a Lecturer and Assistant Professor at Sinop University. He earned his undergraduate degrees in Computer and Control Teaching from Marmara University, Computer Engineering from Karabük University, and Software Engineering from Fırat University. He completed his master's degree in Computer and Control Education and his Ph.D. in Computer Engineering at Marmara University. Dr. Lokman has more than 15 years teaching and research experience. He teaches computer science and artificial intelligence related courses. Since 2009, he has been involved in editorial and peer review roles for various international journals. In 2023, he served as the Secretary for ATAConf'23 and was the editor of the conference proceedings.

Rustem Baris YESILAY, Prof. Dr., Ege University Aviation Higher Vocational School (HVS).



Prof. Dr. Yesilay is director of the Ege University, Aviation Higher Vocational School (HVS). He was the vice director of the school between 2017 – 2021 and founding head of Ege University, Aviation HVS, Civil Aviation Management Program. He is the vice director of Ege University Product Lifecycle Management (PLM) Research and Application Excellent Center. He earned his Ph.D. from Dokuz Eylul University, Institute of Social Sciences, Department of Economics, and he has master's degree from Istanbul University, Institute of Social Sciences, Department of Fiscal Economics. Dr. Yesilay has 22 years teaching and research experience. He teaches aviation and economics related courses. He has publications on sustainable development, innovation, entrepreneurship, aviation management, and PLM. He has experience in skills development for technicians, accreditation of training, university-industry cooperation and improving the competitiveness of companies. Dr. Yesilay has taken active role as a coordinator or researcher in eleven national and international (Leonardo da Vinci, Erasmus + etc.) projects. Dr. Yesilay is the academic member of Aerospace Cluster Association - Izmir (ACA) and was co-leader of Skills Working Group of European Aerospace Cluster Partnership (EACP) between 2013 - 2021. He is also member of Istanbul University Faculty of Economics Graduates Society.

About the Contributors

Ayşegül Özden Acehan is currently pursuing her doctoral studies in the Department of Civil Engineering at Hacettepe University.

Feti Adar has been working in various positions within the electronics sector in Turkey for over 25 years. He holds a Master's degree in Product Lifecycle Management from Ege University and a Bachelor's degree in Business Administration from Anadolu University. He graduated from Technical Electronics in Vocational High School and Computer Hardware in Associate Degree. He began his career as an R&D assistant for military electronic systems at Yüksek Teknoloji A.Ş. and gradually advanced to the position of Electronic R&D Manager. At Politeknik Elektronik Ltd. Şti., he has expertise in project management, electronic circuit design, PCB layout, electronic component testing, and production planning. He specializes in the design of advanced technology products such as RFID, GPRS, Wi-Fi, Bluetooth, and LoRaWAN-based IoT devices. He has successfully managed and completed public-supported KOSGEB and TÜBİTAK projects, and has provided leadership in hardware design and applications for both military and civilian projects. He is skilled in following innovative technologies, continuous learning, creating creative solutions, and process improvement, and holds professional competency certifications. He continually updates his knowledge through scientific publications and seminars.

Reza Aghazadeh received his bachelor's degree in Mechanical Engineering from Iran University of Science and Technology in February 2008. He obtained his master's and doctoral degrees from the Middle East Technical University in Mechanical Engineering in September 2013 and September 2017, respectively. His research interests include the modeling of functionally graded microbeams and microplates, composite materials, structural analysis, computational mechanics, vibration, and control systems. At the University of Turkish Aeronautical Association, he served as a lecturer in the Department of Aeronautical Engineering from 2015 to 2017, as an assistant professor in the Department of Mechatronics Engineering from December 2017 to February 2021, and as an assistant professor in the Department of Aeronautical Engineering from February 2021 to August 2023. Dr. Aghazadeh has been serving as an Associate Professor in the Department of Aeronautical Engineering since 2023.

Kamil B. Alici received his bachelor's and doctorate degrees from the Department of Physics at Bilkent University in 2004 and 2010, respectively. He worked as a Research Assistant Professor in the Department of Electrical and Electronics Engineering at the University of Arkansas and as a Postdoctoral Researcher in the Department of Physics at the University of Texas between 2010 and 2013. After returning to Turkey, he held various positions at TÜBİTAK Institutes from 2013 to 2024. Assoc. Prof. Dr. Kamil B. ALICI was awarded the TÜBA-GEBİP Outstanding Young Scientist Award in 2020.

Emre Apa graduated from Mechanical Engineering Department, Engineering Faculty of Dokuz Eylül University in 2016 as first rank student with high honour degree. After a year, he completed the Industrial Engineering Department, Engineering Faculty of Dokuz Eylül University in 2017 as a Double Major Programme with an honours degree. During his university life, he made great achievements with two Bachelor Science Degrees. His dissertation in Mechanical Engineering was supported by the Scientific and Technological Research Council of Turkey (TUBITAK). As of 2018, he started to work at Turkish Aerospace as a design engineer for the helicopter platforms and he participated in different structural and system & equipment installation design activities. Afterwards, he joined AIRBUS and he currently has been working at commercial aircraft platforms as a design engineer. He graduated from Aerospace Engineering Master Programme, Faculty of Aeronautics and Astronautics of Ankara Yıldırım Beyazıt University in 2024. His research and area of interests are mainly structural design/assembly activities and structural analysis for aircrafts and helicopters, metallic and composite parts, tolerancing, structural repair, fasteners.

Mert Atas graduated from Vefa High School in 2019 and subsequently began his undergraduate studies in Aeronautical Engineering at the University of Turkish Aeronautical Association. During his second year, he participated in the Erasmus program and completed a six-month course at the Czestochowa University of Technology. Throughout his academic tenure, he engaged in various projects and research on propulsion systems, aeroelasticity, and aircraft design. During his education, he completed two internships. In 2021 His first internship was at MC Aviation as a maintenance planning engineer, where he gained knowledge about the processes involved in planning aircraft maintenance. In 2022 His second internship was at AMAC Aerospace in the quality control department, where he contributed to ensuring that all work adhered to strict aviation

procedures, emphasizing the critical importance of thorough inspections and compliance. Mert Atas completed his undergraduate education in 2023. Currently, he works at Turkish Airlines in the Fleet Planning and Aircraft Procurement Department, where he is responsible for managing new aircraft acquisition agreements and related negotiations with original equipment manufacturers (OEMs). Additionally, following his graduation, in 2024 he began his master's degree in Aeronautical Engineering at the National Defense University.

Hasan Aydoğan, a faculty member in the Department of Mechanical Engineering at Selçuk University Faculty of Technology, completed his PhD at Selçuk University in 2011. His research interests include energy, heat transfer, fuels, and combustion. He has authored over 30 articles and 4 books.

Hakan Aygun has worked an Associate Professor in the Department of Aircraft Maintenance and Overhaul in the Firat University since 2021 and worked as a Research Assistant in the Faculty of Aeronautics and Astronautics between 2016-2021 at Eskisehir Technical University. Moreover, he has graduated PhD education in 2021 and completed his BSc in 2015 from the Faculty of Aeronautics and Astronautics at Anadolu University.

A. Fevzi Baba received BS degree in Electrical and Electronics Education from Marmara University, Faculty of Technical Education, Istanbul, Türkiye, in 1986 and MSc, PhD degrees from the Institute of Science and Technology at Marmara University in 1989 and 1995, respectively. He completed the teacher-training course in Electronic Engineering at Purdue University School of Technology, West Lafayette, IN, in 1990. His research interests include intelligent control systems, fuzzy logic, and engineering technology education.

Husnu Deniz Basdemir received the B.Sc., MSc., and Ph.D. degrees in Electronics and Communication Engineering from Cankaya University, Ankara, Turkey, in 2008, 2010, and 2014, respectively. He also received the second B. Sc. Degree in the Department of Public Administration from Anadolu University in 2024. In 2009, he joined the Department of Electronics and Communication Engineering, Cankaya University, where he was a Research Assistant from 2009 to 2015, and an Assistant Professor and an Associate Professor from 2015 to 2020. He was an Associate Professor in the Department of Electrical and Electronics Engineering, Konya Food and Agriculture University, Konya between 2020-2022. He has been full Professor in the Department of Electrical and Electronics Engineering, Sivas Science and Technology University from 2022. He is

the sole author of more than 30 internationally refereed journal articles. His research area includes mainly to asymptotic techniques in electromagnetic and optics scattering. The study of diffraction and propagation of electromagnetic waves with applications to physical problems are also inside his area of interest. In addition, analysis of different shaped antennas, radar system design, and optical communication systems is inside his research field. Dr. Basdemir received the International Union of Radio Science (USRI) Young Scientists Award in 2011.

Cahit Bilgi studied Aircraft-Engine Maintenance at Eskişehir Anadolu University between 2005 and 2010. During his student years, he worked as an intern engineer at TAI, 1st Jet Main Base, and THY TECHNIC Inc. He started working as an aircraft revision maintenance engineer at THY TECHNIC Inc. in 2010 and graduated from Sakarya University Industrial Engineering in the same year. In 2013, he started working as a lecturer at Istanbul University Aircraft Technology Program. He currently works as a lecturer at Istanbul University-Cerrahpaşa Aircraft Technology Program. He graduated from Karabük University Mechanical Engineering master's degree in 2014 and from Karabük University Mechanical Engineering PhD program in 2024. He researches nano and hybrid composites, non-destructive testing (NDT) methods, and thermographic inspection.

Ahmet Cevat Biricik is currently pursuing his master's studies in the Department of Civil Engineering at Hacettepe University.

Bora Bostancı graduated from the Department of Mechanical Engineering at TOBB Economics and Technology University in 2023. He is currently working at Aselsan and continues his research in the fields of production technologies, artificial intelligence, system dynamics, and control.

Mete Cantekin graduated from the Aircraft Structure and Engine Maintenance Department of Anadolu University's School of Civil Aviation in 2012. From 2013 to 2015, he worked as a Production and Planning Engineer at SunExpress Airlines. Since 2015, he has been serving as a lecturer at Nişantaşı University's Vocational School and School of Civil Aviation. In 2024, he completed his Master's degree in Artificial Intelligence Engineering at Nişantaşı University's Graduate School of Education. His areas of interest include maintenance planning and natural language processing.

Mehmet Burcin Coskun, Coast Guard Search and Rescue Helicopter Pilot, Turkish Coast Guard Command. He is currently serving as a search and rescue helicopter pilot at Turkish Coast Guard Air Command. Mehmet Burcin Coskun graduated from the Naval Academy in 2012 with degrees in Officer Training and Industrial Engineering. He served for two years on a Coast Guard vessel. In 2015, he earned the right to attend flight training, successfully completed the course, and became a Coast Guard search and rescue helicopter pilot. From 2016 to 2023, he served at Izmir Coast Guard Air Command. In 2019, he began his master's degree in Occupational Health and Safety at Ege University, completing his thesis titled "The Effect of Noise and Vibration on Personal Working Hours in Rotary-Wing Aircraft" in 2022, earning his master's degree. Since 2023, he has been serving as a search and rescue helicopter pilot at Samsun Air Group Command.

Efe Kerem Deniz Çeltak completed his high school education in 2021 at Şehit Polis Demet Sezen Vocational and Technical Anatolian High School, specializing in Aircraft Maintenance. He graduated in 2024 from the Aircraft Technology Program at Ege University Vocational School of Aviation. His areas of interest include non-destructive testing, aerodynamics, and materials science.

Elif Çiçek is an Assistant Professor at Hacettepe University, Department of Civil Engineering. She holds the title of Associate Professor in Transportation Structures Engineering, specializing in Transportation and Traffic, as well as Geotechnics, according to YÖK (Council of Higher Education).

Bilge Demir was born in 1970 in the Pazar district of Tokat. Prof. Dr. Bilge DEMİR graduated from Pazar secondary school in 1984, TCDD Sivas Practical Art School in 1986, Sivas Industrial Vocational and Technical High School in 1988, Gazi University technical education faculty in 1993, He graduated from Gazi University Institute of Science and Technology in 1997 with a master's degree and in 2003 with a doctorate. 1986-1995 TCDD, 1995-1999 Research Assistant at Gazi University TEF, 1999-2000 Factory Manager at Ak-Çelik Iron and Steel Company (Izmir AOSB), 2000-2004 ZKÜ TEF Lecturer, 2004-2010 Assistant Professor, Karabük University He worked as an Associate Professor in manufacturing engineering between 2010-2015 and as a Prof. Dr. between 2015-2017. 2017-currently working as a Prof. Dr. at Karabük University, Faculty of

Engineering, Department of Mechanical Engineering. Member of YÖK Vocational School group, member of İşkur MEDAK and RAYTEK (Rail systems technology committee) as YÖK representative, and Various Administrative duties; He worked in many positions such as Department Head, Deputy Dean and Dean, TOBB Vocational School director, KABUSEM deputy director, etc. He is currently the Chairman of the Karabük Provincial Employment Board. He continues to work in the fields of damage analysis, metals, polymers and their composite structures, microstructure and material characterization, mechanical properties, heat treatments, welding science and technology, powder metallurgy, etc. Bilge Demir, an education volunteer and fluent in English, is married and has three children.

Beyza Nur Demirkoparan graduated from the Department of Electrical and Electronics Engineering at Sivas Cumhuriyet University in 2021. She has going towards the master's degree at Sivas Science and Technology University. In her master's thesis, she has been working on the design and production of graphene-based fractal microstrip patch antennas. Also, she has been interested in the fields of metamaterials and piezoelectricity.

Alperen Dođru graduated from the Aircraft Body and Engine Maintenance Department at Kocaeli University in 2010 and from the Industrial Engineering Department at Sakarya University in 2012. He completed his thesis-based master's degree in Mechanical Engineering at Manisa Celal Bayar University between 2011 and 2014 and obtained his PhD in Materials Science and Engineering from Izmir Kâtip Çelebi University in 2022. During his doctoral studies, he participated in a Research Scholarship Program at the University of Alberta, Canada. Since 2010, he has been serving as a Lecturer at Ege University Vocational School of Aviation. He was also involved as a researcher in the TÜBİTAK 1505 University-Industry Cooperation project titled “Advanced Imaging-Based Non-Destructive Testing Magnetic Particle Testing Device” during 2022-2023. His academic interests include non-destructive testing, materials science, polymeric materials, composites, and additive manufacturing.

Uđur Ertunç graduated from the Department of Mechanical Engineering at TOBB Economics and Technology University in 2024. He is currently pursuing a master's degree at Budapest University of Technology and Economics, where he is working on system design and autonomous vehicles.

Mustafa Şamil Futtu graduated from the Department of Aeronautical Engineering at the Turkish Aeronautical Association University in 2023. He is currently pursuing a master's degree in Mechanical Engineering with a focus on Thermo-Fluid Sciences at Istanbul Technical University. In 2021, he completed an internship at AMAC Aerospace Turkey, where he gained experience in the Engineering Department, preparing maintenance packages for Dassault Falcon 2000 Classic, 2000 EX, and 2000 EXEASy aircraft, as well as working in quality control. The following year, he interned at BAYKAR, contributing to the Structural Design and Structural Test Engineering Department on unmanned aerial vehicles. From November 2022 to March 2023, he served as a Trainee Engineer in the System Installation Design and Harness Engineering Department at Turkish Aerospace Industries (TAI). He continued in this role as a Part-Time Engineer from March 2023 to August 2023. Since August 2023, he has been working as a System Installation and Design Engineer at TAI.

Coşkun Harmanşah graduated from Marmara University, Department of Electronics and Computer Education in 1989. Between 1990 and 1994, he worked as a PC and Network Systems Manager at Kalafatoğlu Computer Technology and Entegre Companies. In 1994, he spent eight months at Manchester College of Arts and Technology (MANCAT) in the UK as part of the YÖK-World Bank project to establish the Computer Hardware Program at Ege University Vocational School. From 1995 to 2009, he worked as a Lecturer in the Computer Hardware and Computer Programming Departments at Ege Vocational School, where he completed his master's and doctoral studies on radiation measurement and counting systems at the Institute of Nuclear Sciences, Ege University. In 2009, he was appointed as Dr. Öğr. Üyesi in the Computer Technology Program at Ege University Vocational School. From 2010 to 2016, he served as the Program Coordinator for Computer Programming at Ege University Vocational School. Since 2019, he has been the Deputy Director of the Product Lifecycle Management Excellence Application and Research Center (EGE PLM) and has been a member of the Management Board of Ege University Vocational School of Aviation since 2016. He was also a project manager for the TÜBİTAK 1505 University-Industry Cooperation project titled “İleri Görüntüleme Tabanlı Tahribatsız Muayene Manyetik Parçacık Test Cihazı” during 2022-2023. Additionally, since 2020, he has been involved as a coordinator in the TÜBİTAK 2237-A Scientific Education Activities Support Program training on "Endüstri 4.0 – PLM." His research interests include computer-controlled systems, embedded systems, software and hardware development for radiation measurement and counting systems, server operating systems, and web-based systems.

Abdullah İkiz graduated from Mechanical Engineering Department of Istanbul Technical University in 2018. Then he completed his master's degree in the Department of Aeronautics and Astronautics at the same university. He is currently continuing his academic career as a PhD student at the same department. He has also been working as a structural design engineer in UAV, aircraft and helicopter projects at Turkish Aerospace since 2018. Impact behavior, impact resistance and impact tolerance of composite and sandwich structures are among the main topics of his academic research activities.

İbrahim Furkan İnce received his Ph.D. in Information Technology Design from the Graduate School of Digital Design, Kyungshung University, Busan, South Korea, in 2010. He conducted postdoctoral research at the University of Tokyo, Japan, from 2010 to 2012. From May 2012 to May 2014, he worked as a Senior Research Engineer at Hanwul Multimedia Communication (HMC) in Busan, South Korea. Additionally, he served as an Assistant Professor in Computer Engineering at Gediz University in İzmir, Turkey, from November 2014 to July 2016. He also worked as a Lecturer at the Department of Computer Engineering, Nişantaşı University, Istanbul, Turkey, from October 2019 to June 2024. Currently, he is a Lecturer at the Department of Software Engineering, İstinye University, Istanbul, Turkey. His research interests include image processing, computer vision, pattern recognition, and human-computer interaction.

Umud Efe Karaçay, Lecturer, National Defence University Air NCO Higher Vocational School. Lecturer Karaçay currently serves in the Mechatronics Program under the Department of Technology Sciences at the National Defense University Air NCO Vocational School. He graduated from the Mechatronics Engineering at Erciyes University in 2017 and subsequently completed his degree in Business Administration at Anadolu University in 2019. Between 2017 and 2018, he briefly worked as a Maintenance Engineer at a company in Kayseri. In February 2019, he was appointed as a Lecturer at the National Defense University Air NCO Vocational School in İzmir. In 2023, he began his postgraduate studies in the Electrical and Electronics Engineering Program at Marmara University.

Ünver Kaynak completed his undergraduate education in 1979 at the Department of Aircraft Engineering, Istanbul Technical University. He earned his master's degree in Mechanical Engineering from Stanford University in 1981 and completed his PhD in Aeronautics and Astronautics at Stanford University in 1986. He is currently serving in the Department of Aerospace Engineering at Ankara Yıldırım Beyazıt University.

Mehmet Kirmizi completed his undergraduate education in Anadolu University, Faculty of Aeronautics and Space Sciences, Airframe and Powerplant Maintenance Department in 2014. He earned his Master's degree from Gaziantep University, Institute of Sciences, Department of Aeronautics and Astronautics Engineering. He started his doctorate in 2020 at Eskisehir Technical University, Airframe and Powerplant Maintenance and still continues. His research topics are focused on aviation propulsion system analysis. Lecturer Kirmizi is currently at Ege University, Aviation Higher Vocational School (HVS), Aircraft Technology Programme.

Zahit Mecitoğlu was born in 1958 in Antalya, Turkey. Prof. Mecitoğlu graduated from Aeronautical Engineering Department of Istanbul Technical University (ITU) in 1982. Then he received MS and PhD degrees from Aeronautical Engineering Program of Istanbul Technical University in 1984 and 1988, respectively. Dr. Mecitoğlu employed as assistant professor between 1989 and 1990 and associate professor between 1990 and 1996 in Aeronautical Engineering Department of İstanbul Technical University. He has been working as professor in Astronautical Engineering Department of the same university since 1996. He worked as a visiting scientist in Aerospace Department of Georgia Institute of Technology in 1991 and participated the project named "Structural Integrity of Sikorsky MH-53J Helicopters. Dr. Mecitoğlu has worked in many projects such as National Wind Turbine Prototype System Development and Production Project, Tactical UAV (Catapult / Parachute) Development Project, Aerospace Research and Application Project, Tramcar Development Design and Production Project. He is dean of the Faculty of Aeronautics and Astronautics, ITU since 2020. His research areas are dynamics of aerospace structures, structural design and testing, wind turbine design, composite structures, experimental mechanics and finite element method.

Onur Osman graduated from ITU Electrical Engineering Department in 1994 and completed his master's degree at ITU Electrical Engineering in 1998. He received his doctorate from Istanbul University Electrical and Electronics Engineering in 2004. He started his career as an R&D engineer and later worked as a lecturer at many universities. He worked as an executive in TÜBİTAK and Development Agency projects, and served as a consultant in R&D projects of many companies.

Ibrahim Ozkol is currently working at Istanbul Technical University in the Faculty of Aeronautics and Astronautics as a professor. He received B.S., M.S., and Ph.D. degrees from Istanbul Technical University in 1985, 1988, and 1992, respectively. His research interests are fluid mechanics, heat transfer, applied mathematics, and the dynamics of robotic systems.

Orhan Özçelik, after completion of Bachelor Science at Gazi University, completed the Post Graduate Programme and Doctorate Programme at University of Oklahoma in 2008 and 2015, respectively. He is currently a lecturer at Faculty of Aeronautics and Astronautics of Ankara Yıldırım Beyazıt University and his research areas can be named mechanical vibrations, structural dynamics, aeroelasticity, composites. He gives courses at the university from undergraduate to doctorate level. He actively publishes articles in his area and participates in academic community organizations. Lastly, he is also Vice Department Chair at the same university.

Yavuz Öztürk graduated from the Department of Electrical and Electronics Engineering at Ege University in 2000. He completed his Master's degree with a thesis in the same field at Ege University between 2000 and 2003, and earned his PhD in the same department in 2010. He conducted postdoctoral research in Canada from 2010 to 2011. Since 2021, he has been working as an Associate Professor in the Department of Electrical and Electronics Engineering at Ege University. During 2022-2023, he was a researcher in the TÜBİTAK 1505 University-Industry Cooperation project titled “Advanced Imaging-Based Non-Destructive Testing Magnetic Particle Testing Device.” His academic interests include nanoscale materials, optics and photonics, magnetic materials, and non-destructive testing.

Damla Pehlivan graduated from the Departments of Chemistry and Mechanical Engineering at Atatürk University in 2010 and 2011, respectively. She is currently pursuing her doctoral studies at the Department of Mechanical Engineering, Selçuk University Faculty of Technology. Her research interests include composite structures, smart materials, and heat transfer.

Furkan Mert Sağel graduated from the Department of Mechanical Engineering at TOBB Economics and Technology University in 2023. He is currently pursuing postgraduate education and conducting research in project management and process improvement.

Hüseyin Enes Salman graduated from the Department of Mechanical Engineering at Middle East Technical University (METU) in 2009. He completed his master's degree in 2012 and his doctoral degree in 2018, also at METU. He is currently serving as a faculty member in the Department of Mechanical Engineering at TOBB Economics and Technology University.

Esma Nur Savrangüler graduated from Bursa Plato College in 2015. She completed her undergraduate degree in Mechanical Engineering at Manisa Celal Bayar University in 2021. Subsequently, she obtained her Master's degree in Mechanical Engineering with a thesis from İzmir Demokrasi University in 2024, earning the title of Mechanical Engineer. She gained valuable research experience as a Master's Scholar during 2022-2023 at Ege University. Her academic interests include Non-Destructive Testing, Magnetic Particle Testing, Magnetic Materials, Crack Detection, Electronic and Magnetic Devices, Electrical and Magnetic Fields, and Magnetic Nanoparticles. She has published various scientific papers in these fields.

Aysun Soysal received her PhD from Mathematical Engineering Department of İstanbul Technical University, İstanbul, Türkiye. Her research area is analytical and numerical solutions of differential equations, modeling and simulation of dynamic systems in engineering. He has been serving as the Dean of the Faculty of Engineering at İstanbul Topkapı University since February 2023. His fields of study are image processing, signal processing, machine learning, deep learning, biomedical systems, multi-antenna communication systems. There are over 40 SCI articles and the h-index is 13.

Onder Turan is a Professor of Eskisehir Technical University Faculty of Aeronautics and Astronautics. He received his BSc and MSc in the School of Civil Aviation and Graduate School of Sciences at Anadolu University in 1998 and 2000, respectively. He has published many papers at various national and international scientific journals, while he has authored several books. His research areas include propulsion, turbomachinery, flight mechanics, aerodynamics, renewable and sustainable energy, energy conversion and management, fuels and energy.

Bahadır Türker graduated from the Department of Mechanical Engineering at TOBB Economics and Technology University in 2023. He is currently continuing his work in the fields of control systems, electrical systems, and electric motors.

Caglar Uyulan is currently working at Izmir Katip Celebi University in the Faculty of Mechanical Engineering as an Associate Professor. He received his B.S. degree from Dokuz Eylul University and his M.S. and Ph.D. degrees from Istanbul Technical University in 2008, 2010, and 2017, respectively. His research interests are control theory applications, mechatronic systems, and machine learning.

Erol Uzal is a professor in Department of Mechanical Engineering at İstanbul University-Cerrahpaşa, İstanbul, Türkiye. His research area is aeronautical and astronautical engineering, structural technologies, and aeroelasticity.

Oğuz Varhan is student at the Ege University Product Lifecycle Management Master Program and currently working as a PLM Engineer at the Turkish Aerospace Industry. Previously, he worked as an R&D and Design Engineer at Olgun Steel Company within ILab Holding. He first worked as an Engineering Applications Specialist at CademDigital. He completed his education as Mechanical Engineering at Erciyes University and Izmir High Technology University Engineering Management Non-Thesis Master's Degree. In his business life, he has worked successfully in national and international automotive and defense industry projects.

Mustafa Murat Yavuz graduated from Gaziantep University, Department of Mechanical Engineering in 2008. He carried out various stress studies using numerical methods in his master's and doctoral studies. He teaches and conducts research in the field of mechanical science.

Mustafa Tolga Yavuz received his B.S. and M.S. degrees from Istanbul Technical University in 2011 and 2014, respectively. Now, he continues his Ph.D. studies on thermal structures under the supervision of Professor Ibrahim Ozkol at the Faculty of Aeronautics and Astronautics at Istanbul Technical University. His research interests include computational mechanics, aircraft structures, control theory, structural dynamics, and aeroelasticity.

Uğur Yolum graduated from Mechanical Engineering Department of TOBB University of Economics & Technology (ETÜ) in 2010. After completing his master's degree at Esslingen University, he worked as a structural analysis engineer in the automotive sector in Germany. He started working at Turkish Aerospace in 2014. He is working as a chief engineer in the structural analysis unit of the Helicopter Group. He received his PhD degree from Mechanical Engineering Department at TOBB ETÜ.

Editor's Introduction

We are honoured to present this book, the culmination of significant conferences that have greatly contributed to its maturation and finalization. In collaboration with Ege University Aviation Higher Vocational School and National Defence University Air NCO Higher Vocational School, the "Ulusal Havacılık Teknolojileri Kongresi - UHAT (National Congress of Aviation Technology and Applications)" has been successfully organized five times: in 2012, 2013, 2015, 2017, and 2021. This esteemed congress has seen the participation of over 600 academicians and industry professionals, and more than 250 valuable studies have been shared and discussed. The primary aim of UHAT was to facilitate the exchange of information on aviation and defence among various stakeholders. To this end, the Congress brought together institutions and organizations that provide technical training in aviation and defence, as well as those engaged in R&D and production technologies within the sector. The objectives were multifaceted: to share scientific research and its applications in aviation and defence, to foster collaboration between practitioners and academics, to identify and address areas requiring development, and to disseminate current advancements to educational institutions and the industry.

In 2023, UHAT evolved into an international event, the "Aviation Technologies and Applications Conference (ATAConf)." Hosted by the National Defence University Air NCO Higher Vocational School, in collaboration with the Aviation Higher Vocational School of Ege University, ATAConf took place in İzmir, Türkiye, on October 20-21, 2023. This conference continued to uphold its tradition of excellence, promoting interaction among academics and industry representatives to present and discuss innovative studies. The distinguished contributions of the participants have been instrumental in maintaining the high standards of the conference. Our primary objective moving forward is to ensure the seamless continuation of this now-international conference. We aim to enhance international participation in future conferences, thereby increasing the number and quality of research contributions in the fields of aviation and defence. We extend our heartfelt gratitude to all individuals and organizations that have played a pivotal role in the inception and growth of these conferences. This book compiles a selection of the best papers presented at the 2023 Aviation Technologies and Applications Conference (ATAConf 23). The selected papers were invited to be published as book chapters, and the final chapters were refined through a rigorous peer review process. We sincerely appreciate the contributions of all authors and believe that this book presents high-quality studies in the field of aerospace and defence to the global scientific community.

This book comprises a total of 20 chapters, each authored by experts in their respective fields, providing in-depth analyses and insights. Following this introductory section, brief summaries of each chapter's main findings and focus areas are presented. These summaries aim to offer readers an overview of the book's content and scope. Additionally, the importance of the topics covered in each chapter and their contributions to the existing literature are highlighted. This allows readers to gain a preliminary understanding of the subjects explored and the outcomes of these analyses.

In Chapter 1, the authors explore the influence of optical aperture geometry on image quality within earth and space observation systems. By increasing the aperture diameter from 35 cm to 110 cm, they observed a notable improvement in the correlation coefficient, rising from 0.672 to 0.917. Although larger obscuration sizes negatively impact image quality, restored images display a nuanced behavior with a slight increase followed by a decrease in quality. Furthermore, the authors find that, for telescopes with three, four, and five spider arms at a thickness of 19.8 mm, the variations in image quality remain minor.

Chapter 2 analyses the global buckling behavior of metallic skin-stringer and honeycomb sandwich panels in helicopter fuselage sections using finite element simulations. It compares different stringer cross-sections (z-, c-, and omega-section) and honeycomb panel variants (with or without doublers). Findings show omega stringer panels have 15.6% higher buckling strength than z stringer panels. Among honeycomb panels, those with transverse doublers are 12.6% more durable than those without. Honeycomb panels also offer superior buckling strength per unit weight compared to skin-stringer panels, highlighting their suitability for helicopter fuselage side panels.

Chapter 3 includes a study investigating the field of aeroelasticity, focusing on the interaction between elastic structure deformation and aerodynamic forces. In this study, static aeroelasticity is investigated by theoretical and analytical approaches, necessary equations are derived and wind tunnel data up to maximum speeds are analyzed. The study uses ANSYS for flow analysis using galvanized steel for the bar material and NACA 2411 airfoil for optimum results. The study includes analysis results including lift and drag coefficients, and demonstrates the agreement between theoretical and analytical findings in the simulation of aircraft wing structures.

In Chapter 4, the authors present a review of smart antenna systems and their impact on wireless communications. They explain how smart antennas use adaptive element weights and direction-of-arrival algorithms to improve signal reception and reduce interference, and highlight advances such as blind channel estimation and space-time coding that offer advantages over traditional antennas, such as better coverage and spectral efficiency. The authors also introduce a smart antenna structure that they propose for military and civilian use, and share its theoretical basis and numerical effectiveness.

Chapter 5 includes a study examining microcracks in the chrome coating of the Boeing B737-800 landing gear and their effects on structural integrity. Using SEM, FPI and HRC hardness tests, the study concludes that excessive heat during grinding is the main cause of macrocracks. The study highlights problems such as machine bearing clearances and inadequate cooling, and suggests solutions to reduce friction, develop special ceramic grinding wheels and improve coolant flow to prevent damage and improve coating quality.

In Chapter 6, the authors investigate the enhancement of aerospace composites by incorporating functionalized graphene nanosheets (FGNP) into Araldite LY5052 epoxy. Testing FGNP concentrations of 0.5%, 1%, and 1.5%, they found that 0.5% and 1% significantly improved the material properties and optimum dispersion was observed using UV-Vis spectroscopy at these levels. Overall, the study demonstrated that the incorporation of FGNP enhances the functionality and performance of aerospace composites.

Chapter 7 investigates the development of autopilot systems aimed at achieving fully automatic drone landings on aircraft carriers. In their research, the authors chose a basic propeller aircraft as a model to demonstrate the design and implementation of these systems and FlightGear and Simulink software for simulation. The study also outlines the basic steps to create simple yet effective autopilot systems for aircraft carrier deck landings.

In Chapter 8, the authors examine the use of digital simulations and deep reinforcement learning (DRL) to train aircraft agents. The study focuses on training four aircraft agents in Unity3D to navigate a race track with checkpoints using Proximal Policy Optimization (PPO) and a reward-punishment system. The study also integrates Unity3D ML-Agents examples to optimize PPO parameters, demonstrating that reinforcement learning can solve real-world problems in gaming, robotics, and autonomous flight.

Chapter 9 examines the interactions between the SHELL model flight crew leadership and other operational modules, focusing on identifying and reducing potential errors. In the study, the authors aim to improve flight and ground safety for helicopter search and rescue missions by evaluating error probabilities and impacts within the SHELL framework. A total of 25 accident factors are identified in the study, and their probabilities of occurrence and error impact scores are evaluated. This chapter emphasizes Crew Resource Management (CRM) and improving aviation safety awareness to prevent potential accidents and incidents.

In Chapter 10, the authors examine the increasing use of composite materials and the need for early detection of defects such as fatigue, impact damage, and manufacturing defects. The focus is on thermographic inspection methods, examining their effectiveness in detecting defects in laminated and sandwich composites. The chapter discusses nondestructive testing techniques, composite material terminology, and various types of interruptions, and shows that both heating and cooling processes are effective for thermographic inspections. The authors emphasize that cooled thermographic inspection is particularly sensitive in detecting areas of delamination.

Chapter 11 highlights the growing role of UAVs in disaster management and their fundamental contributions to emergency response. The authors focus on how UAVs enhance pre-disaster terrain mapping, improve communication during crises, and support post-disaster damage assessment. The study outlines the technical specifications required for UAVs to perform tasks such as photogrammetric imaging and communication, highlighting their ability to meet these demands. The chapter demonstrates that UAVs provide rapid and effective assistance in disaster areas, significantly improving both response times and overall effectiveness in emergency situations.

Chapter 12 highlights the increasing importance of non-destructive testing (NDT) in environmentally friendly industrial processes. Focusing on Fluorescence Magnetic Particle Testing (FMPT), this chapter examines how different current values affect test quality to detect defects in ferromagnetic materials. The authors perform statistical analysis and optimization of test parameters using pre-processing techniques on test images. The chapter is written in Turkish and shares insights to improve NDT applications in various industries.

The authors of Chapter 13 examine foam-cored sandwich composites under medium-velocity impacts (10-50 m/s) using a finite element model to estimate damage and residual strength. Unlike studies focusing on low- or high-velocity impacts, this research validates the model through experiments and Abaqus/Explicit simulations. Results show that despite a 50% strength loss at 10 m/s, the structure maintains significant load-carrying capacity after impacts up to 40 m/s.

In Chapter 14, the authors analyse how isentropic efficiency (IE) affects turboprop engine performance, focusing on the air compressor (AC), gas turbine (GT), and free turbine (FT). They find that increasing IE from 0.8 to 0.98 significantly boosts thermal and exergy efficiency, with improvements ranging from 28.9% to 37.1% for AC, 26.6% to 36.9% for GT, and 27.12% to 33.2% for FT. Exergy destruction also decreases with higher IE. The results suggest that innovative manufacturing processes could improve fuel economy in turboprop engines.

Chapter 15 presents an optimized energy management system for UAV operations. The system autonomously identifies the nearest charging station when battery levels drop below 20%, detects available charging units using image processing techniques, and ensures precise landings. The Euclidean Method calculates distances to charging stations, selecting the shortest route. A Raspberry Pi supports the flight computer, managing detection and positioning via GPS. This autonomous system minimizes the need for human intervention during the charging process, enhancing operational efficiency and reducing maintenance.

Chapter 16 explores ice formation on UAV wings and emphasizes electrothermal heating to maintain aerodynamic efficiency. Analyzing the NACA0012 airfoil at various angles of attack and Reynolds numbers, the study uses finite volume methods to solve fluid and energy equations. Results show that high Reynolds numbers cause rapid temperature convergence to external conditions, necessitating internal heat generation to prevent ice. The chapter highlights how internal heating can counteract significant heat loss and maintain acceptable temperatures.

In Chapter 17, the design of wind turbine blades is analysed using Timoshenko and Bernoulli-Euler models. The study reveals that compression increases vibration frequencies, while tension decreases them. The Timoshenko model generally predicts lower frequencies and earlier failure under compression. Shorter blades show more distortion, especially in the Bernoulli-Euler model. Increasing the geometric coupling term also affects vibration modes. The Timoshenko model is recommended for thicker blades and rotational motion.

Chapter 18 explores active control of wing vibrations caused by store separation in aircraft. Using a mass-spring-damper model and LQR control, the study addresses vibrations that occur when external stores like missiles are released. Simulations show that active control significantly reduces harmful vibrations, improving aircraft safety and stability. The research underscores the value of advanced control techniques in enhancing wing performance during critical events.

The authors of Chapter 19 discuss the integration of advanced systems engineering approaches and PLM (Product Lifecycle Management) processes to address the increasing complexity in industrial product and service management. As technology progresses, managing complex products and services becomes more challenging. Systems engineering aims to streamline this complexity, while PLM systems enhance organization, automation, and traceability. This chapter focuses on how the aerospace and defence industries utilize these methods to improve efficiency, accuracy, and safety in their highly complex and sensitive products. It also explores future sector needs and the potential benefits of these innovative approaches.

In Chapter 20, the author examines how root and tip vane positions affect wing properties, using a NACA 2024 airfoil profile modelled with finite element methods. Various wing configurations, including different angles and bending geometries, were analysed. The study found significant bending and torsional responses at modal frequencies and used computational fluid dynamics to calculate drag coefficients. The findings offer valuable insights for future wing design.



CHAPTER 1

Aviation Technologies and Applications
E-ISBN:978-605-338-471-7
2025, chap. (1) , pp.1-19.

STUDY OF QUALITY METRICS FOR SATELLITE BASED IMAGING: EFFECTS OF OPTICAL APERTURE OBSCURATIONS

Kamil B. ALICI^{1,*}

ABSTRACT

After providing general information on earth observation and space observation systems, we investigated the effects of optical aperture geometry on image quality. When the optical aperture diameter was changed from 35cm to 110cm, the correlation coefficient increases from 0.672 to 0.917. Obscuration size negatively affects image quality; however, for restored images we saw a slightly increasing then decreasing quality behavior. As the telescope size increase, the number of spider arms holding the secondary mirror might also increase for mechanical purposes. For three, four, and five, spider arm cases, image quality variation remained minor in terms of correlation coefficients when the spider arm thickness was 19.8mm.

Keywords: Apertures, optical transfer functions, image restoration, optical diffraction, image chain simulation

1. INTRODUCTION

We can divide space-based observation studies into two main categories: i) earth observation, and ii) space observation. Below we provide general information for each of these domains that were depicted in Figure 1. This chapter is an extended version of our previous conference paper on image quality analysis of annular optical apertures with varying obscuration sizes[1].

1.1. Space Based Earth Observation Systems

Earth observation systems (EOS) require the telescope in use to be in relatively close distance to the object. Such a requirement implies utilization of low earth orbits (LEO) for space-based satellites. In radiometry, signal received from ground objects depends on the angle between sun, earth surface, and satellite (SZA).

*Corresponding Author: kamil.alici@tubitak.gov.tr
1 0000-0003-2924-7464, Remote Sensing Group, TÜBİTAK Space Technologies Research Institute, Ankara, Turkey

CHAPTER 1: STUDY OF QUALITY METRICS FOR SATELLITE BASED IMAGING: EFFECTS OF OPTICAL APERTURE OBSCURATIONS

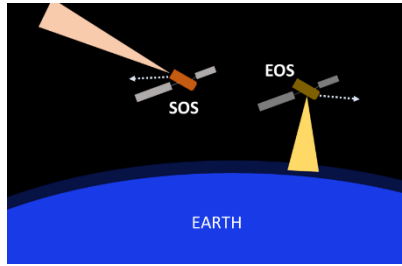


Figure 1. Schematics of Space Based Systems.

While choosing LEO, consideration was given to the SZA. Near polar orbits benefit from earth's rotation for imaging different regions of earth and obtaining reasonably constant SZA. Keeping the SZA almost constant enables comparing different images of the same region in terms of radiometric quantities. Sun synchronous orbits satisfy such a condition, and near polar, sun synchronous LEOs were desired for most EOS systems[2]. Earth observation systems have applications in surveillance, reconnaissance, agriculture, cartography, environmental monitoring, forestry, land use planning, and oceanography.

EOS utilize mirror based, spectrally invariant, reflective telescopes operating at the visible and NIR regimes. A number of telescope designs including Cassegrain architecture were utilized in satellite telescopes. Cassegrain and its variants were commonly utilized in Earth observation systems. There is a central obscuration due to secondary mirror back face at the Cassegrain architecture. Additionally, secondary mirror was fixed to its location via a number of spider arm support structures[2, 3].

1.2. Space Based Space Observation Systems

For the problem of habitable planet identification, direct imaging of exoplanets is essential. Ratio of planet light to the light of its star is typically 10^{-10} to 10^{-11} . In order to cover this ratio, standard space telescope Cassegrain architectures require aperture sizes of 15m to 30m. Such a large telescope size requires segmentation as monolithic fabrication is not possible. Segmented telescopes include not only gaps between segments but also shadows due to supporting spider arm structures. In order to reduce undesired diffraction rays emanating from central patterns, curved spider arms were introduced and corresponding pupil shape was named as pinwheel pupil. Such a design significantly cuts down rays flowing out from central radiation patterns. This allows simpler apodization masks, and more accurate image restoration. Its performance was compared to

circular, annular, and 60-degree segmented hexagonal pupils[4]. Utilization of such a pupil cuts down effects of anisotropic point spread function (PSF) and results in improved image processing. It was shown that curved arcs at the pupil do not introduce significant diffraction patterns at the image plane. There appears 10^4 diffraction magnitude difference between straight line and curved support structures [5]. In order to eliminate diffraction effects that obscure exoplanet images, curved segmented mirrors and curved supporting structures were utilized [6]. Such curved spider arms were actually proposed at an early date by Werenskiold. If the curved spiders were precise arcs of a circle, the diffraction flares will be spread into a uniform distribution and mostly eliminated[6].

For the necessary angular resolution and gathered radiation power, space telescope aperture sizes of 15 to 30 meters are required. Such large area mirrors could be assembled in space or be folded on earth before launch. Such structures are typically composed of hexagonally arranged discontinuous concave surfaces. Such gaps and related structures diffract light in an undesired fashion[7].

In standard Cassegrain architecture, central aperture has obscurations due to support structures and secondary mirror shadow. For larger size telescopes, hexagonal segments were utilized in the primary mirror. They introduced diffraction noise at the image plane. In the pupil plane, instead of straight lines, curved segment edges and spider arms were utilized in order to reduce the diffraction noise. Such variations reduce the complexity of absorbing apodizing masks. Increased performance in radiometric calibration and image restoration is possible[4].

Diffraction spikes typically accompany star images in astronomical telescopes. They reduce the image quality and could be mitigated by some measures. One of them is to use long pipe to attach secondary mirror, another is to use curved spider arms. Such structures reduce diffraction spikes and improve image quality. One of the commonly utilized image criterion is the Strehl ratio that is the ratio of aberrated PSF peak value to diffraction limited peak value[6].

Wave front error (WFE) introduced by telescope segmentation and phasing error in segmented telescope coronagraphy were studied in literature. The flux ratio of radiation from star and its planet is at least on the order of 10^{10} at visible wavelengths. This problem requires utilization of large size primary mirrors with mass, cost, and launch vehicle considerations. The common solution to these problems is utilization of segmented primary mirrors. Segmentation brings in extra diffraction patterns at the image

plane. Misalignments of segments and mirror structure deformities introduce additional WFEs. Such WFEs yield extra radiation patterns and degrade imaging performance[8].

Various telescope apertures have been studied in terms of secondary obscurations, spider arms, and segmentation gaps. One technique is introduction of an area of deep contrast (dark hole) region by using coronagraphy techniques at the focal plane. For the construction of high contrast instruments, wavefront control and sensing techniques were implemented[8].

Mechanical and thermal instabilities of optical components throughout the optical axis affect detectability of point sources. Segmented apertures change wavefront quality and WFE stability requirements. One example telescope, The Nancy Grace Roman Space Telescope designed to supply 10^9 contrast levels[8].

Main implication of utilizing segmented mirrors is the manufacturing bounds of monolithic mirror sizes. For space based large area optical telescopes, such limits need to be surpassed. Segmented mirrors mostly have hexagonal tiling. For such architectures, figures of segments are fraternal and form an aspherical surface in the combined form[9].

Hexagonally segmented primary mirrors of large aperture telescopes were also studied in terms of co-phasing errors. Large telescopes provide higher light collecting capacity and resolution. In such telescopes, a number of segments were used to set up large aperture mirror in addition to active optics. Co-phasing analysis includes theoretical formulation of telescope PSF and relationship between co-phasing errors. Ray tracing simulations supply point diagrams, Strehl ratio, and MTF values. Segmentation errors and manufacturing errors shape the basics of co-phasing errors. Piston, tip-tilt, decenter errors form the segmentation errors while radius of curvature, conformity, and surface misfigure errors are included as manufacturing errors. Figures of merit utilized in image quality analyses of astronomical telescopes are PSF and Strehl ratio[10].

Segmented-mirror telescopes achieve light level ratios of 10^6 depending on their size. In such a case, segmentation geometry, gaps between segments, secondary mirror-based obscurations, spider arm obscurations, segment misalignment errors, segment misfiguring errors, and segment reflectivity variations introduce diffraction effects of various order. Segment misalignment errors can be detailed as piston, tip-tilt errors of primary mirror, segment piston, segment tip-tilt, aberrations, and global radius of curvature errors[11].

Direct observation of exoplanets requires 10^{10} contrast ratio. For this purpose, space-based telescopes include segmented large area apertures, coronagraphs, wave front sensors, and wavefront controls. Coronagraphs reduce the starlight while keeping the exoplanet signal fixed. Such imaging tools were proposed in order to solve the 10^{10} contrast problem. The primary mirror phasing errors significantly affected performance of such telescopes. Optical simulations of instruments are required to test system hardware and algorithms. The simulation software Coronagraphic Focal Plane Wave-front Estimation for Exoplanet Detection (COFFEE) is able to calculate wavefront aberrations with high resolution[12].

Large area space telescopes not only have large collecting area but also provide increased angular resolution. Segmented architectures are much difficult to stabilize and assemble with respect to monolithic ones. Large size is of critical importance for space telescopes in exoplanet detection. Not only for monolithic mirror manufacturing limits but also for launch campaigns, segmentation of primary mirrors is necessary. By the aid of recent coronagraph designs, high contrast levels of 10^{10} were achieved. PSF for the segmented architecture needs to be broken down to segmentation effects[13].

Special attention needs to be put into error budgets in order to obtain and preserve stable high contrast imaging. Error budget covers imaging performance and degrading effects during and after system development. Optical end-to-end simulation provides effects of segment phasing, optical surface quality, jitter, thermal drift based aberrations[13]. Method of error budget estimation relies on generating random distribution of degrading effects and introducing confidence intervals for operating points[13]. Results indicating challenging requirements that appear in order to obtain 10^{10} contrast ratio: such as 20 pm rms piston phasing error[13].

PSF of telescopes with hexagonally segmented primary mirrors was computed by using symmetry relations. There is a resemblance in theoretical expressions between diffraction gratings and hexagonal segmentation. As the size of the telescope increases, more light was delivered to the image sensors and aperture diffraction related resolution increases. Due to manufacturing limitations, after a diameter value, segmented architecture is preferred. Presently, large binocular telescope with 8.4m diameter single mirror is the largest ground-based telescope. By taking the squared modulus of the Fourier transform of the pupil function, we evaluate the point spread function of the system. One way to calculate hexagonally segmented telescope PSF is by getting the convolution of triangular grid with hexagonal pupil function[14].

CHAPTER 1: STUDY OF QUALITY METRICS FOR SATELLITE BASED IMAGING: EFFECTS OF OPTICAL APERTURE OBSCURATIONS

There are three main criteria for high-contrast imaging and spectroscopy: sensitivity, resolution, and contrast. This requires large area optical apertures. For transportation and manufacturing purposes, large-scale mirrors are produced in segmented form. In addition to telescope architectures, coronagraphs are applied to eliminate the starlight while keeping the exoplanet light. Lyot-style coronagraph is suitable for various apertures and utilized in addition to focal plane masks in order to reduce diffraction effects. Such a device provided planetary data so far[15]. This contrast objective sets requirements on observatory stability that might be mitigated with wavefront sensing and control strategies[15].

Hexagonal pattern tiling is commonly used in today's ground and space telescopes with large sizes. Overall, these segments act as unique aperture. There forms a fixed pattern noise on the image plane, which plays an additional effect on exoplanet detection. By using a so-called pinwheel segment geometry, such a diffraction pattern noise could be reduced. While wave front aberrations are caused due to the mirror surface fabrication errors, polarization aberrations are mainly sourced due to mirror coatings[16].

In order to estimate the amount of exoplanet's life sustaining properties, spectral light signal needs to be transferred. The reflected light amount ratios between the parent star and its planet could be on the order of 10^{10} to 10^{11} [16].

For manufacturing purposes, mirror substrate fabrication requires large aperture area, low areal density, and high stiffness. Throughout this direction, supporting systems needs to be designed, and correction of mirror figure errors is required. Diffraction is present due to segment edges and segment gaps. Such diffraction effects need to be eliminated[17]. Advanced mirror technology development (AMTD) provides 10 pm per 10-minute wave front stability. AMTD design and modelling tools include mirror modeler, sensitivity and performance evaluator, MTF calculator, and telescope response simulator[17].

James Webb Space Telescope (JWST) performs alignment and maintenance while orbiting. Accurate wavefront phase determination is present by the way of several diagnostic instruments. Additionally, alignment errors were corrected by employing a point target. Pupil function of a segmented Fresnel primary mirror (SFPM) can be stated as convolution of a circular pupil aperture with a set of two-dimensional Dirac delta functions[7].

As mentioned, due to diffraction effects, star images generated by telescopes include light rays emerging from star centers. By modelling diffraction, image sensor, and image adjustments, a computational framework was established. An image prediction framework composed of two sequential windows was presented in literature[18].

Direct imaging and spectroscopic characterization of exoplanet systems is the objective of Habitable-Zone Exoplanet Observatory Mission (HabEx). Its primary mirror is $4m$ diameter and wavefront stability of a few tens of picometers was achieved. This objective is one of the challenges of NASA[19].

In this mission, for a telescope/coronagraph system providing 10^{10} contrast, maximum irradiance throughput needs to be supplied. Small inner working angle depends on small stable PSF. Surface figure error (SFE), gravity sag, and coefficient of thermal expansion (CTE) are main contributors for primary mirror effects. Another criterion is the line of sight (LOS) stability specification, which is typically one tenth of PSF radius. LOS stability is based on mechanical and thermal effects. There are slow rigid body motions of optical components that can be corrected. Jitter is the mechanical vibration due to reaction wheels, cryo-coolers, and etc. Also, WFE toleration of coronagraphs needs to be determined. A WFE stability error budget was studied yielding signal to noise ratio (SNR) and coronagraph contrast values. Homogeneous CTE introduces defocus error and inhomogeneous CTE yields temperature dependent WFE. Coronagraphy requires ultra-stable wavefront, which is much easier to achieve with monolithic mirrors[19].

2. FRAMEWORK OF THE ANALYSES

Paths of light are investigated in the radiometric calculations of the image chain. Not only the light reflected from target reaching the detectors, but also other light paths are taken into account. Signal of the electro-optics system depends on the spectral characteristics of optics and image sensor components. In visible band imaging systems, top of the atmospheric sun light acts as incoherent light source. During its propagation, part of the visible band sun light was absorbed with atmosphere based spectral dependence. Light reflected from the target reaches the image sensor and acts as signal source. Light reaching the image sensor from other paths acts as the background noise.

CHAPTER 1: STUDY OF QUALITY METRICS FOR SATELLITE BASED IMAGING: EFFECTS OF OPTICAL APERTURE OBSCURATIONS

Depending on the field of view of the optical system, some light rays reach the image plane and image circle. This radiation amount is calculated in Eq.1 by the G-number formula:

$$G_{\#} = \frac{1 + 4f_{\#}^2(1 + M_0)^2}{\pi\tau_{obs}\tau^N} \quad (1)$$

Here $f_{\#}$ is the ratio of effective focal length to optical system aperture diameter. M_0 is the magnification constant, τ_{obs} is the transmission loss due to obscuration, τ is the mirror reflection ratio, N is the number of mirrors.

Light reaching the image plane was filtered due to atmospheric and transmission effects. Depending on the image sensor filter and absorber material, a spectral portion of the light is absorbed and converted into photoelectrons. Absorption level is a function of local electric field strength and in the present study, metaxel unit cells were utilized, and absorbed light levels were calculated.

The number of photoelectrons generated by incident 100 photons yields the quantum efficiency (QE) as percentage. There are two noise sources at the signal: photon noise and dark noise. Photon noise obeys Poisson statistical distribution while dark noise obeys Gaussian statistical distribution.

2.1. Optical Transfer Function Analyses

Image of a point source located at the object plane is called the impulse response or point spread function (PSF) in two-dimensions. When we take PSF into account as a Fourier series, coefficients at high spatial frequencies get small values, while coefficients at low spatial frequencies get large values. The Fourier transform of PSF here is the optical transfer function (OTF). When we shift a point light source at the object plane, if the PSF also shifts at the image plane while keeping its form and values, then the optical system is identified as shift invariant. When the magnitude of light source increases, if the image magnitude also increases, then the system satisfies the multiplicity property. When we have a number of point sources at the object plane, if the overall image is the sum of individual PSFs, then the system satisfies additivity property. If the system satisfies these three properties all together, then it is linear shift invariant system (LSI). For LSI systems, image is calculated as the convolution of object and PSF. In the presence of optical aberrations, the system requires a different PSF for each region and it is linear shift invariant.

The formula of convolution is given as follows[20]:

$$i[x, y] = h[x, y] ** o[x, y] \quad (2)$$

Here x and y are the coordinates and $i[x, y]$ represents image points, $h[x, y]$ is the impulse function, and $o[x, y]$ is the original object function.

In order to estimate system image, we need to model impulse function or optical transfer function of the system. When OTF/MTF of each system component is identified, the overall OTF is formed by computing the composite function. These components could be listed as atmosphere, optics, image sensor, and platform motion. Initial models utilized are aperture diffraction, detector footprint, platform linear motion, and detector TDI. They are formulated with the following formulas[21], respectively:

$$PSF(x, y) = \frac{\left(\frac{1}{\lambda f}\right)^2 |FT\{p(x, y)\}|^2_{f_x=\frac{x}{\lambda f}, f_y=\frac{y}{\lambda f}}}{\iint_{-\infty}^{+\infty} p(x, y) dx dy} \quad (3)$$

Here, λ is the operation wavelength, f is the effective focal length, $p(x, y)$ is the pupil function.

$$OTF(f_x, f_y) = sinc(d_x f_x) sinc(d_y f_y) \quad (4)$$

Here, d_x, d_y are the physical length of the photosensitive area in each direction.

$$OTF(f_x, f_y) = sinc(d_{ysmear} f_y) \quad (5)$$

Here, d_{ysmear} is the length of smear in the y-direction.

$$OTF(f_x) = \frac{\sin(\pi N_{TDI} d_{CCV} \tan \theta f_x)}{N_{TDI} \sin(\pi d_{CCV} \tan \theta f_x)} \quad (6)$$

$$OTF(f_y) = \frac{\sin(\pi N_{TDI} d_{error} f_y)}{N_{TDI} \sin(\pi d_{error} f_y)} \quad (7)$$

Here, N_{TDI} is the number of TDI stages, d_{CCV} is the vertical detector pitch, θ is the angle between the image motion and TDI direction, d_{error} is the actual location and image location difference at the first pixel.

2.2. Image Restoration Analysis

Original images can be restored from degraded image by using the following formula in Eq. 8:

$$I[f_x, f_y] = H[f_x, f_y] \cdot O[f_x, f_y] \quad (8)$$

Here we got the Fourier transform of the convolution equation. $O[f_x, f_y]$ is the scene spectrum, $I[f_x, f_y]$ is the image spectrum and $H[f_x, f_y]$ is the OTF. If we multiply the terms of equation with $WI[f_x, f_y] = 1/H[f_x, f_y]$ we get:

$$O[f_x, f_y] = WI[f_x, f_y] \cdot I[f_x, f_y] \quad (9)$$

We apply inverse Fourier transform to $O[f_x, f_y]$ and get the original scene image.

In the presence of noise the filter is replaced with Wiener-Helstrom filter[22]:

$$W[f_x, f_y] = \frac{H^*[f_x, f_y]}{|H[f_x, f_y]|^2 + \frac{|N[f_x, f_y]|^2}{|F[f_x, f_y]|^2}} \quad (10)$$

Here $H^*[f_x, f_y]$ is the complex conjugate of the OTF, $F[f_x, f_y]$ is the original undegraded object spectrum, and $N[f_x, f_y]$ is the spectrum of the noise.

3. RESULTS OF APERTURE EFFECTS

We investigate effects of main aperture diameter, central obscuration diameter and number of spider arms on image quality.

3.1. Effect of Main Aperture Diameter

Our analyses start with demonstration of aperture structure variation as schematics. It is followed by estimation of images in the presence of the effect and corresponding image restoration results. Data is finalized with correlation coefficient and GIQE variation as a function of the parametric change.

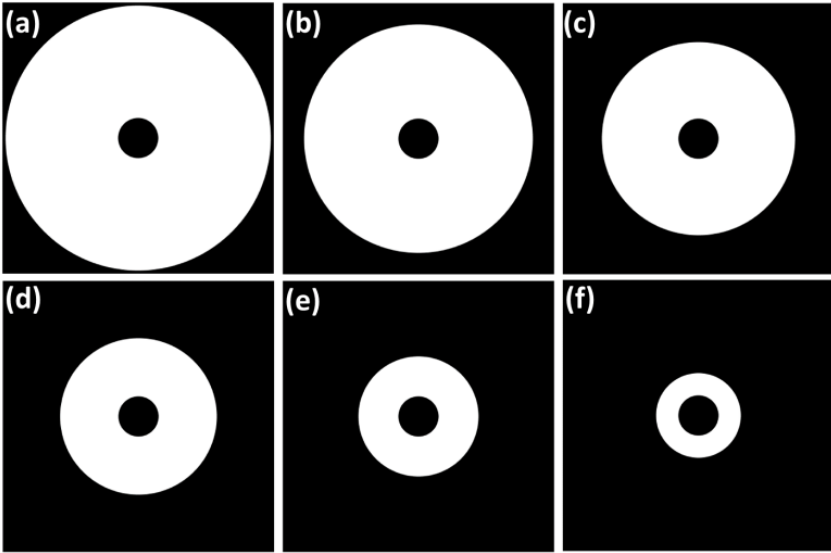


Figure 2. Variation of optical aperture diameter. Aperture diameter values (a) 110 cm, (b) 95 cm, (c) 80 cm, (d) 65 cm, (e) 50 cm, (f) 35 cm.

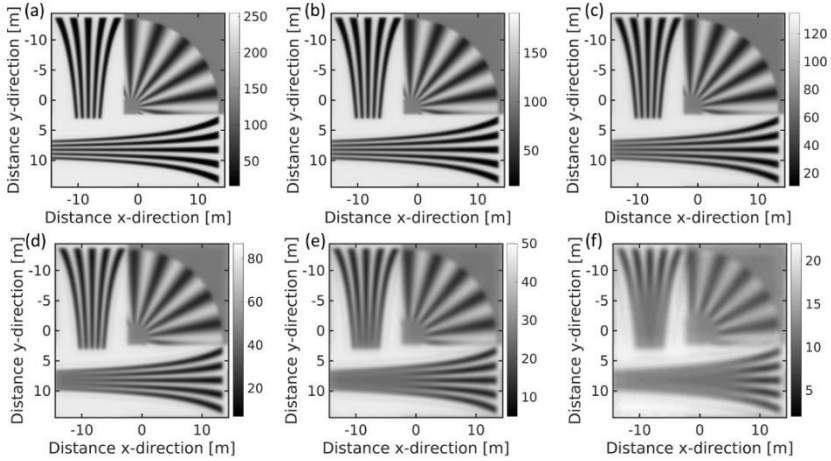


Figure 3. Image estimations as a result of image chain simulations for aperture diameter values (a) 110 cm, (b) 95 cm, (c) 80 cm, (d) 65 cm, (e) 50 cm, (f) 35 cm.

**CHAPTER 1: STUDY OF QUALITY METRICS FOR SATELLITE BASED IMAGING:
EFFECTS OF OPTICAL APERTURE OBSCURATIONS**

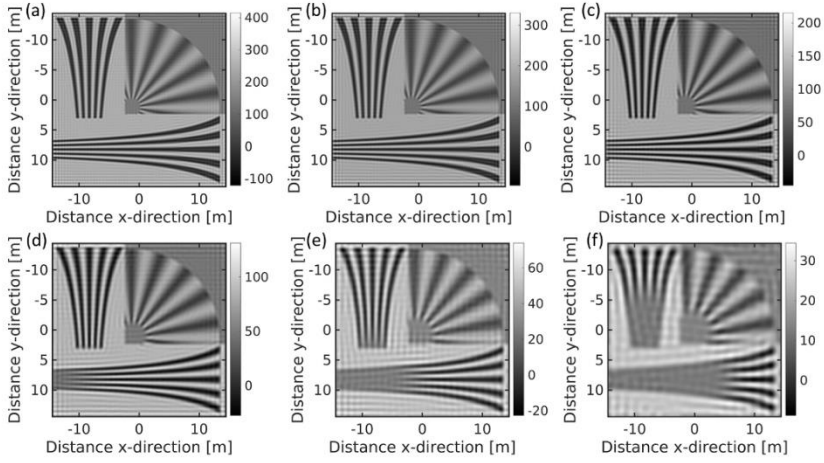


Figure 4. Image restoration results as a result of Wiener filter application for aperture diameter values (a) 110 cm, (b) 95 cm, (c) 80 cm, (d) 65 cm, (e) 50 cm, (f) 35 cm.

Table 1. Image quality metrics for aperture variations: i) optical aperture size, ii) obscuration diameter, iii) number of spider arms. Correlation coefficient and structural similarity index measures were calculated by using degraded images while GIQE values were calculated by using restored images.

Case	Corr. Coeff. Degraded	Corr. Coeff. Restored	GIQE 4.0
D = 35cm	0.672	0.785	
D = 50cm	0.772	0.875	
D = 65cm	0.836	0.912	
D = 80cm	0.877	0.922	
D = 95cm	0.901	0.918	
D = 110cm	0.917	0.935	
D _{obs} = 0cm	0.842	0.909	6.034
D _{obs} = 9.4cm	0.841	0.911	6.040
D _{obs} = 19.0cm	0.833	0.912	6.041
D _{obs} = 28.4cm	0.811	0.914	6.043
D _{obs} = 38.0cm	0.771	0.914	6.045
D _{obs} = 42.7cm	0.747	0.912	6.040
N _{spider} = 3	0.834		
N _{spider} = 4	0.838		
N _{spider} = 5	0.833		

The first key parametric change is the variation of the main aperture diameter. While other parameters were kept as the same, we increased and decreased the aperture diameter of the benchmark system. The benchmark value of the main mirror diameter was 65 cm. We reduced it to 50 cm and 35 cm, and increased it to 80 cm, 95 cm, and 110 cm values. The corresponding schematics are shown in Figure 2. For each aperture diameter, image estimate of the synthetic ground truth is shown in Figure 3. From visual inspection, we see that as the aperture diameter increases minimum resolvable dimension reduces. Sine wave star pattern, minimum resolvable diameter starts from smaller values with large diameter apertures. As the diameter increases image quality of the estimates improves. In the following Figure 4, we show the results of image restoration. The quality of restored images were significantly better than degraded ones. There is a visible quality decrease as the aperture size becomes smaller. The final parametric study demonstrates variation of image quality metrics as the aperture size varies. All of the results were tabulated in Table 1.

3.2. Effect of Obscuration Diameter Size

We show the obscuration diameter variation in Figure 5. As the size of the obscuration diameter was changed from zero to a maximum value of 42.7mm, we investigated the image chain simulation estimates as shown in Figure 6. How the image quality degrades for the case of obscuration diameter variation is demonstrated clearly in Figure 6. We see an increasing blurring trend as the size of the central obscuration increases.

**CHAPTER 1: STUDY OF QUALITY METRICS FOR SATELLITE BASED IMAGING:
EFFECTS OF OPTICAL APERTURE OBSCURATIONS**

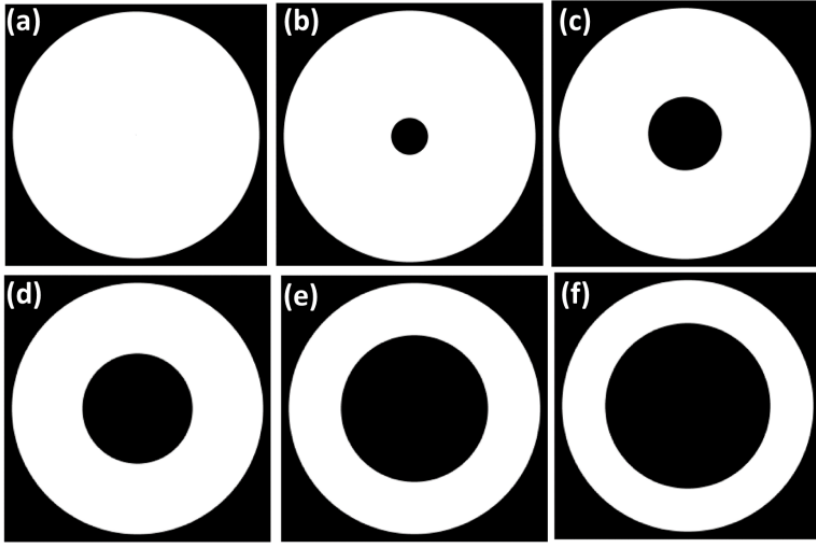


Figure 5. Variation of central obscuration diameter. Obscuration diameter values (a) no obscuration, (b) 9.4 cm, (c) 19.0 cm, (d) 28.4 cm, (e) 38.0 cm, (f) 42.7 cm.

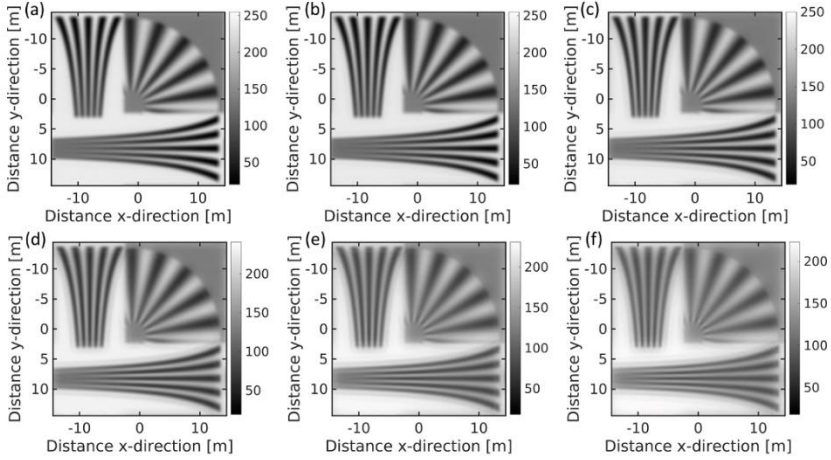


Figure 6. Image estimations using image chain simulations for obscuration diameter values of: (a) no obscuration, (b) 9.4 cm, (c) 19.0 cm, (d) 28.4 cm, (e) 38.0 cm, (f) 42.7 cm.

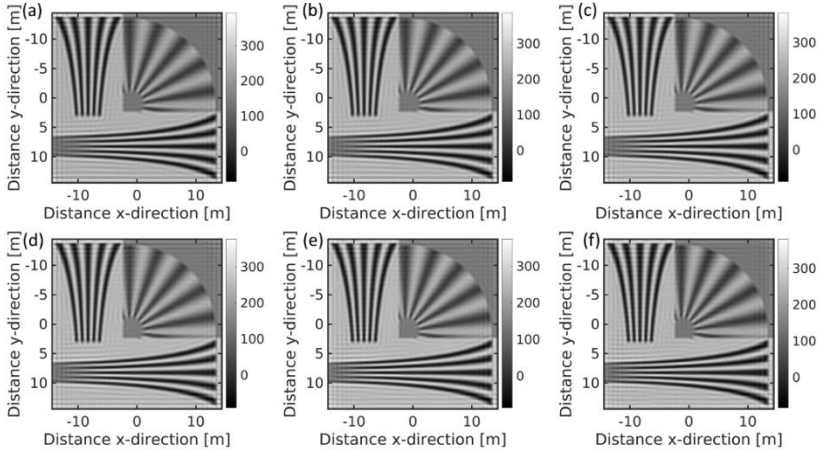


Figure 7. Image restoration results using Wiener filter method for obscuration diameter values (a) no obscuration, (b) 9.4 cm, (c) 19.0 cm, (d) 28.4 cm, (e) 38.0 cm, (f) 42.7 cm. The difference between restored images are minor and we only show one of the restored images in Figure 7. There is a clear quality recovery compared to the degraded images. In order to quantitatively compare images and image quality, we calculate the GIQE values. We plot these values as a function of obscuration diameter in Figure 8, and observe a first increasing then decreasing trend. GIQE 4.0 values get a maximum value when obscuration diameter is equal to $D_{obs} = 38.0cm$. Results are also tabulated in Table-1.

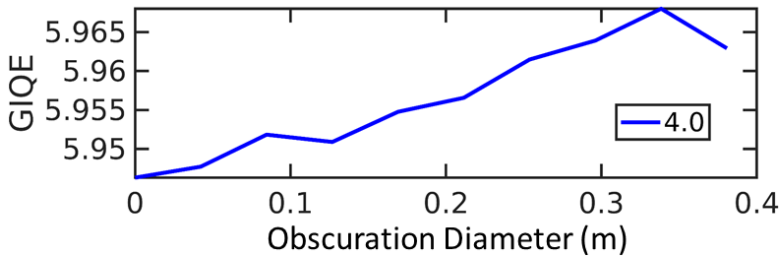


Figure 8. General image quality equation (GIQE) variation as a function of obscuration diameter.

3.3. Effect of Number of Spider Arms

We studied the case when there are three, four, and five spider arms to hold the secondary mirror in stable position. As the sizes of the main mirror and secondary mirror increases, the number of spider arms needed to increase for mechanical stability. In Figure 9, we show the geometry of apertures with three, four, and five spider arm cases.

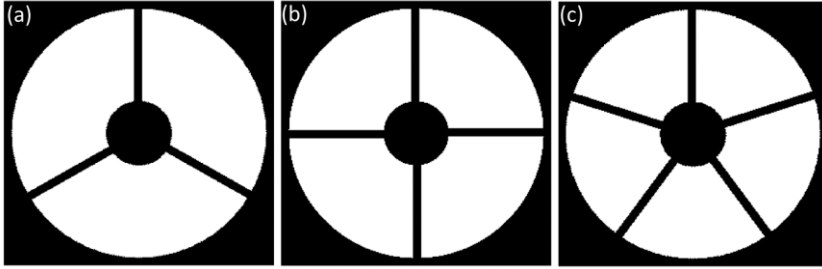


Figure 9. Schematics of the apertures with (a) 3 spider arms, (b) 4 spider arms, (c) 5 spider arms.

In Figure 10, ICS results were shown for the three cases. The visible inspection yields almost equal degradation among images. In Figure 11, we show the restored image cases. We see a significant image quality improvement for the restored images. However, difference between different number of spider arms cases was minor.

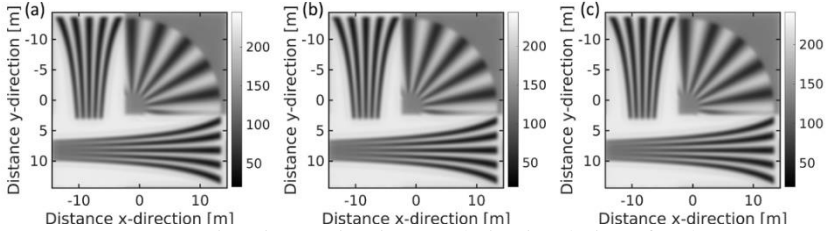


Figure 10. Image estimations using image chain simulations for the apertures with (a) 3 spider arms, (b) 4 spider arms, (c) 5 spider arms.

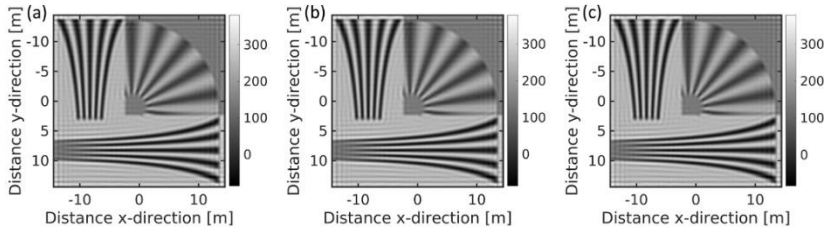


Figure 11. Image restoration results using Wiener filter method for the apertures with (a) 3 spider arms, (b) 4 spider arms, (c) 5 spider arms.

Finally, we tabulate the correlation coefficient values for the three cases in Table 1. We see that number of spider arms does not change the correlation coefficient value significantly. It was varied from 0.834 to 0.838, and 0.833 from 3 to 4, and 5 arms.

CONCLUSIONS

Optical aperture geometry has critical effect on image quality for both space-based earth observation and space-based space observation systems. We show that for optical aperture diameter variation from 35cm to 110cm, the correlation coefficient changes from 0.672 to 0.917. Moreover, for obscuration diameter variation from zero to 42.7cm, the correlation coefficient changes from 0.842 to 0.747, and general image quality equation (GIQE) value changes from 6.034 to 6.040. Furthermore, when the number of spider arms holding the secondary mirror increased from three to four, and five, we saw the correlation coefficient changes from 0.834 to 0.838, and 0.833. As the image restoration algorithms applied to the degraded images, the image quality increased significantly for all cases. For the obscuration size study, we saw a slightly increasing then decreasing behavior in both GIQE and correlation coefficient values.

Acknowledgements

The author (KBA) has been supported by the Turkish Academy of Sciences (TÜBA), in the framework of the Young Scientist Award Program (TÜBA-GEBİP/2020). The research study presented in this article was based on the views of the authors and does not reflect on the official policy of the TÜBİTAK, the Ministry of Industry and Technology, or the Turkish government.

Conflict of interest

No conflict of interest was declared by the authors.

Author contributions

All authors have contributed equally to the relevant work.

REFERENCES

- [1] K. B. Alici, "Halka Biçimli Optik Açıklıkların Uydu Görüntü Kalitesine Etkisi," presented at the Aviation Technologies and Applications Conference (ATAConf23), İzmir, 2023.
- [2] J. R. Schott, Remote sensing: the image chain approach: Oxford University Press on Demand, 2007.
- [3] J. Schott, A. Gerace, S. Brown, M. Gartley, M. Montanaro, and D. C. Reuter, "Simulation of image performance characteristics of the Landsat data continuity mission (LDCM) thermal infrared sensor (TIRS)," *Remote Sensing*, vol. 4, pp. 2477-2491, 2012.
- [4] J. B. Breckinridge, J. E. Harvey, K. Crabtree, and T. Hull, "Exoplanet telescope diffracted light minimized: the pinwheel-pupil solution," pp. 510-519.
- [5] J. E. Harvey, J. B. Breckinridge, R. G. Irvin, and R. N. Pfisterer, "Novel designs for minimizing diffraction effects of large segmented mirror telescopes," pp. 121-134.
- [6] J. E. Harvey and C. Ftaclas, "Diffraction effects of telescope secondary mirror spiders on various image-quality criteria," *Applied Optics*, vol. 34, pp. 6337-6349, 1995.
- [7] L. Zhu, P. Yang, L. Wen, L. Zhao, C. Guan, and B. Xu, "An image-based alignment errors correction method for segmented fresnel primary mirror," *IEEE Photonics Journal*, vol. 12, pp. 1-14, 2020.
- [8] I. Laginja, R. Soummer, L. M. Mugnier, L. Pueyo, J.-F. Sauvage, L. Leboulleux, L. Coyle, and J. S. Knight, "Analytical tolerancing of segmented telescope co-phasing for exo-Earth high-contrast imaging," *Journal of Astronomical Telescopes, Instruments, and Systems*, vol. 7, pp. 015004-015004, 2021.
- [9] N. Lee, S. Pellegrino, and Y.-H. Wu, "Design algorithm for the placement of identical segments in a large spherical mirror," *Journal of Astronomical Telescopes, Instruments, and Systems*, vol. 1, pp. 024002-024002, 2015.
- [10] S.-D. Shen, X.-Q. Cui, and Y. Zhang, "Simulation and analysis of co-phasing errors of the segmented primary mirror tiled by hexagonal segments in LOT," *Research in Astronomy and Astrophysics*, vol. 21, p. 245, 2021.
- [11] M. Troy and G. Chanan, "Diffraction effects from giant segmented-mirror telescopes," *Applied Optics*, vol. 42, pp. 3745-3753, 2003.
- [12] Y. Zheng, L. Tang, B. Liang, and Y. Li, "Primary mirror segmentation for large optical telescopes: an inverse map projection approach," *Applied Optics*, vol. 60, pp. 6015-6022, 2021.
- [13] L. Leboulleux, J.-F. Sauvage, L. A. Pueyo, T. Fusco, R. Soummer, J. Mazoyer, A. Sivaramakrishnan, M. N'diaye, and O. Fauvarque, "Pair-

- based Analytical model for Segmented Telescopes Imaging from Space for sensitivity analysis," *Journal of Astronomical Telescopes, Instruments, and Systems*, vol. 4, pp. 035002-035002, 2018.
- [14] S. Itoh, T. Matsuo, H. Shibai, and T. Sumi, "Point spread function of hexagonally segmented telescopes by new symmetrical formulation," *Monthly Notices of the Royal Astronomical Society*, vol. 483, pp. 119-131, 2019.
- [15] R. Pourcelot, E. H. Por, M. N'Diaye, H. Benard, G. Brady, L. Canas, M. Carbillet, K. Dohlen, I. Laginja, and J. Lugten, "Low-order wavefront control using a Zernike sensor through Lyot coronagraphs for exoplanet imaging-II. Concurrent operation with stroke minimization," *Astronomy & Astrophysics*, vol. 672, p. A73, 2023.
- [16] J. B. Breckinridge, T. Hull, and J. E. Harvey, "Innovative aperture segmentations control image plane diffraction," pp. 2055-2071.
- [17] H. Philip Stahl, "Advanced ultraviolet, optical, and infrared mirror technology development for very large space telescopes," *Journal of Astronomical Telescopes, Instruments, and Systems*, vol. 6, pp. 025001-025001, 2020.
- [18] M. Lendermann, J. S. Q. Tan, J. M. Koh, and K. H. Cheong, "Computational imaging prediction of starburst-effect diffraction spikes," *Scientific reports*, vol. 8, p. 16919, 2018.
- [19] H. Philip Stahl, G. Kuan, W. R. Arnold, T. Brooks, J. Brent Knight, and S. Martin, "Habitable-Zone Exoplanet Observatory baseline 4-m telescope: systems-engineering design process and predicted structural thermal optical performance," *Journal of Astronomical Telescopes, Instruments, and Systems*, vol. 6, pp. 034004-034004, 2020.
- [20] R. D. Fiete, *Modeling the imaging chain of digital cameras*: SPIE press Bellingham, 2010.
- [21] K. B. Alici, F. S. Oktem, O. Karci, A. S. Yilmaz, and O. Selimoglu, "Image Chain Simulation for Earth Observation Satellites," *IEEE Journal of Selected Topics in Applied Earth Observations and Remote Sensing*, vol. 12, pp. 4014-4023, 2019.
- [22] R. E. Introne, N. R. Block, and J. R. Schott, "Comparison of monochromatic and polychromatic modeling of sparse-aperture image quality," pp. 1944-1962.



CHAPTER 2

Aviation Technologies and Applications
E-ISBN:978-605-338-471-7
2025, chap. (2) , pp.20-40.

A COMPARATIVE NUMERICAL STUDY ON BUCKLING BEHAVIOUR OF SKIN-STRINGER AND SANDWICH PANELS

Emre APA^{1,*}, Orhan ÖZÇELİK²

ABSTRACT

In this study, global buckling behaviour of the metallic skin-stringer and honeycomb sandwich panels, which are used on the helicopter fuselage sections, is analysed. The metallic skin-stringer having different stringer cross sectional areas (z-, c-, and omega-section) and the metallic honeycomb sandwich panels in three variants (panels with longitudinal doublers, with transverse doublers, and without doublers) are examined with finite element simulations. The linear eigenvalue buckling analysis is used to calculate the critical global buckling load for simply supported boundary conditions.

The most durable skin-stringer panel against the global buckling failure is determined to be the panel reinforced with the omega stringers. The panel with z stringers is found to be the least durable configuration against global buckling. The buckling strength of the panel with omega stringer is 13.1 and 15.6 percent higher than the panels with c and z stringers, respectively. The most durable honeycomb sandwich panel configuration against global buckling is determined to be the panel with transverse doublers. The panel without any doublers is found to be the least durable configuration against global buckling. The buckling strength of the panel with transverse doublers is 11.8 and 12.6 percent higher than the panels with longitudinal doublers and without any doublers, respectively.

Honeycomb sandwich panels exhibit higher buckling strength compared to the skin-stringer panels. Critical buckling loads of the sandwich panels per kilogram are greater than those of the skin-stringer panels. Considering the structural, manufacturing, and environmental requirements, metallic honeycomb sandwich panels can be utilized as side panels of a helicopter fuselage and they can give better buckling performance per unit weight. Two panel concepts also can be used on different sections of a helicopter fuselage as long as they meet the structural requirements.

Keywords: Stiffened panel, sandwich panel, global buckling, linear buckling analysis.

*Corresponding Author: emre.apa.93.20@gmail.com

¹0009-0001-6029-0981, Aerospace Engineering, Faculty of Aeronautics and Astronautics, Ankara Yıldırım Beyazıt University, Ankara, Turkey

²0000-0002-4353-5246, Aerospace Engineering, Faculty of Aeronautics and Astronautics, Ankara Yıldırım Beyazıt University, Ankara, Turkey

1. INTRODUCTION

Aluminium alloys have consistently served as the predominant material for structural components in aircraft. The preference for aluminium is rooted in considerations such as performance characteristics, cost-effectiveness, adherence to design specifications, feasibility in manufacturing, and easy supply chain.

Buckling, stemming from compression, shear, or their combination, represents the usual load scenarios for fuselage or wing structures. In aerostructures, there is a defined threshold of acceptable buckling that structures can undergo before reaching ultimate load conditions that indicate the catastrophic failures.

In this study, metallic curved skin-stringer panels which have the different types of stringer cross section areas and metallic curved honeycomb sandwich panel that possess the distinct variants such as longitudinal and transverse doublers are examined numerically with finite elements methods in terms of global buckling behaviour to contribute to a side panel of a helicopter fuselage section. In order to carry out the study, the linear eigenvalue buckling analysis is used under particular boundary conditions. Totally, six different panel configurations are investigated to reach the best global buckling behavior among them.

Although numerous studies on stiffened panel structures exist in the literature, this study is managed due to the deprivation of research studies that specify the most efficient types of stringer cross sections concerning linear buckling behaviours. Additionally, there is a gap in studies addressing the linear buckling behavior of metallic honeycomb sandwich panels, prompting a focused investigation in this area that is related to the aero panel structures.

Furthermore, research in the literature reveals numerous boundary conditions that may not be sufficiently advantageous for aerospace structures. To address this gap, this study applies the closest boundary conditions to the panel structures.

1.1. Literature Survey

Two distinct literature surveys that are related to buckling of stiffened and sandwich panels are given under this subtitle of the study.

1.1.1. Stiffened Panel Structure Literature Review

Aluminium alloys have secured their position in pivotal locations and components of aircraft ever since the aviation industry diverged from other engineering sectors. Among these applications, the utilization of aluminium alloys is notably evident in the construction of skin-stringer panel structures.

CHAPTER 2: A COMPARATIVE NUMERICAL STUDY ON BUCKLING BEHAVIOUR OF SKIN-STRINGER AND SANDWICH PANELS

In conventional aircraft design practices, the incorporation of stringers aligned in the longitudinal direction and frames arranged in the circumferential direction constitutes a fundamental strategy for reinforcing the skin of the aircraft. Stringers serve as pivotal components in preventing various failure modes, particularly the onset of buckling and bending failure modes.

Research on plate buckling commenced in the early 19th century, with Claude-Louis Navier being credited for deriving the stability equation for a rectangular thin plate. This derivation, dating back to 1822, is rooted in the assumptions laid out by Gustav Robert Kirchhoff [1]. Bryan, in 1891, has formulated the critical buckling stress equation for a rectangular thin plate subjected to uniaxial compression load and featuring a simply supported edge condition [1].

In Paul et al.'s study, they have focused on a standard transport aircraft wing and conducted a buckling analysis. The initial design showed susceptibility to buckling, prompting several design modifications to enhance its resilience. The study employed both finite element analysis and theoretical approaches to ensure realistic results in the wing buckling analysis for an aircraft [1].

Timoshenko and Gere have addressed the buckling problem using an alternative method. Their assumption involved the plate buckling into multiple sinusoidal half waves in the direction of compression. Additionally, they explored the buckling behaviour of uniformly compressed rectangular plates, featuring simple support along the edges perpendicular to the direction of the applied load. Simultaneously, the other two edges were subjected to various end conditions [2]. Timoshenko and Gere's research highlights that alternative stringer configurations, such as diagonal stringers, exhibit superior buckling behaviour compared to a conventional rectangular stringer stiffened structure. Timoshenko and Gere have provided a solution for an infinitely long isotropic simply supported plate, with the result being approximately 6.5% higher than the exact solution. Consequently, employing this approach may entail an expected error of this magnitude [2].

Stein has demonstrated that diagonal stiffeners possess distinct advantages over conventional rectangular stringers, particularly in terms of buckling resilience and he has compared symmetric/antisymmetric buckling patterns for a plate [3].

Thielemann has presented approximate solutions for boundary conditions involving free, clamped, and simply supported edges specifically for orthotropic materials and he compared the results each other. He has also added to the special reference in his study. Additionally, he has carried on the stability equation of a plate under uniform shear and axial loads and determined the buckling loads [4].

Paik and Thayamballi have shown a buckling behaviour for isotropic stiffened plate. The problem involving differential equations is analogous to the buckling problem of a plate with elastic restraints. This issue is resolved using the Kantorovich method, and a precise determination of the critical local buckling load is obtained through exact calculations that are accepted in the literature [5].

Yu has conducted a study on the buckling behavior of rectangular plates under mid and end loads, encompassing considerations for both elastic and plastic buckling behavior. The study also examines the influence of different plate aspect ratios, and boundary types on buckling. The considered plate is simply supported along two opposite edges parallel to the direction of applied loads while the remaining two edges can assume any combination of clamped, simply supported, and free edge boundary conditions that are specific for his study [6].

1.1.2. Sandwich Panel Structure Literature Review

Sandwich structures stand out as notably lightweight components when contrasted with other structures like metallic alloys in aerospace engineering. The utilization of metallic sandwich panel structures is prevalent in aircraft platforms where elevated mechanical properties are necessary.

Concerning the potential of buckling failure mode, this specific subassembly assumes a pivotal role. Notably, metallic sandwich panels exhibit considerable resilience against the threats of both buckling and bending failure modes, which could otherwise lead to severe consequences for an aircraft or rotorcraft.

Luqman and Farzana have studied on comparison of buckling strength between metallic and composite panel experimentally [7]. This experiment was conducted with specific parameters which includes boundary conditions etc. and the subsequent results were analysed in accordance with these inputs. Upon evaluating the outcomes, it became evident that the aluminium carbon fibre reinforced polymer sandwich panel exhibited

superior buckling strength when compared to the pure aluminium sandwich panel of the same dimensions. Furthermore, a noticeable trend was observed wherein the buckling load carrying capacity of the aluminium carbon fibre reinforced polymer sandwich panel decreased as its thickness was reduced.

Sayyad and Ghugal have shown bending, buckling and free vibration of laminated composite and sandwich beams, but mostly it has been about to civil engineering applications [8]. They have presented that there are many theories such as equivalent single layer, layerwise/zigzag, finite element method, Carrera unified formulation etc. to design a sandwich panel. Similar to study of Sayyad and Ghugal, Abrate and Di Sciuva have presented equivalent single layer theories for composite and sandwich structures including classical, first, second and third order formulations, polynomial and non-polynomial displacement methods [9].

Hua et al. have introduced a novel finite element model for determining the global and local buckling behaviours of sandwich beams [10]. The suggested one-dimensional finite element model was formulated upon a comprehensive kinematics model tailored for investigating both global and local instability modes in a sandwich structure. They observed that the critical load determined through the one-dimensional numerical element model compared to the critical loads derived from the two-dimensional numerical element model, demonstrated satisfactory agreement [10].

Vinson has introduced specific models to analyse buckling behavior modes and post-buckling failure modes under in-plane compressive loads. Vinson's objective was to demonstrate the optimal design of composite honeycomb sandwich panels under uniaxial compression [11].

Coburn and Weaver have showed the analysis, design, and optimization of variable-stiffness sandwich panels, including buckling considerations [12]. The study conducted by Coburn and Weaver also involved subjecting the panels to in-plane compressive loads and examining phenomena such as panel buckling, shear crimping, skin wrinkling, and more.

2. THEORY OF BUCKLING FOR THIN PLATES

Buckling is an instability phenomenon that commonly occurs in compressed slender elements, such as airframe stringers, and skin etc. It can be identified by abrupt displacements in the transverse direction, perpendicular to the direction of compression. This behaviour is critical to understand in the design and analysis of structures to prevent potential failures and ensure the overall structural integrity of the components.

Buckling in structures can be triggered either by direct pure compression loads or by shear loads. In both cases, the stability of the structure may be affected, potentially leading to a loss of load-carrying capacity and structural integrity. Elastic buckling is characterized by the point at which a structure loses its stability, leading to the emergence of significant out-of-plane deflections [13]. The elastic buckling load is the beginning point of this behavior, typically linked to the structure's minimum eigenvalue. Within this range, the stresses applied remain below the yielding point. Consequently, when the structural element is unloaded, this element returns to its initial shape.

On the other hand, flat sheets, as illustrated in Figure 1, play a crucial role as essential structural elements and find widespread use within the aerospace industry. Geometrically, they can have either straight or curved lines. Similar to beams, plates or sheets do not demonstrate only function as structural components but can also cover entire structures, as seen in examples like aircraft panels that includes skin-stringer structures or metallic sandwich panels. They can possess different boundary conditions. Given the presence of compression loads acting on these structural elements, a comprehensive understanding of the stress intensities that may lead to the buckling of thin sheet panels becomes imperative [13]. The critical value of the compression stress on a flat sheet can be found with Eq. (equation) 1.

$$\sigma_{xv} = \frac{(N_x)_{cr}}{h} = \frac{k_c \pi^2 E}{12(1 - \nu^2)} \frac{t^2}{b^2} \quad (1)$$

where; k_c is buckling coefficient, E is modulus of elasticity, ν_e is elastic Poisson's ratio, b is short dimension of plate or loaded edge, t is sheet thickness.

The Figure 1 depicted also illustrates curves designed to determine the buckling coefficient across different boundary or edge conditions, in relation to the " a/b " ratio of the thin sheet.

The letter " C " at the edge signifies a clamped or fixed condition against rotation, while the letter " F " indicates a free edge. " SS " stands for simply supported or hinged. As per Figure 1, the smallest critical loads are evidently acquired at the free edges. Under such circumstances, the plate exhibits behavior akin to that of a column and is denoted as a wide column.

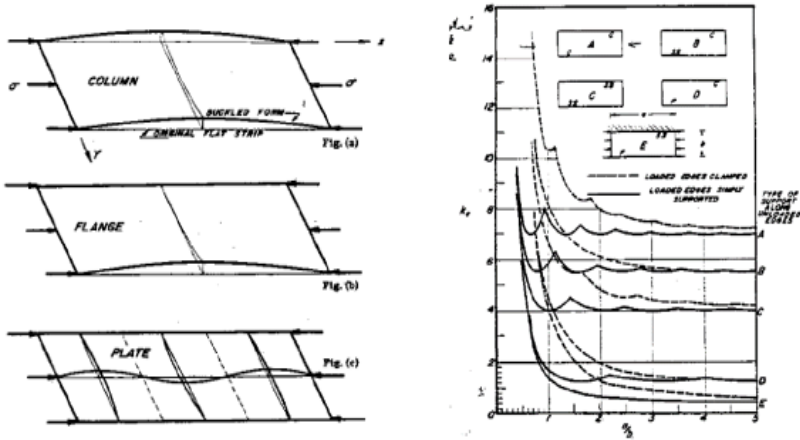


Figure 1. General boundary conditions of buckling situation [13].

2.1. Linear and Nonlinear Buckling Analysis

Linear buckling is an engineering concept using linear theory. The structure can only maintain a certain load level in compression. Linear buckling analysis can be applicable and effective for column and plate structures under certain conditions, especially when dealing with slight manufacturing imperfections or slightly eccentric loading.

The process of linear buckling analysis isolates the buckling modes of a structure based on distinct loading and boundary conditions, assuming that stiffness remains constant throughout the analysis [14]. Additionally, it is assumed that the structure in the pre-buckled configuration is perfectly straight and elastic. Nevertheless, in real-world scenarios, once the initial buckling mode emerges, the stiffness within the buckled region undergoes changes, thereby causing significant shifts in the internal load distribution within the structure. To ensure reliable outcomes for linear buckling, it becomes essential to incorporate the engineering judgments of experts in the assessment process.

Nonlinear buckling analysis considers pre-buckled deformations, geometric nonlinearity, and material nonlinearity effects [14]. This type of analysis is generally more accurate compared to linear analysis. However, it is not automatically more accurate; rather, its advantage lies in its ability to account for additional physical effects and calculate the true physical behaviour of structures. Nonlinear analysis methods do not yield a specific

buckling load value directly. Instead, the onset of buckling needs to be determined from the analysis results. This can be achieved by gradually increasing the applied load on the model until a deviation in the linear proportionality of the load-deformation relationship occurs. In nonlinear analysis, the stiffness matrix is updated at each step of the analysis as a result of the deformations occurring under loading increments [14].

2.2. Local and Global Buckling Approach

Local buckling is commonly associated with detailed components of the structure, such as skin buckling occurring between stringers or elements of stringers and frames. These localized buckling phenomena can arise due to the interaction of various structural elements, and they play a crucial role in the overall structural integrity and performance of the aircraft. Local buckling does not cause distortion in the axis of the entire member, but it jeopardizes the strength of the cross-section of the structural member.

Global buckling is the most critical type of buckling as it results in the overall structure's inability to carry any additional load, often leading to catastrophic failure. In many cases, local buckling tends to occur in the structure before global buckling takes place. Global buckling is characterized by a significant distortion or buckling of the longitudinal axis of the member, which can lead to catastrophic failure of the structure.

3. NUMERICAL ANALYSIS METHODS AND MODEL DEFINITIONS

3.1. General Approach to Linear Eigenvalue Buckling Analysis

Linear buckling analysis, alternatively referred to as eigenvalue buckling analysis, identifies the elastic critical instability loads and their corresponding modes of instability under loads [14]. This kind of analysis does not include material or geometrical nonlinearities and imperfections. Additionally, it estimates the sensitivity of a structure that is subjected to a specific parametric loading, to particular deformation patterns. In this sort of the finite element analysis, achieving the critical buckling load involves a singular stiffness matrix solution [14].

In linear eigenvalue buckling analysis, the lowest value of the eigenvalues is taken into consideration and the subsequent eigenvalues have relevance mainly for local buckling and should be interpreted cautiously, as they may not always carry physical significance [14] and the critical buckling load is given in Eq. 2.

$$P^B = \lambda_i Q^B \quad (2)$$

where; Q^B is incremental load, λ_i is extracted eigenvalues, and P^B is critical buckling load. In a nutshell, once the related eigenvalue is acquired and it is multiplied by the applied load, it signifies the initiation of panel buckling when the calculated buckling is localized in a specific area. Afterwards, when the critical buckling load is calculated on the panel, it signifies global buckling and, thus, the maximum load-carrying capacity of the panel is determined.

3.2. Metallic Stiffened Panel Design

A skin contains multiple fuselage panels, whereas a shell or a stiffened panel is formed by the assembly of longitudinal stringers and panels. Main functions of the skin are to bear and transfer the load induced by aerodynamic forces, to collaborate with the stringers to support bending and buckling forces, to resist torsional forces against shear stress, to safely maintain fuel pressure within the aircraft.

Skin-stringer assembly is essentially known as cover of an aircraft and plays a crucial role for structural integrity. Stringers that lie in longitudinal direction can be riveted or bonded to the skin. Skin-string assembly commonly is used in numerous sections of an aircraft. For example, while the upper covers are designed to bear buckling that causes compression instability, the lower covers are tailored to withstand ultimate tensile and fatigue loads.

The fuselage, except for helicopter fuselages, experiences loading due to pressurization which affects some sections and mechanical forces like buckling, bending and, shear stress. In order to support these loads, the fuselage panels often need to be strengthened using frames and stringers. Stringers are responsible for picking up longitudinal loads, frames carry transverse loads and distribute concentrated loads into fuselage shell, and the skin transfers both loads to whole structure through fasteners, adhesives.

3.3. Metallic Sandwich Panel Design

Another viable configuration for metallic panel structures is the sandwich structure. This design consists of a low-density core positioned between two face sheets. Essentially, this concept benefits the principles that are akin to plate structures, involving skin and stringers. In this scenario, the face sheets handle the normal or axial forces while the sandwich core

between them fulfils the role of providing diagonal shear functionality. However, the distinctive characteristic of the sandwich structure lies in its ability to carry loads in two directions. These structures find widespread application in assemblies like fuselage sidewall panels, floor and ceiling panels etc.

Typically, a sandwich structure is made of two face sheets that are bonded with adhesive to a thick and lightweight core relative to face sheets or plates. Since face sheets serve as the primary load carrying components within sandwich structures, they should have adequate thickness. When it comes to metallic honeycomb cores that have fairly low density, these components give good mechanical properties in terms of shear and compressive loading condition. The utilization of sandwich structures is rooted in their favourable ratio of flexural strength that means buckling and bending stiffness to weight. In other words, there are stiffness increases more against minimal weight gain.

3.4. Metallic Panel Model Definitions

In this study, six different metallic panel structure configurations are given and these panels are employed for linear eigenvalue buckling analysis. All three-dimensional panel models are created by using CATIA V5 6R2020 Software and all geometrical properties of the panel elements are given in the Table 1.

Table 1. Geometrical and material properties of metallic panels.

	Z Stringer	Omega Stringer	C Stringer	Outer Skin	Inner Skin	Honeycomb Core	Longitudinal Doubler	Transverse Doubler
Thickness (mm)	1.016	0.6	0.8	1.016	0.3	24.7	0.3	0.3
Length (mm)	1100	1100	1100	1100	1069	1070	1100	70
Height (mm)	25	25	25	N/A	N/A	N/A	N/A	N/A
Width (mm)	29	42	22	560	530	531	70	560
Material	Al 2024 T3	Al 2024 T3	Al 2024 T3	Al 2024 T3	Al 2024 T3	Al 5052	Al 2024 T3	Al 2024 T3

In order to implement the finite element analysis steps, the Hyperworks software that covers each progress is used as pre-processor and post-processor. In this study, the shell elements with four nodes are used for modelling the metallic panels. Thin panels no matter they are flat or curved are modelled as a shell structure in the finite element analysis since the shell models offer accurate responses for thin-walled structures without calculating the stresses along the thickness of the plate.

3.4.1. Metallic Skin-Stringer Panel Numerical Model Description

CQUAD4 element type, quadrilateral element, is used in order to model the skin-stringer metallic panels and it uses six degrees of freedom per each node. The models are created with very fine mesh, approximately 2x2 mm element size. Therefore, such a dense mesh configuration results in pretty much precise forecast of displacements, stresses, and linear buckling behaviour in reasonable processing time for this study. Quantities of the numerical elements for each component on the related panels can be seen in Table 2 and Figure 2 demonstrates the skin-stringer panels mesh view, respectively.

Table 2. Number of elements for each skin-stringer panel.

Panel Type	Number of Elements
Z Section Stringer-Skin Assembly	228250
Omega Section Stringer-Skin Assembly	277150
C Section Stringer-Skin Assembly	247500

As a contact property, TIE contact property is used to define the interface between the lower surface of the stringers and the upper surface of the skin. This definition is surface to surface discretization. TIE contact restricts the relative displacements between nodes is zero. TIE contact is based on multi point constraints.

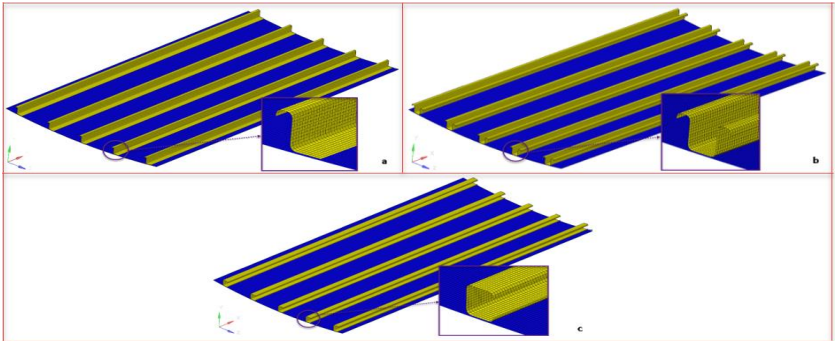


Figure 2. Different stringers-skin assembly mesh view: (a) z cross section stringer-skin panel; (b) omega cross section stringer-skin panel; (c) c cross section stringer-skin panel.

3.4.2. Metallic Honeycomb Sandwich Panel Numerical Model Description

Conventional layered shell elements models are used in order to model the metallic honeycomb sandwich panel numerically. This method offers excellent global buckling behaviour since it has simplicity and practical. CQUAD4 element type, quadrilateral element, is used in order to model

the sandwich panels and it uses six degrees of freedom per each node. Similar to the skin-stringer panels, the models of the sandwich panels are created with very fine mesh, approximately 2x2 mm element size in order to get exact forecast of displacements, stresses, and linear buckling behaviour in reasonable processing time for this study. Quantities of the numerical elements for each panel can be seen in Table 3 and Figure 3 demonstrates the honeycomb sandwich panels.

Table 3. Number of elements for each honeycomb sandwich panel.

Panel Type	Number of Elements
Honeycomb Sandwich Panel Assembly	155100
Honeycomb Sandwich Panel Assembly with Longitudinal Doublers	155100
Honeycomb Sandwich Panel Assembly with Transverse Doublers	155100

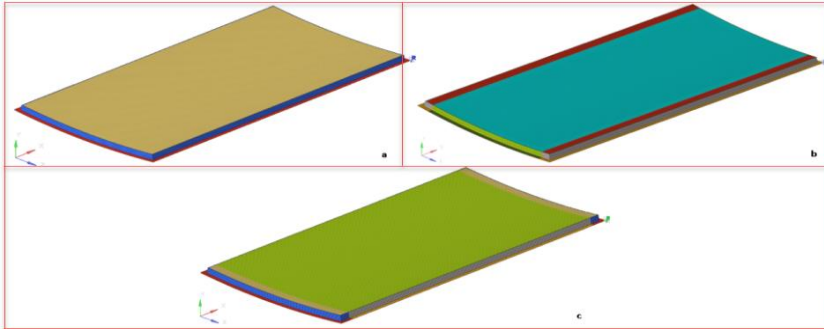


Figure 3. Different honeycomb sandwich panel mesh view: (a) panel without doublers; (b) panel with longitudinal doublers; (c) panel with transverse doublers.

3.5. Boundary Conditions and Loads

Both metallic skin-stringer panels and metallic honeycomb sandwich panel are very common structure in different sections on aircraft or rotorcraft structures. The analyses conducted in this study take into account the status and characteristics of the panels situated on the side of a helicopter fuselage.

Since boundary conditions typically work to describe constraints that mirror the real-world limitations of the structure and its mating parts. Theoretically, boundary conditions maintain the enforced rotations and displacements by other structures. In other words, they do not have exactly the dynamics of the real-world limitations. Nonetheless, boundary conditions are the representatives for showing a proximity of what occurs in real life.

CHAPTER 2: A COMPARATIVE NUMERICAL STUDY ON BUCKLING BEHAVIOUR OF SKIN-STRINGER AND SANDWICH PANELS

In this study, simply supported boundary conditions are used on the long and short edges of the panels which have the rectangular shape with curvatures for simplification. Boundary conditions are one of major inputs for panel design of aircrafts or rotorcrafts so they must be employed in appropriate ways.

The boundary conditions that are applied on the panel structures is shown in Table 4 and Figure 4. While “U” signs to the translational movement, “Rot” shows the rotational movement and the numbers 1, 2, and 3 which are used with translational and rotational movement symbols indicate X, Y, and Z axis, respectively. All axes are compatible with aircraft global axis.

Table 4. Boundary Conditions.

Boundary Code	Suppressed DOF's
1	U ₂ and Rot ₃
2	U ₂ and Rot ₁
3	U ₁ and U ₃ (except for end nodes)

In this study, only longitudinal uniaxial compression loading which is perpendicular to the short edges is taken into account. This loading is applied on the both short edges. All applied loads are considered to be applied gradually enough that inertia effects can be disregarded. In addition, pressure, temperature, and humidity effects are omitted for this study.

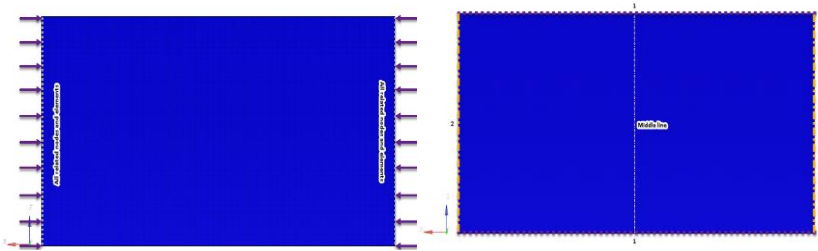


Figure 4. Boundary conditions and loads.

In this study, only longitudinal uniaxial compression loading which is perpendicular to the short edges is taken into account. This loading is applied on the both short edges. All applied loads are considered to be applied gradually enough that inertia effects can be disregarded. In addition, pressure, temperature, and humidity effects are omitted for this study.

Compression force is applied on the panels is 1 N in the $\pm X$ direction, as demonstrated typically in Figure 4. This force is separated to all related nodes equally so that all panels undergo to the same loading condition. Otherwise, the whole system can fall down as local at the weakest region of the structure.

4. NUMERICAL ANALYSIS RESULTS

4.1. Metallic Flat Skin Panel Buckling Analysis Results

Linear eigenvalue buckling analysis is carried out on the flat skin panel in order to demonstrate complying with the analytical solution that is calculated via Eq 2.1. This analysis result creates a sanity check for the other analysis. This metallic flat skin panel has the same dimensions in terms of thickness, width and length like the curved skin panel that is unique panel for this study.

Stress and displacement distribution for the flat skin panel is demonstrated in Figure 5. Higher displacements predominantly occur on the short edges of the panel and their further, like estimated. In other words, the middle of the panel has the minimum displacements. Figure 5 also illustrates the acquisition of eigenmode configurations corresponding to various equilibrium states. In this study, four different buckling modes are calculated for this panel configuration. Because after the first four modes, the buckling modes get meaningless shapes. It is important to highlight that the critical load of the panel aligns specifically with the first buckled form featuring four mode or waves.

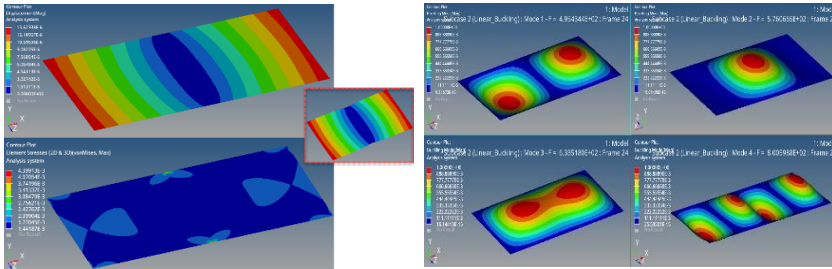


Figure 5. Linear static analysis and eigenvalues results for flat skin panel.

According to the linear eigenvalue buckling analysis result, the value of the first extracted eigenvalue is 495 and since the applied load is 1 N, the critical buckling load that indicates the global buckling behaviour is 495 N. On the other hand, analytical solution, the corresponding answer of the numerical solution, is 492.5 N by using Eq 2.1. The numerical result has a good correlation with analytical result and the deviation is under 1%. This

is desired result in terms of accuracy [14]. Table 5 shows the critical buckling loads for analytical and numerical solution on the simply supported metallic flat skin.

Table 5. Comparison between analytical and numerical solution for metallic flat panel.

	Analytical Solution	Numerical Solution	Difference
Critical Global Buckling Load [N]	492.5	495	0.507%

4.2. Metallic Curved Skin-Stringer Panel Buckling Analysis Results

Linear eigenvalue buckling analysis is carried out on all stringer-skin panel configurations in order to calculate the critical buckling load. In Figure 6, the stress and displacement distribution for each panel is illustrated. The observed distribution proves satisfactory and the higher displacements predominantly occur at the center of the panel for each panel and on the middle stringer, like estimated. Figure 6 also depicts the capture of eigenmode configurations corresponding to different equilibrium states for each panel which has different buckling modes. For instances, there are different 5, 6, 4 buckling modes for z cross section stringer-skin panel, omega cross section stringer-skin panel, and c cross section stringer-skin panel, respectively. Because after these modes, the buckling modes get meaningless shapes. It is important to highlight that the critical load of the panel aligns specifically with the first buckled form featuring these modes. Table 6 includes the critical global buckling loads for each stringer-skin panel.

Table 6. Critical global buckling loads for each stringer-skin panel.

Panel Type	Critical Global Buckling Load [N]
Z Section Stringer-Skin Panel	33868
Omega Section Stringer-Skin Panel	39141
C Section Stringer-Skin Panel	34610

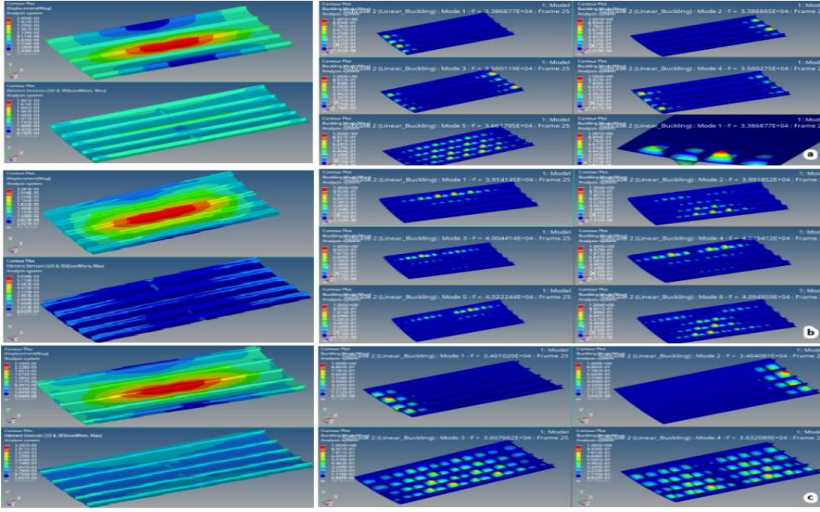


Figure 6. Linear static analysis and eigenvalue results for skin-stringer panels: (a) z cross section stringer-skin panel; (b) omega cross section stringer-skin panel; (c) c cross section stringer-skin panel.

4.3. Metallic Curved Honeycomb Sandwich Panel Buckling Analysis Results

Linear eigenvalue buckling analysis is carried out on all honeycomb sandwich panel configurations in order to calculate the critical buckling load. In Figure 7, the stress and displacement distribution for each panel is illustrated. The observed distribution proves satisfactory under the geometrical and boundary conditions like estimated. Relatively high stress distribution can be seen on the short edges because of the panel geometry. Figure 7 also depicts the capture of eigenmode configurations corresponding to different equilibrium states for each panel which has different buckling modes. For instances, there are different 6, 4, 6 buckling modes for honeycomb sandwich panel without doublers, honeycomb sandwich panel with longitudinal doublers, and honeycomb sandwich panel with transverse doublers, respectively. Because after these modes, the buckling modes get meaningless shapes. It is important to highlight that the critical load of the panel aligns specifically with the first buckled form featuring these modes. Table 7 includes the critical global buckling loads for each honeycomb sandwich panel.

CHAPTER 2: A COMPARATIVE NUMERICAL STUDY ON BUCKLING BEHAVIOUR OF SKIN-STRINGER AND SANDWICH PANELS

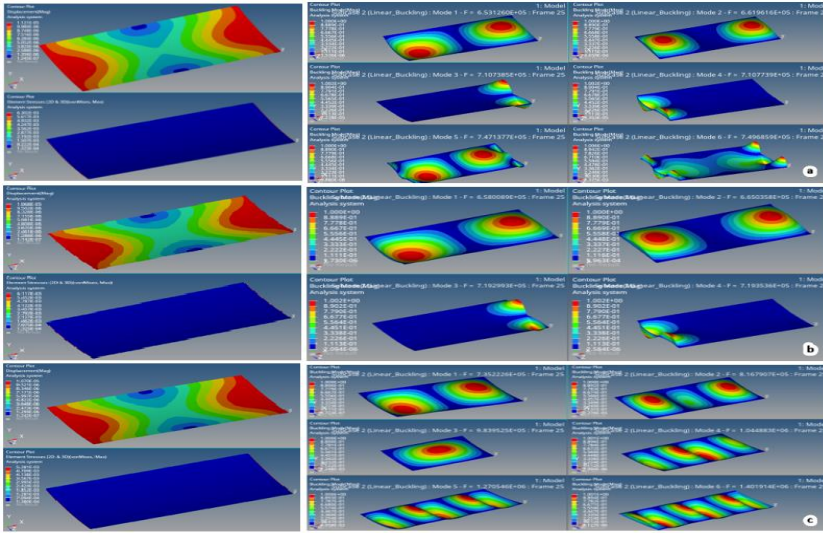


Figure 7. Linear static analysis and eigenvalue results for honeycomb sandwich panels: (a) panel without doublers; (b) panel with longitudinal doublers; (c) panel with transverse doublers.

Table 7. Critical global buckling loads for each honeycomb sandwich panel.

Panel Type	Critical Global Buckling Load [N]
Honeycomb Sandwich Panel without Doublers	653126
Honeycomb Sandwich Panel with Longitudinal Doublers	658008
Honeycomb Sandwich Panel without Transverse Doublers	735222

5. CONCLUSION

According to the Table 6, even though the critical global buckling loads are similar to each other, the panel which has omega cross section stringer-skin combination is the most durable configuration among other panels, since the omega cross section stringer has one more outer flange compared to the other variations. The omega cross section stringer can be thought as coupling two z design stringers in a back-to-back adjustment. After the omega cross section stringer-skin panel combination, the panel that has c cross section stringers ranks as second in terms of global buckling performance. When it comes to the last stringer type, the panel which possesses z cross section stringer is very close to c cross section stringer-skin panel when the global buckling performance is thought since the inertia which influences the global buckling behaviour of a panel is similar.

According to the fuselage sections of the helicopters and desired requirements, all panel variants can be used to eradicate global buckling behaviour. All stringer types offer notable compression resistance against buckling.

In a nutshell with numbers in term of the critical global buckling loads, the panel which has omega cross section stringers shows approximately 13.09% better performance than the panel which has c cross section stringers, while demonstrating about 15.57% better performance than the panel which has z cross section stringers. When it comes to the comparison between the panel which has c cross section stringers and the panel which has z cross section stringers, c cross section stringer-skin panel combination has better than z cross section stringer-skin panel combination with 2.19%.

In addition, the structural design requirements such as manufacturability, assembly requirements, and maintainability issues should be taken into consideration to design these kind of panels and for usage of these stringers.

Each panel configuration has the same weight, approximately 2.57 kg because of the equivalent of geometrical and material properties. Since Al 2024 T3 is used for each panel, there will not be a difference in terms of corrosion, lightning, and electricity etc.

Secondly, according to the Table 7, The honeycomb sandwich panel that has transverse doublers along the short edges is the most resistant to the global buckling behaviour compared to the other panels, since transverse doublers give an additional continuous thickness on loaded edges. In other words, this creates extra strength for the whole panel. Although the thickness of these transverse doublers is very thin, the influence on the overall buckling strength is massive. Secondly, the honeycomb sandwich panel that has longitudinal doublers ranks as second in terms of global buckling performance. However this configuration is the heaviest panel type. Contribution of the different sorts of doubler can be seen on the metallic honeycomb sandwich panel which has not any doublers. Therefore, this panel is end of the list in terms of the global buckling behaviour.

In a nutshell with numbers in term of the critical global buckling loads, the honeycomb sandwich panel that has transverse doublers shows approximately 11.74% better performance than the honeycomb sandwich panel that has longitudinal doublers, while demonstrating about 12.56%

CHAPTER 2: A COMPARATIVE NUMERICAL STUDY ON BUCKLING BEHAVIOUR OF SKIN-STRINGER AND SANDWICH PANELS

better performance than metallic honeycomb sandwich panel which has not any doublers. When it comes to the comparison between the panel which has longitudinal doublers and the panel which has not any doublers, the honeycomb sandwich panel that has longitudinal doublers has better than the counterpart which has not any doublers with 0.75%. According to the fuselage sections of the helicopters and desired requirements, all panel variants can be used to eradicate global buckling behaviour and they offer remarkable buckling resistance thanks to the excellent flexural strength which implies the ability of the resistance under loads.

Similar to the skin-stringer panels, the structural design requirements such as manufacturability, assembly requirements, and maintainability issues should be taken into consideration for usage of these panels. Moreover, Al 2024 T3 and Al 5052 are used for each panel, there will not be a difference in terms of corrosion, lightning, and electricity etc.

Each panel configuration has different weight because of the presence or absence of the doublers. Mass of the honeycomb sandwich panel that has not any doublers is 2.92 kg, the mass of the honeycomb sandwich panel that has longitudinal doublers is 3.00 kg and the mass of the honeycomb sandwich panel that has transverse doublers is 2.96 kg. The most important idea here is that minimal weight gain gives stiffness increases more in terms of buckling behaviour. Sandwich panel's values can be seen in Table 8.

Table 8. Critical global buckling loads per kg for each panel.

Panel Type	Critical Global Buckling Load per Kg [N]
Z Section Stringer-Skin Panel	13178.2
Omega Section Stringer-Skin Panel	15230.1
C Section Stringer-Skin Panel	13466.9
Honeycomb Sandwich Panel without Doublers	223673.3
Honeycomb Sandwich Panel with Longitudinal Doublers	219336.1
Honeycomb Sandwich Panel without Transverse Doublers	248385.8

Based on the finite element analysis results, metallic honeycomb sandwich panels have global buckling strength more compared to metallic skin-stringer panels. Furthermore, the critical global buckling load magnitudes on metallic honeycomb sandwich panels per each kg is greater than metallic skin-stringer panels. These values can be seen in Table 8. In other words, bigger global buckling critical load values with minimum weight increase can be received by using metallic honeycomb sandwich panels.

In terms of manufacturability, the metallic honeycomb sandwich panels reduce the material consumption and they have fewer structural components such as bolts, nuts etc. since they are bonded together. This also signs reduced weight, cost, and effort. It is easy to assemble them. Nonetheless, the manufacturing and repair processes might be costly. They are very susceptible to water ingress and bonding problems that weakens structural capability.

When it comes to the metallic skin-stringer panels, they are conventional fuselage shell or wing shell structures. The reasons of this that they have generally costless, familiar, proven and traditional designs compared to the metallic honeycomb sandwich panels.

Consequently, three different kinds of metallic skin-stringer panels and three different types of metallic sandwich panels are investigated for a side of a helicopter fuselage in terms of the global buckling behaviour. All panels have good resistance to the global buckling behaviour under compression loads and the metallic honeycomb sandwich panels can be used in addition to the metallic skin-stringer panels for this purpose. Based on the structural and manufacturing requirements, their usage can be purposed for a side of a helicopter fuselage and it can give better buckling performance as well as weight. In addition, two panel concepts can be used together at the same time if they are in line with the structural requirements which are used in aerostructures.

Acknowledgements

No Acknowledgements was declared by the authors.

Conflict of interest

No conflict of interest was declared by the authors.

Author contributions

Orhan ÖZÇELİK contributes to the theoretical examination and research sections of thin plates in terms of buckling. Emre APA has provided primary contributions to the following areas: conceptual work and requirements determination of the project, structural design and analysis activities, technical literature review, theoretical and numerical examination of the project, and interpretation of the results.

REFERENCES

- [1] Paul, A., & George, S. P. (2014, October). Buckling analysis of wing upper skin panels of a transport aircraft. *International Journal of Science, Engineering and Technology Research*, 3(10), 2868-2872
- [2] Timoshenko SP, Gere JM. *Theory of Elastic Stability*. Second ed. New York: Mc Graw-Hill; 1961.
- [3] Stein, M., Ne, J., Buckling stresses of simply supported rectangular at plates in shear, NACA-TN-1222, 1947.
- [4] Thielemann, W. (1950). Contribution to the problem of buckling of orthotropic plates, with special reference to plywood (No. NACA-TM-1263).
- [5] Paik, J. K., & Thayamballi, A. K. (2000). Buckling strength of steel plating with elastically restrained edges. *Thin-Walled Structures*, 37(1), 27-55.
- [6] Yu, C. (2003). Buckling of rectangular plates under intermediate and end loads. MS Thesis, National university of Singapore, Department of civil engineering, Singapore.
- [7] Ahamed, S. R., Luqman, S. M., Purushotham, G., Dsouza, V., & Farzana, S. (2018). Comparison of buckling strength between metallic and composite panel. *Materials Today: Proceedings*, 5(1), A1-A10.
- [8] Sayyad, A. S., & Ghugal, Y. M. (2017). Bending, buckling and free vibration of laminated composite and sandwich beams: A critical review of literature. *Composite Structures*, 171, 486-504.
- [9] Abrate, S., & Di Sciuva, M. (2017). Equivalent single layer theories for composite and sandwich structures: A review. *Composite Structures*, 179, 482-494.
- [10] Hua, H., Belouettar, S., Potier-Ferry, M., and Makrادی, A., 2009, "A Novel Finite Element for Global and Local Buckling Analysis of Sandwich Beams," *Composite Structures*, 90, pp. 270–278.
- [11] Vinson, J. R. (1986). Optimum design of composite honeycomb sandwich panels subjected to uniaxial compression. *AIAA journal*, 24(10), 1690-1696.
- [12] Coburn, B. H., & Weaver, P. M. (2016). Buckling analysis, design and optimisation of variable-stiffness sandwich panels. *International Journal of Solids and Structures*, 96, 217-228.
- [13] Bruhn F.R. *Analysis and Design of Flight Vehicles Structures*, 1973.
- [14] ABAQUS, "Version 6.14 user's manual", SIMULIA, World Headquarters, Providence, RI, USA, 2014.



CHAPTER 3

Aviation Technologies and Applications
E-ISBN:978-605-338-471-7
2025, chap. (3) , pp. 41–58.

NUMERICAL AEROELASTICITY ANALYSIS OF WINGS

Mert Atas^{1,*}, Mustafa Şamil FUTTU², Reza AGHAZADEH³

ABSTRACT

Aeroelasticity is the term used to decipher the field of study related to the interaction between the deformation of an elastic structure in air flow and the resulting aerodynamic force. The purpose of this article is to study the science of Aeroelasticity theoretical and analysis as Static Aeroelasticity. This study is carried out under two main headings: theory and analysis. First, the necessary equations are derived. The angle changes up to the maximum speed at which the wind tunnel can exit have been obtained one by one. The obtained data is analyzed to prove its correctness. Various flow analyses are performed using the ANSYS program. The properties and structure of the material to be used in the analysis and theory section. Galvanized steel has been selected as the material for the rod. It is considered a metal commonly used in aviation. During the airfoil selection, a preference was given to choosing a chamfered airfoil. In this article, NACA 2411 airfoil is selected to obtain more optimal results. The analysis of this airfoil is conducted, and results are obtained using the XFLR5 program. The lift coefficient and drag coefficient are obtained, followed by testing the compatibility of theoretical values with the analysis results. It observes the values obtain here are consistent at a speed of 20 *m/s*. In conclusion, this article demonstrates the compatibility between the analysis and theoretical experiments of the airfoil taken at a specific cross-section, simulating aircraft wing structures.

Keywords: Aeroelasticity, airfoil, aerodynamic force

*Corresponding Author: mertatas17@gmail.com

1 0009-0001-4743-2471, Faculty of Aeronautics and Astronautics, University of Turkish Aeronautical Association, Ankara,

TÜRKİYE, mertatas17@gmail.com

2 0009-0004-8400-6510, Faculty of Aeronautics and Astronautics, University of Turkish Aeronautical Association, Ankara,

TÜRKİYE, mustafafuttu1@gmail.com

3 0000-0003-4549-7068, Assoc. Prof., Faculty of Aeronautics and Astronautics, University of Turkish Aeronautical Association, Ankara, TÜRKİYE, raghazadeh@thk.edu.tr

ABBREVIATION

Abbreviation	Definition
C_D	Drag Coefficient
L	Lift Force
D	Drag Force
	Lift Coefficient
C_L	Distance from Leading Edge to
x_0	Shaft Position
m	Mass of Airfoil
x_{ac}	Distance from Leading Edge to
	Aerodynamic Point
	Moment Coefficient
M_{ac}	Distance from Leading Edge to
x_{cg}	Airfoil CG
k	Rotational Stiffness Coefficient
θ	Angle of Twist
α	Angle of Attack
α_r	Rigid Angle of Attack
q	Dynamic Pressure
	Rigid Lift Force
L_{rigid}	Rigid Lift Force Coefficient
$C_{L\alpha}$	Velocity
U	Density of Fluid
ρ_∞	Gravitational Acceleration
g	Polar Moment of Inertia
J	Radius of Rod
R	Shear Modulus
G	Weight of Airfoil
W	Chord of Airfoil
c	Mean Aerodynamic Chord
C_{Mac}	Coefficient
S	Wing Area
L	Length of Rod

1. INTRODUCTION

Aeroelasticity, the study of the interaction between aerodynamic forces, structural dynamics, and elastic deformations, stands as a crucial field influencing the design and performance of aircraft. In this article, the examination of static aeroelasticity has emerged as a critical area, focusing on understanding the structural response of aircraft components to aerodynamic loads.

To comprehend the intricate interplay between static aeroelasticity and nonlinear effects, recent research has concentrated on a select group of references, specifically within the range of [1-4]. These references have been instrumental in shedding light on the nuanced interactions between structural deformations and aerodynamic forces, providing valuable insights that contribute to the advancement of aerospace engineering. Researchers have extensively investigated static aeroelasticity aspects to unravel the complexities governing the behavior of flexible structures subjected to aerodynamic loads. This literature review draws upon key contributions from seminal works, specifically referencing [5], [6], and [7], to provide a comprehensive overview of the advancements in the realms of static aeroelasticity.

This research centers around a theoretical evaluation of static aeroelasticity utilizing a wall-mounted model as a representative platform. Additionally, a theoretical model incorporating a galvanized steel shaft has been analyzed in detail to investigate the consistency between theoretical and analytical values. The theoretical model has been examined through mathematical and analytical methods, and the results have been compared with analyses conducted at an airspeed of 20 m/s. Significantly, a concurrence between theoretical and analytical assessments has been observed at this velocity, indicating the alignment of theoretical predictions with practical observations.

The harmony derived from the combination of theoretical and analytical results contributes to the fundamental understanding of static aeroelasticity. Furthermore, the use of a galvanized steel shaft in the theoretical model plays a significant role as a potential step in material selection. Although limited to theoretical and analytical assessments, this article aims to provide a foundation for future research in aerospace engineering and materials science, shedding light on potential advancements in the field.

2. FUNDAMENTALS OF THEORETICAL ANALYSIS

2.1. Static Aeroelasticity

Static aeroelasticity is the study of deflection of flexible aircraft structures under aerodynamic loads where the forces and motions are independent of time. These loads cause the wing to bend, twist, and change the angle of attack, resulting in a change in the aerodynamic flow. This usually changes the load and deflection acting on the wing until equilibrium is reached. The interplay between wing structural deflection and aerodynamic loading

determines the wing bending and twisting at each flight condition and must be considered to model the static aeroelastic behavior. Air speeds at which the elastic torsion rapidly increases and breaks down are called divergent airspeeds. Simply put, divergence occurs when the lifting surface deforms under aerodynamic load, increasing the applied load, and the increased load eventually deflects the structure further to the point of failure. Such failures are not simply the result of excessive loads for the designed structure. Instead, aerodynamic forces interact with the structure and effective stiffness is lost.

Hodges and Pierce [1] conducted static aeroelasticity analysis for wall-mounted model of the wind tunnel model. Wing model is assumed to be rigid and two-dimensional. That is, the shape of the airfoil is independent of spanwise position, and the span is large enough that the lift and pitching moment are independent of spanwise coordinates.

2.2. Wall Mounted Model

In the wall mounted model, after supporting a particular wing on both sides with torsionally elastic support, angle changes are required to be observed in the wind tunnel. The model can be seen in figure 1.

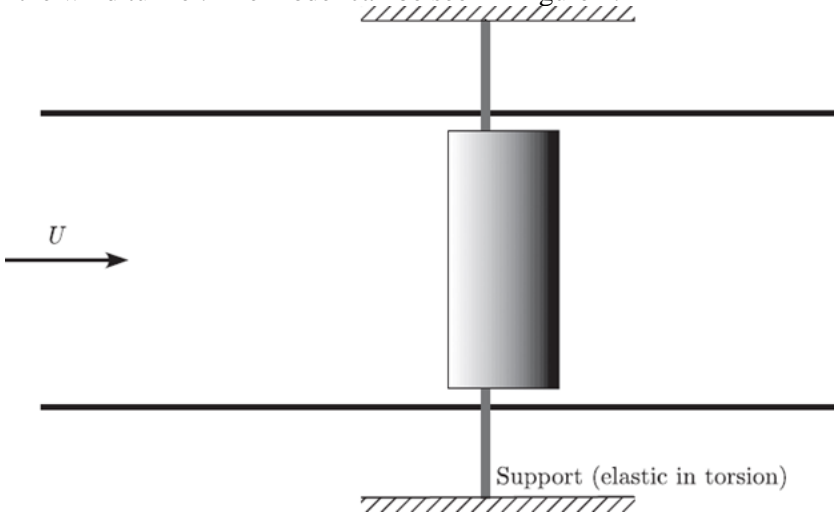


Figure 1 Wall Mounted Model Top View [1]

In the model, the movement will be in one dimension. Time is an independent variable while the angle change is observed. The support is flexible in torsion, which means that it restricts the pitch rotation of the wing in the same way as a rotational spring would. The airfoil side section is given in figure 2.

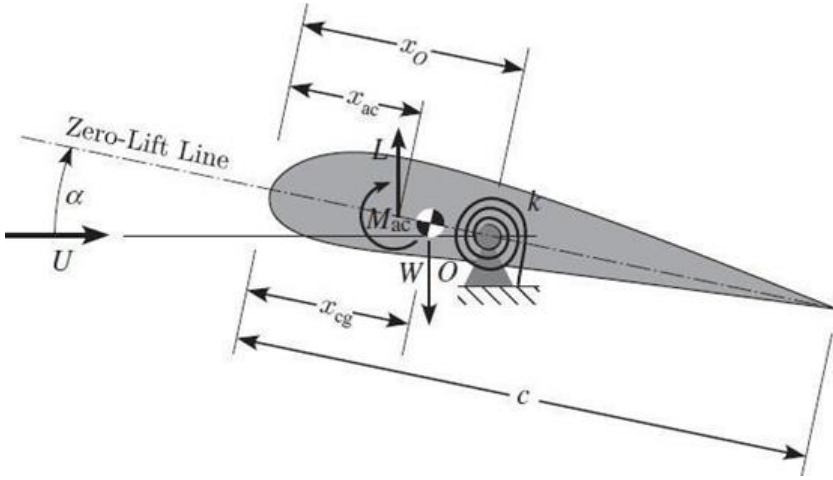


Figure 2 Side View of Airfoil in Wall Mounted Model [1]

At the selected O point, all moments become equal to zero. Thus, the equations are listed in Eq. (1).

$$M_{ac} + L(x_0 + x_{ac}) - W(x_0 + x_{cg}) - k\theta = 0 \quad (1)$$

The angle of attack α_r is positive nose up in Eq. (2). The elastic part of the pitch angle is denoted by θ . That means positive nose-up. Accordingly, the angle of attack formula of the wing is in Eq. (2).

$$\alpha = \alpha_r + \theta \quad (2)$$

Angle of attack is found by summing angle change and support angle of attack. The treatment herein is restricted to incompressible flow, but compressibility effects may be considered by means of Prandtl-Glauert. Airfoil is assumed to be "thin" for this model. Lift rigid formula is given in Eq. (3).

$$L_{rigid} = qSC_{L\alpha}\alpha_r \quad (3)$$

This pressure formula is given in Eq. (4). Lift formula is given in Eq. (5).

$$q = \frac{1}{2}\rho_\infty U^2 \quad (4)$$

$$L = qSC_{L\alpha}(\alpha_r + \theta) \quad (5)$$

For positive θ values, L is not equal to L_{rigid} .

$$M_{ac} = qScC_{Mac} \quad (6)$$

The moment of aerodynamic forces about aerodynamic center is given in Eq. (6). If the angle of attack is small, C_{Mac} can be as a constant. According to linear aerodynamics, the lift curve slope $C_{L\alpha}$ is constant. According to the two-dimensional thin-airfoil theory, a further simplification may be that $C_{L\alpha} = 2\pi$. When the equations obtained in Eq. (1) are written instead of, in Eq. (7) deflection formula is obtained [1]

$$\theta = \frac{qScC_{Mac} + qSC_{L\alpha}\alpha_r(x_0 - x_{ac}) - W(x_0 - x_{cg})}{k - qSC_{L\alpha}(x_0 - x_{ac})} \quad (7)$$

Here, the torsional support value for the k coefficient is performed in Eq. (8). J is the polar moment of inertia for the rod that is performed in Eq. (9).

$$k = \frac{GJ}{L} \quad (8)$$

$$J = \frac{\pi}{2}R^4 \quad (9)$$

NACA 2411 airfoil parameters is shown in table 1. These values are obtained from 20 cm × 14 cm airfoil section.

Table 1 NACA 2411 Airfoil Parameters [11]

c (m)	S (m ²)	C_{Mac}	C_L	α_r (°)	x_0 (m)	x_{cg} (m)	x_{ac} (m)	x_{cp} (m)
0.2	0.28	0.018	6.283	5	0.09	0.05	0.045	0.045

The standard assumptions are given in table 2. The experiment was planned to be conducted at sea level.

Table 2 Standard Assumption at Sea Level [1]

ρ_∞ (kg/m ³)	g (m/s ²)
1.225	9.80665

The diameter and moment of inertia of the rod and its length are given in table 3.

Table 3 Variable Parameters of Rod

R (m)	J (m ⁴)	L (m)
0.008	4.0212e-10	0.14

List of materials to be experimented with angle changes is calculated with Galvanized Steel for the theoretical section. The material properties can be seen in table 4.

Table 4 Material Properties

Material	m (gr)	G (GPa)	W (N)
Galvanized Steel	155.00	80	1.52055

2.3. Airfoil Selection

XFLR5 [8] is an open-source software specifically used to analyze and optimize the aerodynamic performance of wing and plane designs. Although it was originally developed for foils and low Reynolds number flows, it has a wide range of applications. XFLR5 allows users to evaluate the aerodynamic performance of wing and plane designs using various computational methods such as potential flow theory, boundary layer theory and the Vortex Lattice Method (VLM). The program also supports a more advanced calculation method known as the Panel Method. The airfoil to be produced for theoretical has been designated as NACA 2411. Thus, the selected airfoil SOLIDWORKS program [10] was drawn at the desired values and analyzed from the XFLR5 program. The analysis consists of twelve steps. The steps are determined according to Reynolds number and Mach number. Mach number equivalent to 1 m/s was found for the first step. (Calculated according to sea level.) Then, the Mach number was calculated again by increasing 5 m/s for each step. The Mach number at speed of 40 m/s is found to be 0.13. To calculate the Reynolds Numbers, the kinematic viscosity is taken as $1.48 \times 10^{-5} \text{ m}^2/\text{s}$ at 15°C. According to the speed, Reynolds number has changed. For the last step, the Reynolds Number is set at 650000. It was written by increasing the Reynolds Number within twelve steps in appropriate proportions. In the XFLR5 program, the airfoil number of panel was increased to 201 and the analysis was made. As a result of the analysis, the results were obtained for the twelve steps. The desired values in the equations are obtained from figure 3.

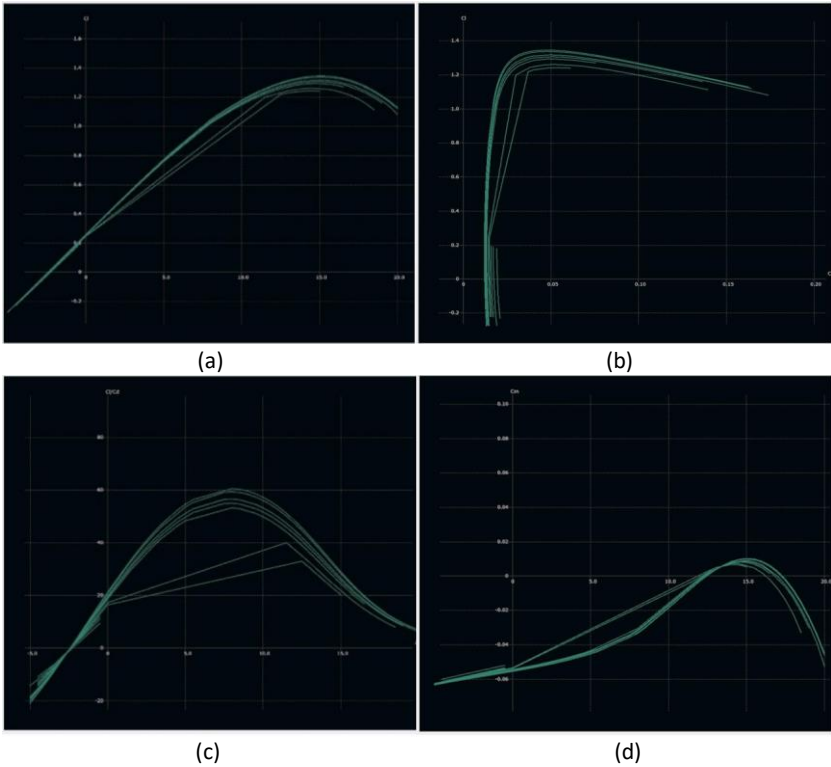


Figure 3 (a) C_L vs α (b) C_L/C_D vs α (c) C_L vs C_D (d) C_M vs α graphs from XFLR5 Program [8]

In figure 3 (a), C_L vs α graph is illustrated for different Reynolds Numbers. Despite the different Reynolds Numbers, the graph is not very different from each other. In figure 3 (b), C_L vs C_D graph is shown for the taken Reynolds Numbers. C_D range starts from 0 and it continues to 0.2. C_L range starts from -0.2 and it continues to 1.4. In addition, C_L/C_D vs α graph is given in figure 3 (c). $C_{M\alpha}$ value is found to be -0.018 in figure 3 (d) [8].

3. AIRFOIL SUPPORT DESIGN

In order to mount the airfoil in the wind tunnel, an appropriate support structure is designed to fix the airfoil from both sides. For this purpose, the structure is modeled using SOLIDWORKS program. The structure has a variable angle of attack between 0° and 5° . The design is shown in figure 4.

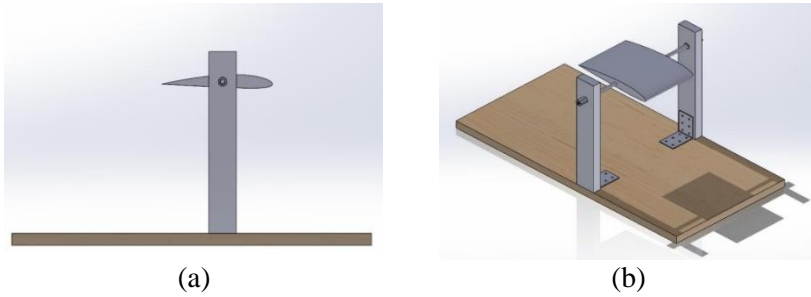


Figure 4 (a) Right View (b) Isometric View of Support Structure [10]

The support points of the design are planned to be made of wood. The remaining shaft is made from galvanized steel. Besides, airfoil is made of organic filament.

4. MATERIALS and METHODS

In today's dynamic engineering landscape, efficient design and optimization of complex systems are imperative. ANSYS [9], a widely embraced simulation and analysis software suite, caters to diverse industries like aerospace, automotive, manufacturing, and energy. It equips engineers with powerful tools for modeling, simulating, and analyzing physical phenomena, aiding informed design decisions, and achieving optimal performance.

Specifically, within this project, one-way Fluid-Structure Interaction (FSI) analyses utilizing ANSYS computational fluid dynamics (CFD), and static analyses were conducted. FSI explores the dynamic interaction between fluid flow and structural response, crucial in applications like aerodynamics on flexible aircraft wings or water-induced vibrations in offshore structures.

The chosen ANSYS version for this project is the student version. The one-way FSI analysis in ANSYS involves simulating fluid flow using CFD, employing tools like ANSYS Fluent. The CFD analysis yields crucial boundary conditions for the subsequent static analysis, performed using the student version of ANSYS. This approach ensures accurate predictions of structural values, such as stresses, deformations, and twist angles, influenced by fluid forces.

The report primarily focuses on CFD and static structural analyses. Initial CFD analysis provides pressure values, utilized in subsequent static analysis to derive desired outcomes.

4.1. Computational Fluid Dynamics (FLUENT) Analysis (2.5°)

CFD analysis calculates aerodynamic parameters like pressure, lift, and drag on a model immersed in a fluid. Meshing is vital in ANSYS analysis, relying on the finite element method. The model is divided into the smallest elements, and values on these elements combine to determine the overall outcome. A circle is drawn at the airfoil center, and a mesh is generated specifically for this circle. This approach ensures better element qualities around the wing, enhancing analysis results. The overall mesh has a 20 *mm* element size, while elements covering the circle have a 4 *mm* size. Edge sizing with 100 divisions and inflation improves the quality of elements around the wing.

Set air density and viscosity as constants in the material section without additional edits. Specifying weather conditions, chosen from the boundary condition section, and setting the air's direction and velocity. For this analysis, incoming air flows through the leading edge to trailing edge with a velocity of 20 *m/s*.

In this analysis, a general method assigned by ANSYS is chosen which gives values close to the values obtained by different methods. As aerodynamic parameters to be obtained as a result of the analysis, lift force, drag force, lift coefficient, and drag coefficient are entered.

The model is initialized, and the solution process starts with iterations. To provide a consistent result of the analysis, the predicted iteration value is 1000.

The analysis converges in approximately 80-90 iterations. Table 5 illustrates the aerodynamic results for a wing with an angle of attack of 2.5°.

Table 5 CFD Analysis Result Parameters 2.5°

C_L	0.0085 N
C_D	0.0004 N
L	3.5758 N
D	0.1756 N

As a result of the analysis, the pressure distribution on the wing is shown in table 5.

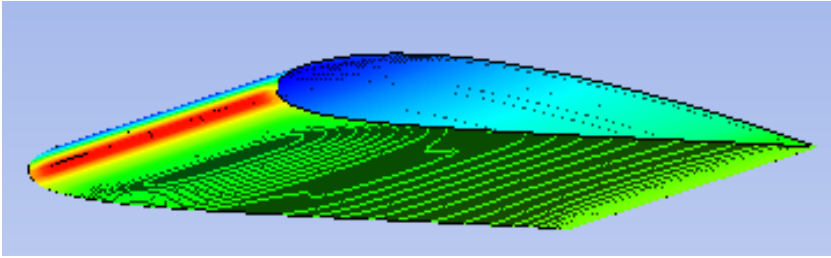


Figure 5 Pressure Distribution as a Result of CFD Analysis at 2.5° [9]

4.2. Static Structural Analysis

Static analysis calculates deformations and stresses due to stresses on the model. To explain this analysis in detail: It is a static analysis using CFD data, therefore no pressure value is entered manually; instead, the pressure value obtained from the CFD analysis is used.

The properties of the filament material of the wing are entered into the engineering data. The material of the airfoil, filament, from the ANSYS library, and the material of the shaft, galvanized steel, from the SOLIDWORKS library were added to the analysis, and these values are presented in table 6.

Table 6 Properties of Materials

	Filament	Galvanized Steel
Young Modulus (<i>MPa</i>)	2013.5	2.074e+6
Poisson's Ratio	0.3	0.29
Density (<i>kg/m³</i>)	1250	7850

The wing geometry is entered into the ANSYS database, the angle of attack is determined and then the model is created. In figure 6 and figure 7, the materials created in the model section, galvanized steel, and filament, are assigned to the wing and shaft.

CHAPTER 3: NUMERICAL AEROELASTICITY ANALYSIS OF WINGS

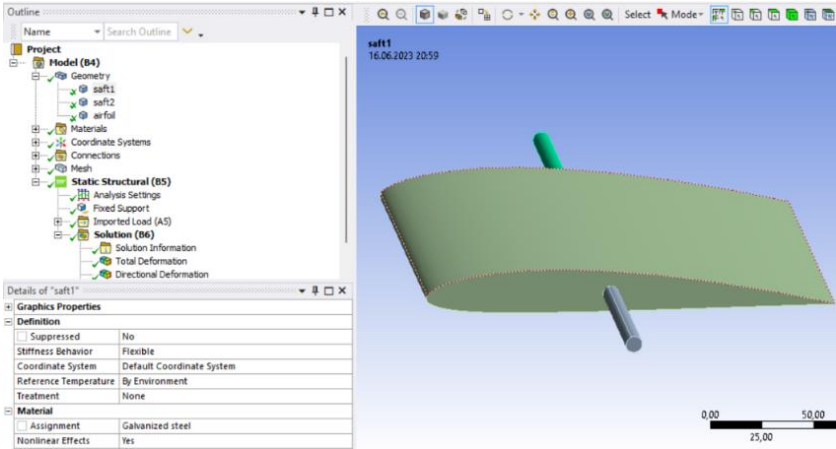


Figure 6 Galvanized Steel Material Assignment for Rod [9]

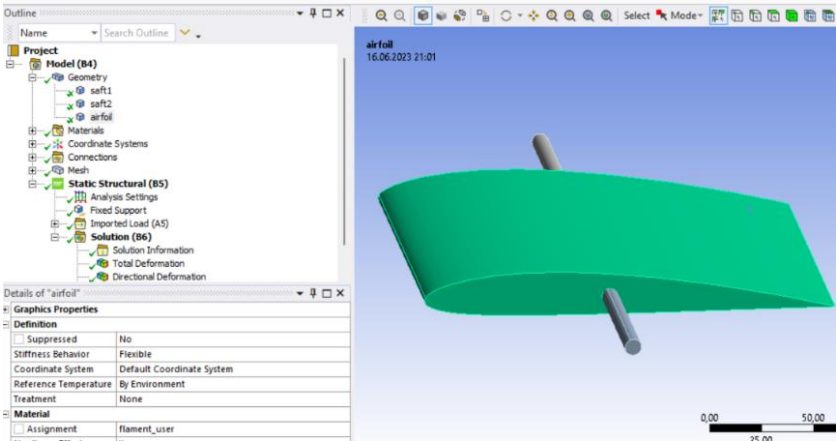


Figure 7 Filament Material Assignment for Airfoil [9]

After assigning the necessary material properties, the connections are checked, and the mesh is applied. In the mesh part, the 'multizone' method is used in both the shaft and the wing because the small elements produced in static analysis are essential. Furthermore, consistent results come from 'Hexa' elements. Therefore, this method is chosen. The element size is set at 2 *mm* for shafts and 3 *mm* for blades. The mesh is illustrated in figure 8.

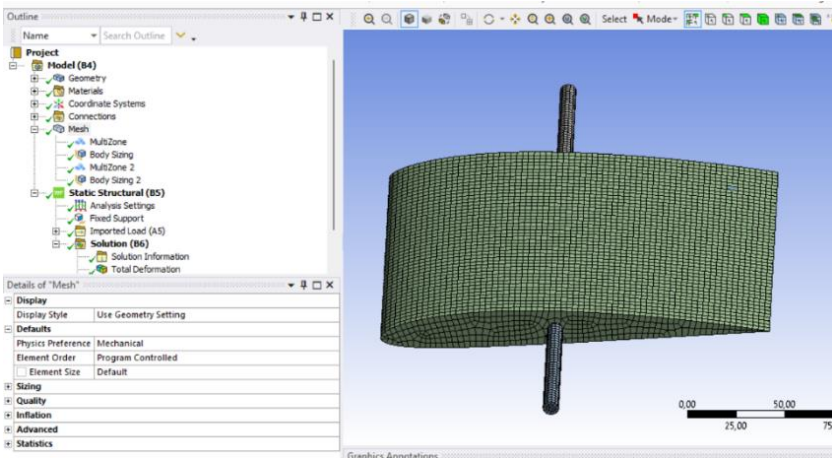


Figure 8 The Mesh Applied on the Shaft and the Wing [9]

Upon completion of the meshing phase, as indicated in figure 9, the model is secured at both ends of the shaft.

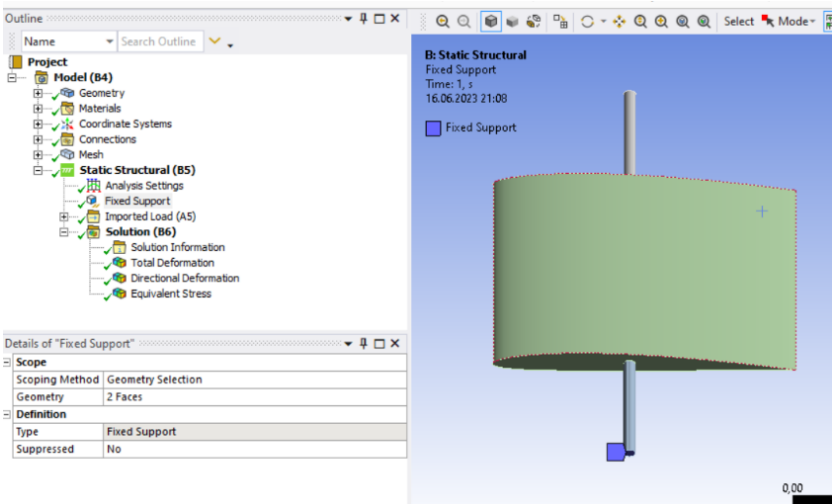


Figure 9 Both Sides Fixed Support [9]

The pressure distribution on the wing obtained from CFD Analysis is formed. The analysis is solved by determining the desired values. As a result of the analysis, deformation and equivalent stress in the y-axis are found. Along with the deformation in the y-axis, the twist angle on the shafts is found. Figure 10 illustrates the values and animation for the y-direction deformation of the wing.

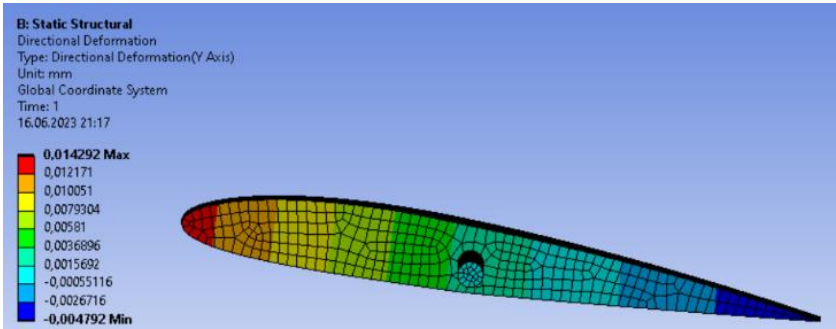


Figure 10 Deformation in Y Directions [9]

Eq. (10) and Eq. (11) are used to find θ from the values taken at figure 10.

$$S \times \theta = Z \tag{10}$$

$$\theta = Z/S \tag{11}$$

Distance from the shaft to leading edge of the wing is denoted as S and displacement from the shaft to leading edge of the wing is denoted as Z .

$$\theta = \frac{0.014}{90} rad = 0.009^\circ$$

Total deformation and equivalent stress distributions are shown in figure 11 and figure 12.

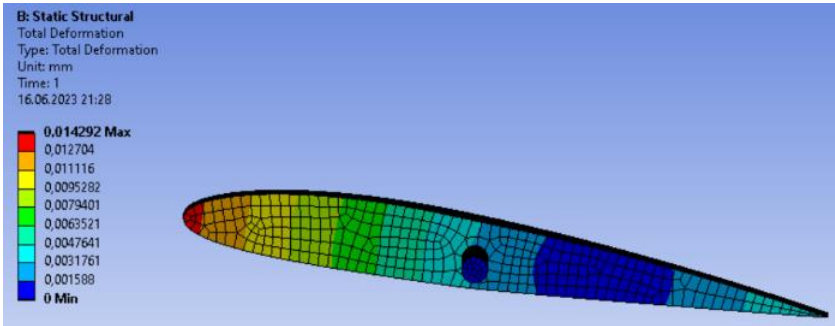


Figure 11 Total Deformation [9]

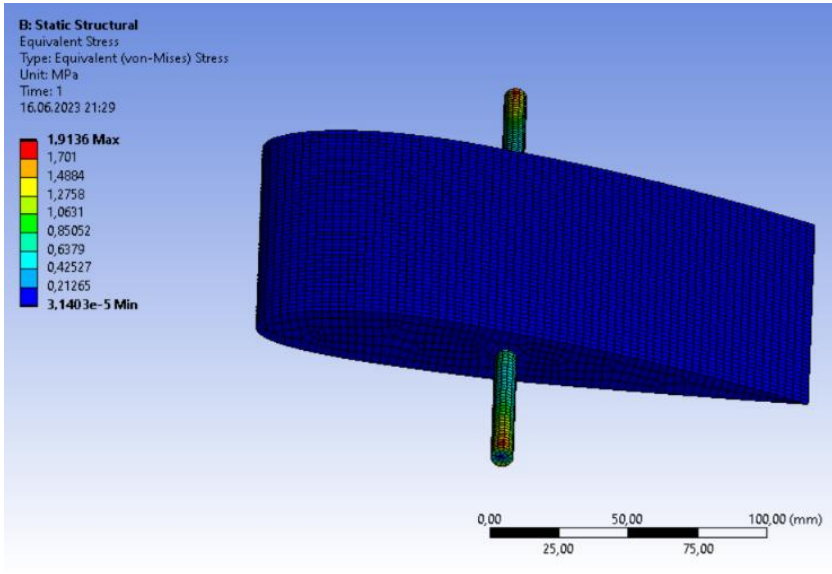


Figure 12 Equivalent Stress [9]

4.3. One Way FSI Analysis (5°)

CFD and static analyses for the wing with an angle of attack of 2.5° are described in detail. The wing with 5° angle of attack was analyzed in the same way and no changes were made. The materials, mesh elements and methods used are the same. The pressure distribution, equivalent stress, deformations, and twist angle values obtained from this analysis are illustrated in figure 13 and figure 14.

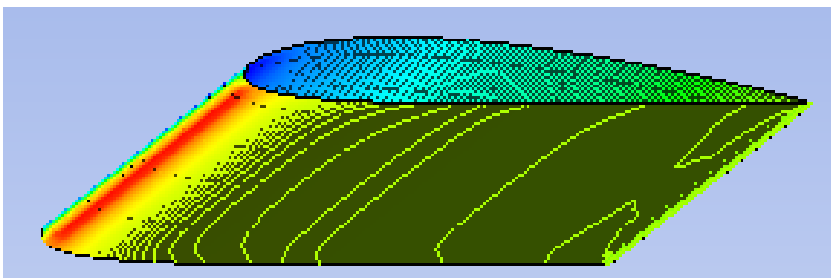


Figure 13 Pressure Distribution Bottom View for 5° [9]

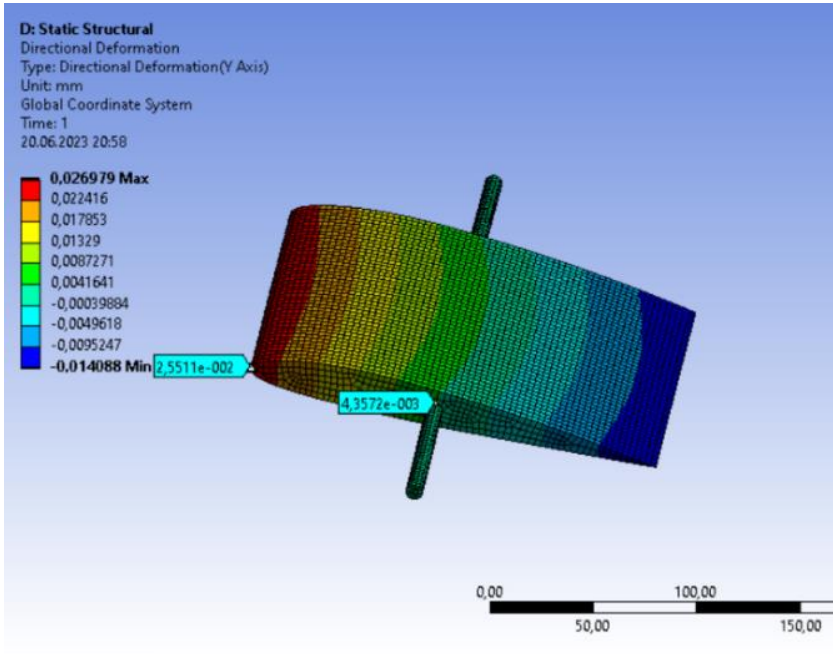


Figure 14 Deformation in Y Direction for 5° [9]

Eq. (10) and Eq. (11) are used to find θ from the values taken at figure 14.

$$\theta = \frac{0.026}{90} rad = 0.017^\circ$$

5. RESULTS and DISCUSSION

In this research, a wall-mounted model was utilized to scrutinize a specific airfoil section at defined dimensions within the realm of static aeroelasticity. Notably, the examination conducted at an airspeed of 20 *m/s* revealed that both the analysis and theoretical equations rendered identical values. This noteworthy observation signifies that, under the specified conditions, both theoretical approaches and analytical methods in table 7 consistently generate results that are not only congruent, however also dependable. The conformity between theoretical predictions and empirical findings enhances confidence in the reliability and accuracy of the chosen methodologies for assessing static aeroelastic behavior. This consistency supports the robustness of the employed analytical framework and contributes valuable insights to the understanding of airfoil behavior in the given aerodynamic context.

Table 7 Angel of Twist Values at 2.5° and 5° Angles at 20 m/s Speed

Result (20 m/s)	Theoretical	Analysis
2.5°	0.009°	0.009°
5°	0.018°	0.017°

6. CONCLUSION

The findings presented in this study have implications for the development of materials used in designs in the aviation industry. In particular, the examination of the suitability of galvanized steel for an airfoil highlights a remarkable convergence between theoretical predictions and real-world applications. The study underlines the theoretical precision in predicting the performance of materials commonly used in aircraft engineering and thus contributes significantly to the formulation of design and safety standards in the industry.

This research not only validates the theoretical basis governing material selection, but also highlights its practical importance in the complex aviation environment. The agreement shown between theoretical predictions and empirical results supports the improvement and development of robust materials for better aircraft performance and safety. As the aviation industry continuously evolves, these insights need to be extended to studies covering different weather conditions and a wider range of material options. This article provides a pathway for future research efforts to further advance our understanding and optimization of materials vital to the aviation industry.

Acknowledgements

No Acknowledgements was declared by the authors.

Conflict of interest

No conflict of interest was declared by the authors.

Author contributions

All authors have contributed equally to the relevant work.

REFERENCES

- [1] Dewey H. Hodges, G. Alvin Pierce. (2011). Introduction to structural dynamics and Aeroelasticity. (Cambridge aerospace series)
- [2] Santos, L. G. P. D., & Marques, F. D. (2021). Nonlinear aeroelastic analysis of airfoil section under stall flutter oscillations and gust loads. *Journal of Fluids and Structures*, 102, 103250
- [3] Shao, S., Zhu, Q., Zhang, C., & Ni, X. (2011). Airfoil Aeroelastic Flutter Analysis based on modified Leishman-Beddoes model at low Mach number. *Chinese Journal of Aeronautics*, 24(5), 550–557.
- [4] Shao, S., Zhu, Q., Zhang, C., & Ni, X. (2011). Airfoil Aeroelastic Flutter Analysis based on modified Leishman-Beddoes model at low Mach number. *Chinese Journal of Aeronautics*, 24(5), 550–557.
- [5] Djojodihardjo, H. (2023). Aeroelastic Optimization of Tapered Wing Structure. In H. Djojodihardjo (Ed.), *Aeroelastic Optimization of Tapered Wing Structure* (pp. 791–803).
- [6] Nejatbakhsh, H., Ghasemi, A. R., Gharaei, A., & Najafabadi, H. R. (2023). An Analytical-Numerical coupled model for an aeroelastic analysis of tail flutter based on Bending–Torsional coupling. *Mechanics of Composite Materials*, 59(4), 757–768.
- [7] Haught, J. A., & Sivaneri, N. T. (2023). AEROELASTIC ANALYSIS OF COMPOSITE PLATE WINGS BASED ON A NEW HSDT FINITE ELEMENT—MONNA. *Aeroelastic Analysis of Composite Plate Wings Based on a New HSDT Finite Element—MONNA*
- [8] XFLR5. (n.d.). Retrieved from <https://www.xflr5.tech/xflr5.htm>
- [9] Students. (2023, October 3). Retrieved from <https://www.ansys.com/academic/students>
- [10] SOLIDWORKS 3D CAD. (2022, September 29). Retrieved from <https://www.solidworks.com/product/solidworks-3d-cad>
- [11] Airfoil tools. (n.d.). Retrieved from <http://www.airfoiltools.com/>



CHAPTER 4

Aviation Technologies and Applications
E-ISBN:978-605-338-471-7
2025, chap. (4), pp.59-74.

SMART ANTENNA SYSTEMS AND APPLICATIONS: A REVIEW

Husnu Deniz BASDEMIR^{1,2,*}, Beyza Nur DEMIRKOPARAN³

ABSTRACT

In wireless communications, antennas are essential components. The ability of an antenna array to hammer spatially spread radio waves for more dependable data reception is widely established. The theories of phased antenna arrays, adaptive beamformers, and optimal array processing have all been utilized in the development of modern smart antenna technology. Over the previous few decades, these theories have been explored and improved. More recent advancements in antenna array technology include blind channel estimation and equalization, space-time coding for multiple transmitters or multiple receivers, and more. When compared to traditional antenna, smart antennas greatly increase coverage area, spectral efficiency, and channel capacity.

A basic description of the smart antenna (SA) system is given in this publication. By adaptively updating the weights associated with each antenna element, SAs can steer nulls toward potential interference. Thus, most of the co-channel interference is cancelled by SAs, improving reception quality, and reducing dropped calls. SAs can also utilize direction of arrival algorithms to track a user within a cell. The basic principle of smart antennas is to raise the gain in a particular direction to boost the wireless communication system's performance. By pointing the principal lobes of the antenna-beam patterns in the desired users' direction, they can be targeted.

In this study, the use of smart antenna systems in different areas is explained. Also, smart antenna structure was suggested which can be used in military communications as well as civilian communications. The proposed structure determines the location of maximum signal strength of incoming wave and radiates the same way or forming the beam to same location. The theories of proposed structure and numerical results were explained to analyze the structure.

Keywords: Smart Antenna Systems, Communication, Defense Industry, Applications of Smart Antenna Systems

*Corresponding Author: denizbasdemir@gmail.com

¹ 0000-0002-2797-3772, Faculty of Aviation and Space Sciences, Sivas University of Science and Technology, Sivas, Turkey

² Department of Electrical and Electronics Engineering, Sivas University of Science and Technology, Sivas, Turkey

³ 0000-0002-7658-9507, Defence Technology Programme, Sivas University of Science and Technology, Sivas, Turkey

1. Introduction

To improve coverage range, system capacity, and reduce multipath fading, adaptive smart antenna systems (SAS) have been the subject of intense research recently [1-4]. It has been demonstrated that those solutions significantly improve coverage and capacity while also mitigating multipath fading when the base station's antenna array and appropriate signal processing techniques are used. It is commonly known that adaptive SAS maximizes the output signal-to-noise ratio by combining the weighted signals received by each antenna to achieve high antenna gain [5].

Service providers are growing more concerned about the constrained capacities of their current networks due to the rapid increase in the number of digital cellular subscribers. Due to this worry, smart antenna systems have been installed in all the major urban cellular markets. Multibeam technologies, that have been demonstrated via intensive analysis, simulation, and experimentation to deliver significant performance increases in FDMA, TDMA, and CDMA networks, have generally been used in these smart antenna systems [6-10]. Typically, reserved frequencies (FDMA), reserved timings (TDMA), or reserved codes are used by all users to communicate on the same base station (CDMA). Users can be assigned one or more frequency bands or channels on an individual basis with FDMA. Like any other multiple access system, FDMA distributes access across multiple users in an equitable manner. A channel access method (CAM) called time division multiple access (TDMA) is utilized to enable interference-free channel sharing. A transmission channel can be shared and used by several stations thanks to TDMA, which splits signals into discrete time slots. Users use their allotted time slots and transmit in quick succession. As a result, several stations (like cell phones) may share a frequency channel yet only utilize a portion of its capacity [7]. A broad name for several multiplexing or media access control techniques based on spread spectrum technology is CDMA (Code-Division Multiple Access) [8]. Conversely, smart antenna systems introduce a new method of user separation. Space Division Multiple Access (SDMA) is another name for this method [9]. It separates users spatially to maximize utilization of the frequency spectrum [10].

Multibeam designs for FDMA and TDMA systems enable the simple implementation of the smart antenna as a non-invasive add-on or appliqué to an existing cell site, without requiring significant modifications or unique interfaces[11]. Applying SAs to demand-based frequency allocation in hierarchical system techniques yields the greatest results

(Flexible antenna patterns obtained electronically and receiving antennas do not need to be physically moved). Reduced inter-symbol interference, reduced co-channel interference, and reduced adjacent channel interference are benefits of using SAs in cellular systems. They also improve bit error rate (because they cause less multipath and ISI), boost receiver sensitivity, lower power consumption, and reduce radiofrequency pollution. Smart antennas are best suited for cognitive radio applications (software radio technology offers flexibility), and their highest security level is by far their greatest asset [12].

2. What is a Smart Antenna System?

A control unit, a network for integrating and dividing signals, and several radiating devices make up a smart antenna system. Digital signal processors (DSP) are typically used to implement the control unit, which is also referred to as the smart antenna intelligence. Using a variety of inputs, the processor modifies the antenna's feeding characteristics to maximize the communications link. This illustrates that intelligent antennas are more than simply an antenna; they are an entire transceiver concept [13].

Antenna systems are intelligent antennas themselves are not. An antenna array and digital signal processing power are combined in a smart antenna system, which is typically co-located with a base station, to enable adaptive, spatially sensitive transmission and reception. Put differently, a system of that kind is capable of automatically adjusting the directionality of its radiation patterns based on the signal environment it is in [14]. To put it another way, their digital signal processing facilities are where their intelligence is housed. In addition to preventing multipath fading, smart antennas help reduce interference. It makes use of adaptive combining methods and diversity. Due to their high-power consumption and significant system complexity, SA methods have primarily been investigated for base stations up until this point. Lately, mobile stations or handsets have begun using clever antenna techniques [15], [16].

3. Types of Smart Antenna Systems

Intelligent antennas, phased arrays, SDMA, digital beam forming, adaptive antenna systems, and spatial processing are some of the terms that are frequently used to refer to different parts of smart antenna system technology. That being said, smart antenna systems are often classified into two primary categories: switching beam and adaptive array systems.

Switched beam antenna systems create a number of fixed beams that are more sensitive in specific directions. When the mobile device moves across the sector, these antenna systems switch between multiple fixed, predefined beams and detect the strength of the signal. Switched beam systems, as opposed to sculpting the directed antenna pattern with the metallic characteristics and physical design of a single element, produce precisely sectorized (directional) beams with improved spatial selectivity by combining the outputs of numerous antennas (like a sectorized antenna) are depicted in Figure 1.

Adaptive antenna technology is currently the most sophisticated smart antenna approach available. The adaptive system leverages its versatility in locating and tracking different kinds of signals to dynamically decrease interference and maximize intended signal reception by employing a range of novel signal-processing techniques.

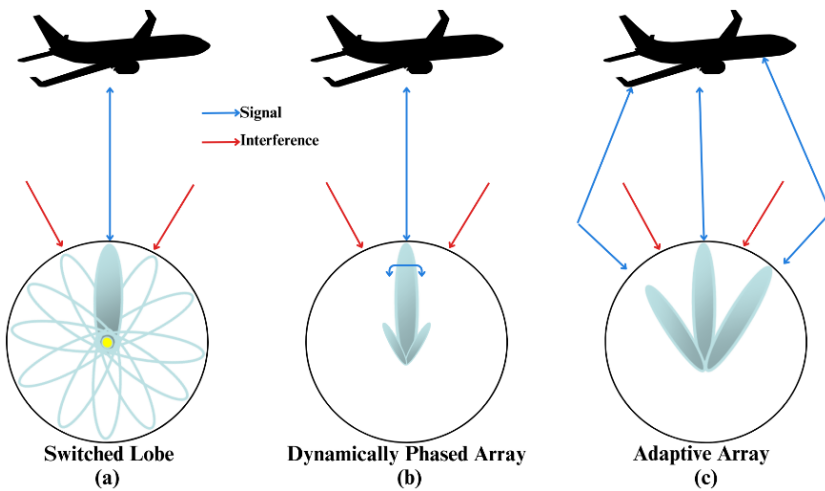


Figure 1. Switched beam system coverage patterns for different array structures.

Both systems try to maximize gain based on the user's location; however, only the adaptive system offers the best gain while concurrently detecting, tracking, and reducing interference signals as shown Figure 1 (c).

4. Smart Antenna Systems Applications

An antenna array and digital signal processing power are combined in a smart antenna system to provide adaptive, spatially sensitive transmission and reception. In reaction to the signal environment, such a system automatically modifies the directionality of its radiation pattern [17]. The main objective of a smart antenna is to dynamically establish the optimal weights for antenna components using an adaptive algorithm. Applying optimal criteria, such as maximum signal-to-noise ratio (SNR), least square error (LSE), and minimum mean square error, can result in a successful solution (MMSE) [18]. Based on these requirements, many adaptive algorithms have been proposed. To achieve broadcast and receive diversity, smart antennas can be utilized in mobile stations as well as base stations. Utilizing one or more antennas at the receiver, receive diversity combines the received signals dynamically. When compared to a traditional antenna, this does not require any additional power. The performance of a smart antenna in terms of diversity gain, bit error rate (BER) reduction, and noise suppression for a direct sequence code division multiple access (DS-CDMA) system is the main emphasis of this research employing a smart antenna system. The effects of antenna configuration and the performance of different adaptive algorithms were evaluated. The emphasis in CDMA systems is on adaptive algorithms created especially for the smart antenna. The enhancement of system performance with the smart antenna is next investigated and the simulation results of two distinct algorithms are displayed [19]. For CDMA systems, two blind adaptive digital beamforming methods have been applied, and simulation results are presented. By comparing the findings with a traditional single-element antenna, the advantages of these methods are illustrated. Additionally, the effects of different design parameters on the smart antenna system performance were also examined [19]. The study found that the smart antenna outperformed the traditional antenna by providing an antenna gain of 6.02 dB for the 4-element antenna and 7.78 dB for the 6-element antenna. Two techniques in bit error rate given in Figure 2 are very appropriate for CDMA systems. When compared to a traditional single-element antenna, which offers BER performance in the range of 10^{-1} - 10^{-2} , they dramatically lower BER [17]. When it comes to antenna element count given in Figure 3, four or six elements yield the best results. The optimal performance in terms of antenna element spacing is attained with 0.5 wavelength spacing is shown in Figure 4.

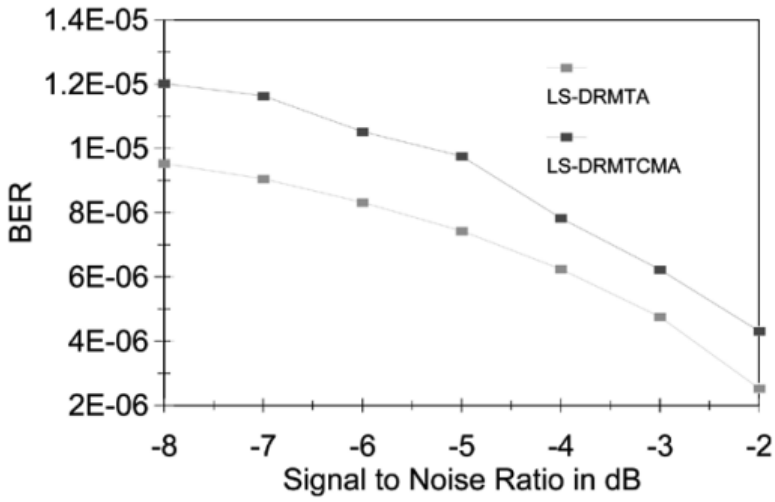


Figure 2. BER versus E_b/N_0 [19]

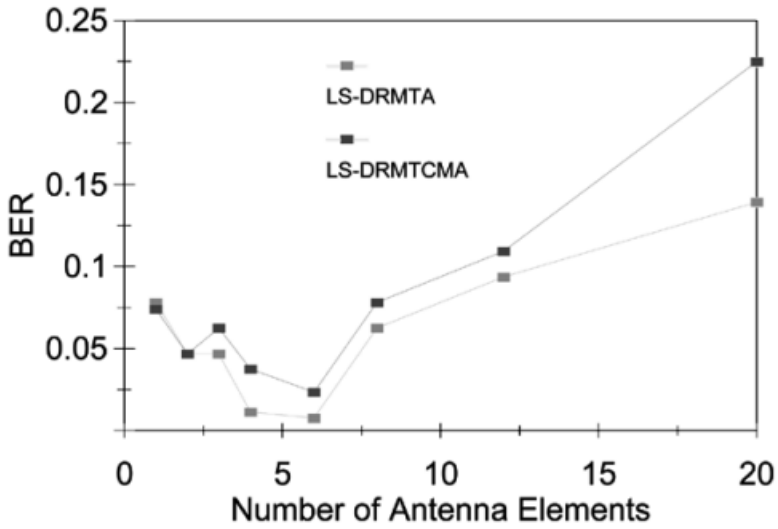


Figure 3. BER versus number of antenna elements [19]

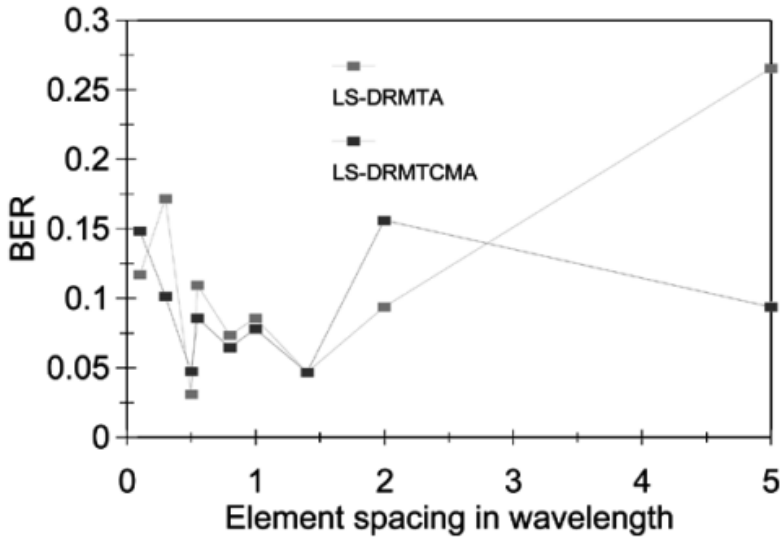


Figure 4. BER versus element spacing [19]

Comparing a smart antenna (with four to six elements) to a traditional single-element antenna, the average gain can be between 6 and 8 dB. Performance of a smart antenna is optimal when it has four or six elements. A six-element scheme has been proposed for CDMA2000 systems, whereas a four-element scheme is proposed for the UMTS. Half the wavelength is the most ideal distance between antenna elements. Nevertheless, BER is increased by less than a factor of two when element spacing is smaller than a wavelength. The performance is independent of the user data rate. This indicates that any type of user, voice, or data can be handled by the system. The smart antenna system can be readily scaled by adding more output modules. The number of elements has no bearing on the highest number of users it can accommodate. Even when coming from the same direction, distinct users can be distinguished by the smart antenna. This is accomplished by investigating the intrinsic orthogonality of various users' gold codes. Bit errors typically cluster around a single user. In other words, rather than affecting every user, errors typically affect one or two of them. Error is more likely to occur among users who are close to the sector boundary [19]. It is explained in another application that smart antenna systems are used to detect brain tumor. In recent years, microwave imaging-based cancer detection has emerged as a promising field of study. The significant dielectric differential between the tumor and healthy tissue serves as the foundation for the operating principle [20]. The signals that are back scattered can be used to identify the tumor. Numerous methods

are based on the detection of cancer using microwave images. Microwave tomography is one method [21]. It resembles magnetic resonance imaging (MRI), which uses scattered energy to create an image of the body's cross-section. The full picture of body tissue is one of the benefits of microwave tomography; yet each tissue is not easily distinguishable [22]. Moreover, non-linear functions must be solved due to the complexity of signal processing. Another possible tactic is to use ultra-wideband (UWB) antennas [23], which pulse briefly into the body [24], [25]. The reflected signals are then detected by one or more receiver antennas that are placed in different locations. Furthermore, by using phase or time shift, more sets of signals can be obtained for calibration to reduce noise and clutter. [26]. This paper described a microwave imaging system for brain cancer detection that is based on smart antenna arrays. It has been discovered that the antenna array emits more energy when it is focused on the tumor than when it is not focused on the tumor. By turning the antenna array around the head, the tumor's location can be ascertained using this information. Moreover, two approaches to the rotation of the antenna array around the head are compared. The UV Plane's array performed far better than the UW Plane's rotating antenna array. It is possible to identify brain cancer using a UWB antenna-based imaging system, according to the simulation results. The application of a smart antenna system in WiMAX technology has been examined. The WiMAX (Worldwide Interoperability for Microwave Access) system, like all other wireless communications solutions, consists of two primary types of antennas: base station antennas and terminal antennas. These days, base stations can use adaptive antennas and MIMO antennas, two new categories of base station antenna options made available by cutting edge technology (multi-input-multi-output). Depending on the end user's degree of mobility, the antenna solutions are split into two groups for the user's terminals: For both stationary and mobile terminals, including those found in vehicles, buses, trains, etc. The terminal antenna solution for mobile and fixed applications is shown in Figure 5 [27].

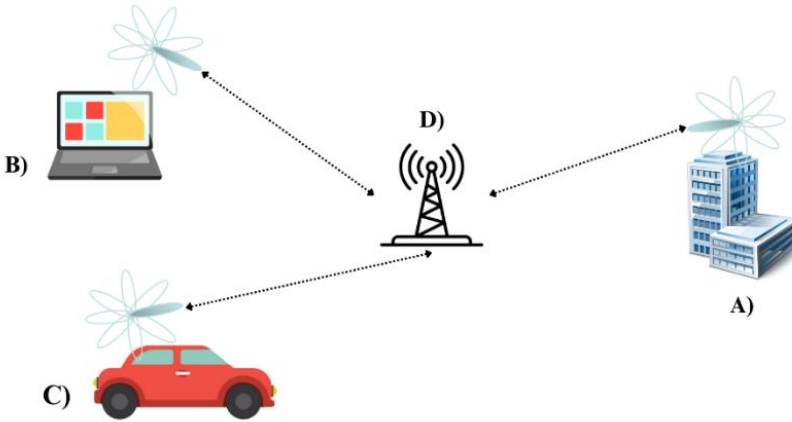


Figure 5. User terminal antenna system for WiMAX

As seen in Figure 5, A) is outside fixed terminal antenna, B) is indoor fixed terminal antenna, C) is antenna for a mobile terminal and D) is antenna of the base station. Through the integration of antenna arrays with modulators and digital signal processors on base stations and user terminals, adaptive antenna technology increases the coverage area, channel capacity, and system throughput of wireless systems. These types of antennas have some benefits. These benefits are, signal to noise ratio rises due to coherent signal summing, the effect of fading on system performance is lessened by the spatial diversity of array members, adaptive beam formation reduces interference by creating the array elements, the radiation pattern consists of maximums in the intended direction and minimums in the interference direction, multiplexing of spatial channels[27]. Smart antenna systems have application in automobile applications, radar, and UAV detection research. As demonstrated by the provided application examples, smart antenna systems have applications in daily communication, healthcare, and even the defense sector.

5. A New Design Proposal for Smart Antenna Systems

As a new approach, the adaptation of smart antenna systems to the defence sector is explained. In the commercial communication systems, the smart antennas are in based stations. Thus, beam forming is made in these stations, but this operation overloads the system for reaching to all end users. In this study, it is proposed that the smart antennas placed in each end users instead of one base station. Therefore, energy efficiency and more clear communication can be achieved since the static station does not

try to determine to all user's location. In addition, the end user's antenna does not radiate to all direction but radiate the direction where the maximum energy strength is determined. Thus, it is also providing easier communication and increase the efficiency of the antennas. The same approach can also be applicable for military systems. Instead of radiating in all directions, determining the direction where the strength of the incoming signal is the highest and radiating in that direction can be more suitable for energy efficiency and healthy communication. Below is the design of the smart antenna system recommended for use in the defence industry.

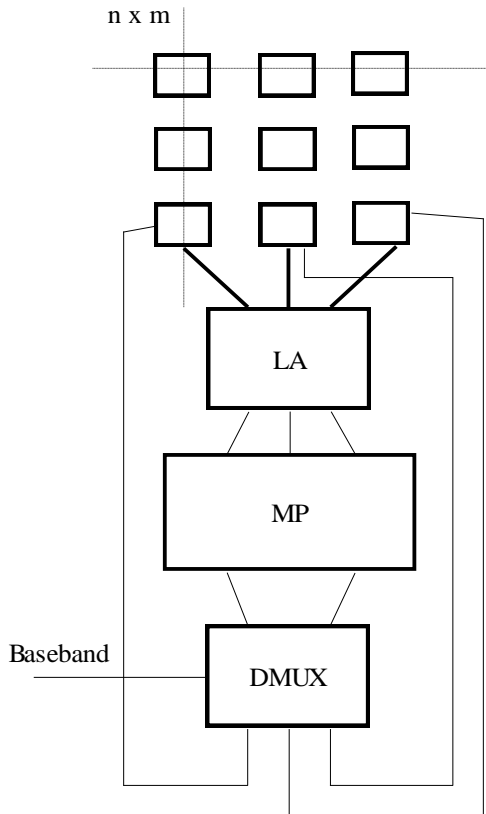


Figure 6. Designed smart antenna system [28]

The proposed antenna structure's radiation diagram drawings, which feature the $n \times m$ matrix array utilized in Figure 6, are provided in section 6. Because of its frequency sensitivity, the lock-in amplifier (LA) in this system is employed to separate the signal from the noise and amplify it. The microprocessor receives the signals from the LA that have been

amplified (MP). Here, the signal's group column is identified by the CPU, which then transmits this information to the multiplexer (DMUX). It also determines which group column the baseband signal should be transmitted to while controlling the DMUX with the signal it will send. Finding the direction where the signal is greatest is the goal here, as is determining whether the antenna should radiate in that direction. Here, DMUX functions something like a switch [28].

6. Materials and Methods

Analytically, existing array structures were analysed and equations giving the relevant radiation patterns were derived. According to the derived equations, the radiation graphs were analysed numerically to provide optimum radiation for different array sizes and numbers. Radiation diagrams of the designed smart antenna system, which is recommended to be used in the defence industry, were drawn with the help of MATLAB program. Its changes were recorded according to various matrix layouts and received wavelength values. The following results were obtained with the antenna design in Figure 7.

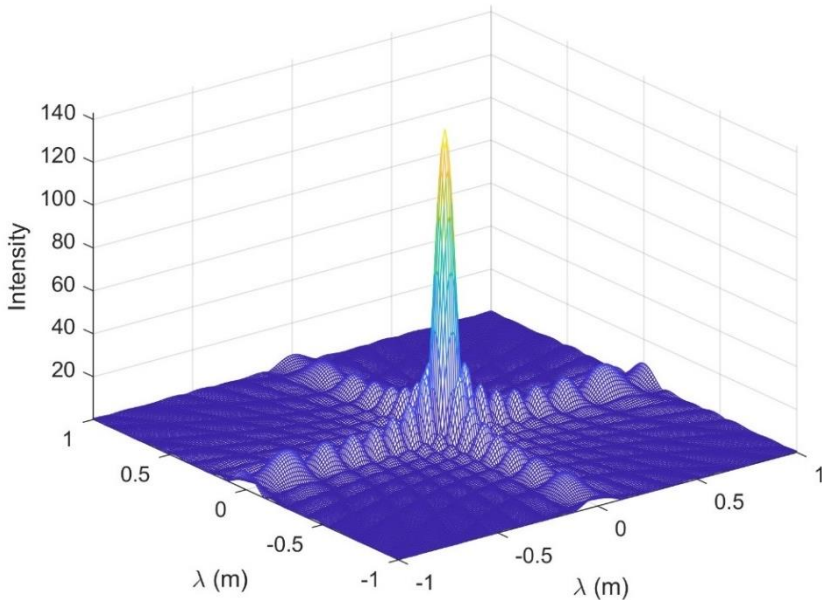


Figure 7. Array antenna radiation diagram [28]

Figure 7 illustrates how the radiation produced by the array antenna is focused in one direction. Here, the matrix is 10 x 10, and the wavelength is the distance between each antenna [28].

The matrix's elements are represented as 20 x 20 in Figure 8, and the wavelength again determines the separation between each member. It is possible to observe that Figure 7 and Figure 8 differ in that the side lobe amplitude levels and the main beam's sharpness have decreased [28].

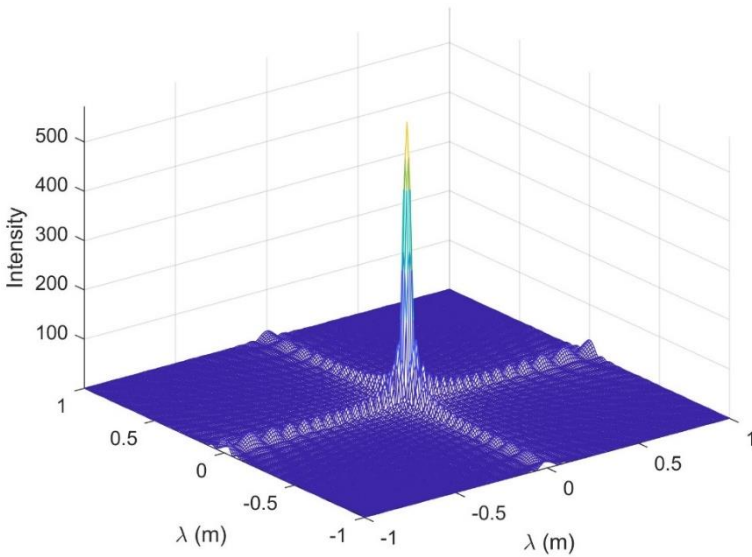


Figure 8. Array antenna radiation diagram [28]

The matrix in Figure 9 is 10 x 10, but the separation between the elements is assumed to be equal to two wavelengths. It was found that the matrix in this instance produced many beams. This image illustrates that one wavelength should be the ideal separation between each matrix element [28].

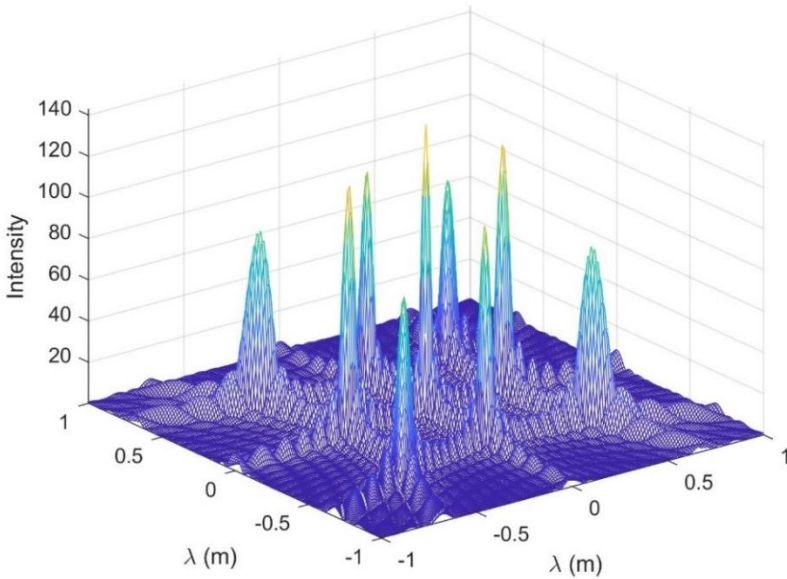


Figure 9. Array antenna radiation diagram [28]

Despite using a 10×10 matrix, Figure 10 treats the separation between the elements as half of a wavelength. In this instance, there was a drop in the main beam's value and an increase in the side lobes' radiation-influencing effect [28].

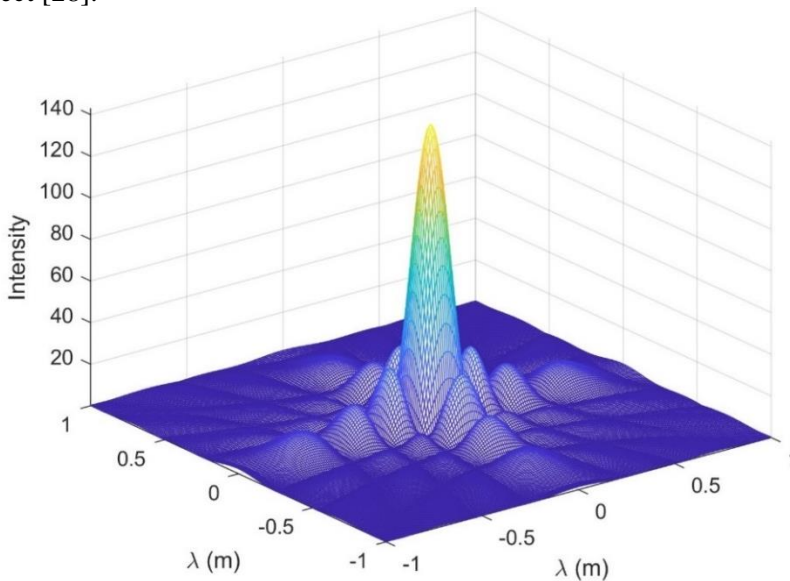


Figure 10. Array antenna radiation diagram [28]

7. Discussion and Conclusion

In this review, a detailed description of smart antenna systems and their various usage areas are explained. Smart antenna systems have a range of uses from brain tumour detection to UAV detection. Its use in systems such as WiMAX systems and universal mobile communication systems is explained with examples. The examples given show that smart antenna systems are more advantageous than standard antennas in many areas. In line with past research, the benefits of using smart antennas in daily communication (for example, mobile phones) have been explained. This method is also recommended for use in military. Here, it is recommended that smart antenna structures can be used in mobile units rather than static stations. Instead of radiating in all directions, determining the direction where the strength of the incoming signal is the highest and radiating in that direction can be more suitable for energy efficiency and healthy communication. There is a chance for a longer range because smart antenna systems are more directed and omnidirectional than sectorized antennas. Put differently, smart antennas have the ability to direct their energy toward specific users rather than other superfluous elements like omnidirectional antennas. Base stations can therefore be positioned farther apart. In sparsely populated areas, where radio coverage is more important than capacity, smart antenna systems are also particularly suitable. Systems with smart antennas are safe. With society becoming more and more reliant on trading personal data and conducting commerce, security is a critical concern. Because the intruder must be positioned in the same direction as the user as seen from the base station in order to effectively tap a connection, smart antennas make it more difficult to tap a connection. Smart antenna systems can be utilized for any location-specific service, including emergency person location, because of their spatial sensing capabilities [29]. It is seen that the designed antenna array will work more accurately with a structure with a distance between the elements of half a wavelength, despite the application of a 10×10 matrix.

Acknowledgements

No Acknowledgements was declared by the authors.

Conflict of interest

No conflict of interest was declared by the authors.

Author contributions

Beyza Nur Demirkoparan contributed to the literature review, preparation of figures, and writing of the chapter. Husnu Deniz Basdemir contributed to the literature review, writing of the chapter, antenna designs, and MATLAB coding.

REFERENCES

- [1] P. Balaban and J. Salz. Optimum diversity combining and equalization in digital data transmission with applications to cellular mobile radio - part i: theoretical considerations. *IEEE Trans. on Communications*. May 1992, 885–894.
- [2] S. S. Jeng, G. Xu, H. P. Lin, and W. J. Vogel. Experimental study of antenna arrays in indoor wireless applications. *Conference Record - Asilomar Conference on Signals, Systems and Computers*, 1995.
- [3] J. G. Proakis, *Digital communications*. McGraw Hill Book Company, 1989.
- [4] B. Suard, A. F. Naguib, G. Xu, and A. Paulraj. Performance of CDMA mobile communication systems using antenna arrays. *ICASSP, IEEE International Conference on Acoustics, Speech, and Signal Processing - Proceedings*, 1993.
- [5] S. Y. Kim and G. Xu. Antenna gain for adaptive smart antenna systems. *IEEE Vehicular Technology Conference*, 1997.
- [6] L. T. & S. S. R. Agius A A. Leach S M. Suvannapattana P. Intelligent handheld antenna for mobile communications beyond the 2nd generation. p. 12.
- [7] Trent K, Are Smart Antennas the way to Non-Line-of-Sight?
- [8] Litwa J. *Digital Beam forming in wireless communications*, 1996.
- [9] Steyskal H. Digital Beam forming antennas. *Microwave J.* 1987, pp. 107–124.
- [10] M. G. Martin Cooper. Intelligent antennas: spatial division multiple access. *Annual Review of Communications*, 1996.
- [11] S. D. Gordon, M. J. Feuerstein, and M. A. Zhao. Methods for measuring and optimizing capacity in CDMA networks using smart antennas. *Wireless Personal Communications*, 2005.
- [12] S. K. N. A. RK Jain. Smart antenna for cellular mobile communication. *VSRD-IJEECE*, vol. 1, pp. 530–541, 2011.
- [13] P. E. M. L. J. G. B. B. G. B. Widrow. Adaptive antenna systems. *Proc IEEE*, vol. 55, pp. 2143–2159, Oct. 1967.
- [14] R. S Kwitkar. Calculation of spatial signatures in smart antenna systems. Feb. 2002, p. 131.
- [15] J. H. Winters. Signal acquisition and tracking with adaptive arrays in the digital mobile radio system IS-54 with flat fading. *IEEE Trans Veh Technology*, vol. 42, no. 4, 1993.
- [16] R. S. Kawitkar and R. K. Shevgaonkar. Design of smart antenna testbed prototype. *ISAPE 2003 - 2003 6th International Symposium on Antennas, Propagation and EM Theory, Proceedings*, 2003.
- [17] Smart antenna systems tutorial. *ArrayComm, Inc.* [Online].

- [18] T. K. Lo J. Litva. *Digital Beamforming in Wireless Communications*. MA: Artech House, 1996.
- [19] V. K. Garg, S. R. Laxpati, and D. Wang. Use of smart antenna system in universal mobile communications systems (UMTS). *IEEE Antennas Wirel Propag Lett*. 2004 vol. 3, no. 1.
- [20] Y. W. A. A. M.E. Bialkowski. UWB microwave monopulse radar System for breast cancer detection. *ICSPCS*. 2010, pp. 1–15.
- [21] X. Li, S. C. Hagness, B. D. Van Veen, and D. Van der Weide. Experimental investigation of microwave imaging via space-time beamforming for breast cancer detection. *IEEE MTT-S International Microwave Symposium Digest*, 2003.
- [22] S. C. Hagness, A. Taflove, and J. E. Bridges. Two-dimensional FDTD analysis of a pulsed microwave confocal system for breast cancer detection: Fixed-focus and antenna-array sensors. *IEEE Trans Biomed Eng*. 1998, vol. 45, no. 12.
- [23] O. K. F. S. F. Thiel. Contrast agent-based tumour detection by ultra-wideband radar: A model approach. *EuCAP*, 2010.
- [24] D. Gibbins, M. Klemm, I. J. Craddock, J. A. Leendertz, A. Preece, and R. Benjamin. A comparison of a wide-slot and a stacked patch antenna for the purpose of breast cancer detection. *IEEE Trans Antennas Propag*. 2010, vol. 58, no. 3.
- [25] E. Pancera. Medical applications of the ultra-wideband technology. *Loughborough antennas and propagation conference*, 2010.
- [26] H. Zhang, A. O. El-Rayis, N. Haridas, N. H. Noordin, A. T. Erdogan, and T. Arslan. A smart antenna array for brain cancer detection. *LAPC 2011- 2011 Loughborough Antennas and Propagation Conference*, 2011.
- [27] Michael Parnes. *Smart Antennas in WiMax system*.
- [28] H.D. Basdemir. 0934.TGSD.2014 numaralı Akıllı Mobil Anten projesi. Sanayi ve Teknoloji Bakanlığı, 2014.
- [29] Constantine A. Balanis. *Antenna theory analysis and design third edition*. 2005.



CHAPTER 5

Aviation Technologies and Applications
E-ISBN:978-605-338-471-7
2025, chap. (5) , pp. 75-91.

INVESTIGATION OF DAMAGES OCCURRED DURING GRINDING OF B737-800 MAIN LANDING GEAR INNER CYLINDER CHROME COATING

Cahit BİLGİ^{1,*}

ABSTRACT

Most of the landing gear and landing gear parts of B737-800 Aircraft consist of high-strength steel such as 4340M. To protect the landing gear steels against corrosion, they are coated with chrome, which has very high corrosion resistance. The crack problem visible to the naked eye in the chrome plating can only be seen in the inner cylinder coating. BOEING SOPM 20-42-03 chrome plating section considers inspection under light with the naked eye sufficient as a quality control criterion and does not allow macro cracks visible to the naked eye. Considering the environment and geometry in which the chrome-plated landing gear is operated, it is essential that the coating is done properly and accurately, as it is not possible to apply repeated heat treatment. In this study, the formation of microcracks that cause macrocracks was examined experimentally using scanning electron microscopy (SEM), Fluorescence Penetrant Method (FPI) and Rockwell C (HRC) hardness tests. Although the cause of damages in the chrome plating and the base metal depends on many parameters, it has been determined that the main reason for the current defects is the out-of-limit (high) heat accumulation during grinding. It has been observed that the thermal damage that occurs during grinding is caused by gaps in the machine beds, balance problems, appropriate grinding wheel selection, and insufficient cooling fluid. The friction caused by the bearing gap in the machine is reduced by approximately 4 times from $\mu = 0.0035$ to 0.001 ; Extruded ceramic particles (sintered alumina) with appropriate porosity are developed and produced with different length/width ratios; Damages that may occur during grinding were prevented by using a grinding wheel from $TG = 4/1$ to $TG = 8/1$ and increasing the coolant flow rate by 1 L

Keywords: B737-800, Landing gear, Chrome plating, Nital etching

1. INTRODUCTION

Many landing gear parts of Boeing aircraft consist of high-strength steel such as 4340M, heat treated at 180-220 ksi pressure values. These alloys are preferred in aircraft structures because they provide low weight and high strength[1]. Compared to other ultra-high-strength steels, AISI/SAE 4340 steel has a structure that combines hardness, toughness, high ductility, and strength[2].

*Corresponding Author: cahit.bilgi@iuc.edu.tr

¹ ORCID ID: 0000-0002-7432-2817, Aircraft Tecnology, Vocational School of Technical Sciences, İstanbul University-Cerrahpaşa, İstanbul, Türkiye

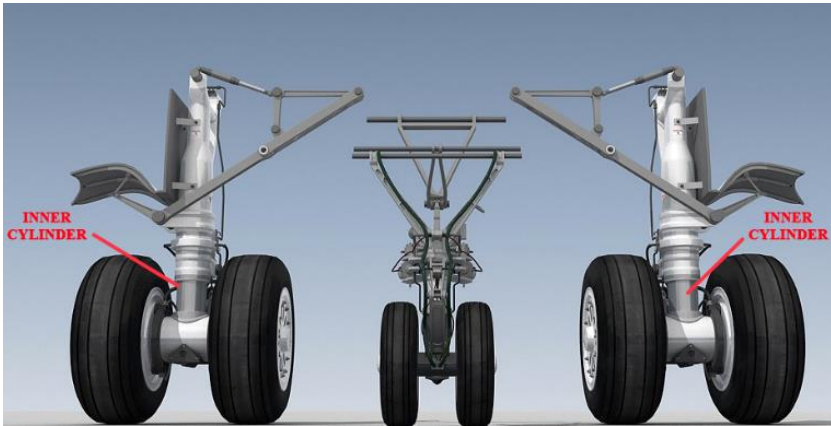


Figure 1. B 737-800 Landing Gear Inner Cylinder

It is known in the literature that microcracks in the chrome layer result from the formation of unstable chromium hydrides with different shapes[3]. E.N. Atabay stated in her study that any material is not suitable when considering the hard coating chrome alternative, repeatability of the coating, geometry of the parts, environments in which the parts are operated, and heat treatment conditions. In addition, the reason why the chrome plating hardness was lower than the value given in the literature (700-1000 HV) was evaluated as heat treatment. When they examined the microstructure pictures, they found that the chrome plating was more complete, homogeneous, and without porosity[4]. M. Nascimento et al showed in their studies that electroplated hard chrome has a lower micro crack density than conventionally coated hard chrome[5]. M. Nascimento et al explained that hard chrome plating with the shot peening method is an effective method to improve fatigue strength[6]. In their study, N. Eliaz et al found that the chrome coating in the front hairline cracks of the main landing gear structure of a cargo plane was exposed to excessive local heating during grinding[7]. In his study on the B747 main landing gear, S. Barter found that cracks existed after each revision and that the cracks progressed due to fatigue. In addition, during the last revision maintenance before the main landing gear was destroyed, the damage-free inspection performed with the magnetic particle method showed that there were acceptable cracks according to the component maintenance manual[8]. H. Henning explained that micro-cracks are harder and have higher resistance, and at the same time, corrosion progresses very quickly when a piece reaches the macro crack structure[9].

The use of high O and S during coating causes the corrosion proceeding through the coating cracks and pores to remove the coating exchange. To increase the corrosion resistance of the coating, the brittleness of the coating must be reduced[10].

The chrome plating of the landing gear inner cylinder parts of the Boeing B737-800 aircraft, shown in Figure 1, are renewed during major overhaul maintenance. The crack problem visible to the naked eye in the chrome plating can only be seen in the inner cylinder coating. BOEING SOPM 20-42-03 chrome plating section accepts naked eye inspection under light as a quality control criterion and does not allow macro cracks that can be seen with the naked eye, as seen in Figure 2[11]. Therefore, no micro-level control is made for chrome plating. Because at the micro level, all hard chrome coatings already have a cracked morphology, it is impossible to see these cracks with visual inspection.

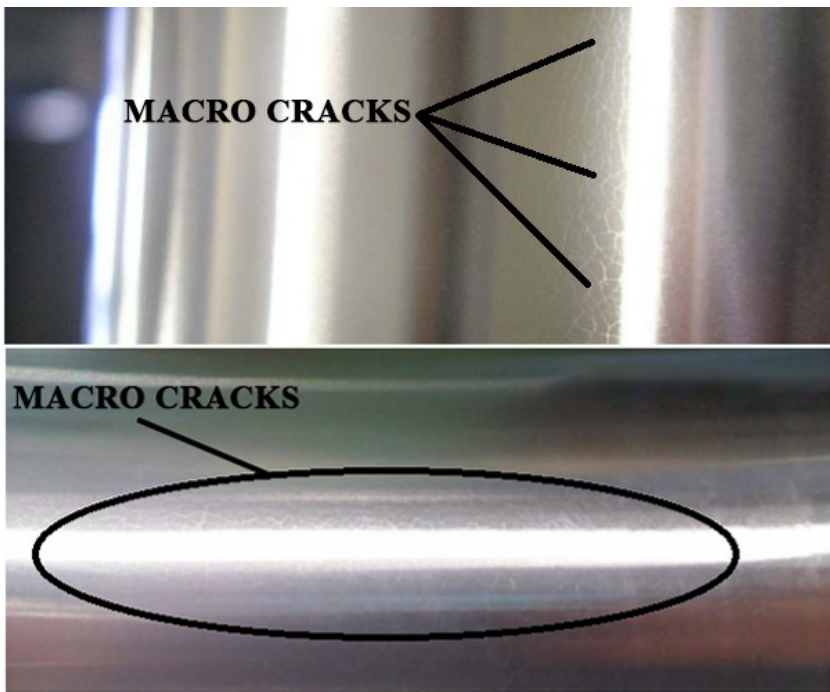


Figure 2. B737 – 800 Main landing gear inner cylinder macro cracks

CHAPTER 5: INVESTIGATION OF DAMAGES OCCURRED DURING GRINDING OF B737-800 MAIN LANDING GEAR INNER CYLINDER CHROME COATING

Boeing Aircraft Corporation (BAC) applies the 5855 Low-stress grinding of coatings standard for the chrome coating grinding on the main landing gear struts of Boeing aircraft. According to this standard, the upper limit for grinding progress is 0.0002"[12]. Grinding is used to remove the chrome layer, but also to obtain a shiny surface after chrome plating[13] and to clean chrome residues.

There is a problem of grind burning[14] of the steel under the coating during grinding. Fast rotation of the grinding wheel and lower grit number decrease productivity[12]. It is available in the literature that fatigue cracks occurring in chrome coatings are caused by the grinding device rotating at thousands of revolutions, damaging the chrome in the chamber[15]. If the hardness of the abrasive stone used during grinding is higher than the hardness of the coating, the abrasive penetrates the coating, grinding burns occur and micro-fractures occur as small chips separate[16]. At the same time, sharpening or deformation of the grinding wheel initiates fatigue cracks[17] due to high temperatures.

In this study, it was aimed to experimentally determine the causes of macro cracks in the inner cylinder of the main landing gear struts of B737-800 aircraft in Figure 3(b).

This study is to examine with experimental methods the formation of micro cracks that cause macro cracks in the chrome coating on the inner cylinder of the main landing gear struts of the B737-800 aircraft, shown in Figure 3 (a). It also aims to provide solutions to complete the maintenance of landing gear struts without damaging the strut, to extend the life of the strut and to reduce the costs that may arise from strut damage.



(a)



(b)

Figure 3. Chrome plating (a); B737 – 800 Main landing gear inner cylinder (b).

2. MATERIALS and METHODS

2.1. AISI/SAE 4340 M Steel

The main landing gear, which carries the load of the aircraft and can absorb all the potential energy during each landing, is made of AISI/SAE 4340 steel. Since it contains the elements given in Table 1, it has properties that are superior to these elements. It has deep hardenability, high ductility, toughness, strength, and high fatigue and creep resistance. It is frequently used in places where heavy service conditions exist and high strength is required in heavy sections. In thin sections, this steel air hardens; in practice, it is usually quenched with oil. It is especially resistant to anger vulnerability. It does not soften easily at high temperatures; that is, they exhibit good power retention. Hydrogen embrittlement is a problem for 4340 heat treated to higher tensile strengths than about 1400 MPa (200 ksi)[18,19]. Parts exposed to hydrogen during processes such as pickling and plating must then be baked[20,21]. This steel has extremely poor resistance to stress-corrosion[22,23] cracking when tempered to a tensile strength of 1500 to 1950 MPa (220 to 280 ksi)[24].

Table 1. Chemical composition of AISI 4340 steel (% weight)[19].

	Fe	C	Mn	Si	P _(max)	S _(max)	Cr	Ni	Mo
SAE 4340	Balance	0.38–0.43	0.60–0.80	0.15–0.35	0.04	0.04	0.70–0.90	1.65–2.00	0.20–0.30

During component design, eliminating or minimizing areas of stress concentrations is a key objective. Special attention is given to protective finish runouts adjacent to stress concentration details. Any rework or repair must not increase stress concentrations that degrade component durability.

2.2. Maintenance of main landing gear 4340 M steel

During repair, personnel must observe the plating runouts specified in the component maintenance manual (CMM) sections and SOPMs 20-10-01 and 20-42-03[25]. For example, when a coating such as chrome or nickel plating is applied to surfaces to prevent wear or corrosion, the coating must exhibit proper runouts that terminate before the tangent of fillet radius, edges, or other shape changes. Boeing SOPM guidelines should be followed for the rework of any component and all types of plating or

CHAPTER 5: INVESTIGATION OF DAMAGES OCCURRED DURING GRINDING OF B737-800 MAIN LANDING GEAR INNER CYLINDER CHROME COATING

coating. Rework or overhaul of components should not introduce stress concentrations, or otherwise increase stresses, which can reduce the service life of a component below that of the original design configuration. Stress concentrations can lead to the initiation of cracking by fatigue, stress corrosion, or hydrogen-assisted stress corrosion[26–28].

Plating conditions and runout controls that are not by design standards:

During overhaul, many landing gear components are completely stripped to replace nickel and chrome plating. In most instances, these repairs involve rework of the base metal. The new plating deposits frequently are thicker than the original design configuration. In all cases, it is important to adhere to the SOPM recommendations. This will ensure that the restored plating is of high quality and that it does not terminate with an abrupt edge. Thickness cracks in chrome plates (generally present where there is evidence of chicken wire cracking) can lead to corrosion at the base metal interface and deterioration of the plating adhesion. In addition, in these repairs on chrome plating, thermal damage may sometimes occur due to incorrect grinding, as shown in Figure 4. Through-thickness cracking also can lead to fatigue or stress corrosion cracking of the base metal beneath the plating.



Figure 4. B737-800 MLG inner cylinder strut area where thermal damage occurs

Routine or non-routine landing gear checks in aviation, according to BOEING SOPM 20-10-02 Alloy steel processing department standards, do not allow thermal damage on the main metal surface in the control made after nital etching. In these cases, if there is a margin (maximum error limit diameter: 4.4680"), the part must be reprocessed by following the steps given in Table 2. There is no micro-level control for chrome plating in the aviation industry. Because all hard chrome coatings already have a cracked morphology at the micro level and it is impossible to see these cracks with visual inspection, visible macro cracks are given in Figure 2.

Table 2. Process after thermal damage

	Process
1	Electrolytic remove chromium plate
2	Grinding the damaged diameter
3	Nital etching testing
4	Re-grinding the diameter to max. allowable limit (4.4680 inches)
5	Nital etch testing
6	Hardness measurement
7	Final grinding
8	Hardness measurement (HRC)
9	Bake
10	FPI – Flouresan penetrant inspection

In this study, the main landing strut inner cylinder of the B 737-800 aircraft was imaged with SEM and FPI at different stages and hardness tests were performed. An attempt was made to determine at what stage the damage occurred.

3. RESULTS

Although the cause of damages/defects in the chrome plating and the base metal depends on many parameters, the main reason for the current defects is the out-of-limit (high) heat accumulation during grinding. Thermal damage that occurs especially in the base metal strongly confirms this. SEM of cracks in the coatings is given in Figure 5.

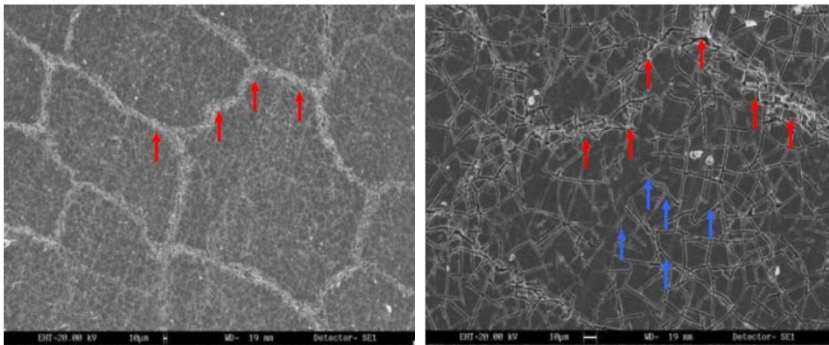


Figure 5. SEM image of natural micro-cracks (blue arrows) and macro-cracks (red arrows) in chrome plating

CHAPTER 5: INVESTIGATION OF DAMAGES OCCURRED DURING GRINDING OF B737-800 MAIN LANDING GEAR INNER CYLINDER CHROME COATING

While the average hardness of the B737-800 MLG inner cylinder was 55 HRC, the average hardness of the heat-damaged area was measured as 44 HRC. Figure 6 shows the hardness measurement graph, figure 7 shows etching, FPI, and grinding photographs, and figure 8 shows FPI images of thermal damage occurring during grinding.

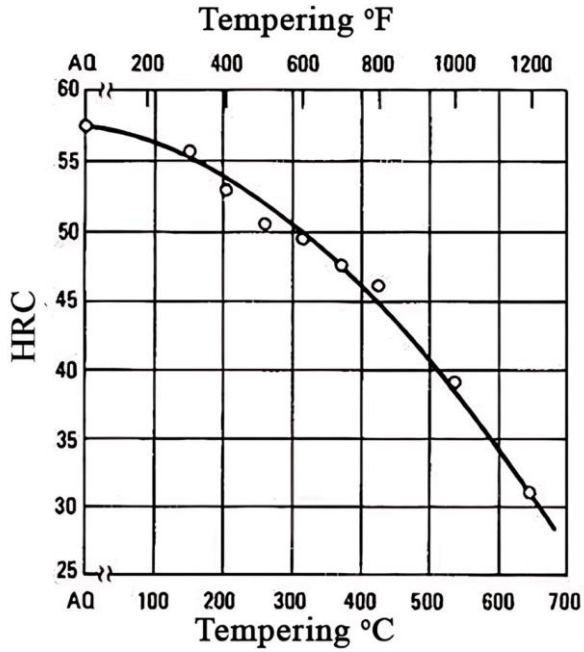
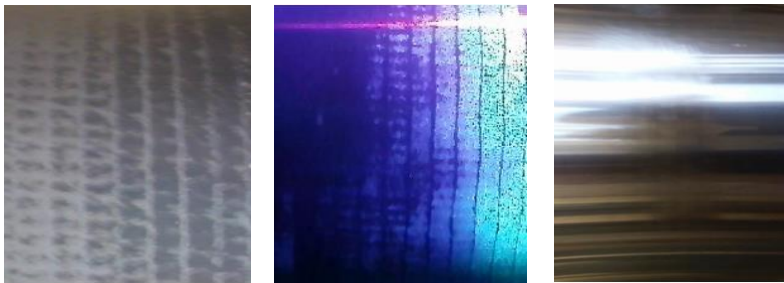


Figure 6. B737-800 MLG inner cylinder HRC chart



(a) Nital etching **(b)** FPI **(c)** Final grinding
Figure 7. Nital etching (a); FPI (b); Final grinding (c)

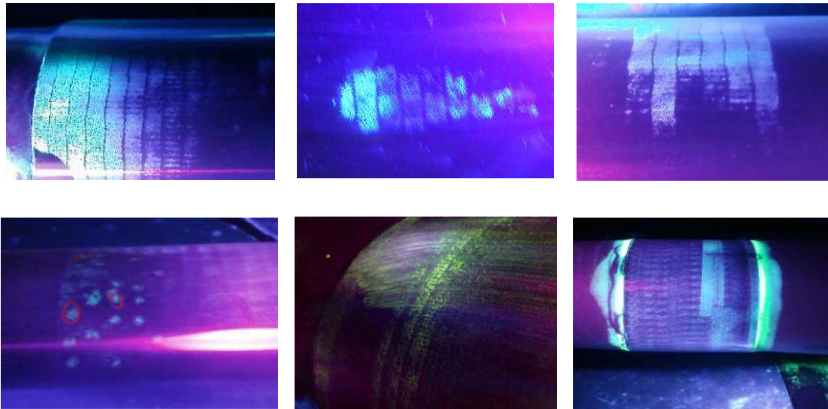


Figure 8. FPI images of thermal damage caused by poor grinding

3.1. Examination of Heat Damages

Incorrect material removal procedures make the part too hot and cause heat damage. The etch inspection procedure helps you find retempering burns, re-hardening burns, grinding or machining burns, and other heat-related damage. Visually examine all completed holes and completed machined surfaces for the correct surface roughness and to see if they became too hot. The surface quality (such as local differences from the specified contour, nicks, gouges, and scratches) must agree with standard industry practices. Parts are unserviceable if they have color changes (such as a blue or dark gray tint) because they became too hot, or if they have tears, chatter marks, or cracks. The surface roughness of holes must be 125 microinches or smoother unless overhaul instructions are different. No sign of corrosion is permitted[29–31].

4. DISCUSSION

Although the cause of damages/defects in the chrome plating and base metal depends on many parameters, the main reason for the current defects is the accumulation of out-of-limit (high) heat (≥ 435 °C) during grinding.

Cracks can result from grinding burns, or scorches, caused by localized frictional heating during grinding. Grinding burns vary in severity from a lightly tempered condition to fresh, untempered martensite. Sometimes, only a shallow layer, 0.0025 to 0.0075 mm (0.0001 to 0.0003 in.) deep, is affected, but heavy grinding produces much deeper burned layers. Heavy grinding causes localized heating sufficient to raise the surface temperature to the austenitizing temperature of 760 to 870 °C (1400 to 1600 °F).

Subsequent rapid quenching by the grinding coolant results in brittle surface layers of untempered martensite. Also, if the surface contains residual compressive stresses, such as those developed during carburizing, heating the surface to its austenitizing temperature will relieve these beneficial compressive stresses.

Mild grinding burns[32] consist of shallow layers that have only been tempered; maximum surface temperatures do not exceed Ac1. In many respects, mild grinding burns resemble heat-affected zones (HAZ) in steel weldments. A similar shallow, tempered layer exists beneath the untempered layer of a severe grinding burn. These tempered layers, although less brittle than untempered layers, are nevertheless regions where material properties differ from those in the interior of the part.

Tempering[33] can induce changes in surface stresses formation of cracks or both. Because the heated area is localized, its ability to contract is restricted by surrounding harder and stronger martensitic regions that have not been heated (tempered) during grinding. The tempered regions subsequently contain residual tensile stress. If this residual tensile stress is great enough to exceed the strength of the tempered material, cracks form.

Grinding burns can be revealed by etching the ground surface in a Nitric acid solution[34]. A surface that contains grinding burns exhibits a series of dark-gray streaks on a light-gray background. The streaks follow the grinding direction, and the severity varies from a few very small streaks to an almost completely dark gray surface. In general, abusive machining[35] promotes higher temperatures and excessive plastic deformation. Gentle machining operations occur when a sharp tool is employed and when machining conditions result in reduced machining forces.

Thermal damage that occurs especially in the base metal strongly confirms this. It has been determined that thermal damage occurring during grinding occurs due to the following 3 main reasons.

4.1. Gaps and Balance Problems in the Bearings of the Grinding Machine

It has been observed that the maximum pass required during grinding of chrome plating is given much more uncontrollably due to the bearing gap in the machine, and the heat generated due to excessive friction (≤ 4 times) ($\mu = 0.001$ to 0.0035) causes morphological changes on the base metal and chrome surface.

When the GIORIA grinding machine was checked after the problems, the ball bearings were damaged, so the machine was taken into maintenance and the damaged bearings were replaced with roller bearings. Although the cause of damages/defects in the chrome plating and base metal depends on many parameters, the main reason for the current defects is the accumulation of out-of-limit (high) heat (≥ 435 °C) during grinding.

4.2. Inappropriate Grinding Wheel Selection

The currently used grinding wheels were domestically produced grinding wheels given in figure 9 (a). It has been determined that these grinding wheels produce more heat because they have low porosity, and it has been observed that they are not effective in reducing the heat.

Extruded ceramic grains (sintered alumina) recommended by BOEING given in Figure 9 (b) are developed and produced with different length/width ratios; TG = 4/1 to TG = 8/1. The elongated shapes of the grains lead to a random orientation during the mixing process and hence to open porosity and high permeability without the use of any pore formers.

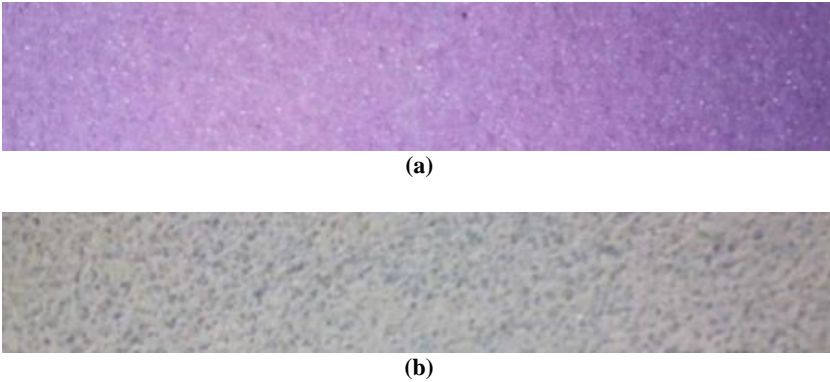


Figure 9. Domestic production low porosity alumina-based grinding wheel (a); High porosity grinding wheel recommended in the BOEING manual (b).

When unsuitable stone is used, mud, sediments, and residues remain around the grinding stone and negatively affect the surface quality. A cleaning water system for the abrasive stone is needed to get rid of residues[36]. The correct wheel requires lower grinding forces and causes less plastic deformation, thus resulting in lower form determination[37].

4.3. Insufficient Cooling Fluid

The function of the cooling fluid during grinding is to remove the heat produced by friction from the part surface. If the flow rate of the liquid is insufficient, it may cause thermal damage to the coating and base metal as the heat produced cannot be removed from the part.

In the measurements, it was determined that the coolant was below the limit and there was a need to increase the flow rate (1L), and the flow rate was increased by installing a suitable pump.

Insufficient cooling oil will cause insufficient cooling capacity. Additionally, increasing the viscosity of the cooling oil slows down the cooling cycle and causes heating during grinding[37]. The location of the cooling system and the distribution system are very important in terms of cutting force and tangential component force during grinding under hard conditions[36].

5. CONCLUSION

The use of correct stone prevents the accumulation of mud layers on the surface, and the surface quality increases as the damage caused by mud and other residues on the surface is minimized. It has also been observed that the higher thermal conductivity of the high porosity grinding wheel recommended by BOEING provides faster cooling and reduces possible damage. The aspect ratios of ceramic stones made of sintered alumina are suitable for use from $TG = 4/1$ to $8/1$. Increasing the distance between sintered alumina on a micro scale allows the transfer of heat and cooling occurs faster.

It has been observed that when the cooling liquid is sufficient, thermal damage is greatly reduced. Before operating the machine, the cooling liquid must be checked and not be operated when the cooling liquid drops below the critical level. In cases where there is insufficient coolant (cooling oil), the viscosity increases, the time it takes for the coolant to complete the cycle is prolonged, and therefore damage due to overheating occurs. The coolant should not be less than 5L.

Periodic maintenance of the grinding machine should not be interrupted and periodic calibration is recommended. In addition, before each operation, a general visual inspection should be made, especially the gaps that may occur in the grinding wheel due to bearing failure. It causes an

increase in tangent forces due to bearing failure and increases the wear coefficient by approximately 4 times. The temperature becomes out of limit (≥ 435 °C), causing thermal damage to the chrome plating and the underlying 4340M steel.

In summary, the damages that occurred during grinding on the chrome plating of B737-800 MLG 4340M steel were successfully detected. Beneficial outputs were obtained for the aircraft maintenance industry.

Originality

In this study, for the first time, the formation of micro-cracks that cause macro cracks in the inner cylinder of the main landing gear struts of B737-800 aircraft was examined and explained with experimental methods.

Suggestions

It has been observed that the gaps formed in the grinding machine may cause damage to the base metal and coating. Therefore, the grinding machine must be checked before use. The machine should not be used beyond its economic life. Periodic maintenance of the machine must be done on time. The machine needs to be calibrated.

Acknowledgements

This study was supported by the Scientific Research Project Coordinator of Karabük University within the scope of the KBÜBAP-21-DR-080 project. TURKISH TECHNIC Inc. supported some of the experimental studies. The author greatly appreciates the sponsorships of the abovementioned universities and companies for their generous support.

Conflict of interest

No conflict of interest was declared by the authors.

REFERENCES

- [1] B.L. Boyce, T.B. Crenshaw, M.F. Dilmore, SANDIA REPORT The Strain-Rate Sensitivity of High-Strength High-Toughness Steels, 2007. <http://www.ntis.gov/help/ordermethods.asp?loc=7-4->.
- [2] R. Araujo Barros, A.J. Abdalla, H.L. Rodrigues, M. dos Santos Pereira, Characterization of a AISI/SAE 4340 steel in different microstructural conditions, in: Materials Science Forum, Trans Tech Publications Ltd, 2014: pp. 136–140. <https://doi.org/10.4028/www.scientific.net/MSF.775-776.136>.
- [3] F. Sánchez Lasheras, J.A. Vilán , P.J. García Nieto, J.J. del Coz Díaz, The use of design of experiments to improve a neural network model in order to predict the thickness of the chromium layer in a hard chromium plating process, *Math Comput Model* 52 (2010) 1169–1176. <https://doi.org/10.1016/j.mcm.2010.03.007>.
- [4] E.N.A. Durul, M. Nurbas, Corrosion Behavior of Different Thermal Spray Coatings and Hard Chromium Electroplating on A286 Super Alloy, *Adv Mat Res* 154–155 (2010) 226–229. <https://doi.org/10.4028/www.scientific.net/AMR.154-155.226>.
- [5] M.P. Nascimento, R.C. Souza, W.L. Pigatin, H.J.C. Voorwald, Effects of surface treatments on the fatigue strength of AISI 4340 aeronautical steel, *Int J Fatigue* 23 (2001) 607–618. [https://doi.org/10.1016/S0142-1123\(01\)00015-9](https://doi.org/10.1016/S0142-1123(01)00015-9).
- [6] M.P. Nascimento, R.C. Souza, I.M. Miguel, W.L. Pigatin, H.J.C. Voorwald, Effects of tungsten carbide thermal spray coating by HP/HVOF and hard chromium electroplating on AISI 4340 high strength steel, *Surf Coat Technol* 138 (2001) 113–124. [https://doi.org/10.1016/S0257-8972\(00\)01148-8](https://doi.org/10.1016/S0257-8972(00)01148-8).
- [7] N. Eliaz, H. Sheinkopf, G. Shemesh, H. Artzi, Cracking in cargo aircraft main landing gear truck beams due to abusive grinding following chromium plating, *Eng Fail Anal* 12 (2005) 337–347. <https://doi.org/10.1016/j.engfailanal.2004.10.004>.
- [8] S.A. Barter, Investigation of a Boeing 747 wing main landing gear trunnion failure, *Eng Fail Anal* 35 (2013) 387–396. <https://doi.org/10.1016/j.engfailanal.2013.03.026>.
- [9] H.F. Henning, Chromium plating, *Annals of Occupational Hygiene* 15 (1972) 93–97. <https://doi.org/10.1093/annhyg/15.1.93>.
- [10] Q. Zhang, J. Wang, W. Shen, F. Huang, Y. Zhao, Failure Analysis of Chromium Plating Layer on the Surface of the Piston Rod of the Hydraulic Jack, *Coatings* 12 (2022). <https://doi.org/10.3390/coatings12060774>.
- [11] Commercial Airplanes 777 Service Bulletin, 2011.

- [12] D.S. Parker, K. Legg, Validation of HVOF WC/Co Thermal Spray Coatings as a Replacement for Hard Chrome Plating on Aircraft Landing Gear, 2004. <https://www.researchgate.net/publication/259088399>.
- [13] M. Marek, M. Novák, K. Šramhauser, MANUFACTURING TECHNOLOGY, 19 (2019). <http://www.scopus.com>.
- [14] E. Security, ESTCP Cost and Performance Report Development of Ferrium® S53 High-Strength, Corrosion-Resistant Steel, 2009.
- [15] P.J. Cote, M.E. Todaro, M. Witherell, FACTORS AFFECTING CHROME LOSS IN GUN TUBES, 2003.
- [16] Q. Wang, S. Luo, S. Wang, H. Wang, C.S. Ramachandran, Wear, erosion and corrosion resistance of HVOF-sprayed WC and Cr 3 C 2 based coatings for electrolytic hard chrome replacement, Int J Refract Metals Hard Mater 81 (2019) 242–252. <https://doi.org/10.1016/j.ijrmhm.2019.03.010>.
- [17] C.R. Gagg, Failure of components and products by “engineered-in” defects: Case studies, Eng Fail Anal 12 (2005) 1000–1026. <https://doi.org/10.1016/j.engfailanal.2004.12.008>.
- [18] W.-S. Lee, T.-T. Su, Mechanical properties and microstructural features of AISI 4340 high-strength alloy steel under quenched and tempered conditions, 1999.
- [19] M.F. de Souza, L.F. Serrão, J.M. Pardal, S.S.M. Tavares, M.C. Fonseca, Tempering influence on residual stresses and mechanical properties of AISI 4340 steel, International Journal of Advanced Manufacturing Technology 120 (2022) 1123–1134. <https://doi.org/10.1007/s00170-022-08880-3>.
- [20] D.J. Figueroa Gordon, HYDROGEN RE-EMBRITTEMENT SUSCEPTIBILITY OF ULTRA HIGH STRENGTH STEELS, n.d.
- [21] S. Laliberté-Riverin, J. Bellemare, F. Sirois, M. Brochu, Internal hydrogen embrittlement of pre-cracked, cadmium-plated AISI 4340 high strength steel with sustained load tests and incremental step-loading tests, Eng Fract Mech 223 (2020). <https://doi.org/10.1016/j.engfracmech.2019.106773>.
- [22] L. Weng, J. Zhang, S. Kalnaus, M. Feng, Y. Jiang, Corrosion fatigue crack growth of AISI 4340 steel, Int J Fatigue 48 (2013) 156–164. <https://doi.org/10.1016/j.ijfatigue.2012.10.015>.
- [23] S. Ramamurthy, W.M.L. Lau, A. Atrens, Influence of the applied stress rate on the stress corrosion cracking of 4340 and 3.5NiCrMoV steels under conditions of cathodic hydrogen charging, (2011). <https://doi.org/10.1016/j.corsci.2011.03.028>.
- [24] Handbook of Materials Selection for Engineering Applications - Google Kitaplar, (n.d.).

- https://books.google.com.tr/books?hl=tr&lr=&id=60tZDwAAQBAJ&oi=fnd&pg=PA149&dq=Thoni+V.+Philip,+Thomas+J.+McCaffrey%3B+ASM+Handbook,+Volume+1,+Ultrahigh-Strength+Steels,+4340+Steel&ots=gPj-9X3a_y&sig=GvnwiKZIVJ4BKN0Yy1Z68UZVlS8&redir_esc=y#v=onepage&q&f=false (accessed March 22, 2024).
- [25] Commercial Airplanes 777 Service Bulletin, 2011.
- [26] X. Lin, R. Zhang, Y. Mei, L. Yang, F. Yang, B. Dou, Y. Wei, Corrosion electrochemical behavior of cadmium-plated 4340 steel in aircraft landing gears under thin electrolyte layers of potassium acetate deicing fluid, *New Journal of Chemistry* 43 (2019) 14435–14442. <https://doi.org/10.1039/c9nj02535a>.
- [27] B.T. Daymond, N. Binot, M.L. Schmidt, S. Preston, R. Collins, A. Shepherd, Development of Custom 465® Corrosion-Resisting Steel for Landing Gear Applications, *J Mater Eng Perform* 25 (2016) 1539–1553. <https://doi.org/10.1007/s11665-015-1830-5>.
- [28] B. Krstic, L. Rebhi, D. Trifkovic, N. Khetrou, M. Dodic, S. Peric, M. Milovancevic, Investigation into recurring military helicopter landing gear failure, *Eng Fail Anal* 63 (2016) 121–130. <https://doi.org/10.1016/j.engfailanal.2016.02.018>.
- [29] Commercial Airplanes 777 Service Bulletin, 2010.
- A. Bussiba, M. Kendler, Microstructure Modifications due to Abusive Grinding Resulted in Unexpected Catastrophic Failure of Main Landing Gear in Civilian Aircraft, *Journal of Failure Analysis and Prevention* 23 (2023) 671–681. <https://doi.org/10.1007/s11668-023-01601-2>.
- [30] S. Sun, ; Da, Q.; Liu, M.; Brandt, M.; Janardhana, G. Clark, Microstructure and mechanical properties of laser cladding repair of AISI 4340 steel, n.d. <https://researchrepository.rmit.edu.au/esploro/outputs/conferenceProceeding/Microstructure-and-mechanical-properties-of-laser/9921858642101341>.
- [31] E. Security, ESTCP Cost and Performance Report Development of Ferrium® S53 High-Strength, Corrosion-Resistant Steel, 2009.
- A. AlSumait, Y. Li, M. Weaser, K. Niji, G. Battel, R. Toal, C. Alvarez, O.S. Es-Said, A Comparison of the Fatigue Life of Shot-Peened 4340M Steel with 100, 200, and 300% Coverage, *J Mater Eng Perform* 28 (2019) 1780–1789. <https://doi.org/10.1007/s11665-019-03891-w>.
- [32] J. Wen, J. Tang, W. Shao, W. Zhou, W. Huang, Towards Understanding Subsurface Characteristics in Burn Process of Gear

- Profile Grinding, Materials 16 (2023).
<https://doi.org/10.3390/ma16062493>.
- [33] R. M'Saoubi, D. Axinte, S.L. Soo, C. Nobel, H. Attia, G. Kappmeyer, S. Engin, W.M. Sim, High performance cutting of advanced aerospace alloys and composite materials, *CIRP Ann Manuf Technol* 64 (2015) 557–580. <https://doi.org/10.1016/j.cirp.2015.05.002>.
- [34] R.F. Damasceno, R. de S. Ruzzi, T.V. França, H.J. de Mello, R.B. da Silva, P.R. de Aguiar, E.C. Bianchi, Performance evaluation of various cooling-lubrication techniques in grinding of hardened AISI 4340 steel with vitrified bonded CBN wheel, *International Journal of Advanced Manufacturing Technology* 92 (2017) 3795–3806. <https://doi.org/10.1007/s00170-017-0434-7>.
- [35] R.L. Rodriguez, J.C. Lopes, M.V. Garcia, F.S. Fontequê Ribeiro, A.E. Diniz, L. Eduardo de Ângelo Sanchez, H. José de Mello, P. Roberto de Aguiar, E.C. Bianchi, Application of hybrid eco-friendly MQL+W CJ technique in AISI 4340 steel grinding for cleaner and greener production, *J Clean Prod* 283 (2021). <https://doi.org/10.1016/j.jclepro.2020.124670>.



CHAPTER 6

Aviation Technologies and Applications
E-ISBN:978-605-338-471-7
2025, chap. (6), pp.92-106.

FORMATION OF AVIATION EPOXY MATRIX ARALDITE LY5052 SOLUTION WITH GRAPHENE NANO ADDITIVE

Cahit BİLGİ^{1,*}, Bilge DEMİR²

ABSTRACT

Efforts are being made to improve material properties and reduce costs in the rapidly developing aviation industry. Composites, which are multifunctional, high-strength, cost-effective, and lightweight materials, constitute approximately 50% of the structural elements in civil aviation aircraft.

Companies such as AIRBUS and BOEING, the world's largest aircraft manufacturers, have produced more functional and stronger composites using nano additives in composite production. Research and development studies use graphene (GNP) nano additives to produce aviation composites. Due to its high thermal and electrical conductivity, graphene is used in aircraft panels, brake units, and aircraft paints where lightning protection and electrical ice prevention/destruction systems are used. The construction of a compactly interconnected graphene network in Three Dimensions provides a significant increase in the electrical and thermal conductivity of polymer composites.

In this study, Neat - 0.5 – 1 – 1.5% functionalized GNP (FGNP) additive by weight was added to Araldite LY5052, an aviation epoxy used in the aviation industry, to functionalize the GNP surface to improve the properties of composites in the aviation industry and to ensure homogeneous distribution of FGNP in the epoxy without aggregation. Its methodology has been investigated. To measure aggregation, the prepared solution was analyzed by Ultraviolet and visible light (UV-Vis) absorption spectroscopy.

SDS (Sodium Dodecyl Sulfate) surfactant is effective for functionalizing GNP, but the Critical Micellar Concentration (CMC) method must be strictly followed to determine the amount of SDS. In UV-Vis absorption, the 285 nm and 298 nm peaks in the graph are considered to be π - π and n - π grooves, respectively. It is seen that 0.5% FGNP contribution is significantly successful, but 1% FGNP contribution is also quite significant.

Keywords: Graphene Functionalization, Araldite LY5052, UV-Vis, Aviation

1. INTRODUCTION

Airplanes are covered with electrically conductive metals using the Faraday Cage principle, or the conductors are woven in the form of a mesh cover. This cover in the aircraft structure is in the form of an enclosure that protects the internal volume from electrical fields in the external environment and ensures flight safety.

*Corresponding Author: cahit.bilgi@iuc.edu.tr

1 ORCID ID: 0000-0002-7432-2817, Aircraft Technology, Vocational School of Technical Sciences, İstanbul University-Cerrahpaşa, İstanbul, Türkiye.

2 ORCID ID: 0000-0002-3617-9749, Mechanical Engineering, Engineering Faculty, Karabük University, Karabük, Türkiye.

The use of composite materials in aircraft structural parts poses difficulties due to this situation. The use of non-metallic composite materials as aircraft structural materials in the fuselage is a significant disadvantage because they are insulators. For this reason, it is aimed to provide electrical conductivity to polymeric composite materials by applying various applications. In this context, graphene and carbon nanotubes have become the focus of attention in the aviation industry due to their low density and easy-to-mix structures, and mechanical, electrical, and thermal properties[1].

Carbon, denoted C, is a 6-electron substance with an atomic weight of 12.011 g/mol and is located in group 4A in the periodic table. Carbon atoms are bonded only to each other by covalent bonds, and they bond in 3 different ways (sp, sp², sp³) depending on the number of electrons.[2]. Fullerene, which is one of the different allotropes of carbon, is 0-dimensional (0D), carbon nanotubes are 1-dimensional (1D), graphene is 2-dimensional (2D), and diamond and graphite are 3-dimensional (3D)[3].

Table 1. Specifications of Carbon Allotropes

Specifications	Graphene	Carbon Nanotube (CNT)	Graphite	Fullerene
Surface Area (m ² /g)	2630	1315	10	5
Thermal Conductivity (W/MK)	5000	≥3000 (MWCNT)	3000	0.4
Mobility (cm ² /Vs)	15 000	100 000	13 000	0.56
Young Module (TPa)	1	0.64	1.06	0.01
Optical Transmittance (%)	97.7	-	-	-

The use of graphene nanoparticles to create advanced multifunctional composite materials with polymer matrix is an innovative method in the aerospace, automotive, and defense industries[4]. As given in Table 1, graphene has the highest thermal conductivity (5000 W/MK) and Young's modulus (1 TPa) among carbon allotropes, therefore the thermal conductivity and mechanical properties of the nanocomposite to be formed in composites doped with graphene will increase. In addition, its large surface area (2630 m²/g) shows that even a small amount of doping will be

successful. Due to its high thermal and electrical conductivity, graphene is used in aircraft lightning protection (Faraday cage) and electrical ice prevention/destruction system panels, brake units, and aircraft paints[5]. The construction of a compactly interconnected graphene network in Three Dimensions can achieve a significant increase in the electrical and thermal conductivity of polymer composites. In addition, corrosion is a very important and undesirable condition in aircraft structures. Due to its barrier properties, graphene can be used to increase corrosion resistance[6].

Composite materials are 40% lighter than aluminum materials and are preferred in the aviation industry due to their very good mechanical and physical properties [7]. In aviation, composites are produced using carbon fiber-reinforced epoxy polymer matrix. By using graphene nano additives in these composites, it is aimed to produce nanocomposites with higher strength and higher thermal and electrical conductivity.

The mechanical properties of composites with graphene nanoparticle additives at 0, 0.15, 0.25, 0.35, 0.45, and 0.75 by weight were examined and it was observed that the highest tensile strength was the sample containing 0.45% graphene additive and the tensile strength increased by 31.29%. The highest bending strength was seen in the sample with 0.25% graphene content. At this rate, bending strength increased by 34.74% compared to the pure sample[8].

Xiao Huang and colleagues argued that graphene-based filler materials also increase the thermal conductivity of polymer matrices, provided that single-layer graphene has a thermal conductivity of up to approximately 5000 W mK^{-1} at room temperature, and added that it also shows stability at increasing degradation temperature[9] In nanoparticle-added epoxy matrix nanocomposites, the increase in cross-link density, decrease in free volume, and restriction of movement at the molecular level lead to an increase in glass transition temperature (T_g)[10] Hu and his colleagues observed that the addition of graphene oxide in the polystyrene nanocomposite samples they made increased T_g as a result of the difficulty in the movement of the polymer chains[11]

To prevent aggregation in graphene and obtain a homogeneous mixture, its surface must be functionalized. There are methods such as chemical, covalent, and non-covalent to activate the surface, but non-covalent functionalization allows molecules to be attached to the surface of graphene by physical adsorption without forming any chemical bonds. π - π interactions between functional groups and graphene are achieved by

forming van der Waals bonds such as electrostatic attraction and adsorption, and by coating the molecules around the graphene. Homogeneous distribution is ensured in the solution prepared in DMF, tetrahydrofuran (THF), isopropyl alcohol (IPA), dichlorobenzene (DCB), acetone, ethanol, or DI water[12].

SDS is the best surfactant for surface functionalization even in the smallest amounts such as $\sim 10 \mu\text{M}$ for surface modification processes. In addition, SDS gave the best results even when the solution was kept for a time[13].

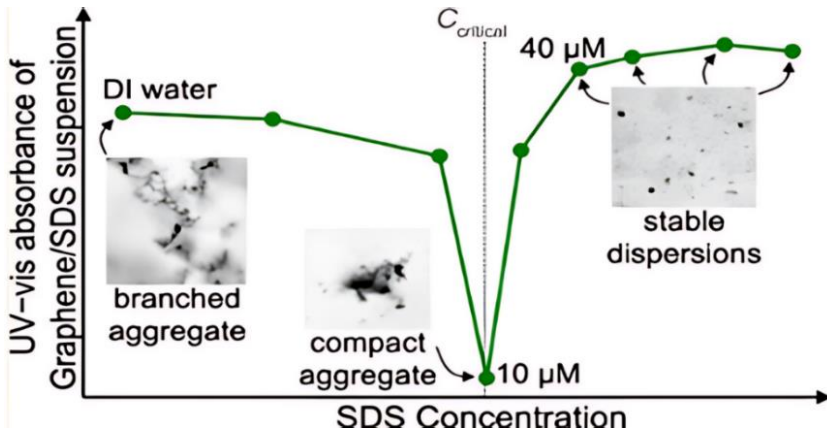


Figure 1. Graphene/SDS solution[13]

This study aims to create graphene solutions with an aerospace polymer matrix to produce graphene-doped nanocomposites that will provide significant advantages in the rapidly developing aerospace and defense industry.

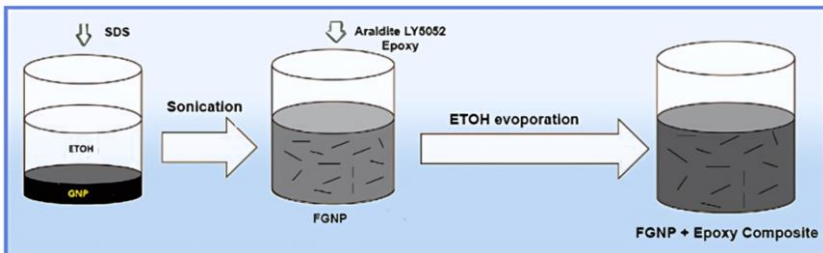


Figure 2. FGNP + Epoxy Solution

2. MATERIALS and METHODS

Graphene was added to 100 ml of ethyl alcohol (Sigma Aldrich 99.9%) in separate containers, and epoxy was added to it at a rate of Neat - 0.5-1-1.5% by weight, and an ultrasonic bath was given at room temperature for 30 minutes. To prevent the graphene from clumping and agglomerating in the epoxy, it will be mixed and homogenized first with a magnetic stirrer for 1 hour at 45 °C, then with a centrifugal mixer for 2 hours at 45 °C. Non-covalent surface modification of graphene with surfactants, ionic liquids, or macromolecules has been successful for highly stable dispersions of graphene sheets in both aqueous and organic media without altering the structural integrity of graphene[14]. Graphene has hydrophobic properties and its dispersion in liquid is not possible without the use of special surfactants[15] SDS surfactant was added to activate and functionalize the graphene surface[16].

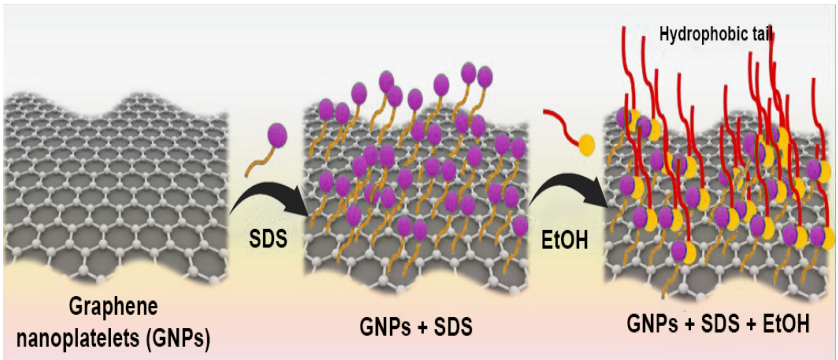


Figure 3. GNP surface modification, and formation of FGNP[17].

The critical Micellar Concentration (CMC) method was used to determine the amount of SDS [18]. In colloidal and surface chemistry, the CMC is defined as the surfactant concentration above which micelles form and any additional surfactants added to the system will form micelles[18] Before reaching the CMC, the surface tension varies strongly with the concentration of the surfactant. After reaching CMC, surface tension remains relatively constant or changes with a lower slope[19]. The CMC value for Sodium Dodecyl Sulfate (SDS) is 0.0082 mol/L.

The result obtained by multiplying the molecular weight of the SDS surfactant and the CMC for one liter of solution will determine the amount of SDS that should be added to the solution.



Figure 4. Ultrasonic Mixer (a); Magnetic Stirrer (b)

Ethyl alcohol used as graphene solvent was evaporated in a magnetic stirrer at 750 RPM and 50 °C for 24 hours and the de-gassing process was performed. After the ethyl alcohol was completely evaporated, 72.47 g of Araldite LY5052 (Epoxy A) was added and mixed in a magnetic stirrer for 15 minutes at 50 °C and de-gassing was performed.

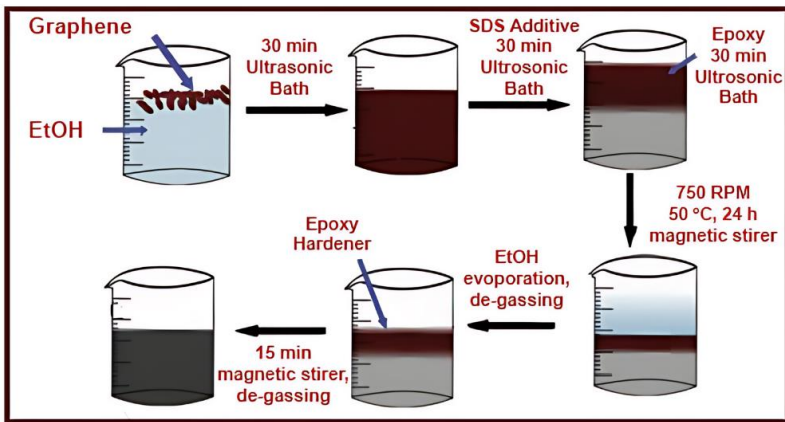


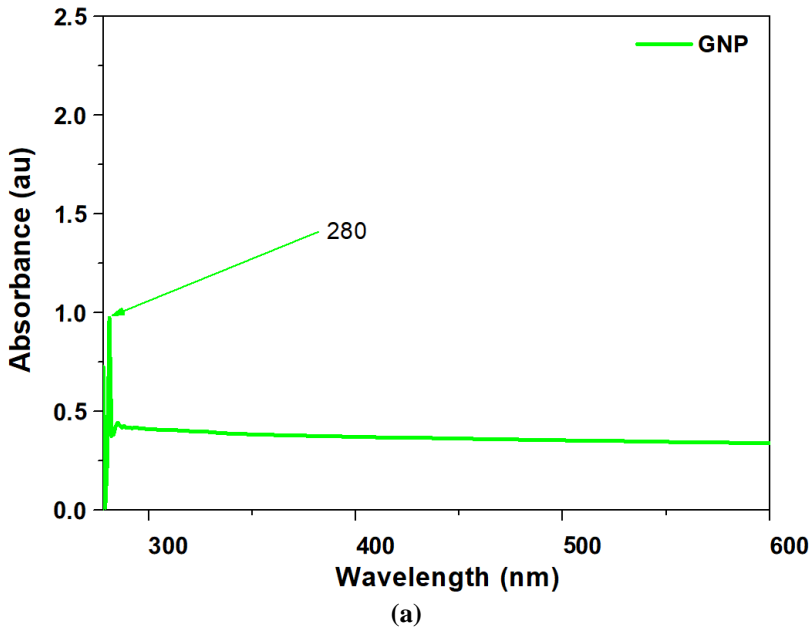
Figure 5. Graphene-added epoxy solution process

Ultraviolet and visible light (UV-Vis) absorption spectroscopy is the measurement of the attenuation of a beam of light after it passes through a sample or is reflected from a sample surface. Decreasing the intensity of light indicates increased absorption. Its concentration is found by measuring its absorption at wavelength. UV-Vis spectroscopy was used to measure molecules or inorganic ions and complexes in the solution.

5. RESULTS

UV and visible light absorption spectra were obtained using a UV–Vis spectrophotometer (Shimadzu UV-1800) operating in the range of 250–800 nm. After sonication, the epoxy suspensions were diluted with Ethyl Alcohol to a concentration of 0.01 mg/ml to obtain detectable transmission during measurements. All samples were diluted to the same concentration. It shows the UV absorption peak (about 285 nm) measured at different times after sonication. The 285 nm and 298 nm peaks in the graph are considered to be π - π and n- π grooves, respectively. Functionalization of the surface of graphene with SDS and Araldite LY5052 epoxy increased the peak value slightly. Figure 5 shows that it successfully functionalized the graphene surface at all contribution rates (0.5-1.5%). However, a 0.5% contribution appears to be significantly successful.

For the results to be inconsistent, the sample prepared without additives must be diluted to the same extent as those with additives.



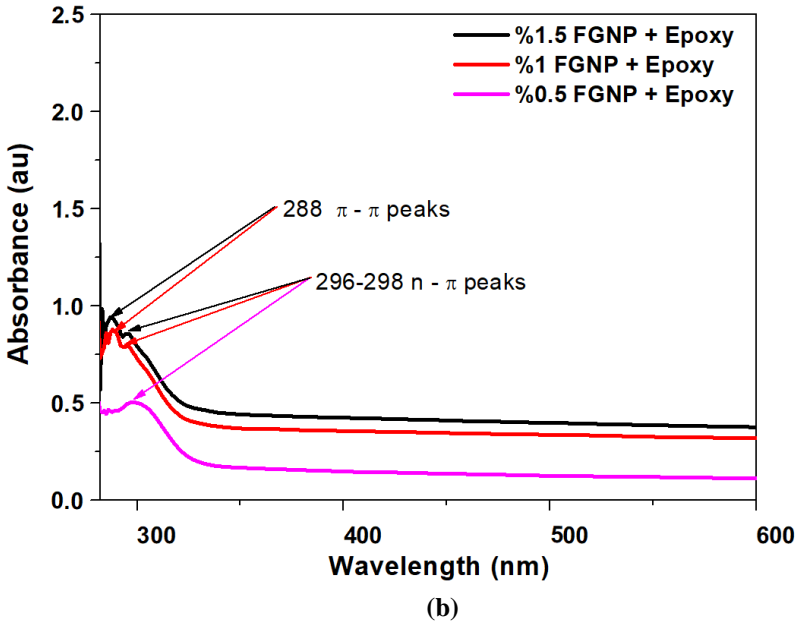


Figure 6. Characterization with UV-Vis Spectrophotometer, GNP+Epoxy (a); FGNP+Epoxy (b)

6. DISCUSSION

There are van der Waals (π - π) [20] bonds between the carbon atoms (C-C) in graphene layers. When added to matrix materials such as epoxy, the attraction between π - π bonds causes graphene agglomerations and the accumulation of layers [21,22]. Carboxyl (-COOH), hydroxyl (-OH), and carbonyl groups (C=O) on the graphene surface cause oxidation in the composite. Agglomeration and oxidation cause the mechanical, thermal, and electrical properties of the composite to decrease [23]. To improve the properties of graphene-doped nanocomposites, it is very important to distribute graphene homogeneously to prevent aggregation and re-layering [24]. Dopings between 0.01% and 0.5% [25] by weight could be made in graphene without [26,27] surface functionalization.

Surfactants reduce the tendency of graphene to aggregate by breaking weak van der Waals bonds [28]. Adding surfactant more than the critical micelle concentration forms micelles on the surface and increases surface tension [19] while adding less than the critical micelle concentration may cause the graphene surface to be inadequately functionalized [18,29,30].

Covalent functionalization[31] improves the properties of the nanocomposite to be produced by grafting graphene into the epoxy matrix by ensuring the best dispersion of graphene in the matrix. Among the covalent functionalization methods, functionalization with SDS under the umbrella of carbon-skeleton functionalization[24] is the most successful. It is possible for SDS to successfully functionalize the graphene surface even with the smallest doping amounts, and the shorter tail and shorter head structure[15] of SDS can provide more doping by increasing the repulsion between graphene layers. In addition, SDS establishes stronger π - π bonds with graphene and hydrogen bonds with epoxy, allowing graphene to act as a bridge[32] by filling the interface in fiber-reinforced polymer matrix composites.

UV-vis spectrophotometer analysis characterizes stability[33] in colloid chemistry by calculating the light absorption index according to Beer Lambert's law. Graphene usually has absorbance peaks between 250 nm and 270 nm still depending on the surface area[34] of the graphene used, the oxygen groups it contains, and the surfactant used, the absorbance value may peak up to 320 nm[35]. In this study, stability was achieved after 300 nm and the peak at 280 nm of unmodified graphene shown in Figure 6(a) corresponds to the π - π transition of aromatic C - C. The shift in the 288 nm peaks shown in Figure 6(b) is due to the formation of stronger π - π (C=C) bonds resulting from SDS + GNP. Additionally, the peaks at 296-298 nm were attributed to n- π (C=O) bonds[35] formed by grafting =O bonds in the SDS hydrophilic head to graphene. n- π bonds indicate that graphene is oxidized[36] during functionalization.

In the open literature, it is known that composites formed by doping SDS-functionalized graphene (FGNP) with epoxy show higher mechanical properties, thermal conductivity, and electrical conductivity[37]. Adding other surfactants[38] in higher amounts by weight to activate the surface may negatively affect the progress of composites as they create external functional groups on the surface of graphene. Even in SDS, the formation of oxygen groups[39] on the graphene surface acted as a diode in FGNP-doped composites and increased the percolation threshold value[40]. It acts as an insulator until the barrier value[41] is exceeded, then it can work as a superconductor[42], but after agglomeration, the conductivity decreases again. SDS-functionalized graphene strengthens the interface between the matrix and reinforcement in fiber-reinforced epoxy matrix composites and delays the formation of microcracks[32] during any damage, thus improving tensile strength, hardness, fracture toughness, and other mechanical properties[43], but mechanical properties decrease after

agglomeration. Likewise, the bridges[44] formed between the fiber and the matrix facilitate heat flow, but restacking also reduces thermal properties. Homogeneous distribution of graphene depends on the repulsive force and distance between graphene layers, and homogeneous distribution is very important to prevent aggregation. However, the only reason for the decrease in the performance of the composite is not agglomeration, but the functional groups formed by the surfactant are also very effective. In determining the amount of SDS, the critical micelle concentration will be effective in reducing excess functional groups that may form on the surface and will allow the production of higher-performance composites.

7. CONCLUSION

The graphene surface was functionalized quite successfully with SDS surfactant. Success was achieved at all weight ratios (0.5-1-1.5%). In UV-Vis absorption, the 285nm and 298 nm peaks in the graph are considered to be π - π and n - π grooves, respectively. It is seen that 1.5% FGNP contribution is significantly successful, but 1% FGNP contribution is also quite significant. The insignificant increase in the absorbance value between 1% and 1.5% created the prediction that doping after 1.5% could cause re-stacking. De-gassing must be applied to the epoxy, the bubbles in the epoxy will cause a broken matrix structure.

Originality

In this study, graphene was added to the epoxy polymer matrix to produce graphene-doped nanocomposites that can be used in aviation. For the solution to be homogeneous, CMC was taken into account and was studied for the first time in an Araldite LY5052 epoxy matrix.

Suggestions

SDS surfactant is effective for functionalizing graphene (GNP), but the Critical Micellar Concentration (CMC) method must be strictly followed to determine the amount of SDS. It has been observed that ethyl alcohol provides a significant advantage for GNP + SDS solution to create FGNP due to its solvent and volatile properties. However, after the epoxy is added and the mixture becomes homogeneous, the ethyl alcohol should have almost completely evaporated. If ethyl alcohol remains in the solution, the mixture will react exothermically and the nanocomposite will swell and change shape. To get positive results from UV-Vis absorption, the solution must be diluted 200 times, otherwise, the result with an absorbance value above 2 will become meaningless.

Acknowledgements

This study was supported by the Scientific Research Project Coordinator of Karabük University within the scope of the KBÜBAP-21-DR-080 project. Some of the experimental studies were supported by the TURKISH AEROSPACE INDUSTRY (TAI). The authors greatly appreciate the sponsorships of the abovementioned universities and companies for their generous support.

Conflict of interest

No conflict of interest was declared by the authors.

Author contributions

Cahit Bilgi: Writing – review & editing, Writing – original draft, Resources, Methodology, Investigation, Formal analysis, Data curation, Conceptualization. Bilge Demir: Writing – review & editing, Writing – original draft, Visualization, Resources, Project administration, Methodology, Investigation, Funding acquisition, Conceptualization.

REFERENCES

- [1] AIRBUS, Nanocomposites for Future Airbus Airframes Nano-ratio, AIRBUS 56 (2008) 6–28.
- [2] H. YILMAZ, Y. ALTIN, A. BEDELOĞLU, Grafen Takviyeli Epoksi Nanokompozitlerin Özelliklerinin İncelenmesi, Journal of Polytechnic 0900 (2020) 0–3. <https://doi.org/10.2339/politeknik.689424>.
- [3] A. Hirsch, The era of carbon allotropes, Nat Mater 9 (2010) 868–871. <https://doi.org/10.1038/nmat2885>.
- [4] T. Monetta, A. Acquesta, F. Bellucci, Graphene/epoxy coating as multifunctional material for aircraft structures, Aerospace 2 (2015) 423–434. <https://doi.org/10.3390/aerospace2030423>.
- [5] D.C. Moreira, M.C.O. Telles, L.A. Sphaier, L.C.S. Nunes, Infrared thermography for estimating the thermal conductivity augmentation of polymeric nanocomposites, High Temp High Press 44 (2014) 3–23.
- [6] H.-M.C. Jinhong Du, The Fabrication, Properties, and Uses of Graphene/Polymer Composites, Macromol Chem Phys 214 (2013) 2683–2693. <https://doi.org/10.1002/macp>.

- [7] P. de T. M. San Juan, O. Martín, F.J. Santos, A. Sánchez, Approach to the Study of Workpiece Damage in Drilling of Carbon Fiber Composites by Using Thermography IR, *Adv Mat Res* 498 (2012) 43–48. <https://doi.org/10.4028/www.scientific.net/AMR.498.43>.
- [8] M.Ç. Tüzemen, F. Khakzad, E. Salamci, Investigation of Tensile Properties of Glass Fiber/Epoxy Nanocomposites Laminates Enhanced with Graphene Nanoparticles, *Fibers and Polymers* 22 (2021) 1441–1448. <https://doi.org/10.1007/s12221-021-0521-0>.
- [9] X. Huang, X. Qi, F. Boey, H. Zhang, Graphene-based composites, *Chem Soc Rev* 41 (2012) 666–686. <https://doi.org/10.1039/c1cs15078b>.
- [10] S. Ganguli, H. Aglan, D. Dean, Microstructural origin of strength and toughness of epoxy nanocomposites, *Journal of Elastomers and Plastics* 37 (2005) 19–35. <https://doi.org/10.1177/0095244305045927>.
- [11] H. Hu, X. Wang, J. Wang, L. Wan, F. Liu, H. Zheng, R. Chen, C. Xu, Preparation and properties of graphene nanosheets-polystyrene nanocomposites via in situ emulsion polymerization, *Chem Phys Lett* 484 (2010) 247–253. <https://doi.org/10.1016/j.cplett.2009.11.024>.
- [12] J. Wei, T. Vo, F. Inam, Epoxy/graphene nanocomposites - processing and properties: a review, *RSC Adv* 5 (2015) 73510–73524. <https://doi.org/10.1039/c5ra13897c>.
- [13] A.G. Hsieh, S. Korkut, C. Punckt, I.A. Aksay, Dispersion stability of functionalized graphene in aqueous sodium dodecyl sulfate solutions, *Langmuir* 29 (2013) 14831–14838. <https://doi.org/10.1021/la4035326>.
- [14] J. Wei, M.S. Saharudin, T. Vo, F. Inam, Effects of surfactants on the properties of epoxy/graphene nanocomposites, *Journal of Reinforced Plastics and Composites* 37 (2018) 960–967. <https://doi.org/10.1177/0731684418765369>.
- [15] M. Poorsargol, M. Alimohammadian, B. Sohrabi, M. Dehestani, Dispersion of graphene using surfactant mixtures: Experimental and molecular dynamics simulation studies, *Appl Surf Sci* 464 (2019) 440–450. <https://doi.org/10.1016/j.apsusc.2018.09.042>.
- [16] I. V. Plastinin, S.A. Burikov, S.P. Gofurov, O.B. Ismailova, Y.A. Mirgorod, T.A. Dolenko, Features of self-organization of sodium dodecyl sulfate in water-ethanol solutions: Theory and vibrational spectroscopy, *J Mol Liq* 298 (2020). <https://doi.org/10.1016/j.molliq.2019.112053>.
- [17] D.D. La, T.N. Truong, T.Q. Pham, H.T. Vo, N.T. Tran, T.A. Nguyen, A.K. Nadda, T.T. Nguyen, S. Woong Chang, W. Jin Chung, D. Duc Nguyen, Scalable fabrication of modified graphene nanoplatelets as

- an effective additive for engine lubricant oil, *Nanomaterials* 10 (2020). <https://doi.org/10.3390/nano10050877>.
- [18] A. Vishnyakov, M.T. Lee, A. V. Neimark, Prediction of the critical micelle concentration of nonionic surfactants by dissipative particle dynamics simulations, *Journal of Physical Chemistry Letters* 4 (2013) 797–802. <https://doi.org/10.1021/jz400066k>.
- [19] S.F. Burlatsky, V. V. Atrazhev, D. V. Dmitriev, V.I. Sultanov, E.N. Timokhina, E.A. Ugolkova, S. Tulyani, A. Vincitore, Surface tension model for surfactant solutions at the critical micelle concentration, *J Colloid Interface Sci* 393 (2013) 151–160. <https://doi.org/10.1016/j.jcis.2012.10.020>.
- [20] P.L. De Andres, R. Ramírez, J.A. Vergés, Strong covalent bonding between two graphene layers, *Phys Rev B Condens Matter Mater Phys* 77 (2008). <https://doi.org/10.1103/PhysRevB.77.045403>.
- [21] A. Amiri, R. Sadri, M. Shanbedi, G. Ahmadi, B.T. Chew, S.N. Kazi, M. Dahari, Performance dependence of thermosyphon on the functionalization approaches: An experimental study on thermo-physical properties of graphene nanoplatelet-based water nanofluids, *Energy Convers Manag* 92 (2015) 322–330. <https://doi.org/10.1016/j.enconman.2014.12.051>.
- [22] H.M. Chong, S.J. Hinder, A.C. Taylor, Graphene nanoplatelet-modified epoxy: effect of aspect ratio and surface functionality on mechanical properties and toughening mechanisms, *J Mater Sci* 51 (2016) 8764–8790. <https://doi.org/10.1007/s10853-016-0160-9>.
- [23] M.K. Hassanzadeh-Aghdam, R. Ansari, H.M. Deylami, Influence of graphene nano-platelets on thermal transport performance of carbon fiber-polymer hybrid composites: Overall assessment of microstructural aspects, *International Journal of Thermal Sciences* 171 (2022) 107209. <https://doi.org/10.1016/j.ijthermalsci.2021.107209>.
- [24] W. Yu, L. Sisi, Y. Haiyan, L. Jie, Progress in the functional modification of graphene/graphene oxide: A review, *RSC Adv* 10 (2020) 15328–15345. <https://doi.org/10.1039/d0ra01068e>.
- [25] Ö.U. Colak, N. Bahlouli, D. Uzunsoy, C. Francart, High strain rate behavior of graphene-epoxy nanocomposites, *Polym Test* 81 (2020). <https://doi.org/10.1016/j.polymertesting.2019.106219>.
- [26] E.F. Sukur, G. Onal, Graphene nanoplatelet modified basalt/epoxy multi-scale composites with improved tribological performance, *Wear* 460–461 (2020). <https://doi.org/10.1016/j.wear.2020.203481>.
- [27] H. Kaftelen-Odabaşı, A. Odabaşı, M. Özdemir, M. Baydoğan, A study on graphene reinforced carbon fiber epoxy composites: Investigation

- of electrical, flexural, and dynamic mechanical properties, *Polym Compos* 44 (2023) 121–135. <https://doi.org/10.1002/pc.27031>.
- [28] P. Gavallas, D. Savvas, G. Stefanou, Mechanical properties of graphene nanoplatelets containing random structural defects, *Mechanics of Materials* 180 (2023). <https://doi.org/10.1016/j.mechmat.2023.104611>.
- [29] T.R. Gahrooe, A. Abbasi Moud, M. Danesh, S.G. Hatzikiriakos, Rheological characterization of CNC-CTAB network below and above critical micelle concentration (CMC), *Carbohydr Polym* 257 (2021). <https://doi.org/10.1016/j.carbpol.2020.117552>.
- [30] A. Beyaz, W.S. Oh, V.P. Reddy, Ionic liquids as modulators of the critical micelle concentration of sodium dodecyl sulfate, *Colloids Surf B Biointerfaces* 35 (2004) 119–124. <https://doi.org/10.1016/j.colsurfb.2004.02.014>.
- [31] A. Kausar, Z. Anwar, B. Muhammad, Recent Developments in Epoxy/Graphite, Epoxy/Graphene, and Epoxy/Graphene Nanoplatelet Composites: A Comparative Review, *Polymer - Plastics Technology and Engineering* 55 (2016) 1192–1210. <https://doi.org/10.1080/03602559.2016.1163589>.
- [32] F. Wang, X. Cai, Improvement of mechanical properties and thermal conductivity of carbon fiber laminated composites through depositing graphene nanoplatelets on fibers, *J Mater Sci* 54 (2019) 3847–3862. <https://doi.org/10.1007/s10853-018-3097-3>.
- [33] M. Mehrali, E. Sadeghinezhad, S.T. Latibari, S.N. Kazi, M. Mehrali, M.N. Bin, M. Zubir, H. Simon, C. Metselaar, Investigation of thermal conductivity and rheological properties of nanofluids containing graphene nanoplatelets, 2014. <http://www.nanoscalereslett.com/content/9/1/15>.
- [34] J. Wei, R. Atif, T. Vo, F. Inam, Graphene Nanoplatelets in Epoxy System: Dispersion, Reaggregation, and Mechanical Properties of Nanocomposites, *J Nanomater* 2015 (2015). <https://doi.org/10.1155/2015/561742>.
- [35] A.F. Mindivan, THE SYNTHESIS AND CHARACTERIZATION OF GRAPHENE OXIDE (GO) AND REDUCED GRAPHENE OXIDE (RGO), n.d.
- [36] A. Hussain Wazir, I. Waseem Kundi, Synthesis of Graphene Nano Sheets by the Rapid Reduction of Electrochemically Exfoliated Graphene Oxide Induced by Microwaves, 2016.
- [37] Y.M. Jen, J.C. Huang, Synergistic effect on the thermomechanical and electrical properties of epoxy composites with the enhancement of carbon nanotubes and graphene nano platelets, *Materials* 12 (2019). <https://doi.org/10.3390/ma12020255>.

- [38] B.B. Feng, Z.H. Wang, W.H. Suo, Y. Wang, J.C. Wen, Y.F. Li, H.L. Suo, M. Liu, L. Ma, Performance of graphene dispersion by using mixed surfactants, *Mater Res Express* 7 (2020). <https://doi.org/10.1088/2053-1591/abb2ca>.
- [39] D. Galpaya, M. Wang, M. Liu, N. Motta, E. Waclawik, C. Yan, Recent Advances in Fabrication and Characterization of Graphene-Polymer Nanocomposites, *Graphene* 01 (2012) 30–49. <https://doi.org/10.4236/graphene.2012.12005>.
- [40] Z. Wang, J.K. Nelson, H. Hillborg, S. Zhao, L.S. Schadler, Graphene oxide filled nanocomposite with novel electrical and dielectric properties, *Advanced Materials* 24 (2012) 3134–3137. <https://doi.org/10.1002/adma.201200827>.
- [41] B. Nazari, Z. Ranjbar, R.R. Hashjin, A. Rezvani Moghaddam, G. Momen, B. Ranjbar, Dispersing graphene in aqueous media: Investigating the effect of different surfactants, *Colloids Surf A Physicochem Eng Asp* 582 (2019). <https://doi.org/10.1016/j.colsurfa.2019.123870>.
- [42] J. Trinidad, B.M. Amoli, W. Zhang, R. Pal, B. Zhao, Effect of SDS decoration of graphene on the rheological and electrical properties of graphene-filled epoxy/Ag composites, *Journal of Materials Science: Materials in Electronics* 27 (2016) 12955–12963. <https://doi.org/10.1007/s10854-016-5434-0>.
- [43] A. Allahbakhsh, S. Mazinani, Influences of sodium dodecyl sulfate on vulcanization kinetics and mechanical performance of EPDM/graphene oxide nanocomposites, *RSC Adv* 5 (2015) 46694–46704. <https://doi.org/10.1039/c5ra00394f>.
- [44] M. Rafiee, F. Nitzsche, J. Laliberte, S. Hind, F. Robitaille, M.R. Labrosse, Thermal properties of doubly reinforced fiberglass/epoxy composites with graphene nanoplatelets, graphene oxide and reduced-graphene oxide, *Compos B Eng* 164 (2019) 1–9. <https://doi.org/10.1016/j.compositesb.2018.11.051>.



CHAPTER 7

Aviation Technologies and Applications
E-ISBN:978-605-338-471-7
2025, chap. (7) , pp.107-127.

AUTONOMOUS LANDING OF A GENERAL AVIATION AIRPLANE ON AN AIRCRAFT CARRIER

**Bora BOSTANCI^{1,*}, Bahadır TÜRKER², Furkan Mert SAĞEL³,
Uğur ERTUNÇ⁴, Hüseyin Enes SALMAN⁵, Ünver KAYNAK⁶**

ABSTRACT

This research is motivated by recent advancements in the development of automatic-landing systems of drones on aircraft carriers. It focuses on the design of an autopilot system for achieving fully automated landings. The approach is demonstrated using a basic propeller aircraft to provide a fundamental perspective on this new development, employing both the FlightGear and Simulink software. Thus, the present paper highlights the fundamental steps being taken in developing simple autopilot systems for landing on carrier decks, and the outcome can contribute to the development of more effective and efficient autopilot systems for UAVs.

Keywords: Autonomous Landing, Autopilot, Classical Control, UAV

1. INTRODUCTION

The design of aircraft extensively relies on flight control systems to oversee and regulate their subsystems, as illustrated in Fig. 1. The evolution of these control systems has played a pivotal role in the advancement of both civil and military aircraft. Modern aircraft are equipped with a diverse array of flight control systems that either assist flight crews in navigation or fully unmanned operations, flight management, and enhancing the aircraft's stability characteristics.

*Corresponding Author: bbostanci@etu.edu.tr

1 Department of Mechanical Engineering TOBB University of Economics and Technology Ankara, Turkey

2 Department of Mechanical Engineering TOBB University of Economics and Technology Ankara, Turkey

3 Department of Mechanical Engineering TOBB University of Economics and Technology Ankara, Turkey

4 Department of Mechanical Engineering TOBB University of Economics and Technology Ankara, Turkey

5 Department of Mechanical Engineering TOBB University of Economics and Technology Ankara, Turkey

6 Faculty of Aviation and Space Sciences Ankara Yıldırım Beyazıt University Ankara, Turkey

Autopilot characteristics may vary according to the field in which the aircraft is used, like military or commercial fields. Autopilot systems need to be tailored considering potentially challenging environmental conditions, such as weather conditions, the air pressure during flight and landing, uncertainty or parameter variations of the aircraft etc.

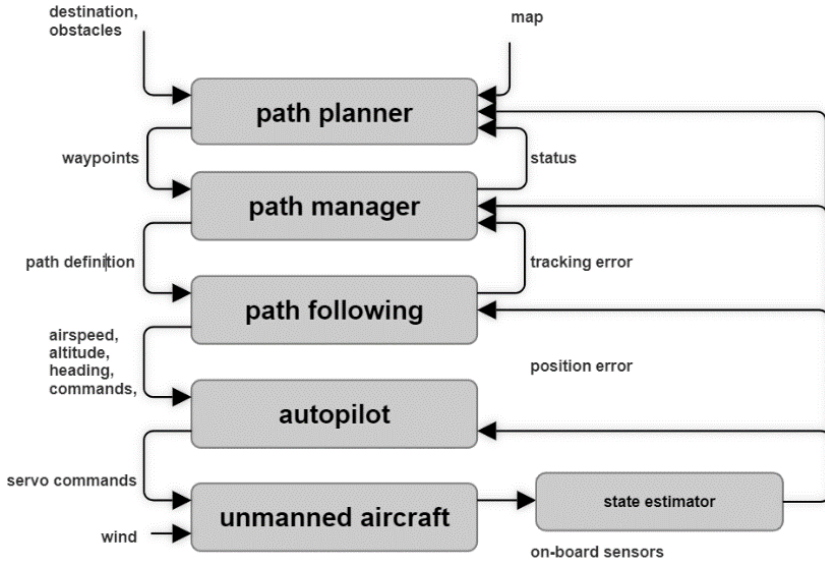


Figure 1. Autonomous system architecture [1]

On the other hand, with the advancement of the field, new challenges have emerged. A major one is landing on a carrier ship autonomously and the first of its kind X-47B. In Turkish aerospace landscape, a specific operational need has arisen. To highlight the intricate challenges of achieving a viable system, the historical context of the X-47 is illustrative. The UCAS-D (Unmanned Combat Air System Demonstrator) program's inaugural flight test occurred in February 2011, followed by the successful catapult launch of the X-47B from Naval Air Station in November 2012. Additionally, the USS Harry S Truman (CVN 75) hosted the first at-sea testing phase, featuring successful deck handling trials that concluded in December 2012 [2]. Notably, domestic initiatives are also underway to establish automatic landing capabilities for a domestically designed piston-propeller UAV on an amphibious assault ship [3].

In the present study, the conceptual design of a landing autopilot is considered by decoupling the dynamical system's representation enabling to classical control system design. The reason behind using that approach

is that the coupling between channels of the system can be considered as disturbance [4] and therefore, increasing the disturbance rejection capacities of the decoupled design provides acceptable results. Furthermore, opting for a fully Multiple-Input Multiple-Output (MIMO) controller introduces complexities that could potentially obscure the comprehension of the landing phenomenon, which aligns with the core focus of this paper. Following the conceptual design, the system is subjected to testing on a simulation platform known as FlightGear. This platform provides a physics-based virtual environment for the evaluation of the autopilot's performance.

2. METHODS

2.1 Equations of Motion

The aircraft is considered as a rigid body and its motion is governed by the equations of rigid body dynamics. Initially, these equations are formulated in the body axis system as depicted in Fig. 2. However, due to the complexities associated with handling the comprehensive set of real-time aerodynamic data required for the 6-degree-of-freedom (6-DOF) equations, the application of small disturbance theory becomes pertinent. This theory is used to linearize the equations of motion, thereby facilitating a more manageable analysis.

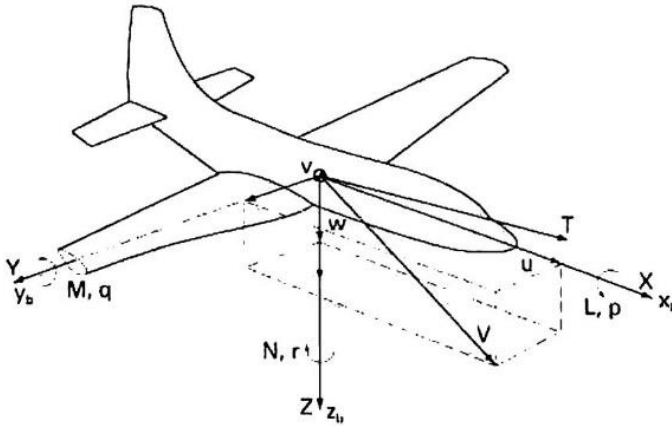


Figure 2. Definition of forces, moments, and velocity components in a body-fixed coordinate

Thus, Eq. (1) is obtained as the longitudinal equations of motion in the state-space form.

$$\begin{bmatrix} \Delta \dot{u} \\ \Delta \dot{w} \\ \Delta \dot{q} \\ \Delta \dot{\theta} \end{bmatrix} = \begin{bmatrix} X_u & X_w & 0 & -g \\ Z_u & Z_w & u_u & 0 \\ M_u + M_{\dot{w}}Z_u & M_u + M_{\dot{w}}Z_w & M_u + M_{\dot{w}}u_u & 0 \\ 0 & 0 & 1 & 0 \end{bmatrix} \begin{bmatrix} \Delta u \\ \Delta w \\ \Delta q \\ \Delta \theta \end{bmatrix} + \begin{bmatrix} X_{\delta} & X_{\delta_T} \\ Z_{\delta} & Z_{\delta_T} \\ M_{\delta} + M_{\dot{w}}Z_{\delta} & M_{\delta_T} + M_{\dot{w}}Z_{\delta_T} \\ 0 & 0 \end{bmatrix} \begin{bmatrix} \Delta \delta \\ \Delta \delta_T \end{bmatrix} \quad (1)$$

Where $\Delta \delta$ and $\Delta \delta_T$ are the aerodynamic and propulsive controls, respectively. Similarly, (2) is obtained in matrix format to find the lateral-directional equations of motion.

$$\begin{bmatrix} \Delta \dot{u} \\ \Delta \dot{w} \\ \Delta \dot{q} \\ \Delta \dot{\phi} \end{bmatrix} = \begin{bmatrix} Y_0 & Y_0 - (u_0 - Y_r) & -g \cos \theta_0 \\ L_0 & P_0 & L_r & 0 \\ N_0 & N_P & N_r & 0 \\ 0 & 1 & 0 & 0 \end{bmatrix} \begin{bmatrix} \Delta u \\ \Delta p \\ \Delta r \\ \Delta \phi \end{bmatrix} + \begin{bmatrix} 0 & X_{\delta r} \\ L_{\delta a} & L_{\delta r} \\ N_{\delta a} & N_{\delta r} \\ 0 & 0 \end{bmatrix} \begin{bmatrix} \Delta \delta_a \\ \Delta \delta_r \end{bmatrix} \quad (2)$$

2.2 Stability Derivatives

When an airplane is in motion, it requires a mathematical explanation of the forces and moments acting upon it. Nevertheless, the exact mathematical representation of the forces and moments is not always obtainable. This is where stability derivations become important. They support to explain how various forces and moments after during an airplane motion [6]. Stability derivatives measure the magnitude of change in a force or moment enforce on the aircraft when a small change occurs in a flight condition parameter, such as angle of attack, airspeed or altitude. These parameters are commonly referred to as "states"[7].

The stability derivatives for the generic unmanned aerial vehicle used in the project can be taken one of the exemplary general aviation aircraft given in [4] and [5]

2.3 Autopilot Design

To decrease the complexity, the longitudinal dynamic equations can be divided into short and long period approximations. These approximations later on are used for instance to build a pitch attitude hold autopilot, airspeed hold, altitude hold autopilots etc. Also, autopilot modes such as heading hold and turn autopilot require lateral-directional approximation. The autopilot modes that are given in this section will be working in parallel to achieve an autonomous flight phase.

2.3.1. Pitch Displacement Autopilot

Assuming no change in x-body axes and dropping X-force in longitudinal motion decreases the complexity [4]. Claiming elevator as an input and output a theta angle enables writing transfer function. Change in pitch rate to the change in elevator angle shown in (3).

$$\frac{\Delta q(s)}{\Delta \delta_e(s)} = \frac{N^q_{\delta_e}(s)}{\Delta_{sp}(s)} = \frac{A_q s + B_q}{A s^2 + B s + C} \quad (3)$$

Table 1. Short period transfer function coefficient values [4]

	$A, A_a \text{ or } A_q$	$B, B_a \text{ or } B_q$	C
$\Delta_{sp}(s)$	1	$-(M_q + M_{\dot{a}} + Z_a/u_0)$	$Z_a M_q / u_0$ $- M_q$
$N^a_{\delta_e}(s)$	Z_{δ_e} / u_0	$M_{\delta_e} - M_q Z_{\delta_e} / u_0$	-
$N^q_{\delta_e}(s)$	$M_{\delta_e} + M_a Z_{\delta_e} / u_0$	$M_a Z_{\delta_e} / u_0$ $- M_{\delta_e} Z_a / u_0$	-

As the output is pitch rate, it must be written in terms of θ If the system is only moving on longitudinal plane, (4) holds in Laplace domain.

$$\Delta q = s * \Delta \quad (4)$$

CHAPTER 7: AUTONOMOUS LANDING OF A GENERAL AVIATION AIRPLANE ON AN AIRCRAFT CARRIER

This autopilot system can be modeled by a controller, servo motor and aircraft response to changes. A typical servo showing characteristics of a first order system can be modeled using transfer function [5]. For a typical servo motor a time constant is considered as 0.1. The transfer function of servo motor is described in (5).

$$\frac{\delta_e}{v} = \frac{k_a}{\tau s + 1} \tag{5}$$

To simply further, the aircraft dynamics are represented by using the short-period approximation [5]. The short-period Aircraft Dynamics transfer function for Cessna-182 Aircraft (General Aviation Airplane) at cruise flight condition can be shown in (6).

$$\frac{\theta}{\Delta\delta_e} = \frac{-40.12s - 94.9}{s^3 + 10.4s^2 + 34.6s} \tag{6}$$

The Ziegler–Nichols tuning method is used for designing a PID controller. The Table 2 shows to use this technique to develop the gains of the controller.

Table 2. Ziegler-Nichols method table

Control Type	K_p	T_i	T_d	K_i	K_d
P	$0.5K_u$	–	–	–	–
PI	$0.45K_u$	$0.83T_u$	–	$0.54K_u$ $/T_u$	–
PD	$0.8K_u$	–	$0.125T_u$	–	$0.10K_uT_u$
Classic PID	$0.6K_u$	$0.5T_u$	$0.125T_u$	$1.2K_u/T_u$	$0.075K_uT_u$
Pessen Integral	$0.7K_u$	$0.4T_u$	$0.15T_u$	$1.75K_u$ $/T_u$	$0.105K_uT_u$
Some Overshoot	$0.33K_u$	$0.5T_u$	$0.33T_u$	$0.66K_u$ $/T_u$	$0.11K_uT_u$
No Overshoot	$0.20K_u$	$0.5T_u$	$0.33T_u$	$0.40K_u$ $/T_u$	$0.066K_uT_u$

Different types of controllers are tested at the end of this part. Selection of the gain K_u can be determined using a root locus plot of the closed loop transfer function. The closed-loop configuration is given by Fig. 3 where the vertical gyro can be modeled by using (5) with suitable parameters.

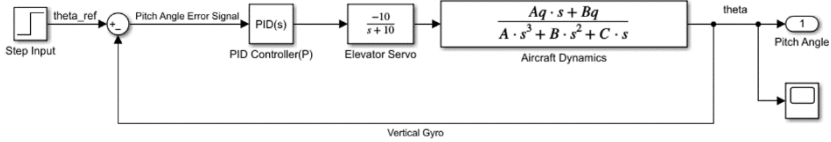


Figure 3. Pitch displacement autopilot

Response is controlled with the Classical PID for the Pitch Displacement Autopilot. A quick comparison between other Ziegler-Nichols methods in the Fig.5.

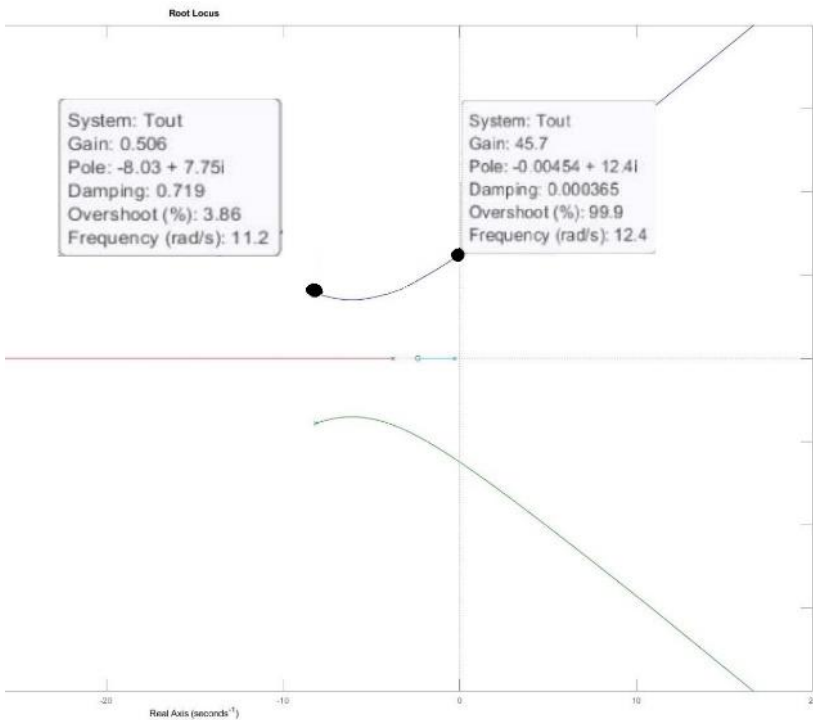


Figure 4. Pitch attitude root locus plot

CHAPTER 7: AUTONOMOUS LANDING OF A GENERAL AVIATION AIRPLANE ON AN AIRCRAFT CARRIER

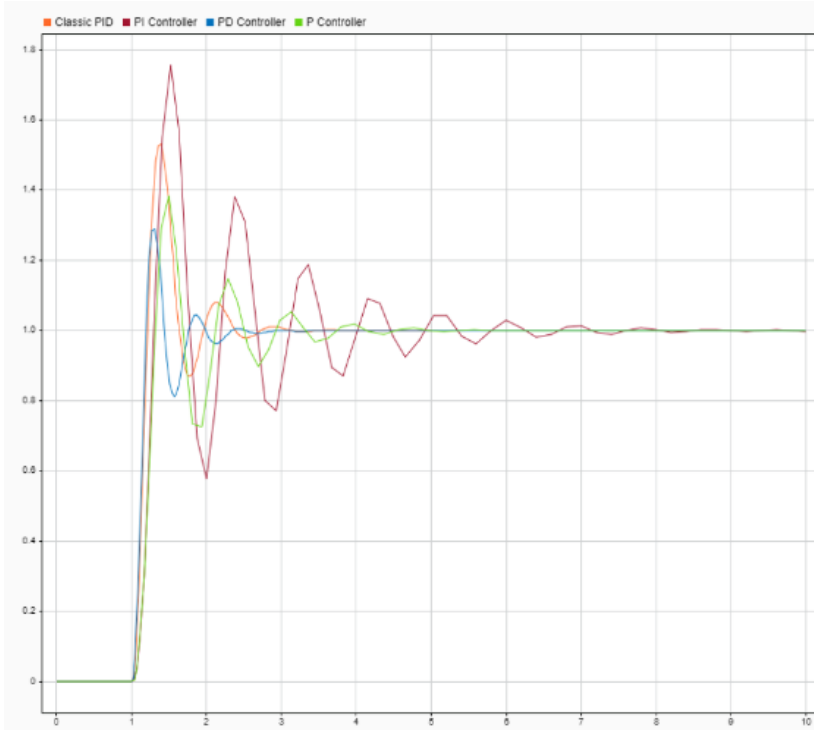


Figure 5. Comparison of P, PD, PI, PID system responses

2.3.2 Airspeed Hold Autopilot

The forward speed of an aircraft can be controlled by varying the generated thrust of the propulsion system. The basic function of speed control is to maintain the flight speed within the desired range. This is achieved by changing the engine throttle for increasing or decreasing the thrust. Fig.8 is a simplified form for a speed control system described in [5]. The speed control system constitutes of compensator, engine throttle, aircraft dynamics, and a feedback path consisting of the velocity and acceleration feedback.

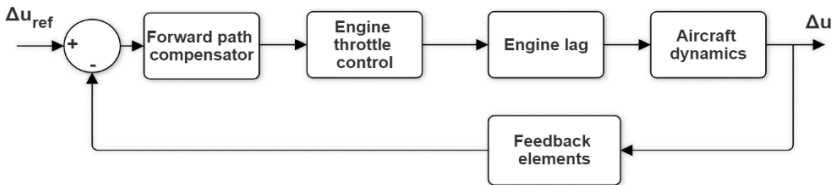


Figure 6. Simple block diagram for a speed control system

The changes in velocity and acceleration are used in the feedback path. The feedback path transfer function is given in the form below (7).

$$H(s) = 10s + 1 \quad (7)$$

The lateral aircraft dynamics for a heading displacement autopilot can be described with the transfer function shown in (8)

$$\frac{\Delta u(s)}{\Delta \delta_T(s)} = \frac{N_{\delta_e}^u(s)}{\Delta_p(s)} = \frac{A_u s + B_u}{A s^2 + B s + C} \quad (8)$$

This control system is modelled in Simulink and then simplified to just a simple closed loop control system with a PID.

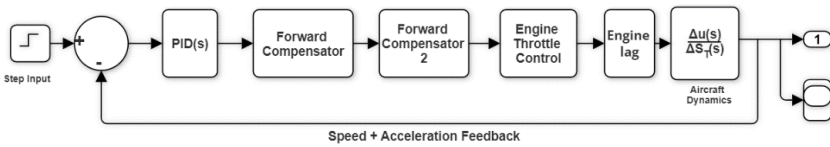


Figure 7. Velocity hold autopilot

Where the aircraft dynamics transfer function block for Cessna 182 can be found as in (9)

$$\frac{\Delta u}{\Delta \delta_T} = \frac{1.483s}{s^2 + 0.03611s + 0.05064} \quad (9)$$

It is known that root locus technique shows the performance of the gains and it is a useful tool to determine gain. However, in some cases, the required performance objectives cannot be reached by only changing the gain. If the performance is not satisfactory, compensator is added to the system. The system reaches or comes closer to the required performance with the compensator. Here, two forward path compensators are used to improve the steady system response to achieve the desired system performance. From the transfer function of this closed loop, the root locus plot in Fig. 8 can be found.

CHAPTER 7: AUTONOMOUS LANDING OF A GENERAL AVIATION AIRPLANE ON AN AIRCRAFT CARRIER

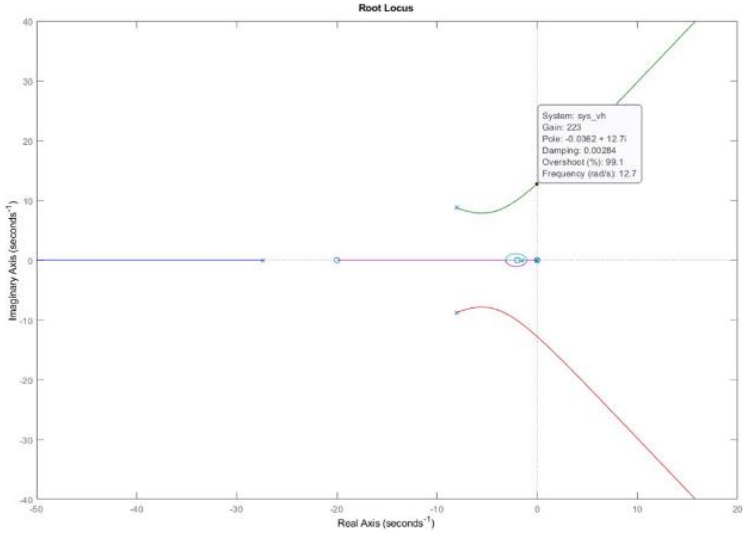


Figure 8. Velocity hold root locus plot

In this section, the ultimate gain K_u is 223, and the Frequency is 12.7. The system response will be controlled with the Ziegler-Nichols Method Classic PID.

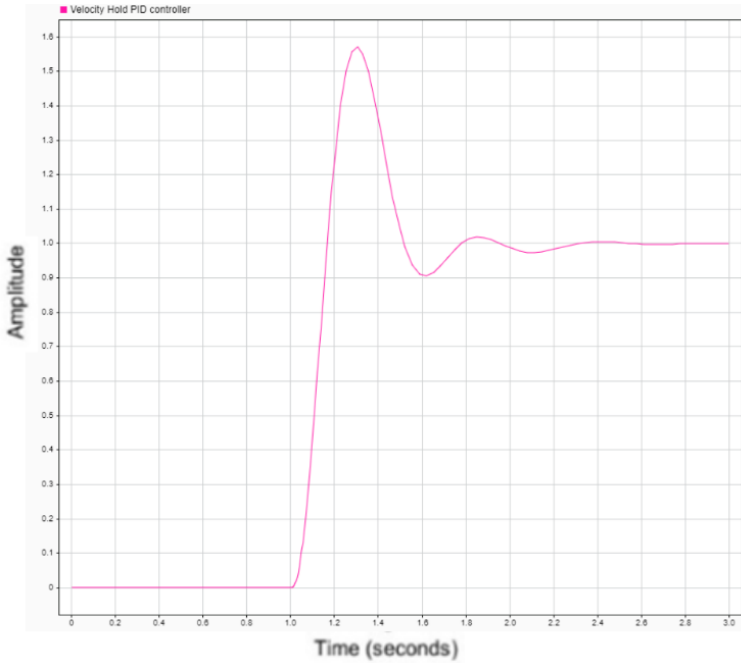


Figure 9. Velocity hold autopilot classical PID step response

2.3.3 Altitude Hold Autopilot

The altitude of an airplane can be maintained by an altitude hold autopilot. A simplified altitude hold autopilot is shown in Fig.10:

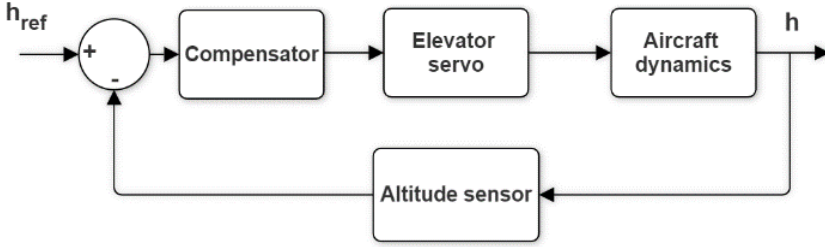


Figure 10. Altitude hold control model [4]

This autopilot is developed to minimize the deviation between current altitude and the desired altitude.

In an ideal scenario, the following assumptions are made: Firstly, the airplane's speed is controlled by a separate control system (hold constant in our case); secondly, any lateral dynamic effect is neglected. With these restrictions, it is assumed that aircraft only moves in the vertical plane. Elevator transfer function can be represented as a first-order lag:

$$\frac{\delta_e}{e} = \frac{k_a}{s + 10} \quad (10)$$

To examine the altitude hold control system, $\delta h(s)/\Delta \delta_e(s)$ transfer function is needed. This function is obtained by Fig.11.

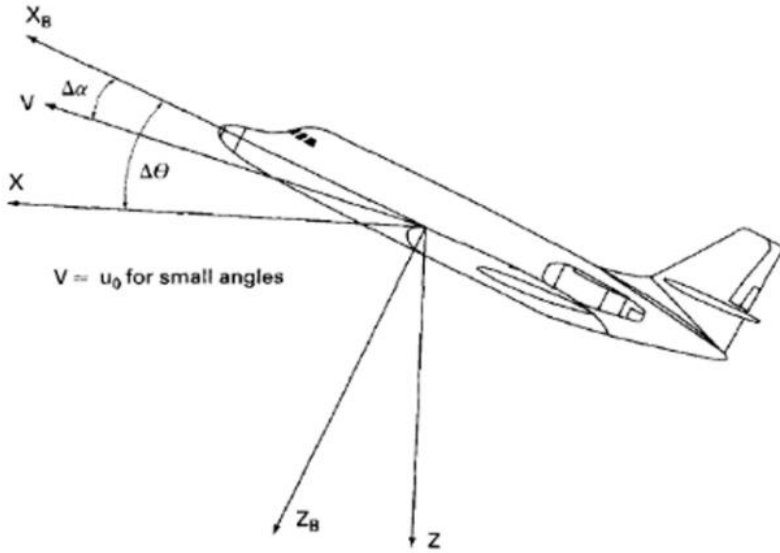


Figure 11. Kinematic relationship for determining vertical rate of climb

Which shows the kinematic relationship between the airplane's rate of climb, pitch angle, and angle of attack. From Fig. 11 we can write the following relationship.

$$\frac{\delta h(s)}{\Delta \delta_e(s)} = \frac{u_0}{s} \left[\frac{\Delta \theta(s)}{\Delta \delta_e(s)} - \frac{\Delta \alpha(s)}{\Delta \delta_e(s)} \right] \quad (11)$$

The transfer function inside (11) can be written as

$$\frac{\Delta \theta(s)}{\Delta \delta_e(s)} = \frac{1}{s} \frac{\Delta q(s)}{\Delta \delta_e(s)} = \frac{A_q s + B_a}{s(A s^2 + B s + C)} \quad (12)$$

And

$$\frac{\Delta \alpha(s)}{\Delta \delta_e(s)} = \frac{A_q s + B_a}{A s^2 + B s + C} \quad (13)$$

The Aircraft Dynamics transfer function for Cessna-182 Aircraft (General Aviation Airplane) at cruise flight condition is shown in (14).

$$\frac{\Delta h(s)}{\Delta \delta_e(s)} = \frac{-159.4s^3 - 1283s^2 + 6.354E04s + 6366}{s^6 + 40.4s^5 + 946.7s^4 + 3118s^3 + 6920s^2} \quad (14)$$

2.3.4 Heading Displacement Autopilot (Lateral)

To control the heading angle of an airplane a directional gyro is employed. The heading angle is basically controlled by setting a certain bank angle and holding that angle until the desired heading change is satisfied [4]. The bank angle control loop is used as the inner loop for the heading control system.

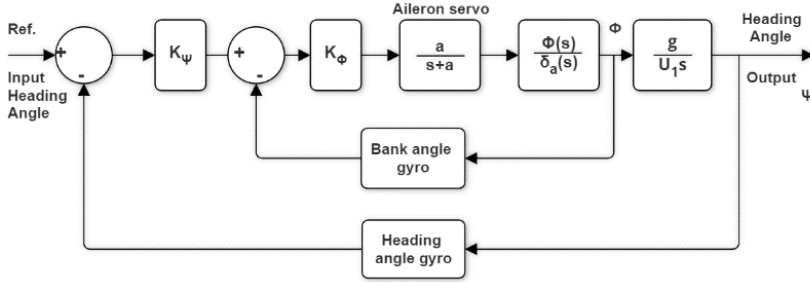


Figure 12. Heading angle hold mode with attitude gyro

Time constants for typical servomotors are generally in the range of 0.05-0.25 s. For this system it is assumed as of 0.1 s.

Bank angle response of the aircraft is given below with pure rolling motion approximation [5].

$$\frac{\phi(s)}{\delta_e(s)} = \frac{L\delta_a}{s(s-L_p)} \quad (15)$$

The relationship between bank angle and heading angle is with the following equation [4], heading autopilot is created. Small angle approximation was used to obtain this equation.

$$\frac{\psi(s)}{\phi(s)} = \frac{g}{U_0 s} \quad (16)$$

Coincident body and wind axes assumption leads to the motion depicted below in earth reference frame. The response of Fig. 12 is depicted in Fig. 13. in earth coordinate system with constant speed approximation.

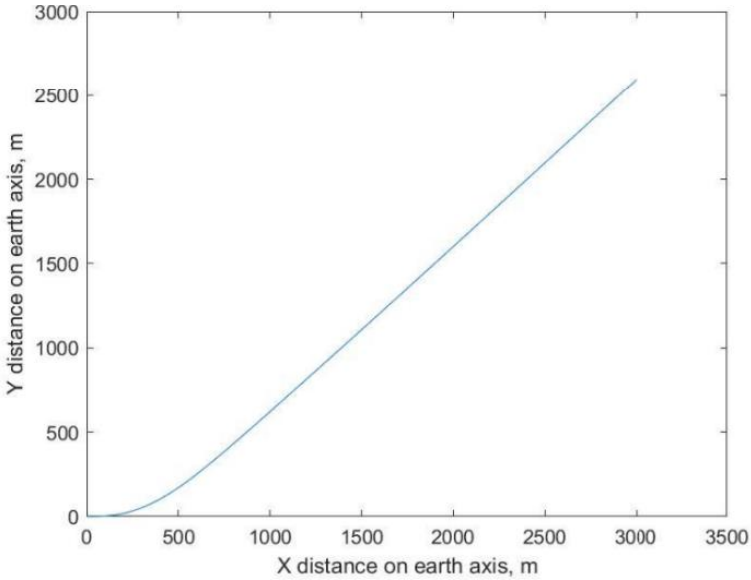


Figure 13. Heading command tracking on a lateral plane

2.3.5 Turn Autopilot

Turn autopilot controls the derivative of heading angle which the airplane's nose turns right or left. The system is composed of an aileron and aircraft's response on the derivative of the heading angle (where the effect of rolling and yawing rates are considered). In Fig. 14, the controller is taken as a PID controller where the gains are optimized by trial and error in order to achieve a system behavior that can track an optimal turn.

Assumptions made on this mode are constant speed and altitude which are controlled by other autopilots. Also transfer function of rolling rate is approximated by pure rolling motion [5] and the yawing rate is approximated by Dutch-Roll Approximation [5]. Aileron Servo's time constant is considered as 0.1 which is same as other autopilot servos. This system is claimed as plant structure of the control system in Fig 14.

From the relationship between the angular velocities in the body frame and the Euler rates [5], it can be readily observed that when Theta is in zero position where the theta can be controlled by pitch autopilot, the relationship between body axis rolling(p) and the derivative of phi angle becomes equal. This relationship simplifies the simulation and modeling for utilizing this autopilot mode in future work, where the aircraft gains autonomous turning capability. With a mathematical manipulation at the bottom below of Fig 14., the motion of the aircraft is demonstrated on 2-dimensional Earth x-y axis

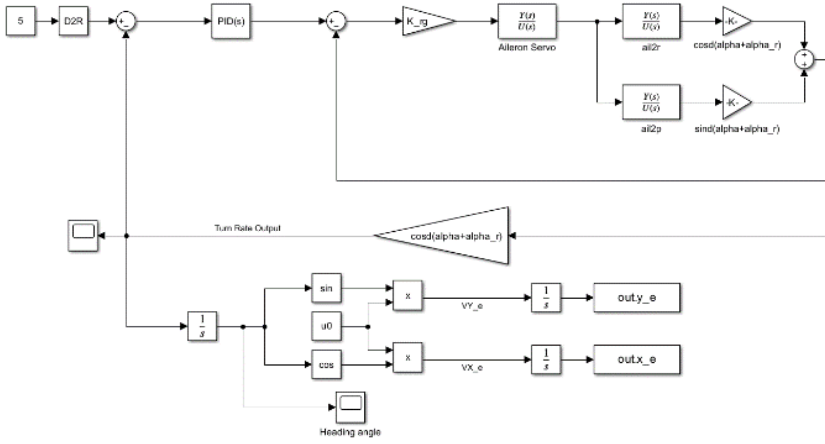


Figure 14. Turn autopilot

Fig. 15 demonstrates the response of the system in earth-fixed coordinate system for a time to airplane to make a circle. It can be noted that the first response of the system is fast that a successful circle is obtained, starting from (0,0)

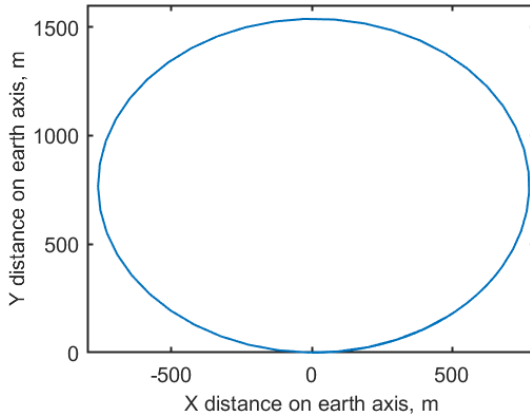


Figure 15. Airplane tracing a circle with turn autopilot

The transfer functions used to model the aircraft response are given below.

$$\frac{\Delta r(s)}{\Delta \delta_a(s)} = \frac{N_{\delta_a}^r(s)}{\delta_D R(s)} = \frac{N_{\delta_a} s - (Y_{\beta} N_{\delta_a} / u_0)}{s^2 - \left(\frac{Y_{\beta} + u_0 N_r}{u_0} \right) s + \frac{Y_{\beta} N_r - N_{\beta} Y_r + N_{\beta} u_0}{u_0}} \quad (17)$$

$$\frac{\Delta p(s)}{\Delta \delta_a(s)} = \frac{L_{\delta_a}}{s - L_p} \quad (18)$$

2.4 Autoland Autopilot

Firstly, glide slope tracking and maneuvering mode are demonstrated. Then, these modes are used to autonomously land a General Aviation Airplane on a carrier. The velocity of the airplane is assumed to be constant during the landing phase; this can be achieved by the velocity hold autopilot. Another important assumption is that the airplane is not moving in a lateral plane.

2.4.1 Glideslope Tracker Mode

Pitch attitude control system is being developed in previous part is used where the PID controller gains are developed by the Ziegler-Nichols method.

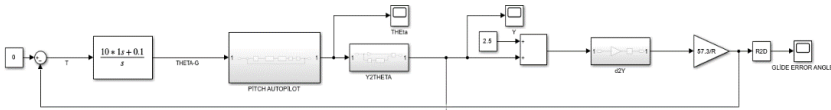


Figure 16. Glideslope tracker navigational autopilot

As the airplane reaches an intercept point, the navigational autopilot is initiated. At this point, any nose position (θ - Euler angle) of an airplane on the longitudinal plane can be controlled with this tracker mode. This navigational mode, where the system in Fig. 16 demonstrated, consists of a glideslope controller, a pitch autopilot, and trigonometric operations (from θ to the distance between the glideslope and the center of gravity of the airplane) in the Laplace domain.

2.4.2 Flare Maneuver Mode

Flare maneuver is necessary to prevent damage to the landing gear during high-velocity landings. The physical representation of the flare movement is shown below in Fig. 17. Since the airplane is unmanned, passenger and crew comfort is not taken into account, but it can be optimized if a need arises in the future. The same pitch attitude control system is used with glideslope tracker.

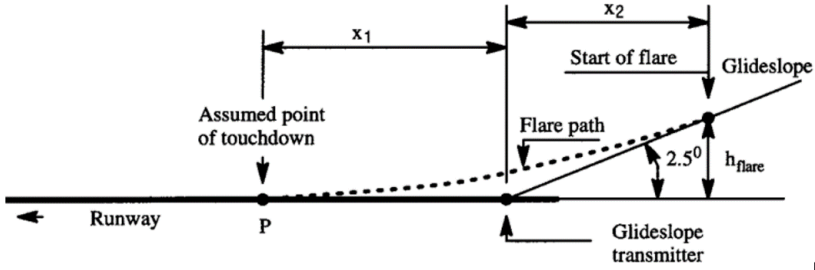


Figure 17. Flare Maneuver Scheme

The flare path function is represented as $h = h_{flare} e^{-\frac{t}{\tau}}$. The initial flare height and time constant depend on the airplane's velocity, the landing duration (assumed to be four times the time constant), and the offset distance due to a gentler landing. Because of the small landing angle, (19) is applicable.

$$x_1 + x_2 = 4\tau U_1 \quad (19)$$

The variables depicted above are defined in Fig.17. This navigational mode consists of a flare controller, a pitch attitude autopilot, algebraic operations (from θ angle onward), and a control law (comprising a time constant) in the Laplace domain. This algorithm assumes that the airplane's starting point is the intercept point. In the glideslope tracker mode, the slope's degree is assumed to be 2.5, and the distance between the point of intercept and the landing point is set at 2000 meters. For the flare maneuver mode, an offset distance of 335.28 meters is considered. During the landing phase, an airplane speed of 32.827 meters per second (approach) is expected.

The flare and glideslope mode combined system (seen in Fig. 18) initially starts at an altitude of 88 meters above the sea level, with the glideslope tracker mode activated. When the airplane reaches the flare height, the glideslope tracker mode disengages, and the flare maneuver initiates. The flare path is drawn, and the pitch autopilot tries to maintain the airplane on that trajectory. With this idea a condition system dependent on height is created. As shown in Fig. 18, pitch controller is used to hold the aircraft in desired pitch, theta to flight path angle converter is used which uses $\gamma = \theta - \alpha$ equality and 2 navigational modes which are designed above are created.

CHAPTER 7: AUTONOMOUS LANDING OF A GENERAL AVIATION AIRPLANE ON AN AIRCRAFT CARRIER

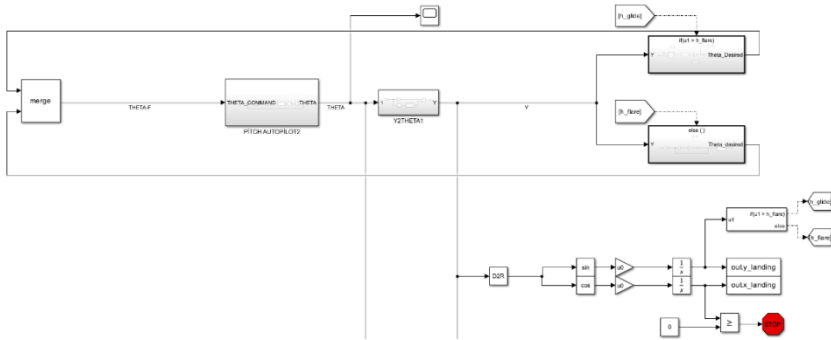


Figure 18. Navigational Landing System

3. SIMULATION

In order to visualize the scope of the project better, a physics-based simulation was utilized. The simulation was created on the simulation software platform Flightgear which has the ability to integrate MATLAB codes.

While using this platform, generated Euler angles and Fixed-frame earth coordinate data from Fig 18. were fed to Flightgear at each time step therefore the position and orientation of the UAV were observed in the environment of the Flightgear at each time step.

The procedure was previously tested for a landing on an airport scenario and lately tested on a landing on a typical carrier scenario. Both scenarios worked properly and fulfilled their main task which is visualization. In those scenarios, the simulation started at the beginning phase of the glideslope line.

3.1 Carrier Landing

In this scenario, it is aimed to complete the landing maneuver of the aircraft along the glide slope curve on the airport’s landing strip. The values of the initial conditions used for the scenario are defined manually.

When the scenario file created under the conditions is started, the following Fig. 19 is obtained from FlightGear.



Figure 19. Demonstration of final approach position, airport scenario in FlightGear

3.2 Airport Landing

In this scenario, it is aimed to perform landing phase on a moving target. Nimitz-class aircraft carrier has been preferred as a moving target because it is relatively close to reality since it is in today's current working cases and also the size and the deck configurations are similar to the TCG ANADOLU carrier. Aircraft was expected to perform the landing maneuver along the glideslope curve. The initial conditions required for landing on the moving carrier were determined and written on the run scrip.



Figure 20. Demonstration of final approach position, carrier scenario in FlightGear

The scenario started to run when the SIMULINK file connected with FlightGear was launched. Landing was completed successfully by applying the landing maneuver created by the designed autopilot modes. The image obtained towards the end of the scenario is shown in Fig. 20.

4. CONCLUSION

In this project, fundamental autopilots like Pitch Attitude Hold, Velocity Hold, Altitude Hold, Heading Displacement, and Turn Autopilots were designed and optimized for specific aircraft and flying conditions. An Autoland control system with glideslope hold and automatic flare modes was also developed. These autopilots work simultaneously during landing, along with airspeed control, localizer hold, and turn modes. The Autoland system can be further improved by adding more autopilot modes, real-time wind conditions, and using complete set of rigid body equations. The system developed in this project provides a foundation for an ideal landing scenario at an undergraduate level. This work used simulation to test designed autopilots for Airport Landing and Carrier Landing scenarios with a Cessna 182 aircraft. Autopilots were successful under specified conditions. Autopilot modes were based on Nelson's conceptual design for longitudinal modes and Roskam's for lateral modes. Aircraft transfer functions were approximated for simplification while preserving system behavior. Autopilot modes were modeled in Simulink and MATLAB for Root Locus Plot optimization using the PID controller Method by Ziegler Nichols. Compensators were modeled in Simulink Control System Toolbox. An Autoland Control System was developed with a Navigation Algorithm based on Roskam's work, with some advancements. The FlightGear system in Aerospace Toolbox in Simulink was used for simulation, with initial condition scenarios and animation running through FlightGear when the run button is pushed in Simulink. In this work a basic level system is created which can be enhanced in future works. A useful transition logic between different autopilot modes are demonstrated, where a smooth and continuous transitions between modes are obtained. As for the future work, more sophisticated multiple input multiple output (MIMO) type autopilot systems should be developed. Finally, moving and heaving carrier flight decks with gusty and crosswinds should be simulated for real type harsh sea environment.

Acknowledgements

We are grateful to Batu Candan, Abdülhamid Han Doğru and Mehmet Karahan, for their assistance and support to the research

Conflict of interest

No conflict of interest was declared by the authors.

Author contributions

Bahadır Türker, Bora Bostancı, Furkan Mert Sağel, and Uğur Ertunç were responsible for model preparation, conducting technical work, and writing the manuscript. Prof. Dr. Ünver Kaynak and Dr. Hüseyin Enes Salman managed the study, determined the technical methods, and oversaw the revision of the manuscript.

All authors have contributed equally to the relevant work.

REFERENCES

- [1] Beard, R. W., & McLain, T. W. (2012). Small unmanned aircraft: Theory and practice. Princeton university press.
- [2] Northrop Grumman, "X-47B UCAS," Available: <https://www.northropgrumman.com/what-we-do/air/x-47b-ucas/>. Accessed: April 7, 2023.
- [3] "Bayraktar TB3 SİHA 2023'te TCG Anadolu'ya Konuşlandırılacak," defenceturk.net. Available: <https://www.defenceturk.net/bayraktar-tb3-siha-2023te-tcg-anadoluya-konuslandirilacak>. Accessed: April 7, 2023.
- [4] J. Roskam, "Airplane flight dynamics and automatic flight controls. Part II," Roskam Aviation and Engineering Corp., 1979.
- [5] R. C. Nelson, "Flight stability and automatic control," New York, NY: McGraw-Hill, 1989.
- [6] B. Etkin, "Dynamics of Flight Stability and Control," New York, NY: John Wiley & Sons, 1982.
- [7] J.G. Ziegler and N.B. Nichols, "Optimum Settings for Automatic Controllers," presented at the IEEE Conference on Decision and Control, Rochester, NY, 1962.



CHAPTER 8

Aviation Technologies and Applications
E-ISBN:978-605-338-471-7
2025, chap. (8), pp.128-149.

UNITY3D ORTAMINDA DERİN PEKİŞTİRMELİ ÖĞRENME İLE EĞİTİLEN UÇAKLARIN PERFORMANSI

Mete CANTEKİN^{1,*}, Onur OSMAN², İbrahim Furkan İNCE³

ÖZET

İçinde yaşadığımız evren, fizik yasalarının geçerli olduğu bir simülasyon ortamı olarak görülebilir. Ne var ki bir robot ya da video oyun karakteri gibi sentetik bir ajana göre kendi yapay dünyaları haricinde herhangi bir evren ya da simülasyon tanımı yoktur. Bu ajanlar karmaşık talimatlar dizisi ile oluşturulmuş sanal dünyalarında, bu dünyanın fiziği hakkında bilgi edinmek istiyorlarsa, geliştiricinin sakladığı değişkenleri öğrenme yoluyla tespit etmeleri yeterlidir. Bu ajanlar fiziksel dünyamızın zaman değişkeniyle sınırlı olmadıklarından, kendi sanal dünyalarında daha hızlı öğrenebilmektedirler. Bu yüzden günümüzde ajan eğitiminin merkezinde dijital ortam bulunmaktadır. Burada kullanılan bilgisayar simülasyonu tabirinden bir algoritmanın çalıştığı ortamı anlamak gerekmektedir. Bu ve benzeri ortamlarda öğrenme süreci çok sayıda eğitim tekrarı gerektirdiğinden, pekiştirmeli öğrenme metodunu algoritma ile simülasyon ya da ajan ve çevre arasındaki boşluğu dolduran bir unsur olarak görmek yerinde olacaktır. Unity3D ortamında derin pekiştirmeli öğrenme ile uçak ajan eğitimi çalışmasında bir başlangıç noktasından harekete geçen 4 uçak ajan, yarış rotasındaki 21 adet kontrol noktasından geçtikten sonra belirli sınırlar içerisinde tekrar başlangıç noktasına dönerek bitiş çizgisine ulaşmaktadır. Dolayısıyla uçak ajanlarının ödül ve ceza sistemi ile oluşturulan bu ortamda, engellere çarpmadan kontrol noktalarından geçebilmesi için eğitilmeleri amaçlanmaktadır. Bu doğrultuda uçak ajanların eylemlerinin sonuçlarına göre politikalarını güncelleyebildiği ve onlara gittikçe daha iyi performans göstermelerini sağlayabildiği için Proksimal Politika Optimizasyonu (PPO) algoritmasından yararlanılmıştır. Ayrıca Unity3D ML-Agents aracının kullanımında Reinforcement Learning: AI Flight with Unity ML-Agents adlı örnek çalışmadan yararlanılmıştır. Böylece ML-Agents aracı sayesinde uçak ajanların sinir ağlarındaki PPO davranış parametreleri optimize edilebilmiştir. Bu durumda yapay sinir ağları değiştirildiğinde, uçak ajanlarının performansının da değişebildiği gözlemlenmiştir. Ne var ki pekiştirmeli öğrenmenin kapsam alanı yakın bir tarihte bilgisayar simülasyonunun ötesine geçecek gibi görünmektedir. Bu kapsamdaki çalışmalar oyun karmaşıklığının dengelenmesi kadar bazı robotik simülasyon ve otonom uçuş gibi gerçek yaşam problemlerine de uygulanabilmektedir. Dolayısıyla bu çalışmalar yapay zeka, dijital oyun ve havacılık gibi farklı alanlarda heyecan verici gelişmelere sebep olmaktadır.

Anahtar Kelimeler: Yapay Zekâ, Oyun Tasarımı, Otonom Uçuş, Derin Pekiştirmeli Öğrenme.

*Corresponding Author: mete.cantekin@nisantasi.edu.tr

1 Öğr. Gör., Nişantaşı Üniversitesi, Sivil Havacılık Yüksekokulu, Uçak Bakım Onarım Böl., İstanbul, Türkiye

2 Prof. Dr., Topkapı Üniversitesi, Mühendislik Fak., Elektrik Elektronik Müh. Böl., İstanbul, Türkiye

3 Dr., İstinye Üniversitesi, Mühendislik ve Doğa Bilimleri Fak., Yazılım Mühendisliği Bölümü, İstanbul, Türkiye

ABSTRACT

The universe we live in can be seen as a simulator environment where physical laws are valid. However, for a synthetic agent like a robot or a video game character, there is no definition of any universe or simulation other than their own artificial worlds. If these agents want to learn about the physics of this world in their virtual worlds created by a complex sequence of instructions, they only need to detect the variables hidden by the developer through learning. These agents are not limited by the time variable of our physical world, so they can learn faster in their own virtual worlds. That is why digital environment is at the center of agent training today. It is necessary to understand the environment where an algorithm works from the term computer simulator used here. In such and similar environments, since the learning process requires a large number of training repetitions, it would be appropriate to see the reinforcement learning method as an element that fills the gap between the algorithm and the simulator or the agent and the environment. In the study of aircraft agent training with deep reinforcement learning in Unity3D environment, 4 aircraft agents moving from a starting point reach the finish line by returning to the starting point within certain limits after passing 21 control points on the race route. Therefore, it is aimed to train the aircraft agents in this environment created with the reward and penalty system to pass the control points without hitting the obstacles. In this direction, the Proximal Policy Optimization (PPO) algorithm was used, which allows the aircraft agents to update their policies according to the results of their actions and to provide them with better performance. In addition, the example study Reinforcement Learning: AI Flight with Unity ML-Agents was used in the use of Unity3D ML-Agents tool. Thus, thanks to the ML-Agents tool, the PPO behavior parameters in the neural networks of the aircraft agents could be optimized. In this case, it was observed that the performance of the aircraft agents changed when the artificial neural networks were changed. However, the scope of reinforcement learning seems to go beyond computer simulation in the near future. Studies in this context can be applied to real-life problems such as robotic simulation and autonomous flight as well as balancing game complexity. Therefore, these studies cause exciting developments in different fields such as artificial intelligence, digital games and aviation.

Keywords: Artificial Intelligence, Game Design, Autonomous Flight, Deep Reinforcement Learning.

1. GİRİŞ

Bu çalışmada uçak ajanlarının, ödül ve ceza sistemi ile oluşturulan ortamda, engellere çarpmadan kontrol noktalarından geçebilmesi için eğitilmesi temel hedef olarak belirlenmiştir [1]. Dolayısıyla uçak ajanların eylemlerinin sonuçlarına göre politikalarını güncelleyerek, onlara daha iyi performans göstermelerini sağlayabildiği için PPO adlı pekiştirmeli öğrenme algoritmasından yararlanılmıştır [2]. Böylece Unity3D ML-Agents Aracı ile eğitilen uçak ajanlarının model hiperparametreleri optimize edilmiştir. Yapılandırma dosyasındaki summary freq., time horizon, batch size, buffer size, hidden units, beta, max. steps değerleri, optimize edilmiş PPO hiperparametre değerleridir. Bu parametreler en iyi

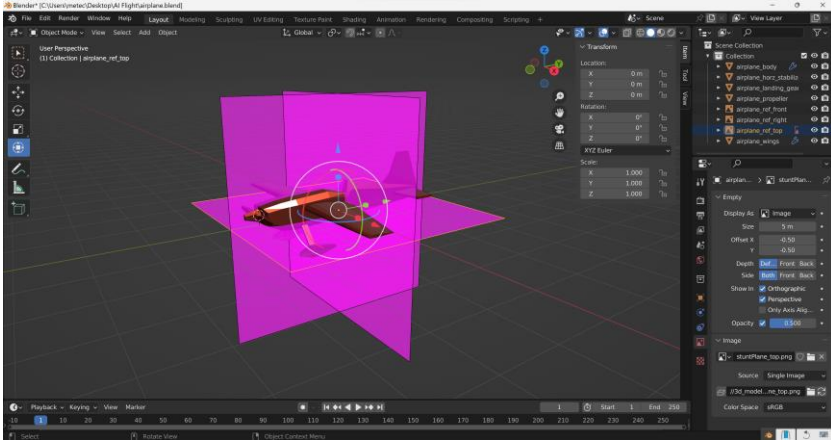
sonucu verebilmeleri için deneme yanılma yönteminden yararlanılarak oluşturulmuştur. Model eğitimi sırasında ise uçak ajanlarının aldığı ortalama ödüle bakılarak eğitimin ilerlemesi kontrol edilmiştir. Böylelikle uçak ajanları, 5000 eğitim adımı sonucunda, belirli sınırlar içerisinde başlangıç noktasına dönerek bitiş çizgisine ulaşmayı öğrenmişlerdir. Uçak ajanı kontrol noktalarından geçişini 4 ödül eşliğini de aşarak tamamladığında, eğitildiği modelin veri kümesindeki tüm eşik değerlerini (Thresholds) görmüş olacağından mükemmel performans ile değerlendirilmektedir. Böylelikle sinir ağının eğitimi başarıyla tamamladığı kabul edilerek, eğitim durdurulmuş ve model kaydedilmiştir. Böylece biri kolay diğeri zor olmak üzere iki farklı yapay sinir ağı eğitilmiştir. Sonuç olarak 1500 deneme sonrası uçakların ortalama parkur tamamlama süresi 1 dakika 55 saniye iken, 2100 deneme sonunda bu değer ortalama 1 dakika 35 saniyeye düşmüştür. Sonuç olarak yapay sinir ağı değiştirildiğinde, uçak ajanlarının performansının da değiştiği gözlemlenmiştir.

2. YÖNTEM

Bu çalışmada bir başlangıç noktasından harekete geçen 4 uçak yarış rotasındaki 21 adet kontrol noktasından geçtikten sonra (checkpoint/waypoint) belirli sınırlar içerisinde başlangıç noktasına dönerek bitiş çizgisine ulaşacaktır. Bu doğrultuda “Reinforcement Learning: AI Flight with Unity ML-Agents” adlı örnek çalışmadan yararlanılmıştır. (<https://immersivelimit.itch.io>, “AI Flight with Unity ML-Agents” 07.12.2023) Böylelikle derin pekiştirmeli öğrenme yöntemlerinde sıklıkla başvurulan PPO algoritması kullanılarak uçak ajanlarının eğitilmesi amaçlanmaktadır [3].

2.1. Uçak ve Çevre Bileşenlerinin Modellenmesi

Uçak ve çevre bileşenlerinin için öncelikli olarak eğitilecek uçak ajanının modellenmesi gerekmektedir. Bu hususta Blender programından yararlanılmıştır. (<https://www.blender.org>, “Blender 4.0” 07.12.2023). Blender programı, özgür ve açık kaynak kodlu bir üç boyutlu modelleme ve canlandırma uygulaması olarak animasyon, görsel efekt, üç boyutlu model, sanal gerçeklik modelleri üretiminde kullanılmaktadır. Blender programı ile bir öğenin konumunu, boyutunu ve yönünü değiştirmek, bir karaktere veya katı bir nesneyi canlandırma yeteneği sağlamak görece basit bir arayüzle mümkün olabilmektedir.



Şekil 1. Blender programında uçak ajan bileşeninin modellenmesi.

2.2. Unity3D Oyun Motoru Araçlarının Kurulumu

Unity3D oyun motorunun kurulumu tamamlandıktan sonra yeni bir Unity projesi oluşturmak adına High Definition Render Pipeline (HDRP) şablonu kullanılmıştır [4]. HDRP, daha yüksek sistem gereksinimlerine ihtiyaç duysa da gelişmiş aydınlatma, gölgeleme ve görsel efektler sağlaması nedeniyle bu projede tercih edilen Unity şablonu olmuştur [5]. Ardından ML-Agents, Cinemachine ve Input System araçlarının kurulumu tamamlanmıştır. (<https://unity.com>, “Cinemachine” 07.12.2023)

2.3. MSV Ortamında Model Klasörlerinin Oluşturulması

Unity3D ortamında ML-Agents kütüphanesi kullanılarak bir uçak ajanı eğitmeyi amaçlarken, ajanın kontrol noktasını geçerek uçuş rotasını tamamladığı her eğitim adımında yapması gereken işlemler Microsoft Visual Studio ortamında oluşturulan dosyalarda tanımlanmaktadır. Bunlar ayrıca ajanın hareketi, patlama efekti, eğitim ve kontrol parametreleri, aksiyonları, gözlemleri, bölüm başlangıcı, kontrol noktaları, hareket işlemi, tüm tetikleyiciler ve çarpışma tepkileri gibi parametrelerin ele alındığı dosyalardır.

2.3.1. Uçak Ajanı ve Çevre Dosyalarının Oluşturulması

Unity ML-Agents kütüphanesini kullanarak bir uçak ajanı oluşturmak için Aircraft Agent dosyasında bir kod dizisi oluşturulmuştur. Böylelikle uçak ajanı yarış parkurunda kontrollü bir şekilde uçmayı öğrenebilecektir. Sezgisel olarak davranan ve AircraftPlayer sınıfına bağımlı olarak

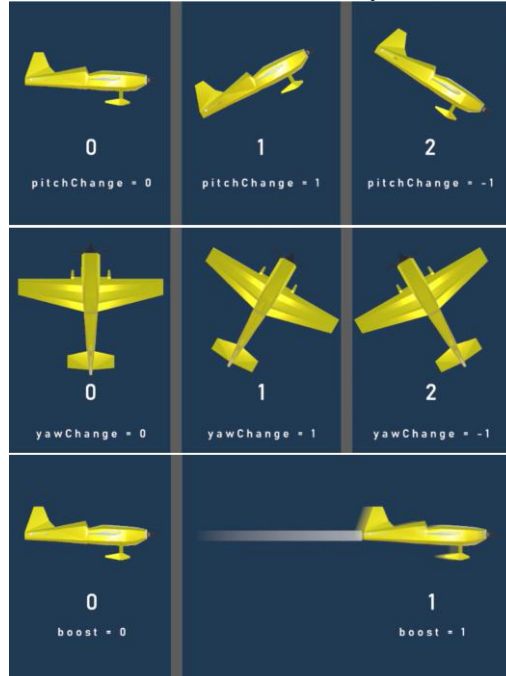
geliştirilen bu kod dizisi, uçağın hareketini, patlama efektini, eğitim ve kontrol parametrelerini, aksiyonlarını, gözlemlerini, bölüm başlangıcını, tüm kontrol noktalarını, hareket işlemini, tetikleyici ve çarpışma tepkilerini tanımlamaktadır. Bu kod dizisi ile ilgili kütüphaneler, Unity ML-Agents, System, Collections, UnityEngine ve InputSystem kütüphaneleridir. Bu kütüphaneler ile kod dizisinde kullanılan tüm sınıflar, metotlar, veri tipleri ve girdi sistemleri oluşturulabilmektedir. Böylece uçağın başlangıçta, her adımda ve her bölümde yapması gereken işlemler kolaylıkla tanımlanabilmiştir. Initialize metodunda uçağın bağlı olduğu bileşenler ve maksimum adım sayısı ayarlanırken, OnActionReceived metodunda ise ajanın aldığı aksiyonlar okunmuş ve uçağın yön değiştirme, hızlanma ve iz bırakma durumları belirlenmiştir. Ardından tanımlanan eğitim modunda ise ajana her adımda küçük bir negatif ödül verilerek, zaman aşımı kontrolü yapılmış ve bir sonraki kontrol noktasına ulaşip ulaşmadığı sorgulanmıştır [6].

AircraftAgent sınıfının içinde uçağın hareket, patlama efekti, eğitim ve kontrol parametreleri bulunmaktadır. Bu parametrelerde uçak ajanlarının itme kuvveti, yatış, sapma ve yunuslama açıları ve hızları, patlama efekti ve eğitimlerindeki zaman aşımı sayısı gibi değerleri tanımlanmıştır. Diğer yandan uçağın bağlı olduğu bileşenler ve eğitiminde kullanılacak değerler de AircraftAgent sınıfının içinde tanımlanmıştır. Bu parametrelerin bazıları kod editöründe ayrıca görünür hale getirilmiştir. Aircraft Agent klasöründe bulunan uçak pervanelerinin ve kontrol noktası kapılarının rotasyonları ile ilgili metotlar oluşturulmaktadır. Ancak bu metotların tanımlanması patlama ve uçakların ardındaki ışın efektinin tanımlanması gibi bu çalışmanın kapsamı alanı dışında tutulmuştur. Örneğin Next Step Timeout bileşeni eğitim modunda kullanılan bir değeri ifade etmektedir. Bu değer uçağın zaman aşımına uğramaması için yapması gereken maksimum adım sayısını belirtir. Eğer uçak ajanları 300 adımın ardından sonraki kontrol noktasına ulaşmadılarsa, negatif bir ödül aldıkları için eğitimleri sıfırlanır. Bunun bir diğer sebebi, eğitimin daha uzun sürmesi halinde, tekrara düşme ihtimalidir.

```
// Controls
private float pitchChange = 0f;
private float smoothPitchChange = 0f;
private float maxPitchAngle = 45f;
private float yawChange = 0f;
private float smoothYawChange = 0f;
private float rollChange = 0f;
private float smoothRollChange = 0f;
private float maxRollAngle = 45f;
private bool boost;
```

Şekil 2. Uçak ajanın 3 temel eksen ve itki değerleri.

Pitch Change, Smooth Pitch Change, Yaw Change, Smooth Yaw Change, Roll Change, Smooth Roll Change bileşenleri uçağın yatış, sapma ve yunuslama açılarındaki değişimleri belirten değerlerdir. Bu değerler ajanın aldığı aksiyonlara ve mevcut dönüş açılarına göre hesaplanmaktadır. Düzgün değişim değerlerinin tanımlanabilmesi uçak ajanının, ani dönüşler yapmak yerine yumuşak dönüşler yaparak seyredildiğini gösterir. Max Pitch Angle, Max Roll Angle bileşenleri uçağın maksimum yatış ve yunuslama açılarını belirten değerlerdir. Bu değerler sayesinde uçağın çok fazla burun aşağı vermesi ya da yana yatması engellenmiş olur. Boost bileşeni uçak ajanının hızındaki artış durumunu belirten mantıksal değeri ifade etmektedir. Bu bileşene göre uçağa takviye itki kuvveti kazandırıldığında iz bırakma durumu da değiştirilir. Diğer yandan AircraftAgent sınıfında uçak ajanının başlangıçta, her adımda ve bölümde yapması gereken işlemler tanımlanmıştır. Initialize bileşeni uçak ajan uçuşa ilk başladığında çağrılan metodu ifade eder. Bu metotta uçağın bağlı olduğu bileşenler ve maksimum adım sayısı ayarlanmıştır. Maksimum adım sayısı eğitim modunda 5000, yarış modunda ise 0 (sonsuz) değeri ile tanımlanmıştır. On Action Received bileşeni uçak ajanının uçuşa başlaması ile birlikte çağrılan metodu ifade eder. Bu metotta uçağın yön değiştirme, hızlanma ve iz bırakma durumları tanımlanmıştır.



Şekil 3. VectorAction değerlerinin açılımları.

Uçak ajana eğitimi sırasında her adımda küçük bir negatif ödül verilerek zaman aşımı kontrolü de yapılmış olur. Böylece uçağın bir sonraki kontrol noktasına ulaşım sağlanmadığı sorgulanmış olur. Collect Observations bileşeni uçak ajanının karar vermek için kullandığı gözlemler tamamlandığında çağrılan metodu ifade eder. Dolayısıyla uçak ajanın etrafındaki dünyayı gözlemlemesini sağlamaktadır. Bu metotta, uçağın hızı, bir sonraki kontrol noktasının yönü ve yönelimi gibi gözlemler Unity M.L. içerisindeki Agent Stunt sensörleri ile VectorSensor nesnesine eklenir. Bu gözlemler, uçak ajanının sanal dünyayı temsil eden veri noktalarıdır. Uçak ajanı böylelikle bu verileri kullanarak çevresi hakkında anlamlı bilgiler elde ederek eylemlerini belirler. Bu esnada uçak hızı, bir sonraki kontrol noktasının konumu ve bu kontrol noktasının yönelimi olmak üzere üç tür gözlem toplanmaktadır. Uçak hızı, uçak ajanının kendi yerel koordinat sistemindeki hızını gözlemler. Böylece ajanın hızı ve doğrultusu bilinmiş olur (1 vector3 = 3 değer). Bir sonraki kontrol noktasının yeri ise uçak ajanının bir sonraki kontrol noktasına olan mesafesi ve yönünü vektörel olarak gözlemler. Böylece ajanın nereye gitmesi gerektiğinin bilmesi sağlanır (1 vector3 = 3 değer). Bir sonraki kontrol noktasının yönelimi de uçak ajanının bir sonraki kontrol noktasına doğru yönünü kendi yerel koordinat sisteminde gözlemler. Böylece ajanın kontrol noktasına nasıl yaklaşması gerektiği bilinmiş olur (1 vector3 = 3 değer).

Sonuç olarak her 3 gözlem için 3'er değer olmak üzere toplam 9 adet gözlem değeri vardır. Got Checkpoint bileşeni uçak ajanı rotasındaki kontrol noktasından geçtiğinde çağrılan metodu ifade etmektedir. Bir sonraki kontrol noktasının indeksi bu metot ile güncellenmektedir. Eğitim modundaki uçak ajanı, her kontrol noktasından geçtiğinde 0,5 değerli bir pozitif ödül kazanarak zaman aşımı değeri de güncellenmiş olur. Process Movement bileşeni uçak ajanının hareketini hesaplayan ve uygulayan metodu ifade eder. Bu metotta ajanın hızlanma durumuna göre sırasıyla bir çarpan belirlenmiştir (Delta Time). Böylelikle uçak ajana kazandırılmak istenen itme kuvveti uygulanmış, yatış, sapma ve yunuslama açılarındaki değişimler hesaplanarak yumuşatılmış ve yeni dönüş açıları sınırlandırılarak dönüş rotasyonu ayarlanmış olur. Diğer yandan pekiştirmeli öğrenme yönteminin temeli olan ödül ceza sistemindeki negatif değerler burada tanımlanmıştır. Delta time terimi bir önceki kareyi tamamlamak için gereken süreyi ifade etmektedir. Bu sayede oyunun akıcılığını ve tutarlılığını sağlamak kolaylaşmaktadır.


```

ProcessMovement();

if (area.trainingMode)
{
    // Small negative reward every step
    AddReward(-1f / MaxStep);

    // Make sure we haven't run out of time if training
    if (StepCount > nextStepTimeout)
    {
        AddReward(-.5f);
        EndEpisode();
    }
}

```

Şekil 4. Uçak ajanının davranışını ödüllendiren değerlerin tanımlanması.

On Collision Enter bileşeni uçak ajanının çarpışma yaşadığı durumlarda, eğer çarpıştığı nesne başka bir ajan değilse, patlama efekti bu metot sayesinde gösterilir. Bu durumda uçak görünmez kılınarak bölüm sonlandırılır. Diğer yandan eğitim esnasında uçak ajanların birbirlerine çarpabilmelerine, tetikleyici unsurlar etkisiz kılınarak izin verilirken, ajan olmayan başka bir nesneye çarptıklarında tetiklenmeleri ve negatif ödül (-1) almaları sağlanmıştır. Explosion Reset bileşeni bu metotta tanımlanan özel işlevler, patlama efektinin kullanılması, ajanın konumunun sıfırlanması ve çarpışan ajanın kaybolması ile ilgilidir. Bu metotta eğitim modunu etkileyen değer, uçak ajanlarının çarpışmadan 1 saniye sonra meydana gelecek (spawn) şekilde ayarlanmış olmasıdır.

Aircraft Area dosyasındaki kod dizininde ise uçakların belli bir güzergahta seyretmesini sağlayan sanal bir yarış pisti oluşturulmaktadır. Burada önce CinemachineSmoothPath bileşeni kullanılarak yarış yolunu tanımlanmış, ardından da kontrol noktaları oluşturulmuştur. Diğer yandan AircraftAgent sınıfı ile tanımlı uçaklar da bu dosyada listelenmektedir. Böylece bir uçağın konumunu sıfırlamak ya da uçağın yeni bir kontrol noktasından başlamasını sağlamak için gerekli metotlar da bu dosyada tanımlanmış olur. Dosyanın devamında yarış pistindeki kontrol noktalarının konumlarını ve yönlerini hesaplamak için gerekli metotlar ve eğitim modundaki uçak ajanlarının spawn olduğunda konumlarını rastgele olarak sıfırlayabilmek için kullanılan bir metot bulunmaktadır.

Diğer yandan bir hava yarışı simülasyonuna eğer biraz rastgelelik eklenirse, uçakların daha öngörülemez hareket etmesi sağlanabilir. Bu durum yarışın sonucunu önceden belirlenemez hale getirerek, yarışı daha ilginç kılabilir. Bu rastgelelik sayesinde uçak ajanların pistin etrafında her zaman aynı yolu izlemesi de engellenmiş olur. Buradaki Random.Range değişkeni 10 değeri ile tanımlandığında, uçaklar tekrar aynı yerde meydana gelerek (spawn), pistin etrafında her zaman için aynı yolu takip ederler.

Bunun asıl nedeni, uçakların kontrolünü sağlayan sinir ağının her zaman aynı girdiyi alması ve bu girdiye dayalı olarak her zaman aynı kararları vermesidir. Dolayısıyla çalışılan ortama biraz rastgelelik eklemek adına Random.Range değişkeni 9 ila 10 aralığında bir değer ile ayarlanmaktadır. Böylece uçak ajanları tekrar spawn olduklarında 1 ila 10 metre arasında rastgele kaydırılarak vücut bulmaları sağlanmaktadır. Bu küçük değişiklik sayesinde uçak ajanların pist etrafında farklı yollar izlemesi ve sinir ağının her zaman aynı kararları vermesi engellenmiş olur. Böylelikle simülasyon ortamına oynanan karakterler eklenmek istendiğinde NPC'ler (non player character) ile aralarında daha gerçekçi ve rekabetçi bir ortam bulmuş olurlar.

2.3.2. Eğitim Dosyalarının Oluşturulması

Bir pekiştirmeli öğrenme ajanının eğitiminde ihtiyaca göre düzenlenmiş özel bir içerik (curriculum) dosyasına her zaman gerek olmasa da bu çalışmadaki uçak ajanının, 3B ekseninde 100 metre aralıklarla uçuşması oldukça karmaşık bir görev olduğundan, davranışını etkileyecek eğitim datasının tanımlanması önemlidir. Bunun için ajanın ödül değerine göre kontrol noktasına uzaklığının nasıl değiştiği hesaplanmıştır. Böylece ajanın öğrenmeye başladıktan sonra görevi kolaydan zora doğru gerçekleştirilmesi sağlanabilecektir. Uçak ajanı bu yapılandırmayı öğrendikçe ödüllendirilecek ve davranışlarını bu ödül ile eşleştirebilecektir. Burada uçak ajanının aşması gereken eşik değerleri (Thresholds) 2.0, 2.0, 4.0 ve 6.0 değerleri ile tanımlanmıştır. Dolayısıyla AircraftLearning.yaml dosyasında tanımlandığı üzere, ajan eşik değerlerini geçtikçe, artan ödül kazanacaktır. Bunun için bir kontrol noktasını geçtikten sonra ilk olarak 50 metreden 30 metreye yaklaştığında 2.0 puan (iyi performans), ardından 30 metreden 20 metreye yaklaştığında 2.0 puan, 20 metreden 10 metreye yaklaştığında 4.0 puan ve 10 metreden 0 metreye yaklaştığında ise 6.0 puan (mükemmel performans) elde edilir. Böylece ajanın başlangıçta bir sonraki kontrol noktasına 50 metre yaklaşması yeterli iken, daha sonra 30, 20, 10 ve sıfır metre ile kontrol noktasına ulaşması sağlanır.

```
AircraftLearning:
  measure: "reward"
  thresholds: [ 2.0, 2.0, 4.0, 6.0 ]
  min_lesson_length: 100
  signal_smoothing: true
  parameters:
    checkpoint_radius: [ 50.0, 30.0, 20.0, 10.0, 0.0 ]
```

Şekil 5. AircraftLearning.yaml dosyasındaki temel değerler.

Thresholds bileşeni öğrenme performansının nasıl değerlendirildiği gösteren ödül eşiklerini ifade etmektedir. Çalışmada kullanılan eşikler 2, 2, 4 ve 6 değerleri ile tanımlanmıştır. Bir uçak ajanın performansı, eşiklerden her birine ulaştığında aldığı ödüle göre değerlendirilir. Bu doğrultuda bir uçağın ödülü 2 değerine ulaştığında uçağın performansı iyi olacak, 6 değerine ulaştığında ise mükemmel olacaktır. Parameters bileşeni öğrenme sürecine eklenen parametreleri belirtmektedir. Bu çalışmada değerlendirilmesi gereken parametrelerden biri de checkpoint_radius değişkeni olmuştur.

Bu parametre uçağın bir kontrol noktasından geçebilmesi için katetmesi gereken mesafeleri tanımlamaktadır. Bu çalışmada uçağın kontrol noktasına gelebilmesi için tamamlaması gereken mesafeler geriye doğru 50, 30, 20, 10 ve 0 metre şeklinde tanımlanmıştır. Dolayısıyla kontrol noktasındaki mesafe sayılarının artması, uçağın daha sık kontrol edilmesine neden olacağından, uçağın performansının da daha iyi izlenmesine yardımcı olmaktadır.

Bu çalışmada uçak ajanlarının doğru davranışı öğrenebilmesi için “trainer_config.yaml” adında biraz daha karmaşık olan bir yapılandırma dosyası daha oluşturulmuştur. Bu dosya aslında bir derin pekiştirmeli öğrenme yöntemi olan PPO algoritmasından ibarettir. Dolayısıyla sınır ağları ve eğitim algoritmaları ile ilgili olan PPO hiperparametrelerini içermektedir. Bu çalışmada bazı PPO hiperparametre değerleri varsayılan olarak bırakılırken, bazıları ise optimize edilerek uygulanmıştır.

2.3.2.1. Varsayılan Değerlerle Kullanılan PPO Hiperparametreleri

Bu çalışmada kullanılan Proximal Policy Optimization algoritması, diğer derin öğrenme algoritmalarına kıyasla daha hızlı ve daha kararlı öğrenme sağladığı ve farklı çevrelerde ve farklı parametrelerde çalışabildiği için seçilmiştir. Dolayısıyla bazı PPO hiperparametreleri, trainer_config.yaml dosyasındaki varsayılan değerleriyle kullanılmıştır [7].

```
default:
  trainer: ppo
  batch_size: 1024
  beta: 5.0e-3
  buffer_size: 10240
  epsilon: 0.2
  hidden_units: 128
  lambda: 0.95
  learning_rate: 3.0e-4
  learning_rate_schedule: linear
  max_steps: 5.0e5
  memory_size: 256
  normalize: false
  num_epoch: 3
  num_layers: 2
  time_horizon: 64
  sequence_length: 64
  summary_freq: 10000
  use_recurrent: false
  vis_encode_type: simple
  reward_signals:
    extrinsic:
      strength: 1.0
      gamma: 0.99
```

Şekil 6. Uçak ajanın varsayılan hiperparametre değerleri.

Epsilon bileşeni PPO algoritmasında kullanılan rastgele eylem alma olasılığını belirtmektedir. Bu parametre, uçak ajanın politikasının çok fazla değişmesini önlemeye yardımcı olarak, ortamı keşfetmesini sağlamaktadır. Bu çalışmada dosyadaki varsayılan değeri olan 0.2 değeri kullanılmıştır. Lambd bileşeni Generalised Advantage Estimation (GAE) algoritmasında da kullanılan indirgenme faktörünü belirtmektedir. GAE, Q öğrenme algoritmalarından daha az bellek gerektirdiği ve daha hızlı öğrenebildiği için geliştirilmiştir. Dolayısıyla bu parametre zamansal fark hatasının önemini kontrol eden parametredir. Böylece uçak ajanın gelecekteki ödülleri tahmin etmesine yardımcı olur. Lamda değeri 0 ile 1 arasında bir değer olarak, 0 değeri tüm ödüllerin ağırlığını eşit olarak ayarlarken, 1 yalnızca en yakın ödülü dikkate alacaktır. Bu çalışmada dosyadaki varsayılan değeri olan 0.95 değeri kullanılmıştır. Learning Rate bileşeni uçak ajanın politika ve sinir ağlarını güncellemek için kullandığı öğrenme hızını belirtmektedir. Daha yüksek tanımlanan değerler, daha hızlı bir öğrenme sağlasa da kararsız olabilir. Bu çalışmada dosyadaki varsayılan değeri olan 3.0e-4 değeri kullanılmıştır. Memory Size bileşeni genellikle Recurrent Neural Network (RNN) kullanan ajanlar için bellek boyutunu belirtmektedir. Böylece ajanın geçmiş deneyimlerinden yararlanmasına olanak tanımaktadır. Dolayısıyla bu parametredeki değer ajanın geçmiş deneyimlerini depolamak için kullanılan belleğin boyutunu ifade etmektedir. Bu çalışmada dosyadaki varsayılan değeri olan 256 deneyim değeri kullanılmıştır.

Num Epoch bileşeni her bir eğitim döngüsünde politika ve sinir ağlarının kaç kez güncelleneceğini belirtmektedir. Daha yüksek tanımlanan değerler, daha iyi bir öğrenme sağlasa da daha yavaş ilerlemeye sebep olmaktadır. Bu çalışmada dosyadaki varsayılan değeri olan 3 döngü değeri kullanılmıştır. Num Layer bileşeni politika ve sinir ağlarında kullanılan gizli katman sayısını belirtmektedir. Daha yüksek değer ile tanımlanması, daha karmaşık bir politikanın belirlenmesine yardımcı olsa da aşırı uyum sorununa (overfitting) sebebiyet verebilir. Bu çalışmada dosyadaki varsayılan değeri olan 2 katman değeri kullanılmıştır. Sequence Length bileşeni RNN kullanan ajanlar için her bir eğitim döngüsünde toplanan ardışık deneyim sayısını belirtmektedir. Daha yüksek bir değer, daha iyi bir bellek kullanımı sağlasa da daha yavaş ilerler. Bu çalışmada dosyadaki varsayılan değeri olan 64 adım değeri kullanılmıştır. Extrinsic bileşeni Extrinsic ödül sinyali, ortamda tanımlanan ödülleri temsil etmektedir. Bu çalışmada varsayılan olarak etkin konumdadır. Bu ödül sinyali, ajanın ortamda başarılı olmasını sağlar. Bu çalışmada ortamdan doğrudan alınan sinyaller ile çalışıldığı için dosyadaki varsayılan olarak extrinsic dışsal ödül sinyali tercihe edilmiştir. Strength bileşeni dışsal ödül sinyalinin gücünü belirlemek için kullanılan bir değerdir. Bu parametre bir sayı olabilir. Bu çalışmada dosyadaki varsayılan değeri olan 1.0 değeri kullanılmıştır. Gamma bileşeni Gelecekteki ödüllerin indirgenme faktörüdür. Gelecekteki ödüllerin politikayı ne kadar etkilediğini belirler. Bu parametre 0 ile 1 arasındaki herhangi bir sayı olabilir. Bu çalışmada dosyadaki varsayılan değeri olan 0.99 değeri kullanılmıştır.

2.3.2.2. Optimize Edilmiş PPO Hiperparametre Değerleri

Bu çalışmada oluşturulan summary freq., time horizon, batch size, buffer size, hidden units, beta, max. steps gibi PPO hiperparametre değerleri ise trainer_config.yaml dosyasındaki en iyi sonucu verebilmeleri için deneme yanılma yönteminden yararlanılarak optimize edilmiş PPO hiperparametre değerleridir [8].

```

AircraftLearning:
  summary_freq: 32000
  time_horizon: 128
  batch_size: 2048 #512
  buffer_size: 20480 #4096
  hidden_units: 256 #128
  num_layers: 2
  beta: 1.0e-2
  max_steps: 5.0e7
  num_epoch: 3
  reward_signals:
    extrinsic:
      strength: 1.0
      gamma: 0.99
    
```

Şekil 7. Uçak ajanının optimize edilmiş hiperparametre değerleri.

Summary Freq bileşeni uçak ajanının eğitim istatistiklerini görselleştirmek için kullanılacak TensorBoard aracında, özet verilerinin kaydedileceği adım aralığını belirtmektedir. Bu çalışmadaki optimize edilmiş değeri 32000 adımdır. Time Horizon bileşeni her bir eğitim döngüsünde toplanan ardışık deneyim sayısını belirtmektedir. Daha yüksek tanımlanan değerler, daha iyi bir ödül tahmini sağlasa da daha yavaş ilerler. Bu çalışmadaki optimize edilmiş değeri 128 adımdır. Batch Size bileşeni her bir eğitim döngüsünde kullanılan deneyim sayısını belirtmektedir. Daha yüksek tanımlanan değerler, istikrarlı bir öğrenme sağlasa da daha yavaş ilerler. Bu çalışmadaki optimize edilmiş değeri 2048 örnektir. Kararsız uçması istenen uçak ajanı için ise bu optimizasyon değeri 512 olarak tanımlanmıştır.

Buffer Size bileşeni eğitim için toplanan deneyim sayısını belirtmektedir. Bu durumda geçmiş deneyimleri depolamak için de kullanıldığından bu değer, Batch Size değerinden büyük olmalıdır. Bu çalışmadaki optimize edilmiş değeri 20480 örnektir. Kararsız uçması istenen uçak ajanı için ise bu optimizasyon değeri 4096 olarak tanımlanmıştır. Hidden Units bileşeni politika ve değer ağlarında kullanılan gizli katmanlardaki nöron sayısını belirtmektedir. Daha yüksek tanımlanan değerler, daha karmaşık bir politika öğrenmeye yardımcı olsa da aşırı uyuma (overfitting) neden olabilir. Bu çalışmadaki optimize edilmiş değeri 256 birimdir. Kararsız uçması istenen uçak ajanı için bu optimizasyon değeri 128 olarak tanımlanmıştır. Beta bileşeni politika kayıplarına eklenen entropi düzenleme teriminin katsayısını belirtmektedir. Entropi düzenlemesi ajanı bir yandan keşif yapmaya teşvik ederken, bir yandan da “istimrar” ile arasındaki dengeyi sağlar. Bu çalışmadaki optimize edilmiş değeri $1.0e-2$ (%1) olarak tanımlanmıştır. Max Steps bileşeni uçak ajanı için eğitimde kalacağı maksimum adım sayısını belirtmektedir. Bu parametre, eğitimin ne zaman duracağını kontrol eder. Dolayısıyla eğitim sona ermeden yapılması gereken maksimum adım sayısını gösterir. Bu çalışmadaki optimize edilmiş değeri $5.0e7$ (50.000.000) adımdır.

2.4. Unity3D Ortamında Uçak Ajan Eğitimi

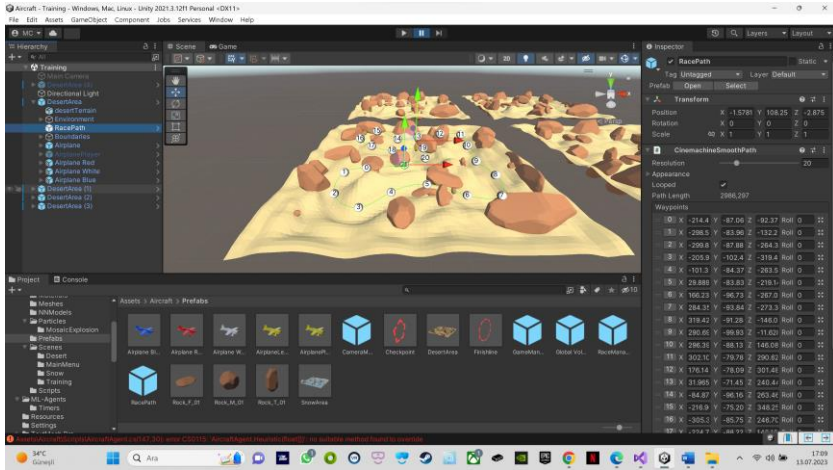
Unity3D ortamında gerçekleştirilecek olan model eğitiminin başlatılabilmesi için bölüm tasarımı sınırlarının belirlenmesi, uçuş rotasının oluşturulması, engel algılama parametrelerinin ayarlanması, uçak ajanlarının davranış parametrelerinin tanımlanması gerekmektedir. Böylece eğitim sırasında uçak ajanlarının aldığı ortalama ödüle bakılarak eğitimin ilerlemesi kontrol edilebilmektedir [9].

2.4.1. Bölüm Tasarımı Limitlerinin Belirlenmesi

Uçak ajanlarının eğitim sırasında simülasyon haritasının dışına çıkmamaları için eğitim alanının çevresinde ve üstünde görünmez duvarlar oluşturulmuştur. Böylelikle uçakların uçuş alanı simülasyon ortamı büyüklüğünde ölçeklendirilirken, maksimum irtifaları da 200 birim şeklinde sınırlanmıştır.

2.4.2. Uçuş Rotasının Oluşturulması

CinemachineSmoothPath özelliği sayesinde 100 metre iz düşümlü aralıklara makul dönüş açıları ile yerleştirilmiş 21 adet kontrol noktası oluşturulmuştur. Dolayısıyla yüksek hücum açıları olmaksızın oluşturulan bir yarış pisti sanal bir döngü içinde 4 uçak ajanının kendi aralarında çarpışma ve nesnelere çarpma ihtimallerinin eğitimi etkileyeceği de düşünülerek tanımlanabilmektedir. Bir başka önemli nokta da ajanların eğitim sırasında irtifa değiştirirken boost parametresini sürekli yüksek itki değerinde kullanmaması gerektiğidir. Uçuş rotası hazırlandıktan sonra uçak ajanlarının eğitim alanı dört konumda çoğaltılmıştır.



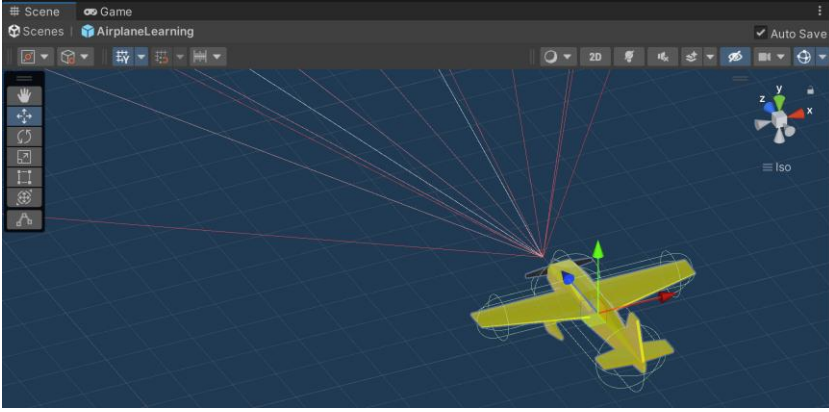
Şekil 8. Uçak ajanının uçuş rotasındaki kontrol noktaları.

2.4.3. Engel Algılama Parametrelerinin Ayarlanması

RayPerceptionSensor3D aracının ray cast tabanlı gözlemleri destekleyen sensörleri sayesinde uçağın önündeki, altındaki ve üstündeki engeller algılanarak (obstacle avoidance), uçağın çarpışmalardan kaçınması için manevralar gerçekleştirmesi sağlanır. RayPerceptionInput adlı arayüzü ise

CHAPTER 8: UNITY3D ORTAMINDA DERİN PEKİŞTİRMELİ ÖĞRENME İLE EĞİTİLEN UÇAKLARIN PERFORMANSI

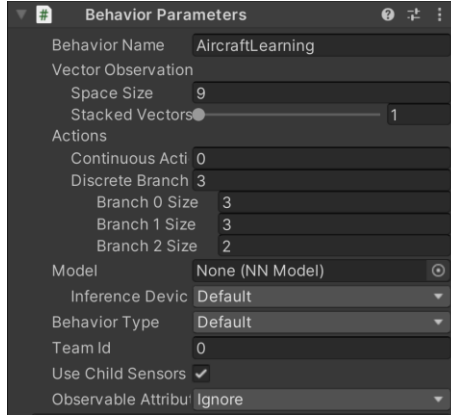
sensörün adını, ışın sayısını, açısını, uzunluğunu, katman maskesini, algılanan nesnelere etiketlerini ve ışınların başlangıç ve bitiş noktalarının dikey ofsetlerini belirler. (<https://docs.unity3d.com>, “Class Ray Perception Sensor Component 3D” 07.12.2023) Transform bileşeni sensörün bağlandığı konumu ve yapılmak istenen manevrayı belirleyen parametredir. Bu çalışmada uçak ajanları için hava hızı yönünde, 18 derece yunuslama aşağı yönde ve 18 derece yunuslama yukarı yönde olmak üzere 3 adet RayPerceptionSensor3D bileşeni oluşturulmuştur. Ray Angles bileşeni ışınların sensörün konumuna göre hangi açılarda yayılacağını belirleyen parametredir. Örneğin ışınlar 0 derecede iken sadece ileriye tararken, 90 derecede sağa doğru, 180 derece ise geriye doğru tarama yapar. Bu çalışmadaki değeri ise 30 derece olarak tanımlanmıştır.



Şekil 9. RayPerceptionSensor3D ışın sensörünün 30 dereceye ayarlanması.

2.4.4. Uçak Ajanlarının Davranış Parametreleri

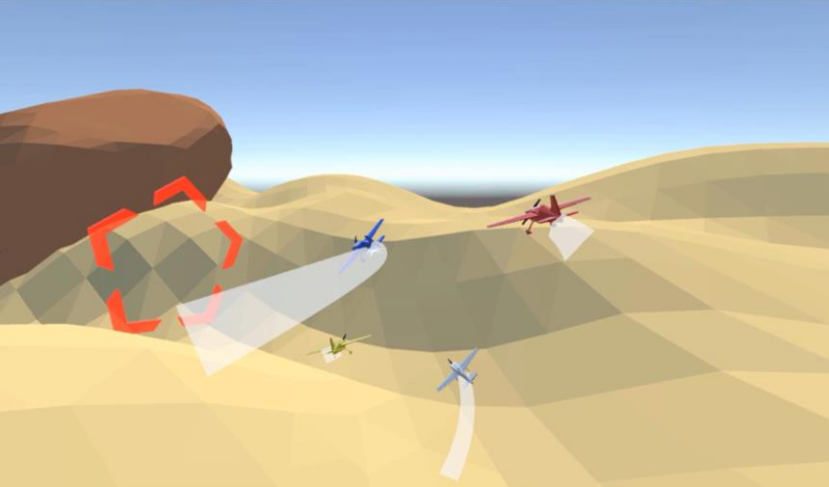
Uçak ajanları sahneye eklenerek engel algılama ayarları tanımlandıktan sonra uçak ajan ayarlarına davranış parametreleri eklenir. Unity3D ortamındaki Behavior Parameters arayüzü ajanın davranış özelliklerini ayarlamak için kullanılan temel bileşenleri barındırmaktadır. Bunlar ajanın davranışıyla ilgili olarak gözlem boyutu, eylem boyutu ve eylem türü gibi bilgileri içermektedir [10]. Vector Observation: Bu alanda tanımlanan “Space Size” değeri, uçakların geliştireceği davranış için topladığı gözlemlerin tümünü ifade eder. Bu çalışmadaki değeri (3+3+3) 9 olarak tanımlanmıştır. Discrete Branch bileşeni bu alanda tanımlanan “Branch 0 Size” parametresi uçağın pitch değişkenlerini temsil ettiğinden 3 değeri olarak, “Branch 1 Size” parametresi uçağın yaw değişkenlerini temsil ettiğinden 3 değeri olarak, “Branch 2 Size” parametresi ise uçağın boost değişkenlerini temsil ettiğinden 3 değeri olarak tanımlanmıştır. Model bileşeni uçak ajan çıkarım modundayken kullanılan sinir ağı modelidir.



Şekil 10. Unity3D ortamında uçak ajanı davranış parametrelerinin belirlenmesi.

2.4.5. Model Eğitiminin Başlatılması

Unity3D ortamında ML-Agents aracını kullanarak uçak ajan eğitime başlamak için Anaconda Prompt üzerinden daha önce kurulan ortamların etkinleştirilmesi gerekmektedir. Böylece eğitim verilerinin bulunduğu klasörler erişilebilir olacaklardır. Burada dosya yolunun doğru kopyalandığından ve tanımlanan uçak ajan adlarının (aircraft_01, aircraft_02, aircraft_03) eğitimde kullanılan benzersiz tanımlayıcılar olduğundan emin olmak gerekmektedir.



Şekil 11. Eğitime başlayan uçak ajanların ekran görüntüsü.

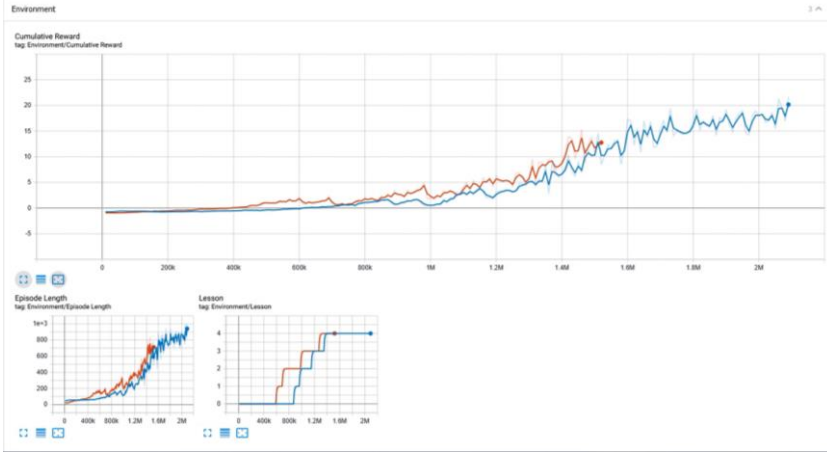
Bu işlemlerin ardından oynat düğmesi ile eğitim başlatıldığında sürecin 20 kat hızlı olduğu, dolayısıyla uçak ajanlarının çok hızlı uçtuğu gözlemlenecektir. Bu durumda Project Setting arayüzünde bulunan “Time” menüsündeki “Time Scale” değerinin 20 yerine 1 olması halinde, uçak ajanların uçuşunun gerçek zamanlı render alma süreleri ile gözlemleneceğini belirtmek gerekir. Diğer yandan uçak ajanlarının “havada tutunabilmesi” için RigidBody sekmesindeki “Use Gravity” değişkeninin de kapalı olması gerekmektedir. Böylece Unity3D ortamının yerçekimi bileşeni etkin olarak kullanılmayacaktır. Uçak ajanın eğitim ilerlemesi bu esnada Anaconda üzerinden ortalama ödülle bakılarak kontrol edilebilmektedir.

Pozitif ortalama ödül ajanın öğrendiğini gösterirken, negatif ortalama ödül ise ajanın öğrenmediğini gösterecektir. Dolayısıyla eğitimin başlangıcında ortalama ödülün negatif olması ajanın henüz çok iyi öğrenmediğini göstermekle birlikte, öğrenmenin biraz zaman alacağını da ifade etmektedir. Aircraft_01_AircraftLearning parametresi ile eğitilen modelin daha hızlı öğrense de daha düşük kayıplar elde ettiği Anaconda üzerinden gözlemlenebilmektedir. Ne var ki Aircraft_02_AircraftLearning ve Aircraft_03_AircraftLearning parametreleri ile eğitimin ilerlemesini daha sağlıklı izleyebilmek için TensorBoard aracının kullanılması gerekecektir. TensorBoard aracı, makine öğrenimi modelinin performansını izlemek için kullanılan bir görselleştirme aracı olarak eğitim bulgularının değerlendirilmesinde büyük fayda sağlamaktadır.

3. BULGULAR

Eğitim ilerlemesini daha sağlıklı izlemek için TensorBoard aracından yararlanılmıştır. TensorBoard aracı, makine öğrenimi modelinin performansını izlemek için kullanılan bir görselleştirme aracı olarak eğitim bulgularının değerlendirilmesinde büyük fayda sağlamaktadır. Böylece eğitilen uçak ajanlarının, derin pekiştirmeli öğrenme ile eğitildiği modelin performansları daha doğru analiz edilebilecektir. Dolayısıyla çalışmadaki kayıp ve doğruluk metriklerine bakarak, modelin performansı hakkında detaylı sonuçlar elde edilebilmektedir. Analizi yapılacak grafiklerde eğitim verileri ve doğrulama verileri olmak üzere iki tür veri bulunmaktadır. Dolayısıyla eğitim verileri, modelin öğrenme sırasında kullandığı verilerdir. Bu veriler, modelin ödül ve ceza mekanizması ile öğrenmesini sağlamaktadır. Böylece model, eğitim verilerinden gelen geri bildirimlere göre ağırlıklarını günceller. Doğrulama verileri ise modelin öğrendiklerini test etmek için kullandığı verilerdir. Bu veriler modelin yeni veya görmediği durumlara nasıl tepki verdiğini ölçmektedir.

Burada model, ağırlıklarını, doğrulama verilerinden gelen geri bildirimlere göre güncellemez. Curriculum Reward grafiğinde ise modelin her görevde ne kadar ödül aldığı gösterilmektedir. Bu modelde eğitilen uçak ajanı daha zor görevlerde daha fazla ödül aldığından, uçak ajanı daha zor görevlere teşvik edilmektedir.



Şekil 12. TensorBoard arayüzünde uçak ajan modellerinin görüntülenmesi.

Kayıp grafikleri (Episode Length), modelin eğitim verileri üzerinde düşük kayıp elde ettiğini, ancak doğrulama verileri üzerinde yüksek kayıp elde ettiğini göstermektedir. Yatay eksen, modelin eğitildiği eğitim örnekleri sayısını göstermektedir. Dikey eksen ise modelin kaybını göstermektedir. Modelin kaybı, modelin eğitim örneklerini doğru sınıflandırmak için yaptığı hata miktarını ölçer. Grafikteki değerler ise modelin kaybının zaman içindeki değişimini göstermektedir. Grafikte görüldüğü üzere modelin kaybı zamanla azalmaktadır, bu da modelin daha doğru hale geldiği anlamına gelmektedir. Bu durum modelin aşırı uyum eğilimi olduğunu göstermektedir. Aşırı uyum, modelin sadece eğitim verilerine uyum sağladığı ancak yeni verilere genelleştiremediği bir durumdur.

Doğruluk grafikleri (Lesson), modelin eğitim verileri üzerinde yüksek doğruluk elde ettiğini, ancak doğrulama verileri üzerinde düşük doğruluk elde ettiğini göstermektedir. Bu da modelin aşırı uyum eğilimi olduğunu göstermektedir. Diğer yandan yatay eksen modelin eğitildiği eğitim örnekleri sayısını gösterirken dikey eksen ise modelin doğruluğunu göstermektedir. Modelin doğruluğu, modelin eğitim örneklerini doğru sınıflandırma yüzdesini ölçer. Dolayısıyla grafikteki değerler modelin doğruluğunun zaman içindeki değişimini göstermektedir. Bu doğrultuda modelin doğruluğunun zamanla arttığı gözlemlenmektedir.

Uçak ajanı kontrol noktalarından geçişini 4 ödül eşliğini de aşarak tamamladığında, eğitildiği modelin veri kümesindeki tüm eşik değerlerini (Thresholds) görmüş olacağından mükemmel performans ile değerlendirilmektedir. Böylelikle sinir ağının eğitimi başarıyla tamamladığı kabul edilerek, eğitim durdurulmuş ve model kaydedilmiştir. Eğitilen modeller NNModels klasörüne kaydedildikten sonra, davranış parametrelerindeki model dosyasından seçilebilmektedir. Böylelikle eğitilen modeller, Unity3D ortamına aktarılarak sinir ağı tarafından kontrol edilen uçak ajanları farklı modları ile gözlemlenebilmektedirler.

Uçak ajanlarının Aircraft_02_AircraftLearning parametresi olarak adlandırıldığı model NNModels klasörüne “AircraftLearning_Hard.nn” olarak kaydedilmiştir. Bunun nedeni uçak ajanlarının uçmayı yüksek düzeyde öğrenmiş olmasıdır. Aircraft_02_AircraftLearning parametresinde model daha yavaş öğrenmekle birlikte, daha yüksek oranda kayıplar elde etmektedir. Diğer yandan bu parametre ile model çok az dalgalanma göstermekte ve doğrulama verileri üzerinde daha iyi performanslar elde etmektedir. Buradan da uçak ajanının daha yavaş veya daha dikkatli bir şekilde hareket etmesini sağlayan bir modele sahip olduğu sonucu çıkmaktadır. Ne var ki bu durumda bir oynanan karakterin yapay sinir ağı tarafından kontrol edilen bu türde uçak ajanlarla rekabet etmesi neredeyse olanaksız olacaktır. Bu durumda yapay sinir ağının eğitimini erken durdurmak, simülasyonu oynanan karakter lehine daha dengeli bir hale getirebilir. Bu işlem simülasyonun farklı zorluk seviyelerinde dengelenmesi anlamına gelmektedir. Bunun için eğitim erken durdurularak yapay sinir ağının farklı bir dosyası olarak yeniden oluşturulmuştur. Bu durum orta seviyede eğitilen uçak ajanlarının Aircraft_03_AircraftLearning parametresi olarak NNModels klasörüne “AircraftLearning_Normal.nn” dosyası şeklinde kaydedilmiştir. Burada ise modelin orta seviyede öğrendiği ve kayıp değerlerinin diğerlerine göre daha dengeli olduğu gözlemlenmektedir. Buradan uçak ajanlarının daha dengeli veya daha ortalama bir şekilde hareket etmesini sağlayan bir modele sahip olduğu sonucu çıkmaktadır. Bu işlem ile simülasyonun farklı zorluk seviyelerinde dengelenebileceği anlaşılmıştır. Böylece biri kolay diğeri zor olmak üzere iki farklı yapay sinir ağı eğitilmiştir.

4. SONUÇ

Derin pekiştirmeli öğrenme yaklaşımı, dijital oyun tasarımında ajanların davranışlarını geliştirmek ve oyunların zorluk seviyesini ayarlamak için kullanılmaktadır. Dolayısıyla bir ajanı hedefleri yok etmeye, görevleri tamamlamaya veya belirli öğeleri toplamaya teşvik etmek için pekiştirmeli öğrenme yönteminden yararlanılmaktadır [11].

Bu çalışmada 1500 deneme sonrası uçakların ortalama parkur tamamlama süresi 1 dakika 55 saniye iken, 2100 deneme sonunda bu değer ortalama 1 dakika 35 saniyeye düşmüştür. Sonuç olarak yapay sinir ağları değiştirildiğinde, uçak ajanlarının performansının da değiştiği gözlemlenmiştir. Oyun geliştirme ortamında pekiştirmeli öğrenmenin en yaygın kullanım alanı NPC'lerin davranışlarını geliştirmek ve oyunların zorluk seviyelerini ayarlamaktır. Oyun geliştiricileri ajanların ne kadar hızlı öğrendiğini ve ödüllendirildiğini kontrol ederek, bu durumu ortamın zorluk seviyesinin ayarlamakta kullanmaktadır. Eğitilen sinir ağlarının platformlar arası bir oyuna entegre edilmesi, game logic ve game balance gibi kavramlar neticesinde olmaktadır. Game logic, oyunun nasıl çalıştığını, oyuncunun oyun dünyasıyla nasıl etkileşime girdiğini ve oyunun kurallarını tanımlayan bir terimdir. Game balance ise oyunun zorluk ve adalet seviyesini ayarlayarak oyunu daha eğlenceli ve tatmin edici hale getirmeyi amaçlayan bir süreçtir. Oyun mekaniği, hedefler, kazanma-kaybetme koşulları, geri bildirim döngüleri gibi unsurlar game logic kapsamında değerlendirilmektedir. Game balance ise ödüller, zorluklar, oyun öğeleri, ekonomi gibi faktörleri içerir. Dolayısıyla game logic, oyunun ne olduğunu anlatırken, game balance, oyunun nasıl olduğu ile ilgilenmektedir. Game logic oyunun temelini oluştururken, game balance oyunun daha eğlenceli hale gelmesini sağlar. (<https://en.wikipedia.org>, “Game Balance”). Simülasyon ortamında geliştirilen yapay zeka uygulamaları oyun karmaşıklığının dengelenmesi kadar, bazı robotik simülasyon ve otonom uçuş gibi gerçek yaşam problemlerinin çözümünde de kullanılmaktadır [12]. Bu doğrultuda otonom uçuş ve otopilot sistemlerindeki güncel geliştirme çabalarına dikkat çekmek gerekir. Otonom uçuş, uçağın pilot veya insan müdahalesi olmadan kendi kendine uçabilmesi anlamına gelmektedir. Dolayısıyla otonom uçuş sistemleri, uçağın sensör verilerini işleyen, rotasını tahmin edebilen ve gerektiğinde uçağa müdahale edebilen dinamik yapıda sistemlerdir. Örneğin Airbus şirketinin uzunca bir süredir otonom uçuş teknolojilerini test ettiği bilinmektedir.

Bu çalışmalarda uçakların, uçuş rotası, arazi ve hava koşulları gibi dış faktörler analiz edilerek yeni rotalar oluşturulması ve bu bilgilerin hava trafik kontrol birimlerine iletebilmesi testten geçirilmektedir. Diğer yandan otopilot sistemleri ise otonom uçuş sistemlerinden farklı olarak bir uçağı pilot gözetiminde yöneten görece statik sistemlerdir. Otopilot sistemi sensörler, bilgisayar görüşü algoritmaları ve yapay zeka teknikleri kullanarak uçağın rotasını, hızını, yüksekliğini ve diğer parametrelerini kontrol etmekte kullanılmaktadır. Airbus şirketinin geliştirdiğini açıkladığı DragonFly adlı pilot asistanı ise yapılan testlerde A350 uçağı pilotunun

görevini yapamadığı acil durumlarda uçağın kontrolünü başarıyla ele alabilmiştir. (<https://www.airbus.com>, “Could The Humble Dragonfly Help Pilots During Flight” 07.12.2023).

Bununla birlikte yeni nesil uçuş kontrol yazılımlarının, yakın gelecekte, ana akım uçuş kontrol mimarileri tarafından da benimsenebileceği tartışılmaktadır. Örneğin Neuroflight Controller çalışması hem çok rotorlu hem sabit kanatlı uçakları uzaktan kontrol edebilen ilk açık kaynaklı uçuş kontrol yazılımı olmuştur. Bu dünyanın ilk sinir ağı destekli uçuş kontrol yazılımında denetleyicileri geliştirmek için temelde robotik kontrolörleri bir nöral ağ ile eğitmek için tasarlanmış olan Gymfc aracından yararlanılmıştır. Neuroflight Controller bu özelliği uçuş kontrolleri için geliştirilmiş bir yazılıma dönüştürürken, aynı zamanda simülasyondan gerçeğe geçerken karşılaşılabilecek zorluklara karşın en iyi uçuş performansını araştırır. (<https://arxiv.org>, “Attitude Control for Fixed-Wing Aircraft Using Q-Learning” 07.12.2023). Havacılık şirketi Boeing ise bir sonraki yeni nesil uçağı için sanal üç boyutlu dijital ikiz kopyalarını ve simülasyonları çalıştırabilen bir üretim sistemi üzerinde çalıştığını açıklamıştır. (<https://www.aviationtoday.com>, “Boeing CEO Talks ‘Digital Twin’ Era of Aviation” 07.12.2023).

Sonuç olarak bazı geliştiriciler simülasyon ajanlarını eğitmek için Unity3D içindeki ML Agents benzeri kütüphanelerden yararlanarak ajanlarını kolayca eğitebilmektedirler. Bu durum oyun motorlarında oluşturulan gerçekçi simülasyon ortamlarındaki algoritmaların daha basit arayüzlere sahip olması sebebi ile eğitim amaçlı çalışmalara da büyük katkı sağlamaktadır.

Teşekkürler

Yazarlar tarafından herhangi bir Teşekkürler beyan edilmemiştir.

Çıkar çatışması

Yazarlar tarafından herhangi bir çıkar çatışması beyan edilmemiştir.

Yazar katkıları

Mete CANTEKİN, uçak ajanı ve çevre bileşenlerine yönelik model klasörlerinin oluşturulması ve eğitim dosyalarının oluşturulması kısımlarına katkı sağlamıştır. Onur OSMAN, derin pekiştirmeli öğrenme uygulamalarının incelenmesi ve araştırma bulgularının değerlendirilmesi kısımlarına katkı sağlamıştır. İbrahim Furkan İNCE, oyun motoru ortamında oluşturulan temel yapay zekâ içeriklerinin incelenmesi ve araştırma bulgularının değerlendirilmesi kısımlarına katkı sağlamıştır.

REFERANSLAR

- [1] Millington I. *AI for Games*. CRC Press, 2019.
- [2] Mnih V, Kavukcuoglu K. Human-level control through deep reinforcement learning. *Nature*, 518(7540):529–533, 2015.
- [3] Cuccu G, Gomez F. Evolving largescale neural networks for vision-based reinforcement learning. In *Proceedings of the 15th Annual Conference on Genetic and Evolutionary Computation*, pages 1061–1068. ACM, 2013.
- [4] Yannakakis G, Togelius J. *Artificial Intelligence and Games*, Springer International Publishing, ISBN: 978-3-319-63518-7, 119, 2018.
- [5] Hawkins B. *Real-Time Cinematography for Games (Game Development Series)*. Charles River Media, Inc., 2004.
- [6] Monfort M, Johnson M, Oliva A, Hofmann K. Asynchronous data aggregation for training end to end visual control networks. *Proceedings of the 16th Conference on Autonomous Agents and Multi-Agent Systems*, pages 530–537. Springer, 2017.
- [7] Wolpert D, Macready W. No free lunch theorems for optimization. *IEEE Transactions on Evolutionary Computation*, 1(1), 1997.
- [8] Gaina R, Liu J. Analysis of vanilla rolling horizon evolution parameters in general video game playing. *European Conference on the Applications of Evolutionary Computation*, pages 418–434. Springer, 2017.
- [9] Koutnik J, Cuccu G. Evolving largescale neural networks for vision-based reinforcement learning. In *Proceedings of the 15th Annual Conference on Genetic and Evolutionary Computation*, pages 1061–1068. ACM, 2013.
- [10] Chaplot D, Lample G. Arnold: An autonomous agent to play FPS games. In *Thirty-First AAAI Conference on Artificial Intelligence*, 2017.
- [11] Udagawa H, Narasimhan T, Lee S. *Fighting Zombies in Minecraft With Deep Reinforcement Learning*. Technical Report, Stanford University, 2016.
- [12] Polceanu M. Mirrorbot: Using human-inspired mirroring behavior to pass a Turing test. In *Computational Intelligence in Games (CIG)*, 2013 IEEE Conference on. IEEE, 2013.



CHAPTER 9

Aviation Technologies and Applications
E-ISBN:978-605-338-471-7
2025, chap. (9) , pp.150-166.

INVESTIGATION OF THE HUMAN FACTOR IN SEARCH AND RESCUE OPERATIONS: SHELL MODEL ANALYSIS

Mehmet Burçin COŞKUN¹, Rüstem Barış YEŞİLAY^{2,*}

ABSTRACT

The human factor has played a significant role in the development process of the aviation sector up to the present day. In addition to setting standards, human decision-making has been a central authority in addressing all aspects related to transportation operations, ground services, as well as flight safety and security.

In this thesis study, the main objective of the SHELL model analysis is to examine the interactions between flight crew and leadership personnel with other modules and to identify the possibilities of errors between the modules. Eliminating identified errors or reducing their probabilities is assessed to contribute to flight and ground safety for flight crews and maintenance personnel involved in helicopter search and rescue missions. Additionally, the aim is to evaluate the data obtained from the SHELL model analysis to elevate the awareness level of personnel in CRM (Crew Resource Management) and aviation safety topics, and to prevent possible accidents or incidents.

A total of 25 accident factors have been identified in the designed SHELL model. In determining these accident factors, errors that could jeopardize flight safety and are likely to be encountered during flights have been identified, and their probabilities of occurrence and error impact assessment scores have been examined. The probabilities of occurrence of accident factors are sorted by sortie, and the error impact assessment scores are determined according to the priority order within the module. In the table examining the probabilities of occurrence of errors affecting flight safety, the probabilities of occurrence of accident factors that may be encountered during flight are provided on a sortie basis. This table has been created using the Helicopter Sortie Tracking database, and the probabilities of occurrence of accident factors identified based on all flights between 2012 and 2022 have been determined. The table examining the error impact assessments consists of data obtained from face-to-face interviews with 10 PIC (Pilot In Command) certified pilots who have flown between 1400 and 2500 hours. In these interviews, pilots were asked to assign a value between 1 (very low impact) and 10 (very high impact) to satellite modules and accident factors identified within the central module in the SHELL model analysis, and the average of the evaluations was taken to determine the error impact score.

The percentages of accident factors and the percentages of the modules within the SHELL model have been calculated by multiplying the probabilities of occurrence with the error impact assessment scores, and the total value of a single accident factor has been compared to the total value of all accident factors within the module to determine the percentage values within that module. In calculating the percentages of the modules within the SHELL model, the values obtained from accident factors within a module have been summed to determine the total value of that module, and the percentages have been created by comparing the total value of all modules.

*Corresponding Author: rustem.baris.yesilay@ege.edu.tr

1 0000-0003-0191-8422, Occupational Health and Safety, Ege University, İzmir, Türkiye

2 0000-0002-0830-8224, Aviation Higher Vocational School, Department of Transportation Services, Ege University, İzmir, Türkiye

Utilizing the tables of accident factors affecting flight safety and the assessment scores of accident factors, the highest accident factor impact percentages have been determined. Among the satellite modules, the highest impact percentage of 34% has been observed in the Liveware module. It has been found that the Liveware module, which is the central module, has an error impact percentage of 20%. The other modules have been determined as follows: Environment (18%), Software (15%), and Hardware (13%).

The results of this study emphasize the impact of the human factor on safety and security performance in the aviation sector. Considering the complexity of the aviation sector, the interaction, skills, and decision mechanisms of individuals are crucial for ensuring flight safety. The research findings demonstrate that the potential risks on the interactions of flight crew and leadership personnel identified by using the SHELL model. This study contributes to the development of strategies for aviation safety by examining the probabilities of occurrence and impact assessment scores of accident factors in detail. The data obtained indicates that the highest-risk areas affecting flight safety are within the Human (Liveware) module. This highlights the importance of CRM training and development programs focusing on the human factor.

In conclusion, this study addresses the contribution of the human factor to safety performance in the aviation sector and examines accident factors affecting flight safety using the SHELL model. The results obtained guide the determination and improvement of strategies for flight safety and security. Effectively managing the human factor is a critical step to enhance the reliability and success of the aviation sector.

Keywords: SHELL, search and rescue, human factors, aviation, helicopter

1. INTRODUCTION

The term "human factor" pertains to a professional discipline concerned with human-machine interactions, emphasizing the psycho-physical aspects influencing decision-making and information processing. Additionally, it encompasses factors like equipment, the physical environment, tasks, and the individuals executing the work [12] and given the inherent fallibility of humans, it's unsurprising that human error plays a prominent role in numerous occupational accidents, notably in civil and military aviation where it's implicated in 70% to 80% of cases [11].

The SHELL Model (Software, Hardware, Environment, Liveware, Liveware) is a performance model created by Elwyn Edwards and later developed by Frank Hawkins with the purpose of analytically explaining human factors in aviation [1]. In connection with safety performance, one of the models created to support the assessment of human factors is the SHELL model. Designed to reveal the impact and interaction of various system and environmental elements on individuals, the SHELL model emphasizes the importance of considering it as a well-known, useful model, integrated into the broader framework of Human Factors in Safety Risk Management (SRM) [2].

2.INTERACTIONS BETWEEN THE COMPONENTS OF THE SHELL MODEL

The SHELL model illustrates the connections between individuals and other components within a system, offering a framework for enhancing the interaction between people and their tasks within the aviation system. Given that any element surrounding Liveware (humans) can directly impact aircraft operations, it's crucial to maintain optimal levels of interaction and interface among these components to uphold efficiency and ensure safety [10]. In a model where individuals taking on leadership or managerial roles in a specific organization are considered the focal point, they are the most sensitive among all satellite modules to the least predictable personal factors (fatigue, alertness, motivation, etc.) and the least predictable environmental factors (temperature, light, noise, etc.). Despite their ability to adapt to changing conditions, their performance exhibits significant variability. Individuals cannot be standardized to the same extent as equipment; therefore, the extremes of this structure are neither simple nor straightforward. In this model, whether the extremes of the structure match or not is as crucial as the inherent characteristics of the structure itself. The lack of alignment may pose a potential source of human error [3].

To achieve a better understanding of human factors, it is necessary to adopt a gradual approach with the assistance of the "SHELL" theoretical model. The Figure 1 illustrates this model using squares representing different elements of human factors. The model's name is derived from the initials of its components: Software (procedures, symbols), Hardware (machines, aircraft), Environment (context in which the L-H-S system operates), and Liveware (the human). This model serves a purely didactic purpose and aims to facilitate a better comprehension of human factors [9].



Figure 1 : SHELL Model [2].

The interaction between the human and workplace components of the SHELL Model, centered around humans, is depicted in Figure 2. The SHELL Model consists of the following components [14]:

- Software: procedures, training, support, etc.
- Hardware: machines and equipment.
- Environment: the working environment that the L-H-S system's remainder needs to operate.
- Liveware: other individuals in the workplace [2].

2.1. Software

The software component of aviation incorporates non-physical, intangible elements that govern the operational structure of aviation and influence how system information is organized, presented, and conveyed to those operating within the system [4]. This component encompasses a wide range of elements, including but not limited to, the software controlling computer hardware operations [5]. It consists of rules, instructions, regulations, emergency procedures, policies, norms, checklists, laws, orders, safety procedures, standard operating procedures, customs, practices, conventions, habits, symbology, supervisor commands, and computer programs. Additionally, software extends to encompass documents such as the contents of charts, maps, publications, emergency operating manuals, training materials, and procedural checklists [6].

2.2. Hardware

Hardware comprises the tangible components of the aviation operational system, encompassing items like aircraft (including controls, surfaces, displays, functional systems, and seating), operator equipment, tools, materials, buildings, vehicles, computers, conveyor belts, and more [13]. In the context of this study, for example; equipment such as pilot night vision goggles, survival vests, pilot/operator helmets, etc. can be included in the hardware module. The hardware module has been identified as the module with the lowest impact percentage in this study, at 13%.

2.3. Environment

The environment in which aircraft and resources within the aviation operational system (software, hardware, liveware) operate is shaped by various factors, including physical, organizational, economic, regulatory, political, and social variables that influence the workers/operators [6]. The internal air transport environment pertains to the immediate work area and encompasses physical aspects such as cabin/cockpit temperature, air pressure, humidity, noise, vibration, and ambient light levels [7]. Meanwhile, the external air transport environment extends beyond the

immediate work area, encompassing factors like weather (visibility/turbulence), terrain, congested airspace, and physical infrastructure, including airports. Additionally, it includes organizational, economic, regulatory, political, and social elements [15].

2.4. Liveware

The Liveware component within the SHELL model comprises individuals involved in the aviation system, encompassing flight crews, cabin personnel, ground crew, schedulers, dispatchers, maintenance workers, as well as management and administration personnel. This component takes into account the cognitive and physical performance, capabilities, and limitations of the users [7]. The highest impact percentage in this study, at 34%, was found in the satellite liveware module. Following it is the central liveware module with a percentage of 20. The fact that the impact percentages of these two modules together account for 54% underscores the significant role of the human factor in aviation.

3.SHELL MODEL INTERFACES

The SHELL model delineates the connections between individuals and other elements of a system, offering a framework for enhancing the interaction between people and their tasks within the aviation system, which is paramount to human factors. Notably, the International Civil Aviation Organization has defined human factors as encompassing individuals in their everyday living and working contexts, their engagements with machinery (hardware), procedures (software), and the surrounding environment, as well as their interpersonal relationships[16]. As per the SHELL model, a discrepancy occurring at the interface of blocks/components, where energy and information exchange takes place, can serve as a potential cause of human error or system vulnerability, ultimately resulting in system failure in the form of an incident or accident [17]. Aviation disasters often exhibit mismatches at the interfaces between system components, rather than catastrophic failures of individual components [6].

3.1. Liveware - Software (L-S) interaction

The interaction between human operators and intangible support systems within the work environment [17]. Involves tailoring software to align with the typical traits of human users and ensuring that the software, such as rules and procedures, can be easily implemented [4]. During training, flight crew members internalize a significant portion of the software, such as procedural details, related to flying and handling emergency scenarios, converting them into memory in the form of knowledge and skills.

However, additional information is acquired through the consultation of manuals, checklists, maps, and charts. While these documents are considered hardware in a physical sense, in terms of information design, meticulous attention must be given to various aspects of the liveware-software interface [6].

3.2. Liveware - Hardware (L-H) interaction

Interaction between human operator and machinery. This relationship involves aligning the physical attributes of the aircraft, cockpit, or equipment with the typical traits of human users, taking into account the specific task or role to be fulfilled [4]. Mismatches at the interface between humans and machines can arise due to various factors, such as inadequately designed equipment, inappropriate or lacking operational materials, poorly situated or coded instruments and control devices, malfunctioning warning systems, and insufficient informational or guidance functions during abnormal situations[18].

3.3. Liveware - Environment (L-E) interaction

The Liveware-Environment (L-E) relationship focuses on the interaction between humans and environmental factors. It encompasses aspects such as temperature, ambient light, noise, vibration, and air quality. It also takes into account external environmental factors like weather, infrastructure, and region [2]. In aviation, this interaction involves aircraft equipment and cockpit-cabin design. In addition to topics such as aircraft equipment and cockpit-cabin design, it also includes correctable errors caused by environmental factors such as illusions [4].

3.4. Liveware - Liveware (L-L) interaction

The interaction between the central human operator and any other individual within the aviation system during task execution [15]. Interactions among humans or groups can significantly impact behavior and performance, shaping the development and adherence to behavioral norms. As such, the human-human or group interface focuses predominantly on interpersonal relations, leadership dynamics, crew collaboration, coordination, communication, social interaction dynamics, teamwork, cultural exchanges, as well as personality and attitude interactions [4][17].

Considering this, the recognition of factors that may contribute to accidents and the understanding of the human role in accidents underscore the necessity for risk analysis. Consequently, specific risk analysis methodologies have been developed for the aviation sector. Among them,

the SHELL model analysis stands out as one of the most widely employed methodologies. It has been crafted to enhance the assessment of human factors concerning safety performance and to discern the influence and interplay of environmental factors and systems on individuals.

The main objective of the SHELL model analysis used in this study is to address the interactions between the flight crew and leading personnel with other modules and to identify the possibilities of errors among the modules. Additionally, the evaluation of the data obtained from the SHELL model analysis aims to raise the awareness level of the personnel in CRM and aviation safety, ultimately preventing possible accidents or incidents from occurring.

Understanding the effects of mismatches in interfaces between various SHELL structures and the central Liveware structure is crucial to preventing risks that could negatively impact human performance and expose aircraft to hazardous situations. The sharp edges in the modules represent inappropriate matches between each module. This understanding can visually aid in identifying the following interfaces among various elements in the aviation sector:

- Liveware and Software (L-S)
- Liveware and Hardware (L-H)
- Liveware and Environment (L-E)
- Liveware and Liveware (L-L)

Comprehending mismatches in these interfaces is critical for making appropriate corrections and enhancing the safety of the system. This effort can contribute to the more effective management of human factors in the aviation industry and improve aviation safety.

4. METHODS

In the SHELL model examination in this study, a SHELL model template was created by taking search and rescue missions performed by air units as an example. The central and satellite modules and their contents were determined based on helicopter search and rescue operations.

In the designed SHELL model, 25 accident factors have been identified. In determining these accident factors, errors that could jeopardize flight safety and are most likely to occur during flight have been identified. The probabilities of occurrence and error impact assessment scores have been examined. The probabilities of occurrence of these accident factors are determined sortie by sortie, while the error impact assessment scores are determined according to the priority sequence within the module.

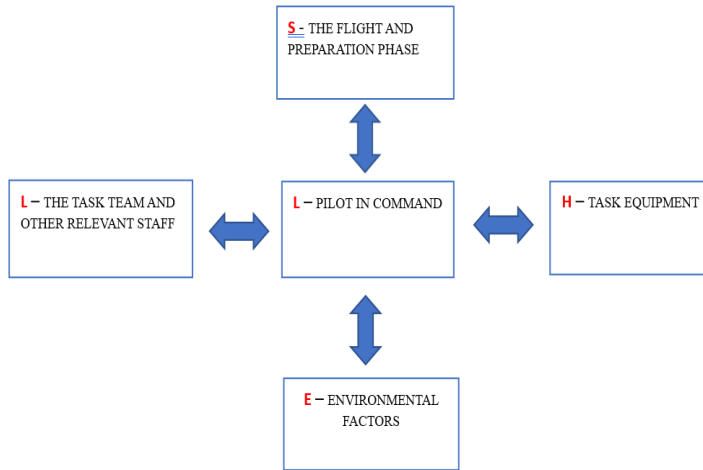


Figure 2 : The main themes of the SHELL model plan and satellite modules

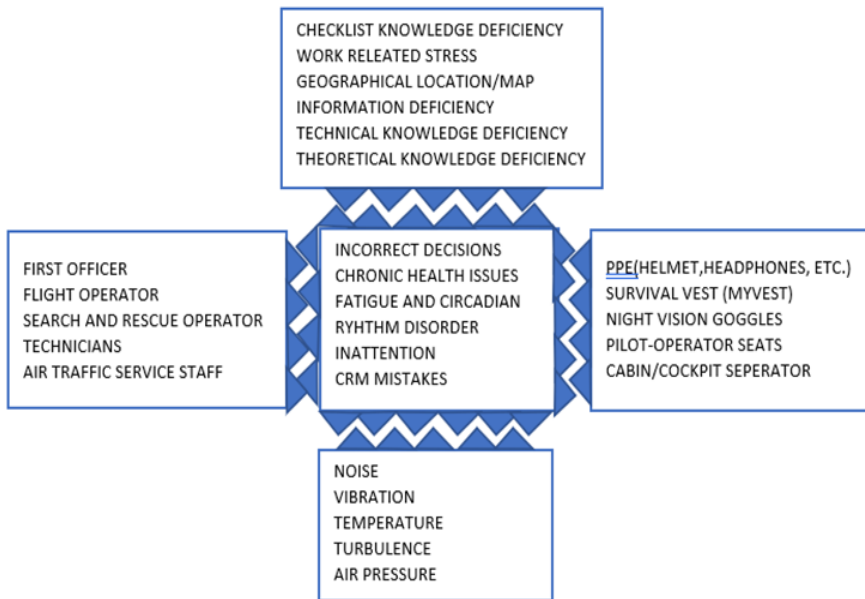


Figure 3 : Accident factors within satellite modules

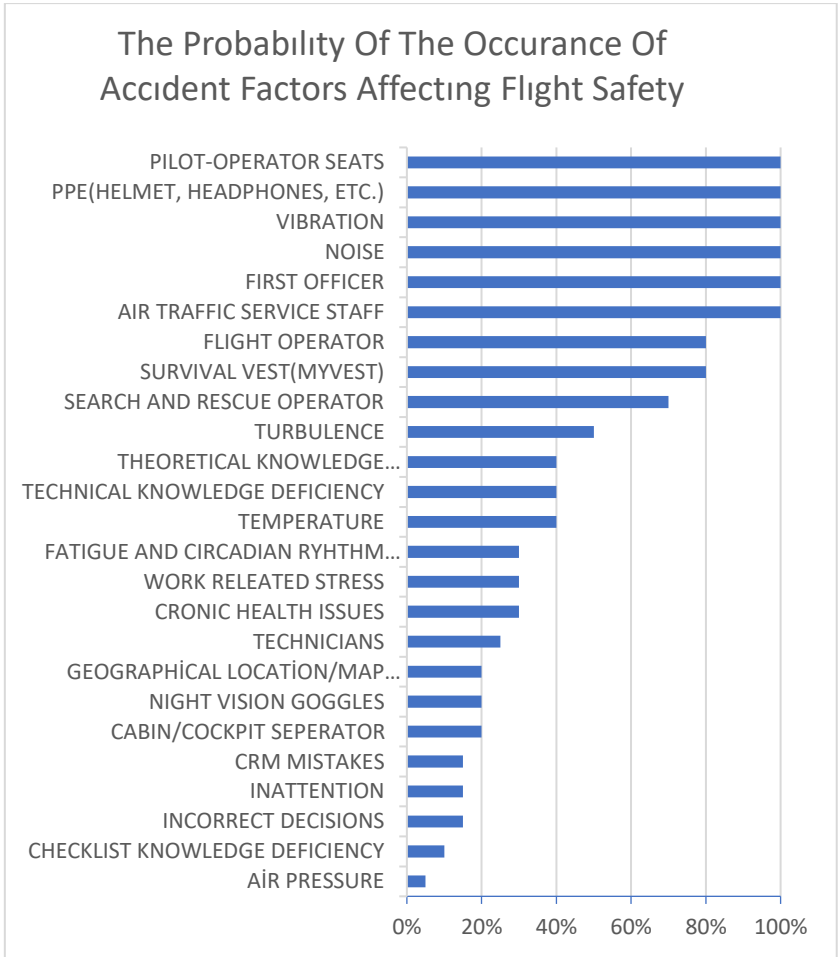


Figure 4 : The probability of the occurrence of accident factor affecting flight safety

The table examining the probabilities of occurrence of accident factor affecting flight safety provides sortie-based probabilities for potential accident factors that may be encountered during flights. According to the table, a high probability of occurrence for an accident factor in a sortie may correspond to a lower impact assessment score within the module. For example, while the accident factor "Pilot-Operator Seat" is encountered in all flights, the accident factor "Night Vision Goggles" is specific to night flights. However, considering the physiological strains arising from the ergonomics of the "Pilot-Operator Seat" and its transmission of platform vibrations, it may have a lower error impact assessment score in terms of

causing accidents. On the other hand, "Night Vision Goggles" can pose challenges to personnel both physiologically and psychologically, especially in terms of weight, position, and potential visual perceptual errors during flights over the sea. Therefore, it may have a higher error impact assessment score when considering its potential contribution to accidents.

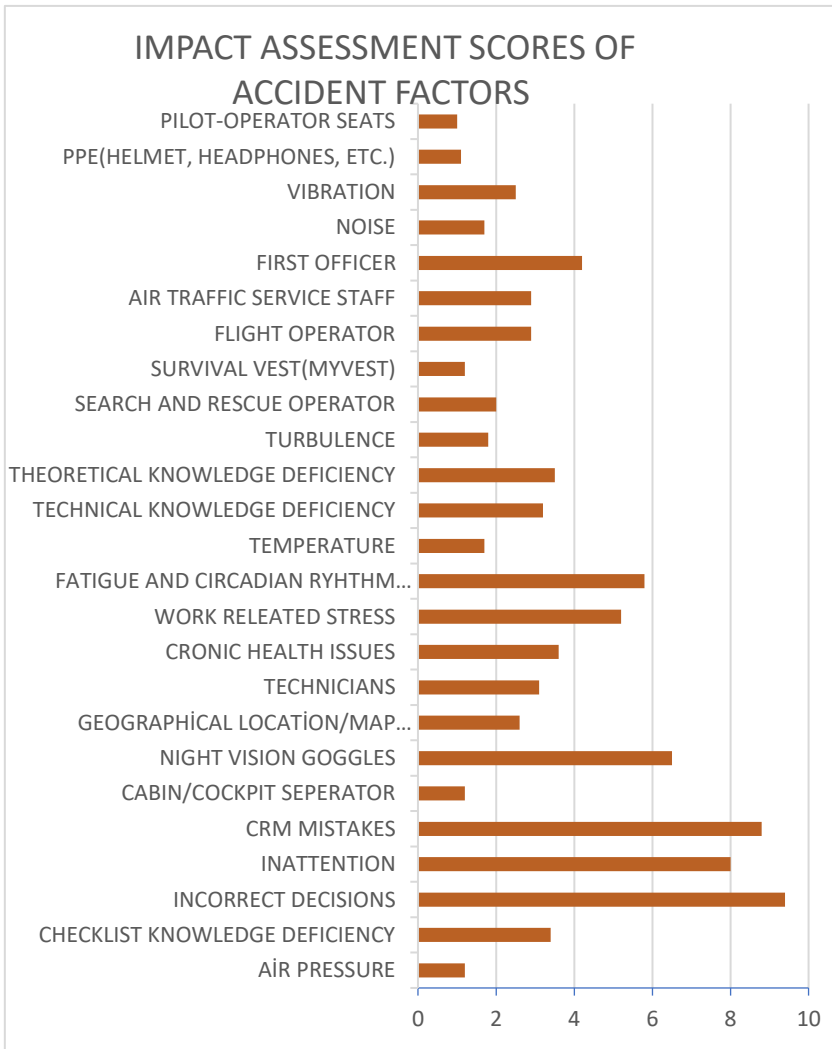


Figure 5 : Impact assessment scores of accident factors

When examining the impact assessments of accident factors (Figure 7), the data is derived from face-to-face interviews with 10 PICs (Pilots in

Command) with flight hours ranging from 1400 to 2500. In these interviews, pilots were asked to assign a value between 1 (very low impact) and 10 (very high impact) to the accident factors determined in the satellite modules and central module of the SHELL model analysis. The average of these assessments was calculated to determine the impact score of each accident factor.

To calculate the impact percentages of accident factors and modules within the SHELL model, the probabilities of occurrence were multiplied by the impact assessment scores. The total value for each accident factor was then determined by dividing it by the sum of all values for the accident factors within the module, resulting in the percentage value within that module. For calculating the impact percentages of modules within the SHELL model, the values assigned to accident factors within a module were summed to determine the total value for that module. This total value was then divided by the sum of all values across all modules to establish the percentage impact within that specific module.

5. FINDINGS

The highest impact percentages of accident factors affecting flight safety were determined by utilizing the tables of the probabilities of occurrence and the impact assessment scores of accident factors created for the analysis. The highest impact percentage, at 34%, was observed in the Human (Liveware) module among the satellite modules. The central module, which is the Human (Liveware) module, was found to have an error impact percentage of 20%. The other modules were determined as follows: 18% for Environment module, 15% for Software module, and 13% for Hardware module.

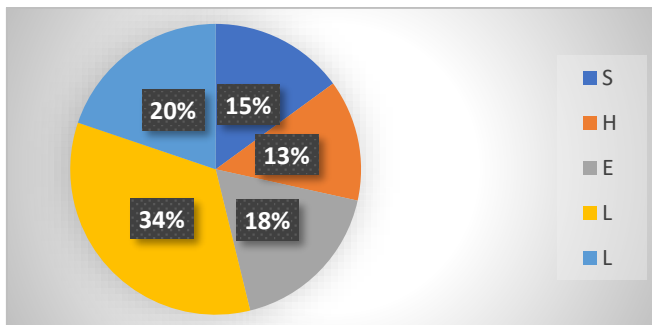


Figure 6 : SHELL Model Error Classification

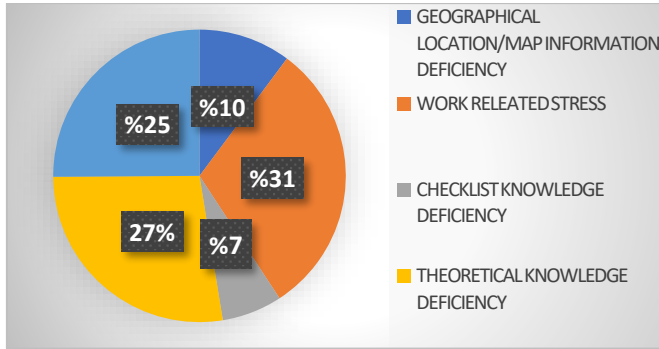


Figure 7 : S – The Flight and Preparation Phase

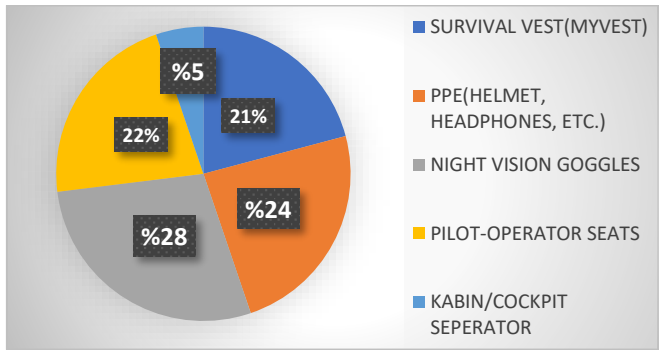


Figure 8 : H – Task Equipment

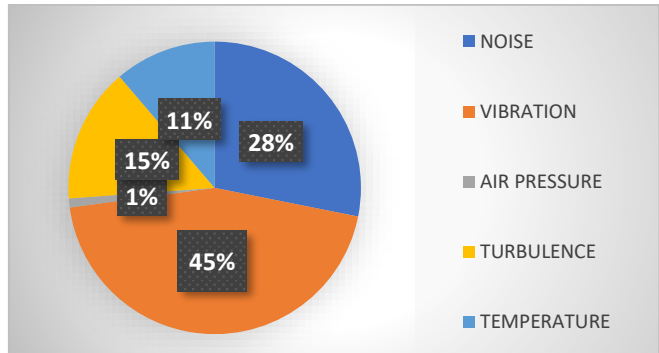


Figure 9 : E – Environmental Factors

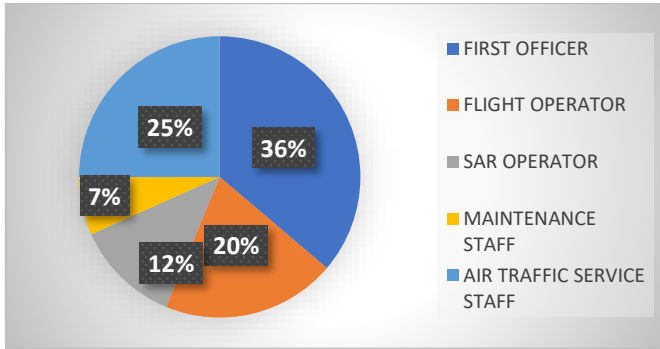


Figure 10 : L – The Task Team and Other Relevant Staff

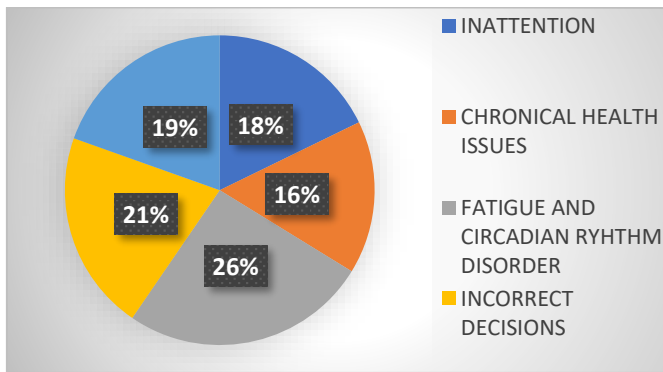


Figure 11 : L – Pilot in Command

6. CONCLUSION

To the best of our knowledge, there are a limited number of publications in academic literature that examine aviation and the SHELL model. Nevertheless, in conclusion, we would like to mention the general features of three studies that can be seen as closer to the content of our study.

In their study Wong and Tong [19] by using A-SHELL Model (Airworthiness-Software-Hardware-Environment-Liveware) tried to understand better of how human factors and errors in aviation maintenance may contribute to an aircraft accident or incident. Their goal was to improve compliance with airworthiness standards, which will raise aviation safety levels. They discussed the impact of human factors on airworthiness compliance in airplane maintenance, and a case study was used to illustrate how the A-SHELL model is applied.

In their study Perboli and others [20] argued that currently there are no established technical standards for automated human factors identification because the existing standard depends on the manual classification carried out by skilled personnel. They examined this problem and suggested machine learning methods by utilizing cutting-edge natural language processing technologies. After that, the methods are modified to fit the standard accident causality model of the Software Hardware Environment Liveware (SHEL) and evaluated on a series of actual incidents. The computational outcomes demonstrate the precision and potency of the suggested approach. Moreover, the implementation of the methodology on actual documents examined by specialists predicts a minimum 30% decrease in time required in comparison to the conventional approaches for human factors detection.

An airport-based study [21] identified the threats that pilots face when flying into airports. The SHEL model was used to create an airport hazard index system that included 14 hazard indices. Lastly, a case study was completed. In the case study, the established hazard index system was used to analyze the airport hazards. The SHEL model was then used to identify 24 hazard elements of the airport under study, including 3 liveware-liveware elements, 13 liveware-software elements, 3 liveware-hardware elements, and 5 liveware-environment elements. As a result, some preventive measures were proposed according to the identified hazard elements for the reference of airports and airlines, aiming to improve their hazard control level.

This study emphasizes the impact of the human factor on safety performance in the aviation sector by taking into consideration the impact assessments of accident factors (Figure 7) and, the data is derived from face-to-face interviews with 10 PICs (Pilots in Command) with flight hours ranging from 1400 to 2500. Considering the complexity of the aviation industry, the interaction, capabilities, and decision mechanisms of individuals play a crucial role in ensuring flight safety. The research results demonstrate that the identified accident factors using the SHELL model highlight potential risks on the interactions of the flight crew and leading personnel.

By thoroughly examining the probabilities of occurrence and impact assessment scores of accident factors, this study contributes to the development of strategies for aviation safety. The data obtained indicates that the highest-risk areas affecting flight safety are within the Human (Liveware) module. This underscores the importance of CRM training and development programs focusing on the human factor.

In conclusion, this study addresses the contribution of the human factor to safety performance in the aviation sector and examines accident factors affecting flight safety using the SHELL model. The results guide the determination and improvement of strategies for flight safety. Effectively managing the human factor is a critical step in enhancing the reliability and success of the aviation industry.

As researchers in the field of aviation safety, it is imperative to recognize the pivotal role of the human factor in shaping safety performance within the aviation sector. The findings of this study underscore the necessity of prioritizing human factors considerations in the development and implementation of safety strategies. Specifically, the utilization of the SHELL model proves to be valuable in identifying potential risks associated with human-machine interactions and decision-making processes.

Moving forward, researchers should continue to delve into the intricacies of human factors within aviation, exploring new methodologies and frameworks for assessing and mitigating risks. Additionally, there is a pressing need for further investigation into the effectiveness of CRM (Crew Resource Management) training and development programs in enhancing flight safety.

Moreover, collaboration between researchers, industry stakeholders, and regulatory bodies is essential to ensure the translation of research findings into practical solutions and policies aimed at improving aviation safety standards. By prioritizing research efforts in this area and fostering interdisciplinary collaboration, researchers can contribute significantly to the advancement of safety practices within the aviation industry, ultimately enhancing the reliability and success of air transportation systems.

Acknowledgements

During this study, I extend my endless gratitude to my academic advisor, Prof. Dr. R. Barış YEŞİLAY, who continuously supported me academically, assisted me in every aspect, and elevated this work to a higher level with his valuable advice. I also thank my colleagues who dedicated their precious time to contribute to this study. Special thanks to my wife, Özge COŞKUN, and my son, Candemir COŞKUN, whose presence provided me strength, energy, and joy in life.

Conflict of interest

No conflict of interest was declared by the authors.

Author contributions

Prof. Dr. Rüstem Barış YEŞİLAY (Section 1 and Section 6 Writing and Research, All sections Review and Regulating). Mehmet Burçin COŞKUN (Section 1 - Section 6 Writing and Research)

REFERENCES

- [1] D.A. Wiegmann, S. A. Shappell, “A Human Error Approach to Aviation Accident Analysis”, The Human Factors Analysis and Classification System, University of Illinois at Urbana-Champaign, Civil Aerospace Medical Institute, Ash Gate e-book, 2003
- [2] ICAO, Doc 9859 Rev. 4
- [3] EHEST, Risk Assessment in Flight, HE5 Training Leaflet
- [4] Hawkins, F.H., & Orlady, H.W. (Ed.). (1993). Human factors in flight (2nd ed.). England: Avebury Technical, 1993.
- [5] Johnston, N., McDonald, N., & Fuller, R. (Eds). (2001). Aviation psychology in practice. England: Ashgate Publishing Ltd, 2001.
- [6] Wiener, E.L., & Nagel, D.C. (Eds). (1988). Human factors in aviation. California: Academic Press Inc, 1988.
- [7] Kiss, C. (2005). The Human Factors SHELL Model. *Academia Edu*, 80, 152-155.
- [8] Terzioğlu, M. (2007). Team Resource Management in Reducing Human Errors as the Cause of Airplane Accidents (Doctoral dissertation, DEU Institute of Social Sciences.
- [9] Dumitru, I. M., & Boşcoianu, M. (2015). Human factors contribution to aviation safety. *International Scientific Committee*, 49.
- [10] Lee, K. S. (2011). A Study on the Impact of Human Factors for the Students Pilot's in ATO-With Respect to Korea Aviation Act and ICAO Human Factors Training Manual. *The Korean Journal of Air & Space Law and Policy*, 26(2), 149-179.

- [11] Wiegmann, D. A., & Shappell, S. A. (2001). A human error analysis of commercial aviation accidents using the human factors analysis and classification system (HFACS).
- [12] Kałużna, E., & Fellner, A. (2014). Metody uwzględnienia czynnika ludzkiego w zarządzaniu bezpieczeństwem systemu transportu lotniczego. *Prace Naukowe Politechniki Warszawskiej. Transport*, (103), 99-111.
- [13] Campbell, R. D., & Bagshaw, M. (2002). *Human performance and limitations in aviation*. John Wiley & Sons.
- [14] Martinussen, M., & Hunter, D. R. (2010). Personnel selection. *Aviation psychology and human factors*, 73-98.
- [15] "ICAO Circular 240-AN/144: Human Factors Digest No 7 - Investigation of Human Factors in Accidents and Incidents". Circular 240-An/144. Montreal, Canada: International Civil Aviation Organization. 1993. Retrieved 25 September 2023
- [16] Keightley, Alan (2004). *Human factors study guide*. Palmerston North: Massey University. 190.216
- [17] Johnston, Neil; McDonald, Nick (31 December 2017). *Aviation Psychology in Practice*.
- [18] Cacciabue, Carlo (17 April 2013). *Guide to Applying Human Factors Methods: Human Error and Accident Management in Safety-Critical Systems*. Springer Science & Business Media. ISBN 978-1-4471-3812-9.
- [19] T. T. Wong and S. Tong, "An airworthiness SHELL model for aircraft maintenance," 2012 IEEE International Conference on Industrial Engineering and Engineering Management, Hong Kong, China, 2012, pp. 1292-1296, doi: 10.1109/IEEM.2012.6837952.
- [20] Guido Perboli, Marco Gajetti, Stanislav Fedorov, Simona Lo Giudice, (2021), *Natural Language Processing for the identification of Human factors in aviation accidents causes: An application to the SHEL methodology*, *Expert Systems with Applications*, Volume 186, 115694, ISSN 0957-4174, <https://doi.org/10.1016/j.eswa.2021.115694>.
- [21] X. Wang, X. Long and L. Yu, "Research on Hazards Identification of Airport Based on SHEL Model," 2022 International Conference on Electronics and Devices, Computational Science (ICEDCS), Marseille, France, 2022, pp. 136-139, doi: 10.1109/ICEDCS57360.2022.00037.



CHAPTER 10

Aviation Technologies and Applications
E-ISBN:978-605-338-471-7
2025, chap. (10) , pp.167-176.

DISCONTINUITY DETECTION IN GLASS FIBER REINFORCED THERMOSET LAMINATED COMPOSITES BY REVERSE THERMOGRAPHIC INSPECTION

Efe Kerem Deniz ÇELTEK¹, Alperen DOĞRU^{2,*}

ABSTRACT

The use of composite materials is increasing in the 21st century. Fatigue, impact, and manufacturing discontinuities may occur in composite materials used in structural parts. Early detection of these discontinuities is critical for safety. In recent years, the use of the thermographic control method has come to the forefront of discontinuity control in composite materials. It has special significance, especially in the inspection of defects in laminated and sandwich composites.

In this chapter, non-destructive testing methods and thermographic inspection method, terminology of composite materials, and types of discontinuities are explained and the performance of the thermographic inspection method in composite samples containing artificial discontinuities is examined. Discontinuities formed in glass fiber-reinforced epoxy matrix laminated composites produced by different methods were examined by thermographic examinations with different temperature ranges. The temperature changes of all specimens were conducted in a similar temperature range with both heating and cooling processes. It was observed that the reverse thermographic examination with cooling has a sensitivity similar to that of heating, which will allow more flexible application of the method and localized controls. It was shown that cooled thermographic examination can be used to identify areas of delamination.

Keywords: Thermographic Inspection, Non-Destructive Testing, Polymeric Composites

1. INTRODUCTION

A composite material is a form of material in which two or more components are physically combined without chemical bonding. The components that make up the composite material have different chemical and/or physical properties[1]. These materials are combined to form a new material with different properties. Today, these composite materials are used in many end products, especially in the structural parts of airplanes[2]. Fatigue, impact, and manufacturing discontinuities may occur in composite materials used in structural parts. Early detection of these discontinuities is critical for safety[3].

*Corresponding Author: alperen.dogru@ege.edu.tr

1 0000-0003-3730-3761, Aircraft Technology Prog., Aviation HVS, Ege University, Izmir, Turkiye

2 0009-0003-6402-6787, Aircraft Technology Prog., Aviation HVS, Ege University, Izmir, Turkiye

CHAPTER 10: DISCONTINUITY DETECTION IN GLASS FIBER REINFORCED THERMOSET LAMINATED COMPOSITES BY REVERSE THERMOGRAPHIC INSPECTION

Traditional non-destructive testing (NDT) methods such as ultrasonic inspection and radiographic inspection are used to detect discontinuities in composite materials[4,5]. In addition, in recent years, the thermographic inspection method, which is defined as modern NDT, which provides discontinuity detection in a short time, has started to be used in composite materials inspections[6].

Thermographic inspection method is an inspection method based on invisible InfraRed (IR) energy (heat) as an imaging method and the general structure of the image is determined by the colors and shapes formed according to IR energy and the heat changes on the parts are examined. Thermography, thermal imaging or thermal video is a form of infrared imaging. Thermographic cameras detect electromagnetic radiation in the infrared part of the electromagnetic spectrum (roughly 900-14,000 nanometers or 0.9-14 μm) and create images from this radiation[7].

Non-destructive control methods used in aerospace require faster and more accurate results than in other fields[5]. Thermography is an indispensable non-destructive testing method with its fast and reliable results, and it provides reliable and accurate results in composite materials used in aerospace. It is especially important in the examination of defects in laminated and sandwich composites[2,3].

The types of damage detected in composite materials during their production and service life are scratches, dents, holes and cracks, adhesion defects (void, gaps, separations), panel edge damage and foreign materials[8,9]. While different non-destructive testing methods are used to detect these damage and defect types, the use of the thermographic method to detect such defects in laminated composites is becoming more widespread[10].

There are some steps to be followed in the process of thermographic examination. Following these steps will increase the accuracy of the inspection and prevent time losses. With the thermography method, the location of the discontinuities is determined with the help of temperature differences on the damaged surface of the part. In thermographic examination, firstly, heat is applied to the part with different heating equipment, the part that reaches a certain temperature and is homogeneously heated is left to cool. The temperature change that occurs during the cooling of the part is recorded and examined step by step with thermal cameras. The change in the cooling rate in areas with discontinuities is detected by the cameras.

In a study in which water (moisture) was detected with a thermal camera in the directional rudders of honeycomb aircraft reinforced with carbon fiber, it was stated that the regions with water appeared darker in the thermal camera and approximately 3050 mm² water was detected [5]. Meola et al. compared thermographic and ultrasonic examination for discontinuity detection in carbon fiber reinforced composites. They found that the TI method is more advantageous for discontinuities caused by impact [11]. Taraghi et al. were able to detect subsurface discontinuities in epoxy matrix carbon fiber reinforced and 0.5 wt% carbon nanotube doped composites by TI method [12]. When the research in the literature are examined, tests were carried out by heating the parts and then cooling the parts to detect discontinuities in polymer matrix composites. In our research study, discontinuity checks were conducted with a reverse cycle in laminated composite materials, and the parts were first cooled and then examined with thermal cameras during the process of coming to room temperature.

In this study, instead of heating the parts to high temperatures, thermal change was achieved by cooling the parts and then bringing them to room temperature. Temperature changes in laminated composite plates produced by different fabrication methods were also examined with thermal cameras to examine the performance of detecting artificial discontinuities created in the samples. In addition, the specimens were both heated and cooled to room temperature over a similar range of temperature changes and the performance of detecting discontinuities in both directions of temperature change was compared.

2. EXPERIMENTAL

2.1. Materials

Epilox® A 19-00 Thermoset Epoxy from Leuna-Harze GmbH and Epilox® H 10-41 hardener were used in our research. TR-WA-E 1220 E-glass fiber product of Metyx company with 0/+45/-45 orientation shown in Figure 1 (a) was used as fiber reinforcement.



Figure 1. (a) Glass Fiber (b) Aluminum Plate

CHAPTER 10: DISCONTINUITY DETECTION IN GLASS FIBER REINFORCED THERMOSET LAMINATED COMPOSITES BY REVERSE THERMOGRAPHIC INSPECTION

A 40 wt% glass fiber reinforcement was applied in the production of all sample plates. The specimen plates were produced by hand lay-up, vacuum infusion, and vacuum bagging. With 3 different production methods, two plates with 140*140 mm dimensions, one without discontinuities and one with artificial discontinuities, were produced. Four layers of glass fiber fabric were used in all of the plates. In the middle layer of the plates containing artificial discontinuities and in the middle part of the plate, 2024-T6 Aluminum plate with 40*40 mm dimensions and 1.65 mm thickness shown in Figure 1 (b) was positioned.

2.2. Samples Production

Within the scope of the study, the samples whose dimensions were determined were produced by 3 different composite production methods: hand lay-up, vacuum infusion, and vacuum bagging. For the samples produced by each method, the glass fiber fabrics were weighed on a precision balance and the epoxy ratios were calculated. All sample plates were produced with 40 wt% glass fiber reinforcement. In each method, the glass fiber fabrics were spread on a flat surface. For the hand lay-up method, the epoxy was applied with a roller brush on this laid fabric. For the vacuum infusion method, the epoxy was applied with a vacuum pump after the glass fiber fabrics were laid and wrapped in a vacuum bag. In the vacuum bagging methods, the epoxy was combined with a roller brush as in the hand lay-up methods, then the sample was covered with a vacuum bag and vacuumed with a pump. Figure 2 shows the images of the composite plates produced with 3 different production methods.

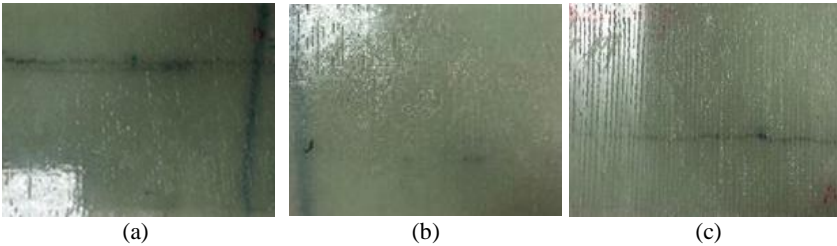


Figure 2. Produced composite plates: (a) Hand Lay-up (b) Vacuum Bagging (c) Vacuum Infusion

All the specimens were produced by these three methods in two different versions, one with an artificial defect and the other with no defect. The aluminum plates representing the artificial defect placed on all specimens are located at the same point and in the same layer. Figure 3 shows composite plates with artificial discontinuities produced by different fabrication methods.

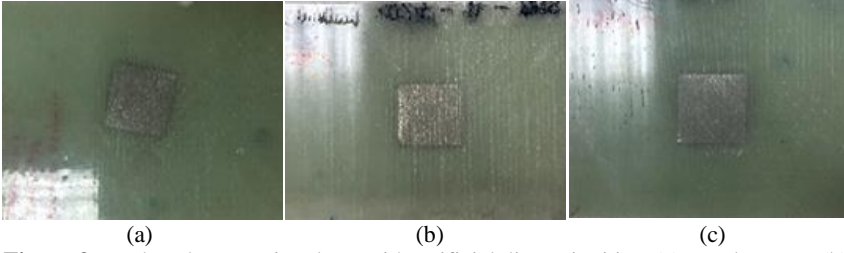


Figure 3. Produced composite plates with artificial discontinuities: (a) Hand Lay-up (b) Vacuum Bagging (c) Vacuum Infusion

2.3. Equipment

To increase the temperature of the produced sample plates, the NKD-250 model oven of Nükleon brand shown in Figure 4 (a) was used. All samples were heated up to 60 °C. For the cooling process, Pic Solution brand cooling spray shown in Figure 4 (b) was used. The temperature of all samples was reduced to -20 °C by using sprays. All thermographic measurements were performed at room temperature and the ambient temperature was recorded with the Fischer Scientific thermometer shown in Figure 4 (c).



Figure 4. (a) Nukleon NKD250 Oven (b) Pic Ice Spray (c) Fischer Scientific Thermometer

Temperature measurements were performed with the UNI-T brand UTi120T model thermal camera shown in Figure 5. The camera has a resolution of 120*90 pixels, an accuracy of +/-2 °C and a frame rate of 25 Hz.



Figure 5. UNI-T UTi120T Thermal Camera

CHAPTER 10: DISCONTINUITY DETECTION IN GLASS FIBER REINFORCED THERMOSET LAMINATED COMPOSITES BY REVERSE THERMOGRAPHIC INSPECTION

In this study, the performance and effects of detection of artificial discontinuities in specimens produced by different production methods with reverse thermal change in thermographic examination were investigated.

2.3. Thermographic Testing

The cooling process was carried out by spraying special cooling chemicals and the heating process was carried out with an oven. The sample plates were first heated to 60 °C and then cooled to room temperature. In addition, the same sample plates were cooled down to -20 °C and brought to room temperature and all these processes were analyzed by thermal camera. Temperature changes in the composite plates were measured at 60-second intervals and images were taken.

3. RESULTS AND DISCUSSION

With the Uni-T UTi120T thermal camera, the temperature change rates of composite plates produced with different production methods, temperature change rates in samples with artificial discontinuities and discontinuity images were analyzed.

All samples were examined three times, and all changing contrasts were recorded with a camera at 60 second intervals. Temperature controls during the cooling and heating processes were measured and recorded with a Fischer Scientific thermometer. Measurements were taken at the center of all specimens where the artificial discontinuity was located. Measurements were made from a fixed distance to measure these regions and with a device that allows the thermal camera to be positioned at an angle of 90 degrees to the part. The minimum and maximum temperature points recorded by the thermal camera in the area determined for measurement were measured and these values were recorded. Figure 6 shows sample images of the temperature changes of discontinuity-free composite plates after cooling.

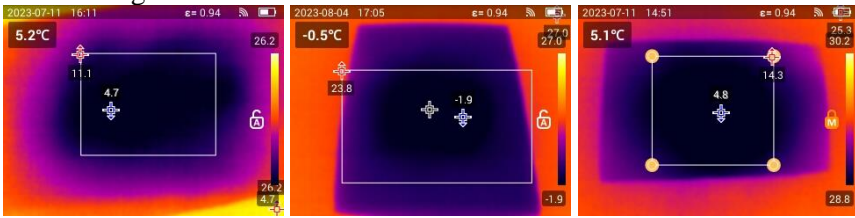


Figure 6. Cooling Cycle Results of Composite Plates without Discontinuities: (a) Hand Lay-up (b) Vacuum Bagging (c) Vacuum Infusion

All samples at $-20\text{ }^{\circ}\text{C}$ were tested to till reach room temperature. As expected, the heat exchange started from the edge surfaces of the plate and progressed towards the center. The reason for this rapid heat exchange is that the edges have more surface area.

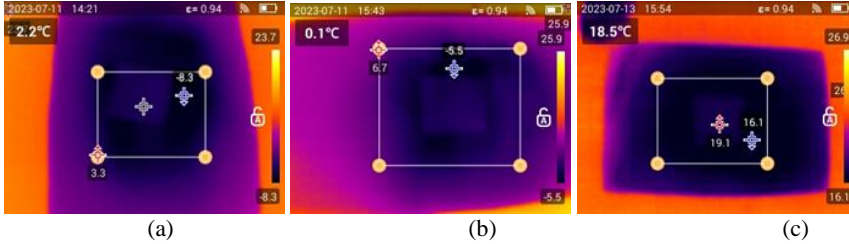


Figure 7. Cooling Cycle Results of Composite Plates with artificial discontinuities: (a) Hand Lay-up (b) Vacuum Bagging (c) Vacuum Infusion

It was found that the heat changes in the area where the artificial discontinuities are positioned are slower. Figure 7 shows sample images of composite plates produced by different methods containing artificial discontinuities. The reason for this situation can be said to be the use of aluminum plates as artificial discontinuities.

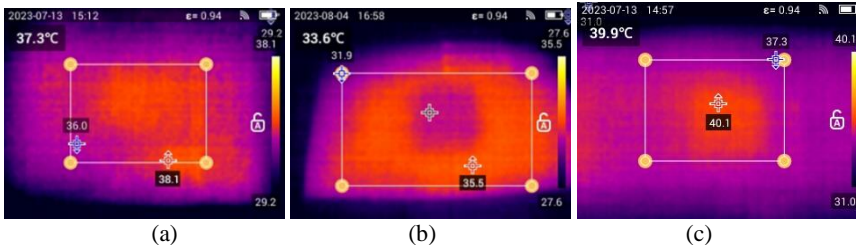


Figure 8. Heating Cycle Results of Composite Plates with artificial discontinuities: (a) Hand Lay-up (b) Vacuum Bagging (c) Vacuum Infusion

In the heating cycle, the thermal changes in all composite plates heated to $60\text{ }^{\circ}\text{C}$ were analyzed. Figure 8 shows example images of composite plates with artificial discontinuities, each produced in a different manufacturing process, where the thermal changes after heating are measured. The tests showed that it is possible to detect artificial defects in both applications, both heating and cooling. In both applications, a significant contrast difference was observed in the regions containing artificial discontinuities. Time-dependent temperature changes of all specimens were plotted using the data recorded from the thermal imaging camera and the slopes of the curves were calculated. It was observed that the slopes were close to each other in the graphs of temperature changes in heating and cooling applications.

CHAPTER 10: DISCONTINUITY DETECTION IN GLASS FIBER REINFORCED THERMOSET LAMINATED COMPOSITES BY REVERSE THERMOGRAPHIC INSPECTION

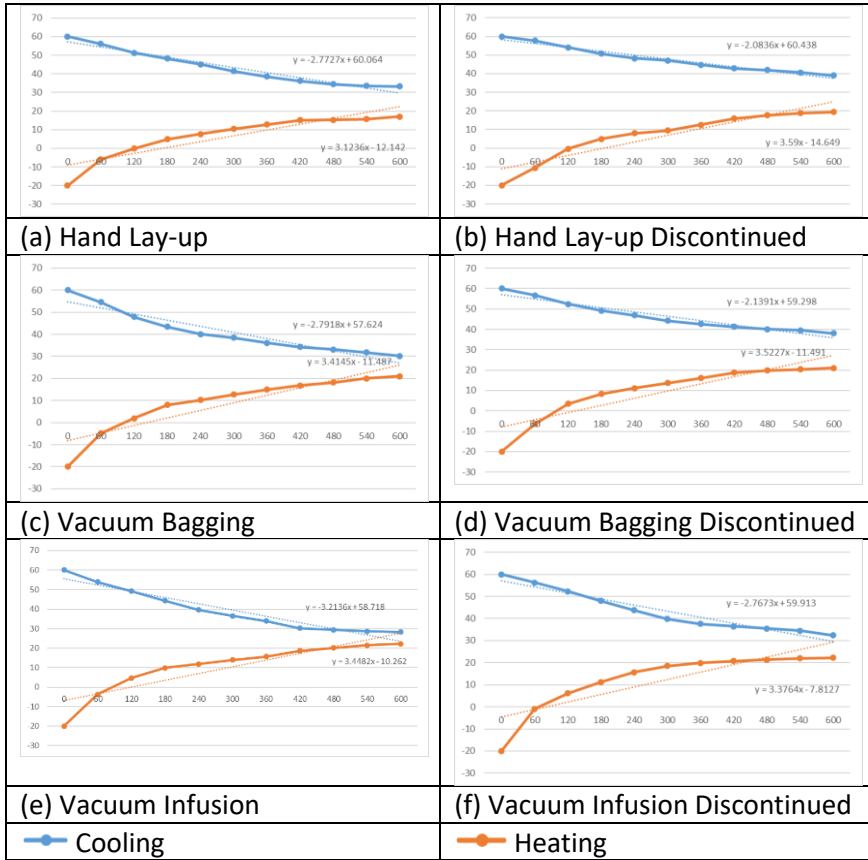


Figure 9. Time Dependent Temperature Change Curves of Samples

As a result of the comparison of these slopes, it was observed that the samples produced by vacuum infusion method showed faster temperature changes. Similar temperature changes were observed when heating and cooling processes were compared. The temperature changes in the samples containing artificial discontinuities were different from the samples without discontinuities, and cooling and heating were slower due to the different thermal conductivity of the aluminum sheet used for the artificial discontinuity.

4. CONCLUSION

In this study, temperature change rates and discontinuity images of composite specimens with artificial discontinuities were analyzed as a result of thermal tests performed on composite specimens produced by different production methods. It was determined that the reverse

thermography performed by cooling process has similar sensitivity to the heating process. The results obtained suggest that the thermal test method to be carried out by cooling will allow more flexible applications. In addition, this system may allow for more localized controls.

Acknowledgements

This study was supported within the scope of TÜBİTAK 2209B University Students Industry-Focused Research Projects Support Program. We would like to thank TÜBİTAK for supporting science and scientists.

Conflict of interest

No conflict of interest was declared by the authors.

Author contributions

Efe Kerem Deniz ÇELTEK, Literature review, article preparation, experimental studies, evaluation of results, and writing. Alperen DOĞRU: Idea/concept formation, method planning, article organization, provision of resources for experimental studies, evaluation of results, and grammar and content review of the article.

REFERENCES

- [1] Mallick PK. Fiber-Reinforced Composites: Materials, Manufacturing, and Design, Third Edition 2007. <https://doi.org/10.1201/9781420005981>.
- [2] Gay D. Composite Materials: Design and Applications 2022. <https://doi.org/10.1201/9781003195788>.
- [3] Shahkhosravi NA, Yousefi J, Najafabadi MA, Burvill C, Minak G. Fatigue life reduction of GFRP composites due to delamination associated with the introduction of functional discontinuities. *Compos B Eng* 2019;163:536–47. <https://doi.org/10.1016/J.COMPOSITESB.2019.01.005>.
- [4] Ibarra-Castanedo C, Tarpani JR, Maldague XPV. Nondestructive testing with thermography. *Eur J Phys* 2013;34:S91. <https://doi.org/10.1088/0143-0807/34/6/S91>.
- [5] Eroğlu E. Non-Destructive Testing by Means of Thermographic Analysis in Aircraft Composite Structures. Eskisehir Osmangazi University, 2019.
- [6] Carosena M. Infrared thermography: Recent advances and future trends. *Infrared Thermography: Recent Advances and Future Trends* 2012. <https://doi.org/10.2174/97816080514341120101>.

CHAPTER 10: DISCONTINUITY DETECTION IN GLASS FIBER REINFORCED THERMOSET LAMINATED COMPOSITES BY REVERSE THERMOGRAPHIC INSPECTION

- [7] Sarawade AA, Charniya NN. Infrared Thermography and its Applications: A Review. Proceedings of the 3rd International Conference on Communication and Electronics Systems, ICCES 2018 2018;280–5. <https://doi.org/10.1109/CESYS.2018.8723875>.
- [8] Heslehurst RB. Defects and Damage in Composite Materials and Structures. Defects and Damage in Composite Materials and Structures 2014. <https://doi.org/10.1201/B16765>.
- [9] Awaja F, Zhang S, Tripathi M, Nikiforov A, Pugno N. Cracks, microcracks and fracture in polymer structures: Formation, detection, autonomic repair. Prog Mater Sci 2016;83:536–73. <https://doi.org/10.1016/J.PMATSCI.2016.07.007>.
- [10] Asif M, Khan MA, Khan SZ, Choudhry RS, Khan KA. Identification of an effective nondestructive technique for bond defect determination in laminate composites—A technical review. J Compos Mater 2018;52:3589–99. https://doi.org/10.1177/0021998318766595/ASSET/IMAGES/LARGE/10.1177_0021998318766595-FIG9.JPEG.
- [11] Meola C, Boccardi S, Carlomagno GM, Boffa ND, Monaco E, Ricci F. Nondestructive evaluation of carbon fibre reinforced composites with infrared thermography and ultrasonics. Compos Struct 2015;134:845–53. <https://doi.org/10.1016/J.COMPSTRUCT.2015.08.119>.
- [12] Taraghi I, Łopato P, Paszkiewicz S, Fereidoon A. State-of-the art non-destructive techniques for defects detection in nanocomposites foam-core sandwich panels containing carbon nanotubes: IR thermography and microwave imaging. Polym Test 2019;73:352–8. <https://doi.org/10.1016/J.POLYMERTESTING.2018.11.047>.



CHAPTER 11

Aviation Technologies and Applications
E-ISBN:978-605-338-471-7
2025, chap. (11), pp.177-190.

UNMANNED AERIAL VEHICLES IN DISASTER MANAGEMENT: AN INNOVATIVE APPROACH TO CIVIL ENGINEERING

Elif CİCEK^{1,*}, Ayşegül ÖZDEN ACEHAN², Ahmet Cevat BİRİCİK³

ABSTRACT

Unmanned aerial vehicles (UAVs) have become integral in various fields due to technological advancements, with significant applications in disaster management. This chapter explores the innovative use of UAVs by focusing on their role in emergency and disaster response. The research emphasizes the importance of UAVs in pre-disaster terrain information, communication during disasters, and post-disaster damage assessment. The study also discusses the technical requirements of UAVs tailored for specific purposes, such as photogrammetric imaging and communication. By this way, faster and more effective transportation will be provided to areas that require intervention in disasters and emergencies, and rapid assistance will be provided.

Keywords: Disaster management, UAV, intelligent cities, artificial transportation vehicles.

1. INTRODUCTION

Unmanned aerial vehicles (UAV) have entered our lives in many different areas with today's advancing technology. Although defense comes first, there are many studies on the possibility of using unmanned aerial vehicles in many areas. One of them is the contribution to human life before and after disasters, traffic monitoring and rescue [1]. Generally, photogrammetric studies were carried out with unmanned aerial vehicles, and the lands of regions at risk of disaster were examined and orthophotos were produced from the collected data, and it was observed that data that would be useful to act quickly during a disaster was observed thanks to these produced orthophotos.

*Corresponding Author: Elif Cicek: elif.cicek@hacettepe.edu.tr

¹ 0000-0002-3575-8079, Civil Engineering, Faculty of Engineering, Hacettepe University, Ankara, Türkiye

² 0000-0002-2801-2551, Civil Engineering, Faculty of Engineering, Hacettepe University, Ankara, Türkiye

³ 0009-0003-7295-2131, Civil Engineering, Faculty of Engineering, Hacettepe University, Ankara, Türkiye

CHAPTER 11: UNMANNED AERIAL VEHICLES IN DISASTER MANAGEMENT: AN INNOVATIVE APPROACH TO CIVIL ENGINEERING

The integration of unmanned aerial vehicles (UAVs) in disaster management marks a significant advancement in civil engineering. In recent years, the integration of UAVs in disaster management has become increasingly pervasive, revolutionizing traditional approaches.

This chapter seeks to unravel the multifaceted applications of UAVs within the broader context of civil engineering, with a particular emphasis on their role in pre-disaster preparation, real-time communication during disasters, and the meticulous assessment of post-disaster damages. The overarching objectives of this chapter are to provide a comprehensive understanding of the diverse roles that UAVs play in disaster management within the field of civil engineering. The specific goals include:

Exploring Pre-disaster Terrain Information: Investigating how UAVs contribute to the creation of pre-disaster terrain information, enabling proactive measures and strategic planning in anticipation of potential disasters.

Enhancing Communication During Disasters: Analyzing the pivotal role of UAVs in facilitating communication and coordination during the critical hours of disaster response. UAVs offer a unique aerial perspective that aids in rapid decision-making and resource allocation.

Advancing Post-disaster Damage Assessment: Delving into the technical requirements and methodologies employed by UAVs in post-disaster scenarios. Emphasis will be placed on their capacity for rapid and detailed scanning, aiding civil engineers in damage assessments and decision-making. It is thought that the use of unmanned aerial vehicles will also be beneficial in post-disaster damage assessment and scanning, in which civil engineers and architects play a major role. It is expected that the damage assessment will be carried out more reliably with the faster and more detailed scanning of the damaged areas thanks to the unmanned aerial vehicles. In light of the data collected by unmanned aerial vehicles, civil engineers can make damage assessments more quickly, determine the extent of the damage and determine the need for repair or reinforcement, thus contributing to the faster execution of the works [2].

Unmanned Aerial Vehicles (UAVs) are still being used by international humanitarian actors and disaster management authorities to produce visual data in the aftermath of disasters to assess initial impacts, like the possible spatial distribution of building and infrastructure damages [3].

2. APPLICATIONS OF UNMANNED AERIAL VEHICLES

There are too many usages of UAV's in the modern area. With developments in the technology too many types of this devices have been presented to the people and access to the UAV's became very easy. Top civilian applications of the UAV's are;

- Photography,
- Shipping and Delivery,
- Rescue and Damage Assessment in Disaster Management,
- Archaeological Survey,
- Safety Inspection,
- Life Observance,
- Weather Forecasting and
- Livestock Surveillance.

Table 1 and Table 2 shows different classification samples for UAV's. In the first table you can see they classified according to their weights. And in Table 2, UAV's classified according to their maximum take-off weight, range, time of fly and data delivery range.

Table 1. Classification of UAVs according to SHGM UAV Systems Instruction [4]

Type	Weight
İHA0	500 gr- 4 kg
İHA1	4 kg- 25 kg
İHA2	25 kg- 150 kg
İHA3	>150 kg

Table 2. Classification of UAV's [4]

	C	W	R	T	L
Micro	Micro	0.10	250	1	<10
Mini	Mini	<30	150-300	<2	<10
Tactical	Too short range	150	3000	2-4	10-30
	Short range	200	3000	3-6	30-70
	Mid-range	150-500	3000-5000	6-10	70-200
	Long range	-	3000-5000	6-13	200-500
	Durable	500-1500	5000-8000	12-24	>500
	Mid-range, Long Durability	1000-1500	5000-8000	24-48	>500
Strategic	Long-range, Long Durability	2500-12500	15000-20000	24-48	>2000
	Mission Based	Militant	250	3000-4000	3-4
Based	Bait	250	50-5000	<4	0-500
	Stratospheric	-	20000-30000	>48	>2000
	Out of Stratospher	-	>30000	-	-

*(C: class, W: Maximum takeoff weight, R: Maximum height-meter, T: Time of fly-hour, L: Data delivery range-km)

2.1. Role of UAV's

UAV's can play a very big role in disaster management. As can be seen in the Figure 1 roads, bridges and other land-based transportation ways can be damaged in disasters like earthquake, storm etc. In situations like this, air transportation plays a high role in disaster management. But landing bigger planes and helicopters will be a problem because airports and other areas can be highly damaged and cannot be used. So, usage of UAV's may determine the how quick can the help reach to the people in that area.



Figure 1. Cracks on Hatay-Reyhanlı highway due to Kahramanmaras earthquakes

The roles of these vehicle types can be expressed as below:

- They can be used for determination of which roads and bridges are damaged or which ones are in a good condition to use after an earthquake.
- They allow quick scanning of damaged areas and identification of damage.
- Thanks to high-resolution cameras and fast flight capabilities, detecting road and bridge damage becomes much faster and more detailed.
- Also, they can be used for buildings.
- They can quickly access areas that are difficult or dangerous for humans to reach.
- By this way, this helps to teams for moving quickly to identify damaged buildings and people who needs to help.

UAV and network technologies are related to data gathering, processing, analyzing, and the integration of new management techniques in addition to extraction, processing, and manufacturing [5]. In the literature there are some studies about new intelligent cities and transportation vehicles. Real-time tracking, real-time analytics, and enhanced decision-making might be made possible by collaboration between UAV, WSN, and IoT. This would help smart cities meet their public safety requirements by delivering such vital infrastructure in the event of a crisis [6]. As aerial evaluation may collect images and videos over broad geographic regions, it is the most efficient and fastest situational awareness device. The R&D community in disaster management has been paying more and more attention to UAV technology in recent years. WSN and multi-UAV systems were combined by Erdelj et al. to generate enhanced disaster management solutions [7]. A cooperation UAV-WSN network [8] has been built for broad area monitoring and to improve the network's overall performance. It is self-configured to boost the capture of environmental data across large areas. As can be seen, Figure 3 shows the UAV-based and multi-type network at the time of disaster, considering the connectivity of UAVs with each other and the environment, this leads to the field of management of studies. With their real-time data collection potential, surveillance capabilities and rapid mobility, UAVs play an important role in the development of disaster response and management strategies in the context of smart urban systems and advanced transportation networks.

Figure 2 shows that the role of various network types in disaster and critical situation management. The diagram includes different communication and data transfer systems such as satellite networks, high-altitude unmanned aerial vehicle (UAV) ad hoc networks, low-altitude UAV ad hoc networks, Wi-Fi networks, cellular networks, and video surveillance. This representation emphasizes the diversity and coordination of communication infrastructure during disaster and emergency situations, showcasing the potential contribution of unmanned aerial vehicles in these processes.

As can be seen in Figure 3, it is clear that integrating different methods will result in a more effective design for disaster monitoring, detection, and management. Disaster management systems must have access to real-time analytics, which includes affordable data storage, connection, and real-time data from numerous sources. The advantages of combining several methods are illustrated [9].

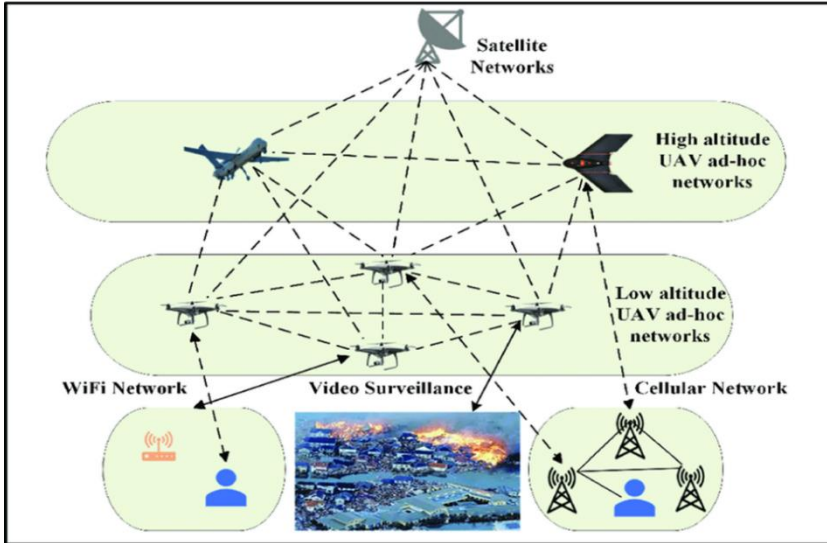


Figure 2. UAV-based and multi-type network in disaster and critical case management. [9]

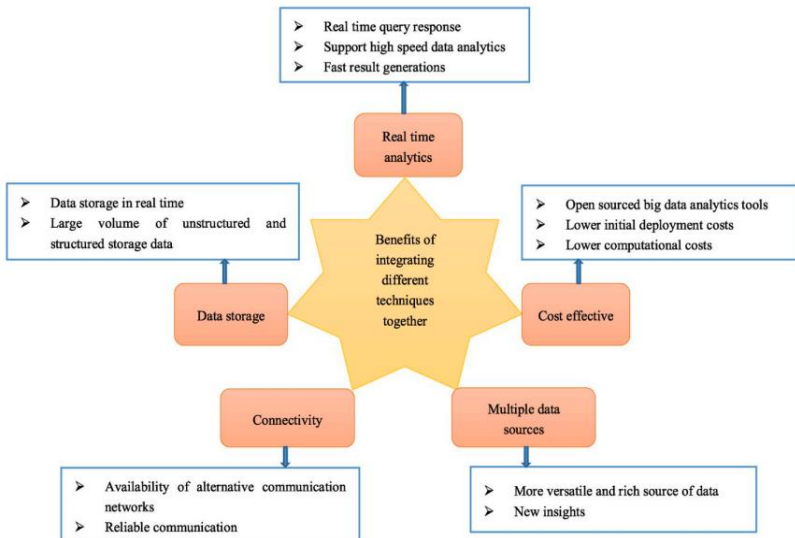


Figure 3. Benefits of UAV-based and multi-type network integrating [9]

The communication and network technologies that can support UAV disaster management systems in scenarios involving early warning systems, search and rescue, data collection, network coverage for emergency communication, and logistic delivery are highlighted by Luo et al. [10]. Regarding catastrophe management and response, the writers also cover the networking technologies that are necessary for UAV deployment in real-world settings [11].

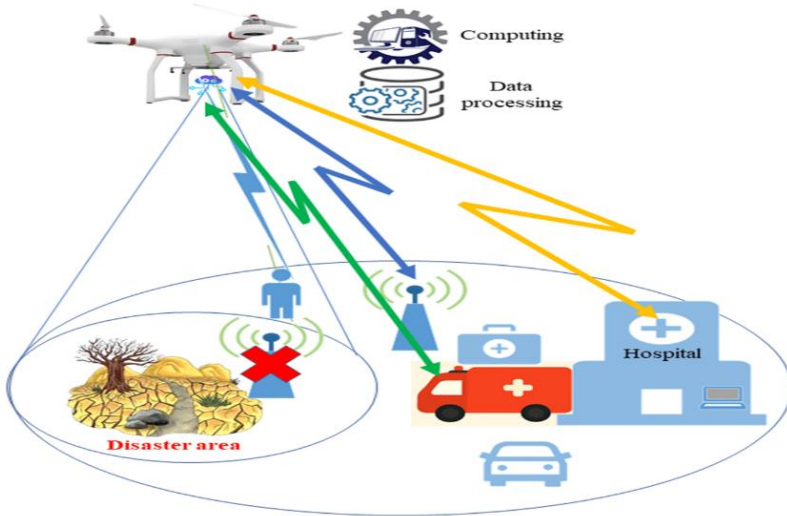


Figure 4. UAV network in disaster area [7]

Figure 4 shows that UAV computing in the disaster area. UAV's can ensure the communication between disaster area and the rescue teams. UAV's scans the disaster area and deliver the images to the rescue teams, so when they reach the area, they won't be losing time by searching for the people to save and they will go to their location immediately. Cooperation between multiple UAVs and search and rescue (SAR) teams plays a key role improving safety and reducing the economic impact of disasters [12].

However, UAV computing still faces some important challenges. First off, the UAV experiences more stress, and its propulsion system uses more energy when edge computing is installed on it. Second, a UAV's service time is shortened, and its battery capacity is limited. This is made worse by users shifting their computing tasks to the UAV, increasing the energy consumption of the UAV for computation [12].

UAVs can be used as mobile assistance units during disaster relief operations. Depending on the kind of crisis and user needs, UAVs can offer food, medical, and networking assistance to survivors. Figure 5 (a,b,c,d) depicts four distinct scenarios.

CHAPTER 11: UNMANNED AERIAL VEHICLES IN DISASTER MANAGEMENT: AN INNOVATIVE APPROACH TO CIVIL ENGINEERING

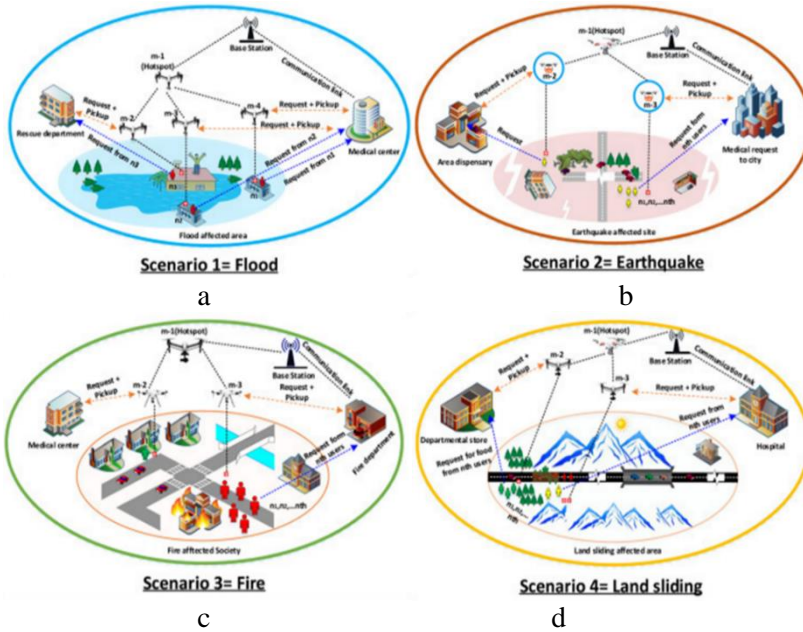


Figure 5. Disaster management types; a. Flood, b. Earthquake, c. Fire, d. Land sliding [12]

In the first scenario, UAVs acting as mobile assistance units can assist flood victims by offering food services, medical attention, and network access in the event that floods block off the major city road. UAVs, or Unmanned Aerial Vehicles, serve as invaluable assets in disaster relief operations, providing mobile assistance units capable of swift response and versatile aid delivery. In the context of flood relief, these UAVs play a pivotal role in addressing the urgent needs of victims stranded by inundated areas. When floodwaters render major city roads impossible, UAVs step in to bridge the gap, offering essential services such as food distribution, medical attention, and connectivity support. By extending their reach beyond conventional means, UAVs as mobile assistance units demonstrate their capacity to adapt to evolving crisis situations. Their agility and versatility empower disaster response teams to deliver comprehensive aid efficiently, enhancing the resilience of communities in the face of adversity. Thus, in the first depicted scenario, UAVs emerge as indispensable allies, leveraging their capabilities to alleviate the hardships faced by flood victims and contribute to the restoration of normalcy in affected areas [12].

In the second scenario, UAV-based mobile assistance units can offer basic medical services and communications coverage in an earthquake-damaged area where access to medical services is limited. Earthquakes often severely impact infrastructure and diminish or entirely obstruct the functionality of healthcare facilities. In such instances, injured individuals and patients may require urgent medical assistance, but reaching healthcare facilities can be challenging. UAVs can swiftly reach affected areas and promptly deliver basic medical services to the injured or those in need of medical attention. For example, a UAV can carry urgent medical necessities such as medication, medical supplies, or even conduct medical consultations and provide first aid services guided by remote medical experts [12]. In conclusion, in the second scenario, UAVs emerge as significant assets to alleviate the challenges faced by earthquake victims and provide critical services to survivors. By offering basic medical services and communication support, they can intervene rapidly as mobile assistance units, thereby expediting the post-disaster recovery process.

In the third scenario, in the event of a sudden fire outbreak, MHU-UAVs can deliver emergency medical services (oxygen, masks, medicine) to fire-affected people. Fires can rapidly escalate, causing injuries and health hazards to individuals in the vicinity. In such situations, immediate medical assistance is crucial for those affected by smoke inhalation, burns, or other fire-related injuries. MHU-UAVs equipped with medical supplies and equipment can swiftly navigate through the affected area, reaching inaccessible or dangerous locations to provide vital medical aid [12].

In the fourth scenario, in the event of glaciers melting as a result of a landslide or severe weather changes in a mountainous region, the loss of roads and communication routes could leave people short of water, medical aid and food. UAV-based mobile assistance units can provide assistance in these areas [13]. The sudden melting of glaciers can endanger water sources and significantly disrupt infrastructure, isolating people. In such situations, prompt intervention is crucial to meet basic needs. UAV-based mobile assistance units can swiftly reach affected areas and transport necessary supplies to address urgent requirements. In the fourth scenario, UAV-based mobile assistance units have the potential to provide rapid and effective aid in disaster situations in mountainous regions. This can help meet the urgent needs of communities facing resource shortages and increase their chances of survival.

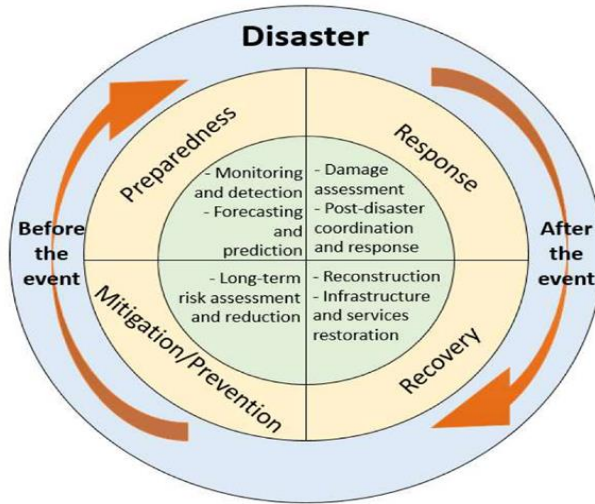


Figure 6. Disaster management cycle can be used as can be seen in figure [15]

In the Figure 6, you can see the phases of disaster management. It can be divided into two sections; things can be done before the event and things can be done after the event.

Pre-Disaster Management:

- Data collecting: Information can collect data of the land and the entire structure using the photography technique and how these data can be used in pre-disaster management.
- Quick Response: UAVs can contribute to communication and coordination in the event of a disaster.
- Preventive Measures: UAVs can help prevent disasters and minimize damage.

Post-Disaster Management

- Communication and Coordination: It is necessary to emphasize the critical role of UAVs in improving post-disaster communication and coordination.
- Damage Detection and Inspection: It can speed up the damage detection and inspection processes of UAVs and thus support the work of engineers and architects.
- Data Analysis: Data collected by UAVs can be analyzed and these analyzes can contribute to the development of post-disaster strategies.

Table 3. Total number of buildings in the provinces which affected by the 2023 earthquake (İçişleri Bakanlığı, MAKS)

Province	Residence	Business	Public Building	Other	Total
Adana	404.502	29.920	8916	7.779	451.117
Adıyaman	107.242	5.765	4.370	3.119	120.496
Diyarbakır	199.138	11.412	11.964	3.165	225.679
Elazığ	106.569	7.221	2.872	7.051	123.713
Gaziantep	269.212	22.829	5.480	8.162	305.683
Hatay	357.467	33.511	10.382	5.489	406.849
Kahramanmaraş	219.351	12.358	6.879	4.565	243.153
Kilis	33.399	1.526	1.651	736	37.132
Malatya	159.896	8.370	6.670	4.051	178.987
Osmaniye	128.163	9.428	3.105	2.384	143.080
Şanlıurfa	347.902	18.847	11.790	4.089	382.628
Total of the Area	2.332.841	161.187	74.079	50.590	2.618.697

Table 4. Damage Assessment Report for every Provinces (ÇİŞDİB)

Province	Total Number of Urgent-Heavily Damaged-Ruined Residence	Moderately Damaged Residence	Slightly Damaged Residence
Adana	2.952	11.768	71.072
Adıyaman	56.256	18.715	72.729
Diyarbakır	8.602	11.209	113.223
Elazığ	10.156	15.220	31.151
Gaziantep	29.155	20.251	236.497
Hatay	99.326	17.887	161.137
Kahramanmaraş	71.519	12.801	107.765
Kilis	215.255	25.857	189.317
Malatya	2.514	1.303	27.969
Osmaniye	16.111	4.122	69.466
Şanlıurfa	6.163	6.041	199.401
Total of the Area	518.009	131.577	1.279.727

As can be seen from the Table 3 and Table 4, a lot of provinces and buildings has been damaged at the 2023 Earthquake. One of the most important things about this earthquake places couldn't get help for weeks because earthquake damaged the roads and bridges so there was no access to city centers and most of the villages more less time. At this point, there were a chance that UAV's could be used and have determined the places that needed help, could carry some supplies to the people at those places because at winter conditions it is really hard to find food or keep yourself warm.

If we go back to the table, preparation of the report includes these tables took about a month. Because experts couldn't reach the area and when they have reached, they couldn't investigate the area in a detailed way. Most of the buildings were ruined and the others were too dangerous to get in and investigate. It was very risky for experts to get in to. Because aftershock earthquakes were happening too so buildings didn't break down, could go down too. At this point, using of UAV's could be very helpful because they can get in to the places humans can't and we would only risk a UAV, not a human's life. With the extra equipment, UAV's can measure the distances, take videos and photographs so experts can estimate the damages.

Additionally, technical features of the unmanned aerial vehicle to be used for photogrammetric purposes and the unmanned aerial vehicle intended to be used for communication have many different aspects. For an unmanned aerial vehicle to be used for photogrammetric purposes, the importance of the camera can be more important than the flight time. Its technical features need to be designed more suitable for imaging. The flight time does not need to be very long because the urgency of these studies is less than after the disaster. However, the flight time of the unmanned aerial vehicles, which can be expected to provide communication and coordination after the disaster, is very important. The need for frequent charging restricts their use, but also seriously reduces the efficiency to be obtained. For this reason, it is clearly seen that a relatively more powerful charging unit is needed for the camera to provide communication. The importance of the camera for those that will be used in damage detection and assessment is once again seen. Because in these determinations, it is necessary to observe the region or structures in detail. Obtaining these data properly and in detail will provide an undeniable convenience in the studies to be carried out [14].

CONCLUSIONS

In the recent times, determining disaster management to a higher level by using unmanned aerial vehicles has a critical role in the world. They can be used for a lot of different areas. Some of these are the determining of pre-disaster terrain information and images, and the fastest use of spatial data during a disaster. In this way, search teams can be able to recognize the area and be organized quickly.

Therefore, new technologies should be used for new city and critical areas. Technical features of the unmanned aerial vehicle to be used for photogrammetric purposes and the unmanned aerial vehicle intended to be used for communication have many different aspects. By these

determinations, it is necessary to observe the region or structures in detail. Obtaining these data properly and in detail can provide an undeniable convenience in the studies to be carried out.

Crisis management has critical effects for human life and disaster determination. They can be more effective and can operate in various places and cases, including those that are challenging or posing high risks for humans. As a result, using intelligent city designs and unmanned aerial vehicles can be an innovative approach for civil engineering disasters.

Acknowledgements

No Acknowledgements was declared by the authors.

Conflict of interest

No conflict of interest was declared by the authors.

Author contributions

All authors have contributed equally to the relevant work.

REFERENCES

- [1] P.Petrides, C.Kyrkou, P.Kolios, T.Theocharides ve C.Panayiotou, «Towards a holistic performance evaluation framework for drone-based object detection,» %1 içinde In 2017 International Conference on Unmanned Aircraft Systems (ICUAS), 2017.
- [2] R.-Y. Kung, N.-H. Pan, C. C. Wang ve P.-C. Lee, «Deep-Learning-Based Aerial Image Classification for Emergency Response Applications using Unmanned Aerial Vehicles,» Advances in Civil Engineering, 2021.
- [3] N. R. Hanifaa, E. Gunawan, S. Firmansyah, L. Faizal, D. A. Retnowati, G. C. Pradipta, I. Imran ve J. A. Lassa, «Unmanned Aerial Vehicles for geospatial mapping of damage assessment: A study case of the 2021 Mw6.2 Mamuju-Majene, Indonesia, earthquake during the coronavirus disease 2019 (COVID-19) pandemic,» Remote Sensing Applications: Society and Environment, pp. 2352-9385, 2022.
- [4] T. i. t. R.-R. Country, A. Symagulov, Y. Kuchin, E. Zaitseva, A. Bekbotayeva, K. Yakunin, I. Assanov, V. Levashenko, Y. Popova, A. Akzhalova, S. Bastaubayeva ve L. Tabynbaeva, «Review of Some Applications of Unmanned Aerial Vehicles Technology in the Resource-Rich Country,» Applied Sciences, cilt 11, no. 10171, 2021.
- [5] Y. Torres, J. Arranz, J. Gaspar-Escribano, A. Haghi, S. Martínez-Cuevas, B. Benito ve J. Ojeda, «a, Integration of LiDAR and multispectral images for rapid exposure and earthquake vulnerability estimation. Application in lorca, Spain,» Int. J. Appl. Earth Obs. Geoinf, cilt 81, p. 161–175, 2019.

- [6] M. Erdelj, M. Krol ve E. Natalizio, «Wireless sensor networks and multi-UAV systems for natural disaster management,» *Computer Networks*, pp. 72-86, 2017.
- [7] S. Alsamhi, F. Almalki, O. Ma, M. Ansari ve M. Angelides, «Performance Optimization of Tethered Balloon Technology for Public Safety and Emergency Communications,» *Telecommunication Systems*, p. 1–10, 2019.
- [8] A. Khan, S. Gupta ve S. K. Gupta, «Multi-hazard disaster studies: Monitoring, detection, recovery, and management, based on emerging technologies and optimal techniques,» *International Journal of Disaster Risk Reduction*, cilt 47, no. 101642, 2020.
- [9] Z. T. AlAli ve S. A. Alabady, «The role of unmanned aerial vehicle and related technologies in disasters,» *Remote Sensing Applications: Society and Environment*, 2022.
- [10] C. Luo, W. Miao, H. Ullah, S. McClean, G. Parr ve G. Min, «Unmanned aerial vehicles for disaster management,» *Geological Disaster Monitoring Based on Sensor Networks*, 2017.
- [11] S. H. Alsamhi, A. V. Shvetsov, S. Kumar, J. Hassan, M. Alhartomi, S. V. Shvetsova, R. Sahal ve A. Hawbani, «Computing in the Sky: A Survey on Intelligent Ubiquitous Computing for UAV-Assisted 6G Networks and Industry 4.0/5.0,» *drones*, 2022.
- [12] R. Masroor, M. Naeem ve WaleedEjaz, «Efficient deployment of UAVs for disaster management: A multi-criterion optimization approach,» *ComputerCommunications*, cilt 177, pp. 185-194, 2021.
- [13] C. Kyrkou ve T. Theocharides, «Deep-Learning-Based Aerial Image Classification for Emergency Response Applications Using Unmanned Uerial Vehicles,» %1 içinde *CVPR WORKSHOP ON COMPUTER VISION FOR UAVS*, 2019.
- [14] O. Villi ve M. Yakar, «İnsansız Hava Araçlarının Kullanım Alanları ve Sensör Tipleri,» *Türkiye İnsansız Hava Araçları Dergisi* , cilt 4, no. 2, pp. 73-100, 2022.
- [15] Alexander, D.E. *Principles of Emergency Planning and Management*; Oxford University Press on Demand: Oxford, UK, 2002; ISBN 9780195218381.



CHAPTER 12

Aviation Technologies and Applications
E-ISBN:978-605-338-471-7
2025, chap. (12), pp.191-204.

FLORESANS MANYETİK PARÇACIK TEST GÖRÜNTÜLERİNDE AKIM DEĞİŞİMLERİNİN ANALİZİ

Alperen DOĞRU^{1,*}, Coşkun HARMANŞAH², Esmâ Nur
SAVRANGÜLER³, Yavuz ÖZTÜRK⁴,
Feti ADAR⁵

ÖZET

Günümüzde atıkların, enerji tüketiminin az olduğu ve çevre dostu endüstriyel üretim süreçleri büyük önem taşımaktadır. Bu durum üretim süreçlerinin kesintiye uğramadan gerçekleşmesi açısından tahribatsız muayene yöntemlerinin tercih edilmesini arttırmaktadır. Tahribatsız muayene (NDT) sayesinde malzemeye kalıcı hasar vermeden ve kullanılabilirliğini etkilemeden olası iç veya yüzeysel kusurlar tespit edilebilmektedir. NDT malzemenin güvenilirliği ve bütünlüğünün korunmasında önemli bir rol oynamaktadır. Otomotiv, havacılık, savunma vb. sektörler başta olmak üzere diğer sektörlerdeki kritik malzemelerin üretim ve bakım çalışmalarında çeşitli NDT yöntemleri kullanılmaktadır.

Floresans Manyetik Parçacık Testi tahribatsız muayene metotları arasında basit kullanımı ve yüksek hassasiyeti nedeniyle ferromanyetik malzemelerin yüzey altı ve/veya yüzeysel süreksizliklerini tespit etmek amacıyla yaygın olarak kullanılan muayene yöntemlerinden birisidir. Manyetik parçacık muayenesi sırasında ferromanyetik parça yüzey ve/veya yüzeye yakın süreksizlikler UV ışığa veya görünür ışığa duyarlı floresans manyetik parçacık kullanılmaktadır. Burada, manyetik parçacıkların konsantrasyonu test sonuçlarını doğrudan etkilemekte ve kusurların daha belirgin hale gelmesinde rol oynamaktadır.

Manyetik parçacık muayenede önemli parametrelerden birisi akım türüdür. Kullanılan akım türü, muayene edilen malzemenin özelliklerine, muayene amacına ve muayene standartlarına bağlı olarak değişir. AC akım yüzeye daha yakın kusurların tespitinde yaygın olarak kullanılırken DC akım yüzey altındaki kusurların tespit edilmesine daha uygun olmaktadır. Piyasada yaygın olarak kullanılan çelikler için 50/60 Hz AC akım ile yapılan MPI uygulamalarında giriciliğin 2 mm'den (0,080") az olmaktadır. Manyetik parçacık muayenesinde akım seçimini yanı sıra uygulanacak akımın değeri de test sonuçları açısından önemlidir.

Bu çalışmada referans blok için farklı alternatif akım değerleri uygulanarak testin kalitesini etkileyen parametreler için veri setleri elde edilmiştir. Çalışma kapsamında elde edilen akım değerleri istatistiksel olarak yorumlanmış ve elde edilen sonuçlar formülize edilmiştir. Testler sırasında alınan görüntü dosyalarına ön işleme teknikleri uygulanarak elde edilen işlenmiş görüntüler ile sonuçlar karşılaştırılmış ve süreç optimize edilmiştir.

*Corresponding Author:coskun.harmansah@ege.edu.tr

¹ 0000-0003-3730-3761, Aircraft Technology, Aviation Vocational School, Ege University, İzmir, Türkiye

² 0000-0003-4946-8344, Computer Programming, Vocational School, Ege University, İzmir, Türkiye

³ 0000-0002-2766-0012, Mechanical Eng., Institute Of Science, İzmir Democracy University, İzmir, Türkiye

⁴ 0000-0002-9650-6350, Electrical Electronics Eng., Engineering Faculty, Ege University, İzmir, Türkiye

⁵ 0000-0003-3295-5840, Politeknik Elektronik, İzmir, Türkiye

1. GİRİŞ

1.1 Malzeme Muayenesi

Üretim ve üretim sonrası aşamasında olan parçaların durum tespitini yapmak ve kalite standartlarına göre uygunluğu kontrol etmek oldukça önemlidir. Bundan dolayı malzeme muayeneleri parçalara uygulanması gereken bir adımdır. Malzeme muayenesi tahribatlı ve tahribatsız olmak üzere iki gruba ayrılmaktadır [1]. Bir malzemenin mekanik özelliklerini belirlemek için de tahribatlı muayeneler ile gerçekleştirilen test sonuçlarına ihtiyaç duyulur. Ayrıca bir malzemede veya parçada meydana gelen süreksizlikler, ondan beklenen performansın elde edilmesini engeller. Bu süreksizlikler malzemenin türüne, üretim yöntemine ve kullanım koşullarına bağlı olarak farklılık gösterebilmektedir. Bu süreksizliklerin tespit edilmesinde ise tahribatsız muayene yöntemleri ön plana çıkar[2].

1.2 Tahribatlı Muayene

Tahribatlı muayene (Destructive Testing-DT), bir malzemenin kalıcı şekil değişikliğine karşı yük altında nasıl davrandığını, dayanıklılığını, mukavemetini ve diğer mekanik özelliklerini belirlemek için kullanılmaktadır. Bu yöntem malzemede kalıcı hasar bırakmaktadır. Bu yöntemde test sonrası meydana gelen kusur tipi ve malzeme özellikleri gibi değişkenlere uygun olarak malzeme veya parçanın mekanik özellikleri uluslararası normlara göre test edilerek raporlanmaktadır [3].

1.3 Tahribatsız Muayene

Günümüzde atıkların, enerji tüketiminin az olduğu ve çevre dostu endüstriyel üretim süreçleri büyük önem taşımaktadır. Bu durumda üretim süreçlerini kesintiye uğratmadan ve hızlı bir şekilde ilerlemesini sağlamak için tahribatsız muayene yöntemleri tercih edilmektedir. Tahribatsız muayene (Non Destructive Testing-NDT) sayesinde malzemeye kalıcı hasar vermeden ve kullanılabilirliğini etkilemeden olası içsel veya yüzeysel süreksizlikler tespit edilebilmektedir. Bu sayede tahribatsız muayene yöntemi atık üretimi ve enerji tüketimi açısından önemli avantajlar sunmaktadır. Ayrıca NDT malzemenin güvenilirliği ve bütünlüğünün korunmasında önemli bir rol oynamaktadır.

Tahribatsız muayene, kalite kontrolün en önemli bölümü olup üretimin tamamlayıcı son kısmıdır. Tahribatsız muayene yöntemi ile malzemeler

hammadde aşamasında, üretim sürecinde veya belli bir süre kullandıktan sonra örneğin, korozyon, stres veya aşınma gibi nedenlerden dolayı oluşan çatlak, içyapıda meydana gelen boşluk, kesit azalması vb. süreksizliklerin tespiti gerçekleştirilir. Bu yöntemler ile malzemelerin test edilmesi süreçlerinde numune almaya gerek yoktur ve testler, doğrudan parça üzerinde yapılır[1,2]. Tahribatsız muayene yöntemleri malzemelerin mukavemet değerleri hakkında bilgi vermez, bu sebeple tahribatlı testlerin alternatifi değildir. Ancak tahribatsız muayene yöntemleri ile bir parçadan veya malzemenin beklenen özelliğinin gerçekleşmesine mâni olabilecek süreksizliklerin tespit edilmesi mümkündür ve bu durum bir benzeri veya belirli bir örneklem gerekmeden tüm parçalara uygulanması sayesinde performans belirleme için kritiktir.

Tahribatsız muayene yöntemleri ile metalik, polimer, seramik veya kompozit malzemeler test edilebilmektedir. Bu kapsamda test edilecek malzemeye ve aranan süreksizlik türüne göre uygun olan Görsel Muayene (VT), Manyetik Parçacık Muayenesi (MPI), Sıvı Penetrant Muayenesi (PT), Ultrasonik Muayene (UT), Radyografik Muayene (RT), Eddy Akımı Muayenesi (ET) yöntemlerinden birisi veya birileri uygulanabilir[2]. Otomotiv, havacılık, savunma, uzay, petrol rafinerisi, çelik konstrüksiyon endüstrileri başta olmak üzere kritik parçaların performans kontrollerinde tahribatsız muayene yöntemleri önemli rol oynamakta ve birçok durumda ve koşulda zorunluluk olarak ele alınmaktadır.

Ayrıca uygulama alanı, kullanım şekli ve malzemenin özelliğine bağlı olarak İleri Tahribatsız Muayene Yöntemleri de kullanılmaktadır. Makine diagnostığı ile hareketli parçaların titreşim ve sıcaklıkları ölçülerek kalan servis ömrünün tespitini yapan yöntemler de mevcuttur[4].

1.4 Floresans Manyetik Parçacık Muayenesi

Floresans Manyetik Parçacık Testi tahribatsız muayene metotları arasında basit kullanımı ve yüksek hassasiyeti nedeniyle ferromanyetik malzemelerin yüzey altı ve/veya yüzeysel süreksizliklerini tespit etmek amacıyla yaygın olarak kullanılan muayene yöntemlerinden birisidir [1].

Tespit edilmek istenilen bulgular için muayene işlemi uygulanacak malzemelerin ferromanyetik özellikte olması gerekmektedir. Otomotiv, havacılık, savunma ve inşaat sektörleri başta olmak üzere diğer sektörlerdeki kritik malzemelerin üretim ve bakım çalışmalarında bu yöntem tercih edilmektedir. Floresans Manyetik Parçacık Muayene’de test sonuçlarını etkileyen birkaç önemli parametre vardır. Bunlardan biri

manyetik parçacık solüsyonudur. Muayene sırasında ferromanyetik parçadaki yüzey ve/veya yüzeye yakın süreksizliklerin tespiti için Ultraviyole (UV) ışığa veya görünür ışığa duyarlı manyetik parçacıklar kullanılmaktadır. Floresans MPI uygulamalarında manyetik parçacıklar, taşıyıcı sıvı ile homojen bir şekilde karıştırılarak manyetik parçacık solüsyonu elde edilmektedir [4]. Burada, manyetik parçacıkların konsantrasyonu test sonuçlarını doğrudan etkilemekte ve kusurların daha belirgin hale gelmesinde rol oynamaktadır. Bundan dolayı Floresans MPI Testi öncesi manyetik parçacık konsantrasyonu ve homojenliği kontrol edilmektedir. Manyetik parçacıklar; yeşil, kahverengi ve kırmızı renklerde olabilmektedir. Burada renkler test ortamında kullanılan görünür veya UV ışık türüne bağlı olarak daha iyi görünürlük sağlamak amacıyla farklı olarak üretilmektedir [5]. Test sırasında kullanılan sıvı AE AMS 3043 ve SAE AMS 2641 Type 1 standartlarını karşılamaktadır. ASME B&PV Code ve EN ISO 9934-2 göre non-koroinoniulfirik ve non-halojenik'tir[1].

Manyetik parçacık muayenede diğer bir önemli parametre ise kullanılan akımın türüdür. Burada kullanılan akım türü, muayene edilen malzemenin özelliklerine, muayene amacına ve muayene standartlarına bağlı olarak değişmektedir. Manyetik parçacık muayenesi akım türleri: Alternatif Akım (Alternating Current-AC), Doğru Akım (Direct Current- DC), Yarım Dalga DC (Half Width DC) ve Tam Dalga DC (Full Width DC)dir. Burada akım türünün seçimi test edilecek süreksizliğin yüzey ve/veya yüzey altındaki derinliğine bağlı olarak yapılmaktadır.

1.5 Alternatif Akım

Alternatif akım (Alternating Current-AC), kolaylıkla temin edilebildiği için manyetik parçacık kontrolünde yaygın biçimde kullanılan en uygun elektrik güç kaynağıdır. Alternatif akım, bir iletkenin yüzeyinde akar. Alternatif akım ile indüklenen manyetik alan, mıknatıslanacak test parçası yüzeyine yakın yerde yoğunlaşır. Bu nedenle alternatif akım ile mıknatıslanma yüzey süreksizliklerinin tespitinde en iyi yol olup yüzey altı süreksizlikleri için aynı şekilde etkin değildir.

1.6 Doğru Akım

Doğru akım (Direct Current-DC), düz akım olup yarım dalga doğru akıma göre daha kuvvetlidir ve alternatif akıma nazaran yüzey altında daha kuvvetli bir manyetik alan yaratır. Test parçasında; yüzey altı süreksizliği araştırılmasında yüzey altına daha yoğun akı oluşturan doğru akım kullanılmalıdır. Bu nedenle doğru akım her ne kadar yüzey süreksizliklerini tespit ediyorsa da yüzey altı süreksizliklerin saptanmasında kullanılmalıdır [1,6].

AC akım yüzeye daha yakın kusurların tespitinde yaygın olarak kullanılırken DC akım yüzey altındaki kusurların tespit edilmesine daha uygun olmaktadır. Piyasada yaygın olarak kullanılan çelikler için 50/60 Hz AC akım ile yapılan MPI uygulamalarında giriciliğin 2 mm'den (0,080") az olmaktadır [7].

Manyetik parçacık muayenesinde akım seçimini yanı sıra uygulanacak akımın değeri de test sonuçları açısından önemlidir. Bundan dolayı, NDT uzmanı manyetik parçacık muayenesinde referans test bloğu; operatörlerin eğitimi, muayene yöntemini doğrulama ve test sürecinin kalitesini belgelendirmek için kullanılmaktadır. Bunun için çeşitli referans test blokları üretilmiş ve bunlar standartlaştırılmıştır [8,9]. NDT uzmanları yapacakları floresans manyetik parçacık testine bağlı olarak standart referans blokları seçerek kullandıkları cihazlarını kalibrasyon yapmak zorundadır. Bunun için kullanılan MPI cihazı belirli periyotlarda kalibre edilerek testlerin doğruluğu garanti altına alınmaktadır.

Bu çalışmada Islak Metot Floresans Manyetik Parçacık Testi'nde farklı yüzey ve yüzey altı süreksizliklere sahip bir referans (test) blok kullanılmıştır. Deneysel çalışmalar Ege Üniversitesi Havacılık Meslek Yüksek Okulu NDT Laboratuvarı'nda bulunan Magnaflux MAG 20 Serisi Floresans Manyetik Parçacık Test cihazı ile gerçekleştirilmiştir. Testler sırasında elde edilen görüntüler, MATLAB ortamında ön görüntü işleme ve filtreleme algoritmaları kullanılarak değerlendirilmiştir.

2. MALZEME VE YÖNTEMLER

2.1 Islak Metot Floresans Manyetik Parçacık Muayenesi Bileşenleri

2.1.1 Floresans Manyetik Parçacık Test Cihazı:

Magnaflux MAG 20 Serisi, ıslak metot Floresans Manyetik Parçacık yöntemi ile yüzey ve yüzey altı yorulma çatlaklarını veya işleme kusurlarını tespit etmek için kullanılan bir test cihazıdır. Magnaflux MAG 20, 500 mm uzunluğa kadar ferromanyetik parçaların kontrolü için tasarlanmıştır. Şekil 1'de deneylerde kullanılan test cihazı gösterilmiştir [10].



Şekil 1:Floresans Manyetik Parçacık Test Cihazı

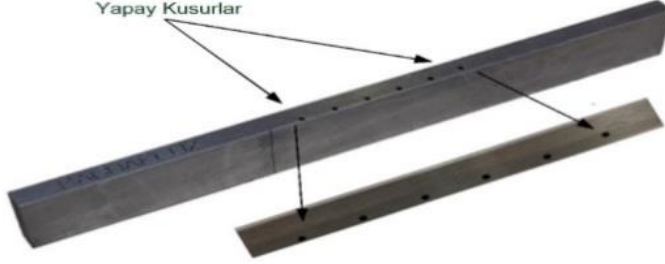
2.1.2 Referans Blok:

Manyetik parçacık muayenesinde test bloğu, cihazın doğru çalıştığından emin olmak, operatörlerin eğitimini sağlamak, muayene yöntemini doğrulamak ve test sürecinin kalitesini belgelemek için kullanılmaktadır. Referans blok, hem ince hem kaba kusurlara, yüzey ve yüzey altı kusurlara ve boyuna ve enine kusurlara sahiptir. Test bloğu standartlaştırılmıştır. Hem dairesel hem de boyuna AC mıknatıslanmayı doğrulamak için çubuğun her iki tarafında iki yönde yüzey çentikleri bulunmaktadır. Aşamalı derinliklerde çoklu yüzey altı kusurları, HWDC ve FWDC alan penetrasyonunun doğrulanmasını sağlamaktadır[11]. Referans bloğun boyutları ve blok üzerinde bulunan yapay kusurlara ait özellikler aşağıdaki Tablo-1’de verilmiştir.

Tablo 1: Referans Blok Özellikleri

Boyut (inç)	10.0 x 1.25 x 0.375
Yüzey Kusurları (Boy x Genişlik x Derinlik)	
Üst (inç)	Boyuna (2.0 x 0.005 x 0.040) Enine (0.063 x 0.005 x 0.020)
Alt (inç)	Boyuna (0.062 x 0.005 x 0.020) Enine (1.25 x 0.005 x 0.020)
Yüzeyaltı Kusurları	
Enine (inç)	0.064 (çap) x 0.75 (delik derinliği) 1. 0.051 (yüzeyden) 2. 0.061 (yüzeyden) 3. 0.071 (yüzeyden) 4. 0.081 (yüzeyden) 5. 0.091 (yüzeyden) 6. 0.131 (yüzeyden)
Boyuna (inç)	0.064 (çap) x 1.75 (delik derinliği) 0.093 (yüzeyden)

Şekil 2’de referans blok ve yapay kusurlar gösterilmiştir.



Şekil 2: Referans Blok ve Yapay Kusurlar

Deneylerde Aerospace Prime ve OEM spesifikasyonlarına uyumlu 365 nm dalga boyunda çalışan UV lamba kullanılmıştır. Islak metot Floresans MPI Testleri 14A floresans manyetik toz ile gerçekleştirilmiştir.

2.2 Islak Metot Floresans Manyetik Parçacık Testi Uygulama Adımları:

2.2.1 Test Numunesinin Hazırlanması:

Test edilecek malzemenin üzerinde bulunan ve yanlış endikasyon-lara yol açabilecek pas, tortu, kir vb. şeylerin uzaklaştırılması için uygun çözücüler ile temizlenir.

2.2.2 Test Örneğinin Mıknatıslanması:

Test edilecek malzemenin şekline ve konfigürasyonuna bağlı olarak mıknatıslanmanın nasıl yapılacağı belirlenmelidir. Yüzey ve yüzeye yakın süreksizliklerin tespitinin çözünürlüğü mıknatıslanma düzeyi ile doğru orantılıdır. Bundan dolayı pratikte mıknatıslanma doyunluğunun yaklaşık %40’ı olabilecek bir mıknatıslanma düzeyinde çalışılması yeterli olmaktadır. Literatürde doyunluk düzeyinin %40’ında çalışılması durumunda derinliği yüzeye 2,5mm’ye kadar olan süreksizlikler kolayca tespit edilebilmektedir.

2.2.3 Manyetik Sıvının Uygulanması:

Islak Metot Floresans Manyetik Parçacık Testi’nde homojen halde bulunan manyetik sıvı mıknatıslanma sırasında test örneği üzerine uygulanır. Sıvı manyetik parçacık akışının süreksizlikleri tespit edilmesinde önemi olduğu için kontrollü bir akış gerçekleştirilmelidir.

2.2.4 Süreksizliklerin Görüntülenmesi Ve Raporlanması:

Test edilecek malzeme manyetik sıvının akışı esnasında mıknatıslanır ve bu sırada görüntüleme yapılır. Elde edilen görüntülemeler yorumlanarak süreksizlikler raporlanır.

2.2.5 Demanyetizasyon:

Test tamamlandıktan sonra malzeme kalan manyetikliği gidermek amacıyla demanyetizasyon işlemi yapılmaktadır. Böylece malzemenin kullanım alanında manyetiklikten kaynaklanabilecek sorunların oluşması engellenir.

Manyetik alana paralel olan süreksizlikler akı kaçacağına neden olmayacağı için test sırasında gözlemlenmemektedir. Bu nedenle kusur tespiti yapabilmek için uygun manyetik alanı sağlamak gerekmektedir.

Islak Metot Floresans Manyetik Parçacık Testinde, referans blok üzerinde bulunan farklı özelliklere sahip yüzey ve yüzey altı kusurları tespit etmek amacıyla dairesel ve boyuna olmak üzere farklı manyetik alanlar uygulanmış ve böylece her iki yönde bulunan yüzey ve yüzey altı kusurlar gözlemlenmiştir. Boyuna mıknatıslayıcı akımda test parçası uzunlamasına mıknatıslanmakta ve bobin kullanımı ile gerçekleşmektedir.

3. TEORİK HESAPLAMALAR

3.1 Referans Blok İçin Dairesel Akım Hesabı

Islak Metot Floresans MPI Testinde dairesel akım hesabı için referans bloğun genişlik-kalınlık ölçümleri Şekil 3'te gösterildiği gibi yapılmıştır. Bloğun; genişliği 1,25 inç ve kalınlığı 0,36 inç olarak ölçülmüştür. Ölçülen geometri özelliklerinin referans bloğun standartları ile uyumlu olduğu gözlemlenmiştir.



Şekil 3: Referans Blok Ölçümleri

Islak Metot Floresans MPI Test için gerekli olan akım değerlerini hesaplama adımları aşağıda verilmiştir ve Denklem 1 ve Denklem 2 kullanılmıştır.

$$\text{Minimum akım değeri} = (\text{Köşegen veya çap uzunluğu}) \times 500 \quad (1)$$

$$\text{Maksimum akım değeri} = (\text{Köşegen veya çap uzunluğu}) \times 800 \quad (2)$$

Referans bloğun köşegen uzunluğu Denklem 3’de hesaplanmıştır.

$$\text{Köşegen Uzunluğu: } \sqrt{(0,36)^2 + (1,25)^2} = 1,3 \text{ inç} \quad (3)$$

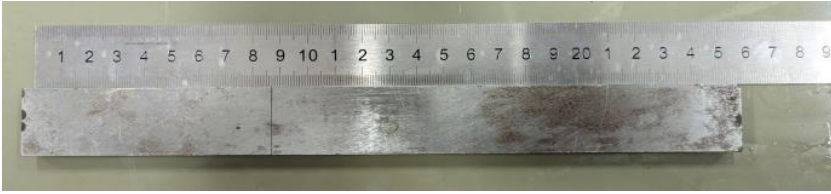
Ardından referans blok köşegen uzunluğu, standartlarda verilen minimum akım değeri için (Denklem 1) 500 ile maksimum akım değeri için (Denklem 2) 800 değeri ile çarpılarak test için gerekli mıknatıslayıcı akım değerleri bulunmuştur.

$$1,3 \times 500 = 650 \text{ Amper} \quad (1)$$

$$1,3 \times 800 = 1040 \text{ Amper} \quad (2)$$

Böylece testte kullanılacak referans bloğu mıknatıslamak için gerekli olan akım değerleri; 650 A ve 1040 A olarak bulunmuştur.

3.2 Referans Blok İçin Boyuna Akım Hesabı



Şekil 4: Referans Blok Uzunluk Ölçümü

Islak Metot Floresans MPI Testi’nde boyuna akım hesabı için referans bloğun uzunluk ölçümleri Şekil 4’te ve genişlik ölçüsü Şekil 3 (a)’de gösterildiği gibi yapılmıştır. Bloğun; uzunluğu 10 inç ve genişliği 1,25 inç olarak ölçülmüştür. Ölçülen geometri özelliklerinin referans bloğun standartları ile uyumlu olduğu gözlemlenmiştir. Islak Metot Floresans MPI Test için gerekli olan akım değerlerini hesaplama adımları aşağıda verilmiştir. Öncelikle Denklem 4 kullanılarak Amper-Sarım miktarı hesaplanmıştır.

$$\text{Amper sarım değeri} = \frac{K}{D} \quad (4)$$

Verilen formülde;

L: Parçanın uzunluğu,

D: Parçanın genişliği,

K: Tüm boyuna mıknatıslanmalar için K faktörü sabit bir sayı olup hesaplamalarda 45.000 olarak kullanılmıştır.

Denklem 4'te verilen formüle referans blok değerleri yerine yazıldığında Amper-Sarım miktarı 5625 olarak hesaplanmıştır.

$$\frac{45000}{\frac{10}{1,25}} = 5625 \text{ Amper-Sarım} \quad (4)$$

Böylece Islak Metot Floresans MPI Testinde kullanılacak Amper-Sarım miktarı belirlenmiştir. Floresans MPI Test için gerekli olan mıknatıslayıcı akım değeri Amper-Sarım miktarının, deneyde kullanılan Bobin Sarım sayısına bölünmesi ile hesaplanmaktadır. Deneylerde 4 sarım bobin kullanılmıştır. Gerekli olan mıknatıslayıcı akım Denklem 5 kullanılarak hesaplanmıştır.

$$\frac{5625}{4} = 1406 \text{ Amper} \quad (5)$$

Hesaplamalar sonucunda boyuna mıknatıslayıcı akım değeri ~1400 Amper bulunmuştur. Ege Üniversitesi Havacılık Meslek Yüksek Okulu NDT Laboratuvarı'nda bulunan cihaz maksimum 1000 Amperde çalıştığı için hesaplamalar ile elde edilen ~1400 A yerine 1000 A kullanılmıştır.

Aşağıda verilen Tablo 2, deneyde kullanılacak olan dairesel ve boyuna akım değerlerini göstermektedir. Denklemler ile hesaplanan amper değerleri referans alınarak oluşturulmuştur.

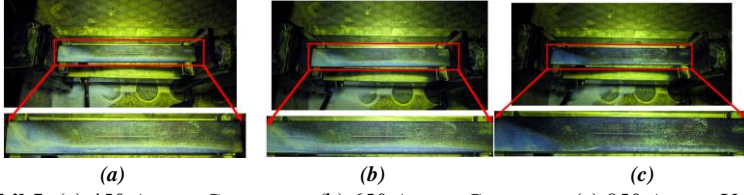
Tablo 2: Deneysel Çalışmada Uygulanan Akım Değerleri

Boyuna Mıknatıslanma		Dairesel Mıknatıslanma	
Test-1	600 Amper	Test-4	450 Amper
Test-2	800 Amper	Test-5	650 Amper
Test-3	1000 Amper	Test-6	850 Amper

4. DENEYSEL SONUÇLAR

4.1 Dairesel Mıknatıslanma

Dairesel mıknatıslanma kullanılarak yapılan Islak Metot Floresans MPI Testi'nde sırasıyla referans bloğa 450, 650 ve 850 Amper mıknatıslayıcı akım verilmiştir. Şekil 5 (a)'da referans bloğa 450 Amper mıknatıslayıcı akım verilmesinin ardından elde edilen görüntü, (b)'de referans bloğa 650 Amper mıknatıslayıcı akım verilmesinin ardından elde edilen görüntü ve (c)'de referans bloğa 850 Amper mıknatıslayıcı akım verilmesinin ardından elde edilmiştir.

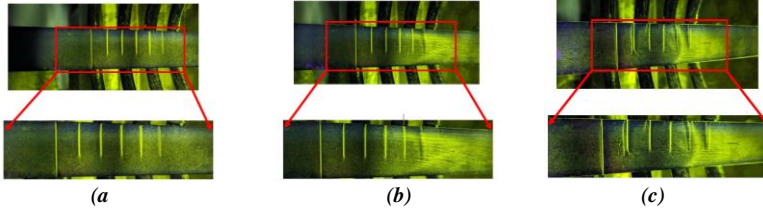


Şekil 5: (a) 450 Amper Görüntüsü, (b) 650 Amper Görüntüsü (c) 850 Amper Yakın Görüntüsü

4.2 Boyuna Mıknatıslanma:

Boyuna mıknatıslanma ve bobin kullanılarak yapılan Islak Metot Floresans MPI Testi'nde sırasıyla referans bloğa 600, 800 ve 1000 Amper mıknatıslayıcı akım verilmiştir.

Şekil 6 (a)'da referans bloğa 600 Amper, (b)'de referans bloğa 800 Amper ve (c)'de referans bloğa 1000 Amper mıknatıslayıcı akım verilmesinin ardından elde edilmiştir.



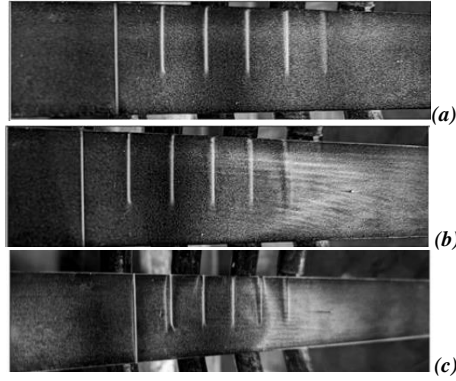
Şekil 6 (a) 600 Amper Görüntüsü (b) 800 Amper Görüntüsü (c) 1000 Amper görüntüsü

5. GÖRÜNTÜ ANALİZLERİ

Islak Metot Floresans MPI Testleri'nde 450 A, 650 A ve 850 A mıknatıslayıcı akım ile elde edilen referans bloğa ait görüntüler MATLAB ortamına aktarılmış ve sonrasında test görüntü dosyaları ön işleme teknikleri uygulanmıştır. Burada resim kenarları ve ince detayları başka bir deyişle referans blok üzerinde yer alan yapay kusurların daha iyi görüntülenmesi amacıyla “Alçak Geçiren Filtre”, “Medyan Filtre”, “Sobel Filtre”, “Prewitt Filtre” ve “Yüksek Artırıcı Filtre” kullanılmıştır. Testlerde uygulanan akımlara ait resimlerin ilk olarak görüntü ön işlemleri gerçekleştirilmiş sonrasında filtreler ile referans bloğa ait görüntüler üzerindeki yapay kusurların ayırt edilmesi ve net görüntülenmesi sağlanmıştır. Böylece farklı mıknatıslayıcı akımlardan elde edilen görüntülerdeki yoğunluk değişiklikleri ve detayları netleştirilmiştir. Görüntü analiz çalışmaları sırasında kullanılan filtreler içerisinde en iyi sonucu veren yüksek artırıcı filtredir. 450 A, 650 A ve 850 A'lik dairesel mıknatıslayıcı akım için yüksek artırıcı filtre uygulanmış görüntüler Şekil 7'de verilmiştir. 600 A, 800 A ve 1000 A'lik boyuna mıknatıslayıcı akım için yüksek artırıcı filtre uygulanmış görüntüler Şekil 8'de verilmiştir.



Şekil 7: Yüksek arttırıcı filtre uygulanmış dairesel mıknatıslayıcı akım görüntüsü (a) 450 A, (b) 650 A, (c) 850 A



Şekil 8: Yüksek arttırıcı filtre uygulanmış boyuna mıknatıslayıcı akım görüntüsü (a) 600 A, (b) 800 A, (c) 1000 A

6. SONUÇ

Çalışma kapsamında elde edilen akım değerleri istatistiksel olarak yorumlanmış ve elde edilen sonuçlar formülize edilmiştir. Referans blok için farklı alternatif akım değerleri uygulanarak test kalitesini etkileyen parametreler için veri setleri elde edilmiştir. Ayrıca uygulanan akım ve yönü arasındaki ilişkiler analiz edilmiştir.

Hesaplamalarda sonucunda; dairesel mıknatıslanma akımı değeri 650-1040 A aralığındayken elde edilen görüntülerin analizleri sonucunda 850 A'lik mıknatıslayıcı akımın referans blokta bulunan yapay kusurların görüntülenmesinde yeterli olabileceği gözlenmiştir. Boyuna mıknatıslanma akımı değeri hesaplamalarda 1406 A iken elde edilen görüntülerin analizleri sonucunda 1000 A'lik mıknatıslayıcı akım ile referans blokta bulunan yapay kusurların görüntülenebilecektir. Belirli bir akım değerinden sonra ise görüntü netliği ve keskinliğinde önemli bir artış olmayıp satürasyona gittiği görülmüştür. Burada uygulanması gereken ideal mıknatıslanma akım değeri elde edilmiştir.

Testler sırasında alınan görüntü dosyalarına ön işleme teknikleri uygulanarak elde edilen işlenmiş görüntüler ile sonuçlar karşılaştırılmış ve süreç optimize edilmiştir. Bu durum MPI operatörünün Floresans Manyetik Parçacık Testi'ni daha kısa sürede ve yüksek bir performansla yapmasını sağlayacaktır. Dolayısıyla operatörler test sonucunda malzemeler üzerindeki ve/veya yüzey altı kusurlardan daha kaliteli görüntüler alabileceklerdir.

Islak Metot Floresans Manyetik Parçacık Testlerinde mıknatıslayıcı akımın yükselmesi ile birlikte görüntü netliğinin ve keskinliğinin arttığı bilinmektedir. Bu çalışmada referans blok testleri ile görüntü netliği ve keskinliğini sağlayacak mıknatıslayıcı akımı belirlenmiştir. Böylece test yapılacak parçalara veya malzemelere daha yüksek mıknatıslayıcı akım verilmesi engellenmiş olacaktır. Diğer taraftan elde edilen sonuçlar operatörler için yardımcı bir rehber niteliği taşımakla birlikte NDT'de MPI uygulamalarının iyileştirilmesine katkı sağlayacaktır. Bu durum NDT operatörlerinin Islak Metot Floresans Manyetik Parçacık Testleri'nde hangi parametrelere dikkat etmeleri gerektiğini ve bu parametrelerin ne kadar etkili olduğunu kavramasını kolaylaştıracaktır. İleriye dönük çalışmalar kapsamında bir TÜBİTAK projesinde geliştirilen ve ileri görüntüleme özelliklerine sahip Islak Metot MPI Test cihazıyla daha detaylı parametre analizleri yapılması planlanmaktadır.

Teşekkürler

Yazarlar tarafından herhangi bir Teşekkürler beyan edilmemiştir.

Çıkar çatışması

Yazarlar tarafından herhangi bir çıkar çatışması beyan edilmemiştir.

Yazar katkıları

Alperen DOĞRU, fikir/kavram oluşturulması, yöntem planlanması, makalenin organizasyonu, deneysel çalışmalar için kaynakların sağlanması, sonuçların değerlendirilmesi ve makalenin dil bilgisi ve içerik kontrolü. Coşkun HARMANŞAH, fikir/kavram oluşturulması, yöntem planlanması, literatür taraması, makale hazırlık çalışmaları, sonuçların değerlendirilmesi ve makalenin dil bilgisi ve içerik kontrolü. Esmâ Nur SAVRANGÜLER, literatür taraması, deneysel çalışmalar için kaynakların sağlanması, makale hazırlık çalışmaları, makalenin dil bilgisi ve içerik kontrolü. Yavuz ÖZTÜRK, makalenin organizasyonu, literatür taraması, deneysel çalışmalar için kaynakların sağlanması, sonuçların değerlendirilmesi ve makalenin dil bilgisi ve içerik kontrolü. Feti ADAR, makale hazırlık çalışmaları, deneysel çalışmalar için kaynakların sağlanması, literatür taraması, sonuçların değerlendirilmesi.

REFERANSLAR

- [1] Kaynak Eğitim ve Muayene Merkezi. (2023). Tahribatlı muayene eğitimleri, Erişim Tarihi: Kasım 2023, <https://www.kemm.org.tr/egitimler-tahribatli-muayene-egitimleri.html>
- [2] TMMOB. (2023). Tahribatsız muayene hizmetlerimiz, Erişim Tarihi: Kasım 2023, <https://www.mmo.org.tr/ankara/tahribatsiz-muayene-hizmetlerimiz>
- [3] YETİŞTİREN, H., ZEREN, A., & FEYZULLAHOĞLU, E. (2007). Taşıma tekniği ekipmanlarının bakımında kullanılan tahribatsız muayene yöntemleri. *Mühendis ve Makina*, 48 (571), 17-24.
- [4] Tu, Z. (2019). Application of Magnetic Particle Inspection in Boiler Inspection. *Appl. Energy. Technol.*, 27-29.
- [5] Gubelj, N., Cvetic, M., Božić, Ž., & Predan, J. (2017). Application of structural integrity assessment procedure on an axle pin of a wind turbine. *Fatigue & fracture of engineering materials & structures*, 40(8), 1284-1294.
- [6] Weizenecker, J., Gleich, B., Rahmer, J., Dahnke, H., & Borgert, J. (2009). Three-dimensional real-time in vivo magnetic particle imaging. *Physics in Medicine & Biology*, 54(5), L1.
- [7] Anonim. (2023). Tahribatsız Muayene, Erişim Tarihi: Temmuz 2023, <https://mak-ndt.com/k/14/Manyetik-Parcacik-Test-Urunleri-.html>
- [8] Türk Hava Yolları. (2010). Manyetik Parçacık Seviye 1.
- [9] Downes, G. (2003). DC or AC Magnetising Waveforms in Magnetic Particle Inspection. *Insight NDT Equipment Ltd.*
- [10] Ürün Föyü: MAG 20 Serisi MPI Cihazı. (2015). Magnaflux: <https://magnaflux.in/IN-Files/Product-Data-Sheets---Equipment/MAG-20-Series-Magnetic-Particle-Inspection-Equipment-Product-Data-Sheet-300715-English.pdf>
- [11] Magnetic Particle Test Bar. (2023). Magnaflux: https://www.magnaflux.com/Files/Product-DataSheets/Accessories/Magnetic-Particle-TestBar_Product-Data-Sheet_English.pdf



CHAPTER 13

Aviation Technologies and Applications
E-ISBN:978-605-338-471-7
2025, chap. (13), pp.205-224.

NUMERICAL AND EXPERIMENTAL INVESTIGATIONS ON THE RESPONSE AND COMPRESSIVE STRENGTH OF FOAM- CORED SANDWICH STRUCTURES SUBJECTED TO MEDIUM- VELOCITY IMPACT

Abdullah İKİZ^{1,*}, Uğur YOLUM², Zahit MECİTOĞLU³

ABSTRACT

The study deals with the material behavior of foam-cored sandwich composites under medium-velocity impact loading conditions. The main focus of this paper is to develop a numerical model based on the finite element method that estimates impact damage and residual compression strength of foam-core/composite-facesheet sandwich structures subjected to medium-velocity impact. It is well known that sandwich materials are vulnerable to out-of-plane loads like foreign object impacts. Medium velocity level of impact, which refers to 10-50 m/s, is one of the out-of-plane load sources that an aircraft can face as hail strikes or runway debris on the ground. Most of the studies focus on low-velocity (0-10 m/s) or high-velocity (50-500 m/s) impacts, and less attention is given to impacts at medium levels of velocity. To verify the numerical model, impact event and post-impact characteristics are examined experimentally as well. Two separate test activities were modeled in Abaqus/Explicit by establishing representing simulations and by creating corresponding material and damage models of different constituents of the sandwich structure. Delamination is the major damage mode under impact loading. Therefore, the cohesive zone modeling method was utilized to get delamination damage. Hashin damage initiation criteria were used to model in-plane behavior, and the crushable foam model was assigned for foam modeling. Residual compressive strength variation according to different impact velocities was investigated numerically. Results show that the foam-cored sandwich structure loses almost 50% of its strength after 10 m/s velocity impact, but it still has remarkable load-carrying capacity even after 40 m/s velocity impact.

Keywords: medium-velocity, impact, foam-core, sandwich, CAI

*Corresponding Author: ikizab@itu.edu.tr

¹ 0009-0004-6324-2450, Istanbul Technical University & Turkish Aerospace, Istanbul, Türkiye

² 0000-0001-7230-4458, Turkish Aerospace, Ankara, Türkiye

³ 0000-0002-9957-9854, Faculty of Aeronautics and Astronautics, Istanbul Technical University, Türkiye

1. INTRODUCTION

Sandwich structures are frequently preferred materials in the aviation industry. Their advantageous properties of low weight and higher flexural stiffness are the main reasons for their widespread usage. But sandwich materials have some drawbacks due to their layered structure which makes them vulnerable to out-of-plane loads like foreign object impacts. The outer skin of an aircraft is generally made from sandwich panels to resist compression and buckling loading, but these exterior regions are more likely to be exposed to impact events like runway debris, hail and bird strikes in service. Some of them create internal cracks and interlaminar debonding faces that cannot be detected by visual inspection. Furthermore, it is mandatory according to the certification process to prove that aircraft structures can withstand the limit load even in damaged situations. Therefore, it is critical to design skin panels safely in terms of impact damage.

There are numerous studies in the literature that investigate various aspects of composite materials and sandwich structures and analyze them with different methods. Analytical methods developed in the literature to examine impact damage focus on simplified analyses such as the spring-mass model, energy conservation model, and wave propagation model, and contact laws used to obtain the force and pressure distribution resulting from contact between two structures during impact. Abrate [1] reviewed different simplified models and contact laws in his work. Sun et al. [2-4] developed new contact laws in their sequential studies and used them for low-velocity impact. Choi and Lim [5] compared existing analytical methods and proposed their own linearized contact law. There are also experimental studies examining the impact damage of composite materials. The behavior of different core and facesheet material combinations under impact conditions was researched in controlled test environments. Anderson and Madenci [6] examined the low-velocity impact behavior of sandwich structures with carbon fiber-reinforced composite facesheets according to facesheet thickness, core material, and density. Chen and Hodgkinson [7] tested the low- and high-velocity impact damage of various composite plates. Aktas et al. [8] included post-impact strength in their research as well as impact damage.

Due to the inadequacy of analytical methods in analyzing complex situations and the high cost of experimental methods, interest in the development of numerical analysis methods has increased recently. Iannucci and Willows [9] examined the impact behavior of woven fabric

composite materials in the numerical model they created using ready software with an energy-based impact mechanics approach. Maimi et al. [10] modeled the in-plane behavior of composite materials, while Gonzalez [11] simulated delamination damage using cohesive elements. Similarly, impact mechanics has been addressed in many aspects in studies using the progressive damage model. Long et al. [12] studied the low-velocity impact behavior of foam sandwich structures. Accurately estimating the damage to the structure in terms of impact mechanics has paved the way for determining the remaining strength after the impact. Tan et al. [13] developed three stages in their numerical model: first capturing the impact damage, then preparing the damaged part for the compression test with new boundary conditions, and finally determining the compressive strength. In this way, the decrease in the strength of the structure can be predicted even when the damage is not visible at low speeds. Using a similar method, the post-impact strength of foam-cored sandwich structures was also determined in other aspects [14-15].

On the other hand, experimental and numerical studies examining high-velocity impact damage also considered the fact that the impactor penetrates the structure. Ivanetz [16] analyzed the high-velocity impact resistance of foam core and glass fiber-reinforced composite facesheet structures with a numerical model. Nasirzadeh and Sabet [17] exposed foam core sandwiches of different densities to high-velocity impact and obtained the performance of the structure with experimental methods.

The main focus of this study is to develop a numerical model based on the finite element method that estimates impact damage and residual compression strength of foam-core/composite-facesheet sandwich structures subjected to medium-velocity impact. Most of the studies focus on low-velocity (0-10 m/s) or high-velocity (50-500 m/s) impacts, and less attention is given to impacts at medium levels of velocity which can reflect hail strikes and runway debris on the ground. Therefore, a velocity range of 10-50 m/s was investigated in the scope of this study. To verify the numerical model, impact event and post-impact characteristics are examined experimentally as well. It is aimed to reduce the need for expensive and time-consuming test campaigns in terms of impact resistance during the design stage of aircraft skin structures by increasing the reliability of the analysis results of the numerical model.

2. NUMERICAL MODEL

The numerical analysis study performed in Abaqus/Explicit includes the determination of material properties and damage models of sandwich constituents and the creation of virtual test setups for impact and compression after impact (CAI) tests. Accordingly, finite element method implementations were considered to get a more accurate and easier solution.

2.1. Material Properties and Damage Models

2.1.1. Sandwich Structure

Sandwich structure in mesoscale finite element modeling requires three different material properties and corresponding damage behavior definitions for the facesheet, interface, and core which are the main constituents of a sandwich. Fiber-reinforced composite laminated facesheets, epoxy-based film adhesive, and foam core were used as the main components of the investigated sandwich in the scope of this study.

Because the sandwich facesheet is a laminated composite, it contains intralaminar and interlaminar scopes of modeling which refer to fiber or matrix failure and delamination, respectively. The continuum damage mechanics (CDM) approach was used to represent the in-plane behavior of composite laminate. Elastic properties according to the fiber orientation angle of the composite layup were determined by related characterization tests and listed in Table 1. The Hashin damage model was implemented as damage initiation criteria which consists of mainly 4 criteria representing 4 different damage modes such as fiber failure under tension and compression and matrix failure under tension and compression. Mathematical expressions defining the Hashin model were given as [18]

Fiber failure under tension ($\sigma_{11} \geq 0$):

$$\left(\frac{\sigma_{11}}{X_{1+}}\right)^2 + \alpha \left(\frac{\tau_{12}}{S_{12}}\right)^2 = 1 \quad (1)$$

Fiber failure under compression ($\sigma_{11} < 0$):

$$\left(\frac{\sigma_{11}}{X_{1-}}\right)^2 = 1 \quad (2)$$

Matrix failure under tension ($\sigma_{22} \geq 0$):

$$\left(\frac{\sigma_{22}}{X_{2+}}\right)^2 + \left(\frac{\tau_{12}}{S_{12}}\right)^2 = 1 \quad (3)$$

Matrix failure under compression ($\sigma_{22} < 0$):

$$\left(\frac{\sigma_{22}}{2S_{13}}\right)^2 + \left[\left(\frac{X_{2-}}{2S_{13}}\right)^2 - 1\right]\left(\frac{\sigma_{22}}{X_{2-}}\right)^2 + \left(\frac{\tau_{12}}{S_{12}}\right)^2 = 1 \quad (4)$$

After damage is initiated, a damage evolution phase takes place until the final failure of the material. A fracture-energy-based linear softening law was provided as the damage evaluation law which can be described graphically as shown in Fig. 1. The material behaves elastically to the damage initiation point as the load increases. After that point, damage begins to grow according to the linear softening law which results in a stiffness reduction of the material. If loading continues to the critical displacement or energy level, the material faces a final failure.

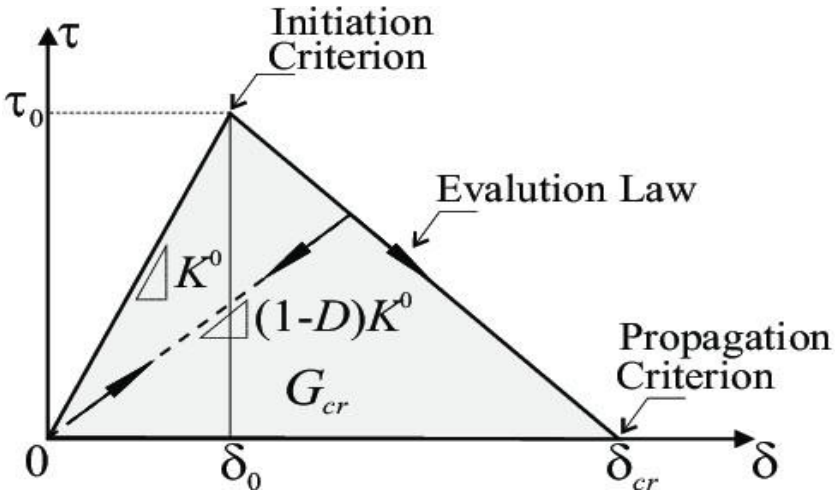


Figure 1. Damage model in terms of initiation and evaluation [19]

The interlaminar behavior of laminate was specified with the cohesive zone model (CZM) method which utilizes traction-separation law for damage initiation and a fracture mechanics-based approach for damage evaluation. Mixed-mode loading was considered according to B&K law [20]. The adhesive between the facesheet and core was modeled in terms of CZM as well. Interlaminar properties of the facesheet and adhesive characteristics of the interface are given in Table 1.

CHAPTER 13: NUMERICAL AND EXPERIMENTAL INVESTIGATIONS ON THE RESPONSE AND COMPRESSIVE STRENGTH OF FOAM-CORED SANDWICH STRUCTURES SUBJECTED TO MEDIUM-VELOCITY IMPACT

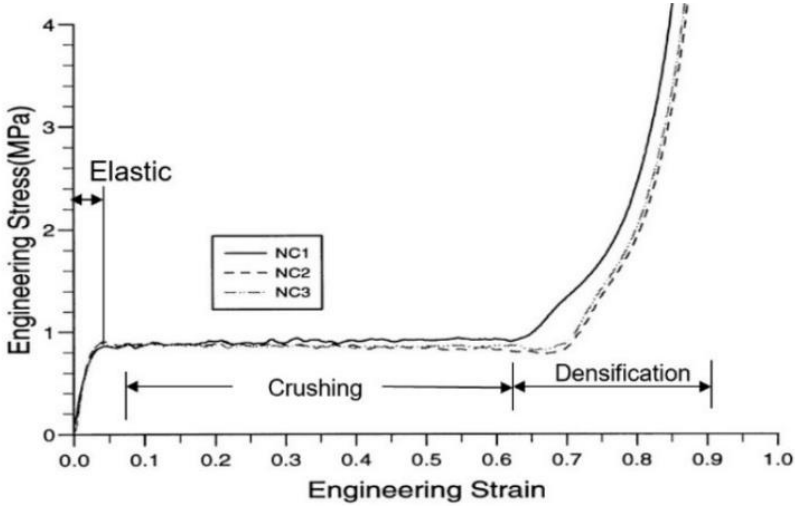


Figure 2. Core material behavior under compression loading [21]

The crushable foam plasticity model available in Abaqus/Explicit was used to identify core damage properties. Representing the material behavior of a closed-cell foam shows three main regimes during compression loading such as elastic, crushing, and densification, as shown in Fig. 2. Other required parameters for the crushable foam model are included in Table 1.

Table 1. Material properties

Definition	Properties
Intralaminar	
Elastic	$E_1 = 120 \text{ GPa}$, $E_2 = 6 \text{ GPa}$, $\nu_{12} = 0.3$, $G_{12} = G_{13} = 3 \text{ GPa}$, $G_{23} = 1.8 \text{ GPa}$
Strength	$X_{1+} = 1.4 \text{ GPa}$, $X_{1-} = 0.9 \text{ GPa}$, $X_{2+} = 40 \text{ MPa}$, $X_{2-} = 150 \text{ MPa}$, $S_{12} = S_{13} = 70 \text{ MPa}$
Fracture	$G_f^{1+} = 81.5 \text{ kJ/m}^2$, $G_f^{1-} = 106.3 \text{ kJ/m}^2$, $G_f^{2+} = 0.28 \text{ kJ/m}^2$, $G_f^{2-} = 0.79 \text{ kJ/m}^2$
Interlaminar	
Elastic	$E_m = 7.63 \text{ GPa}$, $G_m = 2.63 \text{ GPa}$, $E_{nn} = 763 \text{ kN/mm}^3$, $E_{ss} = E_{tt} = 263.1 \text{ kN/mm}^3$
Strength	$t_n^0 = 40 \text{ MPa}$, $t_s^0 = t_t^0 = 70 \text{ MPa}$
Fracture	$G_I^C = 0.28 \text{ kJ/m}^2$, $G_{II}^C = G_{III}^C = 0.79 \text{ kJ/m}^2$, $\eta = 1.45$
Adhesive	
Elastic	$E_a = 3.12 \text{ GPa}$, $G_a = 0.9 \text{ GPa}$, $E_{nn} = 1.64 \text{ kN/mm}^3$, $E_{ss} = E_{tt} = 4.74 \text{ kN/mm}^3$
Strength	$t_n^0 = 72 \text{ MPa}$, $t_s^0 = t_t^0 = 42 \text{ MPa}$
Fracture	$G_I^C = 1.1 \text{ kJ/m}^2$, $G_{II}^C = G_{III}^C = 3.8 \text{ kJ/m}^2$, $\eta = 2.3$
Core	
Elastic	$E_f = 22 \text{ MPa}$, $\nu = 0$
Strength	$\sigma_c^0 = 0.85 \text{ MPa}$, $P_c^0 = 0.82 \text{ MPa}$, $P_1 = 0.082 \text{ MPa}$

2.1.2. Auxiliary Components

In addition to the sandwich, other objects in impact test simulation like impactor, fixing clamps, and supporting plate were modeled as rigid bodies because their deformation was not of interest. A 10 mm-thick support plate is introduced with a cutout region in the middle. The clamp is represented as a cylinder with an 18 mm diameter and the impactor is a semi-ball with the same diameter (Fig. 3).

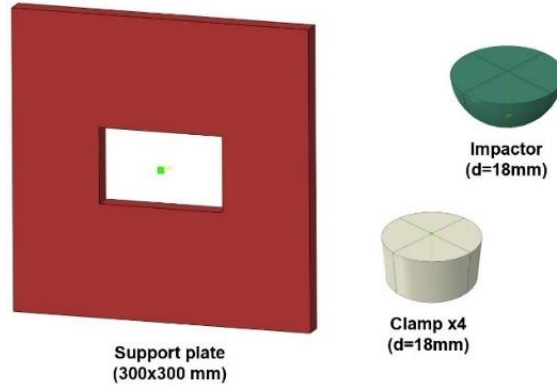


Figure 3. Models of auxiliary components used in impact test simulation

2.2. Simulations

2.2.1. Impact Test

A two-stage simulation was developed to reflect the impact and CAI test. Fig. 4 shows the schematic assembly of parts used in the impact test simulation. The rectangular support plate and the sandwich structure are placed on top of each other so that the directions passing through their midpoints coincide and there is no gap in between. Then, four clamps are positioned at the four corners of the sandwich structure. The ball is added to the assembly so that its end point and the middle point of the upper surface of the sandwich are aligned.

In the assembly created, one surface contact relationship was defined between the ball and the sandwich, one between the sandwich and the support plate, and four between the clamps and the sandwich structure. In this contact relationship, two basic features are defined: in the normal direction, so that the two parts do not pass through each other during the analysis, and in the tangential direction, representing the friction that will occur between the two parts. The tangential friction coefficient was taken as 0.3.

CHAPTER 13: NUMERICAL AND EXPERIMENTAL INVESTIGATIONS ON THE RESPONSE AND COMPRESSIVE STRENGTH OF FOAM-CORED SANDWICH STRUCTURES SUBJECTED TO MEDIUM-VELOCITY IMPACT

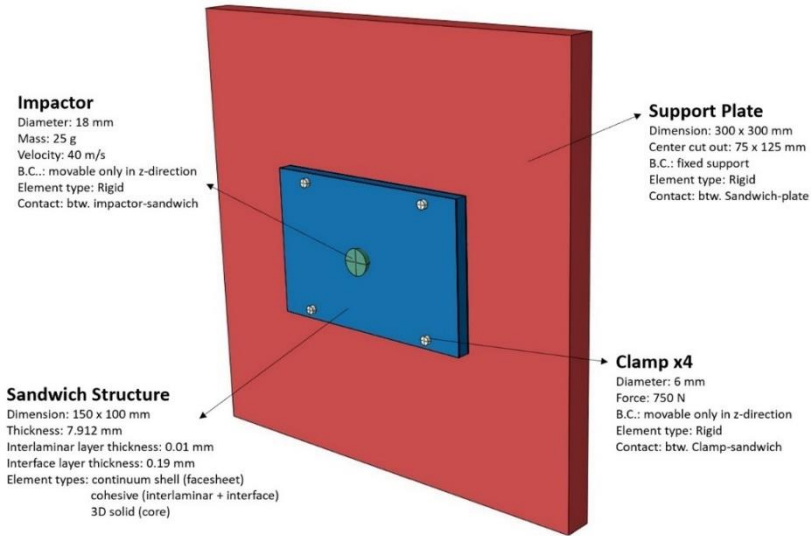


Figure 4. Setup of impact test simulation

All displacements of the support plate are limited to fix all structures. Boundary conditions that allow only translational movement along the impact direction are assigned to the clamp and ball. Since the clamps will apply pressure to the sandwich structure, the displacement force has been defined to simulate this effect. In addition, a constant velocity was entered in one direction for the ball that would cause the impact.

2.2.2. Compression After Impact (CAI) Test

After running the impact simulation, the damaged sandwich part was put in a second simulation referring to the CAI test by using the “restart” option of Abaqus/Explicit. New boundary conditions were assigned to represent compression loading and to avoid out-of-plane buckling deformation during compression, as shown in Fig. 5.

In the numerical model, the impact simulation is copied exactly, and a new model is created. In the compression step, which is added after the impact step without changing the material properties, the boundary conditions and forces that are no longer needed are removed, and new required boundary conditions are defined.

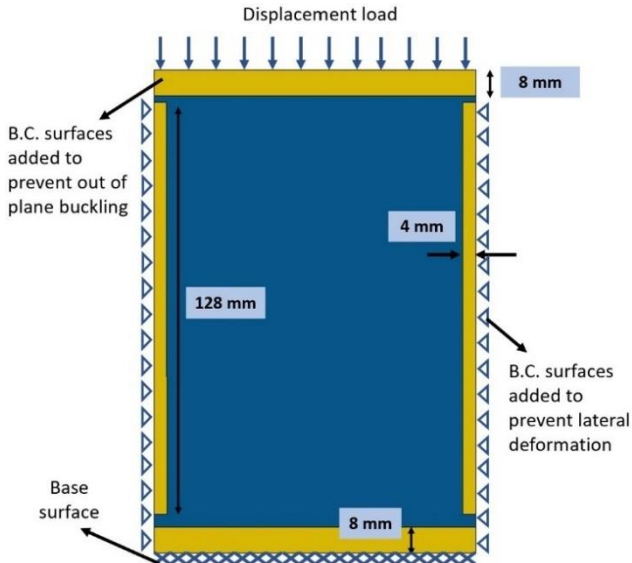


Figure 5. Schematic setup of compression after impact test simulation

On the other hand, one of the short edges is placed on the support plate and fixed in that direction, while a constant-speed compressive force (in the form of displacement) is applied from the other short edge. There is no need to change the analysis type to static for the compression test, which can be considered quasi-static in nature. Considering the high material and geometric nonlinearities, it would be advantageous to continue the analysis with dynamic explicit [22]. By making the necessary adjustments, it is possible to simulate dynamic analysis as if it were stationary analysis. The most important arrangement is that a test that may actually take up to a few minutes can be simulated in a shorter time without deteriorating the accuracy of the results. Because trying to simulate a real-time test in dynamic analysis will require very serious computational effort, will take too long, and will not be efficient. For this reason, it is necessary to get faster results by reducing the simulation time without affecting the accuracy of the result. It should be guaranteed that inertial forces will not be effective in the analysis and kinetic energy will be kept close to zero. Thus, the quasi-stationary structure will be preserved.

2.3. FEM Implementations

Fiber-reinforced composite materials, by their nature, consist of fibers and resin at the micro level, while at the macro level they consist of layers of fabric stacked on top of each other. Due to their complex structure, the

CHAPTER 13: NUMERICAL AND EXPERIMENTAL INVESTIGATIONS ON THE RESPONSE AND COMPRESSIVE STRENGTH OF FOAM-CORED SANDWICH STRUCTURES SUBJECTED TO MEDIUM-VELOCITY IMPACT

scale at which composites will be modeled is important. When using the finite element method, three modeling scales can be mentioned in this sense: micro, meso, and macro- level modeling [23]. While fibers and matrix material are modeled in three dimensions at the micro level, fabric layers consisting of fiber and matrix at the meso scale are subject to modeling and material properties depending on the laying angle are defined for each layer. At the macro level, modeling occurs at the laminate level, fabric layers are not visible separately, and layer sequences are entered within the material properties. These three modeling scales are summarized in Fig. 6.

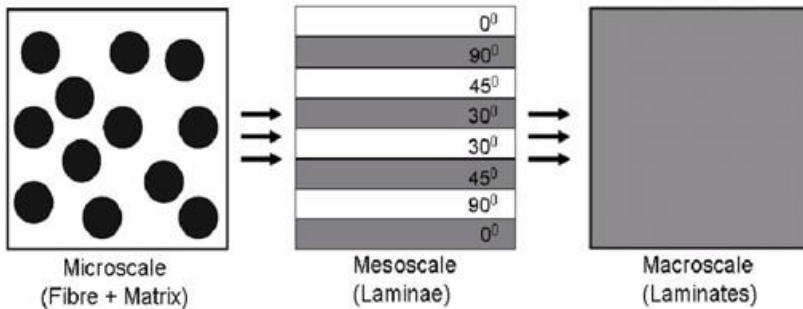


Figure 6. Modeling scales of composites

Since delamination becomes the most critical damage mode in a composite structure subjected to out-of-plane loads such as impact, the numerical analysis model must be able to detect interlaminar separation. Therefore, in order to see the delamination most accurately, the composite facesheets of the sandwich structure should be modeled at the mesoscale [23]. In this way, adhesion areas between layers and between the facesheet and core can be added to the model with a certain thickness at the same scale. Fig. 7 describes how the composite facesheet sandwich structure is modeled with the aforementioned method.

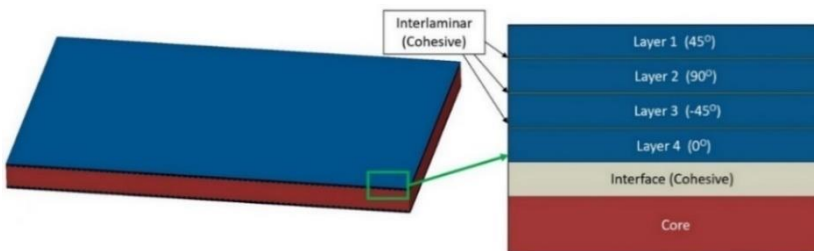


Figure 7. The model of the sandwich in thickness direction

Since the impact caused by small-sized foreign objects causes a very localized effect, it is important to divide the areas in contact with the impactor into smaller-sized elements. Since the impact effect decreases outward from the impact point, the regions close to the edge of the sandwich structure can be represented by relatively larger-sized elements compared to the middle region. Using different element sizes will also positively affect the solution speed of the numerical model. For this purpose, the in-plane incremental dimensioning method, proposed by Gonzalez et al. [22], will be used as well. A rectangular area of 60 mm x 60 mm in the center is divided by elements of 0.3 mm x 0.3 mm, while elements that are gradually increased in size are used outside this area (Fig. 8).

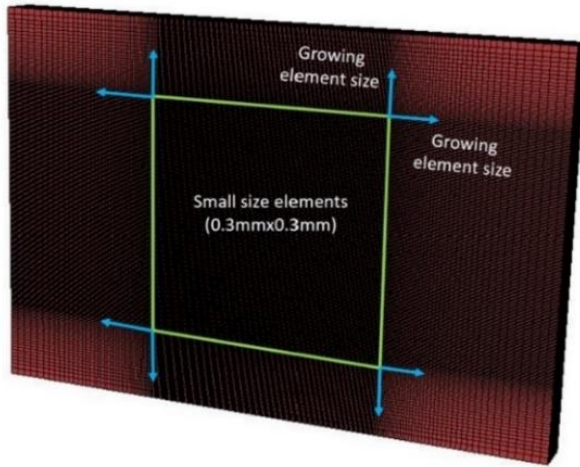
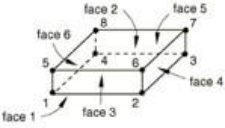
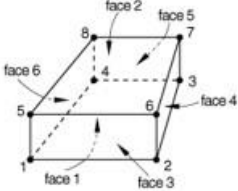
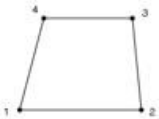


Figure 8. In-plane mesh dimensions of sandwich

The appropriate element type was used for each component forming the sandwich structure. The parts representing the composite facesheet fabric layers will be represented by the continuum shell element with 8 nodes called SC8R. The cohesive regions that form the adhesive material between the fabric layers and between the facesheet and the core will be modeled with the help of three-dimensional, 8-node cohesive elements called COH3D8. Since the core is the part that will undergo the most deformation, a three-dimensional, 8-node solid element coded C3D8R, which has the ability to control this deformation, will be used. Finally, the ball, clamp, and support plate, modeled as rigid, will be included in the mesh through a three-dimensional, 4-node, R3D4 rigid element. All mesh element types used are summarized in Table 2.

CHAPTER 13: NUMERICAL AND EXPERIMENTAL INVESTIGATIONS ON THE RESPONSE AND COMPRESSIVE STRENGTH OF FOAM-CORED SANDWICH STRUCTURES SUBJECTED TO MEDIUM-VELOCITY IMPACT

Table 2. Mesh element types

Material Model	Element Type	Element Presentation
Facesheet, Intralaminar	SC8R	
Facesheet, Interlaminar	COH3D8	
Interface	COH3D8	
Core	C3D8R	
Impactor, Clamp, Support Plate	R3D4	

3. EXPERIMENTAL STUDY

In addition to the numerical model, an experimental study was carried out to verify the numerical model. A rectangular-shaped sandwich plate with in-plane dimensions of 150mm x 100mm and with a foam core was manufactured as the test sample. Both upper and lower facesheets have four carbon-fiber-reinforced unidirectional prepreg plies which are stacked in orientation angle from outer to inner as [+45/0/-45/90]. The foam core material is Rohacell 51-WF produced from 6 mm thick PMI material, and the interface material between facesheet and core is a Cytotec film adhesive coded FM-300K with a thickness of 0.19 mm.

The properties of the sandwich layup and the manufactured part are shown in Fig. 9. Test samples were prepared based on the ASTM test standard D7766 [24]. The dimensions of the material to be manufactured, the lay-up of the composite laminate, and the thickness of the sample have been determined as recommended in the aforementioned standard. Since prepreg materials, by their nature, are semi-finished products impregnated with resin in predetermined proportions, their curing process must be done in an autoclave under controlled environmental conditions. For this reason, the composite facesheet, interface material, and core were packed on top of each other to form a sandwich structure and then cured in an autoclave. The manufacturing of the samples was carried out in the Ankara Kahramankazan facilities of TA-Turkish Aerospace.

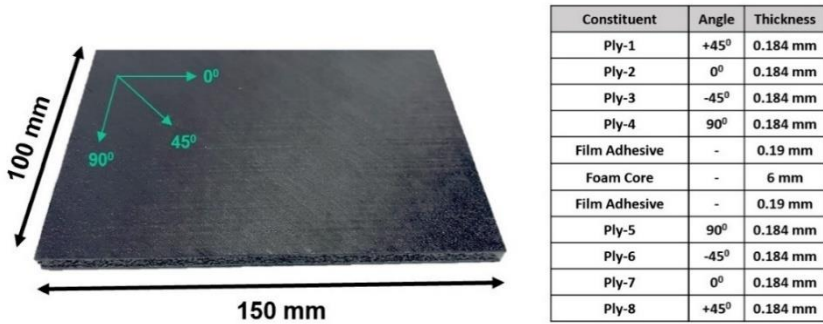


Figure 9. Dimensions, materials and stacking of the sample

3.1. Impact Test

A gas gun-based impact test mechanism of Composite Structure Laboratory of Faculty of Aeronautics and Astronautics at Istanbul Technical University was utilized for impact testing. The gas gun test machine consists of a gas tank, a 40-bar compressor, a 5-liter pressure vessel, a solenoid valve in capacity of maximum 100 bar, a horizontal barrel of 25 mm diameter, a velocity meter and a skeletal structure that serves for locating plate (Fig. 10).

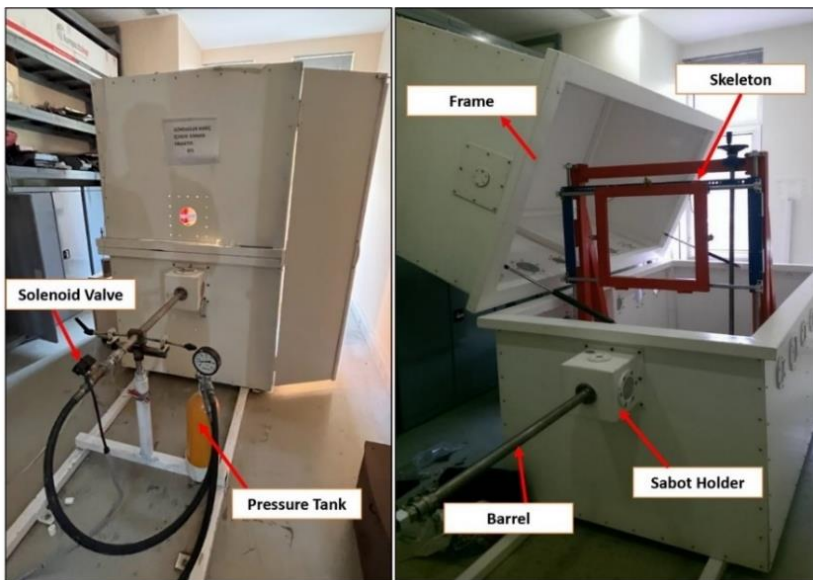


Figure 10. Gas gun impact test mechanism

CHAPTER 13: NUMERICAL AND EXPERIMENTAL INVESTIGATIONS ON THE RESPONSE AND COMPRESSIVE STRENGTH OF FOAM-CORED SANDWICH STRUCTURES SUBJECTED TO MEDIUM-VELOCITY IMPACT

A steel ball with a diameter of 18 mm (25 gram) was used as impactor and it was located in a sabot made of plastic which enables the ball to be centered properly. Four horizontal toggle clamps together with a steel supporting plate were attached to the skeletal structure in order to fix the sandwich sample, as shown in Fig. 11. The velocity of the impactor was kept at 40 m/s by arranging the pressure level.

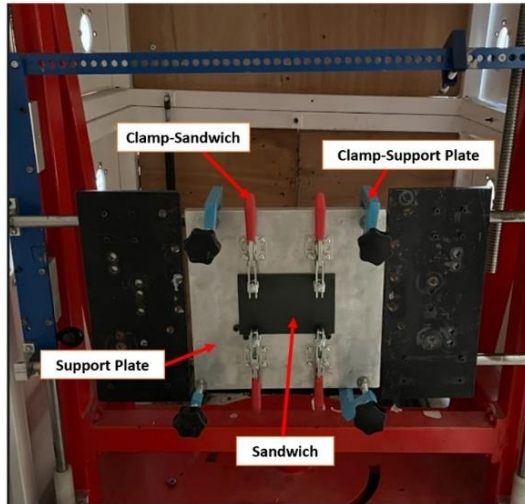


Figure 11. Sample installation to the test mechanism

3.2. Compression After Impact (CAI) Test

The universal test machine was used to determine the compressive strength of both damaged and undamaged samples. For preventing of out-of-plane buckling deformation, the sample sandwich plate was inserted in a 12-piece test fixture made of steel-machined parts according to [25], as shown in Fig. 12.

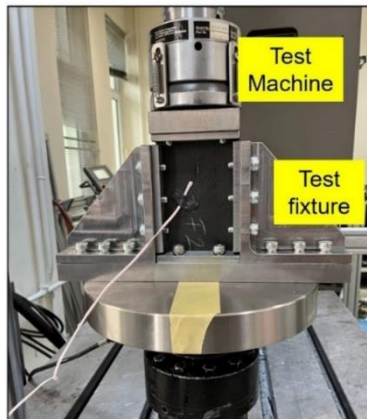


Figure 12. Compression after impact test fixture

4. RESULTS

The impact behavior of a foam-cored sandwich structure was investigated both numerically and experimentally in certain conditions. Damage area, damage modes, dent depth, strength variation after damage, and contact force history during impact are the parameters evaluated. Fig. 13 shows the comparison between the experimental and numerical results of impact damage at a 40 m/s impact velocity. It can be observed that the impact damage occurs in an ellipse shape in the direction of the orientation of the fibers on the top layer. Fiber breakage resulting from tensile elongation in this direction can be clearly detected. In addition, it can be concluded that there is a permanent deformation as a result of core crushing just below the broken fibers. According to the numerical model prediction of the damages, the damage caused by fiber tension extends in the 45°-angle direction as well. Although there is harmony with the experimental results in this respect, it can be seen that the numerical model underestimates the width of the damage. As shown by the green ellipse lines in the figures, the damage in the test samples is in the form of a thicker ellipse, while in the numerical model results it is in the form of a thinner ellipse.

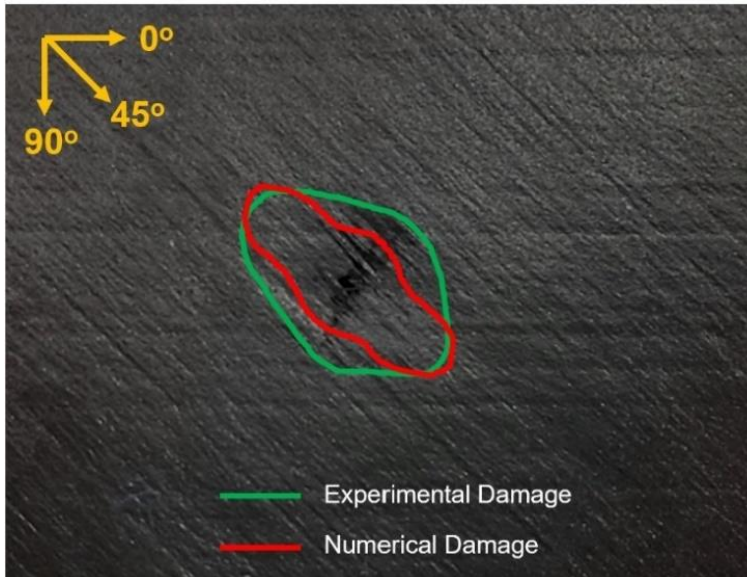


Figure 13. Damage on sample after impact test

Residual compression strength (after 40 m/s velocity impact) obtained experimentally and predicted numerically are listed in Table 3. The experimental value of compressive strength is lower than the numerical

CHAPTER 13: NUMERICAL AND EXPERIMENTAL INVESTIGATIONS ON THE RESPONSE AND COMPRESSIVE STRENGTH OF FOAM-CORED SANDWICH STRUCTURES SUBJECTED TO MEDIUM-VELOCITY IMPACT

one which is possibly due to a manufacturing defect that the sample may have. The numerical model analyses the sandwich in ideal conditions. But the decrease in strength after impact was calculated to be very close to experimental results. Both methods determine strength reduction at approximately 65%.

Table 3. Change in compressive strength

Method	Before Impact Strength	After Impact Strength	Decrease in Strength
Experimental	15 kN	5 kN	66%
Numerical	22 kN	8 kN	64%

Further numerical analyses with different medium-level velocities are performed separately. Fig. 14-15 shows the change in contact force according to contact duration and out-of-plane displacement with different impact velocities. It can be observed from Fig. 14 that contact duration decreases as velocity increases. In lower velocity impacts, it takes more time to end the interaction between the impactor and the sandwich. Moreover, the contact force not only rises with increasing velocity but also its peak value is seen at earlier phases of the whole impact time. Fig. 15 shows that out-of-plane displacement comes back less at 40 m/s velocity impact than at 10 m/s one which indicates more plastic deformation of the core and fiber breakage in the facesheet at higher velocity impact.

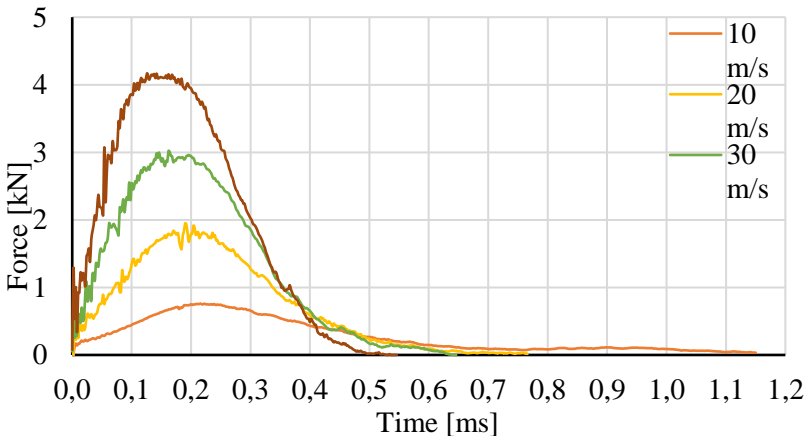


Figure 14. Force-time curves in different impact velocities

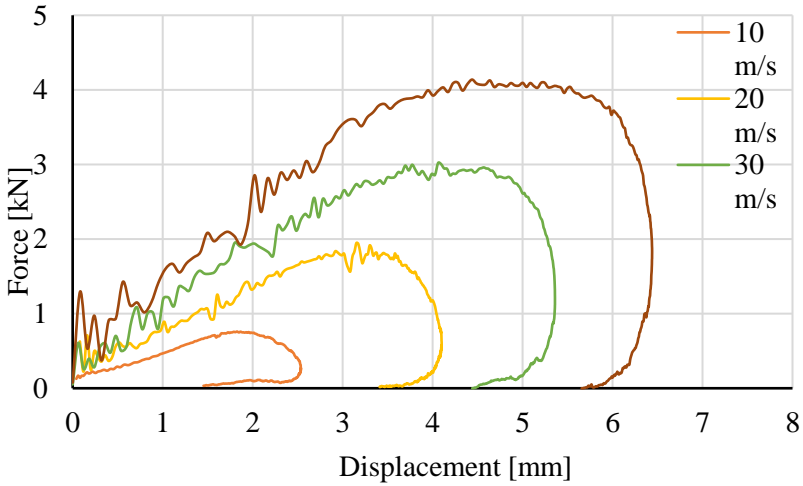


Figure 15. Force-displacement curves in different impact velocities

The reduction of the compression after impact strength with increasing velocity is shown in Fig. 16. An impacted sandwich loses almost 50% of its strength after just 10 m/s velocity impact which shows that impact damage has a significant effect on the compressive strength of the structure.

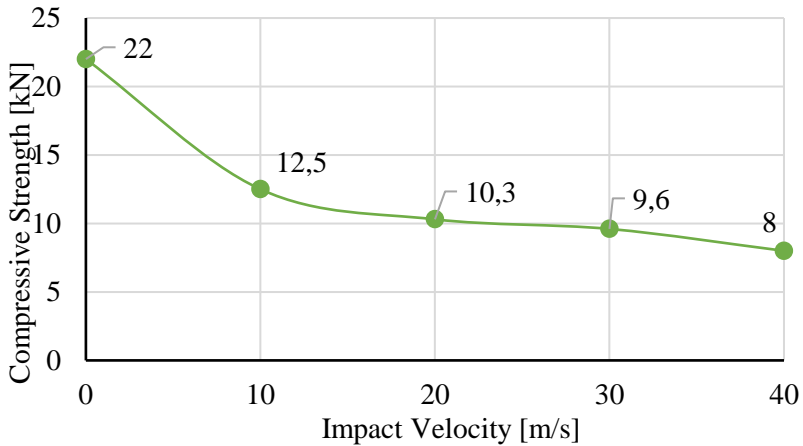


Figure 16. Compressive strength reduction with impact velocity

5. CONCLUSION

Impact damage characteristics were evaluated in terms of facesheet failures such as fiber breakage, matrix cracking, or delamination and in terms of other failure mechanisms like core crushing, shear deformation, and core-

CHAPTER 13: NUMERICAL AND EXPERIMENTAL INVESTIGATIONS ON THE RESPONSE AND COMPRESSIVE STRENGTH OF FOAM-CORED SANDWICH STRUCTURES SUBJECTED TO MEDIUM-VELOCITY IMPACT

face sheet debonding. Permanent damage on the sandwich plate impacted with a velocity of 40 m/s was seen to be formed of obvious fiber breakage lying in the direction of the 45⁰ outermost ply as an elliptic shape on the contact face. Matrix cracking and following delamination failure are expanding from the contact point to the edges in a peanut shape. Further analyses with the numerical model for different velocity levels revealed that contact time decreases, damage becomes more localized, contact force rises, and its peak value is shown at the earlier phase of impact duration as the impact velocity increases. The plastic deformation of the foam core indicates the energy absorption capacity of the structure. An impacted sandwich loses a major portion of its strength after impact, but it still has load-carrying capacity even after 40 m/s velocity impact.

It can be concluded that less effort was given in the literature for not only obtaining the residual properties of sandwich structures subjected to impact but also researching medium velocity range impact events. These two particular topics were combined in this study. The ultimate goal is to create a reliable numerical analysis tool that can be used by designers to reduce required test activities and get more optimized designs in terms of impact. Therefore, the impact and post-impact characteristics of sandwich structures with different core materials are kept to be discovered in many aspects.

Acknowledgements

This work has been conducted in collaboration between Istanbul Technical University and Turkish Aerospace, and supported financially by Turkish Aerospace under the project code 2021-BAP-14.

Conflict of interest

No conflict of interest was declared by the authors.

Author contributions

Abdullah İköz took part in literature research, preparation of the general framework of the publication, creation of the material model, FEM analysis, determination of material properties, manufacturing of test samples, and execution of tests. Uğur Yolum, contributed to the creation of the numerical model, definition of material properties and fabrication of test samples. Zahit Mecitoğlu, contribution was made to the conduct of experimental studies, the use of test devices and the preparation of theoretical infrastructure.

REFERENCES

- [1] Abrate, S. Impact on laminated composite: recent advances. *Appl. Mech. Rev. ASME* 1994; 47(11): 517-44.
- [2] Sun, C.T. An analytical method for evaluation of impact damage energy of laminated composites. *American Society for Testing and Materials, ASTM STP* 1977; 617: 427-40.
- [3] Yang, S.H., Sun, C.T. Indentation law for composite laminates. *American Society for Testing and Materials, ASTM STP* 1981; 787: 425-49.
- [4] Tan, T.M., Sun, C.T. Wave propagation in graphite/epoxy laminates due to impact. *NASA CR* 1982: 168057.
- [5] Choi, I. H., Lim, C.H. Low-velocity impact analysis of composite laminates using linearized contact law. *Composite Structures* 2004; 66: 125-132.
- [6] Anderson, T., Madenci, E. Experimental investigation of low-velocity impact characteristics of sandwich comp. *Composite Structures* 2000; 50: 239-247.
- [7] Chen, F., Hodgkinson, J.M. Impact behavior of composites with different fiber architecture. *Proceedings of the Institution of Mechanical Engineers, Part G: Journal of Aerospace Engineering* 2009; 223: 1009-17.
- [8] Aktaş, M., Balcıoğlu, H.E., Aktaş, A., Türker, E., Impact and post impact behaviour of layer fabric comp. *Composite Structures* 2012; 94: 2809-2818.
- [9] Iannucci, L., Willows, M.L. An energy based damage mechanics approach to modelling impact onto woven composite materials-Part I: numerical models. *Composites: Part A* 2006; 37: 2041-2056.
- [10] Maimi, P., Camanho, P.P., Mayugo, J.A., & Davila, C.G. A continuum damage model for composite laminates: Part II: computational implementation and validation. *Mechanics of Materials* 2007; 39: 909-919.
- [11] Gonzalez, E.V., Maimi, P., Turon, A., Camanho, P.P., Renart, J. Simulation of delamination by means of cohesive elements using an explicit finite element code. *Computers, Materials & Continua* 2009; 9(1): 51-92.
- [12] Long, S., Yao, X., Wang, H. Failure analysis and modeling of foam sandwich laminates under impact loading. *Composite Structures* 2018; 197: 10-20.
- [13] Tan, W., Falzon, B.G., Chiu, L.N.S., Price, M. Predicting low velocity impact damage and compression-after-impact (CAI) behavior of composite laminates. *Composites: Part A* 2015; 71: 212-226.

CHAPTER 13: NUMERICAL AND EXPERIMENTAL INVESTIGATIONS ON THE RESPONSE AND COMPRESSIVE STRENGTH OF FOAM-CORED SANDWICH STRUCTURES SUBJECTED TO MEDIUM-VELOCITY IMPACT

- [14] Wang, J., Wang, H., Chen, B., Huang, H. A failure mechanism based model for numerical modeling the compression-after-impact of foam-core sandwich panels. *Composites Science and Technology* 2017; 151: 258-267.
- [15] Bai, R., Guo, J., Lei, Z., Liu, D., CAI behavior of composite foam-core sandwich panels. *Composite Structures* 2019; 225: 111181.
- [16] Ivanez, I., Santiuste, C., Barbero, E., Saez, S.S. Numerical modelling of foam-cored sandwich plates under high-velocity impact. *Composite Structures* 2011, 93(9): 2392-2399.
- [17] Nasirzadeh, R., Sabet, A.R. Study of foam density variations in composite sandwich panels under high velocity impact loading. *International Journal of Impact Engineering* 2014; 63: 129-139.
- [18] Hashin, Z. Failure criteria for unidirectional fiber composites. *Journal of Applied Mechanics* 1980; 47(3): 329-334.
- [19] ABAQUS/CAE 6.16 user's guide. Providence (RI, USA): Dassault Systemes Simulia Corp.; 2015.
- [20] Benzeggagh, M.L., Kenane, M. Measurement of mixed-mode delamination fracture toughness of unidirectional glass/epoxy composites with mixed-mode bending apparatus. *Composites Science and Technology* 1995; 56: 439-449.
- [21] Li, Q.M., Mines, R.A.W., Birch, R.S. The crush behaviour of Rohacell-51WF structural foam. *Int. J. of Solids and Structures* 2000; 37: 6321-6341.
- [22] Gonzalez, E.V., Maimi, P., Camanho, P.P., Turon, A., Mayugo, J.A. Simulation of drop-weight impact and compression after impact tests on composite laminates, *Composite Structures* 2012; 94: 3364-3378.
- [23] Maimi, P., Camanho, P.P., Mayugo, J.A., Davila, C.G. A continuum damage model for composite laminates: Part I – Constitutive model. *Mechanics of Materials* 2006; 39: 97-908.
- [24] ASTM. Standard Practice for Damage Resistance Testing of Sandwich Constructions (ASTM D7766/D7766M-16), 2016.
- [25] ASTM. Standard Test Method for Compressive Residual Strength Properties of Damaged Polymer Matrix Composite Plates (ASTM D7137/D7137M-17), 2017.



CHAPTER 14

Aviation Technologies and Applications
E-ISBN:978-605-338-471-7
2025, chap. (14) , pp.225-237.

INVESTIGATING ON BEHAVIOUR OF TURBOPROP ENGINE BY CONSIDERING COMPONENT EFFICIENCY

Mehmet KIRMIZI^{1,*}, Hakan AYGÜN², Önder TURAN³

ABSTRACT

To perform the performance analysis of the turboprop engine is of high importance due to increasing environmental impact of gas turbine engines. In this study, influences of isentropic efficiency (IE) of an air compressor (AC), a gas turbine (GT), and a free turbine (FT) are examined. Accordingly, for three units, the isentropic efficiency ranges are set between 0.8 and 0.98. The thermal efficiency of the turboprop engine increases from 28.9% to 37.1% for AC, from 26.6% to 36.9% for GT, and from 27.12% to 33.2% for FT due to the effect of the isentropic efficiencies of the turbomachinery components. On the other hand, exergy efficiency of the AC enhances from 91.4% to 99.1% whereas the exergy efficiencies of the gas turbine and free turbine rise from 92.2% to 99.3% and from 90% to 98.2%, respectively due to raised isentropic efficiency from 0.8 to 0.98. Lastly, exergy destruction of the AC varies between 610 kW-52 kW while those of the gas turbine and free turbine change between 588 kW-45 kW and between 337 kW-65 kW, respectively, with the elevated isentropic efficiency. Based on aero-thermodynamic research, it can be deduced that designing turbomachinery components using innovative manufacturing processes might enhance the fuel economy of turboprop engines.

Keywords: Turboprop, isentropic efficiency, exergy efficiency, turbomachinery.

1. INTRODUCTION

One of the main issues in the gas turbine sector is designing environmentally friendly aero-engines, which is difficult given that the engines have advanced since the 1940s. However, it is noted that compared to prior years, there is a greater requirement for gas turbine engines for both military and commercial applications[1]. The most common gas turbine engines used in aviation are turbojet, turbofan, turboprop and turboshaft engines. These engines generate thrust through propulsion and, as a result, emissions such as NO_x, CO₂, SO_x, H₂O, and CO. Propulsion advancements are of high importance for high-speed air travel on extended flights carrying large payloads [2].

*Corresponding Author: mehmet.kirmizi@ege.edu.tr

1 Lecturer, Ege University Aviation HVS Aircraft Tech., İzmir, TURKIYE, 0000-0003-0510-2981,
mehmet.kirmizi@ege.edu.tr

2 Dr., Firat University, Department of Aircraft Frame and Power-Plant, Elazığ, TURKIYE, 0000-0001-9064-9644,
haygun@firat.edu.tr

3 Prof. Dr., Eskisehir Technical University, Faculty of Aeronautics and Astronautics, Eskisehir, TURKIYE, 0000-0003-0303-4313, onderturan@eskisehir.edu.tr

CHAPTER 14: INVESTIGATING ON BEHAVIOUR OF TURBOPROP ENGINE BY CONSIDERING COMPONENT EFFICIENCY

The main components of gas turbine engines are generally the air intake, air compressor, combustion chamber, turbine and exhaust from front to back. Among these engines, turbojet and turbofan engines, thrust force is obtained from the momentum difference of the gases coming out of the exhaust. Power is obtained from turboprop and turboshaft engines by means of a shaft. However, some turboprop engines produce some of the thrust from the exhaust (residual thrust) and the rest from the air accelerated backwards by the propeller. In some turboprop engines, the propeller is driven by a gas turbine, whereas in others it is driven by an independent turbine called a free or power turbine. The most important advantages of turboprop engines are that they have relatively lower fuel consumption and require shorter runways for take-off. In addition, since their fuel consumption per unit thrust is low, they have a lower environmental impact than other gas turbine engines [3]. Lastly, their noisier operation compared to turbofan engines can be shown as a disadvantage. When considering literature review, there are studies on aviation propulsion systems from many perspectives. Moreover, there are numerous studies pertaining to the thermodynamics analysis of gas turbines [4].

Aydin et al. [5] conducted a thermodynamic analysis on a turboprop engine operating at both full and partial load levels. The turboprop's maximum overall and exergy efficiencies are determined to be 30.7% and 29.2%, respectively. It is determined that the maximum shaft power and the lowest specific fuel consumption are 1948 shp and 0.2704 kg/kWh at maximum load, respectively. Moreover, Atilgan et al. [6] carried out advanced exergy and exergo-economic study of the CT7-9C model turboprop engine for six different torque values. The study's findings include information about the interactions of engine components and avoidable exergy destruction. Furthermore, it was discovered that there was little interaction between the engine's components since the irreversibility that was occurring in them was caused by internal factors, which varied in rate from 65% to 70%. Aygun et al. [7] examined into the effects of propeller efficiency on the energy, sustainability, and performance metrics of a small turboprop engine. The search on influence of propeller efficiency on a turboprop engine was the primary focus compared with earlier research. Additionally, the degree to which the design factors influenced the engine's and its components' energy and performance indicators was ascertained. Balli [8] conducted a conventional and an advanced exergy investigation on a turboprop airplane engine and its components in this study. Exergy destruction rates in engine components are classified as internal/external and avoidable/unavoidable in this context, however the basic exergy

parameters of the engine's primary components were discussed. The engine's energy efficiency values were estimated to be 16.63% in the real case and 17.13% in the unavoidable situation based on the author's results in this study. When the open literature is examined in detail, it is seen that aviation engines have been analyzed from many perspectives [9-12].

This study employs thermodynamic parameters involving isentropic efficiency of the components to investigate a behaviours of turboprop engine used in freight aircraft by considering parametric analysis. The main aim is to examine the impact of the compressor's and the axial turbines' isentropic efficiency on the engine as a whole. In order to observe the engine's behavior, the ranges changing between 0.8 and 0.98 for isentropic efficiency are determined.

2. Methods

In the present study, the AE2100 turboprop engine is the subject of the analysis. The aforementioned engine was employed in a number of aircraft, including the C-130J and C-27 [13]. Figure 1 shows a 2D drawing of the AE2100 turboprop engine as well as main components. When looking at some of the features of this engine, it is seen that it has a 4.11 m diameter propeller and a 14-stage axial compressor with a compressor pressure ratio of 16.6. It also has a two-stage gas turbine and a two-stage free turbine. In addition, it has an air flow rate of 16.3 kg/s and a power generation capacity of 3313 kW in ground operation. This study makes use of the second law of thermodynamics, which deals with entropy and exergy [14].

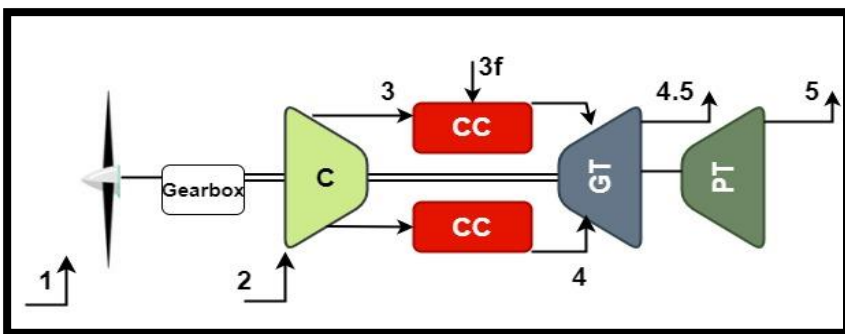


Fig.1 Two-dimensional illustration of AE2100 TPE [4]

Some assumptions are considered while carrying out the analysis. These are presented in table 1.

Table 1. Several assumptions regarding performance analysis of turboprop

Assumptions	
Turbomachinery components	Adiabatic
Gas properties	Ideal
Kinetic exergy	Neglected
Potential exergy	Neglected

2.1 Performance relations

The general statement of isentropic efficiency for a compressor or turbine could be found in eqs. 1 and 2 [14,15].

$$\eta_{comp.} = \frac{\Delta h_{t,isentropic}}{\Delta h_{t,actual}} \quad (1)$$

$$\eta_{turb} = \frac{\Delta h_{t,actual}}{\Delta h_{t,isentropic}} \quad (2)$$

Additionally, equations 3–4 provide the SFC and thermal efficiency formulas [3].

$$SFC = \frac{\dot{m}_f}{ESP} \quad (3)$$

$$\eta_{thermal} = \frac{ESP}{\dot{m}_f LHV} \quad (4)$$

where SFC, ESP, mf and LHV are the specific fuel consumption, equivalent shaft power, fuel mass flow rate and lower calorific value of the fuel, respectively.

2.2 Exergetic relations

The second law of thermodynamics should be studied in order to comprehend the concept of exergy in detail. Rather of focusing on energy's amount, the second law of thermodynamics addresses energy's quality [15, 16]. Exergy is the term used to describe the useful or theoretical work to be obtained from the a system when removing irreversibility system or its components. The purpose of exergy analysis is to provide insight in enhancing system performance by ascertaining the precise locations and accurate magnitudes of irreversibility. A system's overall exergy can be computed as [17, 18];

$$\dot{E}x = \dot{E}x^{PH} + \dot{E}x^{CH} + \dot{E}x^{PT} + \dot{E}x^{KN} \quad (5)$$

where physical, chemical, potential, and kinetic exergies are represented by the superscripts PH, CH, PT, and KN, respectively.

$$\varepsilon^{PH} = C_p (T - T_0 - T_0 \ln \frac{T}{T_0}) + R_a T_0 \ln \frac{P}{P_0} \quad (6)$$

where ε^{PH} and C_p are specific exergy rate and specific heat capacity, respectively [17]. The specific exergy rate and the mass flow rate are used to calculate the exergy rate. Namely, it is calculated by integrating the rules of entropy and energy. [17, 19].

$$\dot{E}x^{PH} = \dot{m} \left[C_p (T - T_0 - T_0 \ln \frac{T}{T_0}) + R_a T_0 \ln \frac{P}{P_0} \right] \quad (7)$$

The following represents the specific heating values for gas and air:

$$c_{p,air}(T) = 1.04841 - 0.000383719(T) + \frac{9.45378(T^2)}{10^7} - \frac{5.49031(T^3)}{10^{10}} + \frac{7.92981(T^4)}{10^{14}} \quad (8)$$

$$c_{p,gas}(T) = 0.9910 + \frac{3.606(T)}{10^5} + \frac{1.552(T^2)}{10^7} - \frac{6.76(T^3)}{10^{11}} \quad (9)$$

The computed difference between the system's inlet and output exergy is called energy destruction.

$$\sum \dot{E}x_{Dest} = \sum \dot{E}x_{in} - \sum \dot{E}x_{out} \quad (10)$$

Another way to calculate the exergy destruction is presented as below:

$$\dot{E}x_{dest} = \sum (1 - \frac{T_0}{T_k}) \dot{Q}_k - \dot{W} + \sum_{in} \dot{E}x_{in} - \sum_{out} \dot{E}x_{out} \quad (11)$$

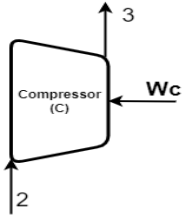
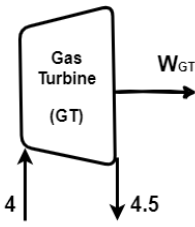
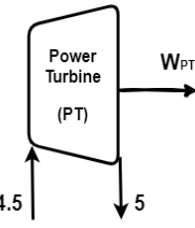
where T_k , T_0 , \dot{W} , $\dot{E}x$ and \dot{Q}_k are the boundary temperature to the kth component, reference (dead) state temperature, work rate, exergy rate of inlet and outlet stream, and output heat rate from the kth component, respectively. Exergy efficiency is obtained from $\dot{E}x_{dest}$ and $\dot{E}x_{in}$.

CHAPTER 14: INVESTIGATING ON BEHAVIOUR OF TURBOPROP ENGINE BY CONSIDERING COMPONENT EFFICIENCY

$$\eta_{ex} = \frac{\dot{E}x_{out}}{\dot{E}x_{in}} = 1 - \frac{\dot{E}x_{dest}}{\dot{E}x_{in}} \quad (12)$$

Table 2 shows applications of both first and second laws of thermodynamics on component basis.

Table 2. Energy and exergy balance equations for turbomachinery units. [20]

Component	Energy and Exergy Balance
	$\dot{E}_2 + \dot{W}_c - \dot{E}_3 = 0$ $\dot{W}_c - \dot{E}x_2 - \dot{E}x_3 = \dot{E}x_{Dest,c}$ $\eta_{ex,c} = \frac{\dot{E}x_3 - \dot{E}x_2}{\dot{W}_c}$
	$\dot{E}_4 - \dot{W}_{GT} - \dot{E}_{4.5} = 0$ $\dot{E}x_4 - \dot{E}x_{4.5} - \dot{W}_{GT} = \dot{E}x_{Dest,GT}$ $\eta_{ex,GT} = \frac{\dot{W}_{GT}}{\dot{E}x_4 - \dot{E}x_{4.5}}$
	$\dot{E}_{4.5} - \dot{W}_{PT} - \dot{E}_5 = 0$ $\dot{E}x_{4.5} - \dot{E}x_5 - \dot{W}_{PT} = \dot{E}x_{Dest,PT}$ $\eta_{ex,PT} = \frac{\dot{W}_{PT}}{\dot{E}x_{4.5} - \dot{E}x_5}$

3. Results and discussion

In this section, effects of isentropic efficiencies on whole turboprop engine are presented. The primary objective is to ascertain the degree to which the compressor and axial turbines' isentropic efficiency impacts the engine as a whole. In order to observe the engine's behavior, isentropic efficiency of the components is splitted to ten points between 0.8 and 0.98. The following table and figures display the results of the analysis. Moreover, it should be noted that while the isentropic efficiency of one component is changed, the isentropic efficiencies of the other components remain at their design values.

The impact of isentropic efficiency on thermal efficiency is presented in Table 3. Additionally, the effect of IE on thermal efficiency is shown in figure 2, the effect of IE on shaft efficiency is presented in figure 3. Moreover, the effect of IE on specific fuel consumption is illustrated in figure 4, while the effect of IE on exergy efficiency is shown in figure 5. IE' the effect of on exergy destruction is demonstrated in figure 6.

Table 3. Variation of thermal efficiency due to changing isentropic efficiency for three components (a. Due to the IE effect of the AC b. Due to the IE effect of the GT c. Due to the IE effect of the FT)

	IE	0.8	0.82	0.84	0.86	0.88	0.9	0.92	0.94	0.96	0.98
$\eta_{thermal}$ (%)	a	28.9	30.1	31.3	32.3	33.2	34.1	34.9	35.7	36.4	37.1
	b	26.6	28.1	29.52	30.8	32.0	33.1	34.1	35.1	36.0	36.9
	c	27.1	27.8	28.48	29.1	29.8	30.5	31.2	31.8	32.55	33.23

As expected, the performance behavior of the turboprop engine is favourably affected by the increasing isentropic efficiency. When the isentropic efficiency elevates from 0.8 to 0.98, the thermal efficiency of the air compressor enhances between 28.9% and 37.1%, whereas the thermal efficiency of GT and FT increase from 26.6% to 36.9% and from 27.12% to 33.2%, respectively. In other words, the thermal efficiencies of the components improve by 8.1%, 10.3% and 6.1% as a result of the increase in the IE of compressor, GT and FT, respectively.

CHAPTER 14: INVESTIGATING ON BEHAVIOUR OF TURBOPROP ENGINE BY CONSIDERING COMPONENT EFFICIENCY

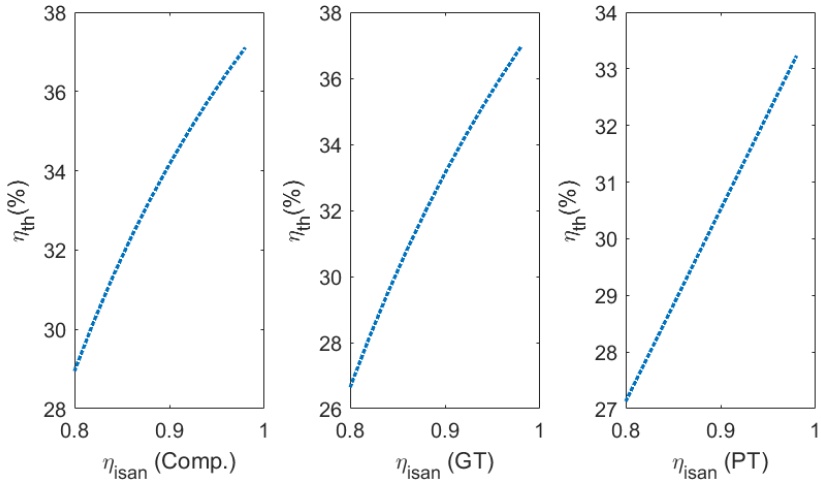


Fig.2 Variation in thermal efficiency due to isentropic efficiency of the components

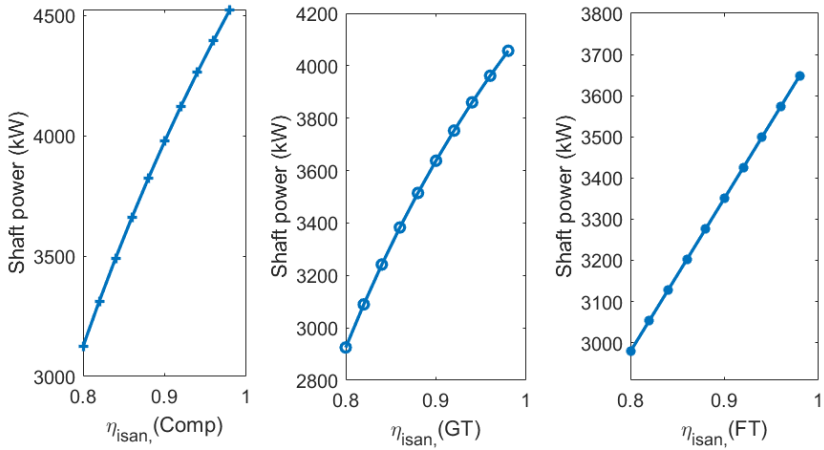


Fig.3 Variation in shaft power due to isentropic efficiency of the components

The effect of component isentropic efficiencies on shaft power is illustrated in figure 3. It is seen that with the increase in component isentropic efficiency, the shaft power of the turboprop engine increases in a similar way to the thermal efficiency. Concisely, shaft power raises from 3124 kW to 4525 kW with the effect of elevated compressor efficiency, from 2925 kW to 4057 kW due to raised efficiency of gas turbine, and from 2978 to 3648 kW owing to enhanced efficiency of free turbine efficiency from 0.8 to 0.98. Shaft power of the engine enhances by 44.84% for air compressor, 38.7% for gas turbine and 22.49% for free turbine due to raising isentropic efficiency

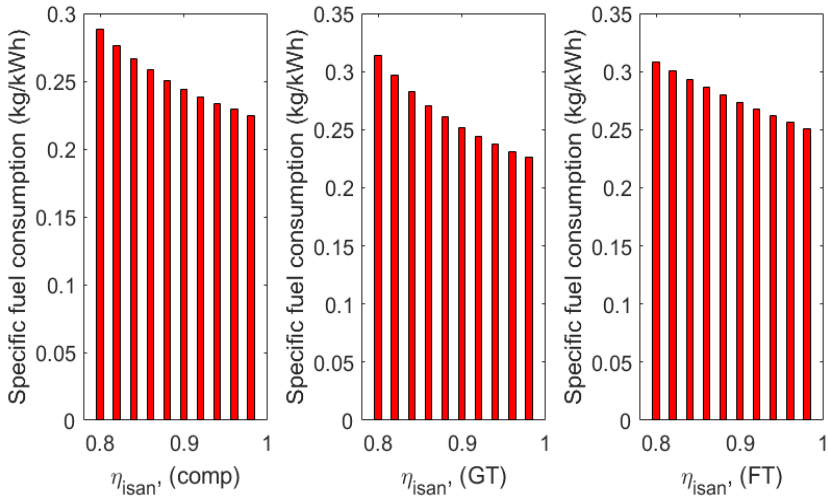


Fig.4 Variation in SFC due to isentropic efficiency of the components

Figure 4 depicts the effect of isentropic efficiency on specific fuel consumption (SFC) of the turboprop engine. As a result of increasing the compressor isentropic efficiency from 0.8 to 0.98, the SFC of TPE improved from 0.288 kg/(kW*h) to 0.224 kg/(kW*h). Only by increasing the isentropic efficiency of the gas turbine from 0.8 to 0.98, the SFC improved from 0.313 kg/(kW*h) to 0.225 kg/(kW*h). Finally, just by changing the isentropic efficiency of the power turbine from 0.8 to 0.98, SFC improved from 0.307 kg/(kW*h) to 0.221 kg/(kW*h). In other words, the largest decrease in SFC was due to the increase in the isentropic efficiency of the gas turbine with 27.9%, and the lowest improvement was due to the effect of the isentropic efficiency of the free turbine with 18.36%. Therefore, it can be inferred that the environmental impact of the turboprop engine decreases with the increase in the isentropic efficiency of the turbomachinery components.

CHAPTER 14: INVESTIGATING ON BEHAVIOUR OF TURBOPROP ENGINE BY CONSIDERING COMPONENT EFFICIENCY

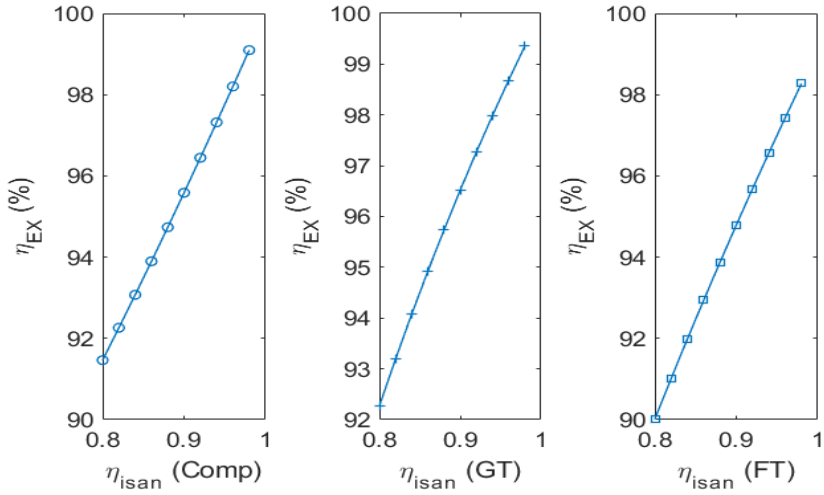


Fig.5 Variation in exergy efficiency due to isentropic efficiency of the components

As mentioned earlier, it is important to note that while the isentropic efficiency of one component is changed, the isentropic efficiencies of other components remain at their design values. When considering isentropic efficiency changing between 0.8 to 0.98, exergy efficiency of air compressor enhances from 91.4 % to 99.1 % whereas it raises from 92.2% to 99.3% for gas turbine and improves from 90% to 98.2% for free turbine, respectively. In other words, increasing isentropic efficiency increased the exergy efficiency of all components.

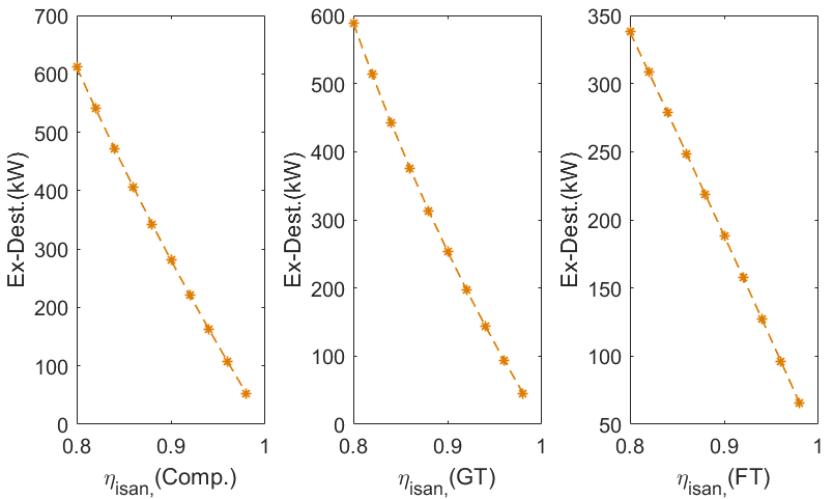


Fig.6 Variation in exergy destruction due to isentropic efficiency of the components

Fig. 6 shows the exergy destruction that occurred in three components since it is crucial to analyze how much irreversibility lowers under the influence of enhanced isentropic efficiency on a component basis. In this regard, the exergy destruction of components decreases more than tenfold for compressors and gas turbines and more than fivefold for free turbines with the enhanced component IEs. That is, the exergy destruction is determined to be minimum at the point where the compressor isentropic efficiency is highest (52 kW) and maximum at the point where the isentropic efficiency is lowest (610 kW). Similarly, as the IE of GT and FT increases, it decreases from 588 kW to 45 kW and from 337 kW to 65 kW, respectively.

4. CONCLUSIONS

It is thought that this study provides guidance for designing turbomachinery components in order to account for the impact of IE on the irreversibility calculation prior to the manufacturing process. The several outcomes are obtained in present study. These are highlighted as:

- It can be said that the shaft power of TPE increases due to the effect of isentropic efficiency. It has been determined that the maximum increase in shaft power becomes 44.84% due to the effect of compressor isentropic efficiency.
- The exergy destruction of the components is prone to decrease due to elevated isentropic efficiency. Moreover, the exergy destruction decreases from 610 kW to 52 kW, from 588 kW to 45 kW and from 337 kW to 65 kW due to the influence of IE of the compressor, GT and FT, respectively.
- Exergy efficiency of turboprop increases from 91.4 % to 99.1 % with influence of the elevated isentropic efficiency of air compressor from 0.8 to 0.98.
- The largest decrease in SFC was due to the increase in the isentropic efficiency of the gas turbine with 27.9%, and the smallest improvement was due to the effect of the isentropic efficiency of the free turbine with 18.36%.

Given the complexity of aero-engines with several subsystems, many engineers have focused on using well-known approaches like thermodynamics to analyse associated systems or components. Namely, these approaches might be used to investigate the components that show promise for improvement. Thus, the question of how much performance enhancement results from increasing the isentropic efficiency of compressor and turbine components is addressed in this study. It is believed that this study provides guidance for designing turbomachinery components such that the impact of IE on the irreversibility calculation may be considered before the manufacturing stage.

Acknowledgements

No Acknowledgements was declared by the authors.

Conflict of interest

No conflict of interest was declared by the authors.

Author contributions

Mehmet Kirmizi: Validation, Software, Methodology, Investigation, Formal analysis, Data curation, Conceptualization. Hakan Aygun: Validation, Software, Resources, Investigation, Data curation, Conceptualization. Onder Turan: Supervision, Conceptualization, Writing-Reviewing and Editing, Validation.

REFERENCES

- [1] Dinc, A., Caliskan, H., Ekici, S. and Sohret, Y.,“Thermodynamic-based environmental and enviroeconomic assessments of a turboprop engine used for freight aircrafts under different flight phases”. *Journal of Thermal Analysis and Calorimetry*, 2022.Vol. 147(22): pp. 12693-12707.
- [2] Balli, O. and Caliskan, H.,“On-design and off-design operation performance assessmentsof an aero turboprop engine used on unmanned aerial vehicles (UAVs) in terms of aviation, thermodynamic, environmental and sustainability perspectives”. *Energy Conversion and Management*, 2021.Vol. 243: pp. 114403.
- [3] El-Sayed, A.F., Aircraft propulsion and gas turbine engines. 2017: CRC press.
- [4] Kirmizi, M., Aygun, H. and Turan, O.,“Performance and energy analysis of turboprop engine for air freighter aircraft with the aid of multiple regression”. *Energy*, 2023.Vol. 283: pp. 129084.
- [5] Aydın, H., Turan, O., Midilli, A. and Karakoc, T.H.,“Energetic and exergetic performance assessment of a turboprop engine at various loads”. *International Journal of Exergy*, 2013.Vol. 13(4): pp. 543-564.
- [6] Atılgan, R., Turan, Ö., Altuntaş, Ö., Aydın, H. and Synylo, K.,“Environmental impact assessment of a turboprop engine with the aid of exergy”. *Energy*, 2013.Vol. 58: pp. 664-671.
- [7] Aygun, H., Kirmizi, M. and Turan, O.,“Propeller effects on energy, exergy and sustainability parameters of a small turboprop engine”. *Energy*, 2022.Vol. 249: pp. 123759.
- [8] Balli, O.,“Advanced exergy analyses of an aircraft turboprop engine (TPE)”. *Energy*, 2017.Vol. 124: pp. 599-612.

- [9] Karabacak, M., Kirmizi, M., Aygun, H. and Turan, O., “Application of exergetic analysis to inverted Brayton cycle engine at different flight conditions”. *Energy*, 2023.Vol. 283: pp. 129054.
- [10] Oruc, R. and Baklacioglu, T., “Modeling of energy maneuverability based specific excess power contours for commercial aircraft using metaheuristic methods”. *Energy*, 2023.Vol. 269: pp. 126819.
- [11] Oruc, R. and Baklacioglu, T., “Modelling of fuel flow-rate of commercial aircraft for the climbing flight using cuckoo search algorithm”. *Aircraft Engineering and Aerospace Technology*, 2020.Vol. 92(3): pp. 495-501.
- [12] Aygun, H., Sheikhi, M.R. and Kirmizi, M., “Parametric Study on Exergy and NO_x Metrics of Turbofan Engine Under Different Design Variables”. *Journal of Energy Resources Technology*, 2022.Vol. 144(6): pp. 062303.
- [13] Available from: <http://www.fi-powerweb.com/Engine/Rolls-Royce-AE-2100.html> (Last accessed 12 04 2024).
- [14] Cilgin, M.E. and Turan, O., “Entropy Generation Calculation of a Turbofan Engine: A Case of CFM56-7B”. *International Journal of Turbo & Jet-Engines*, 2018.Vol. 35(3): pp. 217-227.
- [15] Moran, M.J., Shapiro, H.N., Boettner, D.D. and Bailey, M.B., *Fundamentals of engineering thermodynamics*. 2010: John Wiley & Sons.
- [16] Turan, O., “An exergy way to quantify sustainability metrics for a high bypass turbofan engine”. *Energy*, 2015.Vol. 86: pp. 722-736.
- [17] Şöhret, Y., Ekici, S., Altuntaş, Ö., Hepbasli, A. and Karakoç, T.H., “Exergy as a useful tool for the performance assessment of aircraft gas turbine engines: A key review”. *Progress in Aerospace Sciences*, 2016.Vol. 83: pp. 57-69.
- [18] Balli, O. and Hepbasli, A., “Exergoeconomic, sustainability and environmental damage cost analyses of T56 turboprop engine”. *Energy*, 2014.Vol. 64: pp. 582-600.
- [19] Balli, O., Caliskan, N. and Caliskan, H., “Aviation, energy, exergy, sustainability, exergoenvironmental and thermoeconomic analyses of a turbojet engine fueled with jet fuel and biofuel used on a pilot trainer aircraft”. *Energy*, 2023.Vol. 263: pp. 126022.
- [20] Kirmizi, M., Aygun, H. and Turan, O., “Energetic and exergetic metrics of a cargo aircraft turboprop propulsion system by using regression method for dynamic flight”. *Energy*, 2024.Vol. 296.



CHAPTER 15

Aviation Technologies and Applications
E-ISBN:978-605-338-471-7
2025, chap. (15) , pp.238-264.

AUTONOMOUS ENERGY MANAGEMENT FOR ENHANCED UAV OPERATIONS

Umut Efe KARAÇAY¹, Gürcan LOKMAN^{2,*}, A. Fevzi BABA³

ABSTRACT

In this study, an approach is presented that aims to optimize energy management in Unmanned Aerial Vehicle (UAV) operations. In the designed energy management system, when the battery levels of the UAVs reach a critical threshold (20%), it is aimed to autonomously determine the nearest charging station, approach the station, detect empty units in the station, land on the empty unit and then charge the UAV and continue its missions from where it left off after charging is completed. In our study, the distances to the charging stations for the UAVs are calculated using the Euclidean Method and optimum routes are created by selecting the station with the shortest distance. The system is supported by a Raspberry Pi used as a mission computer in addition to the flight computer. While the detection of charging stations and positioning of the UAVs are carried out via GPS, the determination of suitable charging units and the correct positioning of the UAVs are provided by image processing methods. With this method used in our study, the UAV was also given the ability to make precise landings on the existing charging unit. The proposed autonomous energy management system enables the charging process to be carried out without the need for human intervention and minimizes maintenance requirements.

Keywords: UAVs, Autonomous Charging Management, Autonomous landing, GPS Positioning, Image processing methods.

1. INTRODUCTION

Unmanned aerial vehicles (UAVs) have attracted interest from a variety of academic fields because of their adaptability and extensive range of uses. Numerous studies have examined various aspects of UAV technology, concentrating on their capabilities, possible uses, and the opportunities they bring across all parts of UAV systems, as a result of the field's rapid expansion of study. UAVs are essentially aerial vehicles that run remotely or autonomously without human pilots on board; this description highlights

*Corresponding Author: glokman@msu.edu.tr; gurcanlokman@gmail.com

¹ 0000-0002-4132-8681, National Defence University, Air NCO Higher Vocational School, Izmir, TURKIYE

² 0000-0003-2751-7627, National Defence University, Air NCO Higher Vocational School, Izmir, TURKIYE

³ 0000-0003-4834-0912, Electrics-Electronics Engineering, Marmara University, Istanbul, TURKIYE

how complicated UAVs are because they have several systems and can be controlled in various ways [1]. There are several varieties of UAVs, based on what they are meant to be used for. In general, they fall into two main groups, which are fixed-wing and rotary-wing UAVs, as shown in Figure 1. Fixed-wing drones often offer longer flight times and greater range, while rotary-wing UAVs—also called drones—give better manoeuvrability and the ability to take off and land vertically [2]. When UAVs first came into existence, they were primarily employed for military objectives. However, as time went on, they moved throughout civilian regions and found usage in a wide range of industries, nearly completely taking over our daily lives. Today, UAVs are used in a wide range of industries, including mining, environmental monitoring, agriculture, disaster management and the construction sector [2],[3].



Figure 1. Types of UAVs: a) Fixed-wing UAV b) Rotary-wing UAV

Studies have investigated the effectiveness of UAV surveillance for various tasks, including environmental monitoring, police operations, search and rescue missions, and inspection of power lines and bridges [4]. According to this study, UAVs are devices that can be used for a wide variety of activities in different situations. A visual of the use of UAVs in various areas, including agricultural surveillance, urban surveillance for law enforcement, search and rescue, and environmental monitoring, is provided in Figure 2. Integrating cutting-edge technologies such as artificial intelligence (AI) into UAVs is another area of study in the literature. Hashesh et al. (2022) addressed UAV communication problems and future prospects and conducted a study on the use of AI approaches to improve services in 5G/6G networks [5]. In addition, Keong (2023) proposed integrating UAVs with sector 4.0, aiming to facilitate operations and increase efficiency in the construction sector [6]. Pina and Vieira (2022) used UAVs to collect more precise and in-depth data in areas such as vegetation monitoring, animal surveys, geomorphological mapping, and atmospheric research in Antarctica [7]. According to the study, unmanned aerial vehicles facilitate the counting and morphometry of animals, such as birds, seals, penguins, and whales, without disturbing them.

CHAPTER 15: AUTONOMOUS ENERGY MANAGEMENT FOR ENHANCED UAV OPERATIONS

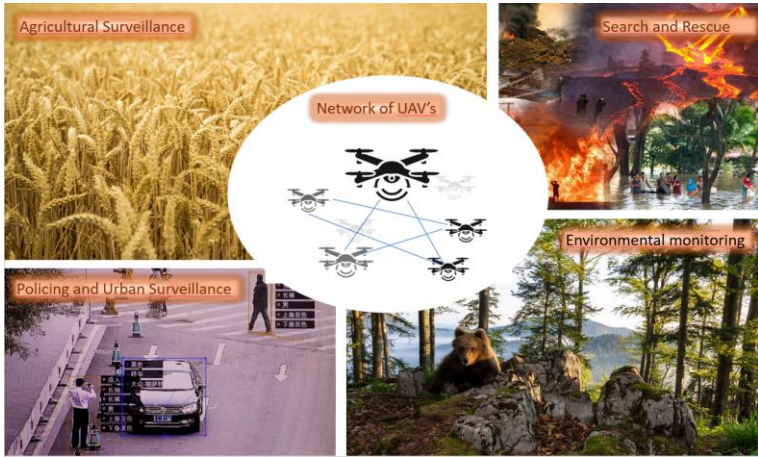


Figure 2. UAV Applications [4]

UAVs are also used in UAV-based delivery systems, real-time multimedia streaming networks, and intelligent transportation systems to improve road safety, monitor traffic flow, and manage infrastructure [8]. It is also stated that UAVs contribute to low-altitude air transportation for goods and people, in addition to conventional land transportation, and significantly improve the safety and reliability of transportation systems, especially in emergency situations [10].

It is stated that their high mobility, autonomous operation capabilities and advanced communication features bring UAVs to an important position in Intelligent Transportation Systems [11]. It is also stated that they are versatile systems used in various fields such as wireless coverage, agriculture, medical applications, environmental monitoring and delivery services [12]. In addition, UAVs are effectively used for commercial delivery purposes, emphasizing their ability to carry medicines, materials and fragile goods to remote locations [13]. Today and in the future, UAVs are expected to play an important role as a transportation system for goods delivery services, as seen in Figure 3. In the literature, studies are being conducted to optimize UAV transportation systems with technological advances such as wireless connectivity with machine learning, blockchain-based task processing systems, and intelligent route planning for collaborative transportation tasks [13],[14],[15]. In addition, studies focused on the cost-effectiveness and feasibility of using UAVs to transport medical supplies, laboratory samples, and blood samples in various environments [16],[17],[18].



Figure 3. The Transportation of Various Materials with UAVs

As discussed above, time and cost play a critical role in both material transportation and emergency situations with UAVs. For these processes, it is obvious that the use of autonomous charging systems during autonomous flights of UAVs can significantly increase UAV operational continuity and performance and provide significant gains in time management. This book chapter introduces an autonomous charging system that aims to extend operational time without the need for human intervention.

In the continuation of this book section, firstly the development process of UAVs, historical milestones and technological advances are discussed in the 2nd section. In the 3rd section, the energy requirements of UAVs and how these requirements are met are explained, while the batteries and battery management systems used in UAV systems, the characteristics of battery types, limitations of their capacities, the effects of charging processes and the operation of general charging systems are examined in detail. The use of image processing techniques for target detection for UAVs is summarized in the 4th section. The autonomous charging system proposed for UAVs is introduced in the 5th section. The book section is completed with conclusions and recommendations.

2. A BRIEF HISTORY OF UAVs

UAVs, commonly known as drones, are technological devices that have been in our history for over a century. It is known that their emergence began with their use for reconnaissance purposes during World War I [19]. As UAVs were used by the US military in the 1980s, their applications grew [20].

The history of UAVs progresses in parallel with the developments in technology and their applications in different areas. It is known that the development of UAVs has come a long way from their first use in military reconnaissance to their modern roles in engineering geology, forest fire detection and emergency rescue missions [21],[22],[23]. It is emphasized that UAVs are preferred in such applications due to their ability to access difficult, remote and dangerous terrains for humans.

The use of UAVs in military operations has revolutionized warfare by providing real-time intelligence, surveillance, and reconnaissance capabilities without risking human life [20]. The history of UAVs in the military dates back to the early 1980s and has created significant changes and improvements in military tactics and strategies. Continuous advances in UAV technology have led to the development of AI-based autonomous UAV networks that increase operational efficiencies [24]. Moreover, combining UAVs with machine learning approaches has brought revolutionary changes in smart agriculture applications, significantly contributing to precise crop monitoring and farmland management [25]. The high-resolution image and data capture capabilities of UAVs have facilitated detailed historical preservation of large-scale infrastructures, contributing to cultural heritage preservation and development planning [26]. With the emergence of electric UAVs, these UAVs have been widely used in disaster and emergency operations in various countries in recent years with their advantages such as small size, light weight, low energy consumption, wide field of view and ease of use.

As shown in Figure 2, UAVs play an important role in these missions with their rotary-wing and fixed-wing variants. While rotary-wing UAVs offer flexibility in narrow and vertical areas with their vertical take-off and landing capabilities, fixed-wing UAVs provide the advantages of longer range and higher speed. UAVs can autonomously determine target information through visual sensing technology and provide positioning information in limited areas or weak signal conditions through visual navigation technology [26]. The integration of these technologies with electric UAVs has the potential to increase the efficiency of rescue operations. Research on reinforcement learning-based approaches for collaborative search architectures for multiple autonomous UAVs highlights efforts to improve UAV capabilities [27], [28]. Additionally, the development of decentralized blockchain-based security monitoring frameworks for UAVs aims to ensure the security and reliability of autonomous UAV systems [29].

Table 1 summarizes the historical development of UAVs from the 1980s to the present. Initially limited to basic flight control systems and radio-controlled technologies during World War I, UAVs progressed with increased use in the US military and improved early navigation technologies in the 1980s. In the 1990s, armed UAVs became operational, providing targeted attacks and surveillance, while in the 2000s, they began to be used in civil and commercial sectors with high-resolution cameras and data collection technologies. In the 2010s, significant progress was made in emergency management and environmental protection with the development of artificial intelligence-based autonomous UAV networks; and in the 2020s, significant steps were taken with UAV-supported mobile edge computing systems and advanced communication technologies. Today, research on advanced autonomy and multi-UAV collaboration continues in agriculture, environmental monitoring, and smart city applications [19],[20],[24],[30].

Table 5. Historical Development of UAVs [19][20][24][30]

Period	Event	Applications	Technological Advancements
World War I	Use of UAVs for reconnaissance missions	Military reconnaissance and surveillance	Basic flight control systems and radio-controlled flights
1980s	Increase in UAV use by the U.S. military and tactical transformations	Advanced military strategies and combat tactics	Improved navigation and early autonomous flight technologies
1990s	First operational use of armed UAVs	Targeted strikes and operational surveillance	Integration of armed payloads and remote-control systems
2000s	Expansion of UAV use into civil and commercial sectors	Environmental monitoring, agriculture, and infrastructure inspections	High-resolution cameras and data collection technologies
2010s	Development of autonomous UAV networks with artificial intelligence	Emergency management, disaster response, and environmental protection	Integration with artificial intelligence and machine learning
2020s	Use of UAV-supported mobile edge computing systems	Fast data processing and emergency communication	Advanced computing and communication technologies for UAV networks
Present Day	Intensive research on advanced autonomy and collaborative capabilities	Agriculture, environmental monitoring, infrastructure inspection, and smart city applications	Enhanced learning and blockchain applications for autonomous operations and multi-UAV collaboration

3. ENERGY SOURCES AND CHARGING OF UAVs

UAVs use batteries as their primary power source. This makes the selection of battery technology important in terms of the performance and operational capabilities of UAVs. Among the existing battery types, Lithium-ion (Li-Ion) batteries are preferred for electric UAVs due to their high energy density and ability to withstand multiple operational cycles [31],[32],[33]. Lithium Polymer (LiPo) batteries also stand out as batteries that can meet the total power requirements of UAVs [34]. Accurately estimating the State of Charge (SOC) of batteries used in UAVs is an equally important factor. Proper assessment of battery power status is critical for the success of UAV missions [35],[36]. In order to increase the operational duration and efficiency of electric (battery-powered) UAVs, studies on autonomous battery maintenance systems are required. These systems play a critical role in extending the operational duration of small-scale UAVs by providing optimum battery performance and lifetime [37]. Innovative studies are being conducted on technologies such as in-flight charging with laser beams and wireless power transfer to overcome the problems caused by battery capacity and charging limitations and to enable UAVs to operate for longer periods without the need for frequent manual charging [38],[39],[40]. Additionally, there are studies in the literature that concentrate on optimizing battery weight, trying to maximize the energy available in UAV-based wireless communications, and making sure UAVs have enough energy to maintain optimal performance while successfully completing their missions [41].

3.1. Capacity Limitations and Charging

Although UAVs have revolutionized various industries due to their versatility and capabilities, one of the critical challenges they face is battery limitations and charging systems, because UAVs are largely dependent on batteries and the limitations of current battery technologies directly affect their operational efficiency and flight capabilities [42]. The limited energy capacity of UAV batteries results in short flight lengths, impeding their ability to carry out long-term missions. Additionally, their short operational duration of less than 1.5 hours limits their use in various applications [43]. Innovative charging methods are being researched to overcome these limitations. For example, wireless power transfer (WPT) technologies aim to increase the operational time of unmanned aerial vehicles (UAVs) by enabling wireless charging and minimizing the need for manual battery replacement. Additionally, in-flight charging mechanisms are being proposed to use mobile unmanned vehicles (MUVs) outfitted with laser beams or laser transmitters to charge batteries while in flight [33]. UAVs will be able to function at maximum battery performance thanks to the development of autonomous battery repair systems, which

will also improve UAVs' overall durability and efficiency [37]. To improve UAV power capacity and endurance, fuel cell technology integration is also being researched in addition to conventional batteries [44]. Charging infrastructure can address the battery limitations of UAV systems, simplify the charging process, reduce downtime, and increase operational efficiency through the design of autonomous refuelling systems and battery swapping stations [45]. Furthermore, strategic positioning of charging stations can make the energy replenishment process more efficient by minimizing the distance UAVs must travel for charging [46].

3.2. Battery Depletion and Mission Interruptions

Battery depletion during a mission can lead to interruptions in UAV operations and especially significant interruptions in critical missions. Battery failure can cause emergency landings and prevent the UAV from continuing its mission. Such interruptions become a major disadvantage for UAVs, especially in long-range and long-duration operations. While UAVs have become indispensable tools in a wide range of areas from surveillance and reconnaissance to delivery services and disaster response, the significant challenges faced by these airborne systems during their missions, due to battery limitations and charging problems, and their reliance on batteries as a power source, imposes limitations on flight autonomy, endurance and operational efficiency [42].

The term "flight duration" refers to the maximum time a UAV can stay airborne before its battery depletes. Environmental factors, such as wind and rain, significantly impact flight duration by affecting the UAV's weight, size, and battery life. Additionally, equipment such as autopilot and GPS plays a crucial role in determining flight duration. While larger UAVs can remain airborne for several hours, the flight duration of smaller UAVs is typically around 20 to 30 minutes [42]. The limited energy capacity of batteries directly affects the flight duration of UAVs, restricting their ability to perform extended missions effectively. Consequently, UAVs are not suitable for applications requiring prolonged flight times, as their operational duration generally does not exceed 1.5 hours [43].

By enhancing endurance and manoeuvrability through the use of WPT technologies, integrated wireless power charging systems for UAVs can significantly improve their operational capabilities and flexibility, enabling them to undertake a broader range of missions [47]. However, UAVs still face limitations due to their short battery life [48]. Further research is required to address these limitations, overcome battery constraints, and enhance the operational capabilities of UAV systems.

3.3. Overview of UAV Charging Systems

Due to limitations in battery capacity, UAVs often need to be replaced or recharged frequently [49]. Studies have suggested autonomous charging stations as a solution to this problem, allowing UAVs to fly longer without the need for human assistance [50]. Studies to lower vehicle weight and lengthen mission duration have also looked at tactics such as abandoning battery modules that run out during flight [51]. Figure 4 illustrates that manual charging is a time-consuming process, highlighting the need for more efficient solutions.



Figure 4. Charging of UAVs

Efforts to optimize UAV mission completion times include studies that take into account factors such as energy consumption, battery life, and charging strategies. For example, path optimization using deep reinforcement learning has been conducted to minimize completion times while complying with energy constraints [52]. Lithium polymer batteries are reported to improve UAV flight times compared to other battery technologies [53]. In addition, advances in battery charging technologies are emphasized to reduce charging times and increase the cost-effectiveness of UAV networks [54]. Complex programming frameworks are being investigated for UAVs that consider factors such as mission planning, flight time, battery risks, and energy efficiency [55]. A study suggests designing autonomous battery swap/charging stations to support small UAV missions lasting longer than three hours [56]. In their study conducted to meet the need for fast charging at low battery levels and autonomously continuing their missions, Arafat and Moh (2022) try to minimize the flight time during deliveries by introducing the Joint Routing and Charging Strategy (JRCS) for logistics drones. This strategy allows drones to prioritize charging at strategically placed stations to minimize downtime and optimize mission completion time [57].

In addition, Huang et al. (2023) proposes the Drone Stations Assisted Flight Planning Approach Beyond Battery Life, which highlights the challenge of limited battery capacity that restricts long-distance flights [58]. Huang et al. (2023) emphasize the importance of innovative solutions such as wireless charging technologies beyond traditional battery swapping services for drones, along with mission-oriented flight paths and charging mechanisms, and state that these technologies enable autonomous management of energy needs and efficient mission execution, allowing uninterrupted operations without manual intervention [59].

Ahmed (2024) emphasizes the importance of exploring methods to extend drone flight times and reduce dependence on conventional battery charging. He suggests enhancing energy collection techniques and integrating efficient power-harvesting devices, such as solar panels or fuel cells [60]. Meanwhile, Alolaiwy (2023) acknowledges the challenges of computational complexity and suboptimal solutions but argues that applying genetic algorithms (GAs) for route optimization in electric and flying vehicles remains a promising approach [61].

To tackle the issues related to battery life and charging processes faced by UAVs, further research is needed on autonomous charging systems. These systems, which allow for the autonomous charging of UAVs during flight or in mission zones, have the potential to greatly enhance operational continuity. By dynamically managing battery capacity, autonomous charging systems can optimize performance and ensure uninterrupted operations during extended missions.

4. IMAGE PROCESSING FOR UAV TARGET DETECTION

Image processing algorithms are essential tools for UAV target recognition and interaction. Advances in target identification technology have emerged from the integration of deep learning algorithms with image processing techniques. Notably, deep learning algorithms have demonstrated significant progress in object detection and tracking within image processing applications [62], [63], [64]. This integration enhances the accuracy and reliability of target identification and tracking, making it a critical component in UAV operations.

Deep learning-based techniques, in particular, have significantly enhanced the success rate of target identification, accelerating and improving the accuracy of image processing tasks [65]. For example, these techniques enable the identification of a target's position as it moves closer, providing real-time updates that enhance positioning accuracy.

Image processing methods play a crucial role in locating and tracking targets; thus, systems for moving object recognition and tracking are vital for the effective execution of UAV missions [66]. UAVs have advanced in their ability to approach targets through the use of image processing techniques, which facilitate the detection of target locations within a given space [67].

5. AUTONOMOUS CHARGING SYSTEM FOR UAVs

In our study, the quadrotor rotary wing UAV (drone) we designed is as shown in Figure 5. As shown in Figure 6, the UAV is equipped with four ESCs and four propellers for four motors. Our design includes a Pixhawk Px4 as a flight computer, a Raspberry Pi as a mission computer and control boards. The design also includes a Here3 GPS module for position detection and flight to specified coordinate points.

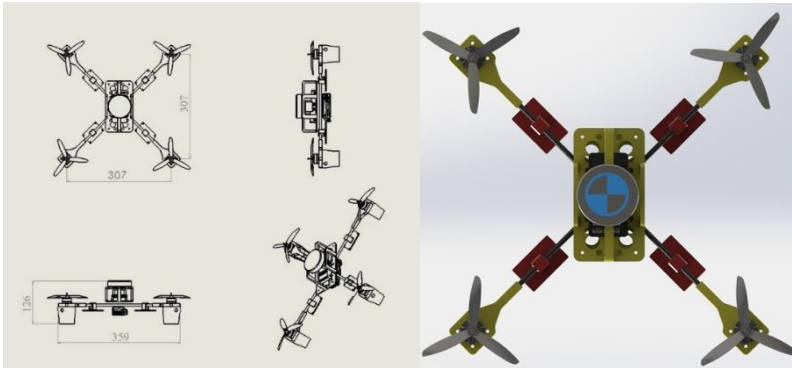


Figure 5. Designed UAV

Liu et al. reported in their research that the positioning errors for UAVs range from 1.75m to 2.07m [68]. Therefore, the designed system includes a camera along with image processing techniques for positioning, since precise positioning is not possible using GPS alone. To ensure accurate positioning, the system includes a camera connected to the Raspberry Pi mission computer that processes images in real time. Additionally, a LIDAR sensor is integrated into the system to prevent altitude-related deviations.

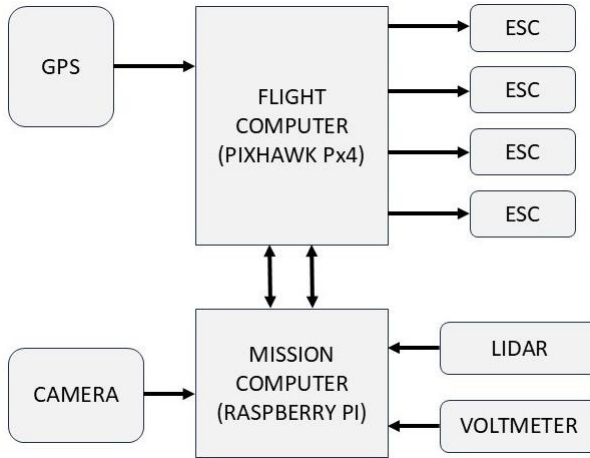


Figure 6. The block diagram of the designed UAV hardware

On the UAV, in addition to these components, there is a Li-Po battery, and the voltage of the battery is continuously transmitted to the mission computer via a voltage sensor. The system also includes a wireless charging circuit, as shown in Figure 7, for charging the battery.

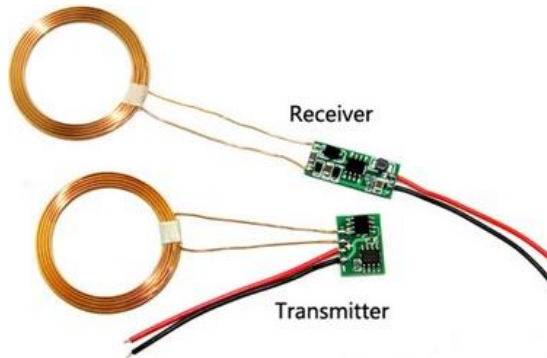


Figure 7. Wireless charging equipment

The basic principle of wireless charging systems is energy transfer through electromagnetic induction. These systems typically consist of a transmitter and a receiver coil. The wireless charging circuit and its operating principle are illustrated in Figure 8 and the transmitter and receiver coils are denoted by the letters L1 and L2, respectively. The transmitter coil is energized with alternating current to generate a magnetic field. Each charging unit contains a transmitter coil. When the magnetic field created here is intersected by the receiver coil, an electric current is induced in the receiver. This process is based on Faraday's law of induction [69].

CHAPTER 15: AUTONOMOUS ENERGY MANAGEMENT FOR ENHANCED UAV OPERATIONS

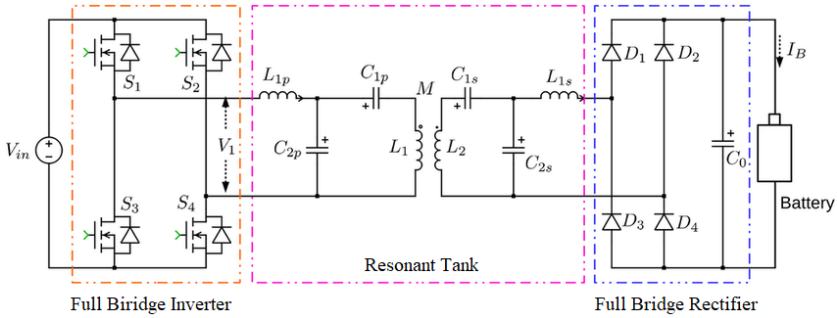


Figure 8. Wireless charging circuit [69]

The receiver coil is installed on the UAV along with the battery charging circuit. If the battery level drops below 20%, the UAV autonomously initiates the charging process and resumes its mission once charging is complete. The flowchart for the mission process and autonomous charging system is shown in Figure 9. This flowchart outlines the steps for managing autonomous operations and charging, ensuring that the UAV can efficiently handle its tasks while maintaining optimal battery levels.

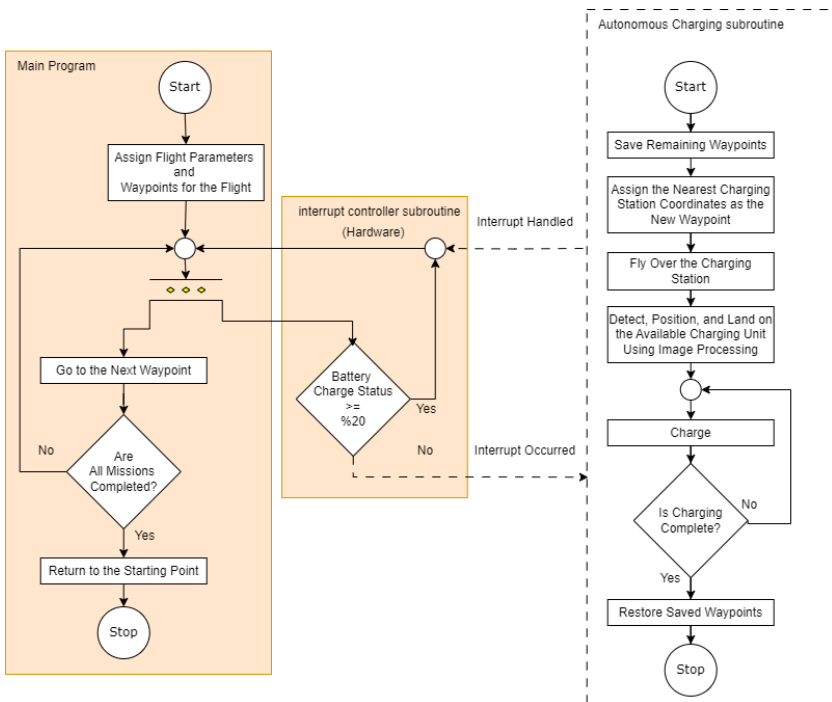


Figure 9. The flowchart for the autonomous mission and autonomous charging system

In the system, the mission computer and the flight computer are connected via USB, enabling them to coordinate and handle mission assignments as needed. The flight computer is the Pixhawk Px4 flight control board, and the open-source software "Mission Planner" is used for flight planning and mission tracking. An example application screenshot is shown in Figure 10. In the study, the stadium depicted in Figure 10, measuring 400m x 100m, has been selected as the mission area. Three waypoint coordinates were defined via the computer to the flight computer, and, in the absence of any input, the UAV is instructed to visit the coordinates shown in Figure 10 and return to the starting point.

During the mission assignment process, the mission data is first uploaded to the mission computer, and the UAV begins executing the tasks. Assuming the battery is fully charged (i.e., it does not drop below 20%), the UAV departs from the home location as shown in Figure 10, visits Waypoints 1 and 2, and completes the mission upon reaching Waypoint 3.



Figure 10. Study Area and Charging Stations Location

Subsequently, three charging stations were added to the mission area, as shown in Figure 10, and their locations were included in the program. When determining the positions of the charging stations, it was ensured that the UAV could reach any charging station from any point in the mission area with a remaining battery of 20%. Thus, in this study, a battery level of 20% was defined as the critical threshold.

If the battery level drops below the critical threshold at any time, the mission computer autonomously assigns a charging task. Before this operation, the current waypoint coordinates are saved, and after the charging task is completed, these saved coordinates are designated as new waypoints. As shown in Figure 11, if the UAV reaches location 2 and the battery level drops to the 20% critical level, the closest charging station, identified as charging station 3, is selected, and the updated waypoints are visualized accordingly.

To determine the nearest charging station, the distances to each charging station are calculated individually. The UAV's current position is denoted as (x_0, y_0) , while the coordinates of the three charging stations on the map are represented as (x_1, y_1) , (x_2, y_2) , and (x_3, y_3) . The distance to each station is calculated using the Euclidean method provided by Equation 1:

$$d_i = \sqrt{(x_0 - x_i)^2 + (y_0 - y_i)^2} \quad (i = 1,2,3) \quad (1)$$

Then, the shortest distance is determined using Equation 2, and the next waypoint is assigned accordingly:

$$d = \min\{d_1, d_2, d_3\} \quad (2)$$

In our study, the Euclidean method was preferred because a small experimental area was chosen. For larger areas, when UAVs need to find the shortest distance between two points on the Earth's surface, the Haversine formula, given by Equation 3, can also be used. This formula is used to calculate the distance between two points on a spherical surface.

$$d = 2r \cdot \arcsin \left(\sqrt{\sin^2 \left(\frac{\Delta\varphi}{2} \right) + \cos(\varphi_1) \cdot \cos(\varphi_2) \cdot \sin^2 \left(\frac{\Delta\lambda}{2} \right)} \right) \quad (3)$$

Here: r is the Earth's radius (approximately 6,371 km $\Delta\varphi = \varphi_2 - \varphi_1$ is the latitude difference. $\Delta\lambda = \lambda_2 - \lambda_1$ is the longitude difference. φ_1 and φ_2 are the latitudes of the two points, while λ_1 and λ_2 are the longitudes of the two points. This formula provides the great-circle distance between two points on the Earth and is useful for long-distance UAV flights.

After the GPS position of the nearest charging station is determined by the system, the most suitable route for these x and y coordinates is assigned as shown in Figure 11, and the UAV resumes its mission from where it left off.



Figure 11. New Route Planning and UAV Guidance to the Nearest Charging Station

After the UAV reaches the charging station, positioning and landing are carried out using image processing techniques due to insufficient GPS accuracy. Each charging station has three charging units, and their arrangement is schematized in Figure 12. Suitable units for charging are indicated by green dots, with one suitable unit randomly selected and represented by a green ‘X’ inside a green dot to facilitate the UAV’s positioning. During the descent process, the UAV performs a precise landing using LIDAR sensor data and camera images simultaneously.

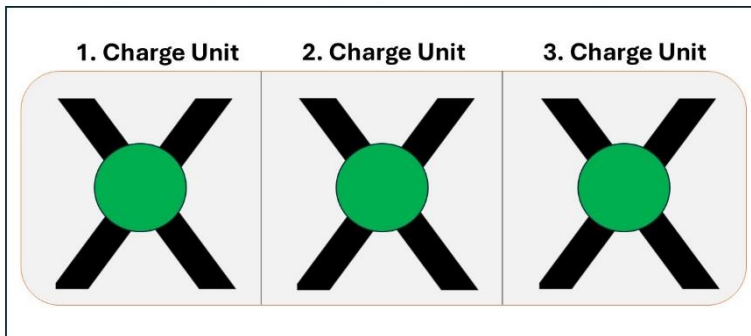


Figure 12. Charging Station Schematic. All units available.

In Figure 13, the unavailable charging unit number 2 is shown. In this case, one of the available units, either number 1 or number 3, will be randomly selected for positioning.

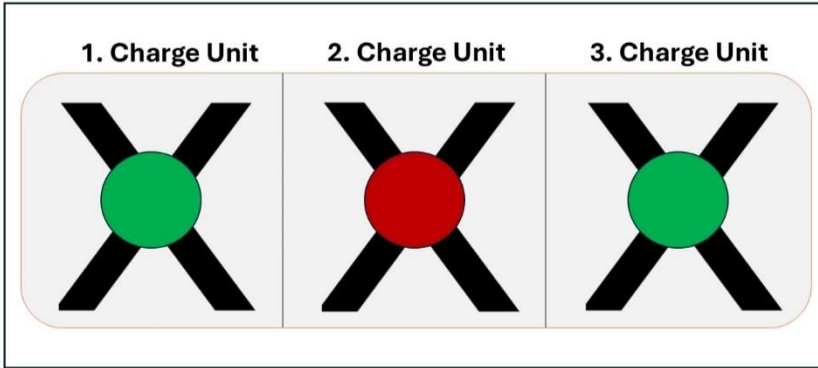


Figure 13. Charging Station Diagram. Second unit is in use.

To locate an available charging station, GPS data is complemented by the RaspiCam on the Raspberry Pi, which captures continuous images. These images are processed to detect the available empty unit, allowing the UAV to position itself accurately on the station. The image processing system integrates deep learning techniques with the Hough Transform and Random Sample Consensus (RANSAC) algorithms to ensure precise target landing location computations. Meanwhile, the RANSAC algorithm enhances the accuracy of the landing process by creating robust models and providing reliable identifications despite the presence of outliers and background noise [70]. This Python-based system exemplifies the effective integration of advanced machine learning methods with traditional image processing techniques. By employing computer vision algorithms, UAVs can autonomously detect accurate landing zones using sensor data [71]. This approach not only improves operational performance in challenging conditions but also enhances the reliability and accuracy of landing procedures.

Once the UAV has landed and charged at the charging station, the power is cut off to fully charge the battery. After the charging process is complete, the last assigned point before charging is reassigned as a task point, and the route between the charging station and the task point is recalculated to continue the mission from where it left off. These processes are repeated whenever the battery percentage drops to a critical level.

The batteries used for the UAV are 3-cell Li-Po with a capacity of 2000 mAh and a voltage of 11.1 V. When fully charged, the batteries have a voltage of 12.6 V. For a single cell, the nominal voltage is 3.7 V, fully charged is 4.2 V, and when fully discharged is around 3 V [72]. At 20% charge, a single cell's voltage is between 3.2 V and 3.4 V [73]. Thus, when the voltage of a three-cell Li-Po battery is in the range of 9.6-10.2 V, the UAV will start the charging task. Although achieving 100% efficiency in wireless charging systems is theoretically possible, it is difficult in practice due to various losses and efficiency decreases. For instance, in inductive power transfer systems, energy losses typically range from 20% to 30% [74]. The UAV charging time can be calculated as follows:

$$\text{Charging Time (hours)} = \frac{\text{Battery Capacity (mAh)}}{\text{Charging Current (mA)}} \tag{3}$$

Using Equation 3, the charging time for a 2000 mAh battery with a 2 A current is approximately 1 hour. However, considering the non-ideal efficiency of wireless charging systems mentioned above and the measured currents of 2 A from the transmitter and 1.5 A from the receiver, the efficiency factor is calculated as:

$$\text{Efficiency Factor} = \frac{P_{\text{receiver}}}{P_{\text{transmitter}}} \times 100 \tag{4}$$

Here, the power values are calculated as follows:

$$P = I \times V \tag{5}$$

$$P_{\text{receiver}} = 12V \times 1.5A = 18W \tag{6}$$

$$P_{\text{transmitter}} = 12V \times 2A = 24W \tag{7}$$

From Equations 4, 6, and 7, the Efficiency Factor is calculated to be 75%. Therefore, the expected charging time of 1 hour will become 1hour/0.75=1.33 hours. Table 2 provides the charging times for different Li-Po batteries with varying capacities using a 2A charging current.

Table 6. Charging Times Calculated for Various Batteries

Cell Count	Nominal Voltage	Capacity	Efficiency Factor	Charging Time
3	11,1 V	1500 mAh	%75	1 hour
3	11,1 V	2000 mAh	%75	1,33 hours
3	11,1 V	2200 mAh	%75	1,47 hours
4	14,8 V	3000 mAh	%75	2 hours
4	14,8 V	4200 mAh	%75	2,8 hours

The technical specifications of the batteries are one of the most important factors that directly affect the flight duration, and the capacity, voltage and chemical composition of the battery determine the energy density [75]. In addition, having a fully charged battery is important to maximize the flight duration [76]. The aerodynamic design and light weight of the UAV reduce battery consumption and extend the flight duration. Flight conditions, especially air currents, wind speed and direction are also factors that directly affect the energy consumption of the UAV [77]. In windy weather, the UAV consumes more energy to stay in the air, change position or maintain its position, which leads to faster battery depletion. The type of mission the UAV performs, the maneuvers it will perform, the altitude it will operate at and the weight of the equipment it carries are also important factors that affect battery consumption [77]. Engine technology is another factor that affects the battery consumption duration, and the efficiency of the engines directly affects energy consumption. In addition, optimization of engine control systems can also contribute to reducing energy consumption and thus extending the flight duration [78].

In our study, due to the aforementioned reasons, a standard duration for UAV flight times, or battery depletion times, has not been established. Instead, real-time monitoring is conducted using a voltmeter, and the Raspberry Pi onboard computer continuously checks the battery status, redirecting the UAV to the charging station as needed. The proposed system is expected to provide significant time advantages for operators during autonomous missions by eliminating the need for human intervention in charging the UAV's battery. Since there is no need for battery removal, replacement, or manual intervention, the system simplifies mission management and offers time savings.

6. CONCLUSION AND RECOMMENDATIONS

This study proposes a new autonomous charging system for UAVs. The research includes a UAV design and experimental studies conducted in a 400m x 100m stadium. With the help of the suggested system, UAVs would be able to self-recharge their batteries and carry out extended missions without the assistance of an operator.

When battery levels fall below a critical threshold (20%), the developed system allows UAVs to locate the nearest charging station, approach the station using GPS coordinates, detect an available charging unit using image processing techniques, land autonomously on the available unit using visual positioning, monitor the charging process, and resume their missions from where they left off once the charging process is finished.

This method provides a novel way to reduce operational disruptions, maximize flight durations, and accomplish effective energy conservation. Furthermore, our research indicates that future UAV operations with cutting-edge technological integration have a wide range of potential applications in terms of boosting the efficacy and continuity of UAV missions.

Precise placement is significantly enhanced when camera-assisted image processing techniques are combined with GPS guidance of the UAV towards the charging station during the charging procedure. According to our research, this technique increases processing efficiency by guaranteeing that the UAV is positioned correctly and approaches the charging station correctly. The wireless charging method preferred in our study eliminates the complexity of traditional plug-and-unplug physical connections, and simplifies the design of the autonomous charging system. In this way, the charging process can be carried out without the need for human intervention and maintenance requirements are minimized. In addition, the integrated use of the UAV's flight computers and mission computers such as Raspberry Pi allows the system to make real-time decisions and perform its tasks quickly and uninterruptedly. Thus, a fully autonomous operation can be made possible without any disruption in the UAV's area of responsibility.

Future research could focus on continuously monitoring the nearest charging station and dynamically calculating the minimum battery level required to streamline route and autonomous charging task assignments. Designs could be developed to work with either fixed or mobile charging stations across various areas rather than a specific location. This would allow for more effective and rapid solutions in UAV operations with mobile stations.

Additionally, research could explore autonomous charging processes for scenarios involving multiple UAVs working on joint missions. The proposed design could be expanded to include scenarios with obstacles, enhancing the development of autonomous charging systems. Lastly, ongoing monitoring of mobile or nearby stations and optimization techniques in the background will provide significant contributions to time management and the development of practical charging applications in future studies.

Acknowledgements

No Acknowledgements was declared by the authors.

Conflict of interest

No conflict of interest was declared by the authors.

Author contributions

All authors have contributed equally to the relevant work.

REFERENCES

- [1] O. VILLI ve M. Yakar, “Unmanned Aerial Vehicles and Geographic Information Systems Applications”, *Türkiye Coğrafi Bilgi Sistemleri Dergisi*, 2023, doi: 10.56130/tucbis.1297245.
- [2] O. VILLI ve M. Yakar, “Usage Areas and Sensor Types of Unmanned Aerial Vehicles”, *Türkiye İnsansız Hava Araçları Dergisi*, 2022, doi: 10.51534/tiha.1189263.
- [3] M. Uysal, M. K. Yılmaz, İ. Tiryakioğlu, ve N. Polat, “The Use of Unmanned Aerial Vehicles in Disaster Management”, *Anadolu Üniversitesi Bilim Ve Teknoloji Dergisi - B Teorik Bilimler*, 2018, doi: 10.20290/aubtdb.489086.
- [4] Z. Fang, “Strategies for Optimized UAV Surveillance in Various Tasks and Scenarios: A Review”, *Drones*, 2024, doi: 10.3390/drones8050193.
- [5] O. Hashesh, S. Hashima, R. M. Zaki, M. M. Fouda, K. Hatano, ve A. S. Tag Eldien, “AI-Enabled UAV Communications: Challenges and Future Directions”, *Ieee Access*, 2022, doi: 10.1109/access.2022.3202956.
- [6] K. F. Keong, “The Adoption of Unmanned Aerial Vehicles (UAV) Technology in the Construction Industry: Construction Stakeholders’ Perception”, *IOP Conf Ser Earth Environ Sci*, 2023, doi: 10.1088/1755-1315/1238/1/012024.
- [7] P. Pina ve G. Vieira, “UAVs for Science in Antarctica”, *Remote Sens (Basel)*, 2022, doi: 10.3390/rs14071610.
- [8] U. Challita, A. Ferdowsi, M. Chen, ve W. Saad, “Machine Learning for Wireless Connectivity and Security of Cellular-Connected UAVs”, *IEEE Wirel Commun*, 2019, doi: 10.1109/mwc.2018.1800155.

- [9] Z. Chen, “A Blockchain-Based Multi-Unmanned Aerial Vehicle Task Processing System for Situation Awareness and Real-Time Decision”, *Sustainability*, 2023, doi: 10.3390/su151813790.
- [10] K. Yakushiji, H. Fujita, M. Murata, N. Hiroi, Y. Hamabe, ve F. Yakushiji, “Short-Range Transportation Using Unmanned Aerial Vehicles (UAVs) During Disasters in Japan”, *Drones*, 2020, doi: 10.3390/drones4040068.
- [11] S. Bhattacharya, M. Hossain, K. Hoedebecke, M. Bacorro, Ö. Gökdemir, ve A. Singh, “Leveraging Unmanned Aerial Vehicle Technology to Improve Public Health Practice: Prospects and Barriers”, *Indian Journal of Community Medicine*, 2020, doi: 10.4103/ijcm.ijcm_402_19.
- [12] N. Zhao vd., “UAV-Assisted Emergency Networks in Disasters”, *IEEE Wirel Commun*, 2019, doi: 10.1109/mwc.2018.1800160.
- [13] M. Inghels vd., “Improving Early Infant Diagnosis for HIV-exposed Infants Using Unmanned Aerial Vehicles Versus Motorcycles for Blood Sample in Conakry, Guinea: A Comparative Cost-Effectiveness Analysis”, 2023, doi: 10.1101/2023.06.16.23291517.
- [14] S. Chung, A. A. Paranjape, P. Dames, S. Shen, ve V. Kumar, “A Survey on Aerial Swarm Robotics”, *Ieee Transactions on Robotics*, 2018, doi: 10.1109/tro.2018.2857475.
- [15] W. Guo ve S. Li, “Intelligent Path Planning for AGV-UAV Transportation in 6G Smart Warehouse”, *Mobile Information Systems*, 2023, doi: 10.1155/2023/4916127.
- [16] M. A. Eichleay, E. Evens, K. Stankevitz, ve C. Parker, “Using the Unmanned Aerial Vehicle Delivery Decision Tool to Consider Transporting Medical Supplies via Drone”, *Glob Health Sci Pract*, 2019, doi: 10.9745/ghsp-d-19-00119.
- [17] C. Parker vd., “Adding Unmanned Aerial Vehicles to HIV Supply Chains in Remote Settings: Modeling Feasibility and Cost in Turkana, Kenya”, *J Glob Health Rep*, 2021, doi: 10.29392/001c.28349.
- [18] T. Amukele, J. Street, K. C. Carroll, H. B. Miller, ve S. X. Zhang, “Drone Transport of Microbes in Blood and Sputum Laboratory Specimens”, *J Clin Microbiol*, 2016, doi: 10.1128/jcm.01204-16.
- [19] D. Wanner, “UAV Avionics Safety, Certification, Accidents, Redundancy, Integrity and Reliability: A Comprehensive Review and Future Trends”, 2024, doi: 10.36227/techrxiv.171328078.80258471/v1.
- [20] G. Macrina, L. Di Puglia Pugliese, F. Guerriero, ve G. Laporte, “Drone-Aided Routing: A Literature Review”, *Transp Res Part C Emerg Technol*, 2020, doi: 10.1016/j.trc.2020.102762.

- [21] D. Giordan vd., “The Use of Unmanned Aerial Vehicles (UAVs) for Engineering Geology Applications”, *Bulletin of Engineering Geology and the Environment*, 2020, doi: 10.1007/s10064-020-01766-2.
- [22] Muid, M. Evita, N. Aminah, M. Budiman, ve M. Djamil, “Determining Forest Fire Position From UAV Photogrammetry Using Color Filtration Algorithm”, *Joiv International Journal on Informatics Visualization*, 2022, doi: 10.30630/joiv.6.4.956.
- [23] P. Tang, “A Review of Electric UAV Visual Detection and Navigation Technologies for Emergency Rescue Missions”, *Sustainability*, 2024, doi: 10.3390/su16052105.
- [24] N. I. Sarkar ve S. Gul, “Artificial Intelligence-Based Autonomous UAV Networks: A Survey”, *Drones*, 2023, doi: 10.3390/drones7050322.
- [25] K. Vijayalakshmi vd., “Smart Agricultural–Industrial Crop-Monitoring System Using Unmanned Aerial Vehicle–Internet of Things Classification Techniques”, *Sustainability*, 2023, doi: 10.3390/su151411242.
- [26] B. E. Berrett, C. A. Vernon, H. Beckstrand, M. Pollei, K. W. Franke, ve J. D. Hedengren, “Large-Scale Reality Modeling of a University Campus Using Combined UAV and Terrestrial Photogrammetry for Historical Preservation and Practical Use”, *Drones*, 2021, doi: 10.3390/drones5040136.
- [27] Y. Bai, “Toward Autonomous Multi-Uav Wireless Network: A Survey of Reinforcement Learning-Based Approaches”, *Ieee Communications Surveys & Tutorials*, 2023, doi: 10.1109/comst.2023.3323344.
- [28] H. Ran vd., “A Novel Cooperative Searching Architecture for Multi-unmanned Aerial Vehicles Under Restricted Communication”, *Asian J Control*, 2021, doi: 10.1002/asjc.2517.
- [29] M. Keshavarz, A. Shamsoshoara, F. Afghah, ve J. Ashdown, “A Real-Time Framework for Trust Monitoring in a Network of Unmanned Aerial Vehicles”, 2020, doi: 10.1109/infocomwkskshps50562.2020.9162761.
- [30] C. Gong, W. Li, D. Gong, T. Li, ve F. Fan, “Energy-Efficient Task Migration and Path Planning in UAV-Enabled Mobile Edge Computing System”, *Complexity*, 2022, doi: 10.1155/2022/4269102.
- [31] D. Andrioiaia, “Predicting the RUL of Li-Ion Batteries in UAVs Using Machine Learning Techniques”, *Computers*, 2024, doi: 10.3390/computers13030064.
- [32] Z. Dou, “Real-Time Online Estimation Technology and Implementation of State of Charge State of Uncrewed Aerial Vehicle Lithium Battery”, *Energies (Basel)*, 2024, doi: 10.3390/en17040803.

- [33] G. Xu, L. Liu, ve X. Zhang, “Modeling and Performance Analysis for Low Altitude Electric UAVs”, 2016, doi: 10.2991/iccte-16.2016.184.
- [34] T. Bose, “QoS Enhancement in Rural Areas Through Energy-Efficient UAV-Assisted NOMA and OMA Data Transmission Utilizing Wide Elliptical Beam”, 2024, doi: 10.36227/techrxiv.171259694.49914104/v1.
- [35] Z. He, D. M. Gomez, A. de la Escalera, P. F. Peña, X. Lü, ve J. M. Armingol, “Battery-Soc Estimation for Hybrid-Power UAVs Using Fast-Ocv Curve With Unscented Kalman Filters”, *Sensors*, 2023, doi: 10.3390/s23146429.
- [36] S. Zhang, Y. Zeng, ve R. Zhang, “Cellular-Enabled UAV Communication: Trajectory Optimization Under Connectivity Constraint”, 2018, doi: 10.1109/icc.2018.8422584.
- [37] N. K. Üre, G. Chowdhary, T. Toksoz, J. P. How, M. A. Vavrina, ve J. Vian, “An Automated Battery Management System to Enable Persistent Missions With Multiple Aerial Vehicles”, *Ieee/Asme Transactions on Mechatronics*, 2015, doi: 10.1109/tmech.2013.2294805.
- [38] Y. N. Saravanakumar, “Power Sources for Unmanned Aerial Vehicles: State - Of - The Art Review”, 2023, doi: 10.20944/preprints202308.1367.v1.
- [39] X. Mou, D. T. Gladwin, J. Jiang, K. Li, ve Z. Yang, “Near-Field Wireless Power Transfer Technology for Unmanned Aerial Vehicles: A Systematical Review”, *Ieee Journal of Emerging and Selected Topics in Industrial Electronics*, 2023, doi: 10.1109/jestie.2022.3213138.
- [40] M. Le, L. H. Truong, T. V Quyen, C. V Nguyen, ve M. T. Nguyen, “Wireless Power Transfer Near-Field Technologies for Unmanned Aerial Vehicles (UAVs): A Review”, *Eai Endorsed Transactions on Industrial Networks and Intelligent Systems*, 2020, doi: 10.4108/eai.31-1-2020.162831.
- [41] H. Yan, S. Yang, Y. Chen, ve S. A. Fahmy, “Optimum Battery Weight for Maximizing Available Energy in UAV-Enabled Wireless Communications”, *Ieee Wireless Communications Letters*, 2021, doi: 10.1109/lwc.2021.3069078.
- [42] S. A. Hassnain Mohsan, N. Q. Hamood Othman, Y. Li, M. H. Alsharif, ve M. A. Khan, “Unmanned Aerial Vehicles (UAVs): Practical Aspects, Applications, Open Challenges, Security Issues, and Future Trends”, *Intell Serv Robot*, 2023, doi: 10.1007/s11370-022-00452-4.

- [43] Y. Qin, M. A. Kishk, ve M. Alouini, "Performance Evaluation of UAV-Enabled Cellular Networks With Battery-Limited Drones", *Ieee Communications Letters*, 2020, doi: 10.1109/lcomm.2020.3013286.
- [44] H. Pourrahmani, C. M. Isabelle Bernier, ve J. Van herle, "The Application of Fuel-Cell and Battery Technologies in Unmanned Aerial Vehicles (UAVs): A Dynamic Study", *Batteries*, 2022, doi: 10.3390/batteries8070073.
- [45] Y. Lozano-Hernández, I. M. de Cruz, O. Gutiérrez-Frías, N. Lozada-Castillo, ve A. Luviano-Juárez, "Design Procedure of a Low-Cost System for Energy Replenishment in a Quadrotor UAV Through a Battery Exchange Mechanism", *Drones*, 2023, doi: 10.3390/drones7040270.
- [46] P.-V. Mekikis vd., "Enabling Wireless-Powered IoT Through Incentive-Based UAV Swarm Orchestration", 2023, doi: 10.36227/tehrxiv.22718374.
- [47] M. Wu vd., "Development and Prospect of Wireless Power Transfer Technology Used to Power Unmanned Aerial Vehicle", *Electronics (Basel)*, 2022, doi: 10.3390/electronics11152297.
- [48] Huang, "MobiPower: Scheduling Mobile Charging Stations for UAV-Mounted Edge Servers in Internet of Vehicles", 2024, doi: 10.21203/rs.3.rs-4370261/v1.
- [49] Y. Wang, "Mobile Wireless Rechargeable UAV Networks: Challenges and Solutions", 2022, doi: 10.48550/arxiv.2203.13139.
- [50] H. Üçgün, U. Yüzgeç, ve C. Bayılmış, "A Review on Applications of Rotary-Wing Unmanned Aerial Vehicle Charging Stations", *Int J Adv Robot Syst*, 2021, doi: 10.1177/17298814211015863.
- [51] F. Morbidi, R. Cano, ve D. Lara, "Minimum-Energy Path Generation for a Quadrotor UAV", 2016, doi: 10.1109/icra.2016.7487285.
- [52] M. Saleh, "Trajectory Optimization of UAV-IRS Assisted 6G THz Network Using Deep Reinforcement Learning Approach", 2024, doi: 10.21203/rs.3.rs-4022303/v1.
- [53] K. Dorling, J. Heinrichs, G. G. Messier, ve S. Magierowski, "Vehicle Routing Problems for Drone Delivery", *IEEE Trans Syst Man Cybern Syst*, 2017, doi: 10.1109/tsmc.2016.2582745.
- [54] B. Galkin, J. Kibiłda, ve L. A. DaSilva, "UAVs as Mobile Infrastructure: Addressing Battery Lifetime", 2019. doi: 10.1109/mcom.2019.1800545.
- [55] H. Ghazzai, H. Menouar, A. Kadri, ve Y. Massoud, "Future UAV-Based ITS: A Comprehensive Scheduling Framework", *Ieee Access*, 2019, doi: 10.1109/access.2019.2921269.
- [56] Trotta, M. Di Felice, F. Montori, K. R. Chowdhury, ve L. Bononi, "Joint Coverage, Connectivity, and Charging Strategies for

- Distributed UAV Networks”, Ieee Transactions on Robotics, 2018, doi: 10.1109/tro.2018.2839087.
- [57] M. Y. Arafat ve S. Moh, “JRCS: Joint Routing and Charging Strategy for Logistics Drones”, IEEE Internet Things J, 2022, doi: 10.1109/jiot.2022.3182750.
- [58] C.-J. Huang, K.-W. Hu, ve H.-W. Cheng, “An Electric Vehicle Assisted Charging Mechanism for Unmanned Aerial Vehicles”, Electronics (Basel), 2023, doi: 10.3390/electronics12071729.
- [59] C. Huang, K. Hu, H.-W. Cheng, ve Y.-S. S. Lin, “A Mission-Oriented Flight Path and Charging Mechanism for Internet of Drones”, Sensors, 2023, doi: 10.3390/s23094269.
- [60] Dr. F. Elrahman Ahmed, “A Survey on Methods to Optimize Power Harvesting in Drones”, Global Journal of Researches in Engineering, 2024, doi: 10.34257/gjreavol24is1pg21.
- [61] M. Alolaiwy, “Multi-Objective Routing Optimization in Electric and Flying Vehicles: A Genetic Algorithm Perspective”, Applied Sciences, 2023, doi: 10.3390/app131810427.
- [62] R. Daş, B. Polat, ve G. Tuna, “Derin Öğrenme İle Resim Ve Videolarda Nesnelerin Tanınması Ve Takibi”, Fırat Üniversitesi Mühendislik Bilimleri Dergisi, 2019, doi: 10.35234/fumbd.608778.
- [63] F. G. Tan, A. S. Yüksel, E. Aydemir, ve M. Ersoy, “Derin Öğrenme Teknikleri İle Nesne Tespiti Ve Takibi Üzerine Bir İnceleme”, European Journal of Science and Technology, 2021, doi: 10.31590/ejosat.878552.
- [64] Z. SAYGILI ve G. Özmen, “İnsansız Hava Araçlarında Gömülü Sistem Üzerinden Derin Öğrenme İle Nesne Tespiti”, European Journal of Science and Technology, 2022, doi: 10.31590/ejosat.1081713.
- [65] B. Aksoy, K. KORUCU, Ö. ÇALIŞKAN, Ş. OSMANBEY, ve H. D. HALİS, “İnsansız Hava Aracı İle Görüntü İşleme Ve Yapay Zekâ Teknikleri Kullanılarak Yangın Tespiti: Örnek Bir Uygulama”, Düzce Üniversitesi Bilim Ve Teknoloji Dergisi, 2021, doi: 10.29130/dubited.1016195.
- [66] T. Öztürk, Y. Albayrak, ve Ö. Polat, “Object Tracking by PI Control and Image Processing on Embedded Systems”, 2015, doi: 10.1109/siu.2015.7130305.
- [67] G. Deniz, “Dört Rotorlu Bir İnsansız Hava Aracının Görüntü Tabanlı Otomatik Kontrolü Ve Hedef Takibi”, Gazi Üniversitesi Mühendislik-Mimarlık Fakültesi Dergisi, 2024, doi: 10.17341/gazimmfd.1198822.
- [68] Z. Liu, X. Miao, Z. Xie, H. Jiang, ve J. Chen, “Power Tower Inspection Simultaneous Localization and Mapping: A Monocular

- Semantic Positioning Approach for UAV Transmission Tower Inspection”, 2022. doi: 10.3390/s22197360.
- [69] Q. Ouyang, G. Xu, K. Liu, ve Z. Wang, “Wireless Battery Charging Control for Electric Vehicles: A User-involved Approach”, 2019. doi: 10.1049/iet-pel.2018.6332.
- [70] K. Tripathi, V. V Patel, ve R. Padhi, “Vision Based Automatic Landing With Runway Identification and Tracking”, 2018, doi: 10.1109/icarcv.2018.8581208.
- [71] H. W. Cheng, T.-L. Chen, ve C. Tien, “Motion Estimation by Hybrid Optical Flow Technology for UAV Landing in an Unvisited Area”, Sensors, 2019, doi: 10.3390/s19061380.
- [72] M. Aktaş, B. Baygüneş, S. Kivrak, B. Çavuş, ve F. Sözen, “Elektrikli Araç İçin Düşük Maliyetli Bir Batarya Yönetim Sistemi Tasarımı Ve Gerçekleştirilmesi”, European Journal of Science and Technology, 2020, doi: 10.31590/ejosat.779720.
- [73] K. KAYSAL, F. O. Hocoaoğlu, ve A. Kaysal, “Pasif Batarya Yönetim Sisteminin ARM Tabanlı Mikroişlemciler Kullanılarak Tasarımı Ve Deneysel Uygulaması”, Gazi Üniversitesi Fen Bilimleri Dergisi Part C Tasarım Ve Teknoloji, 2021, doi: 10.29109/gujsc.811313.
- [74] H. REYHAN, “Elektrikli Araçların Kablosuz Şarj Edilmesinde Kullanılan Güç Aktarım Yöntemlerinin İncelenmesi”, Ömer Halisdemir Üniversitesi Mühendislik Bilimleri Dergisi, 2023, doi: 10.28948/ngumuh.1307910.
- [75] F. AKKUŞ, “Elektrikli Araçlarda Kullanılan Lityum İyon Bataryaların Hava, Sıvı Ve Isı Borulu Termal Yönetim Sistemlerinin İncelenmesi”, Batman Üniversitesi Yaşam Bilimleri Dergisi, 2023, doi: 10.55024/buyasambid.1339607.
- [76] B. KESKİN, E. Ş. Günal, B. Urazel, ve K. Keskin, “Elektrikli Araç Bataryalarının Şarj Durumu Tahmini İçin Bir Model”, Nicel Bilimler Dergisi, 2022, doi: 10.51541/nicel.1117756.
- [77] M. Konar ve E. T. Kekeç, “İnsansız Hava Araçlarının Uçuş Süresinin Termal Hava Akımları Kullanılarak Arttırımı”, European Journal of Science and Technology, 2021, doi: 10.31590/ejosat.874809.
- [78] M. AKÇAY, “Çoklu İHA İle Çok Erkinli Sistemler”, European Journal of Science and Technology, 2022, doi: 10.31590/ejosat.1216730.



CHAPTER 16

Aviation Technologies and Applications
E-ISBN:978-605-338-471-7
2025, chap. (16) , pp.265-278.

İNSANSIZ HAVA ARACI KOMPOZİT KANATLARININ ISIL MODELLEMESİ VE ELEKTROTHERMAL ISITMA UYGULAMASI

Damla PEHLİVAN^{1,*}, Hasan AYDOĞAN²

ÖZET

İnsansız hava araçlarında tercih edilen kompozit yapılarda buzlanma önemli bir problemidir. Kanat yüzeylerinde buzlanmanın önlenmesi, aerodinamik verimlilik ve uçuş performansı açısından oldukça önemlidir. Söz konusu problemin çözümüne yönelik son yıllarda elektrotermal ısıtma tekniği ön plana çıkmaktadır. Bu çalışmada NACA0012 kanat profillerinin türbülanslı akış şartlarında enerji denklemi çözümünü de içeren çözümleri gerçekleştirilmiştir. Bu kapsamda, NACA0012 kanat profili üzerinde akış ve ısı transferi, uçuş değerlerine yakın 3 farklı hücum açısı ve 3 farklı Reynolds sayısında çözülerek sonuçlar kıyaslanmıştır. Bu amaçla, sonlu hacimler yöntemi ile Navier Stokes ve enerji denklemleri, sıkıştırılmaz ve zamana bağlı olmayan akış problemleri için çözülmüştür. Elde edilen ısı transfer katsayıları, ortotropik kanat ve plaka yapılarında doğru ısıtma stratejilerini belirlemek için kullanılmıştır. Yüksek Re sayılarında yüzey ısı akısının şiddeti nedeniyle, kanat sıcaklığı, hızlı bir şekilde dış akış sıcaklığına yakınsamaktadır. Bunu engellemek için, kanat içerisinde ısı üretimi gereklidir. Kanat yüzeyinde buzlanmayı engellemek için gerekli ısı üretimi değerleri araştırılmıştır. Elde edilen sonuçlar grafikler ve tablolarda sunulmuş ve tartışmalara yer verilmiştir. Kanat profili üzerinde taşınım katsayısı, Nusselt sayısı ve ısı akısı parametreleri grafiklerle gösterilmiş, bu parametrelerin Re sayısı ve hücum açısına bağlı olarak değişimine ilişkin tartışmalar ortaya konmuştur. İkinci aşamada, elde edilen ısı taşınım katsayısı değerleri kullanılarak, ortasında ısı üretimi bulunan, alt ve üst yüzeyinden taşınım ısı kaybı olan 3 boyutlu plaka için ısı transferi analizleri gerçekleştirilmiştir. Üst ve alt yüzeydeki yüksek ısı kaybına rağmen plaka ortasına tanımlanan ısı üretim yüzeyi ile sıcaklıkların makul seviyede tutulabildiği ortaya konmuştur.

Anahtar Kelimeler: İnsansız hava aracı, kompozit kanat, termal modelleme

1. GİRİŞ

İnsansız hava araçlarında (İHA) kompozit kanat yapıları, yüksek mukavemet ve düşük ağırlığa sahip olmalarıyla sıklıkla tercih edilmektedir. Kompozit yapıların mukavemet özelliklerinde değişimler, metalik yapılara göre daha dar bir sıcaklık aralığında olmaktadır. Ayrıca, buzlanma problemleri aerodinamik verimliliği ve uçuş dinamiklerini olumsuz yönde etkilemekte, uçuş güvenliği açısından önemli riskler oluşturmaktadır [1,2].

*Corresponding Author: damlapehlvan@gmail.com

0009-0007-9137-6669, Damla PEHLİVAN, Makine Mühendisliği, Teknoloji Fakültesi, Selçuk Üniversitesi (Doktora Öğrencisi), Konya, Türkiye
2 Prof. Dr. Hasan AYDOĞAN, Makine Mühendisliği, Teknoloji Fakültesi, Selçuklu, Konya, Türkiye

Kompozit kanat yapılarında, ısıtıcı tabakalar kullanımı yoluyla buzlanma problemlerin giderilmesine yönelik çalışmalar son yıllarda ön plana çıkmaktadır. Örneğin, Roy vd. [3] tarafından ortaya konulduğu üzere, Güney Kore tarafından geliştirilen KUS-FS hava aracı kanatları, Güney Kore tarafından geliştirilen KUH -1 Surion helikopteri pallerinde bu teknolojiye yararlanılmaktadır. Falzon vd. [4], elektriksel iletkenliği olan bir mat kullanarak karbon kompozit yapılarda ısı transferi davranışını incelemiştir. Laroche [5], deneysel yolla ve sonlu elemanlar analizleri yoluyla, belirli bir bölgesi ısıtılan kompozit plakalarda ısı transferi davranışını incelemiştir.

Literatürde yapılan çalışmalar olmakla birlikte, çalışmalarda taşınım katsayısının bulunması için genellikle 1 boyutlu ve düşük Re sayısında modellerden yararlanıldığı görülmektedir. Bu çalışmada daha doğru bir konvektif ısı katsayısı modellemesi için Navier Stokes denklemlerinin, enerji denklemiyle birlikte çözüm yolu seçilmiştir.

Isı taşınım katsayısı, kanatların termal tasarımı için önemli bir parametredir. Devi vd. [2] NACA0012 kanat profili üzerinde ısı taşınım katsayısının, hıza bağlı değişimini incelemiştir. Çalışma, 2 boyutlu olarak yapılmış, farklı kanat profillerine ve 3 boyuta genişletilmemiştir. Dag vd. [1] NACA4412 kanat profili üzerinde ısı transfer davranışını deneysel olarak incelemiştir. Zohary vd. [6], İHA uygulamaları için NACA0012, NACA4415 kanat profillerini farklı ağ yoğunluklarında çalışarak, aerodinamik katsayıları sayısal olarak tespit etmiştir. Wang vd. [7], NACA23012 kanat profili için farklı buzlanma koşullarında aerodinamik katsayıları hesaplamıştır.

Kompozitlerde ısı iletimi çalışılan önemli konulardan birisidir. Bilhassa karbon kompozitlerde ısı iletim katsayısı önemli ölçüde yöne bağlı olarak değişmektedir. Fiber yönünde iletim değerleri oldukça yüksekken, fibere dik yönde ısı iletimi oldukça düşük kalmaktadır. Karbon kompozitlerle yapılacak ısı transferi çalışmalarında bu durumun göz önünde bulundurulması önemlidir [5-7].

Mutnuri [8] farklı reçinelerin, ısı iletim davranışına etkisini araştırmıştır. Bu çalışmada, ısı iletim katsayısının izotropik olmadığı, ayrıca sıcaklığa bağlı olarak ısı iletim katsayısının bir miktar arttığı gösterilmiştir. Analitik modellerin cam elyaf kompozitlerde, karbon kompozitlere göre daha başarılı olduğunu belirtmiştir.

Szymiczek vd. [9], farklı fiber/reçine kütle oranlarına sahip farklı kompozit plakalar üreterek, kompozitlerin termal (k , C_p) özelliklerini incelemiştir. Test numuneleri üretildikten sonra, ısı iletim katsayıları belirlenmiştir.

Myungsoo vd. [10] kırılmış karbon elyafı ve epoksi reçine matlarının ısıtıcı eleman olarak kullanımına yönelik testler gerçekleştirmiştir. Farklı fiber kütle oranına sahip ısıtıcı matların farklı voltaj değerleri altında ısınma davranışları incelenmiştir.

Aktif elektrotermal yönetime sahip kompozit malzemeler; karbon iplikler(1), constantan telleri(2), elektrik iletken karbon matları(3), karbon nanotüp kağıdı(4), elektrik iletken metal yüzeyler(5) gibi seçeneklerin ısı üretimi amacıyla kullanımı yoluyla üretilebilmektedir. Isıtıcı bileşenlerin;

- Isının uygulandığı bölgede yüzey sıcaklığını aşırı arttırmaması, bununla birlikte tüm yapıda ve bilhassa kanat üzerinde sıcaklığı belli bir eşik değerin üstünde tutarak buzlanmayı önlemesi
- Kompozit yapıda delaminasyona neden olmaması, malzeme mukavemet özelliklerinde önemli bozulmaya yol açmaması
- Yüksek enerji tüketimine ihtiyaç oluşturmaması, verimli yapıda olması önemli parametrelerdir.

Bu kapsamda, içinde ısı üretimi olan ve konvektif hava akımına maruz kalan kanat yapıları için modelleme çalışmaları gerçekleştirilmiştir. Öncelikle kanat yapısı üzerinde, enerji denklemini de içerecek şekilde, Navier Stokes denklemlerinin modellemesi yapılmıştır. Isı taşınım katsayıları, kompozit kanat yapısının termal analizi için elde edilmiştir. Elde edilen ısı taşınım katsayısı değerleri kompozit levhalara uygulanarak, farklı Re ve hücum açısına tekabül eden farklı konveksiyon katsayısı ile farklı ısı üretim büyüklüğü şartlarında sıcaklık dağılımları elde edilmiştir.

Çalışma kapsamında, NACA0012 kanat profillerinin türbülanslı akış şartlarında enerji denklemi çözümünü içeren çözümleri gerçekleştirilmiştir. Bu kapsamda, NACA0012 kanat profili üzerinde akış ve ısı transferi, uçuş değerlerine yakın 3 farklı hücum açısı ve 3 farklı Reynolds sayısında çözümler sonuçlar kıyaslanmıştır. Bayraktar Mini UAV seyir hızına yakın değerler baz alınmıştır. Çözümler; 15, 20, 25 m/s hızlarında yapılmıştır. Çözümde sıkıştırılamaz, zamana bağlı olmayan akış modeli kullanılmıştır. Hızın düşük olması nedeniyle, sıkıştırılamaz akış varsayımı geçerli kabul edilebilir [2,6].

Türbülans modellemesi için gerçekleştirilebilir k-epsilon modeli kullanılmıştır. Giriş hava sıcaklığı için 253 Kelvin değeri kullanılmıştır. Çözümde, basınç temelli bir çözücü kullanılmıştır. Çözümde basınç değerlerinin elde edilmesi için SIMPLE algoritmasından yararlanılmıştır.

C-grid tipi ağ mimarisi ile dörtgen ağ elemanları kullanılmıştır. Kullanılan çözüm ağı elemanları, kanata yakın bölgede küçük, kanattan uzaklaştıkça daha büyük olacak şekildedir.

Yüksek Re sayılarında yüzey ısı akısının şiddeti nedeniyle, kanat sıcaklığı, hızlı bir şekilde dış akış sıcaklığına yakınsamaktadır. Bunu engellemek için, kanat içerisinde ısı üretimi gereklidir. Kanat yüzeyinde buzlanmayı engellemek için gerekli ısı üretimi değerleri çalışılmıştır.

Elde edilen sonuçlar, grafikler ve tablolarda sunulmuş ve tartışmalara yer verilmiştir. Kanat profili üzerinde taşınım katsayısı, Nusselt sayısı ve ısı akısı parametreleri grafiklerle çizdirilmiş, bu parametrelerin Re sayısı ve hücum açısına bağlı olarak değişimine ilişkin tartışmalar ortaya konmuştur.

2. AMAÇ

Çalışmanın amaçları;

- NACA0012 kanat konfigürasyonu ve kanat profilinin akış altında termal karakteristiklerini incelemek
- Farklı kompozit malzemelerin ısı iletim karakteristiklerini incelemek
- Kompozit kanatlarda akış ve ısı transferi modellemeleri gerçekleştirerek, en uygun kanat ısıtma çözümlerini ortaya koymak
- Özgün çözümler üreterek, kompozit kanatların termal açıdan iyileştirilmesine yönelik literatüre katkı sağlamak
- Elde edilen optimum çözümlerden teknolojik olarak yararlanmaktır.

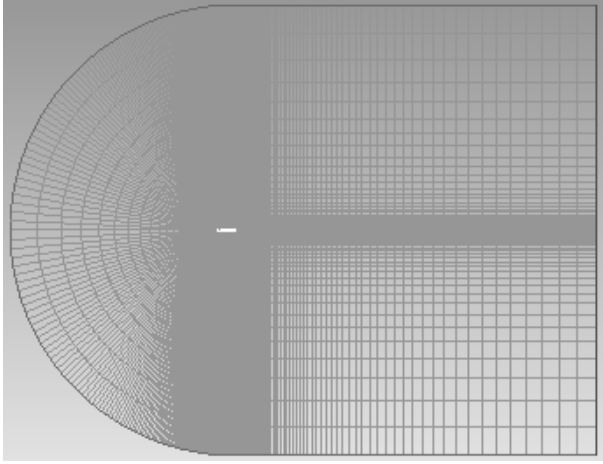
3. YÖNTEM

Çalışmada, her bir çözüm için aşağıdaki yöntem takip edilmiştir:

1. Ağ yapısının oluşturulması
2. Türbülans modelinin seçilmesi
3. Hesaplamalı akışkanlar dinamiği çözümünün enerji denklemini de içerecek şekilde yakınsamaya kadar çalıştırılması

4. Isı transferine ilişkin parametrelerin çözümlerden çıkarılması
5. Isı transferi verilerinin kompozit termal modellemesinde sınır şartı olarak kullanımı
6. Kompozit plaka ve kanatlara yönelik termal modellemelerin gerçekleştirilmesi

Bu amaçla, sonlu hacimler yöntemi ile Navier Stokes ve enerji denklemleri, sıkıştırılmaz ve zamana bağlı olmayan akış problemleri için çözülmüştür. Elde edilen ısı transfer katsayıları, ortotropik kanat ve plaka yapılarında doğru ısıtma stratejilerini belirlemek için kullanılmıştır. Adım 1 kapsamında kullanılan çözüm ağı şematik olarak Şekil 1’de verilmiştir.



Şekil 3. Çözüm ağı yapısı

Çözüm ağına ilişkin parametreler Tablo 1’de verilmiştir.

Tablo 3. Çözüm ağına ilişkin termal parametreler

X koordinatları (m)	-11.5	21.0
Y koordinatları (m)	-12.5	12.5
Hücre tipi	Dörtgen	
Hücre sayısı	20700	
En küçük hücre alanı (m ²)	3.40E-6	
En büyük hücre alanı (m ²)	1.74	
Airfoil uzunluğu	1 m	

Çalışmada, gerçekleştirilebilir k-epsilon modeli kullanılmıştır. Bu model, k-epsilon standart modeline göre daha gerçekçi sonuçlar vermektedir [8]. Türbülanslı akışta duvara yakın bölgelerin nümerik çözümünde Menter-Lechner yaklaşımı kullanılmıştır. Bu yaklaşım, kanat akışları için iyi sonuç vermektedir [5]. (Adım 2)

Navier Stokes denklemleri ve enerji denklemi, çalışma kapsamında çözülmektedir. (Adım 3)

Süreklilik (kütlenin korunumu) denklemi

$$\frac{\partial \rho}{\partial t} + \frac{\partial(\rho u)}{\partial x} + \frac{\partial(\rho v)}{\partial y} = 0 \quad (1)$$

X momentum denklemi

$$\frac{\partial(\rho u)}{\partial t} + \frac{\partial(\rho u u)}{\partial x} + \frac{\partial(\rho v u)}{\partial y} = \frac{-\partial p}{\partial x} + \frac{\partial}{\partial x} \left(\mu \frac{\partial u}{\partial x} \right) + \frac{\partial}{\partial y} \left(\mu \frac{\partial u}{\partial y} \right) + s u \quad (2)$$

Y momentum denklemi

$$\frac{\partial(\rho v)}{\partial t} + \frac{\partial(\rho u v)}{\partial x} + \frac{\partial(\rho v v)}{\partial y} = \frac{-\partial p}{\partial y} + \frac{\partial}{\partial x} \left(\mu \frac{\partial v}{\partial x} \right) + \frac{\partial}{\partial y} \left(\mu \frac{\partial v}{\partial y} \right) + s v \quad (3)$$

Enerji denklemi

$$\frac{\partial(\rho T)}{\partial t} + \frac{\partial(\rho u T)}{\partial x} + \frac{\partial(\rho v T)}{\partial y} = \frac{\partial}{\partial x} \left(\frac{k}{C_p} \frac{\partial T}{\partial x} \right) + \frac{\partial}{\partial y} \left(\frac{k}{C_p} \frac{\partial T}{\partial y} \right) + s T \quad (4)$$

SIMPLE çözüm yaklaşımı, basınç ve hız değerleri arasındaki ilişkiyi tespit etmekte kullanılmaktadır [7]. Bu yaklaşımla, basınç için, süreklilik denkleminde yararlanarak yeni bir denklem üretilmekte ve basınç değerlerine göre hız alanı düzeltilmektedir.

SIMPLE Algoritması:

- Sınır şartlarını ata
- u,v, P değişkenlerine ilk değerlerini ver
- Momentum denklemini çözerek hız değerlerini elde et
- Hesaplama hücre duvarlarında kütle akılarını hesapla
- Basınç düzeltme denklemini çözerek, p'(basınç düzeltme) değerlerini bul

- Basıncı relaksasyon parametresi kullanarak düzelt, $p^{k+1}=p^k + \text{alfa}_p * p'$,
- Hızı relaksasyon parametresi kullanarak düzelt $(u,v)^{k+1}=(u,v)^k + (\text{alfa}_{u,v}) * (u,v)'$,
- Hücrelerdeki net kütle akısı belli bir limite yaklaşıncaya kadar iterasyonları tekrarla

SIMPLE algoritmasında, basınç için süreklilik denkleminde yararlanarak yeni bir denklem üretilmekte ve basınç değerlerine göre hız alanı düzeltilmektedir [4]. Momentum, enerji, k ve epsilon parametrelerinin çözümünde 3. Dereceden MUSCL algoritması kullanılmıştır. Hücum açısı çözümleri, 0,3, ve 6 derece için gerçekleştirilmiştir. Epsilon ve türbülans kinetik enerji hariç tüm parametreler için 1e-6 mutlak hata limiti, bu iki parametre için ise 1e-5 mutlak hata limiti baz alınmıştır.

Nusselt sayısı, ısı taşınım katsayısı ve ısı iletim katsayısı arasındaki ilişkiyi ifade eden bir boyutsuz sayıdır. Sayısal olarak aşağıdaki şekilde hesaplanmaktadır:

$$Nu_L = \frac{\frac{\partial T_w}{\partial n} * L}{T_{wall} - T_{\infty}} \quad (5)$$

Literatürde, Nusselt sayısı ile Reynolds ve Prandtl sayısı arasında ilişkiyi ortaya koyan çeşitli denklemler bulunmaktadır. Boru akışı için Colburn [11] tarafından aşağıdaki denklem önerilmektedir;

$$Nu = 0.023 * Re^{0.8} Pr^{0.33} \quad (6)$$

Samadani ve Morency [12] tarafından denklem 7, ortalama Nusselt sayısı için önerilmektedir:

$$Nu = (0.0289 Re^{0.81} - 257 cl^2) Pr^{1/3} \quad (7)$$

Denklem 7'de yer alan cl terimi, kaldırma kuvveti katsayısıdır. Bu denklem ile üretilen sonuçlar, türbülans modellemesi sonucu çıkan sonuçlarla kıyaslanmış ve iyi bir uyum görülmüştür. Ancak denklem 7, ısı transferinin kanat üzerinde bölgesel değişimini değil, ortalama değerini vermektedir.

4. BULGULAR

Çözümlerin yakınsama karakteristikleri grafiklerle gösterilmiştir. Hücüm açısı ve Re sayısı arttıkça, çözümün yakınsaması için gerekli iterasyon sayısı artmıştır. Ayrıca, artan hücüm açısı ve Re sayısı durumlarında, k ve epsilon terimleri için yakınsama davranışının yavaş olması nedeni ile bu terimlerin relaksasyon değerleri düşürülerek yakınsama davranışı iyileştirilmiştir. Bununla birlikte, çözümlerin tamamı yakınsamıştır.

Elde edilen sonuçlar, kanat üzerinde ısı taşınım ve Nusselt sayısının büyük ölçüde değişkenlik gösterdiğini ortaya koymaktadır. Kanadın arka kısımlarında (fırar kenarına doğru) taşınım katsayısı ve Nusselt sayısının mutlak değeri azaldığı görülmektedir.

Re sayısı arttıkça ısı taşınımının doğrusal olmayan bir şekilde arttığı görülmüştür. Hücüm açısının sıfırdan farklı olduğu durumlarda, kanadın üst yüzeyi ve alt yüzeyi arasında ısı taşınım değerlerinin farklılaştığı gözlemlenmiştir. Simetrik duruma kıyasla, hücüm açısının sıfırdan farklı olduğu durumlarda, kanadın alt yüzeyinde, ısı transferi ve ısı transferine ilişkin katsayıların mutlak büyüklüğü artmakta, üst yüzeyinde ise azalmaktadır. Toplam ısı transferi büyüklüğü, hücüm açısı arttıkça, azalmaktadır. Üst ve alt yüzeylerin ısı transfer katsayıları farkı, kanadın hücüm kenarına yakın kesiminde oldukça fazlayken, bu fark, kanadın fırar kenarına yakın arka kesiminde kapanmaktadır.

Azami ısı transferi noktasının hücüm açısına bağlı değişimi de araştırılmıştır. Hücüm açısı arttıkça azami ısı transferinin gerçekleştiği bölge, hücüm kenarına yaklaşmaktadır. Bu durumda, ısı kaybını telafi etmek ve buzlanmayı önlemek üzere, kanadın hücüm kenarına daha yakın bölgelerinde daha iyi bir ısıtma ihtiyacı oluşabileceği görülmektedir. Kullanılan fiziksel değerler Tablo 2’de verilmiştir [6]. Çözüm alanında Hız girişi sınır şartı ($V_{giriş}=15,20,25$ m/s) ve basınç çıkışı sınır şartları ($P_{çıkış}=0$) kullanılmıştır.

Tablo 4. Fiziksel değerler

Yoğunluk	Cp(J/kgK)	Isı iletim katsayısı (W/mK)	
1kg/m ³	1000	0.0242	
Hız (m/s)	Re	Dinamik Viskozite (Ns/m ²)	Dış Akış Sıcaklığı (K)
15	9.4406e+05	1.6e-05	253 K
20	1.2587e+06		
25	1.5734e+06		

Sınır şartı olarak girişte kullanılan hız değerleri Tablo 3’de verilmiştir.

Tablo 5. Hız değerleri

Hücum açısı (derece)	0 ,3,6
Hız büyüklüğü (m/s)	15,20,25
Hız bileşenleri	
V_x	cosd(hücum)*(15,20,25)
V_y	cosd(hücum)*(15,20,25)

Çözücü relaksasyon parametreleri Tablo 4’te görülmektedir.

Tablo 6. Çözücü relaksasyon parametreleri

Basınç	0.3
Yoğunluk	1
Momentum	0.7
Türbülans kinetik enerji	0.8
Türbülans disipasyon oranı	0.8

Akış ve enerji denklemlerinin kanat profili üzerinde 9 farklı konfigürasyonda çözümü yapılmıştır. Bu konfigürasyonlar Tablo 5’te verilmiştir.

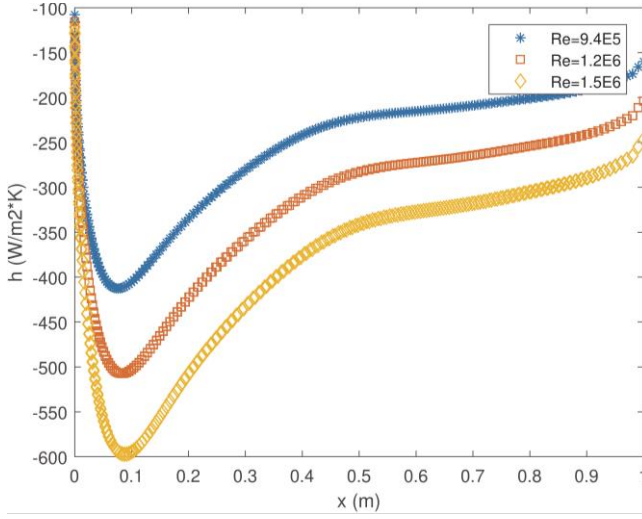
Tablo 7. Çözüm konfigürasyonları

Çözüm No	Hız (m/s)	Sıcaklık(freestream) (K)	Hücum açısı (derece)
1	15	253	0
2	15	253	3
3	15	253	6
4	20	253	0
5	20	253	3
6	20	253	6
7	25	253	0
8	25	253	3
9	25	253	6

Isı taşınım katsayısının, hücum açısı ve Re sayısına bağlı değişimleri, takip eden şekillerde (Şekil 2-4) verilmiştir.

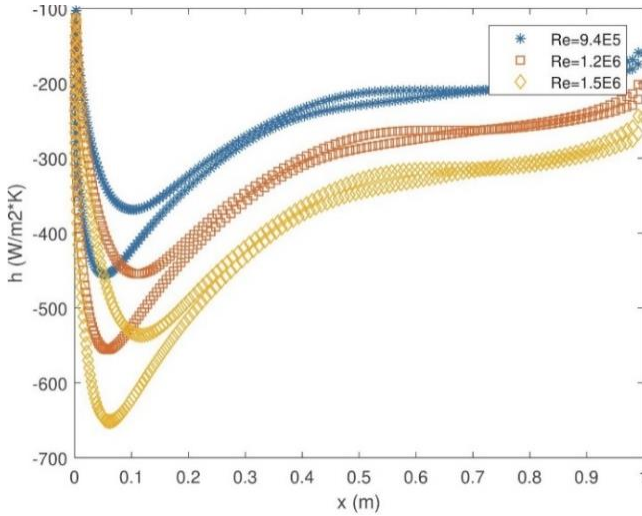
Şekil 2’de Re sayısının ısı taşınım katsayısını arttırıcı etkisi net şekilde görülmektedir.

CHAPTER 16: İNSANSIZ HAVA ARACI KOMPOZİT KANATLARININ ISIL MODELLEMESİ VE ELEKTROTHERMAL ISITMA UYGULAMASI



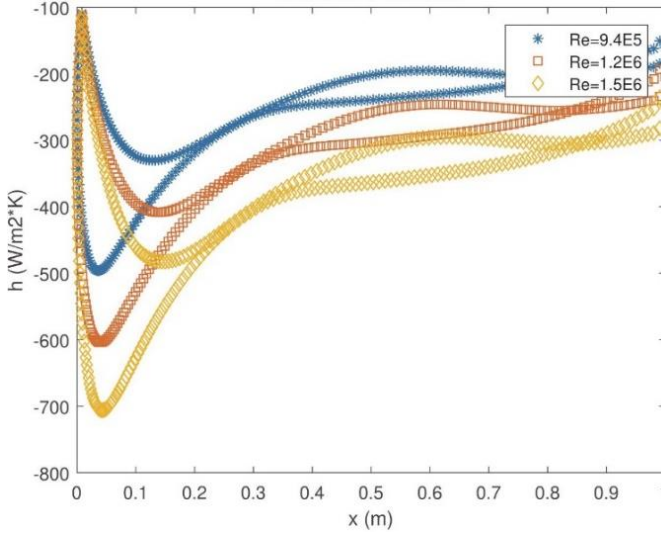
Şekil 4. 0° hücum açısı altında ısı taşınım katsayısı profilleri

Şekil 3’de görüldüğü üzere, kanadın alt ve üst yüzeylerinde ısı taşınım katsayıları farklılaşmıştır. Isı taşınımının maksimum olduğu nokta, kanadın üst ve alt yüzeylerinde tam olarak aynı noktaya denk gelmemektedir. Şekil 2 ile kıyaslandığında alt yüzeyde ısı taşınımının en fazla olduğu nokta, hücum kenarına doğru ilerlemektedir. Üst ve alt yüzeyler ortasında ısı taşınımı açısından önemli farklılık oluşmuştur. Bu durum, ısıtıcı yüzeyin kanadın alt yüzeyine daha yakın olması durumunda daha iyi sonuçlar alınabileceğine işaret etmektedir.



Şekil 5. 3° hücum açısı altında ısı taşınım katsayısı profilleri

Şekil 4’de görüldüğü üzere, kanadın alt ve üst yüzeyleri arasındaki taşınım katsayısı farkı, hücum açısı arttıkça artmaktadır. Bu fark, Şekil 2’de olduğu gibi hücum kenarına doğru giderek azalış göstermektedir.



Şekil 6. 6° hücum açısı altında ısı taşınım katsayısı profilleri

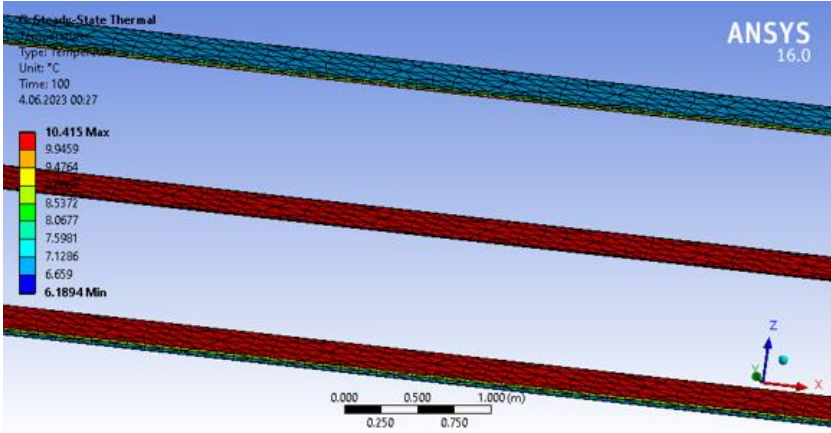
Isıtıcı Yüzey Olan Plaka Çözümleri:

İkinci aşamada, elde edilen ısı taşınım katsayısı değerleri kullanılarak, ortasında ısı üretimi bulunan, alt ve üst yüzeyinden taşınım ile ısı kaybı olan 3 boyutlu plaka için ısı transferi analizleri Ansys Mechanical 16 platformunda gerçekleştirilmiştir. Üst ve alt yüzeydeki yüksek ısı kaybına rağmen plaka ortasına tanımlanan ısı üretim yüzeyi ile sıcaklıklar istenen seviyede tutulabilmektedir.

Tablo 8. Kompozit levha çözümüne ilişkin parametreler

Üst ve alt yüzeyler ısı taşınım katsayısı	$h=400 \text{ W/m}^2\text{K}$
Dış ortam sıcaklığı	-6 derece santigrat
Yan yüzeyler	İzole
Plaka ilk sıcaklığı:	10 derece santigrat
Plaka ısı iletim katsayısı	0.5 W/mK
Plaka ortasında ısı üretimi	$10E^3 \text{ W/m}^2$
Isı üretim levhası kalınlığı	10 mm
Toplam plaka kalınlığı	100 mm
Plaka ebatları	10 m x 1 m x 0.1 m

Çözümler zamana bağlı olmayan ısı transferi şeklinde gerçekleştirilmiştir (Şekil 5). Plakalar arasında sıcaklık eşleme coupling tanımlanmıştır. En altta görülen parçanın üst yüzeyi ile ortadaki parçanın alt yüzeyi aynı sıcaklıktadır. Ortadaki plakanın üst yüzeyi ile üstteki plakanın alt yüzeyi aynı sıcaklıktadır. Analiz sonucunda uygun sıcaklık değerleri elde edilmiştir. Bu şartlar altında buzlanma görülmeyecektir. Isı üretim değerlerine bağlı olarak plaka sıcaklığının önemli ölçüde değiştiği de yapılan sayısal çalışmalarda görülmüştür.



Şekil 7. Isıl analiz sonuçları

5. ÖNERİLER VE SONUÇ

Buzlanma, hava aracı kazalarının en önemli sebeplerinden birisidir[7]. Bu alanda geliştirilecek çözümler önem arz etmektedir. Ayrıca, kanat yüzeylerinde sıcaklık düşüşü neticesinde gelişen buzlanmanın önlenmesi aerodinamik verimlilik ve uçuş performansı açısından da önem taşımaktadır [13,14]. Çalışma, hava aracı kanat profillerinin gerçek uçuş şartlarında, farklı Re ve hücum açılarında modellenmesini içermektedir. Ayrıca, elde edilen ısı akısına göre kompozit kanat tasarımında aktif elektrotermal ısıtmaya yönelik çözümler gerçekleştirilmiştir. Üst ve alt yüzeydeki yüksek ısı kaybına rağmen plaka ortasına tanımlanan ısı üretim yüzeyi ile sıcaklıkların makul seviyede tutulabildiği ortaya konmuştur.

Benzer teknoloji ve sistemler insanlı hava araçları (uçak, helikopter vb.) için de yararlı olacaktır. Aktif termal yönetim sistemine sahip ileri kompozit malzemeler konusunda yapılacak araştırmaların birçok alanda katkı sağlayacağı değerlendirilmektedir.

Uçak kazaları arasında buzlanma önemli bir yer tutmakta olup, aktif termal yönetime sahip malzeme ve yapılar bu kazaların önüne geçilmesi bakımından önem taşımaktadır.

Bu kapsamda, ısıtıcı yüzeyin kompozit kanat içerisinde yerleşimi ve gücüne ilişkin çalışmalar geliştirilebilir. Farklı hücum açılarında akış altında ısı taşınım katsayıları ve Nusselt sayıları çalışılabilir. Sayısal modelleme çalışmalarını müteakip deneysel çalışmalar gerçekleştirilebilir.

Teşekkürler

Yazarlar tarafından herhangi bir Teşekkürler beyan edilmemiştir.

Çıkar çatışması

Yazarlar tarafından herhangi bir çıkar çatışması beyan edilmemiştir.

Yazar katkıları

Damla Pehlivan: Özet, Yöntem, Bulgular kısımlarını hazırlamıştır. Hasan Aydoğan: Giriş, Amaç, Öneriler ve Sonuç kısımlarını hazırlamıştır.

REFERANSLAR

- [1] Dag, Yusuf, Akwaboa, Stephen, Mensah, Patrick. Determination of convective heat transfer for subsonic flows over asymmetric airfoil NACA 4412. In The 15th International Heat Transfer Conference; 2014.
- [2] Devi, P. V. Paulson, V. Madhanraj & Dilip A. Shah, Heat transfer and temperature effects on a dimpled NACA0012 airfoil with various angles of attack. International Journal of Ambient Energy 2017; 39(8): 783-786.
- [3] Roy, R., Raj, L. P., Je-Hyun, J, Min-Young C., Jin-Hwe, K. Myong, R. S. Multiphysics anti-icing simulation of a CFRP composite wing structure embedded with thin etched-foil electrothermal heating films in glaze ice conditions. Composite Structures 2021; 276: 114441.
- [4] Falzon, B. G., Robinson, P., Frenz, S., Gilbert, B. Development and evaluation of a novel integrated anti-icing/de-icing technology for carbon fibre composite aerostructures using an electro-conductive textile. Composites Part A: Applied Science and Manufacturing 2015; 68: 323-335.
- [5] Laroche, A., Comparative Evaluation of Embedded Heating Elements as Electrothermal Ice Protection Systems for Composite Structures. Msc., Concordia University, Montreal, Canada, 2017

- [6] Zohary, A. & Asrar, W. & Aldheeb, M. Numerical Investigation on the Pressure Drag of Some Low-Speed Airfoils for UAV Application. *CFD Letters* 2021; 13: 29-48.
- [7] Wang, Boyu & Agarwal, Ramesh, Numerical Simulation of Flow past an Airfoil with Ice Accretion on Leading Edge. MSc, McKelvey School of Engineering, Missouri, USA, 2021.
- [8] Mutnuri, B., Thermal conductivity characterization of composite materials. MSc, West Virginia University, West Virginia, USA, 2006.
- [9] Szymiczek, M.; Buła, D.; Koczwara, J. Influence of the Reinforcement Structure on the Thermal Conductivity and Surface Resistivity of Vinyl Ester Composites Used on Explosion-Proof Enclosures of Electrical Equipment. *Materials* 2022; 15: 5190.
- [10] Myungsoo Kim, Dae Han Sung, Kyungil Kong, Nari Kim, Byeong-Joo Kim, Hyung Wook Park, Young-Bin Park, Mooyoung Jung, Sang Hwan Lee, Su Gi Kim. Characterization of resistive heating and thermoelectric behavior of discontinuous carbon fiber-epoxy composites. *Composites Part B: Engineering*. 2016; 90: 37-44.
- [11] Colburn, A.P. (1933) A Method of Correlating Forced Convection Heat Transfer Data and A Comparison with Fluid Friction. *International Journal of Heat and Mass Transfer*, 7, 1359-1384.
- [12] Samadani, S., Morency, F. Heat Transfer Correlations for Smooth and Rough Airfoils. *Fluids* 2023; 8(2): 66.
- [13] Ozgen, S. AEE 716 Aircraft Icing Lecture notes; 2011.
- [14] <https://www.baykartech.com/en/uav/bayraktar-mini-iha/> Erişim tarihi: 11.05.2023.



CHAPTER 17

Aviation Technologies and Applications
E-ISBN:978-605-338-471-7
2025, chap. (17), pp.279-299.

ANALYTICAL PARAMETER STUDY FOR A WIND TURBINE BLADE

Aysun SOYSAL^{1,*}, İbrahim ÖZKOL², Erol UZAL³

ABSTRACT

In this study, parameter selection for the design of wind turbine blades are investigated by using two different blade models: Timoshenko model and Bernoulli-Euler model. Firstly, governing differential equations of the models were solved for various boundary conditions of the blade by using an analytical method, named Differential Transform Method. Then, an application is carried out to compare the models in terms of effect of axial load on vibration frequencies and vibration mode shapes, blade length, and geometric coupling term of the blade. The findings of the study showed that for C-F, C-C, and S-S boundary condition, i) regardless of the type of the boundary condition, compared to absence of the axial load case, the compression axial load causes increase in vibration frequencies and the tensile axial load causes reduce in vibration frequencies, ii) for the same material properties, the vibration frequencies of Timoshenko model are less than the vibration frequencies of Bernoulli-Euler model, iii) for the same magnitude of load application, the models begin to fail much earlier in compression load compared to tension load, iv) when the blade length is reduced to $L/4$, the vibration modes of Bernoulli-Euler model are more distorted compared to Timoshenko model; however, when the length is reduced to $L/6$, the vibration modes, especially the second and third modes, are very distorted for both models, and v) when the value of the geometric coupling term is increased in the range of $x_\alpha/2$ to $8x_\alpha$, the vibration modes begin to differ noticeably, but their tendency are almost same in both models. Based on the findings of this study, it can be stated that the structural responses of both models are approximately the same, however, it is suggested that the Timoshenko model is more suitable for the blade design if thicker (stubby) structures and especially rotational motion are needed.

Keywords: Vibration analysis, parameter selection, differential transform method, Timoshenko beam model, Bernoulli-Euler beam model

*Corresponding Author: soysal17@itu.edu.tr

¹ 0000-0003-0708-4529, Department of Mathematical Engineering, Faculty of Science and Letters, İstanbul Technical University, İstanbul, Turkey

² 0000-0002-9300-9092, Department of Aerospace Engineering, Faculty of Aviation and Space, İstanbul Technical University, İstanbul, Turkey

³ 0000-0003-0008-1376, Department of Mechanical Engineering, Faculty of Mechanical, İstanbul University-Cerrahpasa, İstanbul, Turkey

1. INTRODUCTION

The one of the principle aims of wind turbine design is to achieve the maximum possible efficiency during routine energy production. In this process, the blades of wind turbines are the most important critical parts of the wind turbines [1] thanks to their ability to capture energy from the wind [2]. After capturing most wind energy, the blades convert the energy into electricity [3]. Therefore, technically wind turbine blades are the most important components of the design. During the design of the blades, the manufacturing cost is approximately 15-20% of the wind turbine manufacturing cost [4]. Thus, it is of great importance to investigate the design of wind turbine blades not only to increase the efficiency of wind turbines but also to contribute to the cost of blade design.

The importance of beam-type structures in analytically based modeling of wind turbine blades is increasing in the literature. Jokar et al. [5] derived a dynamic model for a wind turbine blade and carried out free vibration analysis by using Rayleigh-Ritz method to investigate the effect of the gravity force, blade rotary inertia, and centrifugal force of the blade on the dynamic characteristics. Ondra et al. [6] conducted free vibration and stability analysis of a blade-tendon system to examine the influence of the number of the attachment points and their location on the diagram of the beam-tendon system which is represented by an axially loaded Euler–Bernoulli beam. The authors used a boundary value problem solver to determine the effect of the axial load on the natural frequencies and mode shapes of the system. Tufekci et al. [7] proposed a simple analytical model for a wind turbine blade, called a novel three-dimensional analytical straight beam model, to obtain the natural frequencies and related mode shapes. Wang et al. [8] presented an analytical approach to analyse the interaction between a wind turbine and tower by using flexible thin-walled beam theory. They carried out free vibration and forced vibration analysis to study the effect of the tower's stiffness on the blade tip deformation. Eslimy-Isfahany and Banerjee [9] used an axially loaded uniform coupled bending torsion beam to predict the response of a cantilever wind turbine blade to deterministic and random loads. In the analysis, they used a normal mode method in the free vibration analysis and modal expansion method in the forced vibration analysis.

The aim of this study is to investigate the effects of parameters for a wind turbine blade from an analytical perspective. For this purpose, two different blade models are used: Timoshenko model and Bernoulli-Euler model. Firstly, the governing equations of the models are solved for

various boundary conditions. Then, the effects of the axial force, length, and geometric coupling term of the blade on the dynamic characteristics of the blade models are investigated for various boundary conditions. A schematic diagram that summarizes the steps of the study is given in Fig. 1.

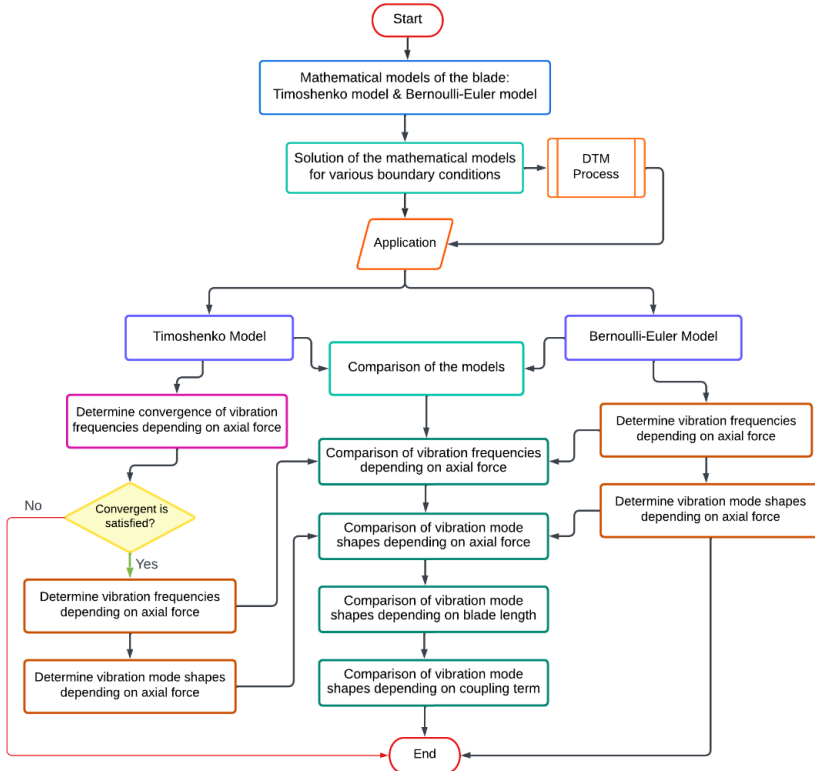


Figure 1. A schematic diagram summarizing the steps of the study.

2. MATERIALS AND METHODS

2.1 Mathematical Model

The wind turbine blades are produced finely to overcome the deformations caused by the bending motion and torsional motion of the wind turbine during operation. [10]. Thus, a coupled bending-torsion beam can be considered to model a wind turbine blade [9]. Fig. 2 shows a wind turbine blade profile with length L . Here, $u(x, t)$ denotes bending translation, $\psi(x, t)$ denotes torsional rotation, and $\theta(x, t)$ denotes the rotation of the cross-section due to bending alone; P is a constant tensile axial force, and x_α is geometric coupling term.

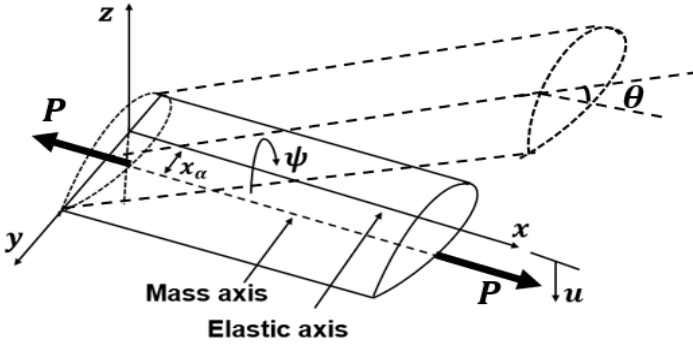


Figure 2. Profile a of wind turbine blade.

The governing equations and boundary conditions of the blade are given in Equation (1) – (9)

(a) Governing equations:

$$EI\theta'' + kAG(u' - \theta) - \rho I\ddot{\theta} = 0 \quad (1)$$

$$kAG(u'' - \theta') + P(u'' - x_\alpha\psi'') - m(\ddot{u} - x_\alpha\ddot{\psi}) = 0 \quad (2)$$

$$GJ\psi'' + P\{I_\alpha/m\}\psi'' - x_\alpha u'' - I_\alpha\ddot{\psi} + mx_\alpha\ddot{u} = 0 \quad (3)$$

with

$$M = -EI\theta' \quad (\text{Bending moment}) \quad (4)$$

$$S = -kAG(u' - \theta) - P(u' - x_\alpha\psi') \quad (\text{Shear force}) \quad (5)$$

$$T = GJ\psi' - \{PI_\alpha/m\}\psi' - Px_\alpha u' \quad (\text{Torque}) \quad (6)$$

(b) Boundary conditions for different end conditions ($x = 0, L$):

$$\text{Clamped-Free (C-F): } u = \theta = \psi = 0, \quad S = M = T = 0 \quad (7)$$

$$\text{Clamped-Clamped (C-C): } u = \theta = \psi = 0, \quad u = \theta = \psi = 0 \quad (8)$$

$$\text{Simply Supported-Simply Supported (S-S): } u = \psi = M = 0, \quad u = \psi = M = 0 \quad (9)$$

where EI , GJ , and kAG are, consecutively, the bending, torsional, and shear rigidities of the blade; I is the second moment of area of the blade cross section; m (i.e., ρA , where A is the cross-sectional area and ρ is density) is mass of the blade per unit length; x_α is geometric coupling term; and I_α is polar mass moment of inertia per unit length of the blade.

2.2 Solution of the Model

In the solution of the model, the solutions are assumed in the following form:

$$u(x, t) = U_n(x)\sin(\omega_n t + \phi_1) \tag{10}$$

$$\psi(x, t) = \Psi_n(x)\sin(\omega_n t + \phi_2) \tag{11}$$

$$\theta(x, t) = \Theta_n(x)\sin(\omega_n t + \phi_3) \tag{12}$$

where $U_n(x)$, $\Psi_n(x)$, and θ_n are vibration modes, ω_n is the vibration frequency, ϕ_1 , ϕ_2 , and ϕ_3 are phase angles, and $n = 1, 2, 3 \dots$.

Substituting Equations (10) – (12) into Equations (1) – (9) reduces the partial differential equations to ordinary differential equations as follows:

$$EI\Theta_n'' + kAG(U_n' - \Theta_n) + \rho I\omega_n^2\Theta_n = 0 \tag{13}$$

$$kAG(U_n'' - \Theta_n') + P(U_n'' - x_\alpha\Psi_n'') + m\omega_n^2(U_n - x_\alpha\Psi_n) = 0 \tag{14}$$

$$GJ\Psi_n'' + P\{(I_\alpha/m)\Psi_n'' - x_\alpha U_n''\} - \omega_n^2(mx_\alpha U_n - I_\alpha\Psi_n) = 0 \tag{15}$$

with the boundary conditions given in Equations (7) – (9) when $u = U_n$, $\psi = \Psi_n$ and $\theta = \Theta_n$.

In the solution of the ordinary differential equations given in Equations (13) – (15), Differential Transform Method (DTM) is applied. According to the theory of the DTM [11], an analytical function $f(x)$ is expanded to a power series with the center x_0 in domain of $f(x)$. Then, the differential transform and inverse transform of $f(x)$ are respectively stated by $F[k]$ and $f[x]$ as follows:

$$F_D[k] = \frac{1}{k!} \left(\frac{d^k f(x)}{dx^k} \right) \Big|_{x=x_0} \tag{16}$$

$$f[x] = \sum_{k=0}^{\infty} (x - x_0)^k F_D[k]. \tag{17}$$

After applying the differential transformation rules of the DTM given in [12], a set of algebraic equations are obtained as follows:

$$T_D[k + 2] = \frac{-kAG(k + 1)U_D[k + 1] + (kAG - \rho I \omega_n^2)T_D[k]}{EI(k + 1)(k + 2)} \quad (18)$$

$$\begin{aligned} & U_D[k + 2] \\ &= \frac{(k + 1)(Px_\alpha(k + 2)\Psi_D[k + 2] + kAGT_D[k + 1]) - m\omega_n^2(U_D[k] - x_\alpha\Psi_D)}{(kAG + P)(k + 1)(k + 2)} \end{aligned} \quad (19)$$

$$\begin{aligned} & \Psi_D[k + 2] \\ &= \frac{(PI_\alpha x_\alpha/m)(k + 1)(k + 2)U_D[k + 2] - I_\alpha \omega_n^2 \Psi_D[k] + m\omega_n^2 U_D[k]}{\left(GJ + \frac{PI_\alpha}{m}\right)(k + 1)(k + 2)} \end{aligned} \quad (20)$$

with

$$M_D[k] = -EI \sum_{k=0}^N kT_D[k]L^{k-1} \quad (21)$$

$$\begin{aligned} S_D[k] = EI \sum_{k=0}^N k(k - 1)T_D[k]L^{k-2} - P \sum_{k=0}^N kL^{k-1}(U_D[k] - x_\alpha\Psi_D[k]) \\ + \rho I \omega_n^2 \sum_{k=0}^N T_D[k] \end{aligned} \quad (22)$$

$$Q_D[k] = (GJ + PI_\alpha/m) \sum_{k=0}^N k\Psi_D[k]L^{k-1} - Px_\alpha \sum_{k=0}^N kU_D[k]L^{k-1} \quad (23)$$

where $U_D[k]$, $\Psi_D[k]$, and $T_D[k]$ are differential transform of $U_n(x)$, $\Psi_n(x)$, and $\Theta_n(x)$, respectively; $M_D[k]$, $S_D[k]$, and $Q_D[k]$ are respectively the differential transform of the bending moment, shear force, and torque. Moreover, in Equations (21) – (23), N denotes the number of terms included in the application of the DTM; and the value of N is determined depending on the convergence of the vibration frequencies.

Then, using the inverse transform formulation given in Equation (17), the vibration mode shapes of the blade are obtained as follows:

$$U_n(x) = \sum_{k=0}^N U_D[k]x^k \quad (24)$$

$$\Psi_n(x) = \sum_{k=0}^N \Psi_D[k]x^k \quad (25)$$

$$\Theta_n(x) = \sum_{k=0}^N \Theta_D[k]x^k. \quad (26)$$

The Equations (24) – (26) are conjunction with the boundary conditions stated in Equations (7) – (9).

Then, using the similar operations for another blade model, Bernoulli-Euler model, based on Bernoulli-Euler theory [9] the solutions of the model are obtained for C-F, C-C, and S-S boundary conditions.

3. RESULTS AND DISCUSSION

Material properties of a coupled bending torsion beam made of an aluminium material are given in Table 1 [13]. Using these properties, the effects of the parameters of a wind turbine blade on the dynamic characteristics are investigated for two different blade models (i.e., Timoshenko model and Bernoulli-Euler model) with various boundary conditions. In this context, for C-F, C-C, and S-S boundary condition, first of all, convergence tests are performed to obtain the first six convergent vibration frequencies of Timoshenko type model; subsequently, the vibration frequencies of Timoshenko model and Bernoulli-Euler model are compared in the case of absence and existence of the axial force; then, vibration mode shapes of Timoshenko model and Bernoulli-Euler model are compared with each other with respect to various magnitude of the axial force, blade length, and the geometric coupling term of the blade.

Table 1. Material properties

EI (Nm^2)	6380
GJ (Nm^2)	43.46
kAG (N)	4.081×10^6
ρI (kgm)	0.251×10^{-3}
m (kg/m)	0.835
I_α ($kg * m$)	0.501×10^{-3}
x_α (m)	0.0155
A (m^2)	3.08×10^{-4}
L (m)	0.82

In Figure 3 – Figure 5, the convergences of the vibration frequencies of Timoshenko model were given for C-F, C-C, and S-S boundary conditions, respectively. These figures showed that when the number of terms included in DTM (N) was increased, the vibration frequencies became more convergent. Moreover, it was seen that the model required the first thirty terms for C-F boundary condition, and forty terms for C-C and S-S boundary conditions to obtain the first six vibration frequencies. 7

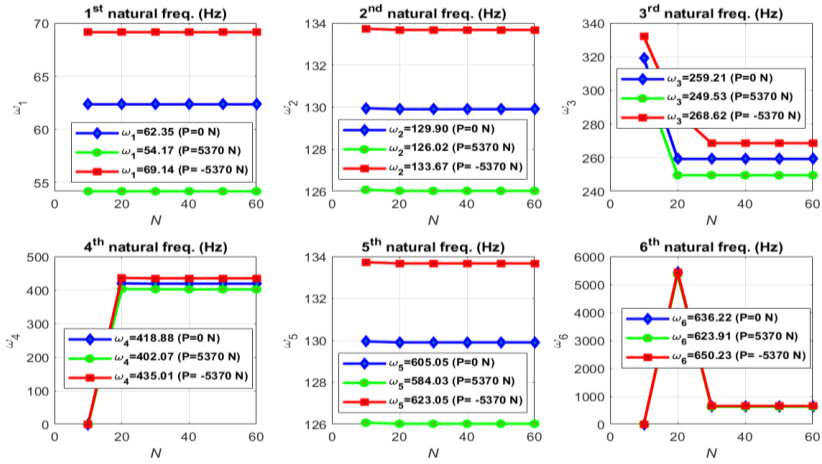


Figure 3. Convergence of the first six vibration frequencies of Timoshenko model with C-F Boundary condition.

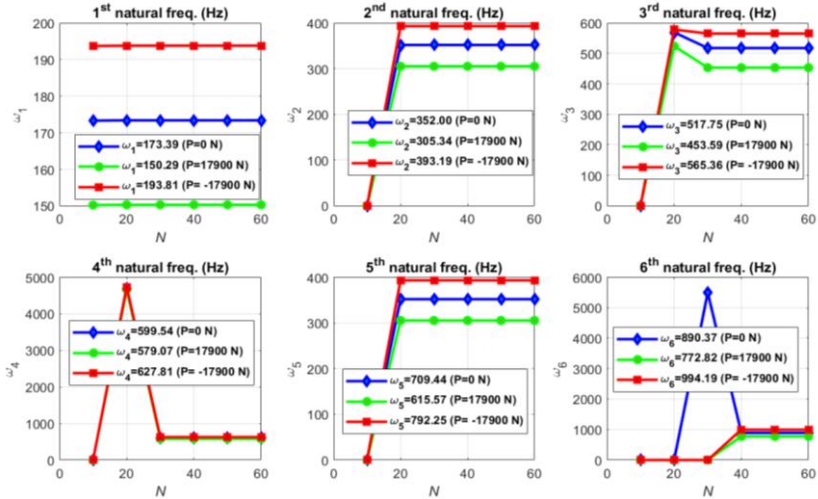


Figure 4. Convergence of the first six vibration frequencies of Timoshenko model with C-C Boundary condition.

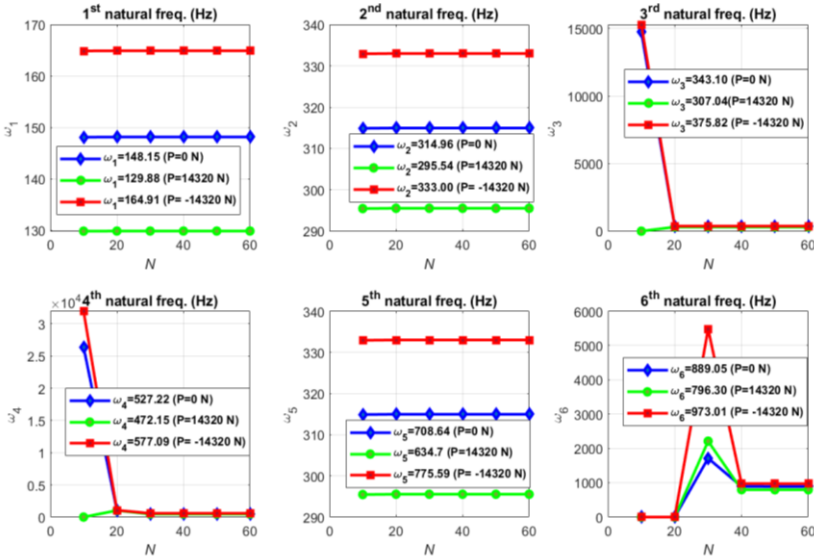


Figure 5. Convergence of the first six vibration frequencies of Timoshenko model with S-S Boundary condition.

Then, the first six vibration frequencies of Timoshenko model for C-F, C-C, and S-S boundary conditions were obtained for various axial load values that do not cause yield stress, as shown in Table 2 – Table 4, and then the results obtained were compared with the results of the study given in [13] whenever the comparison is possible.

Table 2. Vibration frequencies of Timoshenko model with C-F boundary condition

VF (Hz)	P = 0 N		P = 5370 N		P = -5370 N			
	Uncoup.	Coupled	Uncoup.	Coupled	Uncoup.	Coupled		
	DTM	DTM	DTM	DTM	Ref. [13]	ϵ_{rel} (%)	DTM	DTM
ω_1	72.29	62.35	63.98	54.17	54.72	1.00	79.52	69.14
ω_2	89.79	129.90	86.40	126.02	124.46	1.25	93.06	133.67
ω_3	269.38	259.21	259.20	249.53	249.51	0.01	279.19	268.62
ω_4	436.75	418.88	428.08	402.07	401.16	0.23	445.22	435.01
ω_5	448.97	605.05	432.01	584.03	584.11	0.01	465.32	623.05
ω_6	628.56	636.22	604.81	623.91	-	-	651.44	650.23

Table 3. Vibration frequencies of Timoshenko model with C-C boundary condition

VF (Hz)	P = 0 N		P = 17900 N				P = -17900 N	
	Uncoup.		Uncoup.		Coupled		Uncoup.	
	DTM	DTM	DTM	DTM	Ref. [13]	ϵ_{rel} (%)	DTM	DTM
ω_1	179.59	173.39	155.82	150.29	148.56	1.16	200.55	193.81
ω_2	359.18	352.00	311.65	305.34	303.33	0.66	401.11	393.19
ω_3	437.353	517.75	426.28	453.59	449.93	0.81	448.10	565.36
ω_4	538.77	599.54	467.48	579.07	585.79	1.14	601.67	627.81
ω_5	718.36	709.44	623.31	615.57	613.11	0.40	802.22	792.25
ω_6	897.95	890.37	779.13	772.82	-	-	1002.78	994.19

Table 4. Vibration frequencies of Timoshenko model with S-S boundary condition

VF (Hz)	P = 0 N		P = 14320 N		P = -14320 N	
	Uncoup.		Uncoup.		Coupled	
	DTM	DTM	DTM	DTM	DTM	DTM
ω_1	179.59	148.15	160.86	129.88	196.54	164.91
ω_2	201.47	314.96	185.04	295.54	216.65	333.00
ω_3	359.18	343.10	321.72	307.04	393.08	375.82
ω_4	538.77	527.22	482.58	472.15	589.62	577.09
ω_5	718.36	708.64	643.44	634.7	786.16	775.59
ω_6	775.98	889.05	759.62	796.30	792.01	973.01

These tables showed that, irrespective of the type of the boundary condition, compared to absence of the axial load (i.e., $P = 0$ N), when the axial load is compression load (i.e., $P < 0$ N), the vibration frequencies increase, however, when the axial load is tensile load (i.e., $P > 0$ N), then the vibration frequencies decrease. In addition, the tables indicate that regardless of the type of the boundary conditions and existence or absence of the axial force, compared to coupled case ($x_\alpha \neq 0$), in the uncoupled case ($x_\alpha = 0$), there is no general effect (such as reducing or increasing effect) on the vibration frequencies, but there is a specific effect per frequency.

After obtaining the vibration frequencies for both models, in Table 5, Timoshenko model (TM) was compared with Bernoulli-Euler model (BEM) in terms of the vibration frequencies for C-F, C-C, and S-S boundary conditions in the case of absence and existence of the axial load that does not cause yield stress. It was found that for the same material properties, the vibration frequencies obtained by using Timoshenko model are less than the vibration frequencies obtained by using Bernoulli-Euler model regardless of the type of the boundary condition and existence or absence of the axial force.

Table 5. Vibration frequencies of Timoshenko model and Bernoulli Euler model with C-F, C-C, and S-S boundary conditions

BC	VF (Hz)	P = 0 N				P = 1790 N				P = -1790 N	
		TM		BEM		TM		BEM		TM	BEM
		DTM	DTM	Ref. [14]	ϵ_{rel} (%)	DTM	DTM	Ref. [14]	ϵ_{rel} (%)	DTM	DTM
C-F	ω_1	62.35	62.60	62.60	0.00	59.80	60.23	60.23	0.00	64.74	64.84
	ω_2	129.90	130.18	130.18	0.00	128.62	128.42	128.42	0.00	131.17	131.88
	ω_3	259.21	261.15	261.15	0.00	256.02	257.96	257.96	0.00	262.38	264.31
	ω_4	418.88	421.36	421.36	0.00	413.36	415.54	415.54	0.00	424.33	427.10
	ω_5	605.06	612.09	612.09	0.00	598.33	604.60	604.60	0.00	611.44	619.37
	ω_6	636.23	655.86	-	0.00	631.99	652.64	-	0.00	640.64	659.12
C-C	ω_1	173.39	174.08	174.08	0.00	171.22	171.77	171.77	0.00	175.54	176.36
	ω_2	352.00	353.58	353.58	0.00	347.61	349.05	349.05	0.00	356.34	358.07
	ω_3	517.75	522.20	522.20	0.00	512.02	515.85	515.85	0.00	523.34	528.42
	ω_4	599.54	630.19	630.19	0.00	597.26	628.89	628.89	0.00	601.89	631.53
	ω_5	709.44	712.12	712.12	0.00	700.62	703.12	703.12	0.00	718.15	721.01
	ω_6	890.37	893.88	-	0.00	879.31	882.69	-	0.00	901.28	904.92
S-S	ω_1	148.15	148.90	148.90	0.00	145.95	146.20	146.20	0.00	150.32	151.55
	ω_2	314.96	318.06	318.06	0.00	312.61	316.81	316.81	0.00	317.28	319.31
	ω_3	343.10	344.55	344.55	0.00	338.80	339.90	339.90	0.00	347.36	349.15
	ω_4	527.22	529.27	529.27	0.00	520.65	522.45	522.45	0.00	533.71	536.00
	ω_5	708.64	711.30	711.30	0.00	699.83	702.28	702.28	0.00	717.35	720.21
	ω_6	889.05	892.33	-	-	877.99	881.10	-	-	899.97	903.43

In order to determine the effects of axial force on vibration mode shapes of Timoshenko model, the first five consecutive vibration mode shapes of Timoshenko model for C-F, C-C, and S-S boundary conditions in the case of absence and existence of the axial load, that does not cause yield stress, were plotted in Figure 6 – Figure 8, respectively.

Compared with the vibration mode shapes of the study given in [13], it can be seen that Figure 6 shows the same vibration mode shapes of Timoshenko model with C-F boundary condition in the case of the tensile axial load. Moreover, these figures indicated that, irrespective of the type of the boundary conditions, existence of the axial load did not affect the shape of the vibration modes but affected the magnitude of the amplitude of some modes. However, these changes in the amplitudes were in the negligible level. Moreover, in comparison of Timoshenko model with Bernoulli-Euler model in terms of change of the first vibration modes for various value of the magnitude of the axial load, the changes of the first vibration mode shapes of Timoshenko model and Bernoulli-Euler model were observed for various value of the magnitude of the axial load, as shown in Figure 9. Both models were made of aluminium material given in Table 1, and yield stress for this material is approximately 340 MPa [15].

Considering the cross-sectional area of the blade given in Table 1, the yielding stress of the blade was found nearly 104×10^3 N. When the magnitude of the axial load was increased in the range of 0 N to 179×10^4 N, it was observed that the first vibration modes of the models begin to deteriorate significantly starting at $P = 1790 \times 10^2$ N (close to the yield stress for both models). Then, the material began to flow from this point on. Moreover, it was observed that after $P = 1790 \times 10^3$ N, the first vibration modes presented almost the same behavior for both models.

Additionally, for the same magnitude of load application, the material began to fail much earlier in compression load compared to tension load. Furthermore, in comparison of Timoshenko model with Bernoulli-Euler model for various value of blade length, In Figure 10, the change of the first three consecutive vibration modes of both models were observed depending on the blade length. The initial blade length was L . When the blade length was reduced to $L/2$, it was observed that the amplitudes of the vibration modes for both models decreased to half and also the third modes start to break down.

Furthermore, when the blade length was reduced to $L/4$, it was observed that the vibration modes for the Bernoulli-Euler model were more distorted compared to the Timoshenko model. This situation is regarding with the theory of Timoshenko model because while the Bernoulli-Euler model is valid for only slender structures, the Timoshenko model is also valid for both slender and relatively thicker structures. When the length was reduced to $L/6$, it was seen that the vibration modes, especially the second and third modes, were very distorted for both models.

In addition, in comparison of Timoshenko model with Bernoulli-Euler model for various value of the geometric coupling term of the blade, In Figure 11, the changes of the first three consecutive vibration mode shapes of Timoshenko model and Bernoulli-Euler model were given depending on the value of the geometric coupling term. In this figure, it was found that when the geometric coupling term is zero, the first three vibration modes of both models behave same. On the other hand, when the value of the geometric coupling term was increased in the range of $\chi_\alpha/2$ to $8\chi_\alpha$, it was obtained that the vibration modes begin to differ noticeably, but their tendency was almost same in both models.

Coupled Case ($x_\alpha \neq 0$)

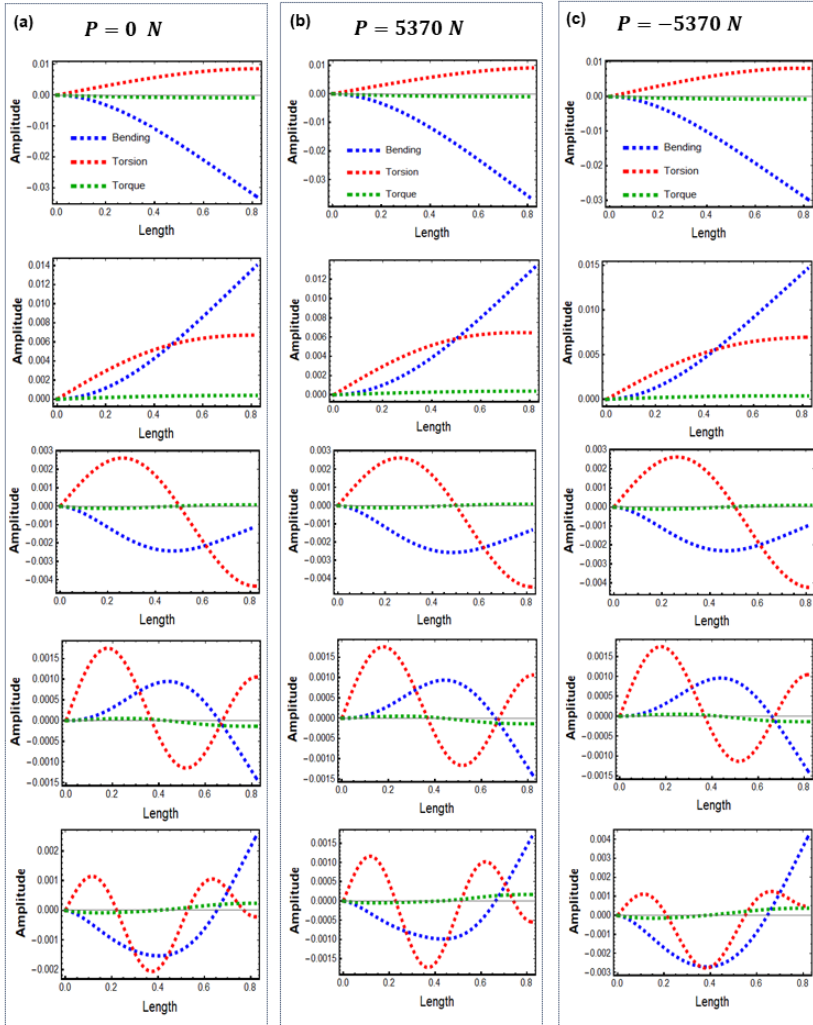


Figure 6. First five consecutive vibration mode shapes of Timoshenko model with C-F boundary condition in the case of absence and existence of the axial force.

Coupled Case ($x_{\alpha} \neq 0$)

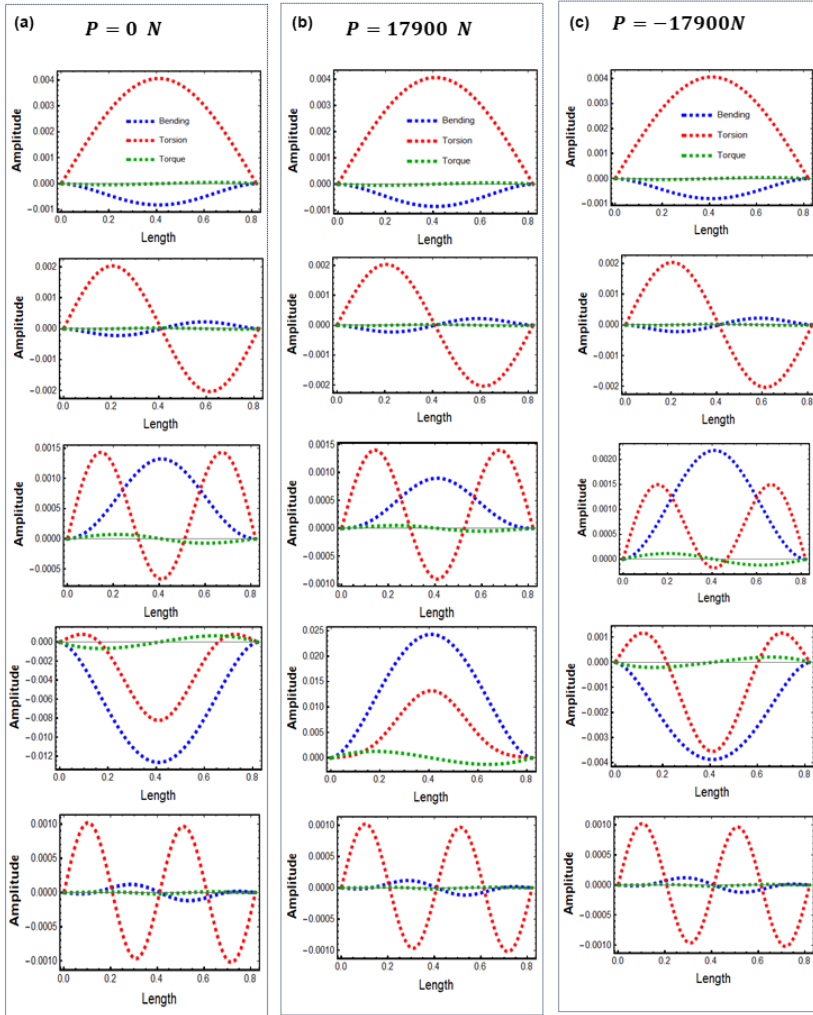


Figure 7. First five consecutive vibration mode shapes of Timoshenko model with C-C boundary condition in the case of absence and existence of the axial force.

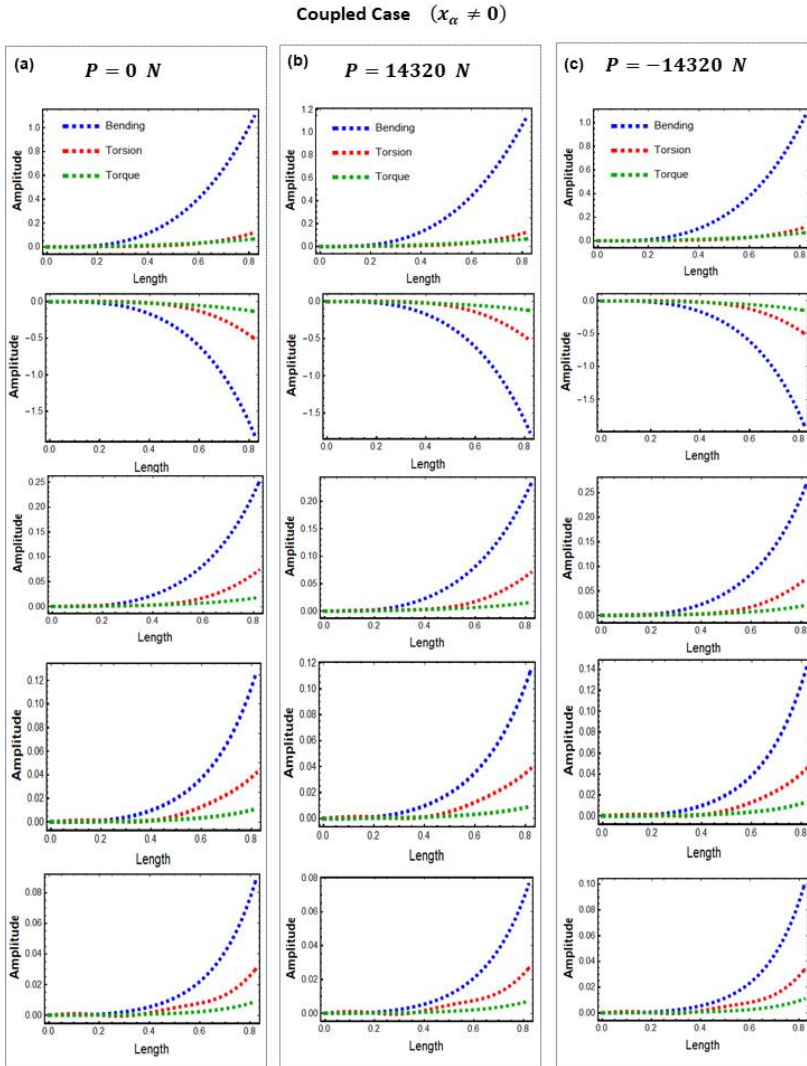


Figure 8. First five consecutive vibration mode shapes of Timoshenko model with S-S boundary condition in the case of absence and existence of the axial force.

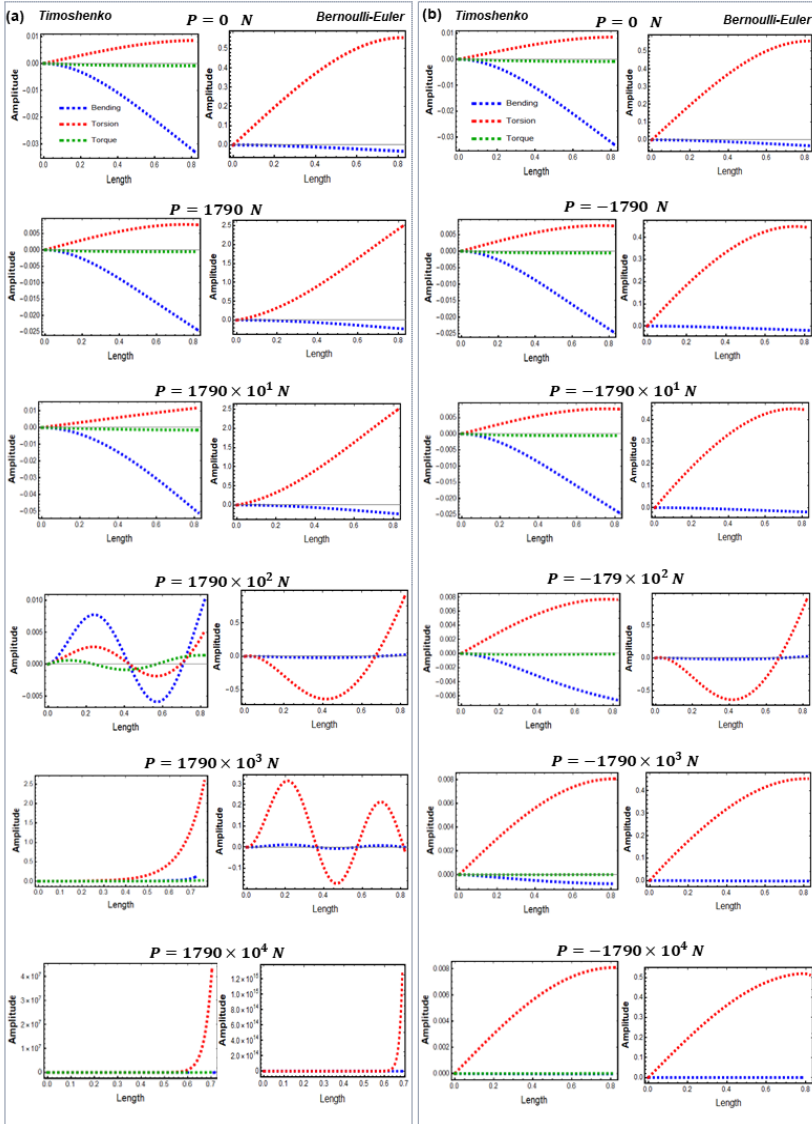


Figure 9. Changes of the first vibration modes of Timoshenko and Bernoulli-Euler model for C-F boundary condition depending on the direction and magnitude of the axial force.

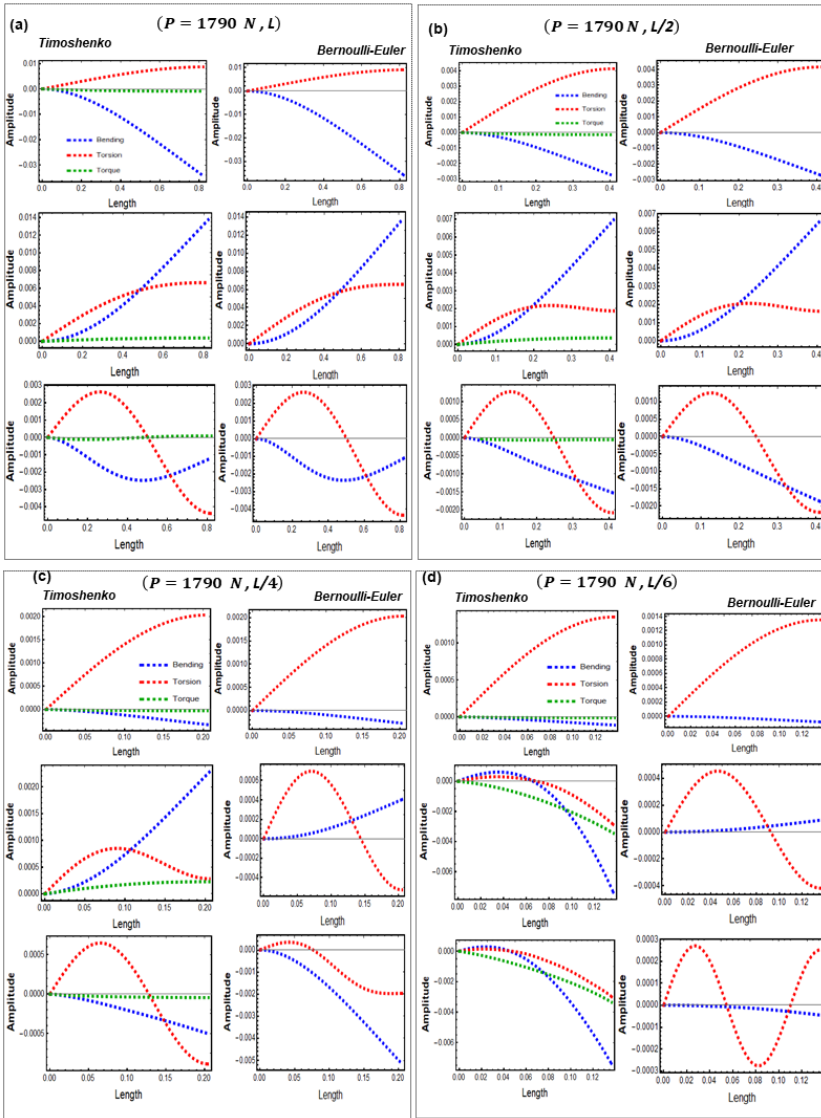


Figure 10. Changes of the first three consecutive vibration mode shapes of Timoshenko and Bernoulli-Euler model depending on the length of the blade.

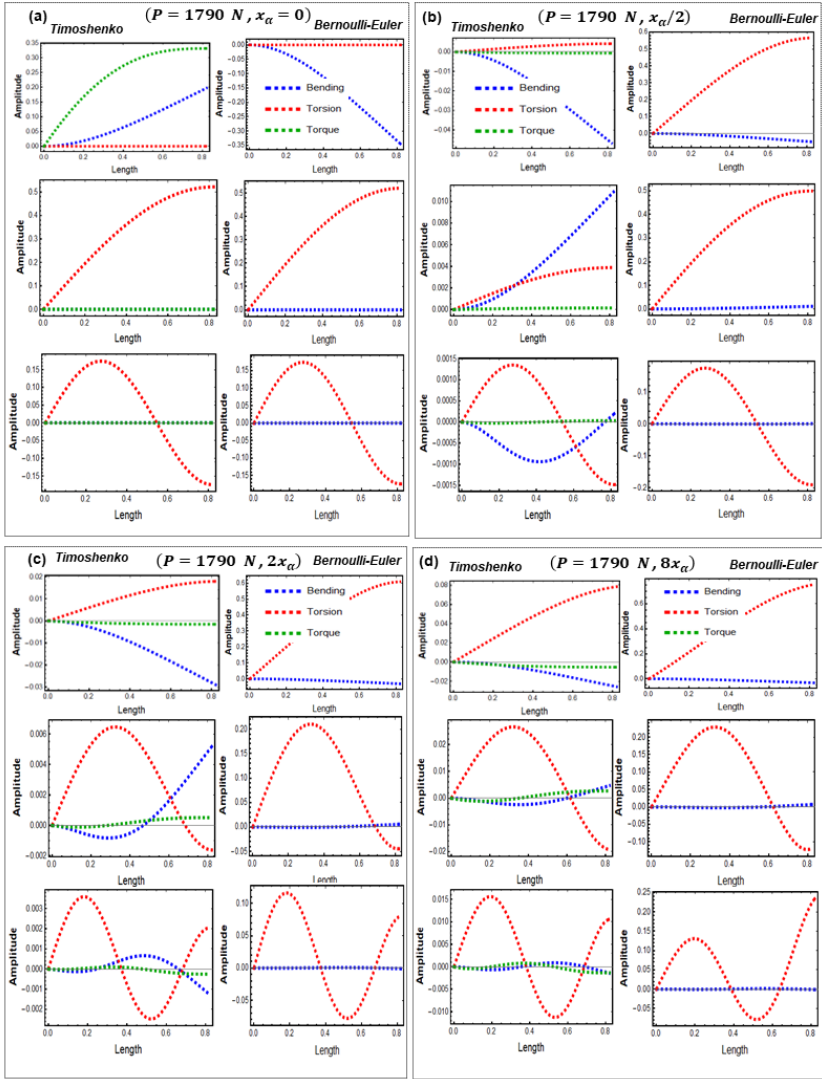


Figure 11. Changes of the first three consecutive vibration mode shapes of Timoshenko and Bernoulli-Euler model depending on the value of the geometric coupling term of the blade.

4. CONCLUSION

Parameter selection in the design of wind turbine blades is significantly important in terms of the efficiency of the wind turbine and reducing the cost. For this reason, in this study, the effects of the parameters of a wind turbine blade on the dynamic characteristics were investigated from an

analytical perspective. In this context, by using two different blade models (i.e., Timoshenko model and Bernoulli-Euler model), the effects of the boundary conditions, the axial force, blade length, and geometric coupling term of the blade on the dynamic characteristics were examined. The findings of this study showed that for C-F, C-C, and S-S boundary condition,

- Regardless of the type of the boundary condition, for both models, compared to absence of the axial load (i.e., $P = 0$ N), when the axial load is compression load (i.e., $P < 0$ N), the vibration frequencies increase, but, when the axial load is tensile load (i.e., $P > 0$ N), the vibration frequencies decrease. Moreover, the uncoupled case ($x_\alpha = 0$) does not have a general effect on the vibration frequencies of Timoshenko model.
- For the same material properties, the values of the vibration frequencies of Timoshenko model are less than the values of the vibration frequencies of Bernoulli-Euler model regardless of the type of the boundary condition and existence or absence of the axial force.
- Irrespective of the type of the boundary conditions, existence of the axial load did not affect the shape of the vibration modes but affected the magnitude of the amplitude of some modes. However, these changes in the amplitudes were in the negligible level.
- For the same magnitude of load application, about the same time, both models began to fail much earlier in compression load compared to tension load.
- When the blade length was reduced to $L/4$, the vibration modes of Bernoulli-Euler model were more distorted compared to Timoshenko model; however, when the length was reduced to $L/6$, the vibration modes, especially the second and third modes, were very distorted for both models.
- When the geometric coupling term was taken zero, the first three vibration modes of both models presented the same tendency in reciprocal modes. On the other hand, when the value of the geometric coupling term was increased in the range of $x_\alpha/2$ to $8x_\alpha$, the vibration modes began to differ noticeably, but their tendency was almost same in both models.

Based on the findings of this study, it can be stated that the structural responses of both models are approximately the same, however, it is suggested that the Timoshenko model is more suitable for the blade design if thicker (stubby) structures and especially rotational motion are needed.

Acknowledgements

This study did not receive any specific grants from funding agencies in the public, commercial, or not-for-profit sectors. We would like to thank our families for their unwavering support throughout our academic studies.

Conflict of interest

No conflict of interest was declared by the authors.

Author contributions

Aysun Soysal, Conceptualization, Methodology, Formal analysis and investigation, Writing- review-and-editing, Resources. İbrahim Özkol, Methodology, review-and-editing, Resources, Supervision Erol Uzal, Methodology, Supervision.

REFERENCES

- [1] Yang B and Sun D. Testing, inspecting and monitoring technologies for wind turbine blades: A survey. *Renewable and Sustainable Energy Reviews* 2013; 22: 515–526, doi: 10.1016/j.rser.2012.12.056.
- [2] Adeyeye KA, Ijumba N, Colton J. The Effect of the Number of Blades on the Efficiency of A Wind Turbine. In *IOP Conference Series: Earth and Environmental Science* 2021, IOP Publishing Ltd, doi: 10.1088/1755-1315/801/1/012020.
- [3] Zhou Q, Liu C, Bian X, Lo KL, Li D. Numerical analysis of lightning attachment to wind turbine blade. *Renew Energy* 2018;116: 584–593, doi: 10.1016/j.renene.2017.09.086.
- [4] Jureczko M, Pawlak M, Męzyk A. Optimisation of wind turbine blades. *J Mater Process Technol* 2005;167: 463–471, doi: 10.1016/j.jmatprotec.2005.06.055.
- [5] Jokar H, Mahzoon M, and Vatankhah R. Dynamic modeling and free vibration analysis of horizontal axis wind turbine blades in the flap-wise direction. *Renew Energy* 2020; 146:1818–1832, doi: 10.1016/j.renene.2019.07.131.
- [6] Ondra V, Titurus B. Free vibration and stability analysis of a cantilever beam axially loaded by an intermittently attached tendon. *Mech Syst Signal Process* 2021; 158, doi: 10.1016/j.ymsp.2021.107739.
- [7] Tüfekci M, Genel OE, Tatar A, Tüfekci E. Dynamic Analysis of Composite Wind Turbine Blades as Beams: An Analytical and

- Numerical Study. *Vibration* 2021; 4: 1–15, doi: 10.3390/vibration4010001.
- [8] Wang J, Qin D, Lim TC. Dynamic analysis of horizontal axis wind turbine by thin-walled beam theory. *J Sound Vib* 2010; 329(17): 3565–3586, doi: 10.1016/j.jsv.2010.03.011.
- [9] Eslimy-Isfahany SHR, Banerjee JR. Dynamic response of an axially loaded bending-torsion coupled beam. *J Aircr* 1996; 33(3): 601–607, doi: 10.2514/3.46988.
- [10] Kong K, Dyer K, Payne C, Hamerton I, Weaver PM. Progress and Trends in Damage Detection Methods, Maintenance, and Data-driven Monitoring of Wind Turbine Blades – A Review. *Renewable Energy Focus* 2023; 44:390–412, doi: 10.1016/j.ref.2022.08.005.
- [11] Zhou JK, Differential transformation and its applications for electrical circuits. Wuhan: Huazhong University Press, 1986.
- [12] Soysal A, Özkol I, and Uzal E. Flexural-torsional-coupled vibration analysis of Euler-Bernoulli beam by using the differential transform method. *Academic Perspective Procedia* 2022; 5(3): 26–33, doi: 10.33793/acperpro.05.03.642.
- [13] Li J, Shen R, Hua H, Jin X. Coupled bending and torsional vibration of axially loaded thin-walled Timoshenko beams. *Int J Mech Sci* 2004; 46(2):299–320, doi: 10.1016/j.ijmecsci.2004.02.009.
- [14] Jun L, Rongying S, Hongxing H, Xianding J. Coupled bending and torsional vibration of axially loaded Bernoulli-Euler beams including warping effects. *Applied Acoustics* 2004; 65(2): 153–170, doi: 10.1016/j.apacoust.2003.07.006.
- [15] Jahangiri A, Marashi SPH, Mohammadaliha M, Ashofte V. The effect of pressure and pouring temperature on the porosity, microstructure, hardness and yield stress of AA2024 aluminum alloy during the squeeze casting process. *J Mater Process Technol* 2017; 245:1–6, doi: 10.1016/j.jmatprotec.2017.02.005.



CHAPTER 18

Aviation Technologies and Applications
E-ISBN:978-605-338-471-7
2025, chap. (18), pp. 300-315.

ACTIVE CONTROL OF STORE SEPARATION INDUCED FLAPWISE BENDING VIBRATIONS ON SIMPLIFIED WING STRUCTURES

Caglar UYULAN¹, Mustafa Tolga YAVUZ^{2,*}, Ibrahim OZKOL³

ABSTRACT

The dynamic behavior of aircraft wings, especially regarding vibrations, holds immense significance in the aircraft design process. Wing vibrations play a crucial role in determining an aircraft's structural integrity, aerodynamic performance, and overall safety during various operational scenarios. Understanding and effectively controlling wing vibrations become especially important in high-performance fighter aircraft, where external store separation events can induce complex and potentially damaging oscillations. This research addresses the active control of flapwise bending vibrations induced by store separation in simplified wing structures. It tackles one of the critical issues stemming from the sudden release of external stores, like missiles or fuel tanks, which has the potential to generate significant and potentially damaging vibrations in the wing structures. The study utilizes a wing vibration model based on equivalent mass-spring-damper elements and integrates a feedback optimal control algorithm to suppress these vibrations effectively. Through virtual simulations encompassing various store release scenarios, the study formulates an active controller based on optimal control approaches. The findings of this study reveal the substantial potential of active control systems in alleviating the adverse impact of store separation on aircraft wing structures, thereby assisting safety and longevity. The research specifically centers on the intricate event of store separation during a fighter aircraft mission, highlighting the paramount importance of the need for effective wing vibration control. Employing the LQR control approach and a mass-spring-damper system model, the study illustrates the controller's effectiveness in significantly reducing vibration motion at critical hard points along the wing. Ultimately, this research underscores the importance of active control strategies in enhancing aircraft safety and stability during store separation events. By employing LQR control in conjunction with a precise mathematical model, the study not only mitigates adverse vibration effects but also lays the groundwork for advancements in aircraft control system design. As research continues to explore innovative control techniques, this study contributes valuable insights to ongoing efforts aimed at improving aircraft structural performance and reliability.

Keywords: Active Vibration Control, Flapwise Bending Vibration, Optimal Control Approach, Store Separation, Vibration Suppression.

*Corresponding Author: yavuzmusta@itu.edu.tr

¹ 0000-0002-6423-6720, Mechanical Engineering Department, Faculty of Engineering and Architecture, Izmir Katip Celebi University, Izmir, Turkiye

² 0000-0001-7728-3713, Aeronautical Engineering Department, Faculty of Aeronautics and Astronautics, Istanbul Technical University, Istanbul, Turkiye

³ 0000-0002-9300-9092, Aeronautical Engineering Department, Faculty of Aeronautics and Astronautics, Istanbul Technical University, Istanbul, Turkiye

1. INTRODUCTION

The stability and integrity of aircraft structures are paramount to their safe and effective operation, and one critical factor that can impact these aspects is the vibrations observed in wing structures. Vibrations in wing structures, stemming from the complex interaction of aerodynamic forces, manoeuvres, and external factors, play a pivotal role in the performance and longevity of aircraft. This challenge becomes particularly noticeable in high-performance fighter aircraft during store separation. The sudden release of external stores, such as missiles or fuel tanks, can induce significant and potentially damaging vibrations in the aircraft's wing structures. To overcome these probable risks, engineers employ various active and passive vibration control techniques. Passive control methods, such as aeroelastic tailoring and viscoelastic coatings, modify the material properties or structural design to absorb or dampen energy naturally. In contrast, active control methods, like the use of piezoelectric actuators, adaptive wing surfaces, and smart materials, involve real-time adjustment to the structure's responses, adapting to changing operation conditions.

In the open literature, various vibration control techniques are discussed, encompassing both active and passive methods, which are utilized to manage and mitigate vibrations in aircraft wing structures. Luber and Becker (1998), and Whalley and Ebrahimi (1998) contrast piezoelectric systems with aerodynamic solutions, underscoring the integration with flight control systems [1-2]. Karpel (1988) introduces an efficient vibration mode analysis method, emphasizing computational efficiency for aircraft with multiple external stores [3]. The adoption of active vibration control technologies, as discussed by Agnes, Whitehouse, and Mackaman (1993), is highlighted for its versatility in applications ranging from sonic fatigue alleviation to active aeroelastic control [4]. Similarly, Mizrahi and Raveh (2019), and Kang et al. (2010) investigate the impact of wing elasticity and the effectiveness of piezoelectric actuators in controlling flow-induced vibrations and store-separation processes, showcasing the dynamic interplay between structural and aerodynamic forces [5-6]. Advancements in control strategies, as presented by Fu, Liu, and Gan (2022), Meirovitch, and Silverberg (1984), and He, Zhu, Swei, and Su (2019), reveal a focus on active boundary control, modal control, and smooth-switching LPV control, respectively [7-9]. The latter study introduces a cutting-edge LPV control strategy for a Blended-Wing-Body flexible airplane wing, emphasizing robust suppression of wing bending displacement through smooth transitions between control states. The synthesis of structural tailoring and adaptive materials in controlling vibrations is elaborated upon by Librescu, Meirovitch, and Na (1997, 2008), and Na and Librescu

(1999), indicating a holistic approach to vibration mitigation [10-12]. Moreover, adaptive and fault-tolerant control strategies by Bialy et al. (2016), Gao and Liu (2021, 2020), and Zhang, Liu, and He (2018) mark significant strides toward addressing the complex dynamics of flexible wings under external disturbances [13-17]. The development in aircraft wing vibration control, from foundational piezoelectric systems to sophisticated control techniques, shows the engineering and materials science advancements dedicated to improving aircraft performance, safety, and longevity. The selection between active and passive vibration control techniques is contingent upon diverse factors, such as the aircraft's design, the specific stores it carries, and the desired level of control. Passive methods, typically simpler and less power-intensive, may not universally offer the same level of effectiveness. In contrast, active methods, though more intricate and power-demanding, provide real-time control and adaptability to dynamic conditions. In the realm of active control techniques, the utilization of piezoelectric patches is a noteworthy choice. This method involves the integration or attachment of piezoelectric materials that can be activated to induce mechanical strains countering undesirable vibrations. Notably effective for real-time vibration control, piezoelectric materials can be strategically embedded within the wing structure. Upon exposure to an electric field, these materials deform, presenting a dynamic means of actively managing and controlling wing vibrations.

The main objective of this study is to design an active control system capable of suppressing store separation-induced wing vibrations effectively alternative to the active/passive vibration control techniques discussed above. To suppress vibration, a Linear Quadratic Regulator (LQR) control approach is employed, which is integrated with a mathematical model of a simplified wing structure with external stores. To thoroughly evaluate the control system's effectiveness and overall performance, various store separation simulations have been conducted. The paper is organized as follows. Section 2 delves into the mathematical modelling of flapwise motion, establishing the theoretical foundation for understanding the dynamic behavior of wing structures during store separation events. In Section 3, the active vibration control approach is detailed, outlining the methodology employed to suppress flapwise bending vibrations in real-time. The subsequent section, Section 4, explores various simulation scenarios that simulate different store release events. Section 5 presents the results of these simulations, providing quantitative insights into the effectiveness of the active control system. Finally, Section 6 concludes the paper, summarizing key findings and potential avenues for future research.

2. MATHEMATICAL MODELING OF FLAPWISE MOTION

The mathematical modelling of flapwise bending motion in wing structures resulting from store separation is a critical endeavor for fighter aircraft. As aircraft undergo various operational phases, including store separation, complex dynamics come into play. The wing structure experiences bending oscillations in the flapwise direction due to the sudden release of external stores, such as missiles or fuel tanks. Understanding and accurately modelling these motions are vital for ensuring the structural integrity, stability, longevity, and safety of the aircraft structures. Through mathematical modelling, engineers can focus on the underlying physics of store separation-induced flapwise bending, providing valuable insights that inform design improvements, structural enhancements, and safety measures for aircraft during critical manoeuvres. The development of a wing equivalent model involves the utilization of mass, spring, and damper elements as depicted in Figure 2. This approach simplifies the complex dynamics of an aircraft wing into a more manageable representation while retaining key characteristics. The mass element accounts for the wing's inertial properties, while the spring element models the stiffness of the structure. The damper element introduces damping effects, representing the dissipation of energy due to various factors such as aerodynamic drag and material damping. By combining these elements, the equivalent model offers a framework to analyse the response of the wing to store separation-induced flapwise bending oscillations.

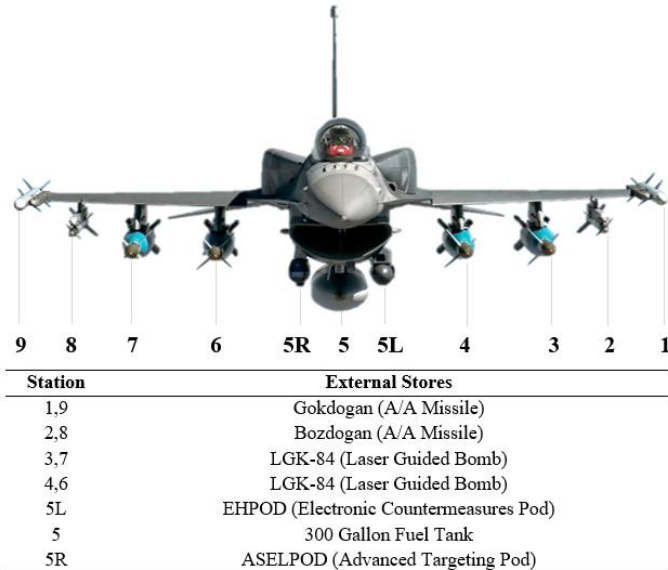


Figure 1. F-16 Block 50 Carrying Configuration with Additional Fuel Tank.

CHAPTER 18: ACTIVE CONTROL OF STORE SEPARATION INDUCED FLAPWISE BENDING VIBRATIONS ON SIMPLIFIED WING STRUCTURES

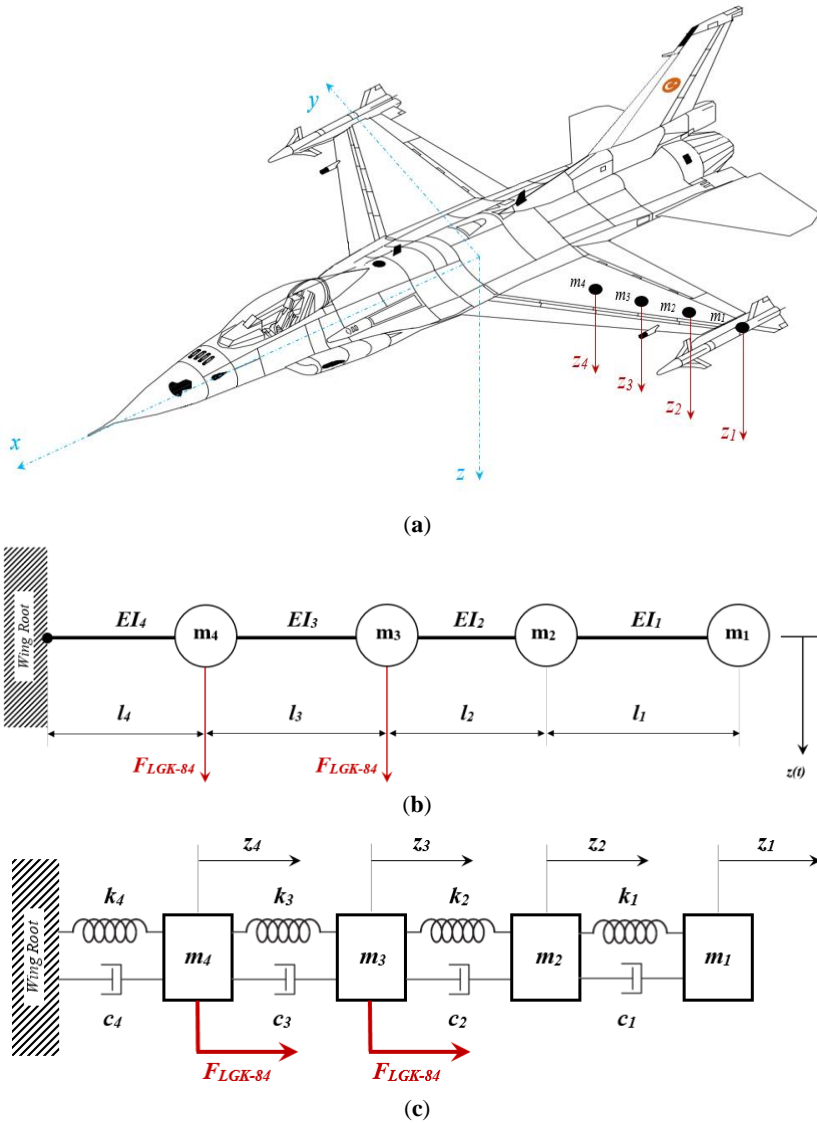


Figure 2. Aircraft Wing Models: (a) Real System with Coordinate System, (b) Equivalent Beam Model, (c) Equivalent Mass-Spring-Damper.

The equations of motion, derived from Newton's second law of motion, provide a fundamental framework for understanding store separation-induced flapwise bending oscillations. These oscillations occur within the real system, whose coordinate system is shown in Figure 2(a). To simplify analysis, a reduced beam model in Figure 2(b) is used. This model captures the core dynamics while simplifying the complexity of the real setup.

Subsequently, an equivalent model depicted in Figure 2(c) is constructed by adding mass-spring and damper elements to each wing station, as illustrated in Figure 1. By dissecting the impulsive forces generated during store separation, this model sheds light on the intricate behavior of flapwise bending oscillations throughout the wing structure. Assuming only flapwise motion in the z-direction, the equations of motion in matrix form are as follows:

$$[m]\ddot{\vec{z}} + [c]\dot{\vec{z}} + [k]\vec{z} = \vec{f}(t) \quad (1)$$

where [m], [c], and [k] are the mass, damping, and stiffness matrices, respectively, and are given by

$$[m] = \begin{bmatrix} m_1 & 0 & 0 & 0 \\ 0 & m_2 & 0 & 0 \\ 0 & 0 & m_3 & 0 \\ 0 & 0 & 0 & m_4 \end{bmatrix}, [c] = \begin{bmatrix} c_1 & -c_2 & 0 & 0 \\ -c_1 & c_1 + c_2 & -c_2 & 0 \\ 0 & -c_2 & c_2 + c_3 & -c_3 \\ 0 & 0 & -c_3 & c_3 + c_4 \end{bmatrix}, \quad (2)$$

$$[k] = \begin{bmatrix} k_1 & -k_2 & 0 & 0 \\ -k_1 & k_1 + k_2 & -k_2 & 0 \\ 0 & -k_2 & k_2 + k_3 & -k_3 \\ 0 & 0 & -k_3 & k_3 + k_4 \end{bmatrix}$$

and \vec{x} and \vec{f} are the displacement and force vectors, respectively, and are given

$$\vec{z} = \begin{bmatrix} z_1 \\ z_2 \\ z_3 \\ z_4 \end{bmatrix}, \vec{f} = \begin{bmatrix} f_1 \\ f_2 \\ f_3 \\ f_4 \end{bmatrix} = \begin{bmatrix} 0 \\ 0 \\ F_{LGK} \\ F_{LGK} \end{bmatrix} \quad (3)$$

Before expressing the state space equations, the equations of motion can be reformulated to facilitate the transition to the state space representation as

$$m\ddot{\underline{x}} + c\dot{\underline{x}} + k\underline{x} = \underline{f} \quad (4)$$

Utilizing a system's foundational dynamics, we can represent the behavior through second-order ordinary differential equations, which articulate the system's equation of motion. The state vector expresses time-varying kinematic interrelations related to the equivalent masses, encompassing both linear displacement and linear velocity. Simultaneously, the input vector is structured to express the distribution of piezoelectric actuators affixed along the wing axis as depicted in Figure 2(a). Disturbance forces are integrated, specifically, into the terminal pair of control surface components within our input vector.

State space representation is a mathematical model that describes a physical system by defining a set of input, output, and state variables interconnected through first-order differential equations [18]. In the context of designing an optimal controller for a multi-input multi-output (MIMO) system, it is essential to express the system's equations of motion in the form of a full state space representation. This representation provides a comprehensive understanding of the underlying dynamics, allowing for a holistic approach to controller design. By utilizing a full-state space representation, a full-state feedback controller capable of effectively addressing the challenges posed by oscillations resulting from store separation in aircraft can be developed. Additionally, the extended state space model of the system can be given as an augmented representation that encompasses both the explicitly defined state variables and additional extended state variables. This formulation allows for a more comprehensive description of the system's dynamics, taking into account unmeasured disturbances, uncertainties, or external inputs that may influence its behavior.

$$\dot{X} = AX + BU = \begin{bmatrix} 0 & 0 & 0 & 0 & 1 & 0 & 0 & 0 \\ 0 & 0 & 0 & 0 & 0 & 1 & 0 & 0 \\ 0 & 0 & 0 & 0 & 0 & 0 & 1 & 0 \\ 0 & 0 & 0 & 0 & 0 & 0 & 0 & 1 \\ \kappa_{11} & \kappa_{12} & \kappa_{13} & \kappa_{14} & \lambda_{11} & \lambda_{12} & \lambda_{13} & \lambda_{14} \\ \kappa_{21} & \kappa_{22} & \kappa_{23} & \kappa_{24} & \lambda_{21} & \lambda_{22} & \lambda_{23} & \lambda_{24} \\ \kappa_{31} & \kappa_{32} & \kappa_{33} & \kappa_{34} & \lambda_{31} & \lambda_{32} & \lambda_{33} & \lambda_{34} \\ \kappa_{41} & \kappa_{42} & \kappa_{43} & \kappa_{44} & \lambda_{41} & \lambda_{42} & \lambda_{43} & \lambda_{44} \end{bmatrix} \begin{bmatrix} x_1 \\ x_2 \\ x_3 \\ x_4 \\ y_1 \\ y_2 \end{bmatrix}_{8 \times 1} + \begin{bmatrix} 0 & 0 & 0 & 0 \\ 0 & 0 & 0 & 0 \\ 0 & 0 & 0 & 0 \\ 0 & 0 & 0 & 0 \\ \mu_{11} & \mu_{12} & \mu_{13} & \mu_{14} \\ \mu_{21} & \mu_{22} & \mu_{23} & \mu_{24} \\ \mu_{31} & \mu_{32} & \mu_{33} & \mu_{34} \\ \mu_{41} & \mu_{42} & \mu_{43} & \mu_{44} \end{bmatrix}_{8 \times 4} \begin{bmatrix} u_1 \\ u_2 \\ u_3 + F_{LGR} \\ u_4 + F_{LGR} \end{bmatrix}_{4 \times 1} \quad (5)$$

$$Y = CX + DU = \begin{bmatrix} x_1 \\ x_2 \\ x_3 \\ x_4 \\ \dot{x}_1 \\ \dot{x}_2 \\ \dot{x}_3 \\ \dot{x}_4 \end{bmatrix} = \begin{bmatrix} 1 & 0 & 0 & 0 & 0 & 0 & 0 & 0 \\ 0 & 1 & 0 & 0 & 0 & 0 & 0 & 0 \\ 0 & 0 & 1 & 0 & 0 & 0 & 0 & 0 \\ 0 & 0 & 0 & 1 & 0 & 0 & 0 & 0 \\ 0 & 0 & 0 & 0 & 1 & 0 & 0 & 0 \\ 0 & 0 & 0 & 0 & 0 & 1 & 0 & 0 \\ 0 & 0 & 0 & 0 & 0 & 0 & 1 & 0 \\ 0 & 0 & 0 & 0 & 0 & 0 & 0 & 1 \end{bmatrix} \begin{bmatrix} x_1 \\ x_2 \\ x_3 \\ x_4 \\ \dot{x}_1 \\ \dot{x}_2 \\ \dot{x}_3 \\ \dot{x}_4 \end{bmatrix}_{8 \times 1} + \begin{bmatrix} 0 & 0 & 0 & 0 \\ 0 & 0 & 0 & 0 \\ 0 & 0 & 0 & 0 \\ 0 & 0 & 0 & 0 \\ \mu_1 \\ \mu_2 \\ \mu_3 + F_{LGR} \\ \mu_4 + F_{LGR} \end{bmatrix}_{8 \times 1} \quad (6)$$

where the parameters, symbolically designated as kappa, lambda, and mu, encapsulate the internal dynamics of the system. Their constitution is inherently derived from the system's intrinsic properties, namely, the mass, spring constants, and damping coefficients.

$$\begin{bmatrix} \kappa_{11} & \kappa_{12} & \kappa_{13} & \kappa_{14} \\ \kappa_{21} & \kappa_{22} & \kappa_{23} & \kappa_{24} \\ \kappa_{31} & \kappa_{32} & \kappa_{33} & \kappa_{34} \\ \kappa_{41} & \kappa_{42} & \kappa_{43} & \kappa_{44} \end{bmatrix} = - \left[\frac{k}{m} \right] \begin{bmatrix} \lambda_{11} & \lambda_{12} & \lambda_{13} & \lambda_{14} \\ \lambda_{21} & \lambda_{22} & \lambda_{23} & \lambda_{24} \\ \lambda_{31} & \lambda_{32} & \lambda_{33} & \lambda_{34} \\ \lambda_{41} & \lambda_{42} & \lambda_{43} & \lambda_{44} \end{bmatrix} = - \left[\frac{c}{m} \right] \begin{bmatrix} \mu_{11} & \mu_{12} & \mu_{13} & \mu_{14} \\ \mu_{21} & \mu_{22} & \mu_{23} & \mu_{24} \\ \mu_{31} & \mu_{32} & \mu_{33} & \mu_{34} \\ \mu_{41} & \mu_{42} & \mu_{43} & \mu_{44} \end{bmatrix} = \frac{1}{m} \quad (7)$$

3. ACTIVE VIBRATION CONTROL APPROACH

To suppress wing vibrations, an optimal control-based feedback controller structure is employed. The preference for this method is rooted in the Linear Quadratic Regulator (LQR) method, which stands out as a premier design technique for addressing the complexities associated with high-dimensional systems, and those with MIMO. The Linear Quadratic Regulator (LQR) stands out as a premier design technique for handling complex systems that are underactuated, exhibit high dimensions, and have multiple inputs and outputs (MIMO). The core idea behind LQR is to derive an ideal control gain matrix, denoted as G , which directs the control input $u(t)$ in the manner $u(t) = -Gx(t)$. This specific control input serves to lessen a quadratic performance criterion.

$$J = \frac{1}{2} \int_{t_0}^{t_f} (x^T Q x + u^T R u) dt \quad (8)$$

Q is a matrix that's real, symmetric, and positive semidefinite, while R is a matrix that's real, symmetric, and positive definite. The time frames t_0 and t_f represent the beginning and conclusion respectively. The gain matrix is given as;

$$G = R^{-1} B^T K \quad (9)$$

The gain matrix can be expressed using the matrix K , which is real and symmetric, and it adheres to the matrix Riccati equation.

$$A^T K + KA + Q - KBR^{-1}B^T K = 0 \quad (10)$$

It's essential to note that the control design outlined assumes a complete availability of the state vector $x(t)$ for feedback, because it takes the input form $u(t) = -Gx(t)$. Yet, in practical scenarios, only the output vector, represented as $y(t) = Cx(t)$, is attainable from r measurements. The matrix C is a constant one with dimensions $r \times (2n+m)$. Hence, the control input gets modified to $u(t) = -G\hat{x}(t)$, with $\hat{x}(t)$ acting as an estimation of the state vector $x(t)$.

The choice of LQR parameters [19], specifically the Q matrix, dictates how quickly state variables converge to a reference value (with a vibration-free reference being zero) for trajectory tracking. Conversely, the R matrix aims to minimize the total energy expended by the actuator. These vectors inherently oppose each other, creating a trade-off. Their nature is conflicting. In determining the Q and R matrices, numerous trial-and-error simulations were run to identify suitable values that achieve the control objectives. Meanwhile, metaheuristic optimization algorithms such as PSO (Particle Swarm Optimization) and GA (Genetic Algorithm) can be employed for meta-optimization of Q - R parameters under the given control performance criteria.

CHAPTER 18: ACTIVE CONTROL OF STORE SEPARATION INDUCED FLAPWISE BENDING VIBRATIONS ON SIMPLIFIED WING STRUCTURES

The Q_i and R matrices for store separation-induced vibration control via LQR are specified differently for each separation scenario illustrated in Figure 3. Specifically, the matrices take the following distinct values for Scenario 1, Scenario 2, and Scenario 3, respectively for the same R matrix.

$$\begin{aligned}
 Q_1 &= \text{diag}([5000 \ 5000 \ 7000 \ 5000 \ 5000 \ 5000 \ 7000 \ 5000]) \\
 Q_2 &= \text{diag}([9500 \ 9500 \ 12000 \ 12000 \ 9500 \ 9500 \ 12000 \ 12000]) \\
 Q_3 &= \text{diag}([5000 \ 5000 \ 7000 \ 5000 \ 5000 \ 5000 \ 7000 \ 5000]) \\
 R &= \text{diag}([0.01 \ 0.02 \ 1 \ 1])
 \end{aligned}
 \tag{11}$$

By emphasizing a quadratic performance criterion, the LQR ensures that system states remain close to desired trajectories while simultaneously minimizing control efforts. Here, the control objectives include achieving a settling time of less than 2.5 seconds and restricting the maximum oscillation amplitude to below 5×10^{-3} meters.

4. SIMULATION SCENARIOS

Various simulation scenarios are illustrated in Figure 3, focusing on the separation of stores from the pylons of the aircraft wing. Each of these scenarios serves a specific purpose in the simulation, helping to analyse how the aircraft wing and control system responds to changes in parameters, weight distribution, and the disturbance forces during the store separation process. By examining various store configurations, engineers can better understand the real-world implications of store release on both the control systems and the structural performance of aircraft wings. The equivalent mass, spring coefficient, and damping coefficient for each scenario are provided, representing the essential parameters of the reduced wing structure after store release in Table 1.



Figure 3. Scenarios of Store Separation from Different Pylons.

Table 1. Equivalent System Parameters for Various Release Scenarios

Scenario	Store	Mass [kg]	Release	m [kg]	k [N/m]	c [Ns/m]	Impulsive Force [N]
1	Gokdogan	161,5	O	173,83	7,01E+06	140,88	0
1	Bozdogan	85,3	O	103,09	4,04E+07	203,25	0
1	LGK-84	0	X	35,61	4,42E+07	406,89	9571,8
1	LGK-84	957,18	O	976,39	2,26E+09	219,52	0
2	Gokdogan	161,5	O	173,83	7,01E+06	140,88	0
2	Bozdogan	85,3	O	103,09	4,04E+07	203,25	0
2	LGK-84	957,18	O	992,79	4,42E+07	406,89	0
2	LGK-84	0	X	19,21	2,26E+09	219,52	9571,8
3	Gokdogan	161,5	O	173,83	7,01E+06	140,88	0
3	Bozdogan	85,3	O	103,09	4,04E+07	203,25	0
3	LGK-84	0	X	35,61	4,42E+07	406,89	9571,8
3	LGK-84	0	X	19,21	2,26E+09	219,52	9571,8

m: Equivalent Mass, *k*: Equivalent Spring Coefficient, *c*: Equivalent Damping Coefficient.

The simulations aim to capture the intricate dynamics involved in store separation events. To analyse and interpret the results of these scenarios, Figure 4 presents a block diagram. This diagram likely encapsulates the mathematical models, control strategies, and feedback systems employed in the simulation setup. Within the diagram, the disturbance inputs simulate the external forces acting on the wing, and the displacement and velocity outputs provide essential data for assessing the wing’s response to these forces. Between inputs and outputs, the LQR controller calculates the necessary control forces to counteract the disturbances, effectively minimizing the resultant vibrations.

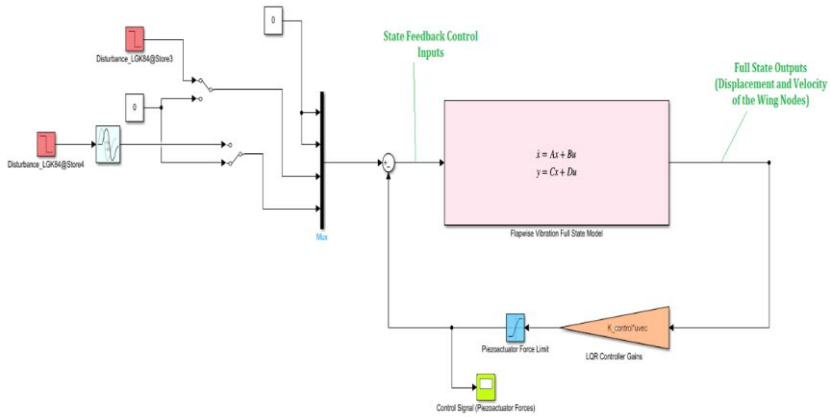


Figure 4. The Feedback Optimal Controller Structure in Simulink.

5. RESULTS

Simulations were conducted using the Matlab/Simulink, employing a variable-step numerical solver with a maximum step size of 1×10^{-4} for 10 seconds simulation. Regarding control actions, the piezo actuators had saturation limits set to ± 400 N. Perturbations introduced at stations 3 and 4 during ordnance release amounted to a step disturbance of 9.57 kN, with a delay of 0.05 seconds. The simulation results, depicted in [Figure 5](#), [Figure 6](#), and [Figure 7](#), showcase the performance of both uncontrolled and controlled closed-loop simulations for various hard points on the wing structure following the sudden release from stations 3 and 4. As seen from the figures, the LQR controller is an effective and simple control approach in significantly dampening vibration motion at different hard points (nodes) along the wing axes.

In the first simulation scenario, the displacement-time graph of the wing between stations 1 and 4 depicted in [Figure 5](#), relative to its initial position, is observed upon releasing the store from station 3. This graph is presented for both controlled (indicated in red) and uncontrolled (indicated in blue) situations. Moving to the second simulation scenario, where the store is released from station 4, the displacement-time graph of the wing between stations 1 and 4 shown in [Figure 6](#), relative to its starting position, is examined. Similar to the first scenario, this graph is illustrated for both the controlled (indicated in red) and uncontrolled (indicated in blue) cases. In the third simulation scenario, involving the release of stores from stations 3 and 4 with a 1-second interval, the displacement-time graph of the wing between stations 1 and 4, relative to its initial position, is evaluated. From these figures, it's evident that the controlled responses demonstrate a significant reduction in displacement amplitude over time, indicating effective vibration suppression. For each hard point, the initial spike in displacement due to the store release is quickly reduced under controlled conditions, stabilizing the wing's motion much faster than in the uncontrolled case. The rapid dampening of vibrations highlights the controller's ability to mitigate disturbances and return the wing to a steady state for the Q - R matrices.

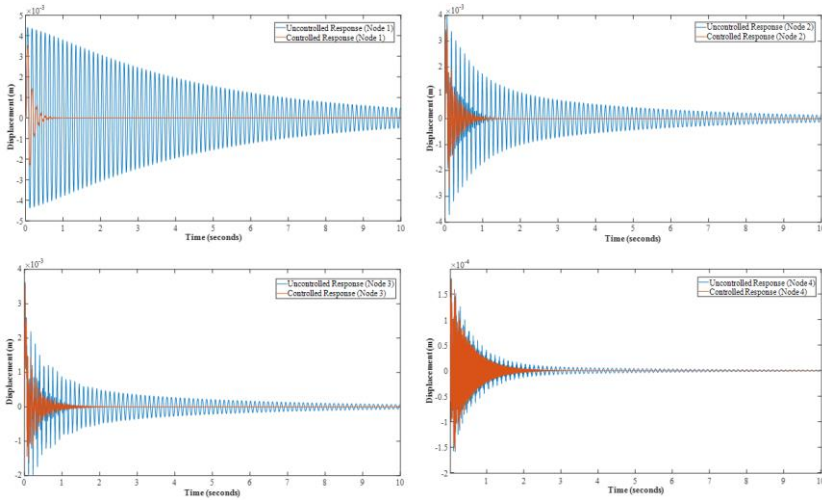


Figure 5. Displacement of Hard Points for Store Release from Station 3 (1st Scenario).

Another result is that the increasing stiffness toward the wing's root leads to a more pronounced decrease in displacement and enhances the effectiveness of the control system, as evidenced by the comparison between Figures 5 and 6. Specifically, the displacement resulting from store release at station 4 is smaller than station 3 for the same disturbance force. Approximately, one second is sufficient to suppress vibration up to the controller's maximum efficiency; therefore, a one-second delay between store releases would allow the active control system to stabilize the wing structure from the effects of the first release before the next store is jettisoned.

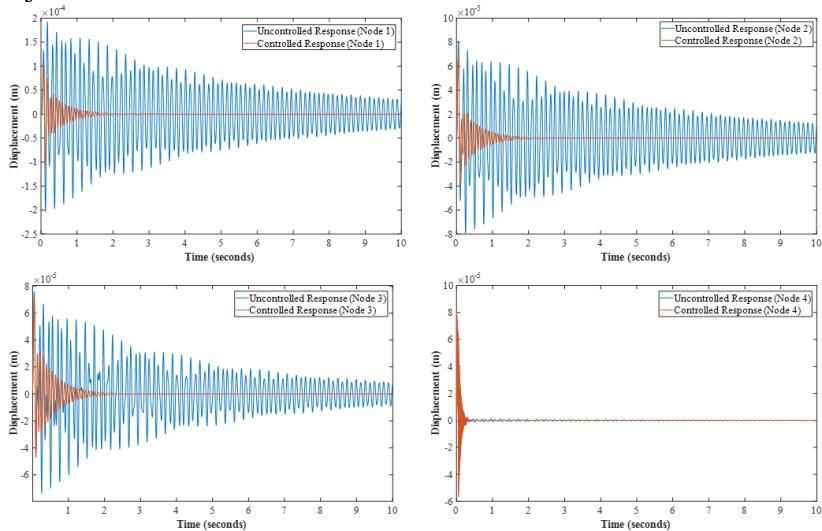


Figure 6. Displacement of Hard Points for Store Release from Station 4 (2nd Scenario).

CHAPTER 18: ACTIVE CONTROL OF STORE SEPARATION INDUCED FLAPWISE BENDING VIBRATIONS ON SIMPLIFIED WING STRUCTURES

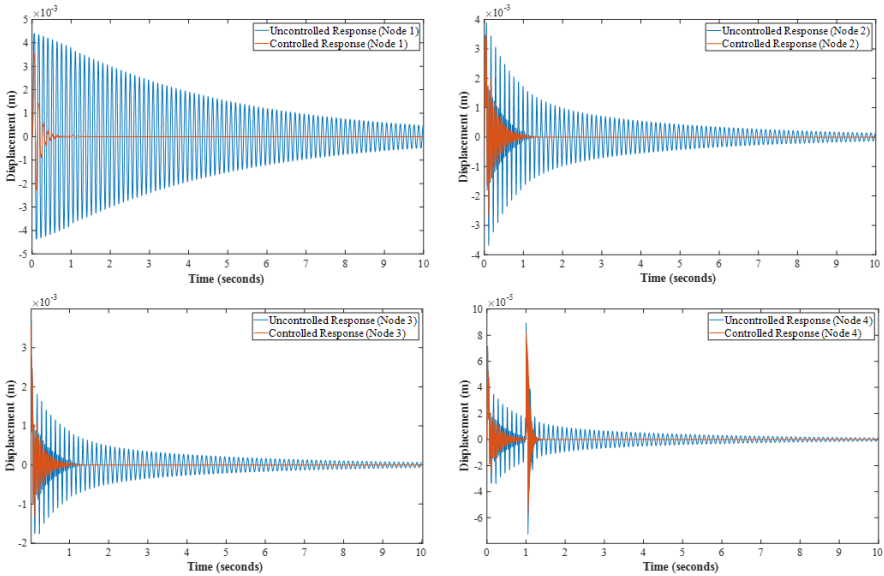


Figure 7. Displacement of Hard Points for Store Release from Station 3 and Station 4 (3rd Scenario).

The conclusion drawn from the graphs indicates the achievement of control objectives in all simulation scenarios. The observed differences in responses across these scenarios can be attributed to variations in the parameters of the equivalent system model. Briefly, it is clear that the effectiveness of active vibration control through optimal feedback control strategies plays a pivotal role in enhancing the overall stability and performance of the system by preventing excessive displacements that could lead to possible structural damage during flight conditions near flutter speeds or other aeroelastic phenomena.

6. CONCLUSION

Wing vibration control in the context of store separation from fighter aircraft emerges as a critical aspect of aircraft wing design. The separation of external stores during a fighter aircraft's mission represents a complex and dynamic event that can induce significant flapwise bending vibrations in the aircraft's wings. Recognizing the paramount importance of effective wing vibration control in this scenario is crucial, as it directly influences the aircraft's aerodynamic performance, mission success, and the safety of both the aircraft and its crew. Therefore, the primary aim of this study is to develop an efficient and simple active control system based on the LQR control approach, suppressing wing vibrations in high-performance fighter

aircraft, triggered by the sudden release of external stores such as missiles or fuel tanks. Also, the investigation into active vibration control, utilizing the LQR control approach and a mass-spring-damper system model, has provided two significant insights. First, the study convincingly demonstrates the controller's effectiveness in significantly reducing vibration motion at critical hard points along the wing axis. Second, the application of LQR control, in conjunction with an accurate mathematical model, not only mitigates adverse vibration effects but also establishes the foundation for further advancements used in subsystems. To sum up, the contribution of this study to the existing literature is twofold. It provides a comprehensive mathematical model of flapwise bending of wing structures in the state space form during store separation, enhancing understanding of the intricate dynamics involved. Furthermore, simulations verify the efficacy of an active control system in mitigating these adverse effects, computing minimum time between store releases for the operational safety and stability of fighter aircraft. To progress this study, future research may explore methods optimizing LQR parameters to better accommodate diverse flight conditions and various store configurations, enhancing the adaptive capabilities of vibration control systems for fighter aircraft.

Acknowledgements

No Acknowledgements was declared by the authors.

Conflict of interest

No conflict of interest was declared by the authors.

Author contributions

C. Uyulan: Methodology, Software, Formal analysis. M. T. Yavuz: Conceptualization, Writing-Original Draft, Visualization. I. Ozkol: Writing-Review & Editing, Supervision.

REFERENCES

- [1] Luber, W., & Becker, J. (1998). Comparison of Piezoelectric Systems and Aerodynamic Systems for Aircraft Vibration Alleviation. 5th Annual International Symposium on Smart Structures and Materials.
- [2] Whalley, R., & Ebrahimi, M. (1998). Vibration and control of aircraft wings. Proceedings of the Institution of Mechanical Engineers, Part G: Journal of Aerospace Engineering, 212(5), 353-365.
- [3] Karpel, M. (1988). Efficient vibration mode analysis of aircraft with multiple external store configurations. Journal of Aircraft, 25(8), 747-751.

- [4] Agnes, G. S., Whitehouse, S. R., & Mackaman, J. R. (1993). Vibration Attenuation of Aircraft Structures Utilizing Active Materials. *Smart Structures and Intelligent Systems*, 1917, 368-379.
- [5] Mizrahi, I., & Raveh, D. E. (2019). Wing Elasticity Effects on Store Separation. *Journal of Aircraft*, 56(3), 1231-1249.
- [6] Kang, L. H., Kim, H. I., Lee, J. H., Park, J. W., & Han, J. H. (2010). Vibration Control of the Composite Wing Model Using Piezoelectric Actuators. *Advanced Materials Research*, 123, 1027–1030.
- [7] Fu, Y., Liu, Y., & Gan, Z. (2022). Active control for a flexible aircraft wing in the presence of external disturbances. *37th Youth Academic Annual Conference of Chinese Association of Automation*, 842-846.
- [8] Meirovitch, L., & Silverberg, L. M. (1984). Active vibration suppression of a cantilever wing. *Journal of Sound and Vibration*, 97(3), 489-498.
- [9] El-Serafi, S. A., Eissa, M. H., El-Sherbiny, H. M., et al. (2006). Comparison between passive and active control of a non-linear dynamical system. *Japan Journal of Industrial and Applied Mathematics*, 23, 139.
- [10] Librescu, L., Meirovitch, L., & Na, S. S. (1997). Control of Cantilever Vibration via Structural Tailoring and Adaptive Materials. *AIAA Journal*, 35(8), 1309-1315.
- [11] Librescu, L., & Song, O. (2008). Dynamics of Composite Aircraft Wings Carrying External Stores. *AIAA Journal*, 46, 568-577.
- [12] Na, S., & Librescu, L. (1999). Optimal vibration control of adaptive aircraft wings carrying externally mounted stores and exposed to blast loading, 3667.
- [13] Bialy, B., Chakraborty, I., Cekic, S., & Dixon, W. (2016). Adaptive boundary control of store-induced oscillations in a flexible aircraft wing. *Automatica*, 70, 230-238.
- [14] Gao, S., & Liu, J. (2021). Adaptive fault-tolerant boundary vibration control for a flexible aircraft wing against actuator and sensor faults. *Journal of Vibration and Control*, 28, 1025 - 1034.
- [15] He, T., Zhu, G., Swei, S., & Su, W. (2019). Smooth-switching LPV control for vibration suppression of a flexible airplane wing. *Aerospace Science and Technology*.
- [16] Gao, S., & Liu, J. (2020). Adaptive neural network vibration control of a flexible aircraft wing system with input signal quantization. *Aerospace Science and Technology*, 96, 105593.
- [17] Zhang Y, Liu J, He W. (2018). Disturbance observer design and vibration control for a flexible aircraft wing. *Transactions of the Institute of Measurement and Control*, 40(13), 3760-3773.

- [18] Ogata, K. (2010). Modern Control Engineering (5th ed.). Prentice Hall Publications.
- [19] Kirk, D. E. (2004). Optimal Control Theory: An Introduction. Dover Publications.



CHAPTER 19

Aviation Technologies and Applications
E-ISBN:978-605-338-471-7
2025, chap. (19), pp. 316-340.

BENEFITS OF END-TO-END TRACEABILITY ON PROJECT PROCESSES WITHIN THE SCOPE OF PLM- DEFENSE AND AVIATION CASE STUDY

Oğuz VARHAN¹, Rüstem Barış YEŞİLAY^{2,*}

ABSTRACT

Industrial technologies are advancing. With advancing technology, the world faces new needs and more expectations. As these needs and expectations increase, the complexity of products and services increases. This increasing complexity makes it difficult to manage a service or product. At the same time, the resources, processes and workforce used for this service or product are increasing. This makes complex product management even more complex. A branch of engineering called systems engineering aims to use certain methods to manage this complexity and envisages the application of these processes in all disciplines. In addition, PLM systems aim to make the processes used to manage these complex structures organized, disciplined, automated and highly traceable. The aerospace and defence industry, which produces highly complex and sensitive products, foresees the use of advanced systems engineering methods and PLM software tools to produce products that are error-free, fast, efficient, safe and many other benefits. In this study, it will be discussed what kind of gains are achieved with the integration of innovative systems engineering approaches and innovative PLM processes used in the sector, which methods are used, what needs the sector may face in the future and what these methods can bring to the sector in the future.

Keywords: Model-Based Systems Engineering, PLM, Aerospace, Defence Industry, RFLP

1. INTRODUCTION

At the international and national level, the aerospace and defence industry produces very complex products. The level of complexity of these products, the size of the organization and the fact that the projects are open to continuous development make it very difficult to manage the product processes. It is planned to integrate customized methods such as Model Based Systems Engineering, System Traceability, Interaction between Requirement-Function-Logical-Physical architectures with the product by using PLM (Product Lifecycle Management) system and tools.

*Corresponding Author: rustem.baris.yesilay@ege.edu.tr

1 0009-0000-2240-4207, PLM, Natural and Applied Science, Ege University, İzmir, Türkiye

2 0000-0002-0830-8224, Aviation Higher Vocational School, Department of Transportation Services, Ege University, İzmir, Türkiye

In this way, it is aimed to produce more efficient and safer products with the innovations gained in the product development process. The v-diagram approach used in systems engineering and specified by INCOSE (International Council on Systems Engineering), the Model Based System Architecture Approach with the SysML language used in systems engineering (Figure 19: Details of the V-Model Approach, Page:325) [12], and some PLM Process approaches determined and proposed by Dassault Systems and Turkish Aerospace Industries were used.

The study has a very unique and complex structure with the use of the SysML language and MBSE (Model Based System Engineering) approach in the PLM environment, which is known to be used in no other industry in the national sense, and with the process methods established for such end-to-end traceability in the aviation and defence industry. With the full use of this methodology, our current domestic fighter jet project is to turn our current domestic fighter jet project into a project that has been developed entirely in a virtual environment, has undergone validation and verification processes in a virtual environment, and production planning and analysis (Digital Factory) have been carried out in a virtual environment.

2.PLM

2.1. What is Briefly?

According to Stark, PLM is the business activity of managing a company's products all the way along their lifecycles; from the very first idea until products are retired and disposed of, in the most effective way [5].

2.2. What is it for?

PLM systems offer a single source to store and manage all information related to a product, including design specifications, bill of materials, manufacturing procedures, quality control data and customer feedback. Data consistency and accessibility across various teams and departments is guaranteed by this centralized method.

It encourages collaboration between cross-functional teams engaged in product development. It makes it possible to easily communicate, share documents and assign tasks, while making sure everyone is collaborating effectively. PLM also improves workflow by automating and monitoring multiple processes, minimizing errors and delays.

CHAPTER 19: BENEFITS OF END-TO-END TRACEABILITY ON PROJECT PROCESSES WITHIN THE SCOPE OF PLM- DEFENSE AND AVIATION CASE STUDY

PLM systems also support version control, which enables effective tracking and management of various product design iterations and revisions, as well as associated documentation. Using this feature, teams can work together on improvements and manage change requests, ensuring everyone has access to the latest information and reducing the potential for errors caused by using out-of-date versions [7].

It connects with other business systems such as Customer Relationship Management (CRM), Enterprise Resource Planning (ERP) and Manufacturing Execution Systems (MES), providing end-to-end visibility and control of the supply chain. Production planning, inventory tracking and customer order fulfilment are all improved with this integration.

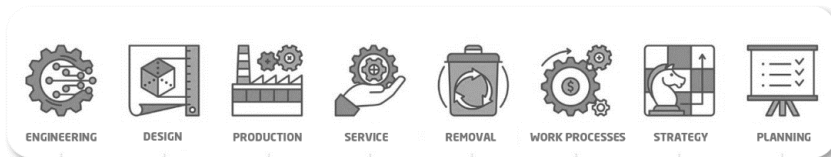


Figure 14:Product Lifecycle Management Concept with Icons (source: istockphoto, 2022)

Facilitates quality assurance processes by collecting and analysing data on the performance and quality of products. It helps track and resolve issues, manage non-conformances and ensure adherence to rules and regulations for the industry. By facilitating traceability and documentation, PLM systems help achieve regulatory requirements and product safety standards.

In summary, PLM is an all-encompassing strategy that enables businesses to effectively manage their product lifecycle, from idea to design to retirement. PLM systems aim to increase profitability and customer satisfaction by improving efficiency, quality, and innovation. They do this by integrating data, streamlining processes, and fostering collaboration.

2.3. Which Business Processes does it Cover in General?

Various procedures are often included in PLM systems to help manage the entire product lifecycle. Depending on the specific demands and requirements of an organization, these procedures may vary, but the following are some typical procedures often found in PLM systems [6][7][8][9][10]:

2.3.1. Product Data Management (PDM):

Design files, specifications and other product-related data are all created, stored, and managed as part of a process known as product data management (PDM). Throughout the product lifecycle, PDM ensures that accurate and up-to-date information is accessible to all stakeholders.

2.3.2. Design and Engineering:

These processes are supported by PLM systems that provide tools for developing and revising product designs. These resources can include simulation capabilities, computer-aided design (CAD) (**Figure 15**) and computer-aided engineering (CAE) (**Figure 16**). PLM makes it easier for design teams to collaborate and captures design iterations and changes for version control.

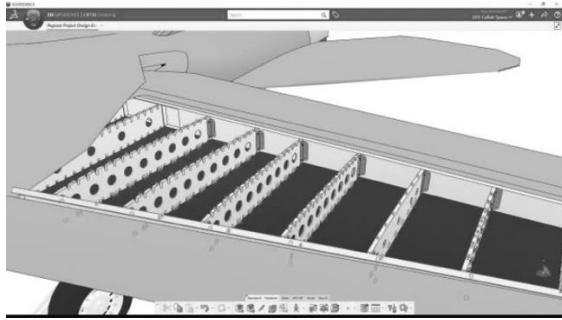


Figure 15: CAD (Wing Frame Design) (Source: Dassault Systemes & Airbus, 2023 (3DEXperience PLM 2023x))

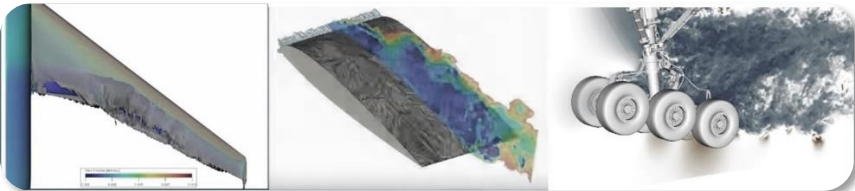


Figure 16: CAE (Wing and Landing Gear Aerodynamic Analysis) (Source: Dassault Systemes & Airbus, 2023 (3DEXperience PLM 2023x))

2.3.3. Change Management:

PLM systems give businesses the ability to manage changes to product designs, specifications, and related documentation. This includes collecting change requests, assessing their impact, and overseeing the implementation of accepted changes while ensuring that proper documentation and team communication is in place.

2.3.4. Bill of Materials (BOM) Management:

BOM management is a critical process in PLM systems. It involves creating and maintaining a hierarchical structure of the components and materials required to produce a product. BOM management provides accurate and consistent information about materials, quantities, and relationships between product components.

2.3.5. Supply Chain Collaboration:

PLM systems facilitate collaboration and communication with suppliers and partners in the product supply chain. This includes exchanging data, managing supplier relationships, monitoring supplier performance (and coordinating purchasing activities. PLM helps optimize supply chain operations by ensuring on-time delivery of components and materials.

2.3.6. Production Process Management:

Supports the management of production processes, including process planning, work instructions, and routing. They enable the creation and management of detailed production instructions, ensuring consistency and adherence to quality standards. PLM also helps optimize production efficiency and monitor work in progress.

2.3.7. Quality Management:

It includes quality management processes to ensure that products meet predefined quality standards. This includes capturing and managing quality requirements, performing inspections and testing, managing non-conformances and monitoring corrective and preventive actions.

2.3.8. Compliance with Legislation:

Help organizations ensure compliance with industry standards and regulatory requirements. They provide tools to track and manage compliance-related documentation, certifications, and approvals throughout the product lifecycle.

2.3.9. Maintenance and Service:

It may include processes related to product maintenance, service and support. This may include managing service requests, tracking product issues, coordinating service activities and providing access to service manuals and documentation.

3. AVIATION SPACE AND DEFENSE INDUSTRY

The main processes used in this sector, how PLM fits with these processes and the details of more innovative and detailed processes such as model-based systems engineering, requirements function logical and physical (RFLP), BOM management, system traceability will be discussed below [9][10].

3.1. What are the Important Processes in Projects?

3.1.1. Requirements Management:

This process (**Figure 17**) involves capturing, documenting and managing requirements for the aerospace or defence project. It involves gathering input from various stakeholders, defining system requirements and managing changes throughout the project lifecycle.

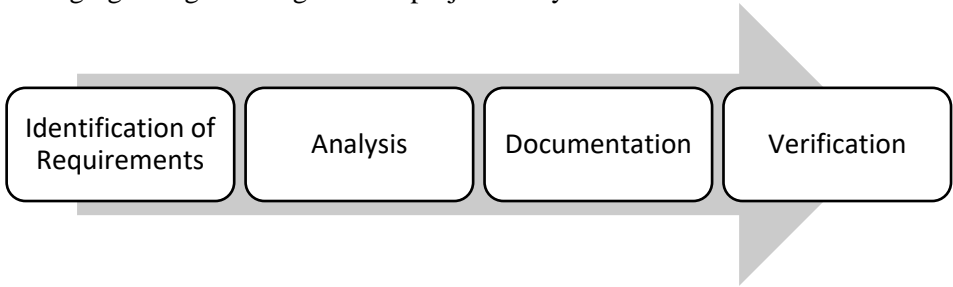


Figure 17: Main items of the requirements process [12].

3.1.2. Systems Engineering:

Systems engineering encompasses the holistic design, integration and verification of complex aerospace and defence systems. It includes defining system architecture (**Figure 18**), subsystems, interfaces and ensuring system-level performance, reliability, and safety [11].

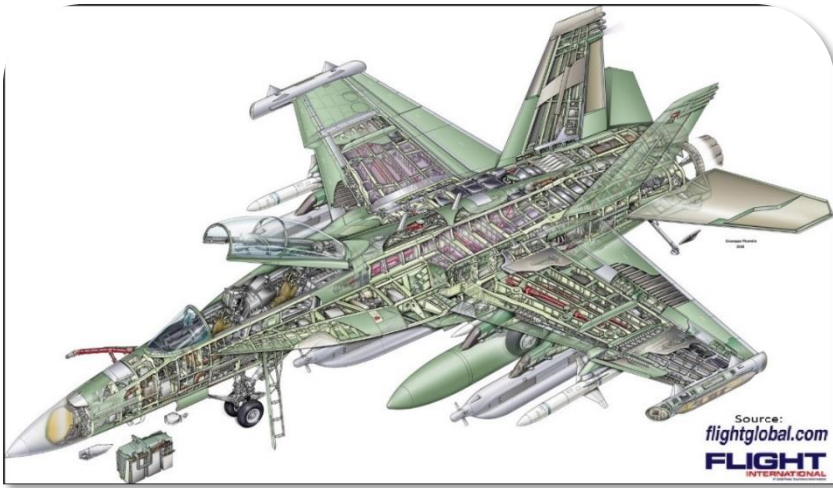


Figure 18: Full System Demonstration of Boeing EA-18G Growler Aircraft (Source: flightglobal.com, 2007)

3.1.3. Configuration Management:

Configuration management is essential in aerospace and defence projects to maintain control over the configuration of systems, components, and related documentation. It includes management of changes, version control and baselining to ensure consistency and traceability throughout the project [1].

3.1.4. Risk Management:

Risk management identifies, assesses, and mitigates risks associated with aerospace and defense projects. It includes risk identification, analysis, prioritization and implementation of risk mitigation strategies to ensure project success and safety.

3.1.5. Supply Chain Management:

Aerospace and defence projects often involve a complex supply chain with multiple suppliers and subcontractors. Effective supply chain management is critical to ensure timely and quality supply of components, ensure compliance, manage supplier relationships and mitigate supply chain risks.

3.1.6. Verification and Validation (Validation & Verification) (V&V):

Validation and verification (Verification) processes are essential to ensure that the aerospace or defence system meets specified requirements and performs as intended. It involves testing, simulation, and analysis to validate the system design and verify its performance against defined criteria [11].

3.1.7. Project Planning and Scheduling:

Effective project planning and scheduling is vital to ensure efficient resource allocation, budget management and on-time completion of aerospace and defence projects. This includes defining project objectives, work breakdown structure, estimating effort and time, and monitoring progress [11].

3.1.8. Configuration Control Panels:

Configuration Control Boards (CCBs) are responsible for reviewing and approving proposed changes to an aerospace or defence system. They ensure that changes comply with requirements, their impact is properly assessed and implemented in a controlled manner [1].

3.1.9. Documentation and Technical Publications:

Aerospace and defence projects generate significant amounts of technical documentation, including design specifications, maintenance procedures and technical publications. Managing and delivering accurate and up-to-date documentation is critical for effective system operation, maintenance, and support.

3.1.10. Compliance and Regulatory Processes:

Aerospace and defence projects must comply with various compliance standards and regulatory requirements. This includes ensuring compliance with safety regulations, export controls, cybersecurity guidelines and industry-specific certifications.

These processes are only a subset of the many processes involved in aerospace and defence projects. Specific processes may vary depending on the complexity, scope and organizational requirements of the project.

3.2. What are the Detailed Processes Used in Domestic Projects?

3.2.1. Model-Based Systems Engineering:

Model-Based Systems Engineering (MBSE) is a methodology used in the development of complex systems. It is a model-based approach where the system is represented through different models that capture its behavior, functions, and physical properties [13] [14].

In MBSE, the system is developed and analysed using computer models and simulations. These models are typically created using specialized software tools that can simulate and analyse the behavior of the system.

MBSE also aims to facilitate communication and collaboration between different stakeholders such as engineers, designers, and customers by providing a common language and framework for understanding the system [2].

It deals with systems engineering, business processes, optimization techniques and risk management tools in very complex and detailed projects in the Aerospace and Defence Industry. It is related to human-centered and technical fields such as industrial engineering, manufacturing systems engineering, process systems engineering, mechanical engineering, production engineering, control engineering, software engineering, electrical engineering, cybernetic engineering, aerospace engineering, organization studies, civil engineering, and project management.

Systems engineering considers all possible aspects of a system or project and integrates them as a whole. In making this integration, it is usually based on the traditional systems engineering approach. The traditional systems engineering approach uses the V-Model Methodology (**Figure 19**).

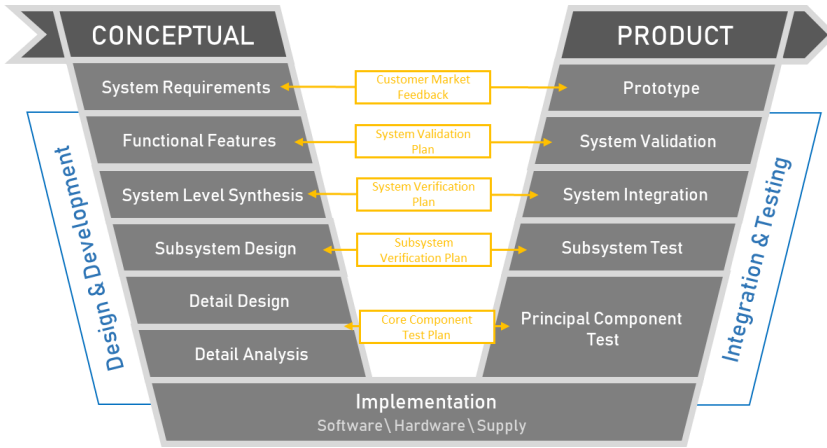


Figure 19: Details of the V-Model Approach [12].

The V model is a graphical representation of a system development life cycle. It is used to produce rigorously developed lifecycle models and project management models.

The left side of the "V" represents the decomposition of requirements and the creation of system specifications. The right side of the "V" represents the integration and verification of parts (**Figure 19**).

However, requirements first need to be validated against higher-level requirements or user needs. There is also such a thing as validation of system models. This can also be done partly on the left-hand side. It may not be correct to claim that verification only takes place on the right side. The easiest way is to say that verification is always against requirements (technical terms) and validation is always against the real world or user needs. The aviation standard RTCA DO-178B states that requirements are verified - confirmed to be correct - and validated to ensure that the final product meets those requirements.

So in short, Validation can be expressed as "Are you building the right thing?" and Verification (V&V) as "Are you building it the right way?".

The system engineering process integrated with PLM is Model Based System Engineering in aerospace and defence industry projects. This approach is based on the v-method approach. However, here the process is more detailed, and the architecture lives with the product. All requirements are first reduced to a system of systems (e.g. the architecture that simulates the landing and take-off of an aircraft), and then progressively to

CHAPTER 19: BENEFITS OF END-TO-END TRACEABILITY ON PROJECT PROCESSES WITHIN THE SCOPE OF PLM- DEFENSE AND AVIATION CASE STUDY

subsystems (e.g. landing gear system, radio communication system, etc.). The hardware (Figure 20), functional and logical architecture of these systems is established, verified, and analysed according to the requirements. Following these processes, the components (hydraulic pump, landing gear parts, etc.) and how they meet the requirements are determined, and the design and development to meet these requirements are made.

As shown in Figure 20 below, the logical architecture of all the aircraft's systems is designed with the help of the program. This architecture is called the system of systems and addresses the 4th part from the left (synthesis at the systems level) of the sequence in the v-diagram (Figure 19).

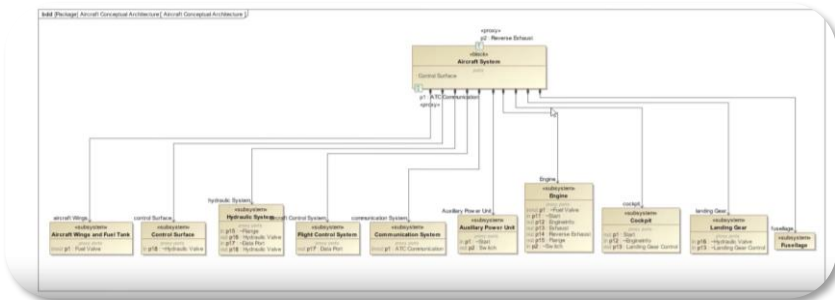


Figure 20: Example Hardware Architecture of an Aircraft Subsystem (Source: Dassault Systemes CATIA Magic, 2022)

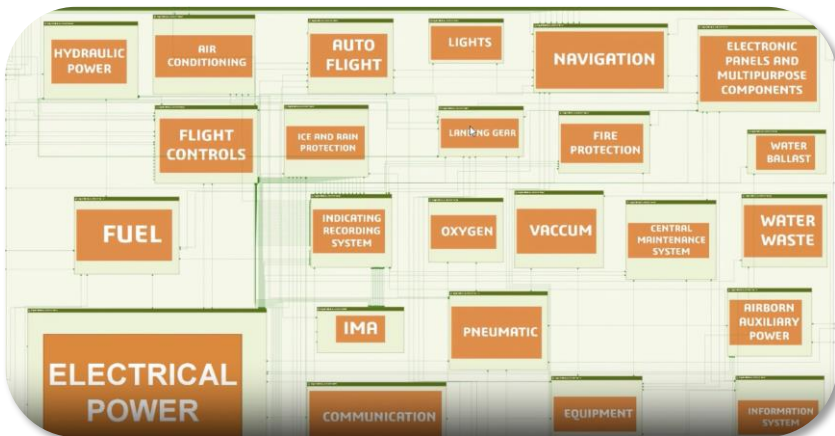


Figure 21: Logical Architecture of Aircraft Subsystems (Source: Dassault Systems, 2021 (3DEXperience PLM 2021x))

The logical design of the landing gear as a subsystem, which is a sub-step of this architecture, is shown in **Figure 22**. This is the last stage before moving on to component level design. Here, even before the design is done, logical analysis can be performed on the system architecture to verify whether the requirements are met (**Figure 23**).



Figure 22: Landing Gear Subsystem Logical Architecture (Source: Dassault Systems, 2021 (3DEXperience PLM 2021x))

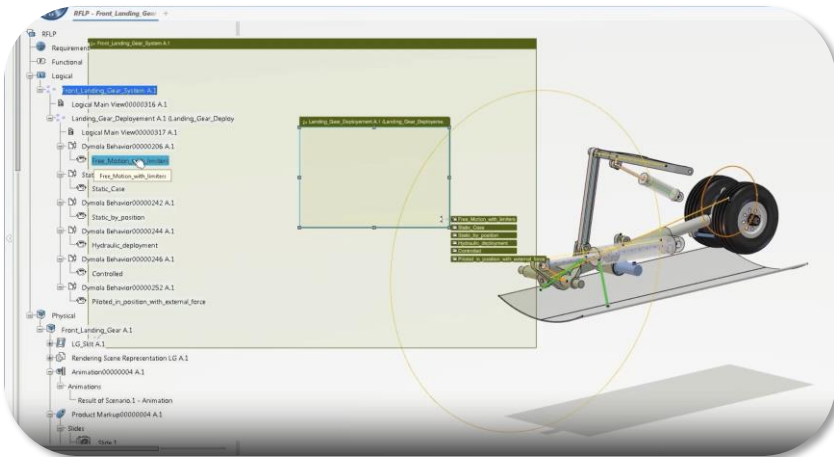


Figure 23: Verification of Landing Gear Subsystem with Logical and Physical Architecture (Source: Dassault Systems, 2021 (3DEXperience PLM 2021x))

3.2.2. System Traceability:

In the aerospace industry, system traceability refers to the capacity to track and record the links between various requirements, design components and other artifacts throughout a product's lifecycle. This traceability is essential to control risk, ensure compliance and support intelligent decision making.

CHAPTER 19: BENEFITS OF END-TO-END TRACEABILITY ON PROJECT PROCESSES WITHIN THE SCOPE OF PLM- DEFENSE AND AVIATION CASE STUDY

PLM (Product Lifecycle Management) systems are essential in the aerospace industry to ensure system traceability. From concept to retirement, these systems provide a consolidated platform to manage and track product data and related information (**Figure 24**).

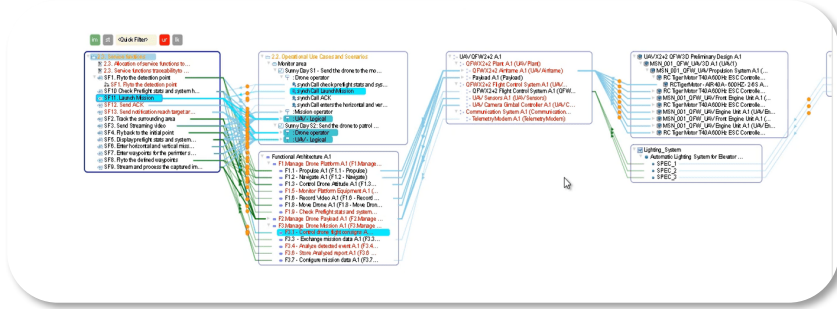


Figure 24: Interaction between System Traceability and RFLP Structure (Source: Dassault Systems, 2021 (3DEXperience PLM 2021x))

In the context of PLM systems for aerospace, system traceability generally aims to provide the following benefits:

- It makes it possible to collect, organize and manage requirements for aerospace products. These requirements are linked to specific components, subsystems and related design components to create traceability.
- It facilitates the management of product configurations by recording and maintaining links between various versions, variants and revisions. This traceability enables changes to be tracked and an understanding of how the system as a whole is affected.
- CAD models facilitate traceability by linking different design artifacts such as requirements, engineering analysis and simulations. Any of these artifacts can track changes and their impact on additional parts or systems can be assessed.
- They ensure that actions related to verification and testing comply with established standards. The requirements they control are linked to test cases, test results and associated artifacts that enable comprehensive coverage analysis and traceability of test operations.
- It makes it possible to track and manage change requests, issues and non-conformities. Traceability guarantees that proposed changes are properly evaluated, accepted, and implemented, considering their impact on the entire system.
- In the aviation industry, compliance with regulations and meeting certification standards is essential. PLM systems provide traceability by maintaining records, documentation, and proof of compliance, which is essential for audits and regulatory inspections.

3.2.3. Requirements, Functional, Logical and Physical Product Tree (RFLP⁴):

RFLP (Figure 26-Figure 27) is a framework that supports the Model Based Systems Engineering process:

In supporting this structure, an architectural structure can be created such that a Level 1 Function meets a Level 2 Requirement, a Level 2 Function meets a Level 3 Requirement (Figure 25).

It is a unified system definition with 4 key aspects:

- **Requirements:** describes all the requirements that a system must fulfil.
- From stakeholders' requirements to the system and design,
- **Functional:** the architecture should provide the system services and the functions and flows provided by its functional components,
- **Logical:** explains the architecture of the system with components. The system, its interfaces and allocated functions and flows.
- **Physical:** describes the actual system components. This is part of the actual design of the product. Structures such as 3D Modelling (Mechanical, Electrical, Fluids... etc.) are established. In this phase 150% BOM logic is applied to these structures. In this way, filtering can be done for all configurations in all BOMs. Instead of creating separate BOMs, a single equipment, design, requirement, etc. represents each configuration. In this way, error-free BOM structures are established. Easier traceability is ensured.

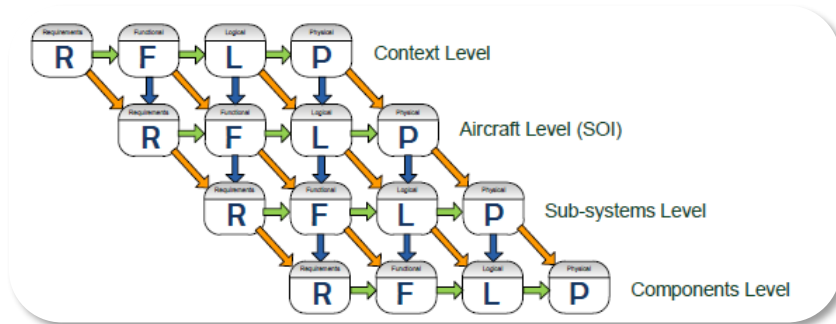


Figure 25: Proposed RFLP model compatible with the Systems Engineering V-model [3].

To be more specific, different variations of aircraft such as *Block0*, *Block10*, *Block20*, etc. are produced. These variations define the aircraft to be used according to its ability to meet the requirements and operational conditions desired by the stakeholders. For example, a *Block0* level aircraft

⁴ RFLP: "Requirement, Functional, Logical and Physical" Engineering Production Tree

is not expected to have a flight computer with intelligent target detection, but *all Block* levels are expected to have a fully functional landing system. Therefore, the Requirements, Functions, Logical Architecture and finally the Physical Architecture of the landing gear system are created in a one-off manner. This structure is matched to all aircraft configurations. The effort spent on the system and the change tracking process is much more efficient in this way. Using a single RFLP Tree (150% BOM⁵), all aircraft were created, and the final result was reached (100% BOM) using filtering logic according to *specific Block* levels.

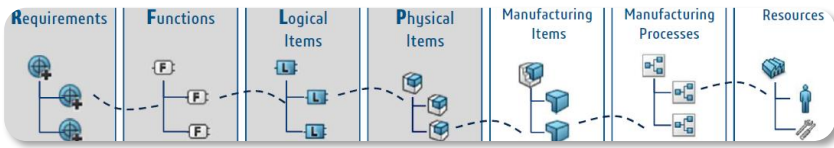


Figure 26:Schematic Representation of RFLP Product Tree Structure [4].

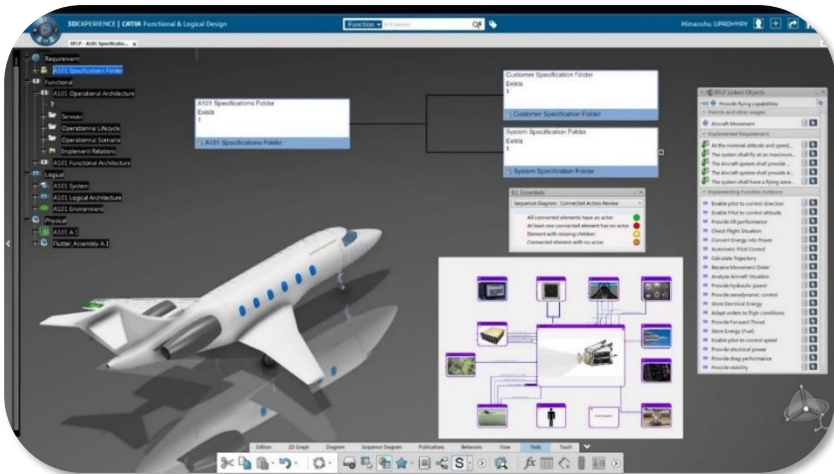


Figure 27:RFLP Structure Representation in 3DEXPERIENCE PLM Application (Source: Dassault Systems, 2021 (3DEXPERIENCE PLM 2021x))

3.2.4. Model Variants and Configurations:

Configuration management (CM) (this is also classified in the literature as Configuration Identification, Change Management, Configuration Status) is a process used to monitor and control changes to a product or system throughout its life cycle. In the aerospace industry, CM is essential to

⁵ BOM: "Bill of Material", i.e. bill of material; It means a product tree or list that constitutes the components of a product.

ensure the safety and reliability of aircraft and spacecraft. The following steps are usually included in CM [1]:

- Identification: The first step is to list every part of the system or product that needs to be identified. This includes both tangible elements such as hardware and software and intangible elements such as information and documentation.
- Control: Once the components are defined, they must be controlled to prevent unauthorized changes. Numerous techniques can be used to do this, such as configuration audits (CA⁶), change control boards (CCB⁷) and configuration checklists (CCL⁸).
- Audit: The CM process needs to be audited to ensure that it is being followed properly. Both internal and external auditors have the ability to perform this.

Monitoring the condition of the system or product is necessary throughout its lifecycle. This includes tracking the progress of any work done on the system or product as well as component changes.

The aerospace industry uses the Configuration Effectivity Matrix (**Table 7**) to manage and track configuration variations and options for aerospace products such as aircraft or spacecraft. It helps to ensure that the right features, systems, and components are included in each specific configuration or variant of the product.

A Configuration Effectiveness Matrix typically consists of rows and columns, where each row represents a specific configuration or variant and each column represents a feature, system or component of the product. The matrix visually presents which features are applicable or enabled for each configuration.

Table 7: Example of Configuration Effectivity Matrix

Configuration Effectiveness Matrix	Avionics System	Wing Type	Engine Type	Structural Architecture
Block 0	Not Available	Type A	Interim Engine	Option 1
Block 10	Available	Type B	Interim Engine	Option 1
Block 20	Available	Type B	Indigenous Engine	Option 2

⁶ Configuration Audits

⁷ Change Control Board

⁸ Configuration Control Lists

PLM (Product Lifecycle Management) systems play a crucial role in managing the Configuration Productivity Matrix in the aerospace industry. These systems provide a comprehensive platform to store, manage and control product data and configurations throughout their lifecycle. Here is how PLM systems contribute to the Configuration Productivity Matrix:

- a) **Centralized Data Management:** PLM systems act as a central repository for all product data, including configuration information. They store the Configuration Productivity Matrix, capturing the relationships between different configurations, features, systems, and components. This ensures that the matrix is easily accessible, up-to-date, and consistent across the organization.
- b) **Configuration Management:** Provides efficient configuration management by associating configuration data with specific product builds and variants. It allows users to define and manage configuration rules such as dependencies and exclusions between features and components. These rules help ensure that only valid configurations are created and maintained.
- c) **Variant Management:** Facilitates effective variant management by providing tools to identify and manage different product variants. They support the creation of variant structures where each variant can have its own features, systems and components. PLM systems ensure that the Configuration Productivity Matrix is linked to these variant structures so that variant-specific configurations are accurately represented and tracked.
- d) **Change Management:** Streamlines change management processes. When changes to configurations or features are proposed, PLM systems enable change requests to be captured, documented, and routed. They provide workflows to evaluate and approve these changes, ensuring that the Configuration Productivity Matrix is updated accordingly.
- e) **Traceability and Impact Analysis:** Supports traceability and impact analysis between configuration changes and other product data. It allows users to track the impact of a configuration change on other components, systems or downstream processes. This capability helps identify potential conflicts, risks and impacts associated with changes in the Configuration Effectiveness Matrix.

- f) **Visualization and Reporting:** Provides visualization and reporting capabilities that enhance the understanding and analysis of the Configuration Effectiveness Matrix. It allows users to view the matrix in various formats such as tables, diagrams or graphs, making it easier to understand and communicate the relationships between configurations and features. In addition, PLM systems enable the generation of reports and analytics on configuration activity, helping stakeholders make informed decisions.

By leveraging PLM systems, aerospace organizations can efficiently manage the Configuration Productivity Matrix throughout the product lifecycle. These systems aim to improve data integrity, help ensure collaboration between stakeholders, support change control processes and provide the tools necessary for effective configuration management in a complex aerospace environment.

3.2.5. E-BOM, M-BOM and S-BOM:

In Product Lifecycle Management (PLM) systems, you typically encounter three types of Bill of Materials (BOM): Engineering BOM (eBOM), Manufacturing BOM (mBOM) and Service BOM (sBOM). Each BOM serves a specific purpose within the product lifecycle. In the aerospace industry, they have more specific scopes, which are defined below:

- a) **Engineering BOM (eBOM):** In the aerospace industry, the eBOM represents the structure and composition of the product from an engineering or design perspective, especially for aerospace products such as aircraft or spacecraft. It includes all components, subassemblies and systems required for the design and functionality of the product. EBOM collects detailed information on aerospace-specific parts such as avionics systems, propulsion systems, airframe components and subsystems such as landing gear, control surfaces or electrical systems. It serves as the basis for production and maintenance processes in the aviation industry.
- b) **Manufacturing BOM (mBOM):** The Manufacturing BOM in the aerospace industry is created based on the E-BOM and is specifically tailored for the manufacturing and production of aerospace products. It includes all components, parts and assemblies needed to build the aircraft or spacecraft. The M-BOM considers aerospace-specific manufacturing issues such as material specifications, tolerances, regulatory requirements and assembly procedures. It includes details

CHAPTER 19: BENEFITS OF END-TO-END TRACEABILITY ON PROJECT PROCESSES WITHIN THE SCOPE OF PLM- DEFENSE AND AVIATION CASE STUDY

on aerospace-specific manufacturing processes such as assembly sequences, tooling requirements, quality standards and test procedures for aerospace components and systems.

- c) Service BOM (sBOM): The Service BOM in the aerospace industry focuses on the support, maintenance, and after-sales activities of aerospace products. It covers components, parts and assemblies required to service, repair, or replace aviation systems and equipment. The S-BOM (Figure 28) includes aerospace industry-specific details such as part numbers, service procedures, compliance information, maintenance schedules and documentation for aerospace systems and components in accordance with industry standards. It ensures that the correct parts and procedures are followed during maintenance, repair and overhaul (MRO) activities in the aerospace industry.

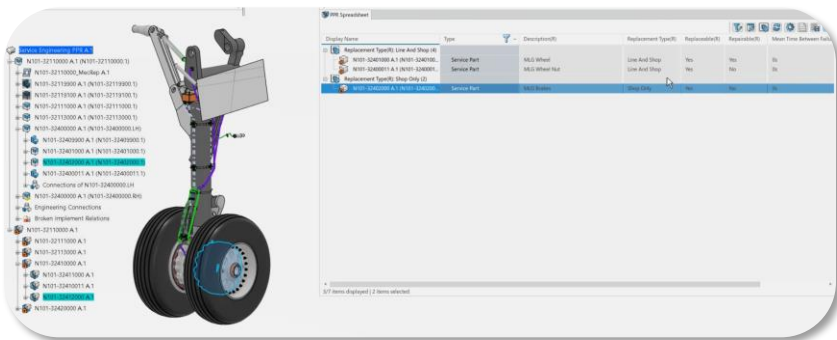


Figure 28: S-BOM Example of Aircraft Landing Gear (Source: Dassault Systems & Airbus, 2023 (3DEXperience PLM 2023x))

These definitions emphasize the special considerations and requirements of the aerospace industry, considering the unique characteristics and complexities of aerospace products, systems, and components. E-BOM, M-BOM and S-BOM, when properly managed within aerospace PLM systems, aim to enable the effective design, manufacture, and maintenance of aerospace products, ensuring compliance with industry regulations, safety standards and efficient lifecycle management.

4. RESULTS OF USING PLM AND INNOVATIVE SYSTEM ENGINEERING PROCESSES

In this section, the innovative PLM and Systems Engineering methods that have been used in the sector and the benefits that the project has gained will be detailed. These topics are identified in a similar way to the benefits of PLM in general, but in detail the contribution to the industry and the project. In addition, the challenges faced are also examined.

4.1. Benefits to The Project

When combined with processes such as Model-Based Systems Engineering (MBSE), RFLP (Requirement, Function, Logical, and Physical) and Configuration Management, the PLM system brings significant innovation and value to domestic projects in the aviation industry. In detail, we can examine the benefits of innovative processes and the use of PLM systems under headings [6][7][8].

4.1.1. Improved Collaboration and Communication:

Provides a centralized platform for collaboration and communication between the customer (SSB, HVKK, etc.) and stakeholders (TAI, TUBITAK, etc.). It enables effective coordination and alignment throughout the product lifecycle, allowing teams to work together, share information and access the latest data. This improves collaboration, reduces errors and improves decision-making.

4.1.2. Advanced Requirements Management:

PLM system integrated with MBSE and RFLP processes enables effective requirements management in the aerospace industry. It facilitates the capture, organization, and traceability of requirements from initial concept to final product. This ensures that all stakeholders have a clear understanding of requirements, their allocation to functions and traceability throughout the design, development and validation processes.

4.1.3. Modern Design and Development:

The PLM system supports modern design and development processes in the aerospace industry. It enables the creation, management, and integration of MBSE models, including logical and physical designs. This allows engineers to develop and validate designs, perform simulations, and optimize system performance. The PLM system ensures that design changes are properly managed, documented and communicated, reducing the time and costs associated with rework.

4.1.4. Full Scope Configuration Management:

The PLM system plays a crucial role in configuration management in the aerospace industry. It provides tools and capabilities to define, control and monitor configurations, including variant management and change management. The system ensures that the correct configurations, including hardware, software and documentation, are used during production, maintenance and support activities. This improves configuration control, reduces errors and improves product quality and safety.

4.1.5. Enhanced Compliance and Certification:

The PLM system helps aerospace companies meet compliance and certification requirements. It enables the integration of regulatory standards and industry specifications into the design and development processes. The system supports documentation, verification, and validation activities, ensuring that the product meets all required regulatory and safety standards. This streamlines the certification process and reduces the risk of non-compliance.

4.1.6. Life Cycle Visibility and Decision Support:

The PLM system supports informed decision making in the aerospace industry, providing comprehensive visibility into the product lifecycle. It offers real-time access to MBSE models, RFLP data and configuration information, allowing stakeholders to analyse and assess the impact of decisions throughout the lifecycle. This supports risk mitigation, performance optimization and cost-effective decision making.

4.2. Challenges Affecting the Project

While PLM systems offer numerous advantages to the aerospace industry when integrated with processes such as MBSE, RFLP, configuration management, etc., there can also be some potential disadvantages. We will examine these challenges in turn.

4.2.1. Implementation Complexity:

Implementing a PLM system and integrating it with MBSE, RFLP and configuration management processes can be complex and require significant upfront investment in time, resources, and infrastructure. Organizations can face challenges during system deployment, data migration and process standardization, which can lead to disruptions and delays if not managed properly.

4.2.2. Learning Curve and Education:

PLM systems often have a learning curve and employees need to be trained on how to use the system and related processes effectively. This can take time and initially impact productivity as employees adapt to new tools and methodologies. Adequate training and change management efforts are essential to mitigate this disadvantage.

4.2.3. Data Integration and Interoperability:

Integrating data from various sources such as CAD systems, simulation tools and legacy systems into a PLM system can be challenging. Ensuring data consistency, accuracy and interoperability across different formats and platforms requires careful planning, data mapping and ongoing maintenance. Poor data integration can lead to errors, inefficiencies, and inconsistencies in the product development process.

4.2.4. Maintenance and Upgrades:

PLM systems require regular maintenance and upgrades to stay current with evolving technologies, industry standards and regulatory requirements. Upgrades can interrupt ongoing projects and require additional training and system validation efforts. Organizations should plan system maintenance and upgrades to minimize potential disruptions and associated costs.

4.2.5. Cost Considerations:

Implementing and maintaining a PLM system can involve significant financial investments, including software licenses, hardware infrastructure, customization, training, and ongoing support. For some organizations, especially smaller organizations with limited resources, the cost of acquiring and maintaining a PLM system can be a disadvantage. Cost-benefit analysis and careful planning are essential to ensure that the potential benefits outweigh the associated costs.

4.2.6. Change Management Challenges

Introducing a PLM system with new processes and methodologies requires effective change management. Resistance to change, lack of user adoption and cultural barriers can hinder the successful implementation of a PLM system. Organizations need to invest in change management strategies, including open communication, stakeholder engagement and training programs to address these challenges and ensure a smooth transition.

It is important to note that although these drawbacks exist, they can be mitigated through proper planning, effective implementation strategies and continuous management and optimization of the PLM system. The potential benefits of improved collaboration, streamlined processes and enhanced product development often outweigh these challenges, making PLM systems a valuable asset in the aerospace industry.

5. CONCLUSION

PLM is considered to offer many benefits for aerospace and other leading technology-intensive industries. In the coming years, these benefits are expected to increase and develop. Integration with procedures such as MBSE, RFLP (Requirements, Functions, Logical and Physical) and configuration management, which are detailed processes in the PLM system, have the potential to significantly improve the domestic aviation industry in the coming years. To illustrate:

- The development of digital twins, virtual representations of real assets, can be realized in the future thanks to the integration of PLM with MBSE and RFLP. Preventive maintenance, predictive analytics and optimization can be made possible by digital twins that provide real-time data on the behavior, performance, and health of an aircraft. To help create and use digital twins for advanced aircraft operations, PLM can make it easier to integrate and utilize data from sensors, simulators, and maintenance records.
- More comprehensive and accurate simulations are possible through the integration of models and data from a variety of disciplines, including aerodynamics, structures, systems, and controls. With better design decisions and shorter development cycles, engineers can evaluate and optimize aircraft performance, fuel efficiency, safety, and other key variables for years to come.
- Integrated Requirements Management Integration can provide end-to-end traceability from high-level system requirements to specific functional and physical requirements. This facilitates efficient change management, improves impact analysis, and streamlines the requirements engineering process. In addition, it facilitates compliance verification and can guarantee that customer and regulatory criteria are met throughout the entire lifecycle of the product.

Finally, all this know-how and virtualized product paves the way for much faster production of real products in the next indigenous projects. Thanks to the ability to store all information resources and the history of what has been learned in a single place without getting lost, and the system's continuous contribution to process improvements, the time it takes to develop and produce aircraft can be reduced from an average of 5-10 years to 1-2 years. The virtual verification of all system modelling and component analyses can enable the aviation industry to achieve challenging elements such as certification, validation, verification, testing, etc. with very low cost, minimum time loss and few iterations, even before the product is actually produced.

Acknowledgements

I would like to thank my esteemed advisor; Prof. Dr. Rüstem Barış YEŞİLAY, who shared his valuable knowledge with me and I will never forget the importance of the information I used in this article, and my colleagues İhsan Anıl TOKMAN, Umut YUL, Kürşad KÜÇÜKKAYA, Emre ERTÜRK, Onur KEMERLİ and Numan SÜME for their help in my study. I would also like to thank all my friends in my team.

Conflict of interest

No conflict of interest was declared by the authors.

Author contributions

Rüstem Barış YEŞİLAY contributed to the review and editing of all chapters. Oğuz Varhan contributed to the research and writing of all chapters.

REFERENCES

- [1] Y. Xu, M. K. Malisetty ve M. Round, «Configuration Management in Aerospace Industry,» Procedia CIRP, no. Volume 11, pp. 183-186, 2013.
- [2] Visure Solutions, Inc., «Model Tabanlı Sistem Mühendisliği (MBSE) Eksiksiz Kılavuz,» Visure, Ocak 2022. [Online]. Available: <https://visuresolutions.com/tr/mbse-rehberi/>.
- [3] G. E. a. S. Liscouët-Hanke, «DEVELOPMENT OF CORE FUNCTIONS FOR AIRCRAFT CONCEPTUAL DESIGN: METHODOLOGY AND RESULTS,» ResarchGate, May 2015.

- [4] N. DALAL, «ENOVIA BOM Management for E2E digital continuity,» 3DEXPERIENCE Dassault Systemes, 4 July 2018. [Online]. Available: https://r1132100503382-eu1-3dswym.3dexperience.3ds.com/#community:38/media:dB0s_peISbyVsb9eUA8Dhg [Reached: June 2023].
- [5] J. Stark, Product Lifecycle Management (Volume 2) The Devil is in the Details, Geneva, Switzerland: Springer, Third Edition (2016).
- [6] J. Stark, Product Lifecycle Management (Volume 3) The Executive Summary, Geneva, Switzerland: Springer, 2018.
- [7] J. Stark, Product Lifecycle Management (Volume 1) 21st Century Paradigm for Product Realisation, Geneva, Switzerland: Springer (ISBN 978-3-319-17440-2), Third Edition (2015).
- [8] J. Stark, Product Lifecycle Management (Volume 4) The Case Studies, Geneva, Switzerland: Springer, 2019.
- [9] E. Gurman, K. Ventura ve H. Soyuer, «PRODUCT LIFECYCLE MANAGEMENT AS A WHOLE BUSINESS MANAGEMENT SYSTEM: AN EXPLORATORY RESEARCH,» PressAcademia (Research Journal of Business and Management), pp. 336-346, 2017 Volume:4 Issue:3.
- [10] H. Gutierrez, «Why Business Processes Are Important for PLM,» SHAREPLM, 27 Kasım 2016. [Online]. Available: <https://shareplm.com/plm-business-processes/>. [Reached: June 2023].
- [11] IEEE Standards Association, «IEEE Standard for Application of Systems Engineering on Defense Programs,» IEEE 15288.1-2014. [Çevrimiçi]. Available: <https://standards.ieee.org/ieee/15288.1/5704/>. [Reached: June 2023].
- [12] INCOSE, Systems Engineering Handbook (A Guide for System Life Cycle Processes and Activities), New York City, USA: Wiley, Fifth Edition (July 2023)
- [13] Procedia Computer Science, Complex System Simulation: Proposition of a MBSE Framework for Design-Analysis Integration, pp. 9 – 68. , 2013 (doi:10.1016/j.procs.2013.01.007).
- [14] JOHNS HOPKINS APL TECHNICAL DIGEST, Model-Based Systems Engineering in Support of Complex Systems Development, VOLUME 32, NUMBER 1, 2013.



CHAPTER 20

Aviation Technologies and Applications
E-ISBN:978-605-338-471-7
2025, chap. (20), pp. 341-356.

INVESTIGATION OF MECHANICAL PROPERTIES OF NACA 2024 DROP WING ACCORDING TO STATIC AND MODAL BEHAVIOUR OF DIFFERENT ROOT AND TIP VETER POSITIONS

Mustafa Murat YAVUZ^{1,*}

ABSTRACT

In the present study, an investigation into the properties was conducted by analysing the impact of the root and tip vane positions on the wing. While the flow characteristics of the wing are extensively documented in the literature, its mechanical properties have been addressed to a lesser extent. The research aims to examine wing configurations featuring front and rear arrow angles, anhedral and dihedral angles, as well as angularly bent wing geometries. A three-dimensional airplane wing was modelled using a NACA 2024 airfoil cross-sectional profile for the analyses. The investigation was conducted utilizing the finite element analysis. Linear elastic isotropic material properties were used as the wing material. Since the wing connection shows a built-in support behaviour, pure bending behaviour was investigated for stress analyses. Modal analysis was included. At the modal frequency, the wing exhibits predominant bending and torsional responses. Additionally, computational fluid dynamics analysis was employed to calculate the drag coefficients. The findings were elaborated upon comprehensively, and the visual outcomes were interpreted. Furthermore, the results procured will furnish insights for future design applications.

Keywords: veterinary length, wing, stress, arrow angle, dihedral

1. INTRODUCTION

Wing structures are the most important design stages of airplanes. Significant scholarly inquiry has been devoted to the study of wings, which play a pivotal role in influencing flight performance and operate across diverse environmental conditions, over an extended duration. The configuration of the wing section, including its shape, length, and sectional characteristics, as well as the sweep angle, is tailored variably in accordance with the specific application requirements. The advent of novel material and production technologies, coupled with the enhancement of experimental and numerical analysis methods, has engendered new domains for modelling and research in the realm of wing design.

*Corresponding Author: murat.yavuz@idu.edu.tr
1 0000-0002-5892-0075, Mechanical Engineering Department, Faculty of Engineering, İzmir Democracy University, İzmir, Turkey

CHAPTER 20: INVESTIGATION OF MECHANICAL PROPERTIES OF NACA 2024 DROP WING ACCORDING TO STATIC AND MODAL BEHAVIOUR OF DIFFERENT ROOT AND TIP VETER POSITIONS

The case studies predominantly concentrated on evaluating the aerodynamic performance and ensuring stability. Airfoil [1] is one of the critical influencing parameters on performance. For instance, the force and pressure effects of straight flaps of different lengths and angles on a NACA 0012 airfoil were [2] investigated, and the utilization of flaps with an angle up to 15 degrees exerted a beneficial influence. Dihedral angle represents a critical parameter, particularly in the context of aircraft wing design, where it has been the subject of various optimization studies [3]. NACA 4412 airfoil was incorporated within a tapered wing design, varying the sweep angle and span length to determine the optimal configuration. This resulted in an aerodynamic efficiency improvement of up to 30%. NACA 0015 airfoil was [5] employed in the construction of a wing with a sweep angle, and the effects of high angles of attack were analysed. Wakes including fluctuations affected stability and was depended on the wing sweep profile. The impact of high Reynolds numbers on friction values was examined by analysing a wing model with a significant sweep angle [6]. A study on a morphing wing structure considered various camber angles, resulting in a reduction of wing loads [7]. The optimization of a morphed winglet, which took into account the angle of twist, sweep, cant, and toe, resulted in a 2% fuel savings [8]. Consideration of an alternative morphing wing design [9] led to reduced take-off and landing distances, as well as an enhanced lift coefficient following optimization. Blended wing body analysis showed [10] that optimized sweep properties influence the lift behaviour. Different sweep angles on a delta wing were [11] analysed and vortex formations were analysed which could cause lift reduction. The influence of dihedral angles on the stability of a tailless aircraft was examined, resulting in the identification of two optimal models [12]. An investigation into a high-pressure capturing wing design incorporated dihedral angles, revealing a correlation between the angle of attack and dihedral angle for enhanced stability [13].

This study includes effect of dihedral and extrusion direction of wing sections for a NACA wing and mechanical/flow behaviour was analysed.

2. MODEL CONSTRUCTION

The geometric section used in the formation of the wing geometry typically features a drop profile. Depending on the type of drop profile structure, they are symmetrical or non-symmetrical structures with a difference in distance between the upper and lower surfaces of the centre of gravity. The wing is fixed using anchored support and the wing section is formed by extrusions such that the cross section narrows along the length of the wing. The pressures on the wing surface are proportional to the surface width.

Therefore, larger forces are generated on the wider wing surface and as a result, these forces produce a larger moment at the wing attachment point. In order to reduce the force and moment caused by the pressure effect, the wing cross-section is reduced as it moves towards the wing tip in order to keep it within certain limits. In this way, the moment effect is limited by reducing the wing surface area.

2.1. Structural Model of the Wing

The basic wing model is shown in Fig. 1. Wing root section width is 1000 mm, wing tip section width is 500 mm and wing length is 5000 mm. The wing aspect ratio is modelled as 1/5 and the wing contraction ratio as 1/2.

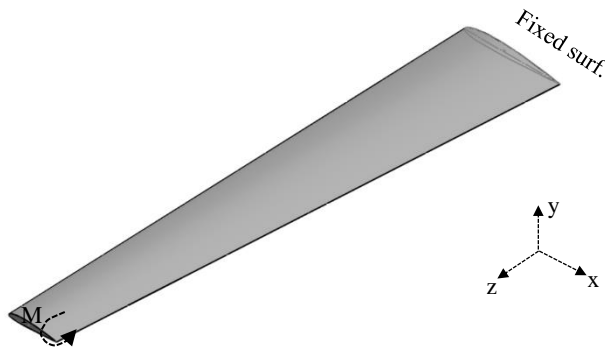


Figure 1. a three-dimensional NACA wing geometry including boundary conditions

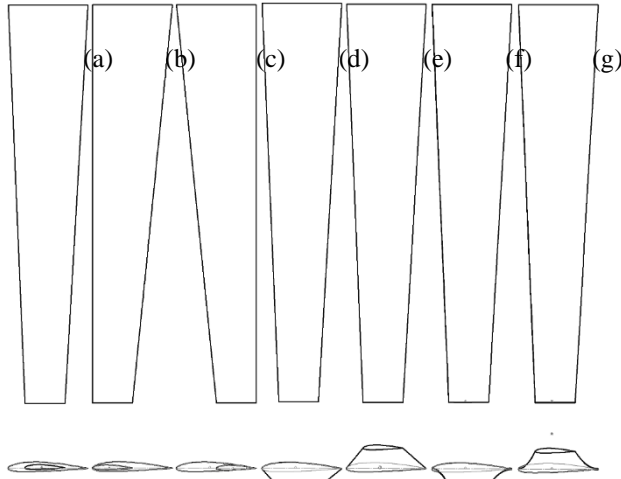


Figure 2. wing cross-section extrude formats: (a) centered; (b) straight; (c) forward-sweep; (d) centered-negative dihedral; (e) centered-positive dihedral; (f) centered-curved negative dihedral; (g) centered-positive curved dihedral.

The wing root location is fixed in all axes and the degree of freedom is zero. A pure bending moment (M) of 1000 Nm was applied downward from the free end of the wing. The airfoil will show mechanical behaviour as a beam subjected to bending in this application. The amount of deformation during bending is related to the material properties. Steel with standard properties was selected as the material to be used. The steel used has a Modulus of Elasticity (E) of 200 GPa and a Poisson's ratio of 0.3. In general, the material behaviour has been adjusted to show linear elastic isotropic material properties. A material in this state does not contain behaviours such as plastic deformation, permanent stress, fracture strength. The different wing models are shown in Fig. 2. Centered, forward/backward, positive/negative straight-curved dihedral structures of the same wing structure are modelled and numbered as case I to case VII, respectively.

2.2. Finite Element Analysis Setup

In general, three different investigation methods (experimental, analytical and numerical methods) are widely used for the investigation of structural behaviour. In order to carry out the experimental investigation, a geometric model must be produced, appropriate boundary conditions must be fully applied, and deformation and strain measurements must be obtained with appropriate devices. Experimental equipment and materials are required. In the analytical method, the inertia of the geometry sections and their moment interaction are analysed using integration methods. Derivative-boundary condition solutions of mathematical equations to be used in deformation calculation are required. Analytical method is difficult especially in models containing geometrical irregularities. In numerical methods, a general mathematical model is solved approximately by using serial methods and including boundary conditions. The method gives an approximate solution to the required results and the solution process requires great solution effort. Therefore, computer programming is used or package programs containing the appropriate numerical solution method are used. In order to investigate the structural behaviour of this study, a package containing the finite element method was used. A general examination method sequence for the solution is given below;

- i. creation of the geometric model
- ii. finite element modelling of the geometric model by fragmentation
- iii. determination of boundary conditions for the modelled finite element model
- iv. numerical solution of the model
- v. obtaining results

All finite elements have nodes and these nodes have bonded each other by edges of elements. If nodes move, the finite elements elongate or shorten which represent deformations. Deformation of finite elements depend on geometries and material properties. So finite element formulation begins with the construction of stiffness (K) and displacement (u) matrices [14] given in Eq. 1.

$$[K]. [u] = [F] \quad (1)$$

[K]: Stiffness matrix

[u]: Displacement matrix

[F]: Nodal external forces on related nodes

The stiffness matrix can be written by deriving the Hooke's Law for linear elastic material behaviour;

$$\sigma = \varepsilon . E \quad (2)$$

$$\varepsilon = \delta / L \quad (3)$$

$$F = \sigma . A \quad (4)$$

$$F = \varepsilon . E . A \quad (5)$$

$$F = E . A . \delta / L \quad (6)$$

$$\delta = u_2 - u_1 \quad (7)$$

$$F = K . (u_2 - u_1) \quad (8)$$

$$K = A . E / L \quad (9)$$

$$\begin{bmatrix} F_1^e \\ F_2^e \end{bmatrix} = \begin{bmatrix} k^e & -k^e \\ -k^e & k^e \end{bmatrix} \cdot \begin{bmatrix} u_1^e \\ u_2^e \end{bmatrix} \quad (10)$$

σ is stress, δ is deformation and ε is the strain of the material/part. The σ for bending condition can [15] be given in the below Eq.

$$\sigma = M . c / I \quad (11)$$

c is perpendicular distance from the neutral axis of the element to the farthest point and I is the second moment of inertia of cross-section.

2.3. Computational Fluid Dynamic Analysis

The drag coefficient (C_d) of is also another important value for a wing. It includes drag force (F_d) which is opposite direction of the aircraft direction. Aircraft thrust force should be greater than the drag force for moving forward. The drag force formula is given in below [16] Eq.

$$F_d = C_d \cdot \rho / 2 \cdot V^2 \cdot A \quad (12)$$

ρ is the density of air (1.225 kg/m^3), A is surface of the wing (m^2) and relative velocity of air to aircraft (m/s).

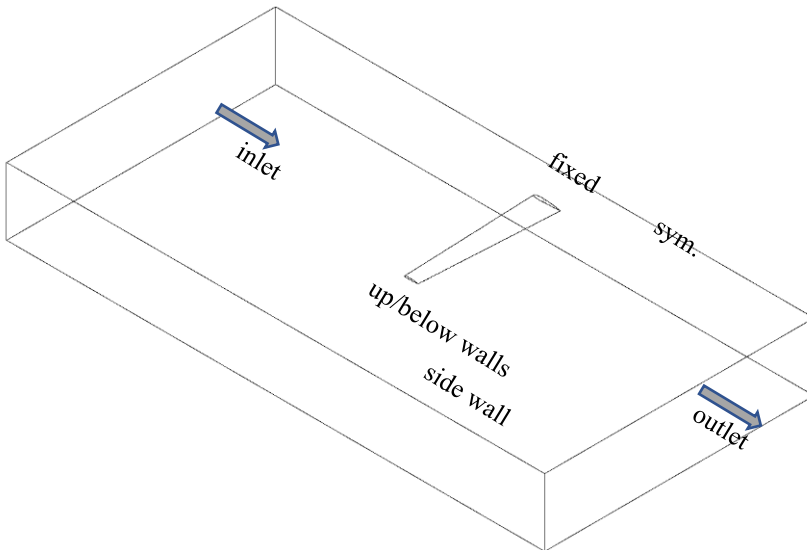


Figure 3. channel shape, wing position and boundary conditions.

The drag coefficient is calculated with a Reynolds number of 100.000. The channel geometry which has 10 m x 2.5 m x 20 m (width, height, length) dimensions is given in Fig. 3. Channel has an inlet, an outlet, a symmetry boundary condition and three wall definitions on the surfaces. The drag coefficient is calculated by the solution of flow analysis. The computational fluid dynamic analysis (CFD) is used and the domain contains approximately 300.000 elements. Standard k-epsilon turbulence model is used for modelling the turbulent regimes. Solution residual is used as $1e-05$.

3. NUMERICAL RESULTS

The results data were taken from a straight path on the upper surface of the wing along the wing. The drop profile of the wing structure creates a cross-sectional geometry that is not fully symmetrical. In this structure, the moment applied vertically downwards not only causes deformation of the wing in the vertical direction, but also causes deformation in the horizontal axis. In Fig. 4, the deformation results on x-direction (horizontal axis) was given for pure bending. The highest x-deformations occurred in case-II-IV-I-V-III-VI-and-VII, respectively. Case I-IV-V nearly on the same path. The forward extrusion of the wing in the bending moment has caused the wing to move further backward. However, the wing extrusion resulted in a minimum x-deformation when it was at the same cross-sectional level, but inclined downward. As the backward arrow angle increased, x-deformation decreased.

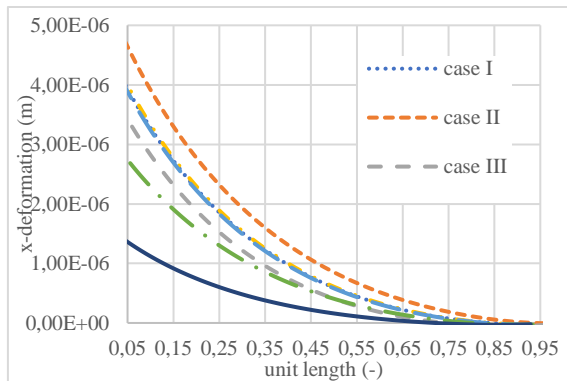


Figure 4. directional deformation at x-axis along the upper surface path of the wing.

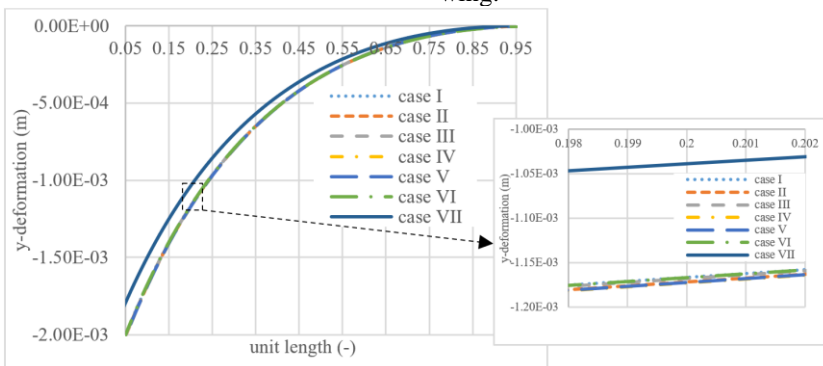


Figure 5. directional deformation at y-axis along the upper surface path of the wing.

CHAPTER 20: INVESTIGATION OF MECHANICAL PROPERTIES OF NACA 2024 DROP WING ACCORDING TO STATIC AND MODAL BEHAVIOUR OF DIFFERENT ROOT AND TIP VETER POSITIONS

Due to the direction of the moment, the deformation of the wing models is predominantly in the vertical direction. Figure 5 shows the deformation results in the y-direction. The largest deformation occurred in the order of case IV-V-II-III-I-VI-VII. The least deformation occurred in the upward curved airfoil (case VII), and the highest deformation occurred in case IV.

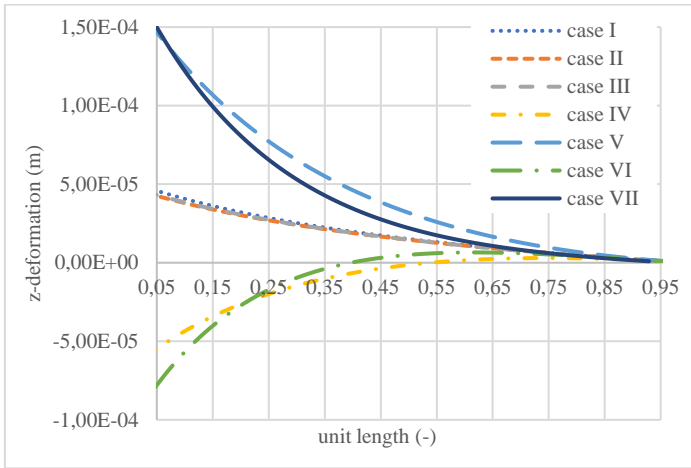


Figure 6. directional deformation at z-axis along the upper surface path of the wing.

Deformations in the z-direction are occurring in the direction of the wing length and the results are shown in Fig. 6. In case IV and case VI results, there was a pronounced deformation observed in the downward direction as the same trajectory direction of created wing. As a result, the z-direction deformation results of case IV and case VI occurred in a negative sign. The highest deformation results appear in case V and case VII. The results of case I, II, and III exhibit proximity to one another and have low deformation values.

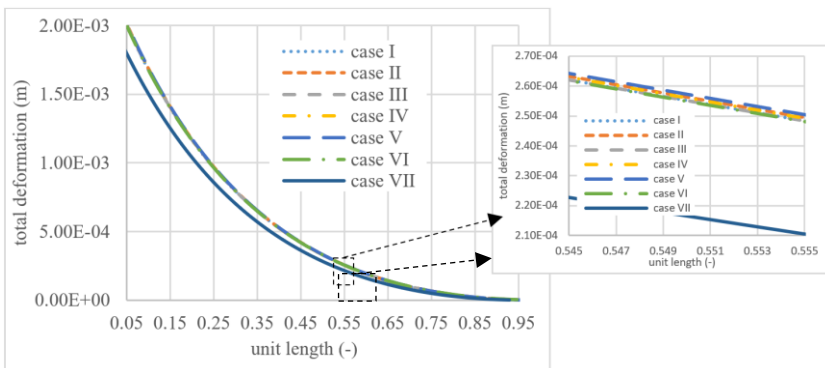


Figure 7. total deformation along the upper surface path of the wing.

The sum of the individual deformations in different directions is shown in Fig. 7. Deformations increased as expected from the wing root to the wing tip. The difference between the result values is less than 1%. Deformations are listed from largest to smallest, as cases V-IV-II-III-I-VI-VII. Minimum principal stress distribution is given in Fig. 8. Cases I-IV-VII have approximately the lowest principal stress values. The only uniform behavior in the distribution appears in the case-VII results. The non-symmetrical structure of the wing section causes the stresses to change suddenly.

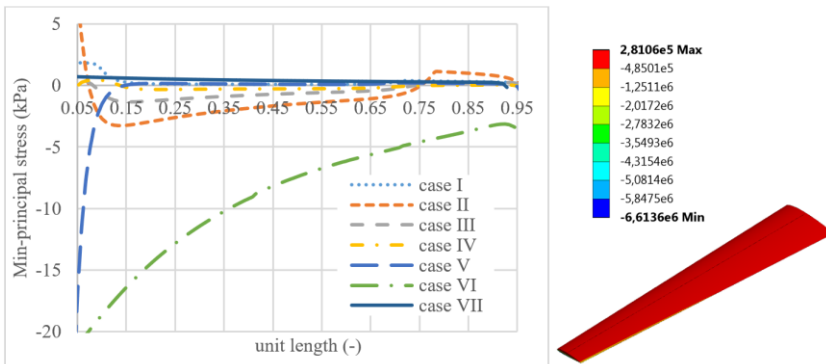


Figure 8. minimum principal stresses along the upper surface path of the wing.

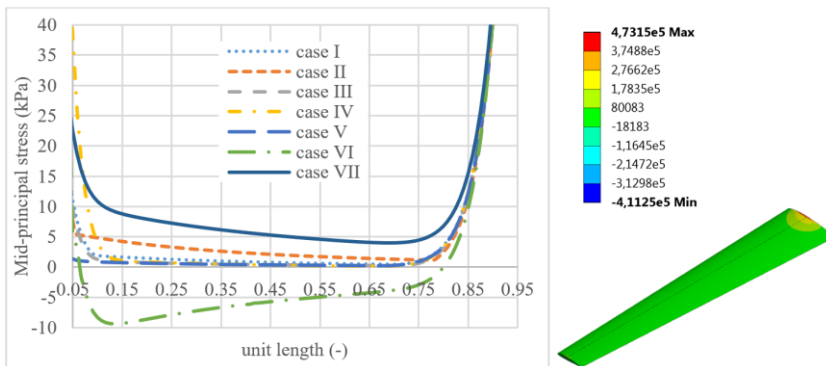


Figure 9. middle principal stresses along the upper surface path of the wing.

The middle principal stresses are shown in Fig. 9. The critical middle principal stresses occur at the fixed location edges of the wing. Upper edges have tension and below edges have compression stress form. The slope created by the curved structure caused lower middle principal stresses and the lowest average values occurred in case VI. In Fig. 10, maximum principal stresses were given. The maximum principal stress

CHAPTER 20: INVESTIGATION OF MECHANICAL PROPERTIES OF NACA 2024 DROP WING ACCORDING TO STATIC AND MODAL BEHAVIOUR OF DIFFERENT ROOT AND TIP VETER POSITIONS

occurred in the case of tensile stress on the upper surface of the wing tip edge, where the bending moment was applied. The highest value of maximum principal stress occurred at case VI result and the lowest value occurred at case III that has a difference about % 1.5. Von-Mises stresses were given in Fig. 11 that have the highest value in case VI and the lowest value in case IV. The moment applied edges and its top/bottom surfaces were the maximum Von-Mises stress locations.

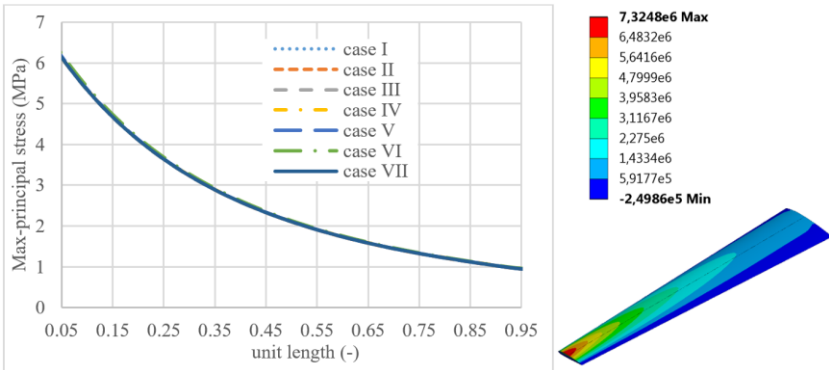


Figure 10. maximum principal stresses along the upper surface path of the wing.

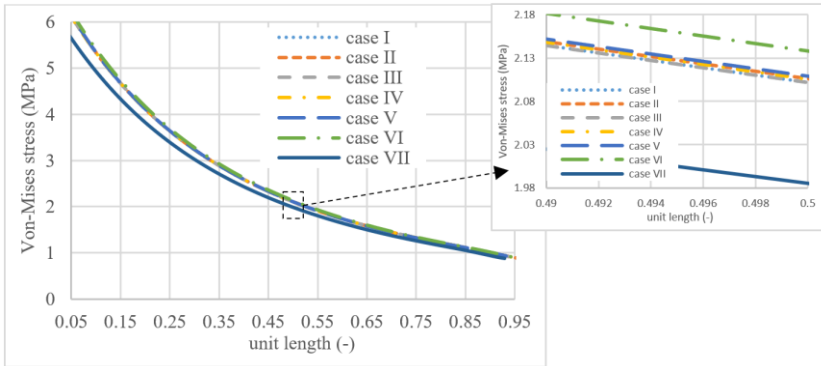


Figure 11. Von-Mises stresses along the upper surface path of the wing.

In Fig. 12, Von-Mises stress contours were given that were obtained fluid-solid interaction solutions. Nearly all the contour plots showed the location of maximum Von-Mises stresses occurred near the fixed location. The red plot location covered more wing surface region in case III and IV.

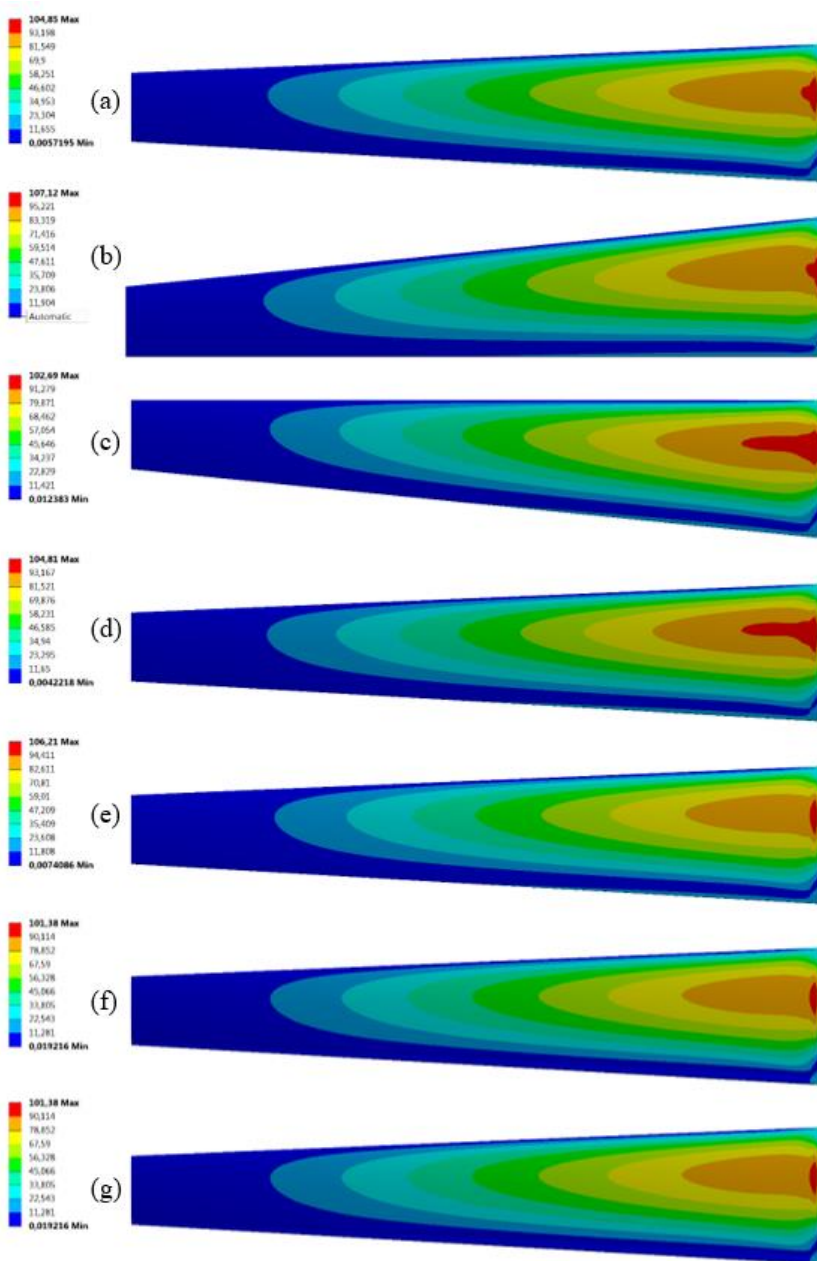


Figure 12. Von-Mises stresses occurring on the upper surface of the wing as a result of solid-fluid interaction; (a) centered; (b) straight; (c) forward-sweep; (d) centered-negative dihedral; (e) centered-positive dihedral; (f) centered-curved negative dihedral; (g) centered-positive curved dihedral.

CHAPTER 20: INVESTIGATION OF MECHANICAL PROPERTIES OF NACA 2024 DROP WING ACCORDING TO STATIC AND MODAL BEHAVIOUR OF DIFFERENT ROOT AND TIP VETER POSITIONS

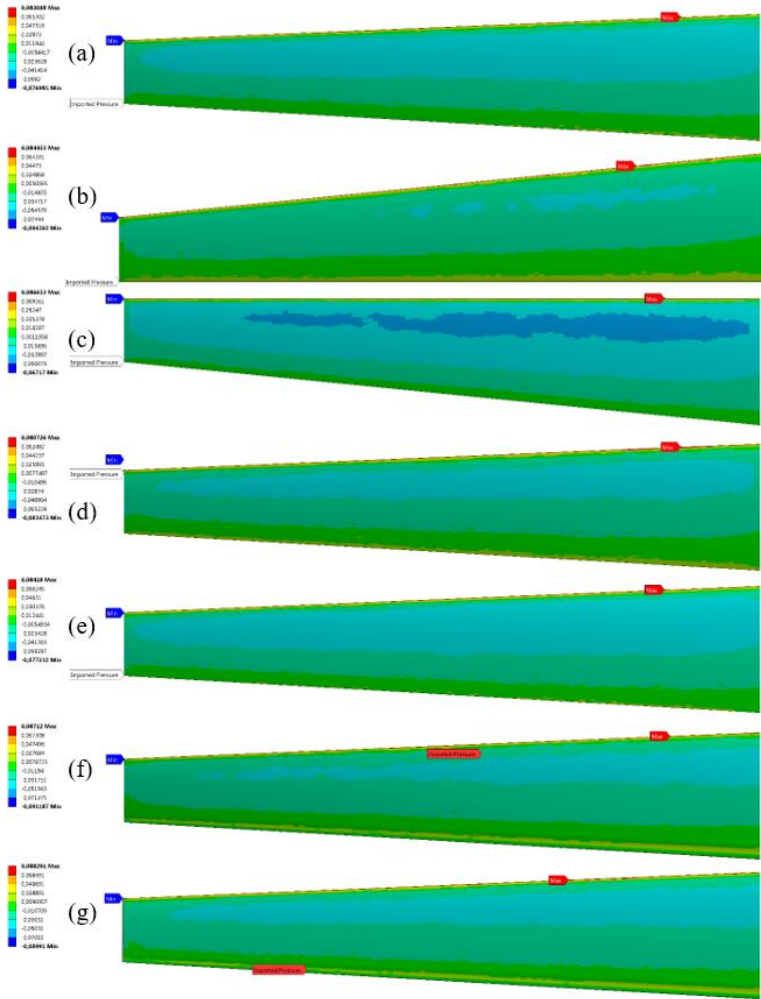


Figure 13. pressure contours due to fluid interaction on the wing surface, sorted from case I (top) to case VII (down); (a) centered; (b) straight; (c) forward-sweep; (d) centered-negative dihedral; (e) centered-positive dihedral; (f) centered-curved negative dihedral; (g) centered-positive curved dihedral.

The pressure contours of wings were given in Fig. 13. It was observed that the highest pressures occurred at the leading edge of the wings, and the lowest (negative) pressure occurred at the front corner of the wings. The regions exhibiting negative pressure on the wing, delineated by a light blue contour, are more pronounced in case-I and case-V compared to the other cases. In case-III, the wing surface exhibits the most significant negative pressure, which facilitates the generation of lift more effectively than in other cases.

Lift and drag coefficient results obtained under steady flow condition are shown in Fig. 14 for different cases. It was observed that the best performance was in the case-II model. Curved models have a higher drag coefficient than straight wings.

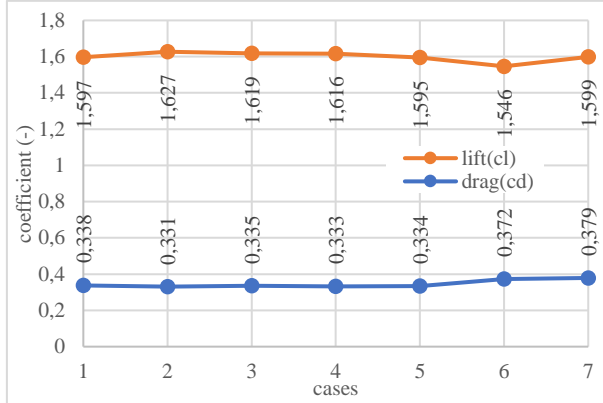


Figure 14. C_d and C_l coefficients of the wing under different cases

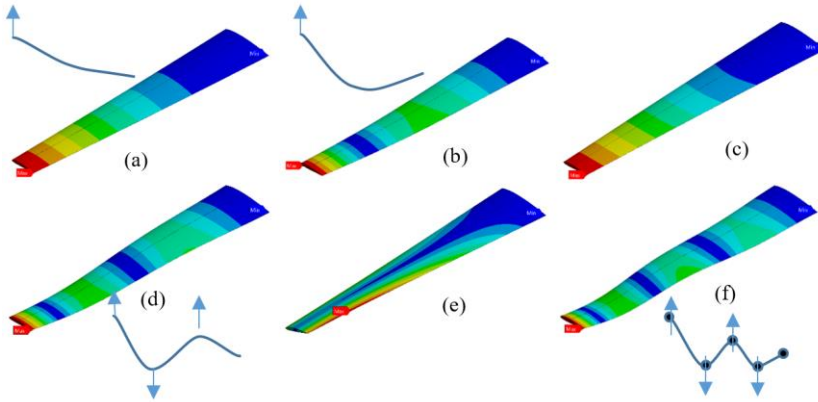


Figure 15. total deformation plots of modal analysis: (a) mod-I; (b) mod-II; (c) mod-III; (d) mod-IV; (e) mod-V; (f) mod-VI

Natural frequencies were calculated, and their behavior was illustrated in Fig. 15. The results were given for case I model. Mod I, II, III, IV, V and VI have natural frequencies 4.35, 18.3, 34.1, 45.4, 62.2 and 85.2 Hz, respectively. The dominant deformation formations can be categorized as; bending the tip up in mod-I, tip bending up and middle bending down in mod-II, the tip side bended in mod-III, tip bending up and two reverse middle bend in mod-IV, tip torsion CCW in mod-V, tip bending up and three middle bend in mod-VI.

4. CONCLUSION

The design of airfoils includes many parameters and a long-term study should be carried out to determine the most suitable values, geometry and material. Flight stability and lift/drag performance of the wing are investigated according to its usage area, and as a result, the effects of mechanical behavior are examined from the results obtained. This study includes front/back arrow angle, up or down straight/curved wing extrusions on a wing made from the same wing cross-section. During the examination of many parameters, experimental equipment or computer-aided flow and mechanical examination methods, which are an alternative examination method against time, were used and the wing results were compared among themselves.

- There are seven inspection models: centred, forward/backward, positive/negative straight-curved dihedral structures of the same wing cross-sections.
- Case VII has the lowest x and y deformations.
- The lowest deformation in the wing direction was obtained in cases I-II-III, which are straight wing profiles.
- While minimum principal stresses occurred at critical values on the lower surface of the wing at the corner where moment was applied to the wing, maximum principal stresses occurred at critical values on the upper surface at the wing tip.
- Middle principal stresses occurred in the wing connection region as tensile stress on the upper edge of the wing and compressive stress on the lower edge of the wing. The lowest values in Von-Mises stresses, where results were obtained from the top of the wing, occurred in case IV.
- In the flow results, the flow pressure effect on the formation of stresses is shown as the Von-Mises stresses on the wing. The lowest results appear in case VI and case VII. The area and values covered by the stress contours appear to be lowest in case VI and case VII. When examined as the negative/positive pressure effect created by the flow results on the wing, it is thought that the wing lift force will occur in the most appropriate case III. This model has a larger negative pressure area and value on the upper surface of the wing. The optimal lift/drag coefficient performance was obtained in case II.
- Due to the lack of wing cross-section and geometric differences, mode shapes and natural frequencies are almost the same in all wing results. In a solid model, the frequencies are lower than in models with spaces inside. Mod shapes are illustrated.

Acknowledgements

No Acknowledgements was declared by the authors.

Conflict of interest

No conflict of interest was declared by the authors.

Author contributions

All authors have contributed equally to the relevant work.

REFERENCES

- [1] Tanürün HE, Akın AG, Acır A. Numerical investigation of rib structure effects on performance of wind turbines. *Journal of Polytechnic*, early view, doi: 0.2339/politeknik.845804
- [2] Genç MS, Özışık G, Kahraman N, Düz flaplı naca0012 kanat profilinin aerodinamik performansının incelenmesi. *J. of Thermal Science and Technology* 2008; 28(1):1-8
- [3] Wang C, Khodaparast HH, Friswell MI. Investigating the benefits of morphing wing tip devices - a case study. *International Forum on Aeroelasticity and Structural Dynamics*, June 28-July 02, 2015, Saint Petersburg, Russia. 1-15.
- [4] Elelwi M, Kuitche MA, Botez RM, Dao TM. Comparison and analyses of a variable span-morphing of the tapered wing with a varying sweep angle, *The Aeronautical Journal* 2020; 124(1278): 1146-1169.
- [5] Ribeiro JHM, Yeh C, Zhang K, Taira K. Wing sweep effects on laminar separated flows. *J. Fluid Mech.* 2022; 950: 1-22. doi:10.1017/jfm.2022.612
- [6] Lin P, Wu J, Lu L, Xiong N, Liu D, Su J, Liu G, Tao Y, Wu J, Liu X. Investigation on the Reynolds number effect of a flying wing model with large sweep angle and small aspect ratio. *Aerospace* 2022; 9(523): 1-16.
- [7] Dimino I, Andreutti G, Moens F, Fonte F, Pecora R, Concilio A. integrated design of a morphing winglet for active load - control and alleviation of turboprop regional aircraft. *Appl. Sci.* 2021; 11(2439): 1-27.
- [8] Queirolo MAC. Impact of morphing winglets on aircraft performance. Master of Science in Aerospace Engineering at the Delft University of Technology, 2018.
- [9] Smith DD, Ajaj RM, Isikveren AT, Friswell MI. Multiobjective optimization for the multi-phase design of active polymorphing wings. *Journal of Aircraft* 2012; 49(4): 1153-1160.

CHAPTER 20: INVESTIGATION OF MECHANICAL PROPERTIES OF NACA 2024 DROP WING ACCORDING TO STATIC AND MODAL BEHAVIOUR OF DIFFERENT ROOT AND TIP VETER POSITIONS

- [10] Siouris S, Qin N. Study of the effects of wing sweep on the aerodynamic performance of a blended wing body aircraft. Proc. IMechE Part G: J. Aerospace Engineering 221; 2007: 47-55.
- [11] Brett J, Ooi A. Effect of sweep angle on the vortical flow over delta wings at an angle of attack of 100. Journal of Engineering Science and Technology 2014; 9(6): 768 – 781.
- [12] Lei S, Hua Y, Yang Z, Haoyu Z, Jun H. Dihedral influence on lateral-directional dynamic stability on large aspect ratio tailless flying wing aircraft. Chinese Journal of Aeronautics 2014; 27(5): 1149–1155.
- [13] Chang S. Xiao Y. Li G. Tian Z. Cui K. Numerical study on hypersonic aerodynamic characteristics of the high-pressure capturing wing configuration with wing dihedral. Aerospace Science and Technology 2023; 143: 1-15.
- [14] Erhan EE. Finite element analysis of a structure consisting of beam elements. Master's thesis, Istanbul University Institute of Science and Technology, Istanbul, 2011.
- [15] Günay D. Fundamentals of the finite element method for engineers. Sakarya University Press, Adapazarı, 1993.
- [16] Anderson JD. Fundamentals of aerodynamics. McGraw, New York, 2009



E-ISBN: 978-605-338-471-7

